International Journal of Fracture Fatigue & Wear

Volume 2, 2014

ISSN 2294-7868

Editor: Professor Magd Abdel Wahab

International Journal of Fracture Fatigue and Wear:

Conference Series proceedings

Volume 2, 2014

Proceedings of the 3rd International Conference on Fracture Fatigue and Wear, FFW 2014, Kitakyushu, Japan, 1-3 September 2014

Published by
Laboratory Soete – Ghent University
Technologiepark Zwijnaarde 903
B-9052 Zwijnaarde, Belgium
http://www.soetelaboratory.ugent.be/
Edited by: Professor Magd Abdel Wahab
ISSN: 2294-7868

3rd International Conference on Fracture Fatigue and Wear, FFW 2014, Kitakyushu, Japan, 1-3 September 2014

Chairman

Professor Magd ABDEL WAHAB
Laboratory Soete, Ghent University
Belgium

Co-chairman

Professor Nao-Aki NODA
Kyushu Institute of Technology
Japan

International Scientific Committee

J ABENOJAR, Universidad Carlos III de Madrid, Spain
K ANYFANTIS, Technical University of Denmark, Denmark
M CHEN, East China Jiaotong University, China
JT CHEN, National Taiwan Ocean University, Taiwan
R DAS, University of Auckland, New Zealand
P DE BAETS, Ghent University, Belgium
JC DEL REAL, Comillas Pontifical University, Spain
M DUAN, China University of Petroleum, China
G DE ROECK, KULeuven, Belgium
W FENG, Shandong University, China
E FERRIER, Université Lyon 1, France
I HILMY, International Islamic University, Malaysia
R HOJJATI, Ghent University, Belgium
K KOSA, Kyutech, Japan
A LI, University of Reims, France
K MATSUDA, Kyutech, Japan
T MIYAZAKI, University of Ryukyu, Japan
K ODA, Oita University, Japan
T QIN, China Agricultural University, China
F REZAI-ARIA, Ecole des Mines d'Albi, France
A RUDAWSKA, Lublin University of Technology, Poland
RV PRAKASH, Indian Institute of Technology, India
Y SANO, Kyutech, Japan
D SCHIPPER, University of Twente, The Netherlands
P SMITH, University of Surrey, UK
LV VANEGAS USECHE, Universidad Tecnológica de Pereira, Colombia
W WANG, Shandong University, China
K WATANABE, Yamagata University, Japan

Editorial

The second volume of the International Journal of Fracture Fatigue and Wear contains the proceedings of the third International Conference of Fracture Fatigue and Wear (FFW) held in Kitakyushu, Japan during the period 1-3 September 2014. The participants of FFW 2014 conference are from 16 different countries including Albania, Algeria, Belgium, Canada, China, France, Germany, Italy, India, Japan, Malaysia, Netherlands, Singapore, Spain, Poland and UK. They presented their research work in several topics related to Fracture Fatigue and Wear.

The organising committee is grateful to Professor Yukitaka Murakami from Kyushu University, Japan for agreeing to deliver the keynote lecture, entitled 'Mechanism of Failure in Fatigue and Tribology from Viewpoint of Small Defects and Small Cracks', at the opening of the conference.

The sponsorship of several Japanese companies, including Fujico Co., Shinko Metal Products Co., Yaskawa Electric Corporation, Japan Casting & Forging Corp., Takagi Co., NS Plant Designing Corporation, Nippon Steel & Sumikin Engineering Co., Toyota Motor Kyushu, Nippon Steel & Sumitomo Metal Corporation, Hamada Heavy Industries, WestJapan Industry and Trade Convention Association, Yoshikawa Kogyo Co. and Kitakyushu city, is highly appreciated.

Most of the papers published in this volume have been sent to reviewers, who are members of Scientific Committee of FFW 2014, to judge their scientific merits. Based on the recommendation of reviewers, the papers were accepted for publication in the conference proceedings and for presentation at the conference venue. The organizing committee would like to thank all members of Scientific Committee for their valuable contribution in evaluating the papers.

The efforts of the local organizers of FFW 2014 at Kyushu Institute of Technology (Kyutech), Japan, Professor Nao-Aki Noda and his team, are highly acknowledged. Special thanks goes to Dr Yasushi Takase for looking after the social events including conference reception, conference dinner, night cruising and barbecue.

Finally, the editor would like to thank to all authors, who have contributed to this volume and presented their research work at FFW 2014.

The Editor
Professor Magd Abdel Wahab

Table of Contents

Damage mechanics based prediction of ductile steel failure under ULCF-conditions
B. Eichler, S. Schaffrath and M. Feldmann
RWTH Aachen University, Institute of Steel Construction, Germany 1-7

Applied studies of fracture mechanics in geological disasters mitigation
Chen Hong-Kai Zhu Xiu-Zhu and Tang Hong-Mei
Institute of Geotechnical Engineering, Chongqing Jiaotong University, China 8-17

SEM in-situ investigation on micro cracking behaviour and threshold failure parameter of pop structure
X.S. Wang, D.Y. Ge, P. Pan and S. Jia
Department of Engineering Mechanics, School of Aerospace, Tsinghua University, Beijing, China 18-24

Strength of adhesive joints of epoxy composites with dissimilar adherends
A. Rudawska
Lublin University of Technology, Lublin, Poland 25-31

Local perturbations in higly prestressed materials
D. Bigoni
University of Trento, Trento, Italy 32-33

Effect of atmospheric plasma torch on ballistic woven aramide
M.A. Martínez and J. Abenojar
Universidad Carlos III de Madrid, Leganés, IAAB, Spain 34-39

Rigid inclusions: stress singularity, inclusion neutrality and shear bands
Francesco Dal Corso[1], Davide Bigoni[1], Giovanni Noselli[2], Diego Misseroni[1] and Summer Shahzad[1]
[1]University of Trento, Trento, Italy
[2]SISSA, Trieste, Italy 40-42

Experimental and Analytical study of bandage strengthening of reinforced concrete short Corbels by bonding carbon fibres fabrics
Jules Assih, Ivelina Ivanova, Alex Li and Yves Delmas
GRESPI/Laboratoire de Génie Civil UFR Sciences, Université de Reims, France 43-49

Analysis on intensity of singular stress for bonded pipe in comparison with bonded plate
Zefeng Wang[1], Nao-Aki Noda[1], Tatsujiro Miyazaki[2], Takumi Uchikoba[1], Guohui Wang[2] and Yoshikazu Sano[1]
[1]Department of Mechanical Engineering, Kyushu Institute of Technology, Japan
[2]Department of Mechanical Engineering Systems, University of the Ryukyus, Japan 50-56

Analysis of intensity of singular stress field for single lap joint under tensile shear load based on crack tip stress method
Tatsujiro Miyazaki[1], Nao-Aki Noda[2], Rong Li[3], Takumi Uchikoba[3] and Yoshikazu Sano[2]
[1]University of the Ryukyus, Okinawa, Japan
[2]Kyushu Institute of Technology, Fukuoka, Japan
[3]Graduate School of Engineering, Kyushu Institute of Technology, Fukuoka, Japan 57-62

Stress intensity factors for small edge interface crack in bonded dissimilar plates under thermal stress
K. Oda[1], T. Shinmoto[2] and N. Tsutsumi[1]
[1]Department of Mechanical and Energy Systems Engineering, Oita University, Oita, Japan
[2]Graduate school of Oita University, Oita, Japan 63-69

A virtual joint element method for numerical simulation of quasi-brittle material failure process
Chunhui Xu and Mingrui Li
College of Science, China Agricultural University, Beijing, China 70-74

Observing the frequency analysis of acoustic emission pattern during tensile test of SAE 1045 steel
M.Mohammad[1], S.Abdullah[2], J.Ganesh[1], N.Jamaludin[2] and O.Innayatullah[3]
[1]Department of Mechanical Engineering, Faculty of Engineering, Universiti Selangor, Malaysia
[2]Department of Mechanical and Materials Engineering, Faculty of Engineering and Built Environment, Universiti Kebangsaan Malaysia , Selangor, Malaysia
[3]Department of Mechanical and Manufacturing Engineering, Faculty of Engineering, Universiti Putra Malaysia, Serdang, Malaysia 75-79

Thermoelectromechanical response of a functionally graded piezoelectric material strip with two parallel cracks in arbitrary positions
S. Ueda and T. Kishimoto
Department of Mechanical Engineering, Osaka Institute of Technology, Osaka, Japan 80-86

Application of singular integral equations to transient elastodynamic crack for piezoelectric solids
P. Zhao[2], T.Y. Qin[1], L.N. Zhang[1] and X.B. Feng[1]
[1]College of Science, China Agricultural University, China
[2]College of Engineering, China Agricultural University, China 87-93

One-dimensional generalized thermoelastic analysis of an electrical conductive thin film subjected to a magnetic field
F. Ashida[1], T. Morimoto[1] and Y. Suzuki[2]
[1] Shimane University, Matsue, Japan
[2] Mitsubishi Motors Cooperation, Tokyo, Japan 94-100

The spread of yield zone at a notch root and its notch size dependence
H. Matsuno
Sojo University, Kumamoto, Japan 101-107

Making smart phone applications in order to have experience of mechanics of materials
T. Tsuji
Chuo University, Tokyo, Japan 108-113

A finite element sub-partition method for simulating crack propagation
C. W. Zhou and Y. L. Sun
State Key Laboratory of Mechanics and Control of Mechanical Structures, Nanjing University of Aeronautics and Astronautics, Nanjing, China 114-120

Stress Intensity Factor during the Propagation of a Crack in a Brittle Material
H. Hamli Benzahar and M. Chabaat
BuiltEnv. Res. Lab., Civil Engineering Faculty, U.S.T.H.B., B P. 32.ElAlia, BabEzzouar, Algiers 16111, Algeria 121-126

Vibration analysis of cracked plate using higher-order shear deformation theory
Loc V. Tran[1], P. Phung-Van[3], Vinh Phu Nguyen[2], M. Abdel Wahab[3] and H. Nguyen-Xuan[1]
[1]Division of Computational Mechanics, Ton Duc Thang University Ho Chi Minh City, Vietnam
[2]Cardiff University, Queen's Buildings, The Parade, Cardiff, UK
[3]Department of Mechanical Construction and Production, Faculty of Engineering and Architecture, Ghent University, Belgium 127-133

Buckling analysis of piezoelectric composite plates using NURBS- based isogeometric finite elements and higher-order shear deformation theory
P. Phung-Van[1,2], M. Abdel-Wahab [2], Loc V. Tran[1] and H. Nguyen-Xuan[3]
[1]Division of Computational Mechanics, Ton Duc Thang University, Vietnam
[2]Department of Mechanical Construction and Production, Faculty of Engineering and Architecture, Ghent University, Belgium
[3]Department of Mechanics, University of Science, VNU - HCMC, Vietnam 134-140

Multi-phase random medium based failure simulation of concrete
Liang Shixue[1,2], Ren Xiaodan[1] and Li Jie[1,3]
[1] School of Civil Engineering, Tongji University, Shanghai, China
[2] Department of Civil and Environmental Engineering, UCLA, Los Angles, CA, USA
[3] The State Key Laboratory on Disaster Reduction in Civil Engineering, Tongji University, Shanghai, China 141-147

Buckling of functionally graded carbon nanotube-fiber reinforced plates under mechanical loads
B. Sobhani Aragh and M. Abdel wahab
Department of Mechanical Construction and Production, Faculty of Engineering and Architecture, Ghent University, Belgium 148-154

Analyzing stress intensity factor and t-stress by stress difference method (SDM) in arc of gas pipeline
Alfred Hasanaj, Alvin Asimi and Mentor Balilaj
Polytechnic University of Tirana, Albania 155-160

Fatigue and fracture in railroad key products
H. Sakamoto
Kochi University of Technology, Japan 161-168

Stress analysis of steam generator tubesheet and main factors affecting fatigue and fracture damage
Qian Hao, Liu Chang, Liang Xingyun, Deng Jingjing, Xie Yongcheng and Lin Shaoxuan
Department of Component Research and Design, Shanghai Nuclear Engineering Research and Design Institute, Shanghai, China 169-174

Numerical investigation of fatigue performance of butt welded joint with undercut
Ezzarhan Abdullah[1,2] and Koji Gotoh[3]
[1]Dept. of Civil and Structural Engineering, Kyushu University, Japan
[2]Dept. of Occupational Safety and Health, Malaysia
[3]Dept. of Marine Systems Engineering, Kyushu University, Japan 175-181

Evaluation of small-crack growth rate in ultrafine grained copper
M. Goto[1], N. Teshima[2], S.Z. Han[3], J.H. Ahn[3], J. Kitamura[1] and S. Kim[4]
[1]Oita University, Department of Mechanical Engineering, Oita, Japan
[2]Oita National College of Technology, Oita, Japan
[3]Korea Institute of Materials Science, Changwon, Republic of Korea
[4]Gyeongsang National University, Chinju, Republic of Korea 182-188

Generation of simulated acceleration and strain signals as the responses of a car coil spring
S. Abdullah[1], T.E. Putra[1], D. Schramm[2], M.Z. Nuawi[1] and T. Bruckmann[2]
[1]Department of Mechanical and Materials Engineering, Universiti Kebangsaan Malaysia, Malaysia
[2]Departmental Chair of Mechatronics, Universität Duisburg-Essen, Germany 189-194

Experimental investigation on the suitable pitch difference improving the fatigue strength significantly for high strength bolts and nuts
X. Chen, N.-A. Noda, H. Maruyama, H. Wang, Y. Sano and Y. Takase
Kyushu Institute of Technology, Kitakyushu, Japan 195-200

Rolling contact fatigue simulation used for full-open type greenhouse
Luyu Wang, Nao-Aki Noda, Qifeng Luo, Hiroyuki Nagatomo, Yoshikazu Sano and Yasushi Takase
Kyushu Institute of Technology, Kitakyushu, Japan 201-206

Fatigue life prediction of composite risers due to vortex-induced vibration (VIV)
X.S. Sun, V.B.C. Tan, L.B. Tan, Y. Chen, R.K. Jaiman and T.E. Tay
Department of Mechanical Engineering, National University of Singapore, Singapore 207-213

Crack nucleation at incubation and early stages of water droplet erosion in TI-6AL-4V
P. Bocher[1], N. Kamkar[1], F. Bridier[1] and P. Jedrzejowski[2]
[1]Mechanical Engineering Department, École de technologie supérieure, University of Quebec, Montreal, Quebec, Canada
[2]Rolls-Royce Canada Ltd. 9545 Cote-De-Liesse, Dorval, Quebec, Canada 214-219

A Unified Fatigue Theory Based on Characteristic Length
S.Q HOU[1,2] and J.Q XU[1]
[1]Shanghai Jiaotong University, Shanghai, China
[2]Shandong Jiaotong University, Jinan, China 220-224

Study of indentation fatigue behaviour of steel weldment through cyclic ball indentation
S Arunkumar and Raghu V. Prakash
Machine Design Section, Department of Mechanical Engineering, Indian Institute of Technology Madras, Chennai, India 225-231

A combined critical distance - stress gradient approach to predict the fretting fatigue crack nucleation risk: application to fem analysis
S. Fouvry, C. Gandiolle and B. Berthel
Ecole Centrale de Lyon, LTDS, France 232-238

Investigation of residual stress effect on fatigue crack initiation for 2024 T351 al-alloy
M. Benachour[1], N. Benachour[1] and M. Benguediab[2]
[1]Tlemcen University, Laboratory of Mechanical Systems and Materials "IS2M", Faculty of Technology, Mechanical Engineering, Tlemcen, Algeria
[2]Sidi Bel Abbes University, Laboratory of Materials and Reactive Systems "LMSR", Mechanical Engineering Department, Sidi Bel Abbes, Algeria 239-245

On the need of the wavelet analysis for fatigue condition monitoring
N. Ismail[1], M.F.M. Yusof[1], C.K.E. Nizwan[1] and S. Abdullah[2]
[1]Faculty of Mechanical Engineering, Universiti Malaysia Pahang, 26600 Pekan, Pahang, Malaysia
[2]Department of Mechanical and Materials Engineering, Faculty of Engineering and Built Environment, Universiti Kebangsaan Malaysia, 43600 Bangi, Selangor, Malaysia 246-249

Fracto-metallographic analysis of fatigue cracking in cold drawn pearlitic steel
J. Toribio[1], B. González[1] and J.C. Matos[2]
[1]Department of Materials Engineering, University of Salamanca, E.P.S. Zamora, Spain
[2]Department of Computing Engineering, University of Salamanca, E.P.S. Zamora, Spain 250-256

Crack shape evolution in plates subjected to cyclic loading
J. Toribio[1], J.C. Matos[2], B. González[1] and J. Escuadra[2]
[1]Department of Materials Engineering, University of Salamanca, E.P.S. Zamora, Spain
[2]Department of Computing Engineering, University of Salamanca, E.P.S. Zamora, Spain 257-262

Influence of fatigue loading on the residual stress induced by cold drawing in prestressing steels
J. Toribio[1], M. Lorenzo[2], D. Vergara[1] and L. Aguado[1]
[1]University of Salamanca, Campus Viriato, Zamora, Spain
[2]University of Salamanca, E.T.S.I.I., Béjar, Spain 263-268

On fretting fatigue behaviour of single bolted lap joint
R. Hojjati-Talmei[1,2], M.A. Wahab[1], T. Yue[1] and L. D'Alvise[2]
[1]Department of Mechanical Construction and Production, Faculty of Engineering and Architecture, Ghent University, Belgium
[2]Geonx Inc., Gosselies, Belgium 269-274

Wear of electrically conductive surfaces
Jian Song, Eugen Silbernagel, Liangliang Wang
Precision Engineering Laboratory, Ostwestfalen-Lippe University of Applied Sciences, Lemgo, Germany 275-280

Friction wear behaviour of carbon based epoxy nanocomposites
J. Abenojar[1], J. Tutor[2], Y. Ballesteros[2], J.C. del Real[2], M.A. Martínez[1]
[1]Universidad Carlos III de Madrid, Leganés, Spain
[2]Universidad Pontificia Comillas, Madrid, Spain 281-287

Study on the sliding wear mechanism of the white metal
K. Masuda[1], S. Ishihara[2], T. Kobata[1] and M. OKane[2]
[1]University of Toyama, Toyama, Japan
[2]Toyama National College of Technology, Toyama, Japan 288-294

Multigrid solution of the 3d elastic subsurface stress field for heterogeneous materials in contact mechanics
H. Boffy and C.H. Venner
University of Twente, Faculty of Engineering Technology (CTW), Department of Engineering Fluid Dynamics, The Netherlands 295-300

Friction and wear behaviour of carburized stainless steel under fretting-reciprocating slidings
L. Haviez[1,2], S. Fouvry[1], R. Toscano[1], G. Yantio[2] and G. Moreau[2]
[1]LTDS - Ecole Centrale de Lyon, Lyon, France
[2]Sagem Défense Sécurité, Paris, France 301-307

Mechanical behavior of dlc coatings under various scratch conditions
G. Pagnoux[1,2,3], S. Fouvry[1], M. Peigney[2], B. Delattre[3], G. Mermaz-Rollet[3]
[1]LTDS, Ecole Centrale de Lyon, Ecully Cedex, France
[2]Laboratoire Navier, Université Paris-Est (Ecole des Ponts ParisTech, IFSTTAR, CNRS), Marne-la-Vallée Cedex 2, France
[3]PSA Peugeot Citroën, Route de Gisy, Vélizy, France 308-313

Wear behaviours of iron composite reinforced with 20wt% silica
Adibah Amir[1] and Othman Mamat[2]
[1]Department of Manufacturing & Materials Engineering, International Islamic University Malaysia, Kuala Lumpur, Malaysia
[2]Department of Mechanical Engineering, Universiti Teknologi Petronas, Tronoh Perak, Malaysia 314-319

Finite element analysis of hydrogen-assisted rolling-contact fatigue in bearings for wind turbines
J. Toribio, V. Kharin, M. Lorenzo and D. Vergara
Fracture of Materials and Structural Integrity Research Group, University of Salamanca, Spain 320-325

FEA of stress singularity in partial slip and gross sliding condition
T. Yue, M. Abdel Wahab and R. Hojjati-Talemi
Department of Mechanical Construction and Production, Faculty of Engineering and Architecture, Ghent University, Belgium 326-332

Experimental study on threshold behavior of intergranular stress corrosion cracking of 316l stainless steel by using fretting fatigue
Tomoya Kishino[1], Yuichi Otsuka[2], Yukio Miyashita[2] and Yoshiharu Mutoh[2]
[1]Graduate School of Engineering, Nagaoka University of Technology, Japan
[2]Nagaoka University of Technology, Japan 333-339

Comparative study on tribological performance of orthopedic plaster reinforced resin
R.M. Nasir [1,2] and M.S.A.M. Sabir[1]
[1]School of Mechanical and Aerospace Engineering, Engineering Campus, Universiti Sains Malaysia(USM), 14300, Nibong Tebal, Seberang Perai Selatan, Pulau Pinang, Malaysia
[2]Cluster of Polymer Composite (CPC), Science and Engineering Research Centre (SERC), Engineering Campus, Universiti Sains Malaysia, Nibong Tebal, 14300, Malaysia 340-346

Proceedings of the 3rd International Conference on
Fracture Fatigue and Wear, pp. 1-7, 2014

DAMAGE MECHANICS BASED PREDICTION OF DUCTILE STEEL FAILURE UNDER ULCF-CONDITIONS

B. Eichler, S. Schaffrath and M. Feldmann

RWTH Aachen University, Institute of Steel Construction, Germany

Abstract: Damage mechanics based concepts are capable of characterizing ductile failure processes in steel material. This even holds true for metallic structures subjected to time-varying loading amplitudes that may result in large alternating strains as in the case of seismic events. In this paper the application of a modified "Effective Damage Concept" (EDC) combined with "Damage Curves" is demonstrated for ULCF-demands by the example of welded beam-column-connections that represent a typical detail of moment-resisting-frames (MRF). As such micromechanical-based approaches require complex and time-consuming Finite Element Analysis (FEA) a more engineering-friendly methodology is proposed using a macro-model where local strain demands are expressed in terms of global rotational capacity by the same Wöhler-lines (S/N-approach) usually given in recommendations for fatigue design of steel structures.

Keywords: damage mechanics; damage curve; ULCF; effective damage concept; S/N-approach

1 INTRODUCTION

Damage caused by load cycles with large plastic amplitudes is frequently reported in civil and mechanical engineering. A typical failure mechanism is the fracture due to ultra-low-cycle-fatigue in case of seismic events. As reported from the devastating earthquakes in Northridge (USA) and Kobe (Japan) steel structures often failed due to insufficient deformation capacity, inappropriate welding work and poor material properties, where ductile fracture was a trigger for subsequent brittle failure [1,2]. As a consequence lots of research was carried out on moment resisting frames (MRF), where the American efforts aimed on the quality of welds and on advanced connection details in order to reduce notch effects. The Japanese focused on welding heat input and material toughness instead. In this context, a European project [3] was initiated several years ago where the key to a safe application of plastic design is the toughness quality of structural steel that controls the resistance of the material against crack initiation.

To ensure a sufficient ductile behaviour, one of the concepts in [3] is based on damage mechanics where toughness demands in the upper-shelf of the transition curve could be related to the first ductile crack initiation in a metallic structure. The major advantages of strain-based damage mechanics theories are:

- Physically based and related to the micromechanical processes in the material matrix; for ductile failure mechanisms the formation of micro voids, coalescence and crack initiation could be described.
- No need to assume crack-like flaws as required for fracture mechanical based concepts.
- The applicability of extended damage approaches to cyclically loaded structures.
- Material parameters to be determined on small-scale tests are size-independent and consider constraint effects and are therefore transferable to structural components and elements.
- The availability of phenomenological based models suitable for complex Finite-Element-Analysis (FEA); despite model parameters are not directly related to the microstructural features of the material.

In this paper, the "Effective Damage Concept" according to *Ohata and Toyoda* [4] in combination with a "Two-Parameter-Criterion" according to Johnson/Cook [5] – here referred to as "damage curve" – was successfully validated for beam-column-connections subjected to cyclic loading with constant and variable amplitudes of large strains. The fundamental procedure was given in [3] and already published in [6]. A re-evaluation of the experimental data and new simulations were carried out within the scope of [7] and are now presented here. Shortcomings of the Effective Damage Concept in case of constant amplitude loading have been conquered and a modified strain accumulation procedure considering the back stress evolution

of the utilized plasticity model is verified. The paper concludes with the development of an engineering-friendly macro-model that is inspired by the S/N-approach for high cycle fatigue applications using Wöhler-curves and that allows a damage assessment for ULCF-straining in terms of a global rotational capacity demand. Such rotational Wöhler-curves not only depend on the structural geometry and the welding details but especially are controlled by the upper-shelf toughness properties of the material as those curves have been derived for the failure criterion crack initiation.

2 TESTS ON BEAM-COLUMN-CONNECTIONS WITH HEA300-PROFILES

2.1 Test setup

Within the framework of [3] eight cyclic tests on welded beam-column-connections (beams: HEA300, columns: HEM300) made of unalloyed structural steel S355 (acc. to EN 10025-2) have been performed. The principle of the rotation tests is a 3-point-bending test with the loading on the column, Fig. 1. Due to the load protocols (see section 2.2) both positive and negative vertical displacements develop at the simply supported beam ends requiring a complex construction using a cross beam that is anchored to the strong floor. Following the “Strong-Column-Weak-Beam-Concept” the welded joint was designed in that way that no plastic deformation or any instability could develop in the columns. Two different types of welds have been examined: a simple field welding with fillet welds (non-sophisticated detail) and a notch-free execution with butt welds where the root was sealed by an additional fillet weld (sophisticated detail). All welds have been examined by means of non-destructive testing (NDT) methods.

Each test specimen was equipped with twelve strain gauges (three at each weld of the tension and compression flanges) in order to measure the local strains 20 mm from the welding. Four wire sensors were applied (two below the column and one in the middle of each beam) to measure the vertical displacements. The relative rotations were recorded by three inclinometers (one at each support and one placed in the column). For the measurement of the reaction forces a load cell was integrated in the hydraulic jack.

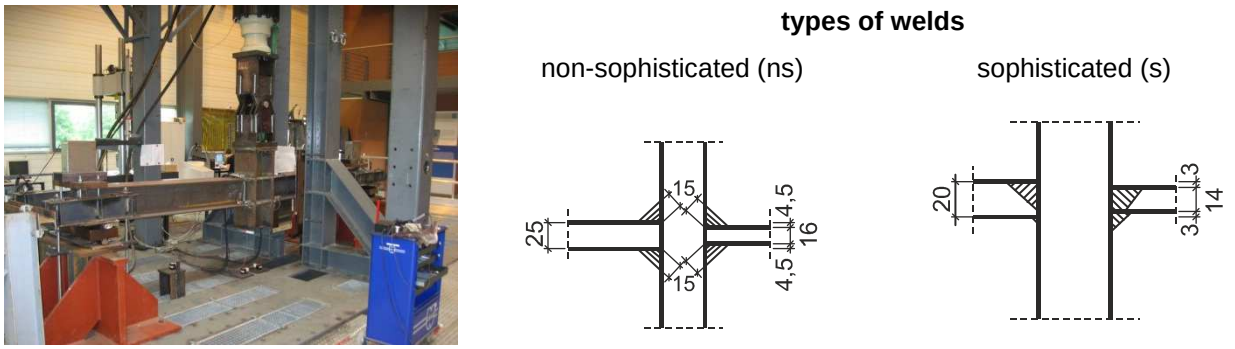

Fig. 1 Rotational test on beam-column-connections with HEA300-beam and two different types of welds

2.2 Load protocols

The tests were performed deformation controlled (6 mm/m) and stepwise under variable and constant amplitude loading conditions. For each type of welding (ns, s), one test with a deformation history according to the ECCS-procedure [8], one test with constant amplitude loading and two tests with analytical derived load protocols from real seismic events (referred to here as “Kobe” and “95 %-fractile”), were carried out.

In the next section, the applied deformation history of test no. 3 is presented. It should be noted that the vertical displacement was taken from the measurements of the wire sensors attached to the column.

2.3 Global deformation and crack initiation behaviour

In all tests, an expressive ductile behaviour could be observed, where the formation of buckles is strongly dependent on the magnitude of the amplitude of the vertical displacements. Therefore, the rotation range of the column could be considered as a measure for the pronouncement of the plastic deformation.

Two types of ductile cracks occurred at the test specimens subjected to cyclic loading:

- Type I: The crack initiates at the toe of the fillet weld between the flanges of the beam and column. For the (ns)-welding detail (fillet welds) the cracks initiated either at the outer or the inner weld toe. The (s)-detail (butt weld + root weld) showed crack initiation only at the root fillet weld at the inside.
- Type II: In the zones of excessive plastic deformation at the plastic hinge location cracks also initiate after a certain number of high amplitude cycles (typically in the vertex of the buckle).

The number of cycles to crack initiation (Type I) could be taken from Fig. 8 in section 4. For the further investigation, only the number of cycles $N_{f,pl}$ above the joint's yield displacement are taken into account as those are the ones that contribute to the biggest extent to the low-cycle fatigue of the welded joints. Fig**. 2** shows the amplitude loading for test no. 3 ("Kobe"-protocol, ns-weld) and the load vs. displacement hysteresis exemplary. The first ductile crack was detected within the 4th package of cycles ($N_{f,pl}$ =12) at a displacement of ±3,2 mm (tensile excursion). Buckling modes of the beam flanges even were observed in the 1st package of cycles followed by visible cracks in the vertex of the buckle after nine packages of cycles. With ongoing deformation history the cracks propagated stable and no brittle fracture was observed.

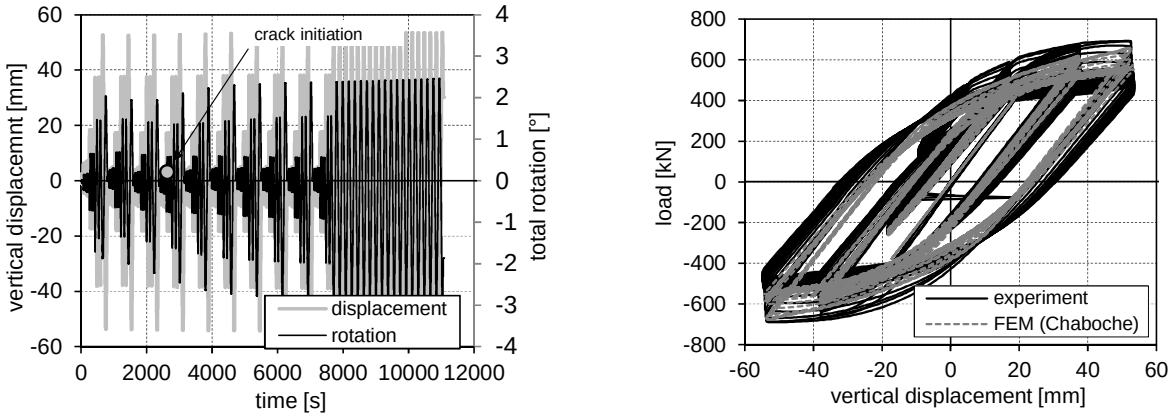

Fig. 2 Experimental results for test no. 3 (RT_HEA_355_ns-4)

3 PREDICTION QUALITY OF THE EFFECTIVE DAMAGE CONCEPT

3.1 Plasticity model

In the numerical simulations (section 3.3), the *Chaboche*-model [9] is used that is an extension of the plasticity model proposed by *Armstrong-Frederick* [10]. This model is based on the *von Mises* yield hypothesis (J2-plasticity) and a combined isotropic and kinematic hardening approach. The *Chaboche*-parameters of material S355J2 were evaluated from cyclic tests with small scale specimens, Table 2.

Table 1 Loading histories

No. 1 + No. 5 (RT_HEA_355_s-2 + RT_HEA_355_ns-2)							
ECCS	number of cycles N [-]	1	1	1	1	3	3+n
	vertical displacement Δ [mm]	±6,5	±13	±19,5	±26	±52	±104
No. 2 + No. 6 (RT_HEA_355_s-3 + RT_HEA_355_ns-3)							
95 %-fractile	number of cycles N [-]	6	5	4	3	2	1
	vertical displacement Δ [mm]	±2,3	±3,8	±5,9	±11,5	±22,6	±43,6
No. 3 + No. 7 (RT_HEA_355_s-4 + RT_HEA_355_ns-4)							
Kobe	number of cycles N [-]	6	5	4	3	2	1
	vertical displacement Δ [mm]	±3,2	±7,7	±8,6	±22	±44	±60
No. 4 + No. 8 (RT_HEA_355_s-5 + RT_HEA_355_ns-5)							
constant amplitude	number of cycles N [-]	x					
	vertical displacement Δ [mm]	±70					

Information: Each line in Table 1 (except "ECCS") represents a package of cycles. The total deformation history was applied several times to each joint until crack initiation occurred.

Table 2 Isotropic and kinematic hardening Chaboche-parameters for S355J2

beam material	$\sigma\|_0$ [MPa]	**C** [MPa]	γ [-]	Q_∞ [MPa]	**b** [-]
S355J2	325	48000	240	10	1,5

3.2 Effective Damage Concept

The micromechanical assumption of the "Effective Damage Concept" proposed by *Ohata and Toyoda* [4] is that ductile crack initiation is the result of the nucleation of micro voids in the soft ferrite phase near the ferrite-perlite-interphase in a structural steel matrix. The engineering approach behind this model uses damage curves as an empirical failure criterion where crack initiation due to monotonic loading is expressed by a plastic equivalent strain limit that depends on the triaxiality parameter η. This triaxiality designates the negative ratio between hydrostatic stress σ_m and the von Mises stress σ_{eq} and quantifies the efficiency of σ_m that is responsible for the enlargement of micro voids. In terms of "constraint" increasing stress triaxiality is synonymous with a decreasing feasibility of plastic deformation demands.
The damage curve shown in Fig. 3 was evaluated from monotonic notched coupon tests with various radii that have been extracted from the beam material where crack initiation was monitored microscopically and by means of electric potential measurements. In addition accompanying numerical simulations were necessary in order to determine the corresponding plastic strain states.

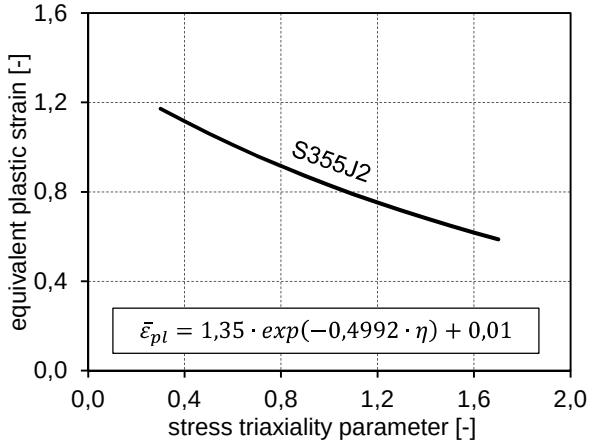

Fig. 3 Damage curve for S355J2 (beam material HEA300)

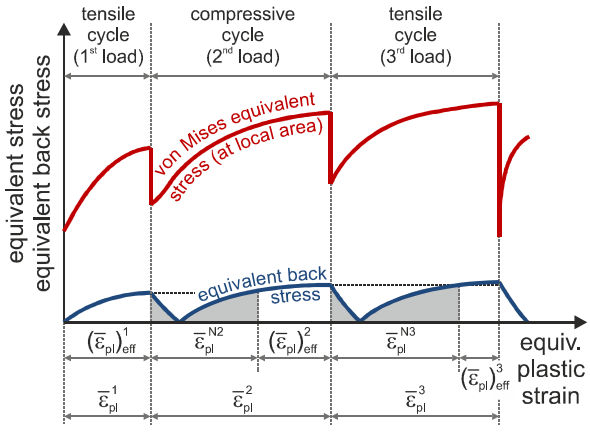

Fig. 4 Determination of effective equivalent plastic strains according to *Ohata and Toyoda* [4]

While incremental tensile strains may be easily accumulated for monotonic loading to check whether the sum of strains reaches the limits given by the damage curve, such a procedure would lead to extremely conservative results for cyclic strains. Therefore, only effective equivalent plastic strains are considered in the strain accumulation that are controlled by the loops of the back stresses α resulting from the kinematic hardening component of the plasticity model. Fig. 4 shows the evolution of the stress components together with the determination of the effective equivalent plastic strains. The principle is that once the cyclic loops of von Mises stresses and equivalent strains are stabilized, there is no contribution from equivalent strains to damage. Hence, only those portions of the equivalent plastic strains are damage effective which belong to the back stresses larger than the maximum α-values related to all of the preceding loops.

For some loading histories this accumulation procedure is unsuitable as the back stress might reach its maximum value in the first half cycles so that the summation of strains stops early in the beginning of a constant amplitude loading history for instance. Then, contrary to the experimental observations the damage criterion would not be fulfilled anymore. Therefore, a slightly modified EDC is proposed, where the accumulation procedure refers to the actual previous half cycle instead of referencing to the maximum value of back stress determined from all of the preceding cycles.

3.3 Finite-Element-Analysis of the rotational tests – Global behaviour

The numerical investigations were carried out with ABAQUS on the basis of the plasticity model in section 3.1 using the *Chaboche*-parameters given in Table 2. A remarkable agreement of the global cyclic rotational behaviour is shown in Fig. 5, where the formation and the amplitudes of the plastic hinges

determined in the calculations correspond to the experimental observations. The quality of the simulations could also be determined from the load-displacement hysteresis represented in Fig. 2.

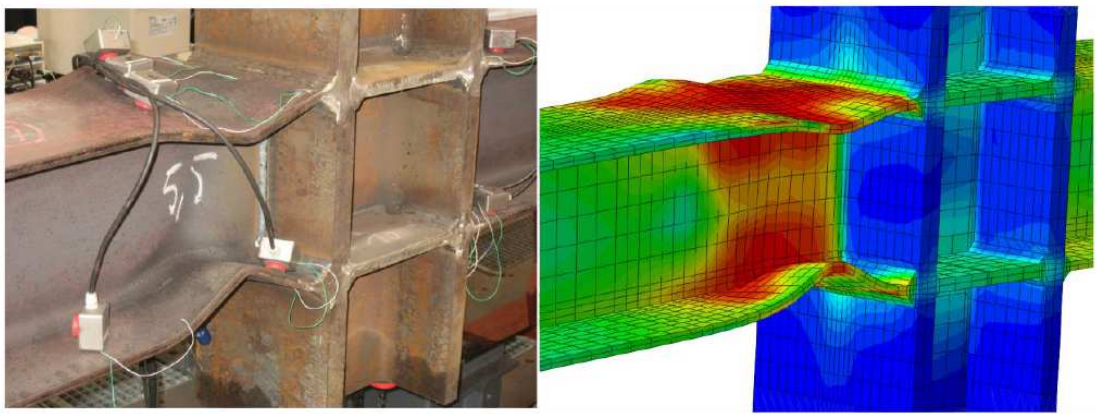

Fig. 5 Structural response with regard to plastic deformations for test no. 3 (RT_HEA_355_ns-4)

3.4 Damage mechanics approach – Local strains

For evaluating the local quantities required for applying the EDC a sub-model technique was used, where the time-dependent values of the state variables saved for the nodes positioned at the interface of a relative coarse global model and a refined sub-model drive the connected boundary nodes of the critical area.

Fig. 6 shows two sub-model levels where level 1 represents the beam flange area connected to the column and level 2 represents a second sub-model (extracted from the level-1-sub-model) at the outer parts of the flanges corresponding to the area of crack type I, cf. 2.3). The weld toe was idealised by a reference radius (r = 1 mm) where the maximum element size was set to 0.06 mm. The distribution of the so-called Ductile Crack Initiation-index is shown, where DCI defines a critical combination of the stress triaxiality parameter and the equivalent plastic strain related to the damage curve. According to this, crack initiation takes place in that specific integration point in a distance of ~10 mm to the flange edges where DCI equals 1,0.

The damage evolution for this respective integration point is plotted in Fig. 7 (stress triaxiality vs. effective equivalent strain) and opposed to the fracture criterion given by the damage curve of S355J2. Crack initiation is indicated after 4.92 packages of cycles according to the “Kobe”-loading protocol which corresponds to a total number of 14 plastic cycles exceeding the joint’s yield displacement. This agrees well with the experimental observations where crack initiation was detected after 12 plastic cycles, cf. 2.3). The overall performance of the model predictions on the basis of the modified EDC is given in Fig. 8.

4 A MACRO-MODEL FOR ULCF

Since damage mechanics calculations are complex and unsuitable with regard to engineering practise, a macro-model for (U)LCF-conditions was established by developing a S/N-line-approach acc. to the log-log domain eq. (1) where the number of plastic cycles to crack initiation is related to the equivalent total rotation range $\Delta\varphi_{tot}$ of the beam-column-connection. Eq. (1) represents a fatigue resistance line with a slope equal to (-1/m).

$$\log(N_{f,pl}) = \log(K) - m \cdot \log(\Delta\varphi_{tot}) \quad (1)$$

The rotation spectra could be determined from rotational histories by means of convenient counting methodologies (Rainflow-Analysis) and were subsequently evaluated with the *Miner*-rule in order to derive a damage equivalent total rotation range as given by eq. (2).

$$\Delta\varphi_{tot} = \{[(\Sigma\Delta\varphi_{tot,i})^{m} \cdot n_i] / \Sigma n_i\}^{1/m} \quad (2)$$

In Fig. 9 the experimental data for the joints with beams HEA300 and the non-sophisticated welding details have been plotted together with additional numerical data determined by means of the modified EDC for

constant amplitude loading (30 mm, 40 mm, 50 mm, 60 mm, 80 mm). The log-log-distribution of the low-scattered data pairs reveals a straight line with a slope parameter of m = 1,87.

The assessment of the slope (-1/m) strictly depends of the definition of the parameter S. Whereas in [11] an inverse slope of m = 3 was validated for LCF-conditions and for S = $\Delta\varphi_{tot}$, from the results in this paper m = 2 is suggested. This is due to the deviating failure criterion in [11] where fracture was not related to the first ductile crack initiation, but was based on a so-called “Energy Reduction Failure Criterion” where failure was defined by a significant drop of the stiffness of the system.

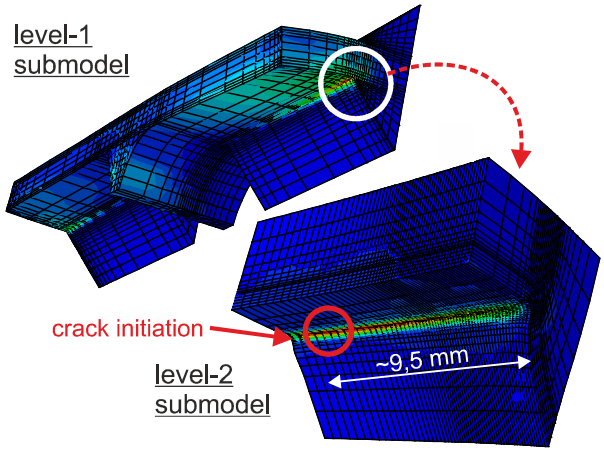

Fig. 6 Level-1- and 2-sub-models of the critical region of the beam flange connection to the column

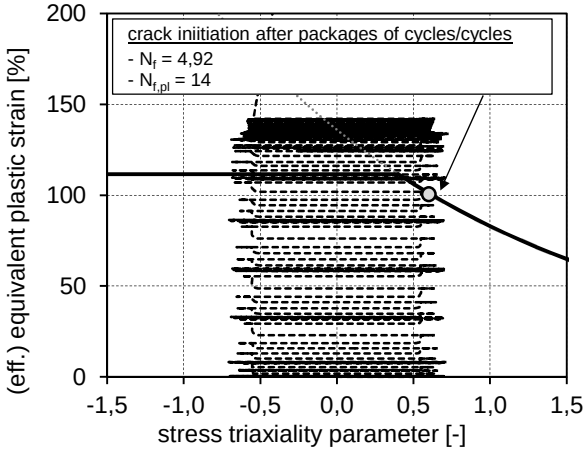

Fig. 7 Prediction of ductile crack initiation acc. to the modified EDC for test no. 3

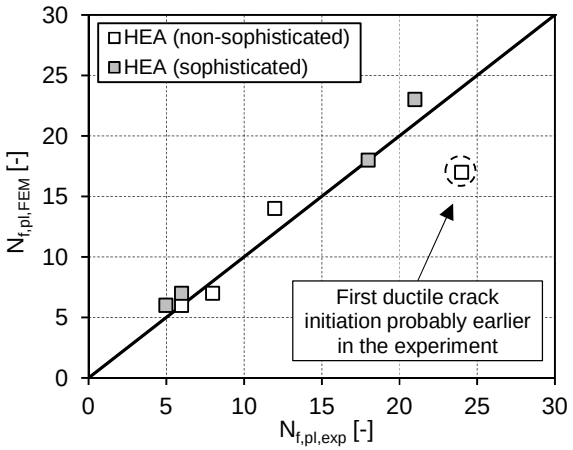

Fig. 8 Plastic cycles $N_{f,pl}$ observed in the rotational tests and determined by the modified EDC

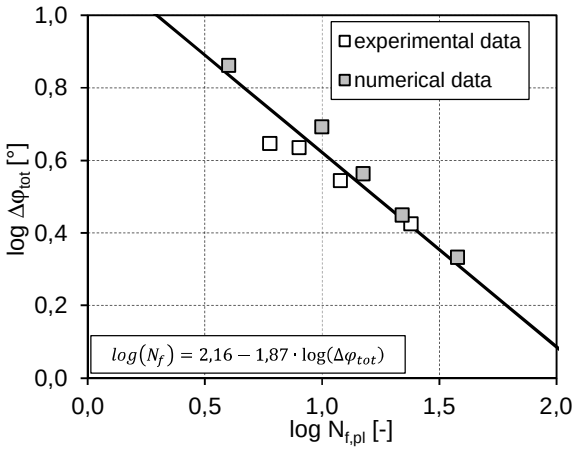

Fig. 9 Rotational Wöhler-curve for beam-column-connections (sophisticated welds and HEA300)

5 CONCLUSIONS

The practicability of a damage mechanics based model for predicting ductile crack initiation for ULCF-loading situations was demonstrated in the framework of [3,7] where beam-column-connections have been exposed to various cyclic large strain protocols. The approach uses a modified effective equivalent plastic strain definition together with a phenomenological crack initiation limit (damage curve). For simplification purposes a more convenient macro-model using a S/N-line based methodology was developed.

6 ACKNOWLEDGEMENTS

The authors would like to acknowledge Prof. Ioannis Vayas and his team (National Technical University of Athens, Laboratory of Steel Structures, Athens, Greece). They were strong partners in the RFSR-CT-2005-0039 project PLASTOTOUGH and provided valuable information in applying the effective damage concept.

7 REFERENCES

[1] E.P. Popov, T.-S. Yang, S.-P. Chang: Design of Steel MRF Connections before and after 1994 Northridge Earthquake. Engineering Structures 20 (12), 1030-1038, 1998.

[2] H. Kuwamura: Fracture of Steel during an Earthquake – State-of-the-Art in Japan. Engineering Structures 20 (4-6), 310-322, 1998.

[3] PLASTOTOUGH: Modern Plastic Design for Steel Structures. Research Fund for Coal and Steel RDT, Final Report, EUR 24227 EN, 2010.

[4] M. Ohata, M. Toyoda.: Damage Concept for Evaluating Ductile Cracking of Steel Structure subjected to Large-Scale Cyclic Straining. Science and Technology of Advanced Materials 5, 241-249, 2004.

[5] G.R. Johnson, W.H. Cook: Fracture Characteristics of Three Metals subjected to various Strains, Strain Rates, Temperatures and Pressures. Engineering Fracture Mechanics 21 (1), 31-48, 1985.

[6] M. Feldmann, B. Eichler et al.: Toughness Requirements for Plastic Design with Structural Steel. Steel Construction 4 (2), 94-113, 2011.

[7] B. Eichler: Untersuchungen in der Zähigkeitshochlage von Stahl im Hinblick auf die Entwicklung eines Kriteriums für die Werkstoffgütewahl für die plastische Bemessung von Stahlbauteilen. Dissertation, RWTH Aachen University, in preparation.

[8] ECCS – Technical Committee 1, Structural Safety and Loadings, Technical Work Group 1 – Seismic Design: Recommended Testing Procedure for Assessing the Behaviour of Structural Steel Elements under Cyclic Loading. 1986.

[9] J. Lemaitre, J.L. Chaboche: Mechanics of Solid Materials. Cambridge University Press, 1990.

[10] P.J., Armstrong, C.O. Frederick: A Mathematical Representation of the Multiaxial Bauschinger Effect. No. CEGP-Report RD/B/N731, Berkeley, UK: Berkeley Nuclear Laboratories, 1966.

[11] C. Bernuzzi, L. Calado, C.A. Castiglioni: Low-Cycle Fatigue of Structural Steel Components: A Method for Re-Analysis of the Test Data and a Design Approach based on Ductility. Journal of Earthquake Technology 37 (4), 47-63, 2000.

Proceedings of the 3rd International Conference on
Fracture Fatigue and Wear, pp. 8-17, 2014

APPLIED STUDIES OF FRACTURE MECHANICS IN GEOLOGICAL DISASTERS MITIGATION

Chen Hong-kai, He Xiao-ying, Tang Hong-mei and Dong Ping

Institute of Geotechnical Engineering, Chongqing Jiaotong University, Chongqing 400074 China

Abstract: Geological disasters engender with high frequency in western China, and seriously threat highways, railways, mines and urban. Undoubtedly, rupture mechanism of geological disasters is one key theoretical issue in geological disasters mitigation. Many geological catastrophic events have identified that fracture phenomena exist everywhere in development of geological disasters such as perilous rock, rock collapse, debris flow, bank collapse, ground fissure, and karst collapse. Paying attention to the sliding perilous rock in this paper, three fracture models to describe rupture mechanism of the perilous rock, the bending moment fracture model, the shear stress fracture model and the compressive stress fracture model, are established in detail. Further, abiding by the classic solutions of fracture models in fracture mechanics, analytical solutions to these fracture models are deduced, and the stability analysis method to character real-time safety of perilous rock is put forward. Finally, two aspects are discussed, one is that fracture mechanics has extensive applicability in rupture mechanism studies of geological disaster, and another is that emergent safety alarms of geological disasters come true by fracture mechanics.

Keywords: geological disasters; fracture mechanics; rupture mechanism; emergent safety alarm; perilous rock

1 INTRODUCTION

Geological disasters are the significant geological safety hidden troubles in construction, maintenance and operation of highways, railways, mines and urban in western China, specially, about 80% in quantity is perilous rock, rock collapse, debris flow and landslide in geological disasters. Serious casualties and property losses produce every year in China [1]. For example, at Oct. 21, 2011, a significant deformation of Wangxia perilous rock suddenly appeared and caused the accident over 30 hours navigation interrupt at Wu Gorge of the Yangtze River, China. At July 25, 2009, one giant avalanche occurs at the Chediguan large-span bridge in Wenchuan county of Sichuan province, China, two bridge piers of the bridge were crushed by the collapse, 6 persons died in the accident. At the last count, about 8000 major geological disasters happen and cause about 8 billion RMB economic losses every year in China [1].

As for geological disasters, some features such as multi-scale, multi-field coupling, randomness, nonlinearity and complexity are concluded by Zhen Xiaojing [2]. Zheng Zhemin actively advocates applied researches of engineering mechanics such as damage mechanics, fracture mechanics and ballistics [3]. Cui Peng emphasizes basic mechanics research in debris flow mitigation [4]. Zheng Yingren et al. discuss the rupture of slope using FLAC3D numerical method [5]. Strom and Korup discuss the kinetic process of slope evolution from rupture of perilous rock and collapse [6]. De Blasio discovers that deposits at the bottom of colluvium are in rheologic status [7]. Frayssines and Hantz analyze fracture mechanism of steep and high slope in limestone area [8]. A mutation model to predict instability of landslide is established by Wang Zhiqiang et al. [9]. In addition, movement uncertainty of debris flow is discussed sketchily by Simoni et al. [10].

Preliminary studies manifest in essence, the rupture of perilous rock and landslide belong to the fracture problem of dominant fissure of perilous rock and sliding surface of landslide, while development of initial debris flow belongs to fracture problem of soil under action of heavy rainfall or seepage. Both rock mesoscopic model and the mapping relationships between mesoscopic model and macroeconomic model are two major research topics in rock strength theory [11]. Wang Sijing emphasizes researches on

essential attribute for rock to rupture [12]. Qi Chengzhi and Qian Qihu discuss the zoning fracture of wall rock in deep mine's roadway [13]. By analogy dominant fissure of perilous rock for type I crack in fracture mechanics, Chen Hongkai, et al. discuss some mechanical problems in evolution of rock slope backward [14]. Meanwhile, by considering the periodic variation of stress intensity factor of dominant fissure under action of water pressure in dominant fissure of perilous rock from intermittent rainfall, Chen Hongkai, et al. analyze the fracture life of dominant fissure [15]. It follows that fracture mechanics has some significant value in studies on rupture mechanism of geological disasters, however, which is in original exploration stage at present. Taking the sliding perilous rock as an example, authors analyze the application of fracture mechanics in geological disaster mitigation in this paper.

2 FRACTURE MECHANICS ANALYSIS OF GEOLOGICAL DISASTERS: A CASE, THE SLIDING PERILOUS ROCK

2.1 Geological model of perilous rock

Geological model for any geological disasters is based on field investigation, measurement and geological survey, which is the key problem to establish mechanical model of the geological disaster. For instance, Wangxia perilous rock, one representative sliding perilous rock shown in Fig.1, locates in Wu Gorge of the Three Gorges of the Yangtze River, China, with 1220 ~ 1230 m a.s.l. at the top, 1137 ~ 1147 m a.s.l. at the bottom, 120 m in length at strike of the cliff, 30 ~ 35 m in thickness perpendicular to the surface of the cliff, and about 40×104m3 in volume. On August 21, 2013, a heavy rainfall happened in area of the Wu Gorge, and aggravated the deformation in eastern part of Wangxia perilous rock and gave rise to collapse frequently with 8 ~ 40 m3 in volume. Especially, at 7:40 on the day, the perilous rock ruptured suddenly. The bottom of the perilous rock slides outward for 10 ~ 15 m and sinks approximately 10 m, which lead to awful fact that the weak mudstone under the perilous rock pushed the subgrade and a great quantity of mudstone debris mixed with heavy weathering rock avalanched downward the slope. For the long term studies on perilous rocks in area of the Three Gorges Reservoir, characteristic geological model of the sliding perilous rock is simplified shown in Fig. 2. Perilous rock is composed of hard rock such as sandstone or limestone; usually there are weak rocks such as mudstone, carbonaceous mudstone and shale below the perilous rock.

Fig. 1 Outline before and after the rupture of Wangxia perilous rock in Wu Gorge of the Yangtze River, China

2.2 Mechanical model of perilous rock

Mechanical model of the sliding perilous rock is shown in Fig.3. Variables describe in the figure are as following, W is the weight unit width of perilous rock (kN/m). P_v is the vertical seismic force acting on the barycentre of perilous rock (kN/m). P_h is the horizontal seismic force acting on the barycentre of perilous rock (kN/m). H is the average height of perilous rock (m). Q is the water pressure in dominant fissure of perilous rock (kN). e is the length of cut-through segment of dominant fissure in perilous rock (m). e_w is the distance between the action point of fissure water pressure Q on dominant fissure and the end point of cut-through segment of dominant fissure (m). c is the width of base below perilous rock (m). $[\sigma_c]$ is the allowable compressive strength of weak rock in base below perilous rock (kPa). β is the average dip angle

of dominant fissure in perilous rock (°). a_c is the horizontal distance from the barycentre of perilous rock to the intersection point between dominant fissure and the bottom of perilous rock (m). b_c is the vertical distance between the barycentre of perilous rock and the bottom of perilous rock (m). O is the end point of cut-through segment of dominant fissure. *C* is the barycentre of perilous rock. *AB* is the bottom of perilous rock.

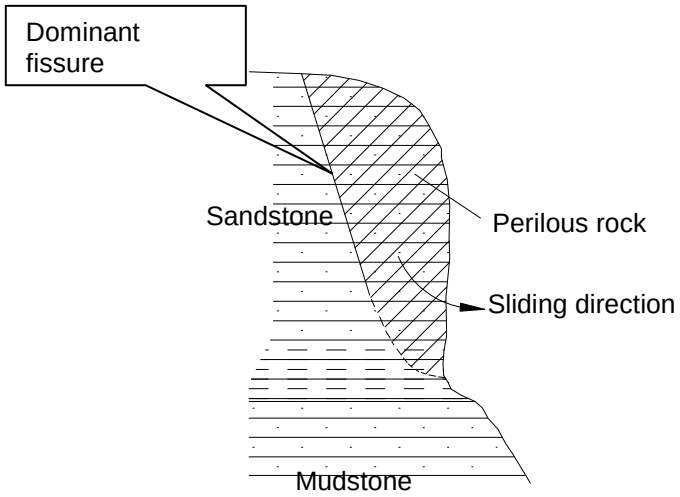

Fig. 2 Characteristic geological model of the sliding perilous rock

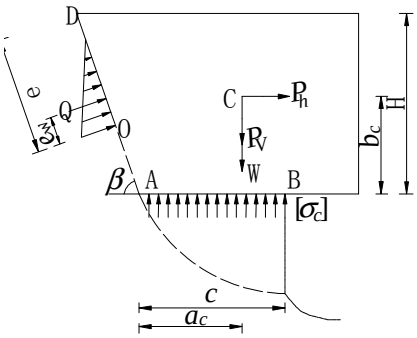

Fig. 3 Mechanical model of the sliding perilous rock

2.3 Loads acting on perilous rock

The function *F* to discriminate the safety state of the sliding perilous rock is defined as:

$$F = P_v + W - c[\sigma_c] - \frac{1}{18}\gamma_w e^2 \sin 2\beta - (H - e\sin\beta)[\tau] \quad (1)$$

Where, [τ] is the allowable shear strength of hard rock at intact segment of dominant fissure (kPa). γw is the water bulk density in dominant fissure (9.8 kN/m3). The other variables are the same as before.

Further, to any concrete perilous rock, we can discriminate it safety state using F value calculated in formula (2), describing as follows.

If F<0, the perilous rock isn't rupture, namely it is in safety state. If *F*=0, the perilous rock is in limit equilibrium state. And if *F*>0, the perilous rock is in rupture state, and there may be two rupture modes, one is pressure-shear rupture when *c*=0, and another is sliding rupture when *c*≠0.

Paying attention to the mechanical model of the sliding perilous rock shown in Fig.3, we transfer loads acting on perilous rock to the dominant fissure of the perilous rock, and obtain three loads, bending moment

M around the end point of cut-through segment of dominant fissure, equivalent average shear stress τ and equivalent average compressive stress σ distributing evenly along the dominant fissure, calculation formulas are in following [1].

$$M = P_h(b_c - H + e\sin\beta) + (W + P_v)(a_c + H\tan\beta - e\cos\beta) + \frac{1}{162}\gamma_w e^3 \sin^3\beta \quad (2)$$

$$\sigma = \frac{[(P_v + W)\cos\beta - P_h \sin\beta - \frac{1}{18}\gamma_w e^2 \sin\beta]\sin\beta}{H} \quad (3)$$

$$\tau = \frac{[(P_v + W)\sin\beta + P_h \cos\beta]\sin\beta}{H} \quad (4)$$

Where, variables are the same as before, however, due to the difference of the transverse wave and the longitudinal wave in earthquake, P_v and P_h are forbidden to consider at the same time.

Based on M, τ and σ at the same time, rupture model of the sliding perilous rock is provided shown as Fig.4.

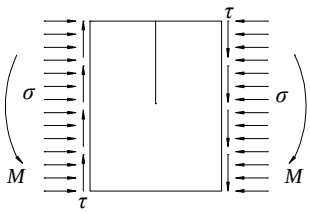

Fig. 4 Rupture model of the sliding perilous rock

2.4 Fracture model of perilous rock

In mesoscopic and microcosmic terms of classic fracture mechanics, fundamental types of crack in material or structures include type Ⅰ (tensile crack), type Ⅱ (shear crack) and type Ⅲ (tensional crack) shown respectively in Fig. 5. The macro performance of material or structure rupture under the action of loads essentially presents as crack forming, extending and cut-through [17]. If we analogy dominant fissure in perilous rock for crack in mesoscopic and microcosmic terms of classic fracture mechanics, we can build fracture model of perilous rock [16], namely, macroscopically fracture models.

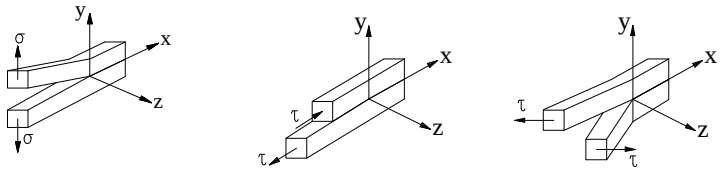

Type I Type II Type III

Fig. 5 fundamental types of crack

By factorization to rupture model of the sliding perilous rock shown in Fig. 6, we establish three fundamental fracture models (Fig. 7), the bending moment fracture model (abbr. M model), the shear stress fracture model (abbr. τ model), and the compressive stress fracture model (abbr. σ model). Apparently, by solving these fundamental fracture models, and combinations with fracture model solutions, we reasonably obtain the fracture mechanics solution of the sliding perilous rock.

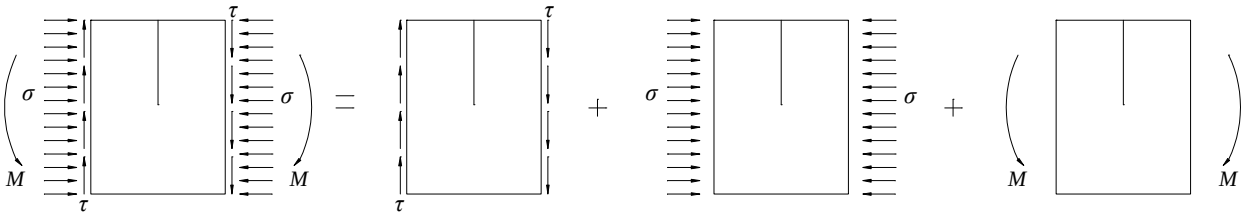

Fig.6 factorization of rupture model of the sliding perilous rock

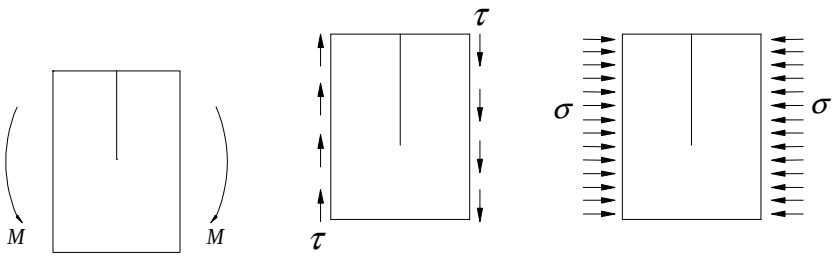

(a) (b) (c)

Fig. 7 Fundamental fracture model of the sliding perilous rock. (a) is the bending moment fracture model (abbr. M model), (b) is the shear stress fracture model (abbr. τ model), and (c) is the compressive stress fracture model (abbr. σ model)

2.5 Fracture model solution of perilous rock

(1) Solution of fundamental fracture model

To M model, by the integral transform method, formulas to calculate stress intensity factor are expressed as following [14].

$$K_{\mathrm{I}}=3.975M\left(\frac{H}{\sin\beta}-e\right)^{-\frac{3}{2}},\ K_{\mathrm{II}}=0 \qquad (5)$$

Where, K_{I} is the stress intensity factor of type Ⅰ, $\mathrm{kPa}\sqrt{\mathrm{m}}$ .K_{II} is the stress intensity factor of type Ⅱ, $\mathrm{kPa}\sqrt{\mathrm{m}}$.

The other variables are the same as before.

To τ model, by the Fourier transform method, formulas to calculate stress intensity factor are expressed as following [14].

$$K_{\mathrm{I}}=0,\ K_{\mathrm{II}}=\tau\sqrt{1.5B\sin\beta}\left(\frac{2H}{B\sin^{2}\beta}+0.2865\right) \qquad (6)$$

Where, *B* is the average width of perilous rock, m. The other variables are the same as before.

To σ model, by the Westergarrd stress function method, formulas to calculate stress intensity factor are expressed as following [14].

$$K_{\mathrm{I}}=-1.5958\sigma\sqrt{\frac{H}{\sin\beta}},\ K_{\mathrm{II}}=0 \qquad (7)$$

Where, the other variables are the same as before.

(2) Fracture model solution of the sliding perilous rock

Focus on the fracture angle θ_0 at arbitrary point *Q* near the end of cut-through segment in dominant fissure in perilous rock (Fig.8), the formula to calculate the union stress intensity factor K_e for rock to fracture along θ_0 direction is deduced using fracture mechanics.

$$K_e = \cos\frac{\theta_0}{2}[K_I \cos^2\frac{\theta_0}{2} - 1.5K_{II}\sin\theta_0] \quad (8)$$

Where, K_e is the union fracture stress intensity factor, $\mathrm{kPa}\sqrt{\mathrm{m}}$. θ_0 is the fracture angle at arbitrary point Q near the end of cut-through segment in dominant fissure. The other variables are the same as before.

In formula (8), when $K_{II}=0$ and $K_I \neq 0$, then $\theta_0 = 0$, which means the dominant fissure will extend along the dominant fissure of perilous rock. However, when $K_{II} \neq 0$, then $\theta_0 \neq 0$ and can be calculated in formula (9).

$$\theta_0 = \arccos[\frac{3+\sqrt{k_0^2+8k_0}}{k_0+9}] \quad (9)$$

Where, intermediate variable by K_I and K_{II} is $k_0 = (K_I / K_{II})^2$.

According to formula (5) ~ (7), K_I and K_{II} of the sliding perilous rock are as follows, respectively.

$$K_I = 3.975M(\frac{H}{\sin\beta} - e)^{-\frac{3}{2}} - 1.5958\sigma\sqrt{\frac{H}{\sin\beta}} \quad (10)$$

$$K_{II} = \tau\sqrt{1.5B\sin\beta}(\frac{2H}{B\sin^2\beta} + 0.2865) \quad (11)$$

Put the formula (10) and (11) into the formula (9), variable θ_0 can be determined. Further, put θ_0, formula (10) and (11) into formula (8), variable K_e of the sliding perilous rock is solved.

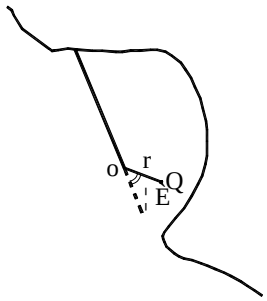

Fig. 8 Polar coordinates at end of cut-through segment of dominant fissure in perilous rock

3 FRACTURE STABILITY ANALYSIS OF GEOLOGICAL DISASTER

Combining the union fracture stress intensity factor K_e of dominant fissure with the fracture toughness K_{IC} of perilous rock, the formula to calculate the coefficient of fracture stability is in followings.

$$F_s = \frac{K_{IC}}{K_e} \quad (12)$$

Where, K_{IC} is the fracture toughness of perilous rock composed of intact rock ($\mathrm{kPa}\sqrt{\mathrm{m}}$), acquired by fracture test in laboratory.

Table 1 provides the evaluation standards of stability for perilous rock [16], and data in the table are the coefficient of fracture stability. Emphatically, due to variation of K_e with σ and τ, as long as we collect the data of σ and τ timely by some transducers, we can identify the stability of perilous rock using formula (12) and table 1 at the same time.

Table 1 Evaluation standards of stability for perilous rock

Type	Instability	Quasi-stability	Stability
sliding perilous rock	<1.0	1.0~1.3	>1.3
toppling perilous rock	<1.0	1.0~1.5	>1.5
falling perilous rock	<1.0	1.0~1.5	>1.5

Case analysis: Taibaiyan in Wanzhou of Chongqing city, locating in area of the Three Gorges Reservoir, China, develops two cliffs, and there are 127 perilous rocks on the cliffs, the individual is 20 ~ 3600 m^3 in volume. Thereinto, the 59# perilous rock is one of representative sliding perilous rocks, composed of feldspathic quartz sandstone, whose geometric and physical parameters are as follows: H=15.5 m,B=6 m, L=20 m, e=11 m, β=85°, c=1.73 m, a_c=3.65 m, b_c=4.59 m, W=2325 kN, K_{IC}=2096 $\mathrm{kPa}\sqrt{\mathrm{m}}$, [$\sigma_c$]=2000 kPa, [$\tau$]=4200 kPa. In the region, the horizontal seismic coefficient μ_h=0.05 while the vertical seismic coefficient μ_v=0.08.

In the course of stability analysis of perilous rock, six working conditions are suggested by Chen HK, et al.[1], i.e.,

- WC1: Rainfall + horizontal seismic action, definitely e_w=2/3e.
- WC2: Rainfall + vertical seismic action, definitely e_w=2/3e.
- WC3: Rainfall only, definitely e_w=2/3e.
- WC4: Natural condition + horizontal seismic action, definitely e_w=1/3e.
- WC5: Natural condition + vertical seismic action, definitely e_w=12/3e.
- WC6: Natural condition only, definitely e_w=1/3e.

Using methods established in the paper, the coefficients of fracture stability of the 59# perilous rock in various working conditions are shown in table 2. Obviously, in rainfall or natural condition, the stability of perilous rock is strongly impacted by vertical seismic action, and in the same seismic action, the stability of perilous rock in rainfall is less than that in natural condition, which is reasonable.

Table 2 Stability analyses of perilous rock at Taibaiyan in Wanzhou of Chongqing, China

Working condition	WC1	WC2	WC3	WC4	WC5	WC6
F_s	0.9494	0.8374	0.9504	1.0820	0.9389	1.0832
Stability evaluation	Instability	Instability	Instability	Quasi-stability	Instability	Quasi-stability

4 DISCUSSIONS

4.1 Fracture mechanics promotes studies on development mechanism of geological disasters

Geological disaster-triggering mechanisms are theoretical evidences to control geological disasters [3,12]. Fracture problems widely exist in development of geological disasters, as mention above, the essential characteristics for perilous rock to rupture is the fracture and extension of dominant fissure of perilous rock [14-16]. To soil bank slope of reservoir or/and river, it is probable to trigger landslide during water level fluctuation, and in the early, a series of tension cracks appear on the surfaces of bank slope (Fig.9). Paying attention to the rupture model of reservoir bank slope, it belongs to tension-shear rupture during the rising of water level, while pressure-shear ruptures during the landing of water level. Many events have indicated that the appearance and extension of tension cracks is the macro characteristics in quasi-soil bank slope of reservoir, for example, Gongjiafang bank slope at Wu Gorge of the Three Gorges of the Yangtze River significantly develops from deformation to rupture during rising of water level (Fig.10). In

studies of development of debris flow, it has been accepted widely in academia for debris flow to start up due to fluidization of soil on slope [4], the mechanical behaviour in initial stage to trigger debris flow is still a fracture problem between particles in soil [20]. In addition, fracture mechanism plays an important role in development of geological disasters such as ground fissures, ground collapse, subgrade collapse, coyote collapse, and earthquake.

The analysis shows that, in development of geological disasters such as perilous rock, collapse, landslide, debris flow, ground collapse, etc. fracture behaviours widely exists. Inferentially, fracture mechanics has important role in researches on developmental mechanism of geological disasters. However, fracture mechanics originated from microscopic analysis of materials and/or structures [11][17], we must pay high attention to the macro analogy for fracture mechanics in researches on development mechanism of geological disasters. For example, to perilous rock disaster, the M model, the σ model and the τ model are stemmed from researches on rupture mechanism, then we can solve the fracture models using the classic solutions of fracture model and obtain the theoretical solutions. At present, it may be the effective way to obtain valuable solutions of geological fracture mechanism using experiments and/or field tests to revise the theoretical solutions.

Fig. 9 Deformation and rupture characteristics of soil bank slope in area of the Three Gorges reservoir

Fig. 10 Rupture process of Gongjiafang bank slope at Wu Gorge of the Three Gorges of the Yangtze river

4.2 Fracture mechanics provides real-time signals need in emergent safety alarm of geological disasters

At present, emergent safety alarm is one of important scientific topics in geological disasters mitigation. For years, it is a frequently-used method to predict geological disasters such as landslide and slope to use time-displacement curves drawn by displacement observation data [21]. Especially, with long-range observation data the method is effective in disaster prediction such as landslide, slope, ground collapse, embankment collapse, and cavity collapse, but doesn't apply in prediction of sudden geological disasters such as perilous rock and earthquake. Meanwhile, as indirect variable such as displacement can't reveal the rupture features of geological disasters such as landslide and slope, disaster predictions by time-displacement curves are out of real-time alerts and/or emergent alarm. As for the essence for geological disasters to rupture such as perilous rock and landslide, stress signals collected at sensitive failure area of perilous rock are effective in calculation of maximum tension stress and maximum shear stress, then the safety of perilous rock can be identified by formula (3) and (4), respectively. Due to the real-time of stress signals, the safety of perilous rock is in real-time, too. In addition, a high-performance transducer to gather stress signals at various positions at the same time is one of key parts in emergent alarm of geological

disasters [16], while another is transmission and processing of signals. Further, the emergent alarm system of geological disaster is composed of transducers, disaster alarm apparatus and signal lines installed in dangerous area of geological disaster, for example, the schematic diagram of emergence alarm system of collapse disaster along highway shown in Fig. 11.

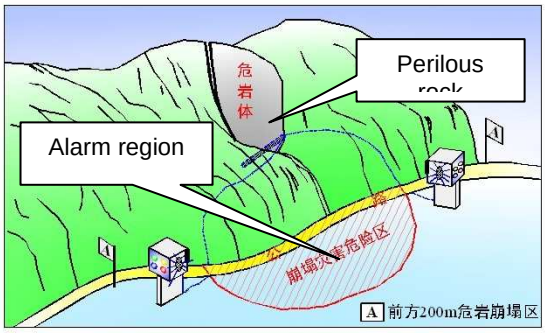

Fig. 11 The schematic diagram of emergence alarm system of collapse disaster along highway

5 CONCLUSIONS

Firstly, researches on rupture mechanism of geological disasters are the key link to control the disasters. As the causes to trigger geological disasters such as perilous rock, landslide, and debris flow, we deduce that fracture mechanics is one practical solution in studies of rupture mechanism of geological disasters.

Secondly, taking the sliding perilous rock as an example, authors establish a method to build fracture model of geological disasters in the paper, i.e., the bending moment fracture model, the shear stress fracture model and the compressive stress fracture model. Abiding by classic solutions of fracture mechanics, the analytical solutions of fracture models of perilous rock are following, and it comes true to represent the real-time stability of perilous rock.

Thirdly, two aspects applying fracture mechanics in geological disasters mitigations are discussed, one is to promote studies on development mechanism of geological disasters, and another is to provide real-time signals need in emergent safety alarm of geological disasters.

6 ACKNOWLEDGMENTS

For a long time, geological disasters widely develop in China. Studies carried out by the scientific group led by professor Chen Hongkai have been supported by the National Natural Fund of China marked 11272185#, 51378521# and 50678182# for tens of year. The authors warmly appreciate the help and encourage in researches have been given from professor Li Jijun, academician of the Chinese Academy of Science (CAS), professor Xian Xuefu and professor Zhou Fengjun, academicians of the Chinese Academy of Engineering (CAE). We wish to thank our colleagues who critically read the manuscript and made useful suggestions. We are also grateful to the Innovation Team for Geological Disasters Mitigation along Highways & Shipping Lane in West China for the field investigations (No. KJTD201305).

7 REFERENCES

[1] Chen Hong-kai, Tang Hong-mei, Wang Lin-feng, Liu Li, He Xiao-ying. Geological hazard theory and its control. Beijing: Science Press, 2011（in Chinese）

[2] Zheng Xiao-jing. Study on mechanism of wind- blown sand movement. Papers on Environmental Mechanics,2007,25(14):22- 27（in Chinese）

[3] ZHENG Zhe-min, ZHOU Heng, ZHANG Han-xin, HUANG Ke-zhi, BAI Yi-long. Developing trends at the beginning of the 21th century. Mechanics and Practice, 1996,18(1):1-8（in Chinese）

[4] Cui Peng. Advances in debris flow prevention in China. Science of Soil and Water Conservation, 2009,7(5):7-13（in Chinese）

[5] Zheng Ying-ren, YE Hai-lin, HUANG Run-qiu. Analysis and discussion of failure mechanism and fracture surface of slope under earthquake. Chinese Journal of Rock Mechanics and Engineering, 2009, 28(8):1714-172（in Chinese）

[6] Strom, A. L. and Korup, O. Extremely large rockslides and rock avalanches in the Tien Shan mountains, Kyrgyzstan. Landslides, 2006, 3(2):125-136

[7] De Blasio, F. V. Rheology of a wet, fragmenting granular flow and the riddle of the anomalous friction of large rock avalanches. Granular Matter, 2009, 11(3):179-184

[8] Frayssines, M. and Hantz, D. Modelling and back-analysing failures in steep limestone cliffs. International Journal of Rock Mechanics and Mining Sciences, 2009, 46(7):1115-1123

[9] Wang Zhi-qiang, Wu Min-Ying, Pan Yue. Fold catastrophe model of slope destabilization and its starting velocity. Journal of China University of Mining & Technology, 2009, 38(2): 175-181（in Chinese）

[10] Simoni, A., Mammoliti, M., and Berti, M. Uncertainty of debris flow mobility relationships and its influence on the prediction of inundated areas. Geomorphology, 2011,132(3-4):249-259

[11] Xie He-ping, Peng Rui-Dong, Zhou Hong-Wei, JU Yang. Research advances in rock strength theory based on fracture and damage mechanics. Advances in Natural Science, 2004, 14(10):1086-1092（in Chinese）

[12] Wang Si-jing. Geological nature of rock and its deduction for rock mechanics. Chinese Journal of Rock Mechanics and Engineering,2009,28(3):433-450（in Chinese）

[13] Qi Cheng-zhi, Qian Qi-Hu, Wang Ming-Yang, Luo Jian. Advance in investigation of zonal disintegration phenomenon. Journal of PLA University of Science and Technology(Natural Science Edition),2011,12(5):472-479（in Chinese）

[14] Chen Hong-kai, Tang Hong-Mei, Wang Lin-Feng, Xian Xue-Fu. Mechanical mechanism for retreat evolution of steep rock slopes with gentle dip. Chinese Journal of Geotechnical Engineering, 2010,32(3): 468-473

[15] Chen Hong-kai, Tang Hong-mei. Method to calculate fatigue fracture life of control fissure in perilous rock. Applied Mathematics and Mechanics, 2007,28(5): 643-649

[16] Chen Hong-kai, Tang Hong-mei, WANG Lin-feng, YE Si-Qiao. Evolution theory for rockfall and its application. Beijing: Science Press, 2009（in Chinese）

[17] Wang Zi-qiang, Chen Shao-hua. Advanced fracture mechanics. Beijing: Science Press, 2009（in Chinese）

[18] The Chinese aviation research institute. Stress intensity factor handbook. Beijing: Science Press, 1981（in Chinese）

[19] CHEN Hong-Kai, TANG Hong-mei. Bored stress sensor and the monitoring method of stress in drill bore. The national invention patent, 2011（in Chinese）

[20] Chen Hong-Kai, Xian Xue-Fu, Tang Hong-Mei, Wang Quan-Cai, Zhang Yuping. Model test of debris flow formation on slope. Journal of Hunan University (Natural Sciences), 2008,35(11):130-134（in Chinese）

[21] Liu Xi-Lin, Huang Zhi-Quan. Study on geological hazards at the western line project of south water to north. Beijing: Geological Press, 2012（in Chinese）

Proceedings of the 3rd International Conference on
Fracture Fatigue and Wear, pp. 18-24, 2014

SEM IN-SITU INVESTIGATION ON MICRO CRACKING BEHAVIOR AND THRESHOLD FAILURE PARAMETER OF POP STRUCTURE

X.S. Wang*, D.Y. Ge, P. Pan and S. Jia

Department of Engineering Mechanics, School of Aerospace, Tsinghua University, Beijing 100084, P.R. China
* Corresponding author: xshwang@tsinghua.edu.cn

Abstract: The three-point bending tests of the complete ultra-large-scale integrated circuits (ULSI) structure by the package on package (PoP) technology were carried out by using *in-situ* scanning electron microscope (SEM). Due the experimental sample involves the multi-layer structure and different elements as well as enough small size, the estimated threshold value of loading response in failure point becomes more and more difficulty, but it is much more significant and necessary in its service, design and reliability analysis. In this work, the micro failure process of PoP structure, including the cracking and fracture behaviours of every element and an instability state of solder balls during the applied bending loading, was exhibited based on the SEM *in-situ* observation images, and the possible failure reasons were analyzed by using the finite element (FE) method based on the cohesive zone model (CZM). These experimental and FE results indicated that the failure process of PoP structure is first to cause the collapse behaviour of solder balls and subsequently to result a discontinuous crack of die, in which is dependence strongly on the adhesive strength, adhesive layer thickness and stress state as well as stress distribution such as σ_{xx}. The deeply understanding the physics-of-failure of PoP structure can assist to improve the current processing technology of PoP structure, to predict, quantify and assure its failure-free performance in the applications.

Keywords: failure analysis; ultra-large-scale integrated circuit; reliability; SEM in-situ; finite element method

1 INTRODUCTION

The ultra-large-scale integrated (ULSI) circuit consists generally of different elements and complex design, fabrication processing as well as small size and micro structure. To assure its failure-free performance in the electronic product applications, we can not only understand the physics failure of an electronic product, but also most importantly, can enable one to predict, quantify a threshold service either condition or state by using the effective qualification test and failure analysis methods [1,2]. In addition, with the increasing requirements for high performance integrated circuit devices have led to the development of multi-die stacking in a single package. Package on package (PoP) is a novel package structure in the field of logic and memory integration, which places one package on top of another to integrate different functionalities while maintaining a compact size. At the same time, it has become the first choice for the some industries [2-5]. The processing package can provide a unique challenge since there is not any gap for the lower die bond wires. There are different types of solutions for stacking the dies including (1) dummy silicon-as-spacer, (2) die attach paste-as-spacer and (3) thick die attach film-as-spacer. The die attach competing technology is different in the package process ability and reliability. Upon structure, the die attach elements were sandwiched in between both dies which need to maintain enough adhesion strength [6,7]. And there is a critical value for these cohesive strengths in the PoP structure in the service time such as what is the carrying capacity of package structure and reliability strength degradation at high temperature or repeated thermal-stress level without a structural fracture.

In previously reported results of our papers [2,7-10], the fracture/fatigue behaviours of surface-mounted technology (SMT) solder joints for the different packages and coating (film)/substrate have been introduced based on the experimental and finite element analysis methods. These results indicated that interface strength including the critical failure stress between the different elements can enable to be estimated by using the coupled approaches such as the scratch test and SEM *in-situ* experimental observation test, even

if in meso-micro scale [10-13]. One of the aims in the present article is to investigate the micro cracking behaviour of PoP structure under three-point bending load by means of the SEM *in-situ* observation technology [14-18]. These results indicated that the failure behaviour of PoP structure exits a strictly hierarchical criterion failure value under mechanical loading which is possible that there are the some typical failure models such as instability failure model of solder balls, crack initiation and fracture of either die layer or adhesive die layer, formed interface crack between dies and bridging cracks evolution process as well as final fracture of PoP structure. Therefore, based on the hierarchical criterion failure behaviour or process of PoP structure, we could deeply understand the failure mechanism and adequately effective predication the failure strength or service time of PoP structure or assure structural reliability of electronic products.

2 SAMPLES AND EXPERIMENTAL PROCEDURES

A PoP structure is widely used in small communication terminals including cell phone, personal digital assistant (PDA), system board, and so on [19]. The size of the PoP structure is about 14 mm×14 mm×1.5 mm (length-width-thickness) and it consists of the top stacked die chip scale package (CSP) and bottom fine-pitch balls grid array (FBGA) package as the cross-section as shown in Fig. 1. The multi-layer microstructure is clearly seen so that the investigation on the failure behaviour of this structure is best way to use the SEM *in-situ* observation technology [2,7,11-14]. At the same time, to estimate the failure criterion and probable failure position of this structure, it should be combined the finite element (FE) analyse and experimental results. Therefore, the simple numerical simulation results are given in this work based on the observed fracture process of dies and die attach adhesives layers by SEM *in-situ* tests. All the SEM *in-situ* tests are controlled by the displacement of about 4.0×10^{-4} mm/s, and the three-point bending span is 10 mm as well as the diameter of the indenter is 2.5 mm. The two types of specimens are shown in Fig. 2 (a)-(b) in which the main difference for these specimens is the different effects of geometrical size, numbers and arranged model of solder balls. Fig. 2 (c) shows a schematic diagram of 3-point bending applied loading in the vacuum chamber (10^{-4} Pa). All SEM *in-situ* observation sections were clearly polished by the abrasive papers (P1000 and P2000) to achieve a surface roughness of approximate R_a=0.1-0.2 μm. These cross-sections can be divided into three main parts including CSP, PBGA and FR4 printed circuit board (PCB).

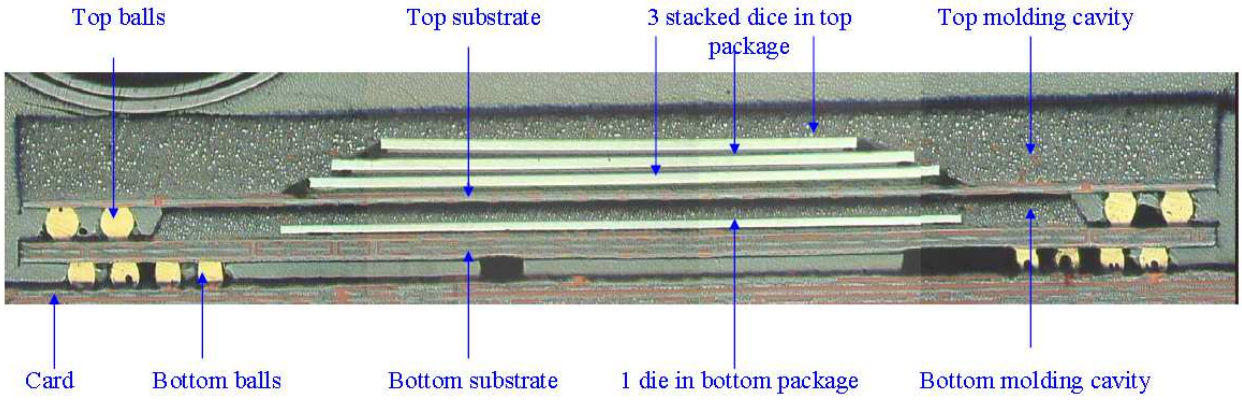

Fig. 1 The cross-section of sample in SEM *in-situ* tests

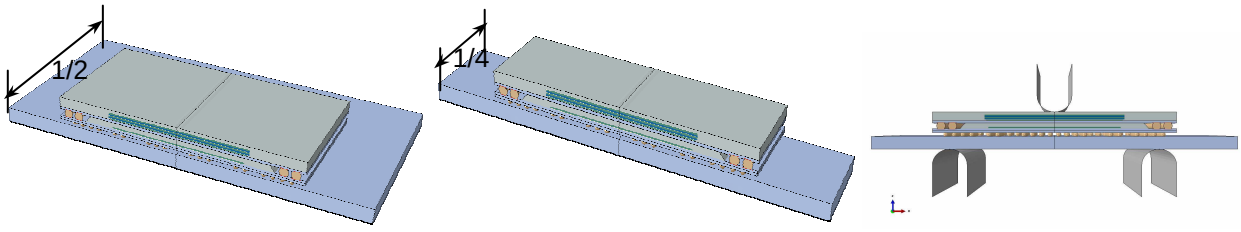

(a) Type A (b) Type B (c) 3-point bending test

Fig. 2 Schematic diagrams of specimens and in 3-point bending test.

3 RESULTS AND DISCUSSIONS

3.1 Failure characterization for type A structure

Figure 3 shows the crack initiation behaviour in the CSP and FBGA structures. It is clearly seen that the crack preferentially occurs at the relative brittleness die layer in the top package but not at the adhesive layer (in Mark A as shown in Fig. 3 (a)) when the applied loading and displacement are 42 N and δ=0.054 mm, respectively as shown in Fig. 3 (b). However, the crack is not linearly propagation in micro scale although it is quickly formed in the different die layers. Its transition direction occurs in the nearly adhesive layer of top and bottom of this die, and there are some obvious plastic vestiges at the near crack tips in both top adhesive layers as shown in Fig. 3 (b). It is clear that the cracking mechanism in the die is a mismatch of deformation between the die layer and adhesive layers in top and bottom of die. With increasing the load and displacement (N=72 N, δ=0.277 mm), the crack passes through the multi adhesive layers and either top die or bottom die, subsequently a main crack is formed by using linked up other cracks occurred in other dies as shown in Fig. 3 (c). At the same time, the main crack propagation direction is to deviate from a tensile stress perpendicular to the crack propagation direction. In addition, the plastic deformation and formed a few interface cracks were accompanied in the crack propagation development. Due the full symmetrical characteristic of PoP structure for type A specimen under 3-point bending test, there is a single failure crack to be seen in the cross-section of PoP structure. Therefore, the critical failure load for one die layer is about 40 N and the critical deflection displacement is about 0.05 mm for type A structure. And the critical failure load and critical deflection displacement for CSF structure are 72 N and 0.28 mm, respectively.

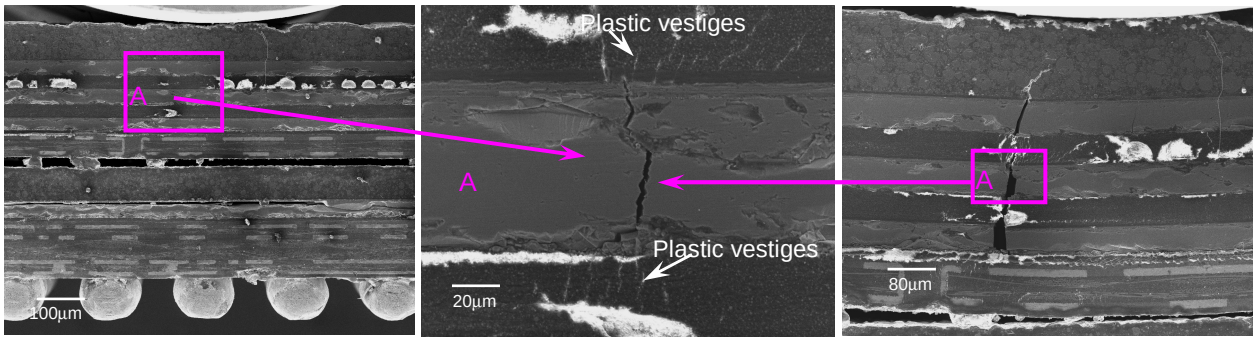

(a) N=0 N, δ=0 mm (b) N=42 N, δ=0.054 mm (c) N=72 N, δ=0.277 mm

Fig. 3 Cracking characterizations of PoP structure under three-point bending

3.2 Failure characterization for type B structure

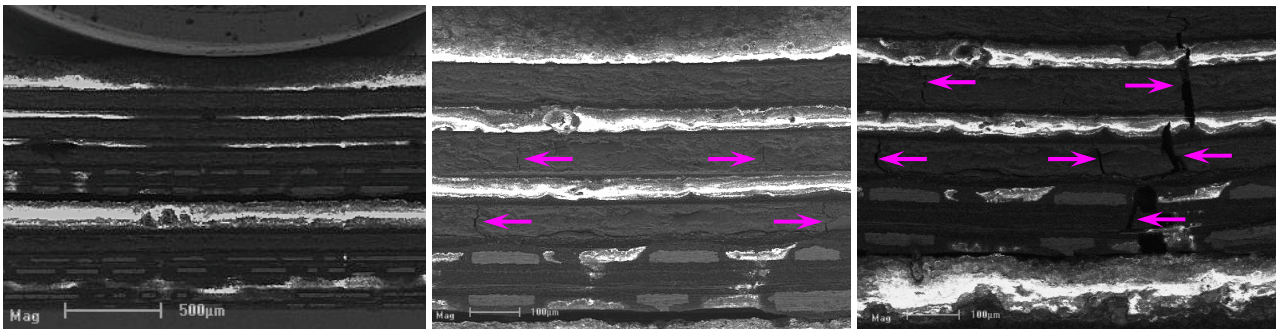

(a) N=0 N, δ=0.0 mm (b) N=7 N, δ=0.11 mm (c) N=14 N, δ=0.21 mm

Fig. 4 Cracking characterizations of PoP structure under three-point bending

Figure 4 shows the cracking characterizations of type B structure under 3-point bending test. When the applied load arrives to the 7 N and the deflection displacement is about 0.11 mm, the multi-cracks occur at the die layers. Compared with the cracking characterization of type A specimen, there are some obvious differences of cracking behaviour. For example, when the deflection displacement for type B specimen

increases obviously, the increase of load is not obvious. In addition, the crack initiation is also preferentially to occur in the dies and the multi cracks occurred in every layer of die. This is because the bending stiffness of type B specimen is rather less than that of type A specimen. That is, the crack initiation behaviour of die should be dominated by the deflection displacement not the applied load. And the effect of adhesive layer on the crack initiation and propagation behaviour is also not ignored. The effect of adhesive layer can be modelling or be explained by the cohesive zone model (CZM) [2,20]. This reflects the fact that a mixed failure model of die attach adhesive is verified based on SEM *in-situ* technology under the 3-point bending test. The stacked CSP can be regarded as a sandwich structure beam. The tensile and shear stresses at the bottom of the die and die attach adhesive layers cause the failure evolution of PoP structure. Therefore, the full failure of type B is about 14 N and deflection displacement is about 0.21 mm. Therefore, for either type A or type B of specimens under 3-point bending loading, the critical failure deflection is approximately same value of 0.20 mm but is not the mechanical parameter of load or stress. This is because there is differently bending stiffness both type A and type B. The deflection displacement of 0.20 mm can be defined as the failure threshold value of PoP structure.

Figure 5 illuminates that the instability of bottom balls to contribute on the crack initiation of die in the bottom package can be not ignored. For example, the die and balls in the FBGA occurred the cracking and instability when the PoP structure is endured by the bending deformation, respectively. Based on the SEM *in-situ* observational results indicated that these failures (both cracking and instability) occurred as in order of instability of balls and crack initiation of die near the bottom balls. However, the geometrical deformations of these bottom balls did not enough resemble as shown in Fig. 5 (a), in which the deformed difference for bottom ball of mark C than that for the bottom balls of mark A and B is much more obvious as shown in Fig. 5 (c). But it is not seen that the interface crack occurs in the top and bottom of deformed ball. That is, the geometrical instability of bottom balls caused enough the brittleness crack initiation and propagation of die. This reflects the fact that the failure of PoP structure is as the order of instability of bottom balls and crack fracture of dies. And the crack initiation seat of die is dependent on the stiffness matching of elements in PoP structure, especially the mechanical parameters and thickness of adhesive layer. This is because the factors of adhesive layer can affect the response or transition of applied loading.

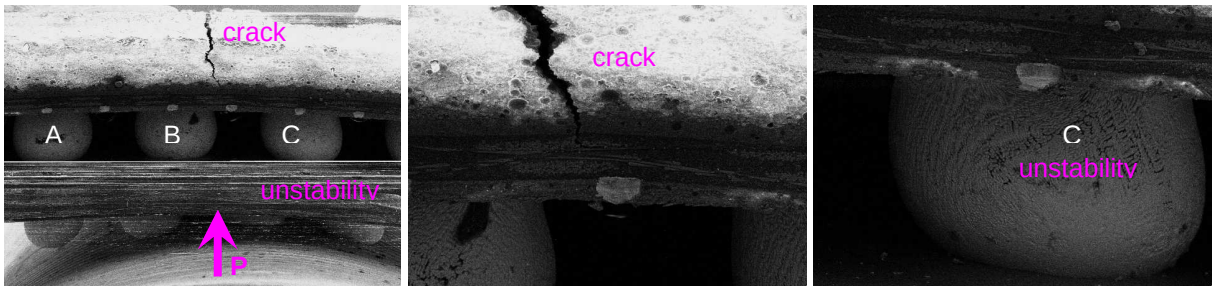

(a) State of failure for FBGA (b) Crack of dia (c) Instability of ball

Fig. 5 Cracking and deformation of FBGA structure under applied load of 23 N

3.3 Numerical simulation on failure stress for PoP structure

The commercial FE software ABAQUS was used to implement the simulation of the failure behaviour of PoP structure in order to understand the failure mechanism. According above mention SEM *in-situ* images and sizes of components, die adhesives with the actual thickness for this PoP structure were carried out, and adhesives element was provided to describe the specification of die adhesives layer as shown in Fig. 1 and the materials constitutive relationship refers the literature [2]. FE modelling under 3-point bending including mesh of all components shows in Fig. 1 and Fig. 6. To reduce the computational cost, a quarter (That is type B specimen as shown in Fig. 2 (b)) of the symmetric geometrical model was created, and three parts (CSP, FBGA and PCB) of PoP structure were partitioned to facilitate the refined mesh. In the FE model, there different layers including three die layers of Die A, Die B and Die C, and die adhesive layers of DA1, DA2 as well as top substrate in CSP structure. In addition, there are layers including one die layer, bottom balls layer and substrate, as well as PCB layer in FBGA structure. When the different applied loads act on the PCB during 3-point bending test, the relationships between the stress response values of elements and displacement (X) away from catch point are shown in Fig. 7 (a) and (b), respectively. With increasing of X displacement away from catch point, the tensile loading of Die C layer increases obviously (to arrive at 250 MPa) and the tensile loading of Die A and B layers is less than about times of 1/5 compared with the tensile loading value of Die C layer so that the crack occurred in the region of Die C

layer is not difficult to understand. At the same time, the simulation result agrees good with the experimental results as shown in Fig. 4 (b), in which the multi cracks occurred at the Die C and Die B, but the cracks in Die C is longer than that in Die B. However, the simulation results in FBGA structure indicated that the maximum tensile stress in PCB is about 40 MPa than that in other components including the one die layer in FBGA which is much less than that in CSP. It means that the bottom balls influence strongly on the response of loading in FBGA structure. This influence is complex stress analysis subsequently it will be investigated. Therefore, the crack fracture of PoP structure occurs easily in CSP but the instability failure occurs easily in FBGA. Compared with crack fracture and instability failure of PoP structure, the crack fracture of CSP much more easily reduce its reliability than that of instability of FBGA.

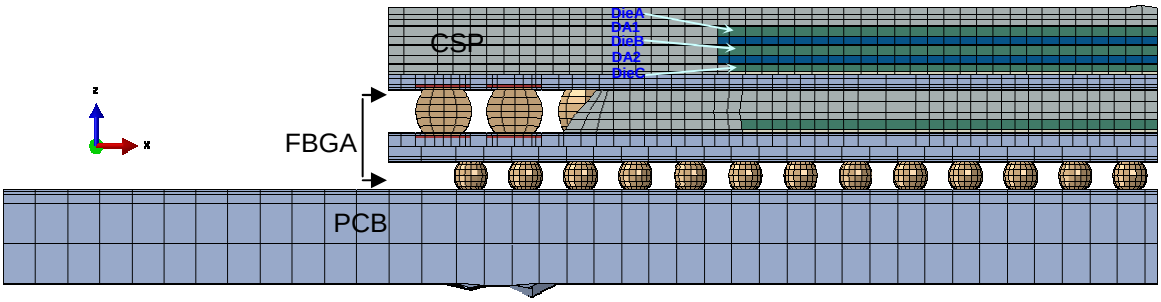

Fig. 6 Simulation model of PoP structure for type B specimen

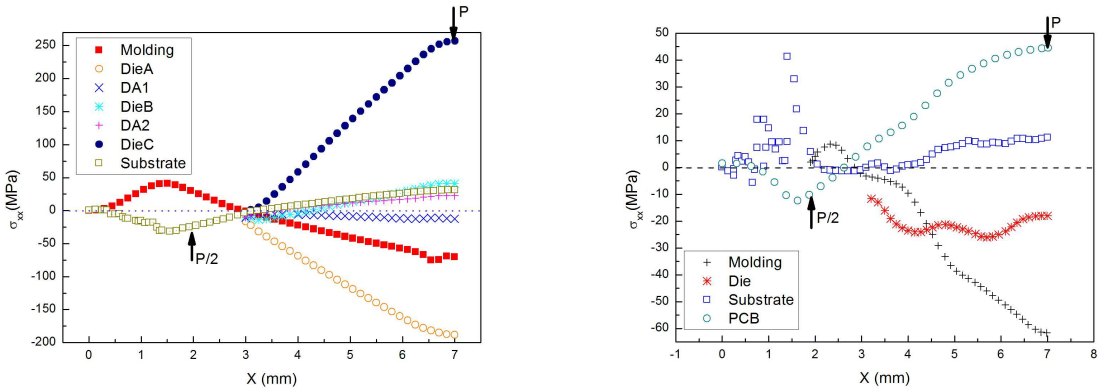

(a) Stress response values of elements in CSP. (b) Stress response values of elements in FBGA.

Fig. 7 The relationships between the stress response values of elements in PoP structure

4 CONCLUSIONS

SEM *in-situ* observation method used to investigate the failure process of PoP structure under three-point bending loading and FE analysis based on the cohesive zone model are carried out. The conclusions are drawn as follows:

1) The cracks occur mainly in dies in CSP, in which there are obvious difference of cracking behaviour for type A and type B. This is because the effect of bending stiffness on the cracking behaviour can be not ignored. These cracking characterizations (the main crack and multi cracks occur in different die layers for different type specimens, respectively) indicate that the dominated parameter is displacement but not loading. It is quantificationally estimated that the failure threshold value of PoP structure under three-point bending test is 0.20 mm. At the same time, the effect of the mechanical property and thickness of adhesive layer between both dies on the resistance and direction of crack propagation is obvious.

2) There are two failure models of PoP structure under three-point bending loading, which are crack fracture model in CSP and instability model in FBGA, respectively.

3) Compared with the two failure models of crack fracture and instability, the crack fracture of CSP much more easily reduce the reliability of PoP structure than that of instability of FBGA.

4) SEM *in-situ* technology combined with FE analysis method is suit for to predicate and estimate the failure model and fracture criterion of PoP structure.

5 ACKNOWLEDGEMENTS

The authors would like to acknowledge the supports of NSFC's projects (Grants No: 11072124, 11272173) and National Basic Research Program of China (Grant No: 2010CB631006).

13 REFERENCES

[1] E. Suhir, Could electronics reliability be predicted, quantified and assured? Microelectronics Reliability 53(7), 925-936, 2013.

[2] H.H. Ren, X.S. Wang, S. Jia, Fracture analysis on die attach adhesives for stacked packages based on in-situ testing and cohesive zone model. Microelectronics Reliability 53, 1021-1028, 2013.

[3] L. Smith, M. Dreiza, A. Yoshida, Package on Package (PoP) stacking and board level reliability results. Proceedings of SMTA International Conference, p.306-312, 2006.

[4] M. Dreiza, A. Yoshida, K. Ishibashi, T. Maeda, High density PoP and package stacking development. Proceedings of 57th Electronic Components and Technology Conference, Reno NV, p. 1397-1402, 2007.

[5] J.Y. Lee, T.K. Hwang, J.Y. Kim, M. Yoo, E.S. Sohn, J.Y. Chung, Study on the board level reliability test of package on package with 2nd level under fill. Proceedings of 57th Electronic Components and Technology Conference, Reno NV, p. 1905-1910, 2007.

[6] S. Stankovic, R. Jones, J. Heck, M. Sysak, V.D. Thourhout, G. Roelkens, Die-to die adhesive bonding procedure for evanescently-coupled photonic devices. Electrochemical Solid ST 14, 326-329, 2011.

[7] X.S. Wang, X.D. Li, H.H. Ren, Y.L. Chen, SEM in situ study on high cyclic fatigue of SnPb-solder joint in the electronic packaging. Microelectronics Reliability 51, 1377-1384, 2011.

[8] X.S. Wang, Y.Q. Li, S.W. Yu, Evaluation of thermal-mechanical fatigue behaviour for 62Sn38Pb bulk solder. Experimental Techniques 27, 31-34, 2003.

[9] X.S. Wang, X.W. Guo, X.D. Li, N. Kawagoishi, Effects of different micro-arc oxidation coating layer types on fatigue life of 2024-T4 alloy. 13th International Conference on Fracture, June 16-21, Beijing, China, 2013.

[10] X.S. Wang, Y. Li, X.K. Meng, An estimation method on failure stress of micro thickness Cu film-substrate structure. Science in China Series E: Technological Science 52(8), 2210-2215, 2009.

[11] Y. Li, X.S. Wang, X.K. Meng, Buckling behaviour of metal film/substrate structure under pure bending. Applied Physics Letters 92(13), 131902, 2008.

[12] X.S. Wang, C.K. Yan, Y. Li, Y.B. Xue, X.K. Meng, B.S. Wu, SEM in-situ study on failure of nanocrystal metallic thin films and substrate structure under three point bending. International Journal of Fracture 151, 269-279, 2008.

[13] J.G, Huang, X.S. Wang, X.K. Meng, SEM in situ study on deformation under three-point bending loading in Cu and Cu/Ni films. Materials Transactions 48(10), 2795-2798, 2007.

[14] S. Jia, X.S Wang, H.H. Ren, Experimental and theoretical analysis of package (PoP structure under there points bending loading. Chinese Physics B 21(12): 126201, 2012.

[15] X.S. Wang, M. Zhang, X.P. Song, S. Jia, Q. Chen, N. Kawagoishi, Fatigue failure mode of TiAl alloy with high Nb content at different temperatures. Materials 5(11), 2280-2291, 2012.

[16] X.D. Li, X.S. Wang, H.H. Ren, Y.L. Chen, Z.T. Mu, Effect of prior corrosion state on the fatigue small cracking behaviour of 6151-T6 aluminium alloy. Corrosion Science 55, 26-33, 2012.

[17] X.S. Wang, J.H. Fan, An evaluation the growth rate of small cracks in cast AM50 magnesium alloy at different temperatures in vacuum environment. International Journal of Fatigue 28(1), 79-86, 2008.

[18] X.S. Wang, F. Liang, J.H. Fang, F.H. Zhang, Investigations on low-cycle fatigue small crack initiation and propagation mechanism of cast magnesium alloys based on in-situ observation with SEM. Philosophical Magazine 86(11), 1581-1596, 2008.

[19] M. Dreiza, A. Yoshida, K. Ishibashi, T. Maeda. High density PoP (package on package) and package stacking development. In: Proceedings of 57th electronic components and technology conference, Reno, NV; May p.1397-1402, 2007.

[20] I. Scheider, W. Brocks. The effect of traction separation law on the results of cohesive zone crack propagation analysis. Key Eng. Mater. 251-252, 313-318, 2003.

Proceedings of the 3rd International Conference on
Fracture Fatigue and Wear, pp. 25-31, 2014

STRENGTH OF ADHESIVE JOINTS OF EPOXY COMPOSITES WITH DISSIMILAR ADHERENDS

A. Rudawska

Lublin University of Technology, Lublin, Poland

Abstract: This paper presents strength test results of adhesive joints of epoxy polymer composites with dissimilar adherends. The analysis was conducted on epoxy-glass, epoxy-aramid and graphite-epoxy composites forming adhesive joints with dissimilar adherends. Epoxy-aramid adhesive joint strength test results allow to conclude that when combined with other composites of the same type, however, formed with a different laminate, epoxy-aramid composites produce higher strength than when combined with a different type of composite. Similarly in strength tests of graphite-epoxy composites, higher strength values were produced by joining the same composite type differing in the type of laminate used to produce it and, in this particular case, in thickness. It can be, therefore, seen that in the majority of the analysed configurations, higher strength values are obtained when the same type of composite, in terms of matrix, yet differing in specific characteristics, rather than by joining different composites. It appears that configurations comprising the same composite promote beneficial adhesive properties, which in turn contributes to higher joint strength, as compared to configurations of different composites.

Keywords: adhesive joints; strength; epoxy composites

1 INTRODUCTION

At present, composites are a material in great demand. One of outstanding features of composite materials is that their properties can be designed. Structural composites comprise a big and diverse group of composite materials. There exists a great variety of component types, which can be used to create composites, the variety of shape and size options for the reinforcement material as well as different technologies of making composites. Nevertheless, all structural composites share a common feature, namely high strength indices, achieved through a careful selection of components. Many composite materials are based upon epoxy resin. Therefore the epoxy polymer composites were tested in this paper.

The choice of a suitable composite is predominantly dictated by conditions of operation; for instance, where environmental conditions require high abrasion resistance or high thermal resistance, metallic matrix composites may be applied. However, when high-temperature conditions are expected, ceramic matrix composites are used [1,2].

The literature devoted to adhesive joining technology related issues, offers plenty information regarding forming adhesive joints (and other adhesive bonds) of the same composite material [3,4]. What has been noted is that recent years indicate a tendency towards joining various types of structural materials of different physical, mechanical or chemical properties; in such a case it is adhesive joining which provides measures to form the joints. In addition, at times it is necessary to join the same material, however, of different dimensions (e.g. thickness). It appears that the type of adherend, together with its various qualities, in such hybrid configurations might be one of the factors relevant for the strength of such a joint. Lots of advantages of adhesive bonding to others form of joining are in improved mechanical response and the ability to bond dissimilar materials [5,6]. Therefore, it appears that the type of adherend, together with its various qualities, in such hybrid configurations might be one of the factors relevant for the strength of such a joint.

Some authors [7] presented lots of problems of composite adhesive joints modelling with dissimilar adherends. Liljedahl et al. [5] presented the some information about modelling of lap shear joints of similar and dissimilar substrates. The one of tested joints was the carbon fibre reinforced polymer (CFRP)

composites and also adhesive joints with dissimilar adherends: aluminium-cfrp-aluminium. Budzik et al. [6] analysed composite-aluminium joints bonded with a slow-curing DGEBA-PAMAM adhesive system.

2 MATERIALS AND METHODS

2.1 Characteristics of joining materials

Conducted research involved different types of epoxy polymer composites: epoxy-glass, epoxy-aramid and graphite-epoxy, the characteristic of which is presented in Table 1.

Table 1 Tested polymer composites characteristics.

No.	Name	Single laminate layer thickness [mm]
1.	Composite 1 – glass laminate 3200-120	0.14
2.	Composite 2 – glass laminate 3200-7781	0.30
3.	Composite 3 – aramid laminate KV-EP 285 199-46-003	0.30
4.	Composite 4 – aramid laminate KV-EP 285 199-46-002	0.30
5.	Composite 5 – graphite laminate GR-EP 199-46-003	0.24
6.	Composite 6 – graphite laminate GR-EP 199-45-003	0.33

The composite substrates were composed of two laminates (2 layers), positioned at an angle of 90° (layer arrangement: [0/90]) and subjected to curing as per technology. The aforementioned composites find application in the aircraft industry as a material for structural elements used in aircraft parts production. The samples of graphical representation of polymer composites surface is shown in Figs. 1 to 3. The presented 3D profiles present substantial differences in the analysed composites topography.

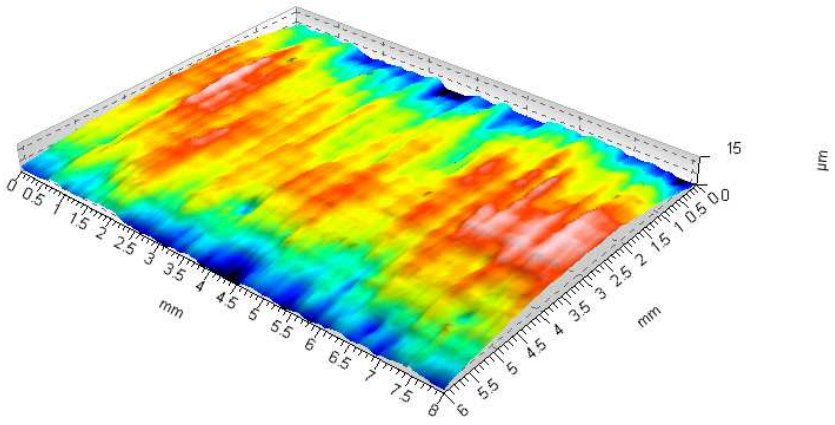

Fig.1 The surface of glass-epoxy composite (1), 3D profiler.

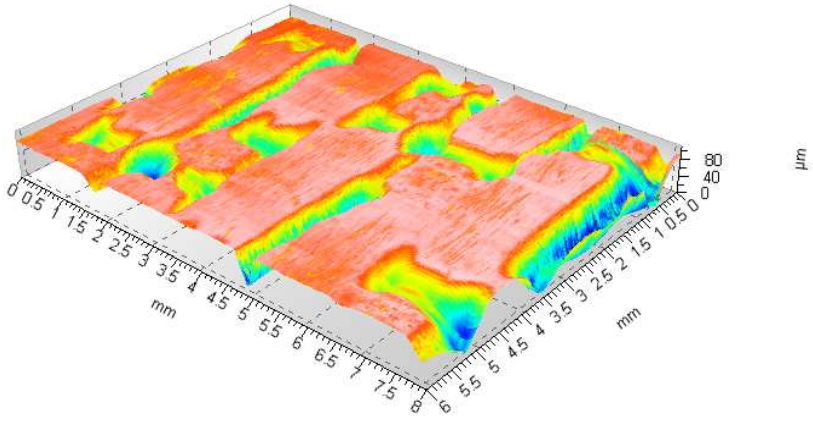

Fig. 2 The surface of glass-epoxy composite (3), 3D profiler.

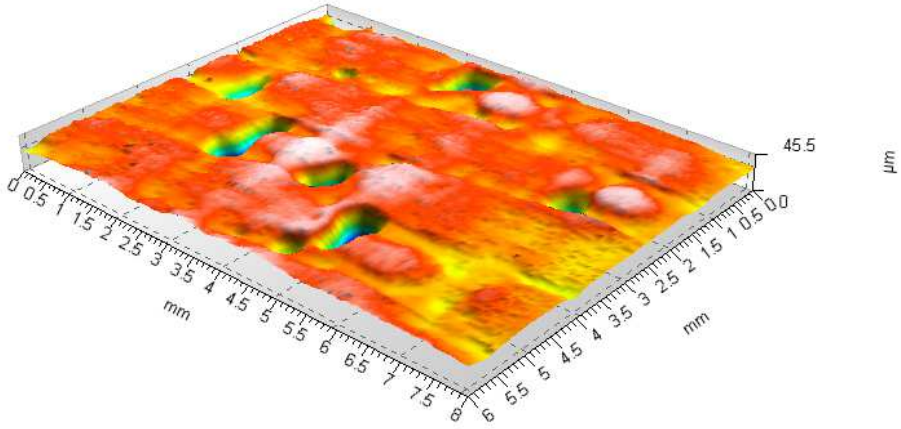

Fig. 3 The surface of glass-epoxy composite (5), 3D profiler.

2.2 Characteristics of adhesive joints

Single-lap adhesive joints of epoxy composites were the subject of experimental tests. The analysed composites were used in hybrid adhesive joints in two configurations: the first consisting of composites of the same laminate, the other, of different laminates.

The characteristics of the joints are as follows:

Group I:

1) epoxy-glass composite '1' - epoxy-glass composite '2';
2) epoxy-aramid composite '3' – epoxy-aramid composite '4';
3) graphite-epoxy composite '5' - graphite-epoxy composite '6';

Group II:

4) epoxy-glass composite '2' - epoxy-aramid composite '3';
5) epoxy-glass composite '2' - graphite-epoxy composite '6';
6) epoxy-aramid composite '3' - graphite-epoxy composite '6';
7) epoxy-aramid composite '4' - graphite-epoxy composite '6'.
8) The model of formed adhesive joints is presented in Fig. 4.

Adhesive joint dimensions were as follows: samples length *ls* = 100±0.8 mm, sample width *ws* = 20±1.02 mm and adhesive layer thickness *ta* = 0.10±0.02. Adherends thickness (samples) *ts* depends on the kind of composites and equals from 0.28±0.02 mm to 0.66 ±0.02 mm. Adhesive joint lap length *la* depends on the kind of composites and adherends thickness and equals from 4.0±0.2 to 8.0±0.2 mm.

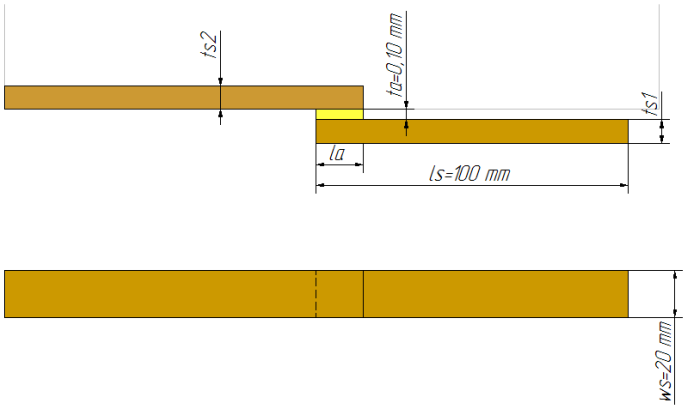

Fig. 4 Tested adhesive joints

2.3 Conditions of forming joints

Test specimens were joined with a two component epoxy adhesive Loctite Hysol 3430. Loctite Hysol 3430 is a two component epoxy adhesive which, once mixed, cures rapidly at room temperature. Elevated temperature may be used to accelerate the cure. Cure time at 22°C is equal to 24 h. It is a general purpose adhesive providing high strength on a range of materials. Some information about this adhesive is presented in [8]. The surface of epoxy composites was subjected to degreasing treatment with using Loctite 7063 degrease agent [9].

For each variant of adhesive joints it was prepare 10 adhesive joints. Adhesive joints were formed at ambient temperature equal to 20± 2°C and humidity equal to 40 ± 2%. Once mixed, the adhesive was applied as quickly as possible to the adherend surface. Formed adhesive joints were subjected to curing processes at ambient temperature for 24 hours. The samples were afterwards subjected to pressure of 0.02 MPa. Conditioning time is 48 hours.

After conditioning time, the joints were subjected to destructive tests, which allowed to determine joint failure force values and adhesive joint shear strength. Tests were conducted on a test stand – materials testing machine Zwick/ Roell Z150 Allround-Line (Fig. 5) according to standard DIN EN 1465 [10]. The rate at which shear tests were carried out was 5 mm/min.

Fig. 5 Testing machine Zwick/ Roell Z150 Allround-Line.

3 RESULTS

Strength test results for the enumerated hybrid composite configurations are presented in Fig. 6 and Fig. 7.

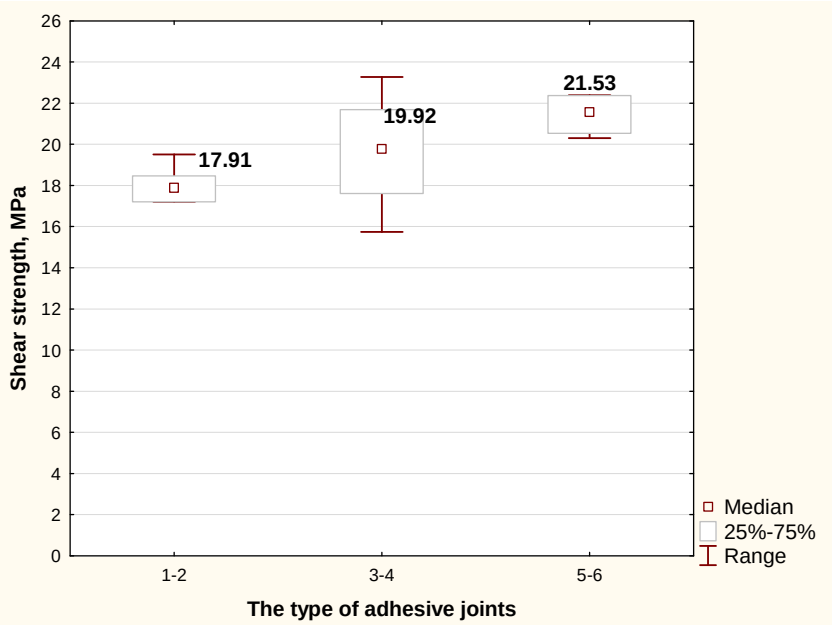

Fig. 6 Shear strength of polymer composite adhesive joints: 1 – glass-epoxy (1) and glass-epoxy (2), 2 – aramid-epoxy (3) and aramid-epoxy (4), 3 – graphite-epoxy (5) and graphite-epoxy (6).

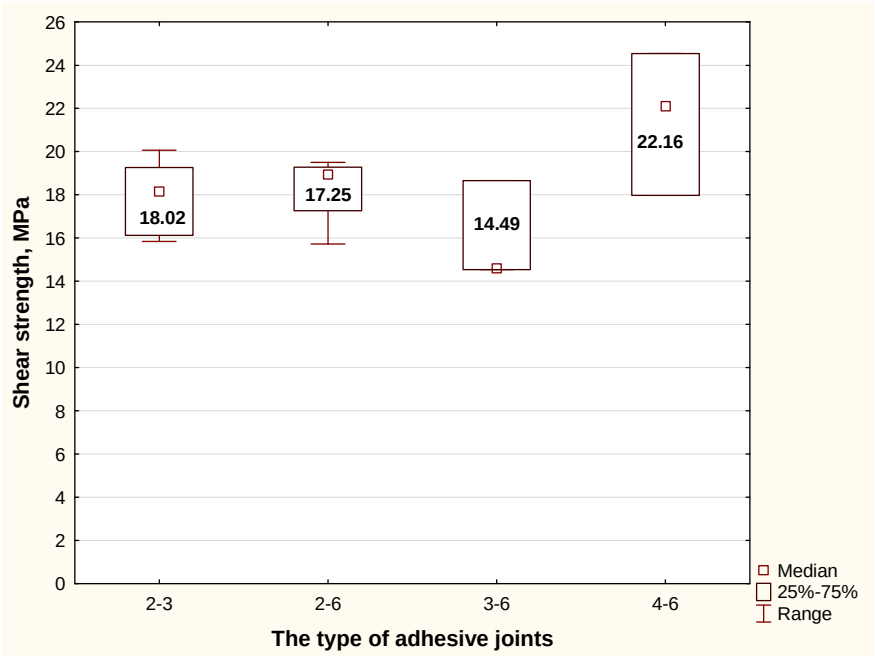

Fig. 7 Shear strength of polymer composite adhesive joints: 1 – glass-epoxy (2) and aramid-epoxy (3), 2 – glass-epoxy (2) and graphite-epoxy (6), 3 – aramid-epoxy (3) and graphite-epoxy (6), 4 – aramid-epoxy (4) and graphite-epoxy (6).

The presented test results data presented in Fig. 6 indicates that the highest strength value, and simultaneously the lowest standard deviation, was achieved in the case of graphite-epoxy composites, whereas the lowest strength was noted in joint configurations with a glass-epoxy adherend. Hence a substantial influence of the selection of materials on joint strength can be indicated. What was noted in the case of the aforementioned composites was the considerable difference in adherends thickness, which

resulted from the formed composite (Table 1). In epoxy-aramid hybrid configuration, however, both adherends were of the same thickness.

It was noted that the standard deviation of adhesive joints strength is the highest for aramid-epoxy composites. The range of strength value is from 15.74 to 23.27 MPa. But for another joints the range of strength value is less. Probably it results from the properties of joining materials. Presumably for this case of joints configuration it will be difficult to obtain the repeatable value of adhesive joints strength. During forming of these joints it could be noticed the precision of forming joints.

Strength test results in Fig. 7 show that it was epoxy-aramid and graphite-epoxy configuration which achieved the highest strength, whereas the lowest was observed in epoxy-glass and graphite-epoxy configurations. For epoxy-glass based hybrid configurations the increase in strength value was visible when joined with epoxy-aramid composite, rather than with another epoxy-glass one (Fig. 7 pos. 2-3) or graphite-epoxy (Fig. 7 pos. 2-6). The similar range of adhesive joints strength of dissimilar adherends was obtained.

In case of epoxy-aramid and graphite-epoxy configuration (Fig. 7 pos. 3-6 and 4-6) the strength is different.

The strength of epoxy-aramid (3) and graphite-epoxy (6) adhesive joints is 66% the strength value of epoxy-aramid (4) and graphite-epoxy (6) adhesive joints. It was the same types of joining composites (epoxy-aramid and graphite-epoxy composites), the same the thickness of adherends in particular configurations but the type of aramid laminate was different. So, it could be supposed that the type of laminate has influence on adhesive properties of surface composite and adhesive joints strength.

4 CONCLUSIONS

Analysis of the results obtained for epoxy-aramid composites leads to the observation that by joining two types of this composite, however, differing in terms of the laminate used in production, contributes to higher strength when compared with epoxy-aramid joined with other types of composites tested. Similarly in the case of graphite-epoxy composites, higher strength is obtained by joining the same composite material, yet different in both the type of laminate used when produced, as well as in thickness.

All things considered, it becomes apparent that higher strength joints are those of the same type of composite, in terms of matrix, different in terms of certain properties, rather than of different types of composites. It is, therefore, justifiable to conclude that hybrid configurations of the same type of composite display higher strength than in configurations with different composite types.

5 ACKNOWLEDGEMENTS

Scientific study financed from funds for science in the years 2010-2013 as research project No N N507 592538.

6 REFERENCES

[1] C. Ageorges, L. Ye, Fusion Bonding of Polymer Composites, Springer, Great Britain, 2002.

[2] A. Boczkowska, J. Kapuściński, Z. Lindemann, D. Witembeg-Perzyk, S. Wojciechowski, Composites. Printed by Warsaw Technical University, Poland, Warsaw, 2003

[3] A.G. Magalhães, M.F.S.F. de Moura, J.P.M. Gonçalves, Evaluation of stress concentration effects in single-lap bonded joints of laminate composite materials, Journal of Adhesion and Adhesives, 25, 313-319, 2005.

[4] H. Moghadamzadeh, H. Rahimi, M. Asadollahzadeh, A.R. Hemmati, Surface treatment of wood polymer composites for adhesive bonding, International Journal of Adhesion and Adhesives, 31, 816-821, 2011.

[5] C.D.M. Liljedahl, A.D. Crocomble, M.A. Wahab, I.A. Ashcroft, Modelling the environmental degradation of adhesively bonded aluminium and composite joints using a CZM approach, International Journal of Adhesion and Adhesives, 27, 505-518, 2007.

[6] M.K. Budzik, J. Jumel, K. Imielińska, Właściwości połączeń klejonych Al/laminat epoksydowy ze wzmocnieniem z włókien węglowych, Inżynieria Materiałowa,1, 42-46, 2008.

[7] P. Molitor, V. Barron, T. Young, Surface treatment of titanium for adhesive bonding to polymer composites: a review, International Journal of Adhesion and Adhesives, 21, 129-136, 2001.

[8] Information on http://www.loctite-kleje.pl.

[9] A. Rudawska, Surface Free Energy and 7075 Aluminium Bonded Joint Strength Following Degreasing Only and Without Any Prior Treatment, Journal Adhesion Science and Technology, 26, 1233-1247, 2012.

[10] Standard DIN EN 1465. Adhesives. Determination of tensile lap-shear strength of bonded joints.

Proceedings of the 3rd International Conference on
Fracture Fatigue and Wear, pp. 32-33, 2014

LOCAL PERTURBATIONS IN HIGLY PRESTRESSED MATERIALS

D. Bigoni

University of Trento, Trento, Italy

Abstract: Perturbations in the form of concentrated forces or dislocations allow the investigation of the mechanical behaviour of a material on the verge of an internal instability. A three-dimensional solution is presented for an infinite body Green's function, together with the relevant boundary integral equations to calculate the stress field near different kinds of dislocations and inclusions in a pre-stressed material. Results show how failure initiates and develops within nonlinear materials.

Keywords: shear bands; material instabilities; dislocations; Green's functions

1 INTRODUCTION

Subjecting a material element to an increasingly severe homogeneous strain, a number of material instabilities can be observed to occur in a sequential order and to concur or compete to bring the material to failure. A typical example of this behaviour is the sequence of events bringing a bar of mild steel to failure, including: (i) necking, (ii) elastoplastic cavitation, (iii) fracture, (iv) shear banding, and (v) final separation. The analysis of these sequential failure mechanisms permits the understanding of the capabilities of a material to resist loading and therefore it allows an improved design for enhancing mechanical performances.

Among different material instabilities, localized deformations in the form of shear bands are examples of microstructures emerging and self-organizing from a slowly varying deformation field of a homogeneous solid. These are known to be the preferential near-failure deformation modes of ductile materials, so that shear band formation is the key concept to explain failure in many materials and, according to its theoretical and 'practical' importance, it has been the focus of a thorough research effort. In particular, research in this field initiated with pioneering works by Hill [1] and Rice [2] and developed –from theoretical point of view- into two principal directions, namely, the dissection of the specific constitutive features responsible for strain localization in different materials and the struggle for the overcoming of difficulties connected with numerical approaches.

The conditions of shear band formation and related instability mechanisms can be analysed with the perturbative approach [3] introduced by Bigoni and Capuani [4]. Following this approach, a material close to failure conditions is incrementally perturbed, and the response analysed. The perturbation can be a pulsating force dipole [5], a stiff and thin lamina [6], a pre-existing shear band [7], or a dislocation [8], see also [9]. For instance, the effects of a perturbing dipole on a highly pre-stressed ductile metal are shown in Fig. 1.

Until now all explored perturbations have been in 2D. Therefore, the aim of the present work is to analyse the case of a three-dimensional perturbation, in the form of a force dipole. In particular, an infinite-body three-dimensional Green's function set (for incremental displacement and mean stress) is derived for the uniform incremental deformation of an incompressible, nonlinear elastic body. Particular cases of the developed formulation are the Mooney-Rivlin elasticity and the J2-deformation theory of plasticity. These Green's functions are used to develop a boundary integral equation framework, by introducing an 'ad hoc' potential, which paves the way for a boundary element formulation of three-dimensional problems of incremental elasticity. Results are used to investigate the behaviour of a material deformed near the limit of ellipticity and to reveal the pattern of shear band development. Within the investigated three-dimensional framework, localized deformations are shown to be organized in conical geometries, rather than in planar bands, something which can perhaps be expected, but has never been explicitly demonstrated. This result may explain the conical failure zone observable in cylindrical specimen of granular material and may be related to the mechanisms of conical fracturing observed in brittle materials and rocks subject to impact.

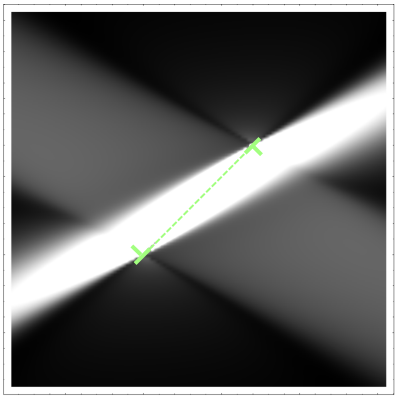

Fig. 1 A perturbation in the form of a dislocation nucleated in a highly-deformed metal produces a localization of strain along a well-defined direction

2 ACKNOWLEDGEMENTS

The author would like to acknowledge the support of the ERC Advanced Grant "Instabilities and nonlocal multiscale modelling of materials" FP7-PEOPLE-IDEAS-ERC-2013-AdG (2014-2019).

3 REFERENCES

[1] Hill, R. Acceleration waves in solids. J. Mech. Phys. Solids 10, 1-16, 1962.

[2] Rice, J. R., The localization of plastic deformation. In Koiter, W.T., ed., Theoretical and Applied Mechanics. Amsterdam, North-Holland, 207-220, 1977.

[3] D. Bigoni, Nonlinear Solid Mechanics - Bifurcation Theory and Material Instability. Cambridge Univ. Press, 2012, ISBN:9781107025417.

[4] D. Bigoni, D. Capuani, Green's function for incremental nonlinear elasticity: shear bands and boundary integral formulation. J. Mech. Phys. Solids, 50, 471-500, 2002.

[5] D. Bigoni, D. Capuani, Time-harmonic Green's function and boundary integral formulation for incremental nonlinear elasticity: dynamics of wave patterns and shear bands. J. Mech. Phys. Solids, 53, 1163-1187, 2005.

[6] Bigoni, D., Dal Corso, F., Gei, M., The stress concentration near a rigid line inclusion in a pre-stressed, elastic material. Part II. Implications on shear band nucleation, growth and energy release rate. J. Mech. Phys. Solids, 56, 839-857, 2008.

[7] Bigoni, D., Dal Corso, F., The unrestrainable growth of a shear band in a pre-stressed material. Proc. R. Soc. A, 464, 2365-2390, 2008.

[8] L. Argani, D. Bigoni, G. Mishuris, Dislocations and inclusions in pre-stressed metals Proc. R. Soc. A 469 no. 2154, 2013.

[9] Information on http://www.ing.unitn.it/~bigoni/.

Proceedings of the 3rd International Conference on
Fracture Fatigue and Wear, pp. 34-39, 2014

EFFECT OF ATMOSPHERIC PLASMA TORCH ON BALLISTIC WOVEN ARAMIDE

M.A. Martínez and J. Abenojar

Universidad Carlos III de Madrid, Leganés, IAAB, Spain

Abstract: The atmospheric plasma torch (APPT) is a cold plasma technique that can be used to treat materials with a polymeric surface in an environmentally friendly way. The treatment indeed modifies the topography and chemistry of the surfaces. In this work, the effect of APPT on aramid fibres used for ballistic fabrics is studied. The shielding laminated with several layers of woven and resin can better resist the projectiles penetration. The greater degree of penetration of the adhesive between the woven fibres offers higher resistance. Aramid woven have low wettability due to their high apolarity and, therefore, the adhesives penetrate the woven fibres with difficulty. APPT treatments increase considerably the polar component of the surface energy and its wettability is improved. In this paper, changes in micro- and nanotopography and in chemical composition are studied, which justify the improvement in the adhesion properties. The adhesion ability with an elastic (polyurethane based) and a rigid (epoxy based) adhesive were determined by adhesion tensile test, T-peel test and impact test.

Keywords: woven aramid; wettability; atmospheric pressure plasma; T-peel test, adhesion tensile test; impact test

1 INTRODUCTION

The wettability characteristics of reinforcement fibres have received great interest due to the strong relationship between the mechanical behaviour of composite material and the fibber matrix-adhesion [1].

Aramid fibres are hot melt Nylon-6,6 derivatives and were first developed in 1965 by Du Pont [2], they present high resistance and low specific weight [3]. They are mainly used in ballistic woven for both flexible and rigid light shield applications. The aramid materials with rigid characteristics are formed by several layers of woven fibres bonded by a polymeric matrix, such as polyester, vinylester, phenolic, epoxy, polyurethane resins, etc., in 9 to 20 wt.%

It has been reported that laminated shields made out of a resin exhibit higher penetration resistance [4] both working at low and high impact speed [5]. This resistance is expected to be a function of the grade of penetration and humectation of the adhesive between the woven fibres [6].

Taffeta type cloths are formed by wavy fibres, thus the energy of a projectile is dissipated with the fibber deformation, shear delamination [7] and fibber breakage (Fig. 1A), causing a reduction in resistance. In order to increase the protection ability against the impact of high energy projectiles, high density ceramic components could be bonded to the surface (Fig. 1B) [5]. However, the adhesion of these materials to the aramid surface is hindered by the fibber low wetting properties.

Due to the aramid low surface energy, low cohesion between layers and the ceramic is obtained, thus fracture energy is low as well.

The treatment of aramid fibres with low pressure oxygen or ammonia plasma are used to modify the material hydrophilic behaviour by creating oxygen and/or nitrogen containing groups [8,9] and increasing the material nano-roughness as a function of treatment time [10,11]. However, the generated UV radiation results in a degradation of the fibber resistance, especially between 300 and 400 nm [2] in a discontinuous process where samples have to be treated under vacuum.

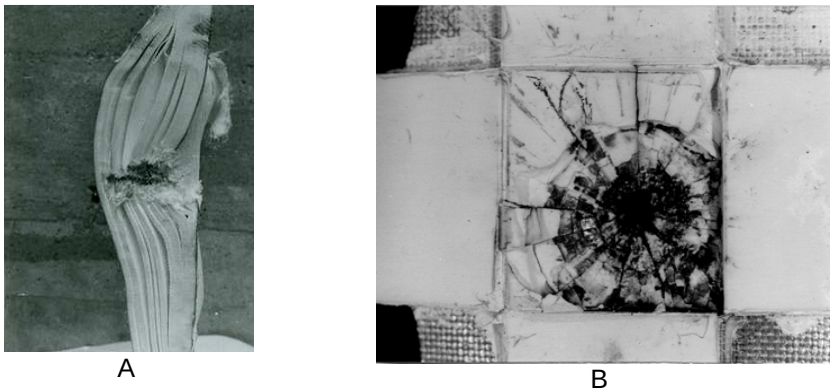

A B

Fig. 1 (A): Delamination and fracture of fibres after the impact of a projectile on an aramid-epoxy rigid shield. B) Impact of a projectile on a rigid layer-ceramic shield [5**Error! Bookmark not defined.**].

On the other hand, atmospheric pressure plasma (APPT) allows treating polymeric surfaces without affecting bulk properties in a fast and environmentally friendly way [12,13]. A compressed air flux is ionized by the action of two electrodes (Fig. 2), modifying the surface when expelled through the nozzle. The creation of hydroxyl and amine type functional groups translates into a higher interaction with the adhesive [14]. This process also presents the industrial advantage of avoiding the vacuum step, thus an in-line procedure can be implemented.

2 EXPERIMENTAL PROCEDURE

2.1. Materials

Taffeta woven aramid material with fibber orientation at 0 and 90º was used, provided by DuPont (Barcelona, Spain). Their main characteristics are shown in Table 1. The used adhesives are elastic polyurethane (SIKAFLEX-252, provided by SIKA S.A.U. Spain) and a rigid epoxy (ARALDITE RAPID provided by Ciba-Geigy, S.A. Spain).

Table 1 Test woven

Fibber	Denier	Threar (nº/cm)	Density (g/cm^2)
Kevlar 129	840	8.5	190

2.2 Atmospheric pressure plasma treatment (APPT)

Material was treated with a device operating at a frequency of 50/60 Hz, 230 voltage and 16 A (PLASMATREAT GMBH, mod. FG 3001, Steinhagen, Germany).

High energy condition (6 mm, 100 mm/s) was tested, without observing a change in colour of the material, which would be indicative of UV radiation degradation (Fig. 2).

2.3 Contact angle and surface energy calculations

Diiodomethane, distilled water and glycerol were the selected liquids for the test, covering a wide range of polar and disperse fractions

Contact angle measurements were performed on the pristine and APPT treated samples. For the contact angle measurements a goniometer Dataphysics Contact angle system OCA 30-2 from DataPhysics Instruments (GmbH, Filderstadt, Germany) was used. The model is able to measure in a range of 1-180º with an accuracy of ± 0.5º. The instrument contains a 3x zoom and a software SCA 202 V.3.11.13 build 162.

The surface energy is calculated with the Owens-Wendt-Rabel-Kaeble method.

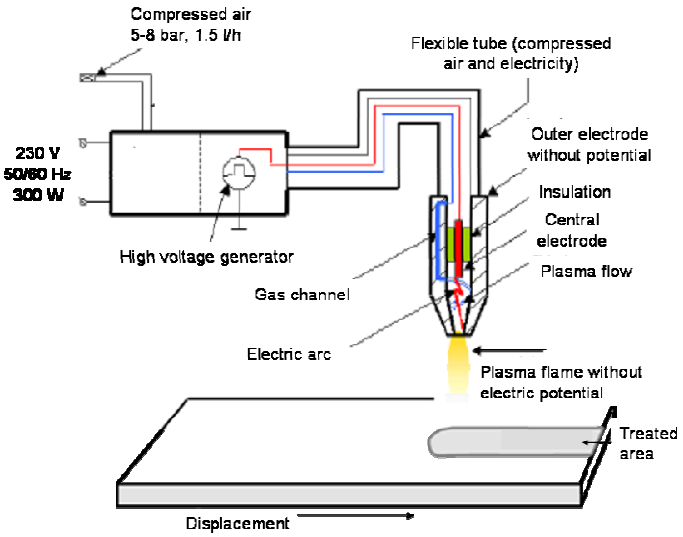

Fig. 2 Atmospheric plasma torch scheme

2.4 Mechanical tests

The quasi-static tests were carried out with a Microtest (Microtest, Madrid, Spain) machine provided with a 1 kN load cell.

Adhesion tensile tests were performed in order to ensure that APPT treatment improves the adhesion strength of rigid materials used for shielding steel or ceramic materials. On the other hand, tensile test method is used to determine the force required to separate an aluminium dolly (20 mm diameter) fixed to a reduced area of the material. The test was performed following the ASTM D 4541 standard. The procedure in this standard was developed for metal substrates, but it may also be suitable for other rigid substrates such as some type of polymers and wood. Woven specimens of 50x50 mm were previously bonded with a rigid adhesive aluminium sheet (to maintain its rigidity) as shown in Fig 3(a). Once the bonding had been cured, the system was tested with the tensile test (relative to the plane of the adhesive bond) at a speed of 1mm/min. The T-peel test was used to prove the resistance variation of the adhesive bonding after plasma treatment. Woven specimens (formed by two pieces) of 40x80 mm were also used, bonded by adhesive (Fig. 3(b)), according to the standard ASTM D1876-08Impact test.

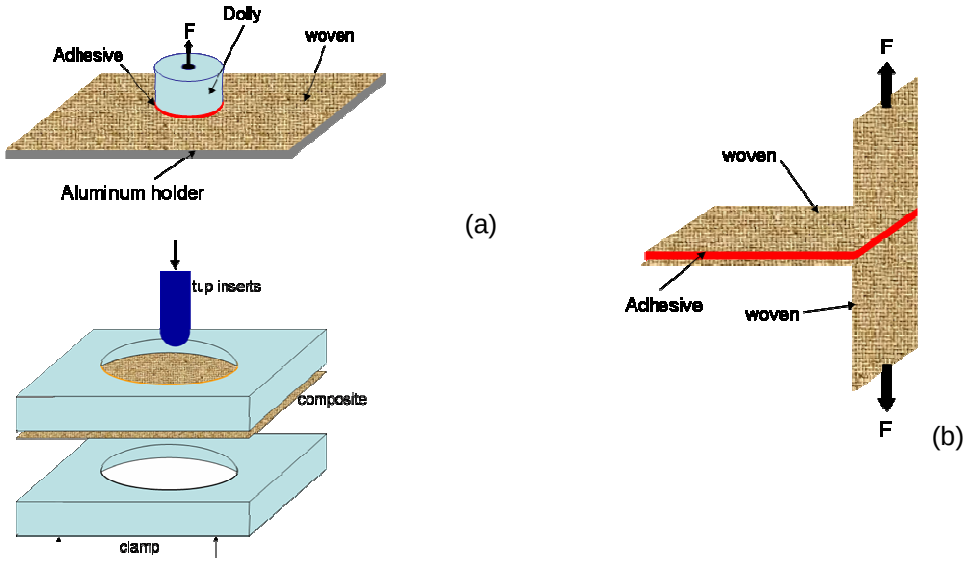

Fig. 3 (a) Adhesion tensile test, (b) T-peel test, (c) Impact test

In this study, 10 samples per condition were tested. The average value of the measurements was obtained by eliminating outliers following the Grubbs method (ASTM E-178:2008). Consequently, applying the Student statistic for small populations, confidence limits of 95% were obtained [15].

Dynamic tests were conducted following the ASTM D 5430 98 standard and a drop-tower impact system (CEAST 9350, Instron Barcelona, Spain). Exploiting suitable instrumentation, the load on the specimen is continuously recorded as a function of time and/or specimen prior to the fracture.

A 3220 g, 20 mm diameter, semi-spherical tube insert was used. 78x78 mm five-layer-woven composites (with and with no APPT treatment) were prepared. The matrices were made of EP (epoxy) and PU (polyurethane) and the samples were set between two clamps with an open surface of 55 mm diameter (Fig. 3(c)).

3 RESULTS AND DISCUSSION

Untreated samples show high contact angle values (above 100º), which is related to a marked hydrophobic behaviour. After the APPT, all the measured values decrease due to the functionalization of the surfaces. The creation of oxidized groups increases the polar fraction of the surface energy, so water and glycerol contact angles decrease in a higher extent than the almost purely disperse diiodomethane.

According to Table 2, surface energy results for the untreated aramid samples present low values and a disperse behaviour. When the fibres are modified by APPT, surface energy reaches values of 52.37 mJ/m^2. This large increase is based on a much more polar character of the woven (increment 90.3%).

Table 2 Variations of surface energy fraction of woven samples untreated and treated with APPT. units are (mJ/m^2)

Surface energy fraction	Untreated	Treated
E_{total}	4.27	56.64
E_{polar}	0.15	51.16
E_{disp}	4.12	5.48

As explained above, this improvement in polarity is caused by two main effects on the aramid fibres surface.

a) Surface chemistry is changed by functionalization with oxygen and/or nitrogen containing groups exhibiting a polar character.

b) SEM micrographs of fibres before and after APPT are observed in Fig. 4. Woven treated with APPT show a smoothening at a micro-scale. An improvement in roughness in some fibres was produced thanks to the creation of grooves as a consequence of to the impact of plasma flux [16,17]. Therefore, at micro-scale level, the woven follow the same tendency found for other polymeric materials. Nonetheless, at nano-scale level, an increase in nano-roughness was found as in other polymers [8].

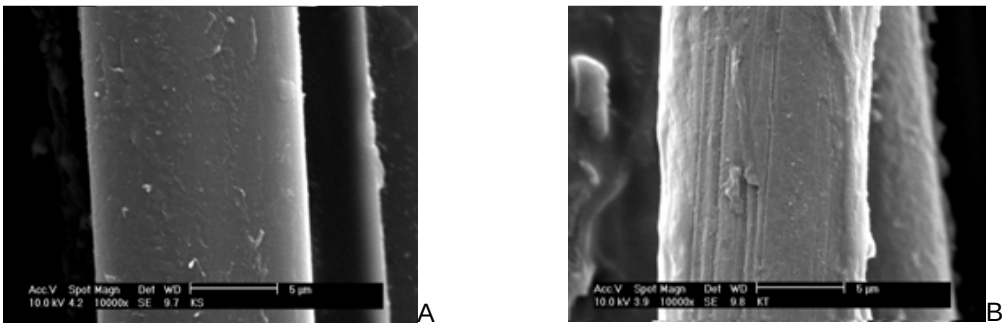

Fig. 4 Kevlar 49 fibres untreated (A) and plasma modified (B).

In view of these results, the adhesion of this tissue with other elements was studied with tensile adhesion test. In Table 3, the obtained values are shown, together with their confidence interval limits.

Table 3 Adhesion tensile test results, measurements in kPa

Adhesive	Untreated	Treated
PUR	306.5 ± 42.7	779.9 ± 113.9
EP	415.2 ± 97.	765.4 ± 169.5

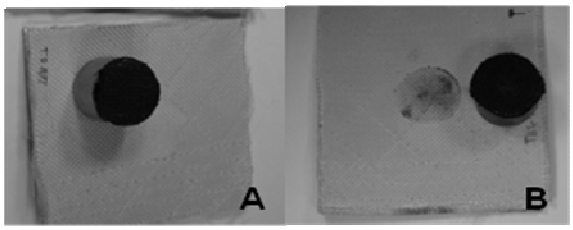

Fig. 5 Samples after tensile test using PUR adhesive. A) Adhesive failure in untreated woven. B) cohesive failure in woven with APPT

In spite of the large data scattering, differences in the type of failure are observed (Fig. 5). With the two adhesives, adhesive failure is obtained in untreated samples (Fig. 5A), and mixed or cohesive in treated samples (Fig. 5B), with a significant increase in bond strength.

The average values in the T-peel test according to the number of threads are presented in Table 4.

Table 4 Mean values obtained in T-peel test and confidence limits. Measurements in N / thread

Adhesive	Untreated	Treated
PUR	0.632 ± 0.1815	1.474 ± 0.1458
EP	1.648 ± 0.1806	2.947 ± 0.45175

The dynamic tests on composites with EP matrix showed that the energy absorbed for delamination is higher for the woven are treated with APPT. On the other hand, for composites with PU matrix, the impact energy is completely absorbed through elasto-plastic deformation in all cases, but the maximum produced deformation is bigger in the samples treated with APPT.

APPT produces significant increase in the resistance of the woven/woven joint (Table 4). Once the outliers are excluded, the results show that the test results present a normal distribution with 95% confidence. Furthermore, the APPT treated woven exhibit a significantly higher strength, in spite of the dispersion of the obtained data.

4 CONCLUSIONS

Contact angle measurements show a change from an almost purely hydrophobic character (water contact angle of 130º) of aramid woven to a hydrophilic and polar behaviour after plasma (water contact angle below 40º). Concerning the surface energy, results are improved after modification in a factor of 13, thus better adhesion properties are expected.

The adhesion tensile tests show that after APPT treatment, the joint, between woven and aluminium (PUR and EP) dollies, has a higher mechanical resistance. Therefore, this treatment improves the tissue union with other materials, such as metals or ceramics. After the plasma treatment, the joint breakage is no longer adhesive but becomes mixed o cohesive.

T-peel tests reveal that the resistance of the adhesion between woven layers increases as well when APPT is carried out.

A statistical analysis of the results leads to a normal distribution for the data obtained with 95% probability, which is a reliability level greater than the one obtained for adhesive bonds.

The composites made with APPT treated woven exhibit an enhanced resistance to impacts since the matrix-fibber joint is more resistant.

5 ACKNOWLEDGEMENTS

Authors acknowledge MINECO financial support through the project MAT2011-29182-C02-02

6 REFERENCES

[1] G. Dorey, The Fibre-Matrix Interface and Composite Strength in Composite Materials in Aircraft Structures, D. H. Middleton (Ed.). Longman Scientific and Technical, New York, 1990, pp. 50-68.

[2] Kevlar Aramid Fibber: Technical Guide. E.I. DuPont de Nemours Company Inc., Wilmington, 1992.

[3] M. Jassal, S. Ghosh, Aramid fibres-An overview Indian Journal Fibre Textile Research, 27, 290-309, 2002.

[4] J.B. Mayo, Jr., E.D. Wetzel, M.V. Hosur, S. Jeelani, Stab and puncture characterization of thermoplastic-impregnated aramid fabrics, International Journal of Impact Engineering, 36, 1095-1105, 2009.

[5] C. Navarro, M.A. Martinez, R. Cortes, V. Sanchez, Some observations on the normal impact on ceramic faced armours backed by composite plates, International Journal of Impact Engineering, 13,145-156, 1993.

[6] A. Akdemir, C. Candan, O.S. Sahin, Effects of Production Parameters and Conditioning upon Ballistic Characteristics of Para Aramid Light Armors, Journal of Composite Materials, 42, 2051-2061, 2008.

[7] B.J. Briscoe, F. Motamedi, The Ballistic Impact Characteristics of Aramid Fabrics: The Influence of Interface Friction, Wear, 158 (1-2), 229-247, 1992.

[8] J. Wang, P. Chen, H. Li, W. Li, B. Wang, C. Zhang, N. Ren, Surface characteristic of Poly(p-pheylene terephthalamide) Fibres with Oxygen Plasma Treatment, Surface and Interface Analysis, 40, 1299-1303, 2008.

[9] S.S. Shyu, T.K. Lin, F.H. Su, S.J.Wu, Effect of Plasma Treatment on Reinforcement-Matrix Interaction in Kevlar Fiber/bismaleimide Composites, Polymer Surface Modification, Relevance to adhesion vol. 2. K.L. Mittal (Ed.) VSP, Zeis, 2000, pp. 199-213

[10] D. Freitas; T.R. Ferreira, T.H.C. Costa, M.C. Feitor, C.M. Bezerra, C. Alves Jr., Tratamento em Plasma de Tecido 100% Aramida para Análise de Molhabilidade. Revista. Brasileira de Aplicações de Vácuo, 25 (4), 215-218, 2006.

[11] S. Manolache, H. Jiang, F. Denes, Generation of nanotopographies on polymeric substrates by cold plasmas Polymer Surface Modification: Relevance to adhesion vol. 5. K.L. Mittal (Ed.). Koninklijke Brill NV, 2009, pp. 45-62

[12] N. Encinas, B. Diaz-Benito, J. Abenojar. M.A. Martinez, Extreme Durability of Wettability Changes on Polyolefin Surfaces by Atmospheric Pressure Plasma Torch, Surface Coatings and Technology, 205, 396-402, 2010.

[13] F. Caiazzo, P. Canonico, R. Nigro, V. Tagliaferri, Electrode discharge for plasma surface treatment of polymeric materials, Journal of Materials Processing Technology, 58, 96-99, 1996.

[14] Polymer Surface Modification: Relevance to adhesion K.L. Mittal (Ed.) VSP, Zeist, 1995

[15] J.N. Miller, J.C. Miller, Statistics and chemometrics for analytical chemistry, Fourth Ed., Pearson, Essex, 2000.

[16] N. Encinas, J.Abenojar, M.A.Martínez, Development of Improved Polypropylene Adhesive Bonding by Abrasion and Atmospheric Plasma Surface Modifications, International Journal of Adhesion and Adhesives, 33, 1–6, 2012.

[17] N. Encinas, M. Lavat-Gil, R.G. Dillingham, J. Abenojar, M.A. Martínez, Cold Plasma Effect on Glass Fibre Reinforced Composites Adhesion Properties, International Journal of Adhesion and Adhesives, 48, 85-91, 2014.

Proceedings of the 3rd International Conference on
Fracture Fatigue and Wear, pp. 40-42, 2014

RIGID INCLUSIONS: STRESS SINGULARITY, INCLUSION NEUTRALITY AND SHEAR BANDS

Francesco Dal Corso[1], Davide Bigoni[1] and Giovanni Noselli[2], Diego Misseroni[1], Summer Shahzad[1]

[1] University of Trento, Trento, Italy
[2] SISSA, Trieste, Italy

Abstract: Analytical solutions in elasticity predict singularities of stress fields at the corners/tips of rigid polygonal/linear inclusions, similarly to the case of void inclusions. On the other hand, a rigid line inclusion is neutral to homogeneous simple shear since a homogeneous stress state is obtained.
We show that: (i) photoelastic experimental investigations validate the rigid inclusion model and therefore the assumptions about infinite stiffness of the inclusion and its complete adhesion with the matrix phase; (ii) when perturbations are superimposed upon a homogeneous pre-stress state, analytical incremental solutions display localization of deformation at the tips of rigid line inclusions and along the shear band directions, confirming experimental observations in ductile and quasi-brittle materials.

Keywords: stiffener; elasticity; failure mechanisms; anti-crack

1 INTRODUCTION

The rigid inclusion model is used to represent inclusions with high stiffness compared to that of the embedding matrix, so that it corresponds to a sort of 'inverse' of a void. Assuming complete adherence to the matrix and the infinite stiffness of the inclusion, the boundary conditions introduced by this model are (differently from a void) of kinematical type, defining the condition that the points of the inclusion can only display a rigid body motion.

Though in the last decades many authors have investigated the theoretical mechanical fields around rigid inclusions, the fundamental task of the validation of this model have been left untouched and it has been only recently investigated [1,2].

On the other hand, a number of instabilities at the micro-scale in form of shear bands have been experimentally observed around thin stiff inclusions in ductile matrixes undergoing large deformation. Application of the perturbative approach to a prestress state close to the ellipticity loss have shown the focussing of deformation in shear bands emerging from the inclusion tips and have disclosed the mechanisms of ductile failure in reinforced materials [3,4,5].

2 VALIDATION OF THE RIGID INCLUSION MODEL

Validation of the rigid inclusion model has been addressed through photoelastic experiments, performed on two-component resin sample containing stiff inclusions of different shapes (thin in [1], polygonal in [2]). The photoelastic fringes obtained with a white circular polariscope are shown in Fig. 1 for the case of a rhombohedral inclusion (left) and a thin inclusion (right) during an uniaxial stress experiment. The photoelastic matrix material has been realized employing a commercial two-part epoxy resin (Translux D180© by Axon, with proportion resin:hardener=1:0.95, for the matrix containing the rhombohedral inclusion; Crystal Resins© by Gedeo, with proportion resin:hardener=1:1, for the matrix containing the steel lamina). The rhombohedral inclusion and the thin inclusion have been realized using solid polycarbonate and steel lamina, respectively.

The photoelastic fringes are reported in Fig. 1 together with the full-field linear elastic solution obtained with the rigid inclusion model. It can be noted that the linear elastic solution is in a very good quantitative agreement with the photoelastic results, confirming the singular behaviour of the stress fields close to the rigid inclusion tips.

Finally, the stiffener neutrality to uniform shear stress states has been verified (again through photoelastic investigation) on a sample subject to a simple shear deformation parallel to the inclusion, Fig. 2. The strain amount can be detected through the visible distortion assumed by the rectangle (drawn on the sample in the undeformed state).

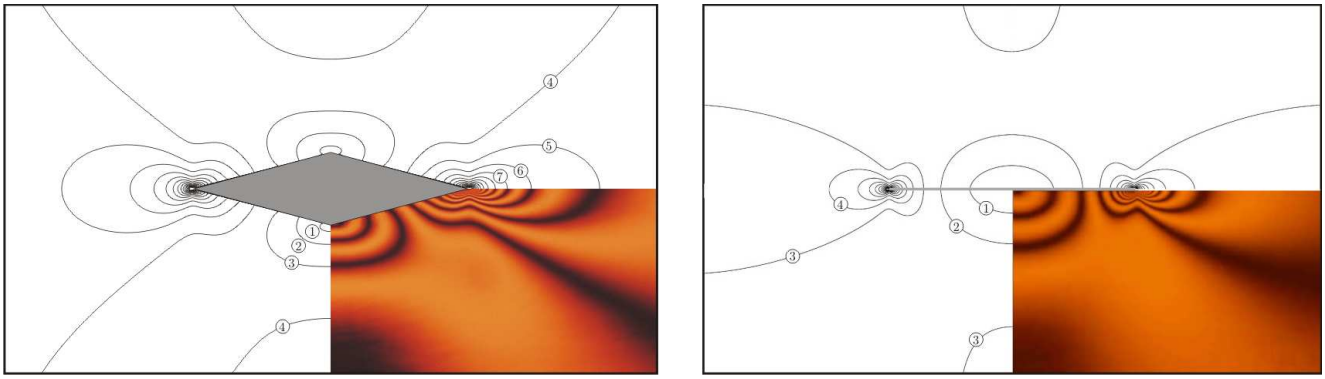

Fig. 1 Photoelastic fringes revealing the stress concentrations around the tips of rhombohedral (left) and thin (right) stiff inclusions during an uniaxial stress experiment.

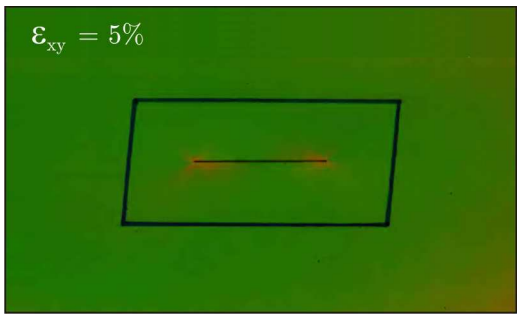

Fig. 2 Photoelastic fringes revealing the stiffener neutrality when the matrix is subjected to a simple shear parallel to the inclusion.

3 THIN RIGID INCLUSIONS PROMOTING FAILURE

Localized deformations in the form of shear bands are experimentally observed to nucleate at the boundaries of stiff inclusions within ductile and quasi-brittle materials.

Assuming the presence of a uniform prestress state, the incremental solutions for uniform Mode I and Mode II perturbations have been obtained for a prestressed material containing a rigid line inclusion [3-5].

Similarly to plane problems for anisotropic materials, the incremental solution is obtained by means of a stream function of complex variables. In particular, the full-field problem is found to be equivalent to a Riemann–Hilbert problem, so that the solutions display square-root singularities at the tips of the rigid inclusion.

Furthermore, since the incremental solution is affected by the prestress amount, exploitation of the solution for prestress states close to the loss of ellipticity shows clearly shear band nucleation and growth at the stiffener tip, Fig. 3, at varying of inclination of the inclusion line with respect to the axes of prestress. The incremental fields are reported for the case of an inclusion embedded in a J_2-deformation theory material with a prestress amount close to the loss of ellipticity condition. In the case of axes of prestress parallel to the inclusion line (left) the symmetry leads to a symmetric nucleation of shear bands, while in the case of axes of prestress not parallel to the inclusion line (right) the shear band closest to the inclusion line is privileged.

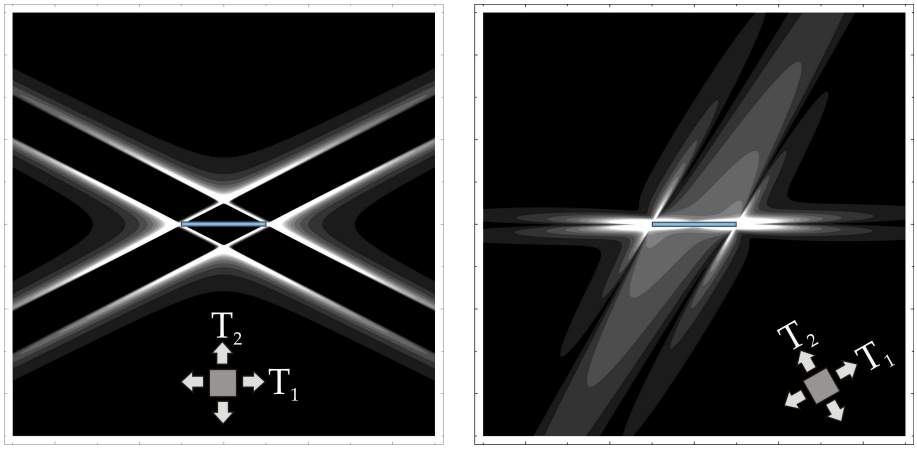

Fig. 3 Level sets of the second invariant of deviatoric incremental strain near a rigid line inclusion for a uniform Mode I perturbation.

4 CONCLUSIONS

The rigid inclusion model has been fully validated by means of photoelastic tests, confirming stress concentration close the inclusion tips of stiff inclusions under Mode I loading and neutrality of rigid line inclusions under Mode II loading, according to analytical solutions in linear elasticity.
The analytical solutions, obtained for the incremental problem of a prestressed material containing a rigid line inclusion, disclose shear band nucleation and growth at the inclusion tips with varying of inclination at varying of the angle between the rigid inclusion line and axes of prestress.

5 ACKNOWLEDGEMENTS

The authors gratefully acknowledge the support by the European Union ERC-2013-ADG-340561-INSTABILITIES.

6 REFERENCES

[1] G. Noselli, F. Dal Corso, D. Bigoni, The stress intensity near a stiffener disclosed by photoelasticity, International Journal of Fracture, 166, 91-103, 2010

[2] D. Misseroni, F. Dal Corso, S. Shahzad, D. Bigoni, Stress concentration near stiff inclusions: validation of rigid inclusion model and boundary layers by means of photoelasticity, Submitted, 2014.

[3] F. Dal Corso, D. Bigoni, M. Gei, The stress concentration near a rigid line inclusion in a prestressed, elastic material. Part I. Full field solution and asymptotics. Journal of the Mechanics and Physics of Solids, 56, 815-838, 2008.

[4] D. Bigoni, F. Dal Corso, M. Gei, The stress concentration near a rigid line inclusion in a prestressed, elastic material. Part II. Implications on shear band nucleation, growth and energy release rate. Journal of the Mechanics and Physics of Solids, 56, 839-857, 2008.

[5] F. Dal Corso, D. Bigoni, The interactions between shear bands and rigid lamellar inclusions in a ductile metal matrix. Proceedings of the Royal Society A, 465, 143-163, 2009.

Proceedings of the 3rd International Conference on
Fracture Fatigue and Wear, pp. 43-49, 2014

EXPERIMENTAL AND ANALYTICAL STUDY OF BANDAGE STRENGTHENING OF REINFORCED CONCRETE SHORT CORBELS BY BONDING CARBON FIBRES FABRICS

Jules Assih*, Ivelina Ivanova, Alex Li and Yves Delmas

GRESPI/Laboratoire de Génie Civil UFR Sciences, Université de Reims, Moulin de la Housse 51687 Reims Cedex 2, France

*Corresponding author: Jules.assih@univ-reims.fr

Abstract: This paper presents damage experimental and analytical study of strengthening reinforced concrete short corbel by bonding carbon fibres sheets. Indeed, the reinforced concrete short corbels are often using in civil engineering, in the building. Of course, the interesting properties of carbon materials: light weight, fire resistance, high mechanical strength, can provide other building approaches. The purpose of the experimental and analytical investigations is to study all changes in behaviour and their contribution to a better understanding of reinforced concrete short corbels. At first, six strengthening reinforced concrete short corbels were examined to carry out of carbon fibres thickness influence. At second, we were interested to study the mechanical behaviour of this structure using the local electrical gauges to measure strains in the steel, concrete and composite material in order to propose an analytical model based on damage theory describing the behaviour of strengthened concrete corbel. The theoretical result was compared with experimental result. The results showed an increase in failure tensile strength of 82%. Three different domains of reinforced concrete corbel are presented. The results show three main failure mode of reinforced concrete corbel: failure by the failure of the composite plate, compression-shear failure, the failure by flexural-shear.

Keywords: reinforced concrete; short corbels; carbon fibres; damage theory; failure analysis

1 INTRODUCTION

Life of concrete structures is between 50 and 100 years. So many of these concrete structures no longer meet the current safety standards or have excessive cracks. Steel corrosion may also cause the occurrence of a large deflection or instability of the structure itself. It is generally manifested by poor performance under service loading in the form of excessive deflections or cracking. Sometimes, even by inadequate ultimate strength.

The introduction of composite carbon fibber [1] in the 1980s in the field of Civil Engineering helps strengthen or repair structures in concrete or reinforced concrete with adhesive. Carbon fibber materials have many advantages: their weight, flexibility, implementation easier and also their physicochemical properties (corrosion) interesting.

This second alternative to carry out a program of strengthening Reinforced concrete corbels [2], [3], and [5] was much more attractive. Maintenance of civil engineering works is to protect them by ensuring better sealing or limiting corrosion, to repair them by trying to compensate for the loss of rigidity and resistance to cracking due to the strengthening and improving performance and durability of structures.

This is a problem of increasing concern since the cost of new structures is becoming higher and repair conditions increasingly difficult. Among the techniques available for over a decade, and one of the most effective structural disorders, is rehabilitating by concrete structures by bonding the external bonded reinforcement.

In this paper, the structure is a reinforced concrete short corbel ($a/d<0.5$) [5]. Corbel is a reinforced concrete member, who is a short-haunched cantilever used to support the reinforced concrete beam element. Corbel is one important element of steel or concrete structure to support the pre-cast structural

system such as pre-cast beam and pre-stressed beam. The corbel is cast monolithic with the column element or wall element. It is interesting to study the mechanical behaviour of this very short element of the structure (corbel) using carbon fibber materials. The costs of these materials become available [1].

While extensive research has been done on corbels, strengthening corbels has received very little attention from researchers. Most of the existing research discussed the behaviour of the corbels.

We are mainly interested in the study of strengthening reinforced concrete short-Corbel. The parameter study is conducted to examine the effects of design variables such as carbon fibber sheet thickness and type of carbon fibber fabrics, on ultimate load, cracking and collapse mechanism under flexural bending. Local behaviour investigation by using the electrical gauges to measure strains in the steel, concrete and carbon fibber sheets is investigated. In this investigation, deformations, cracking and ultimate failure are studied.

However, in this paper, a parameter study is conducted to examine the effects of design variables such as carbon fibber fabrics thickness and the type of carbon fibber fabrics, on flexural behaviour of strengthened reinforced concrete corbels and load failure. We were interested local investigation by using the electrical gauges to measure strains in the steel, concrete and carbon fibber fabrics. In this investigation, deformations, cracking and deflection have been studied.

2 EXPERIMENTAL PROGRAM

This technique for carrying out such improvement was that which involved the bonding of steel plates to the surfaces of the structure. An effective way of eliminating the corrosion problem was to replace steel plates with corrosion resistance materials such as fibber composite materials [1-3]. Many advantages are: low density, corrosion, mechanical properties, good resistance to fatigue and ease of handling.

2.1 Test Specimens

Details and dimensions of the corbels are shown in Figure 1. The column supporting the two short trapezoidal corbels cantilevering on either side was 150 by 300 mm in cross section and 1000 mm long. Corbels had cantilever projection length of 200mm, with thickness of 150mm at both faces of column and the free end [4]. All reinforced concrete corbel specimens have the same dimensions and are reinforced in the same way. The specimens were tested using a single patch load with a shear span to depth ratio; a/d equal to 0.45.

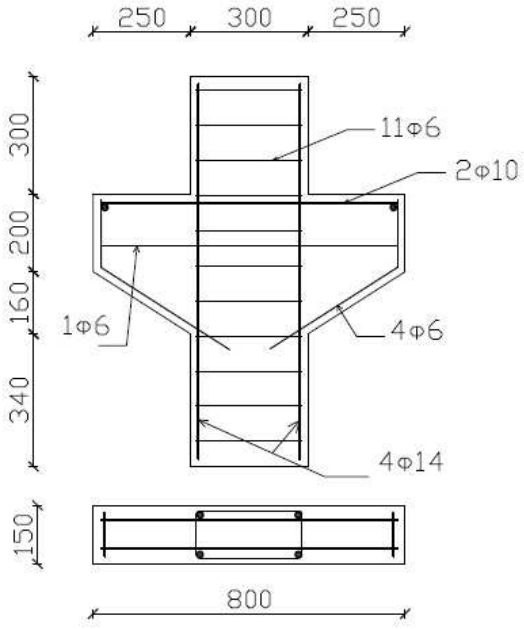

Fig. 1 Details of corbel geometry and steel reinforcement

2.2 Results and discussions

2.2.1 Strain of steel and carbon fibre fabrics

The typical load-strain curves are shown in figure 2 for strengthening reinforced concrete corbels. The results show that bonding carbon fibre fabrics to tensile area of strengthening reinforced concrete short corbel has far greater effect: it increases: the stiffness of corbel structure (at least one third), the ultimate flexural capacity of the corbel (up to 82%) and the range of elastic behaviour (twice). It is seen in figure 2, strain in steel bars, composite sheet. Results show four distinct zones with two characteristic bearing [1].

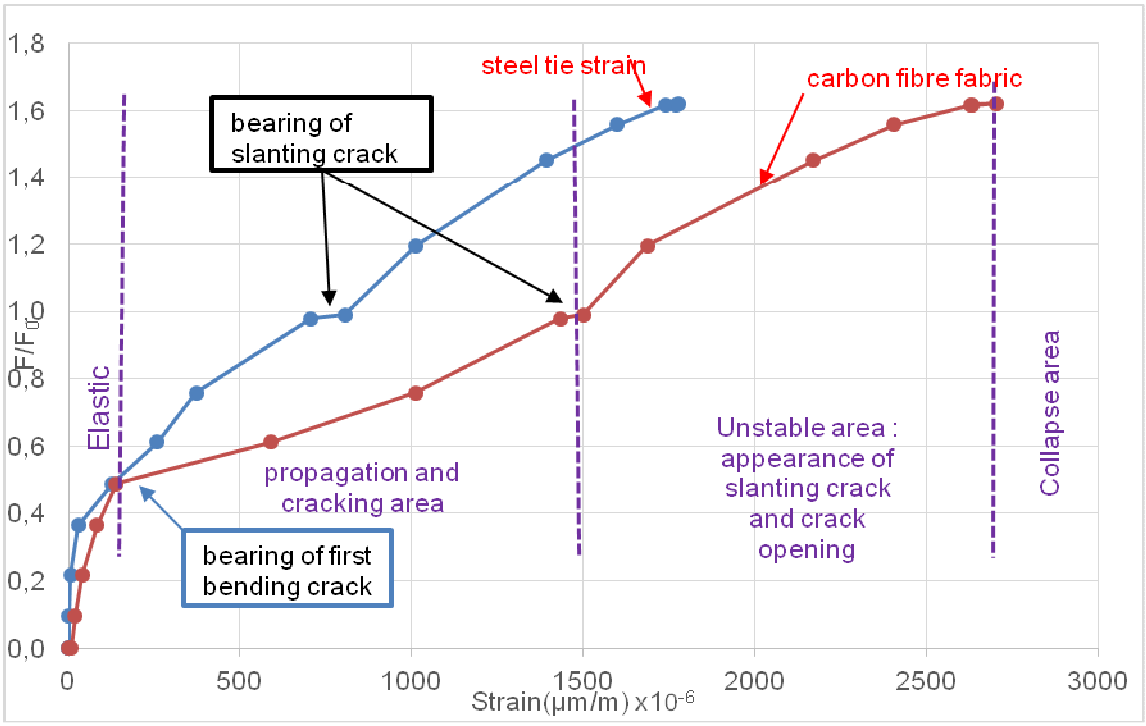

Fig. 2 Curves of Steel and composite plate in strengthening corbel and different areas behaviour

Initial flexural cracks developed in the bending region of corbel as the load increases. When the load was increased more, flexural cracks in the pure bending region propagated more obvious and flexural cracks were observed up to the shear region. Afterwards when the load is added, several diagonal tensile cracks occur in the middle of the beam on the shear span, was developed into diagonal tensile cracks at 45 degree from the neutral axis of the corbel. The diagonal tensile cracks developed simultaneously toward both the loading point and the supports.

When the strengthening reinforced concrete corbel by gluing carbon composite fibre fabric is subject to positive bending moment M, there are several phases:

- Global elastic zone, initially the tensioned concrete, the adhesive seal and plate had the same deformations.
- The field of cracking of the concrete to the top of the lamination steels tensile when the tensile stress on the fibber reaches its lower limit, the concrete will crack. The stresses remain relatively low, concrete, steel plate and continue to behave elastically behaviour after cracking. However, the opening of crack resulting from both sides, a pull of the steel relatively to the sheath with concrete. It remains a permanent opening. Enhanced corbel is definitely characterised when concrete has lost its tensile strength in the plans of cracks. The previous phase ends when steel reaches to this plasticize value. If only the moment is increased, the plasticized material acquires permanent deformation irreversible. The composite plate thus takes all the strength.
- The recovery domain of the composite plate until failure. Strained through the cracks, reaching their elastic limit, frames, therefore plasticized lengthen considerably more power without effective

opposition to the opening of cracks. But this opening crack is slowed by the composite plate and the adhesive joint and precipitating the collapse of the structure by tearing of concrete to steel-concrete interfaces.

2.2.2 Mode of corbel ruptures

Afterwards, six different ruptures of the corbel appeared as shown in Fig. 3. The appearance of first flexural cracks in the concrete was delayed with gluing carbon fibre sheet.

Splitting failure	Compression failure	Bending and Splitting failure
Shearing	Carbon fibre sheet failure	Bending failure and peeling of the end of the plate

Fig. 3 Different modes of strengthening concrete short corbel failures

3 ANALYSIS

The analysis of reinforced concrete corbel strengthened with carbon sheets could be described by a method using damage theory of RC beam [6,7] to predict the mechanical behaviour. The following assumptions were: the deformation distribution at section was linear, the specimen was linear-damageable in tensile zone and linear in compressive zone (Fig. 4). The adherence of sheet and steel bar were perfect. Damage was represented by an operator scalar D which affected the initial stiffness of material.

$$D_t(\varepsilon\varepsilon = \begin{cases} 0 & \text{if} \quad \varepsilon \le \varepsilon_{d0} \\ 1 - \dfrac{\varepsilon_{d0}(1-A_t)}{\varepsilon} - \dfrac{A_t}{\exp(B_t(\varepsilon - \varepsilon_{d0}))} & \text{if} \quad \varepsilon \ge \varepsilon_{d0} \end{cases} \tag{1}$$

$$D_c(\varepsilon\varepsilon = \begin{cases} 0 & \text{if} \quad 0 \geq \varepsilon \geq -\varepsilon_{dc0} \\ 1 + \dfrac{\varepsilon_{dc0}(1-A_c)}{\varepsilon} - \dfrac{A_c}{\exp[-B_c v\sqrt{2}(\varepsilon + \varepsilon_{dco})]} & \text{if} \quad \varepsilon \leq -\varepsilon_{dc0} \end{cases} \tag{2}$$

where D_t is damage factor in tension zone and D_c is damage factor in compression zone; t for tension and c for compression. D_t and D_c were varied between 0 (initial condition) and 1 (condition failure). (A_t, B_t) and (A_c, B_c) typical constants of the material. Figure 4 shows the distribution of strain and stress in rectangular cross section of strengthening reinforced concrete corbel. y_0 was the distance from the top of the beam to neutral axial; ε_{d0} and ε_{d00} were damaged strain; y_{d0} and y_{d00} were the distance from neutral axis to damaged strain in tensile and compression zones; σ_p, σ_s, σ_{bc}, σ were respectively the stress in carbon fibre fabric, steel and concrete; E_b was the concrete modulus of elasticity. A_p: area of steel tie, A_s: area of carbon sheet, b: width of concrete section, A_h: area of second steel, σ_p : stress of carbon sheet, D_c: damage factor in compression, D_t: damage factor in tensile, y_0: position of neutral axis, σ_{s1} and σ_{s2} were stresses of second steel in concrete corbel, E_b: concrete modulus of elasticity, E_s: steel modulus of elasticity, E_p: carbon sheet modulus of elasticity. Two phases of behaviour were distinguished:

Elastic phase:

$$\varepsilon \leq \varepsilon_{d0}, \varepsilon_{d00} \text{ then } \sigma = E_b\varepsilon \tag{3}$$

Damaged phase:

$$\varepsilon > \varepsilon_{d0}, \varepsilon_{d00} \qquad \text{then } \sigma = E_b\varepsilon(1-D_i) \tag{4}$$

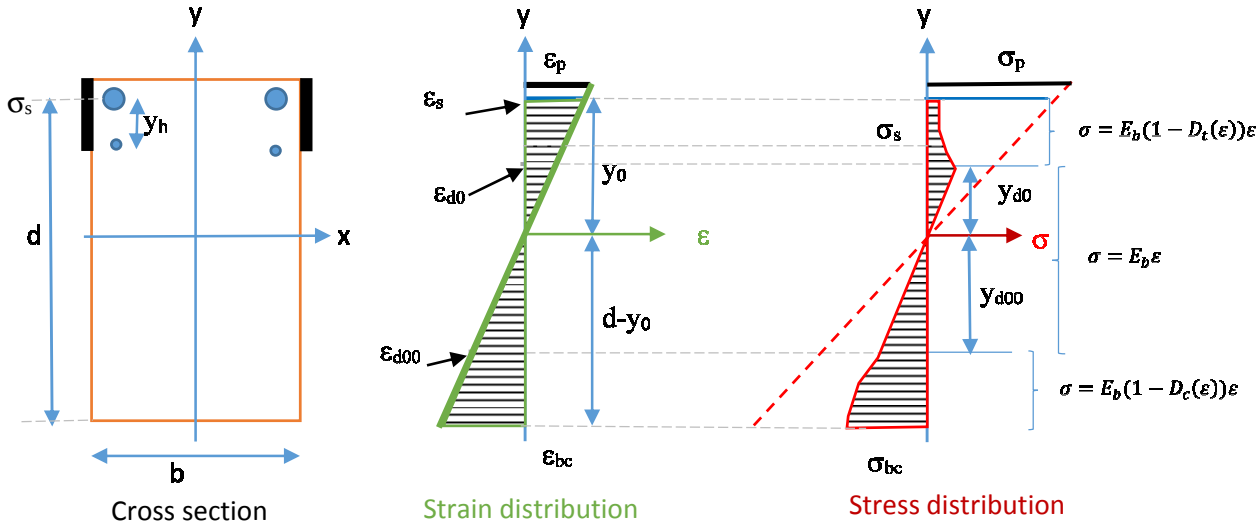

Fig. 4 Strain and stress distribution at cross section

At a section, the equilibrium equations were written for equations (5) and (6) respectively. The resultant strength was given equal zero as follow:

$$A_p\sigma_p + A_s\sigma_{st} + \sum_{i=1}^{2} A_h\sigma_{si} + \int_{-(d-y_o)}^{y_0} b\sigma(\varepsilon)dy = 0 \tag{5}$$

From equation (4), position of neutral axis could be found y_i. Flexural moment was given as follow:

$$A_p\sigma_p y_0 + A_s\sigma_{st} y_0 + \sum_{i=1}^{2} A_h\sigma_{si} y_i + \int_{-(d-y_o)}^{y_0} b\sigma(\varepsilon) y dy = M \quad (6)$$

where A_p, A_s were carbon sheet and steel areas respectively, b was the width of concrete section. Equations (5) and (6) were allowed to determine the behaviour of beam strengthened which was be compared with experimental data in Fig. 5.

The results proved to be a good method to predict mechanical behaviour of strengthened reinforced concrete corbel. The result obtained in fig 5 was a good method to predict mechanical cracking at the first crack load. A little difference is such when stress yield of steel bar passed and gluing effect is not negligible in this test. So search is continue to improve this method.

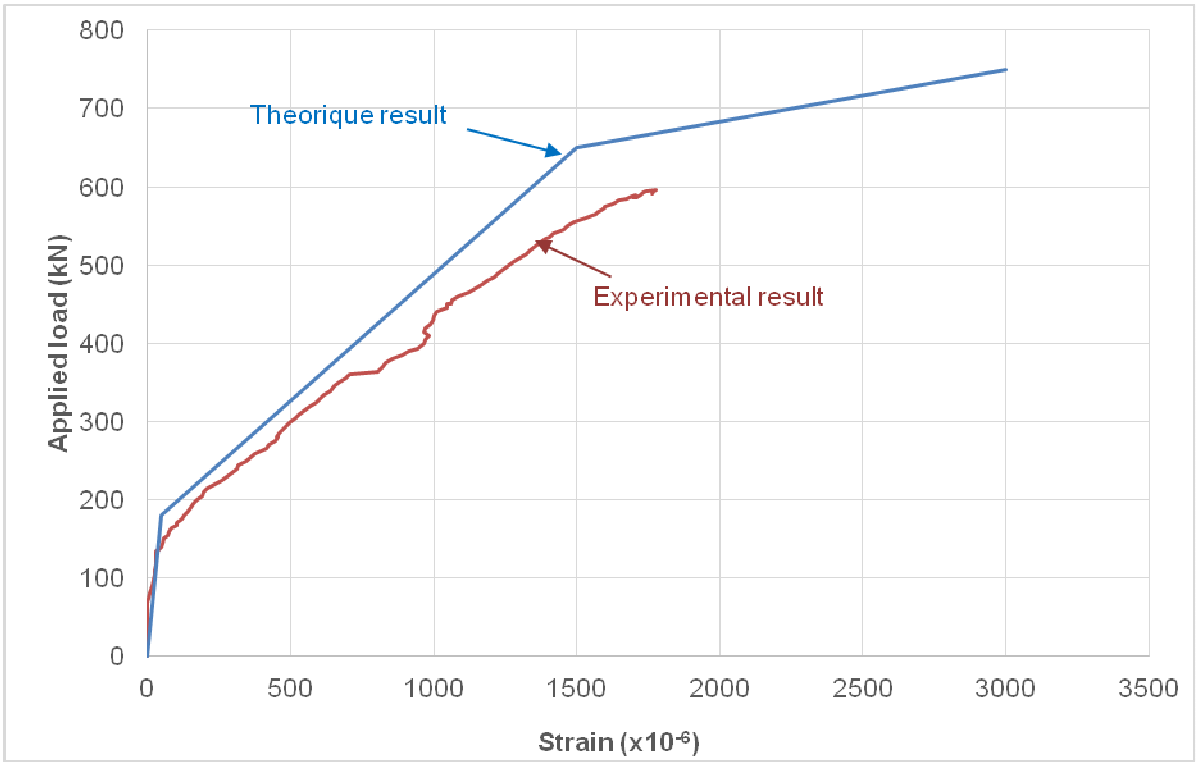

Fig. 5 Comparison of analysis and experimental curves

4 CONCLUSIONS

The results of the tests performed in this study indicated that a significant increase in the flexural strength could be achieved by bonding composite sheets to tensile face of reinforced concrete corbel. The choice of adhesive, surface preparation and damaged steel state were very important in the strengthening technique. Considerable reductions in the deflection and cracks, under loading, were produced by the application of epoxy bonded sheets. The corbel loaded until its ultimate capacity was strengthened successfully (up to 82%). However, any effect on ultimate load of damaged concrete was being noted. Four failures of all corbels were obtained and distinguished tree different zones of mechanics behaviour. The theoretical model developed in this study appeared to be a good method for the prediction mechanical behaviour.

5 REFERENCES

[1] Meier U, Kaiser H. Strengthened of Structures with CFRP laminates, proceeding of the ASCE conference-ACM materials in civil engineering structures, p.224-232, 1991.

[2] Anis A. Mohamad-Ali, Muhammad Abed Attiya, Experimental behaviour of reinforced concrete corbels strengthened with carbon fibre reinforced polymer strips, Basrah Journal for Engineering Science, 2012. pp 31-45.

[3] Assih T., Li A., Delmas Y., Strengthening of Reinforced concrete beams with carbon fibber composite plate, EUROMECH358, Sept. 1997.

[4] Omar Qarani Aziz, Zrar Sedeeq Hothman, Ultimate shear strength of reinforced high strength concrete corbels subjective to vertical load, Al-Rafidain Engineering, vol 18, N°1, January 2010.

[5] Iveline IVANOVA, Comportement mécanique de console courte en béton armé renforcée ou réparée par collage des matériaux composites, thèse de l'Université de Reims champagne Ardenne, décembre 2013.

[6] Mazars J. Application de la mécanique de l'endommagement au comportement non linéaire et à la rupture du béton de structure, Thèse de doctorat d'état, Univ. Paris 6, 1984.

[7] Cedric Giry, Modélisation objective de la localisation des déformations et de la fissuration dans les structures en béton armé, Thèse de l'Université de Grenoble, 10 novembre 2011.

Proceedings of the 3rd International Conference on
Fracture Fatigue and Wear, pp. 50-56, 2014

ANALYSIS ON INTENSITY OF SINGULAR STRESS FOR BONDED PIPE IN COMPARISON WITH BONDED PLATE

Zefeng Wang[1], Nao-Aki Noda[2], Tatsujiro Miyazaki[3], Takumi Uchikoba[2], Guohui Wang[3] and Yoshikazu Sano[2]

[1] Department of Mechanical Engineering, Kyushu Institute of Technology, 1-1 Sensui-cho, Tobata-ku, Kitakyushu-shi, Fukuoka, 804-8550
[2]Department of Mechanical Engineering, Kyushu Institute of Technology, 1-1 Sensui-cho, Tobata-ku, Kitakyushu-shi, Fukuoka, 804-8550
[3]Department of Mechanical Engineering Systems, University of the Ryukyus, 1 Senbaru, Nishihara-cho, Nakagami-gun, Okinawa 903-0213

Abstract: In our previous research, the intensity of singular stress at the end of interface for bonded plate was discussed under arbitrary material combinations. Also, it was found that the bonded strength of butt joint can be evaluated in terms of the singular stress in good accuracy. In this study, the intensity of singular stress for bonded pipe is newly discussed in comparison with the one of bonded plate. The finite element method is applied to calculate the intensity of singular stress with varying the material combination systematically. This method focuses on the result of first node, which locates on the end of the interface. Since few studies are available for bonded pipe, in this study, first, the singular stress field at the end of the interface of the bonded pipe is investigated under several boundary conditions. Next, the effect of the material combination on the intensity of singular stress is discussed. This investigation may contribute to a better understanding of the debonding strength and initial interfacial cracks of bonded pipe.

Keywords: adhesion; fracture mechanics; stress intensity factor; interface; bonded pipe

1 INTRODUCTION

The adhesive pipe joints have been widely used in offshore, space and aviation engineering recent years since it has number of advantages over the traditional pipe joint, such as no welding residual stress, lightweight, lower costs, easy to process and corrosion-resistant. With the rapid growth in the use of adhesive pipe joint, many research works have been done to establish the evaluation criteria of this kind of pipe joint [1-7].

However, the improper selection of material combination will cause stress singularity at the end of interface, which may result in the failure of the joint. Thus a rational selection of material combination is crucial to the strength of the adhesive pipe joint. Noda et al. have investigated the intensity of stress singularity for arbitrary material combination in a boned strip [8]. So far only few researches have considered the stress intensity of adhesive pipe joint, and no result of arbitrary material combination has been obtained.

In order to obtain the stress intensity near the corner interface, a basic result is necessary. Teranishi and Nisitani proposed a highly accurate numerical method named the zero element method to determine the stress intensity factor of a homogenous plate [9]. Anyway, this method cannot be used directly into the problem of adhesive pipe since there are non singular terms in stress components. In this research, the stress intensity will be evaluated by using an extended method proposed by Oda et al. FEM is also employed in this paper.

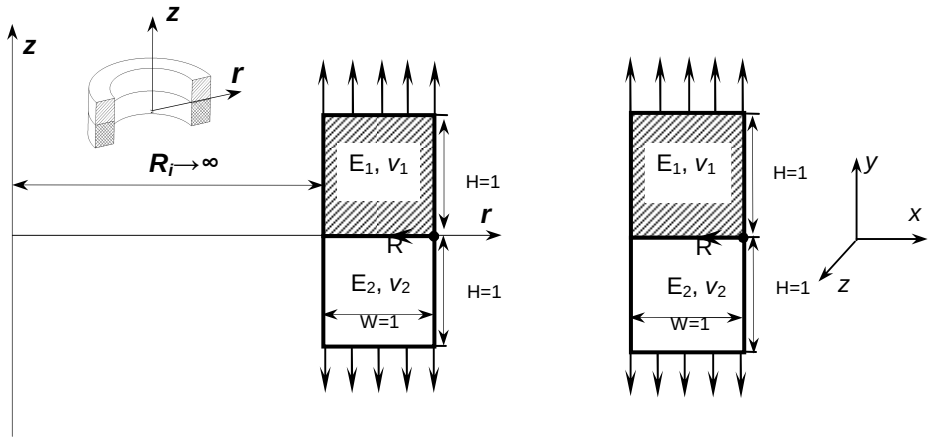

(a) Bonded pipe (b) Plate

Fig. 1 Structure of bonded pipe and reference problem

There are many kinds of adhesive pipe joints; the most commonly used joining methods for pipes are adhesive-bonded socket joints, tubular lap joints, heat-activated coupling joints, and flanged joints. In this research, the basic adhesive bonded pipe shown in Fig.1 is studied. Figure 1(a) shows the structure of pipe joint, and Fig. 1(b) shows the structure of the bonded strip under plain strain condition, which is the reference problem of this research. This research focuses on the intensity of singular stress of arbitrary material combination in a bonded pipe. For the sake of universality, the inner radius of the pipe is chosen as infinite. In this study we assume R_i=10^5.

2 PROBLEM DESCRIPTIONS

The plain strain problem shown in Fig. 1(b) is used as the reference problem, in which the stress near the end of interface can be expressed as

$$\sigma_i^{PLT} = \frac{K_{\sigma_i}^{PLT}}{R^{1-\lambda}} \left(i = x, y, z\right), \tau_{xy}^{PLT} = \frac{K_{\tau_{xy}}^{PLT}}{R^{1-\lambda}} \tag{1}$$

Here R is the distance from the end of interface. This problem has been analyzed by Chen-Nisitani and Noda et al., and the intensity of singular stress was accurately calculated by using body force method (shown in Fig. 2) [10].

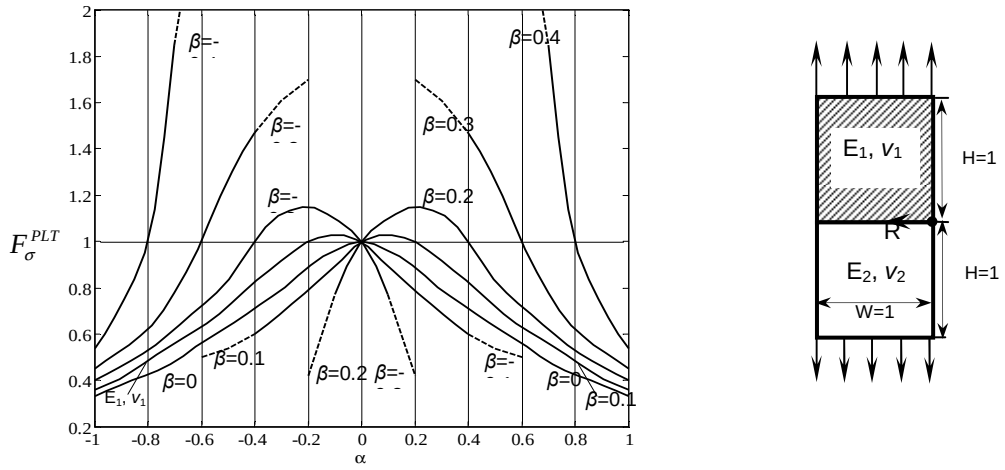

Fig. 2 F_σ for a boned strip in Fig. 1(b)

F_σ is the dimensionless of intensity of singular stress defined by

$$F_\sigma^{PLT} = \frac{K_\sigma^{PLT}}{\sigma_y^\infty (2W)^{1-\lambda}}, \tag{2}$$

While the stress in the unknown problem shown in Fig. 1(a) is expressed as:

$$\sigma_j^{PIPE} = \frac{K_{\sigma_j}^{PIPE}}{R^{1-\lambda}} + \tilde{\sigma}_j^{PIPE} \ (j = r, z, \theta), \ \tau_{rz}^{PIPE} = \frac{K_{\tau_{xy}}^{PIPE}}{R^{1-\lambda}} + \tilde{\tau}_{rz}^{PIPE} \tag{3}$$

This research focuses on the intensity of singular stress of arbitrary material combination in a bonded pipe. To obtain the intensity of singular stress, the zero element method is used. However, according to this method, the stress ratio $\sigma_{ij}^{PIPE}/\sigma_{ij}^{PLT}$ should be consistent with each other and independent of element size when FEM is employed. Table 1 is the results for plate and butt joint. The ratios of all stress components show very good consistent with each other. However the non singular terms in equation (3) can lead uncertainty for the ratio of bonded pipe and plate. Table 2 shows the results of this ratio if we directly apply the zero element method to our new problem. As we can see in Table 1, the ratios of $\sigma_{z0,FEM}$ and $\sigma_{\theta 0,FEM}$ are quite different from that of $\sigma_{r0,FEM}$ and $\tau_{rz,FEM}$.

Table 1 Ratio of $\sigma_{ij0,FEM}^{PLT}/\sigma_{ij0,FEM}^{BJ}$ $(E_1 = 1000, \nu_1 = 0.25548042, E_2 = 113.79748, \nu_2 = 0.20656946)$

	$\sigma_{r0,FEM}^{PIPE}/\sigma_{x0,FEM}^{PLT}$		$\sigma_{z0,FEM}^{PIPE}/\sigma_{y0,FEM}^{PLT}$		$\sigma_{\theta 0,FEM}^{PIPE}/\sigma_{z0,FEM}^{PLT}$		$\tau_{rz,FEM}^{PIPE}/\tau_{xy,FEM}^{PLT}$	
Material	Mat. 1	Mat. 2	Mat. 1	Mat. 2	Mat. 1	Mat. 2	Mat. 1	Mat. 2
$e_{\min} = 2^{-13}$	0.5253	0.5254	0.5254	0.5254	0.5254	0.5253	0.5253	0.5254
$e_{\min} = 2^{-17}$	0.5250	0.5253	0.5252	0.5252	0.5252	0.5252	0.5252	0.5253

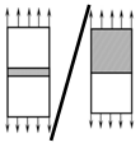

Table 2 Ratio of $\sigma_{ij0,FEM}^{PIPE}/\sigma_{ij0,FEM}^{PLT}$ $(E_1 = 1000, \nu_1 = 0.25548042, E_2 = 113.79748, \nu_2 = 0.20656946)$

	$\sigma_{r0,FEM}^{PIPE}/\sigma_{x0,FEM}^{PLT}$		$\sigma_{z0,FEM}^{PIPE}/\sigma_{y0,FEM}^{PLT}$		$\sigma_{\theta 0,FEM}^{PIPE}/\sigma_{z0,FEM}^{PLT}$		$\tau_{rz,FEM}^{PIPE}/\tau_{xy,FEM}^{PLT}$	
Material	Mat. 1	Mat. 2	Mat. 1	Mat. 2	Mat. 1	Mat. 2	Mat. 1	Mat. 2
$e_{\min} = 2^{-13}$	1.0207	1.0207	***1.0148***	***1.0135***	***-0.12834***	***0.88466***	1.0206	1.0207
$e_{\min} = 2^{-17}$	1.0204	1.0204	***1.0163***	***1.0154***	***0.22911***	***0.92672***	1.0204	1.0203

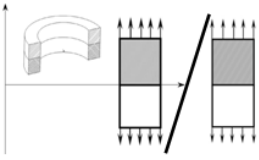

Therefore the zero element method can not be employed directly. It is necessary to eliminate the affect of these non singular terms in Eq.(3) for the use of zero element method. Then next chapter will mainly focus on how to make the zero element method suitable for the new unknown problem shown in Fig. 1(a).

3 NUMERICAL METHOD FOR THE ANALYSIS OF THE STRESS INTENSITY FOR BONDED PIPE

At the end of interface, the second terms in equation (3) have the expressions as

$\left(\tilde{\sigma}_{r0}^{PIPE}\right)^{mat1}, \left(\tilde{\sigma}_{z0}^{PIPE}\right)^{mat1}, \left(\tilde{\sigma}_{\theta 0}^{PIPE}\right)^{mat1}, \left(\tilde{\tau}_{rz}^{PIPE}\right)^{mat1}$ in material 1;

$\left(\tilde{\sigma}_{r0}^{PIPE}\right)^{mat2}, \left(\tilde{\sigma}_{z0}^{PIPE}\right)^{mat2}, \left(\tilde{\sigma}_{\theta 0}^{PIPE}\right)^{mat2}, \left(\tilde{\tau}_{rz}^{PIPE}\right)^{mat2}$ in material 2.

These 8 stress components should meet the boundary conditions of bonded interface and free edge of the outer surface. And the compatibility of deformation should also be satisfied. As a result, these components should conform to the following equations.

$$\left(\tilde{\sigma}_{r0}^{PIPE}\right)^{mat1} = \left(\tilde{\sigma}_{r0}^{PIPE}\right)^{mat2} = \left(\tilde{\tau}_{rz}^{PIPE}\right)^{mat1} = \left(\tilde{\tau}_{rz}^{PIPE}\right)^{mat2} = 0 \tag{4}$$

$$\left(\tilde{\sigma}_{z0}^{PIPE}\right)^{\text{mat1}}=\left(\tilde{\sigma}_{z0}^{PIPE}\right)^{\text{mat2}}=\tilde{\sigma}_{z0}^{PIPE} \tag{5}$$

$$\left(\tilde{\varepsilon}_{\theta 0}^{PIPE}\right)^{\text{mat1}}=\left(\tilde{\varepsilon}_{\theta 0}^{PIPE}\right)^{\text{mat2}}=\tilde{\varepsilon}_{\theta 0}^{PIPE} \tag{6}$$

$$\left(\tilde{\varepsilon}_{r0}^{PIPE}\right)^{\text{mat1}}=\left(\tilde{\varepsilon}_{r0}^{PIPE}\right)^{\text{mat2}}=\tilde{\varepsilon}_{r0}^{PIPE} \tag{7}$$

Transpose Eq. (6), and substitute Eq. (4), (5) into it gives

$$\left(\tilde{\varepsilon}_{\theta 0}^{PIPE}\right)^{\text{mat1}}-\left(\tilde{\varepsilon}_{\theta 0}^{PIPE}\right)^{\text{mat2}}=\frac{1}{E_1}\left[\left(\tilde{\sigma}_{\theta 0}^{PIPE}\right)^{\text{mat1}}-\nu_1\left(\tilde{\sigma}_{z0}^{PIPE}\right)^{\text{mat1}}\right]-\frac{1}{E_2}\left[\left(\tilde{\sigma}_{\theta 0}^{PIPE}\right)^{\text{mat2}}-\nu_2\left(\tilde{\sigma}_{z0}^{PIPE}\right)^{\text{mat2}}\right]=0$$

Thus

$$\left(\frac{\nu_1}{E_1}-\frac{\nu_2}{E_2}\right)\tilde{\sigma}_{z0}^{PIPE}=\frac{\left(\tilde{\varepsilon}_{\theta 0}^{PIPE}\right)^{\text{mat1}}}{E_1}-\frac{\left(\tilde{\varepsilon}_{\theta 0}^{PIPE}\right)^{\text{mat2}}}{E_2} \tag{8}$$

Similarly, for Eq. (7), there is

$$\frac{\left(\tilde{\sigma}_{\theta 0}^{PIPE}\right)^{\text{mat1}}}{\left(\tilde{\sigma}_{\theta 0}^{PIPE}\right)^{\text{mat2}}}=\frac{1+\nu_2}{1+\nu_1}\cdot\frac{E_1}{E_2} \tag{9}$$

From Eq. (8) and Eq. (9) we can obtain

$$\frac{\left(\tilde{\sigma}_{\theta 0}^{PIPE}\right)^{\text{mat1}}}{\tilde{\sigma}_{z0}^{PIPE}}=-\frac{\nu_1-\frac{E_1}{E_2}\nu_2}{\frac{\nu_1-\nu_2}{1+\nu_2}} \tag{10}$$

and

$$\frac{\left(\tilde{\sigma}_{\theta 0}^{PIPE}\right)^{\text{mat2}}}{\tilde{\sigma}_{z0}^{PIPE}}=-\frac{\nu_2-\frac{E_2}{E_1}\nu_1}{\frac{\nu_2-\nu_1}{1+\nu_2}} \tag{11}$$

For axis symmetric problem under cylindrical coordinate system, there is

$$\begin{cases}\varepsilon_r=\dfrac{\partial u_r}{\partial r}\\ \varepsilon_\theta=\dfrac{u_r}{r}\\ \gamma_{rz}=\dfrac{\partial u_r}{\partial z}+\dfrac{\partial u_z}{\partial r}\end{cases} \tag{12}$$

Recall Eq.(6) we can obtain:

$$\left(\tilde{\varepsilon}_{\theta 0}^{PIPE}\right)^{\text{mat1}}=\left(\tilde{\varepsilon}_{\theta 0}^{PIPE}\right)^{\text{mat2}}=\tilde{\varepsilon}_{\theta 0}^{PIPE}=\varepsilon_\theta=\frac{u_r}{r}=\frac{1}{E_1}\left\{\left(\tilde{\sigma}_{\theta 0}^{PIPE}\right)^{\text{mat1}}-\nu_1\left[\left(\tilde{\sigma}_{r0}^{PIPE}\right)^{\text{mat1}}+\left(\tilde{\sigma}_{z0}^{PIPE}\right)^{\text{mat1}}\right]\right\}=-\frac{\left(1+\nu_1\right)\nu_1E_2-\left(1+\nu_2\right)\nu_2E_1}{\left(\nu_1-\nu_2\right)E_1E_2}\tilde{\sigma}_{z0}^{PIPE}$$

Thus

$$\left(\tilde{\sigma}_{z0}^{PIPE}\right)^{\text{mat1}}=\left(\tilde{\sigma}_{z0}^{PIPE}\right)^{\text{mat2}}=\tilde{\sigma}_{z0}^{PIPE}=-\frac{\left(\nu_1-\nu_2\right)E_1E_2}{\left(1+\nu_1\right)\nu_1E_2-\left(1+\nu_2\right)\nu_2E_1}\frac{u_r}{r}=-\frac{\left(\nu_1-\nu_2\right)E_1E_2}{\left(1+\nu_1\right)\nu_1E_2-\left(1+\nu_2\right)\nu_2E_1}\frac{u_{r0}^{PIPE}}{R_i+W} \tag{13}$$

Substituting Eq. (13) into Eq. (10), (11) gives

$$\left(\tilde{\sigma}_{\theta 0}^{PIPE}\right)^{\text{mat1}}=\frac{\left(1+\nu_2\right)\left(\nu_1E_2-\nu_2E_1\right)E_1}{\left(1+\nu_1\right)\nu_1E_2-\left(1+\nu_2\right)\nu_2E_1}\frac{u_{r0}^{PIPE}}{R_i+W} \tag{14}$$

$$\left(\tilde{\sigma}_{\theta 0}^{PIPE}\right)^{\text{mat2}}=\frac{\left(1+\nu_1\right)\left(\nu_1E_2-\nu_2E_1\right)E_2}{\left(1+\nu_1\right)\nu_1E_2-\left(1+\nu_2\right)\nu_2E_1}\frac{u_{r0}^{PIPE}}{R_i+W} \tag{15}$$

And recall Eq. (4)

$$\left(\tilde{\sigma}_{r0}^{PIPE}\right)^{\text{mat1}} = \left(\tilde{\sigma}_{r0}^{PIPE}\right)^{\text{mat2}} = \left(\tilde{\tau}_{rz}^{PIPE}\right)^{\text{mat1}} = \left(\tilde{\tau}_{rz}^{PIPE}\right)^{\text{mat2}} = 0 \tag{16}$$

So far, all the eight non singular terms in Eq. (3) have been solved and can be eliminated from the singular stress calculated by FEM, so that the first element method can be applied to this new unknown problem.

4 NUMERICAL RESULTS AND DISCUSSION

Figure 3 shows one of the FEM model for the bonded pipe. There are two models in this research with the minimum element sizes 2^{-13} and 2^{-17} respectively.

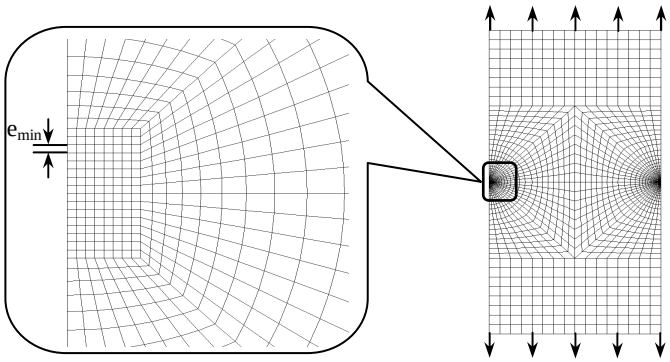

Fig. 3 FEM model

Since the non singular terms have been expressed as shown in Eq.(13)-(16), the ratio $\sigma_{ij}^{PIPE}/\sigma_{ij}^{PLT}$ should be independent of element size when using FEM.

Next we will introduce the results in Eq.(13)-(16) to eliminate the non singular terms. When $e_{min}=2^{-13}$, the displacement of the first node locating on the end of interface (outer surface) is

$$u_r = -73.7971190230$$

And outer radius $R_i+W=100001$, thus

$$\varepsilon_\theta = \frac{u_r}{r} = \frac{-73.7971190230}{100001} = -7.3797\times10^{-4}$$

Submit ε_θ into Eqs.(13)-(15), we can get a perfect result of $\sigma_{ij}^{PIPE}/\sigma_{ij}^{PLT}$, which have at least 4 significant digits (See Table 3).

Table 3 Ratio $\sigma_{ij}^{PIPE}/\sigma_{ij}^{PLT}$ excluding non singular terms when $e_{min}=2^{-13}$

$e_{min}=2^{-13}$	$\sigma_{r0,FEM}^{PIPE}/\sigma_{x0,FEM}^{PLT}$		$\frac{\sigma_{\theta0,FEM}^{PIPE}-\tilde{\sigma}_{\theta0,FEM}^{PIPE}}{\sigma_{z0,FEM}^{PLT}}$		$\frac{\sigma_{z0,FEM}^{PIPE}-\tilde{\sigma}_{z0,FEM}^{PIPE}}{\sigma_{y0,FEM}^{PLT}}$		$\tau_{rz0,FEM}^{PIPE}/\tau_{xy0,FEM}^{PLT}$	
Material	Mat. 1	Mat. 2	Mat. 1	Mat. 2	Mat. 1	Mat. 2	Mat. 1	Mat. 2
Average	1.0207		1.0207		1.0207		1.0207	
Separate	1.0207	1.0207	1.0207	1.0207	1.0207	1.0207	1.0206	1.0207

Table 4 Ratio $\sigma_{ij}^{PIPE}/\sigma_{ij}^{PLT}$ excluding non singular terms when $e_{min}=2^{-17}$

$e_{min}=2^{-17}$	$\sigma_{r0,FEM}^{PIPE}/\sigma_{x0,FEM}^{PLT}$		$\frac{\sigma_{\theta 0,FEM}^{PIPE}-\tilde{\sigma}_{\theta 0,FEM}^{PIPE}}{\sigma_{z0,FEM}^{PLT}}$		$\frac{\sigma_{z0,FEM}^{PIPE}-\tilde{\sigma}_{z0,FEM}^{PIPE}}{\sigma_{y0,FEM}^{PLT}}$		$\tau_{rz0,FEM}^{PIPE}/\tau_{xy0,FEM}^{PLT}$	
Material	Mat. 1	Mat. 2	Mat. 1	Mat. 2	Mat. 1	Mat. 2	Mat. 1	Mat. 2
Average	1.0204		1.0204		1.0203		1.0203	
Separate	1.0204	1.0204	1.0204	1.0204	1.0204	1.0204	1.0204	1.0204

The result when $e_{min}=2^{-17}$ (see Table 4) also shows the same good consistency as shown in Table 1. It is also found that the ratios are almost independent of element size; the accuracy is up to 4 decimal places. Therefore the zero element method is available for the problem in this research. And the intensity of singular stress in bonded pipe F_{σ}^{PIPE} can be expressed as the multiple of $\sigma_{ij,FEM}^{PLT}$, which has already been solved accurately.

$$F_{\sigma}^{PIPE}=\frac{\sigma_{ij,FEM}^{PIPE}}{\sigma_{ij,FEM}^{PLT}}F_{\sigma}^{PLT}$$

So in this research we mainly consider the ratio $\sigma_{z0,FEM}^{PIPE}/\sigma_{y0,FEM}^{PLT}$ when α, β are fixed. For plane strain problems, the Dunder's parameter α and β can fully control the intensity of singular stress near the end of interface, however, for the bonded pipe (axis symmetric problem), the intensity of singular stress can't be totally dominated by these parameters. Figure 4 is the result when α=0.5, β=0.2. Fig. 4 (a) shows that v_2 varies from 0.1177 to 0.3182 while v_1 varies from 0 to 0.5; Fig. 4 (b) shows that E_2/E_1 varies from 0.3284 to 0.3994 while v_1 varies from 0 to 0.5. Fig. 4 (c) shows that $\sigma_z^{PIPE}/\sigma_y^{PLT}$ varies from 0.9532 to 1.3796 with the variation range of 42.64%.

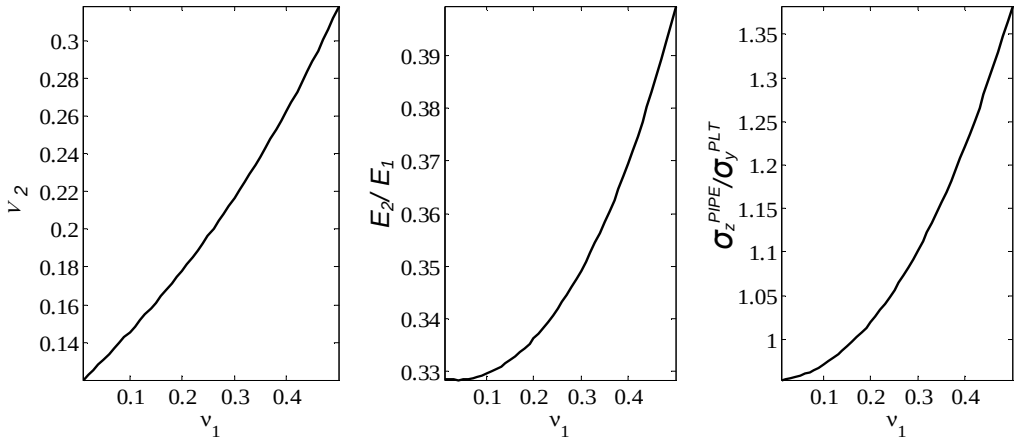

(a) (b) (c)

Fig. 4 $\sigma_z^{PIPE}/\sigma_y^{PLT}$ varies when α and β are fixed as (0.5, 0.2)

Therefore in this study only the maximum and minimum value of $\sigma_{z0,FEM}^{PIPE}/\sigma_{y0,FEM}^{PLT}$ are considered. Figure 5 shows this result. In this research, only the results for $\alpha\geq 0$ in α-β space have been investigated since switching material 1 and 2 (mat. 1↔mat. 2) will only reverse the sings of α and β ((α, β)↔(-α, -β)). So it is unnecessary to draw full map about α and β. When α<0, the result is the same as that when α is positive.

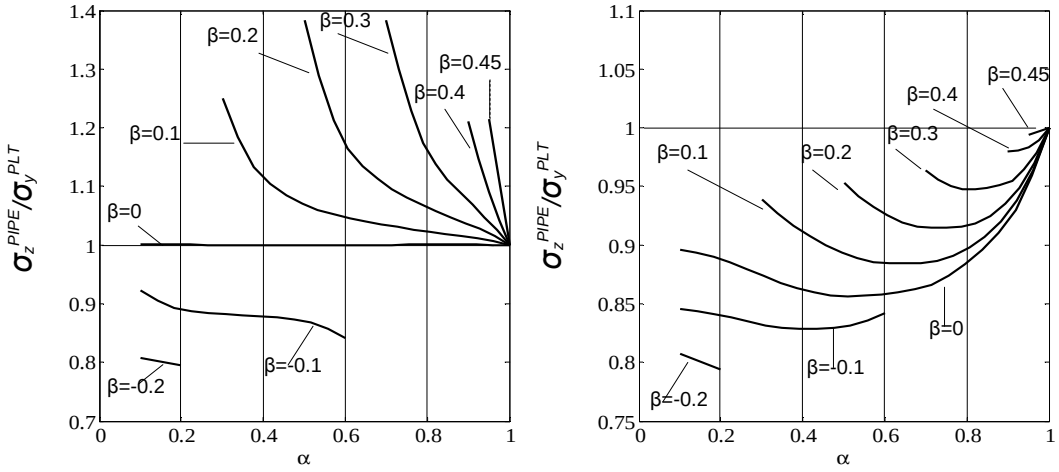

(a) Maximum value of $\sigma_z^{PIPE}/\sigma_y^{PLT}$ (b) Minimum value of $\sigma_z^{PIPE}/\sigma_y^{PLT}$

Fig. 5 Maximum and minimum value of $\sigma_z^{PIPE}/\sigma_y^{PLT}$

5 CONCLUSIONS

In this study the intensity of singular stress for bonded pipe is newly discussed in comparison with the one of bonded plate. First, the non singular terms in stress components of bonded pipe were derived and eliminated so that the proportional method can be applied. This method focuses on the result of first node, which locates on the end of the interface. Then, finite element method is applied to calculate the intensity of singular stress with varying the material combination systematically. And finally the following conclusions can be obtained.

1) The numerical results showed very good consistency among all the ratios of stress components, verifying the rightness of the previous derivation of non singular terms.
2) It is found that the minimum value of stress ratio between axis symmetric problem and plane strain problem is always less than 1, while the maximum value varies from 0.8 to nearly 1.4. The stress ratio for all material combinations converge to 1 if the material combination can reach α=1 or α=-1.
3) Notably, the maximum value keeps constant to 1 when β=0. This result can provide a basic understanding of the intensity of singular stress near the end of interface on a bonded pipe.
4) This investigation may contribute to a better understanding of the debonding strength and provide a better choice of material combination for bonded pipe.

6 REFERENCES

[1] J. Arenas, J.J. Narbon, C. Alia. International Journal of Adhesion & Adhesives, 30, 160-165 (2010).
[2] M. Afendi, T. Teramoto, H. B. Bakri. Int J of Adhesion & Adhesives, 31, 402-411(2011).
[3] S. Azari, M. Papini, J. K. Spelt. Engineering Fracture Mechanics, 78, 153-162 (2011).
[4] D. Hunston, Z. Miyagi, et. al. Mechanics of Time-Dependent Materials, 7, 71-88 (2003).
[5] J.H. Park, J.H. Choi, J.H. Kweon. Composite Structures, 92, 2226-2235(2010).
[6] Y. Suzuki. Transactions of the Japan Society of Mechanical Engineers, A-53, 514-522(1987).
[7] A.A. Neves, E. Courinho, A.Poitevin. Dental Materials, 25, 4-12 (2009).
[8] Noda, N.A, Shirao, R., Li, J. and Sugimoto, J.S., Intensity of Singular Stress at the End of a Fibber under Pull-out Force, International Journal of Solids and Structures, 44(13), (2007), pp.4472-4491.
[9] Teranishi T, Nisitani H. Determination of highly accurate values of stress intensity factor in a plate of arbitrary form by FEM. Trans JSME 1999; A65:16–21.
[10] Zhang Yu, Noda Nao-Aki, Takaishi Ken-Taro, Lan Xin. Effect of Adhesive Thickness on the Interface of Singular Stress at the Adhesive Dissimilar Joint. Transactions Of The Japan Society Of Mechanical Engineers Series A ,77(774), 360-372, 2011.

Proceedings of the 3rd International Conference on
Fracture Fatigue and Wear, pp. 57-62, 2014

ANALYSIS OF INTENSITY OF SINGULAR STRESS FIELD FOR SINGLE LAP JOINT UNDER TENSILE SHEAR LOAD BASED ON CRACK TIP STRESS METHOD

Tatsujiro Miyazaki[1], Nao-Aki Noda[2], Rong Li[3], Takumi Uchikoba[3] and Yoshikazu Sano[2]

[1] University of the Ryukyus, Okinawa, Japan
[2] Kyushu Institute of Technology, Fukuoka, Japan
[3]Graduate School of Engineering, Kyushu Institute of Technology, Fukuoka, Japan

Abstract: In this paper, the crack tip stress method (CTSM) is extended so that the intensity of the singular stress field of the single lap joint (SLJ) with two real stress singularity orders can be analyzed. Two types of the reference models are proposed; one is the tensile force model; the other one is the shear force model. The intensities of the singular stress field of the SLJ are calculated by superposing those of the reference models. The intensities of the singular stress fields of the reference models are calculated by the reciprocal work contour integral method (RWCIM). Then the validity of the reference models and the accuracy of the present method are discussed by comparing the present results with the solutions which are calculated by the RWCIM.

Keywords: intensity of singular stress field; FEM; single lap joint; crack tip stress method

1 INTRODUCTION

In recently years, single lap joints (SLJs) have been widely used to bond dissimilar material members particularly in aircraft and automobile structures. The authors reported that debonding fracture criterion of the SLJs can be expressed with the critical intensity of the singular stress field. However, it is not easy to calculate the intensity of the singular stress field of the SLJ.

Nisitani et al. developed the crack tip stress method (CTSM) [1,2] in order to solve the elastic problems with the notch and crack. Then, the CTSM was extended so that the interface crack and interface corner edge can be analyzed. The authors applied the CTSM to the SLJ and analysed the singular stress field at the interface corner edge of the SLJ under the tensile shear load [3, 4]. In the earlier study, the SLJ is used as the reference model. However, when the various SLJs are analyzed, the simple reference model is desired.

In this study, the reference model suitable for the analysis of the SLJ is examined. Then, the intensities of the singular stress field are solved by the CTSM and the reciprocal work contour integral method (RWCIM) [5]. The intensities of the singular stress field are compared, and the validity of the present reference model and the accuracy of the CTSM are examined.

2 CRACK TIP STRESS METHOD

Figure 1 shows the schematic illustration of the SLJ model and boundary condition. l_1 and t_1 are adherend length and adherend thickness, respectively; l_2 and t_2 are overlap length and adhesive thickness, respectively; E is Young's modulus, ν is Poisson's ratio, and subscripts 1 and 2 refer to the adherend and the adhesive, respectively.

The singular stress field is formed at the corner edge of the interface between the adherend and the adhesive. The singular stress field is governed by the order of stress singularity, $\lambda-1$. The eigenvalue λ can be obtained by solving the eigenvalue equation, which was derived by Bogy. In the case of the corner edge as shown in Fig. 1, the eigenequation is given by the following equation [6,7].

$$4\sin^2(\pi\lambda)\left\{\sin^2\left(\frac{\pi\lambda}{2}\right)-\lambda^2\right\}\beta^2+4\lambda^2\sin^2(\pi\lambda)\alpha\beta+\left\{\sin^2\left(\frac{\pi\lambda}{2}\right)-\lambda^2\right\}\alpha^2$$
$$-4\lambda^2\sin^2(\pi\lambda)\beta-2\left\{\lambda^2\cos(2\pi\lambda)+\sin^2\left(\frac{\pi\lambda}{2}\right)\cos(\pi\lambda)+\frac{1}{2}\sin^2(\pi\lambda)\right\}\alpha+\sin^2\left(\frac{3\pi}{2}\lambda\right)-\lambda^2=0 \quad (1)$$

Here, α and β are Dundurs' parameters [8] and defined as follows

$$\alpha=\frac{G_2(\kappa_1+1)-G_1(\kappa_2+1)}{G_2(\kappa_1+1)+G_1(\kappa_2+1)},\ \beta=\frac{G_2(\kappa_1-1)-G_1(\kappa_2-1)}{G_2(\kappa_1+1)+G_1(\kappa_2+1)},\ \kappa_m=\frac{3-\nu_m}{1+\nu_m}(\text{plain stress}),\ 3-4\nu_m(\text{plain strain}) \quad (2)$$

Here, G_m ($m=1,2$) is the shear modulus of elasticity.

The stresses at a radial distance r from the point O on the interface, σ_θ and $\tau_{r\theta}$, are expressed as follows.

$$\sigma_\theta=\frac{K_1}{r^{1-\lambda_1}}f_{\theta\theta}(0,\lambda_1)+\frac{K_2}{r^{1-\lambda_2}}f_{\theta\theta}(0,\lambda_2)=\frac{K_{\sigma,\lambda_1}}{r^{1-\lambda_1}}+\frac{K_{\sigma,\lambda_2}}{r^{1-\lambda_2}},\ \tau_{r\theta}=\frac{K_1}{r^{1-\lambda_1}}f_{r\theta}(0,\lambda_1)+\frac{K_2}{r^{1-\lambda_2}}f_{r\theta}(0,\lambda_2)=\frac{K_{\tau,\lambda_1}}{r^{1-\lambda_1}}+\frac{K_{\tau,\lambda_2}}{r^{1-\lambda_2}} \quad (3)$$

Here, K_1 and K_2 are real numbers, $f_{\theta\theta}(\theta,\lambda_k)$ and $f_{r\theta}(\theta,\lambda_k)$ are non-dimensional functions of the angle θ, λ_k, Dundurs' parameters (α, β). Because four intensities of the singular stress field, K_{σ,λ_1}, K_{σ,λ_2}, K_{τ,λ_1} and K_{τ,λ_2} are determined by two real numbers K_1 and K_2, the singular stress field in the vicinity of the corner edge is also determined by them. In this paper, four intensities of the singular stress field are analyzed by the CTSM.

In this paper, two reference models as shown in Fig. 2 are introduced in consideration of the mechanical condition at the interface corner O in Fig.1. (a) is the tensile force model; (b) is the shear force model. When $T=T_0$ and $S=S_0$,the singular stress field near the interface corner edge of the SLJ is reproduced. In the CTSM, when the reference models and unknown model are analyzed by FEM, the same mesh pattern and the same materials are used as shown in Figs 2 and 3. The stresses at the interface corner edge, $\sigma_{y0,FEM}^{SLJ}$ and $\tau_{xy0,FEM}^{SLJ}$, are expressed as follows.

$$\sigma_{y0,FEM}^{SLJ}=T_0\,\sigma_{y0,FEM}^{T}\big|_{T=1}+S_0\,\sigma_{y0,FEM}^{S}\big|_{S=1}$$
$$\tau_{xy0,FEM}^{SLJ}=T_0\,\tau_{xy0,FEM}^{T}\big|_{T=1}+S_0\,\tau_{xy0,FEM}^{S}\big|_{S=1} \quad (4)$$

Here, $\sigma_{y0,FEM}^{T}|_{T=1}$ and $\tau_{xy0,FEM}^{T}|_{T=1}$ are stresses at the interface corner edge of the tensile force model under $T=1$ by FEM, $\sigma_{y0,FEM}^{S}|_{S=1}$ and $\tau_{xy0,FEM}^{S}|_{S=1}$ are stresses at the interface corner edge of the shear force model under $S=1$ by FEM. The loads T_0 and S_0 can be obtained by solving the simultaneous equation (4). Then, the intensities of the singular stress field of the SLJ can be obtained by superposing the intensities of the singular stress fields of the two reference models as follows.

$$K_{\sigma,\lambda_k}^{SLJ}=T_0\,K_{\sigma,\lambda_k}^{T}\big|_{T=1}+S_0\,K_{\sigma,\lambda_k}^{S}\big|_{S=1}$$
$$K_{\tau,\lambda_k}^{SLJ}=T_0\,K_{\tau,\lambda_k}^{T}\big|_{T=1}+S_0\,K_{\tau,\lambda_k}^{S}\big|_{S=1} \quad (5)$$

Here, $k=1,2$, $K_{\sigma,\lambda_k}^{T}|_{T=1}$ and $K_{\tau,\lambda_k}^{T}|_{T=1}$ are the intensities of the singular stress field of the tensile force model under $T=1$, $K_{\sigma,\lambda_k}^{S}|_{S=1}$ and $K_{\tau,\lambda_k}^{S}|_{S=1}$ are the intensities of the singular stress field of the shear force model under $S=1$.

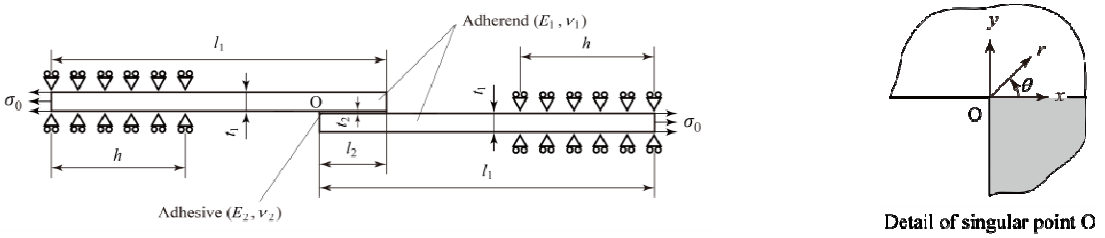

Fig. 1 Schematic illustration of the SLJ

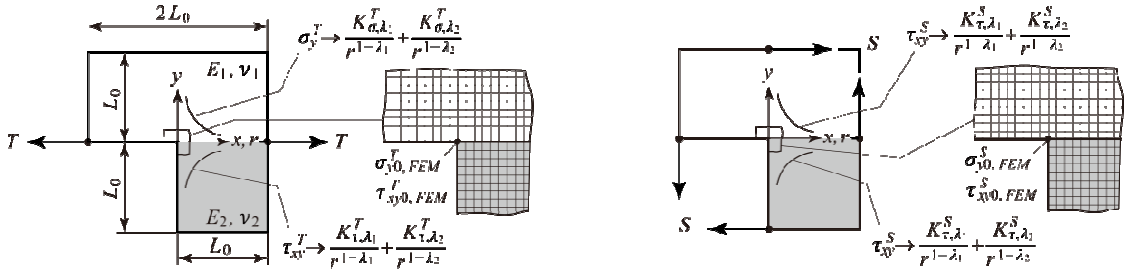

(a) Tensile force model (b) Shear force model

Fig. 2 Reference models used for analysis of SLJ

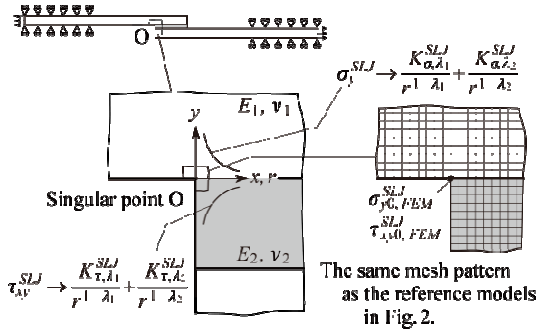

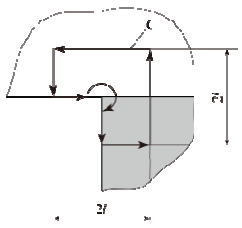

Fig. 3 SLJ model used for analysis **Fig. 4** Contour integral path

3 COMPARISON CTSM WITH RWCIM

In this section, the numerical simulations are performed for four kinds of material combinations: $(\alpha, \beta) = (-0.3, 0.0), (0.3, 0.0), (0.6, 0.0)$ and $(0.8, 0.3)$. In these material combinations, the eigenequation (1) has two different real roots. Then, the validity of the reference models and the accuracy of the CTSM are examined through the simulation results.

The intensities of the singular stress fields of the tensile force model and the shear force model under $L_0 = 1$ mm and $T = S = 1$ N were determined by the RWCIM. The plane strain condition was assumed in the FEM analyses. The commercial FEM code MSC Marc 2008 R1 was used. Figure 4 shows the contour integral path C. Eight node iso-parametric quadrilateral element was used. Table 1 shows the eigenvalues λ_1 and λ_2. Table 2 shows the intensities of the singular stress fields of the reference models.

Table 1 eigenvalues λ_1 and λ_2

Mat. comb.	α	β	λ_1	λ_2
1	-0.3	0.0	0.558760	0.962655
2	0.3	0.0	0.530697	0.821357
3	0.6	0.0	0.517317	0.703330
4	0.8	0.3	0.544319	0.588069

Table 2 Intensities of singular stress field of the reference models

Mat. comb.	Tensile force model				Shear force model			
	K^T_{σ,λ_1}	K^T_{τ,λ_1}	K^T_{σ,λ_2}	K^T_{τ,λ_2}	K^S_{σ,λ_1}	K^S_{τ,λ_1}	K^S_{σ,λ_2}	K^S_{τ,λ_2}
1	0.02303	-0.01225	-0.8423	-0.1162	-0.06735	0.03583	0.04017	0.005542
2	0.02593	-0.01436	-0.3538	-0.1108	-0.05370	0.02973	-0.005941	-0.001860
3	0.02542	-0.01434	-0.1261	-0.05264	-0.04789	0.02701	0.002428	0.001013
4	0.005374	-0.03806	0.001316	0.005596	-0.02639	0.1869	-0.05136	-0.2184

K^T_{σ,λ_k} , K^T_{τ,λ_k} , K^S_{σ,λ_k} , K^S_{τ,λ_k} : $\mathrm{MPa}\cdot\mathrm{m}^{1-\lambda_k}$

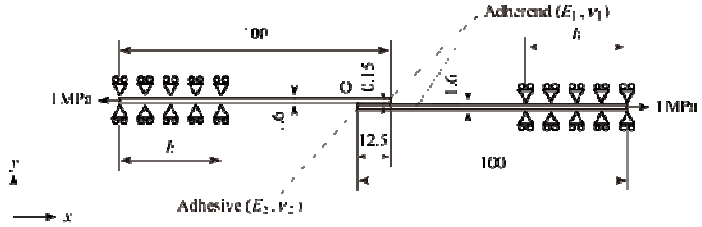

Fig. 5 Analysis model of SLJ (JIS K6850)

Table 3 FEM analysis results of $(\alpha,\beta)=(0.8,0.3)$ when $e_{\min}=3^{-6}$, 3^{-12} and $h=0$

$e_{\min}$	$\sigma^T_{y0,FEM}\big\vert_{T=1}$ $\tau^T_{xy0,FEM}\big\vert_{T=1}$	$\sigma^S_{y0,FEM}\big\vert_{S=1}$ $\tau^S_{xy0,FEM}\big\vert_{S=1}$	$\sigma^{SLJ}_{y0,FEM}$ $\tau^{SLJ}_{xy0,FEM}$	T_0 S_0
3^{-6}	7.217509 -19.25787	-53.96143 46.90953	19.88394 -28.67493	0.8772241 -0.2511529
3^{-12}	143.1043 -396.0553	-982.6654 1223.759	372.3804 -654.7021	0.8766007 -0.2512911

Figure 5 shows the schematic illustration of the SLJ and the boundary conditions. This model is based on JIS K6850. The adhesive thickness $t_2=0.15$ mm, the tensile stress $\sigma_0=1$ MPa, the grip length $h=37.5$ mm were set. In the FEM analyses for RWCIM, eight node iso-parametric quadrilateral element was used near the interface corner edge; four node iso-parametric quadrilateral element was used in the other area. On the other hand, four node iso-parametric quadrilateral element was used in the FEM analyses for CTSM. Table 3 shows the FEM analysis results, T_0 and S_0. The intensities of the singular stress field of the SLJ are obtained from the T_0 and the S_0. Figure 6 shows the relative difference between the results of the CTSM and the RWCIM. The relative differences of the $K^{SLJ}_{\sigma,\lambda_1}$ values and the $K^{SLJ}_{\sigma,\lambda_2}$ values are almost constant independent of the element size. Then, there is little difference between the analysis results of the CTMS and the RWCIM

Table 4 shows four intensities of the singular stress field of the SLJ, $K^{SLJ}_{\sigma,\lambda_1}$, $K^{SLJ}_{\sigma,\lambda_2}$, K^{SLJ}_{τ,λ_1} and K^{SLJ}_{τ,λ_2} which were determined by the CTSM and the RWCIM. There is little difference between the analysis results of the CTMS and the RWCIM. Therefore, the accuracy of the CTSM can be confirmed.

As mentioned above, in the CTSM the intensity of the singular stress field of the SLJ can be obtained from the stress values at the interface corner edge of the reference models and the SLJ model which are calculated by FEM under the same material constants and the same mesh pattern. Therefore, when the intensities of the singular stress field of the reference models are solved on the various material

combinations which are presented with Dundurs' parameter (α, β) in advance, the intensity of the singular stress field of arbitrary SLJ can be obtained easily and promptly.

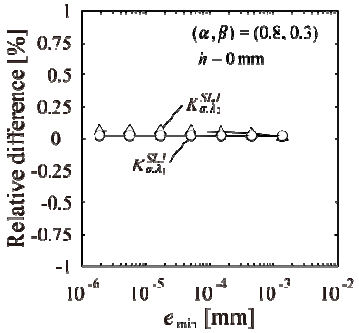

Fig. 6 Relative difference between $K_{\sigma,\lambda_k}^{SLJ}$ values by the present method and RWCIM

Table 4 Intensities of singular stress field when $e_{\min} = 3^{-12}$

(a) $h = 0$ mm

Mat. comb. (α, β)	CTSM		RWCIM	
	$K_{\sigma,\lambda_1}^{SLJ}$	K_{τ,λ_1}^{SLJ}	$K_{\sigma,\lambda_1}^{SLJ}$	K_{τ,λ_1}^{SLJ}
	$K_{\sigma,\lambda_2}^{SLJ}$	K_{τ,λ_2}^{SLJ}	$K_{\sigma,\lambda_2}^{SLJ}$	K_{τ,λ_2}^{SLJ}
1	0.03561	-0.01895	0.03566	-0.01897
(-0.3, 0.0)	-0.7622	-0.1051	-0.7608	-0.1050
2	0.03529	-0.01954	0.03531	-0.01955
(0.3, 0.0)	-0.3012	-0.09434	-0.3009	-0.09423
3	0.03399	-0.01917	0.03400	-0.01918
(0.6, 0.0)	-0.1078	-0.04500	-0.1078	-0.04497
4	0.01134	-0.08034	0.01134	-0.08032
(0.8, 0.3)	0.01406	0.05979	0.01405	0.05975

$K_{\sigma,\lambda_k}^{SLJ}$, K_{τ,λ_k}^{SLJ}, $K_{\sigma,\lambda_k}^{SLJ}$, K_{τ,λ_k}^{SLJ} : MPa · m$^{1-\lambda_k}$

(b) $h = 37.5$ mm

Mat. comb. (α, β)	CTSM		RWCIM	
	$K_{\sigma,\lambda_1}^{SLJ}$	K_{τ,λ_1}^{SLJ}	$K_{\sigma,\lambda_1}^{SLJ}$	K_{τ,λ_1}^{SLJ}
	$K_{\sigma,\lambda_2}^{SLJ}$	K_{τ,λ_2}^{SLJ}	$K_{\sigma,\lambda_2}^{SLJ}$	K_{τ,λ_2}^{SLJ}
1	0.03289	-0.01750	0.03290	-0.01750
(-0.3, 0.0)	-0.7052	-0.09728	-0.7036	-0.09705
2	0.03256	-0.01803	0.03255	-0.01802
(0.3, 0.0)	-0.2801	-0.08772	-0.2797	-0.08758
3	0.03134	-0.01768	0.03133	-0.01767
(0.6, 0.0)	-0.1005	-0.04196	-0.1004	-0.04192
4	0.01034	-0.07326	0.01033	-0.07316
(0.8, 0.3)	0.01261	0.05363	0.01258	0.05352

$K_{\sigma,\lambda_k}^{SLJ}$, K_{τ,λ_k}^{SLJ}, $K_{\sigma,\lambda_k}^{SLJ}$, K_{τ,λ_k}^{SLJ} : MPa · m$^{1-\lambda_k}$

4 CONCLUSIONS

In order to apply the CTSM to the SLJ, the tensile force model and the shear force model were introduced. Then, the validity of two reference models and the accuracy of the CTSM were examined by performing the numerical simulations on JIS type SLJ for $(\alpha, \beta) = (-0.3, 0.0), (0.3, 0.0), (0.6, 0.0)$ and $(0.8, 0.3)$. It was confirmed that four intensities of the singular stress field of the SLJ, $K_{\sigma,\lambda_1}^{SLJ}$, $K_{\sigma,\lambda_2}^{SLJ}$, K_{τ,λ_1}^{SLJ} and K_{τ,λ_2}^{SLJ}, can be obtained by superposing the intensities of the singular stress fields of two reference models. Then, when the results by the CTSM were compared with those by the RWCIM, there is little difference between them.

5 REFERENCES

[1] Nisitani, H., et. al., Determination of Highly Accurate Values of Stress Intensity Factor or Stress Concentration Factor of Plate Specimen by FEM, Trans. Jpn. Soc. Mech. Eng., Ser. A, 65-629 (1999), 26-31.

[2] Zhang, Y., et. al., Effect of Adhesive Thickness on the Interface of Singular Stress at the Adhesive Dissimilar Joint, Trans. Jpn. Soc. Mech. Eng., Ser. A, 77-774 (2011), 360-372.

[3] Noda, N. –A., et. al., Intensity of Singular Stress for Single Lap Joint, Trans. Jpn. Soc. Mech. Eng., Ser. A, 78-789 (2011), 651-655.

[4] Miyazaki, T., et. al., Debonding Criterion for Single Lap Joints from the Intensity of Singular Stress Field, Journal of Japan Institute of Electronics Packaging, 16-2 (2013), 143-151

[5] W. C. Carpenter and C. Byers, A Path Independent Integral for Computing Stress Intensities for V-notched Cracks in a Bimaterial, Int. J. Fract., 35, (1987), 245 - 268.

[6] Bogy, D. B., Edge-bonded dissimilar orthogonal elastic wedges under normal and shear loading, Transaction of the ASME, Journal of Applied Mechanics, Vol. 35, (1968), pp. 460-466.

[7] Bogy, D. B., Two edge-bonded elastic wedges of different and wedge angles under surface tractions, Transaction of the ASME, Journal of Applied Mechanics, Vol. 38, (1971), pp. 377-386.

[8] Dundurs, J., Discussion of edge-bonded dissimilar orthotropic elastic wedges under normal and shear loading, Journal of Applied Mechanics, Vol. 36, (1969), pp. 650-652.

Proceedings of the 3rd International Conference on
Fracture Fatigue and Wear, pp. 63-69, 2014

STRESS INTENSITY FACTORS FOR SMALL EDGE INTERFACE CRACK IN BONDED DISSIMILAR PLATES UNDER THERMAL STRESS

K. Oda[1], T. Shinmoto[2] and N. Tsutsumi[1]

[1] Department of Mechanical and Energy Systems Engineering, Oita University, Oita, Japan
[2] Graduate school of Oita University, Oita, Japan

Abstract: This paper deals with the analysis of the thermal stress intensity factor for small edge interfacial crack in bonded dissimilar plates subjected to uniform change of temperature by using the crack tip stress method. The stress intensity factor of edge interface crack is strongly controlled by the singular stress field at the interface edge of the bonded plates without the crack when the crack becomes extremely short. In this study, the small edge interface crack problem under thermal stress is solved by superposing the uniaxial tension problem with edge singularity and the problem subjected to temperature change and uniaxial compression with no edge singularity. The calculation shows that the stress intensity factors of the small edge interface crack under thermal stress can be evaluated from four factors related only to the Dundurs' parameters.

Keywords: stress intensity factor; interface crack; thermal stress; FEM; crack tip stress method

1 INTRODUCTION

In bonded dissimilar plates, delamination and interface crack at the free edge of interface are often induced by thermal stress due to the elastic and thermal mismatch of the materials. Then, the evaluation of stress intensity factor (SIF) for interface crack under thermal boundary conditions is a subject of practical importance. Although a large number of studies have been made on the interface crack problem under thermal stress [1,2], little is known about the effect of the free edge singularity on the stress intensity factors of the edge interface crack when the crack is extremely short. In the uniaxial tension problem, Noda et al have been shown the SIF of small edge interface crack is strongly dominated by the free-edge singularity of the bonded dissimilar plates without the crack [7,8].

In this paper, single-edge interface crack problem subjected to uniform change of temperature is considered as shown in Fig.1. In Fig.1, G_j, ν_j, η_j (j=1, 2) and ΔT are shear modulus, Poisson's ratio, linear coefficient of thermal expansion and temperature change, respectively. The thermal stress intensity factors for small edge interfacial crack are analysed by using the crack tip stress method. This method is based on the fact that the singular stress field near the interface crack tip is controlled by the stress values at the crack-tip-node calculated by FEM. To determine the SIFs under thermal stress, the stresses at the interface crack tip calculated by FEM are used and are compared with the results of reference problem shown in Fig. 2 under the same mesh pattern near the crack tip [3-6]. In this study, a small edge interface crack in a bonded rectangular plate will be examined with varying crack length and changing material combination. Then, the effect of material combination and relative crack size on the SIF for interface crack will be discussed.

2 CRACK TIP STRESS METHOD

Recently, the effective method was proposed for calculating the stress intensity factor by using FEM [5-6]. The method utilizes the stress values at the crack tip by FEM. From the stresses σ_y, τ_{xy} near the interface crack tip, stress intensity factors are defined as shown in Eq.1.

$$\sigma_y + i\tau_{xy} = \frac{K_1 + iK_2}{\sqrt{2\pi r}}\left(\frac{r}{2a}\right)^{i\varepsilon}, \quad \varepsilon = \frac{1}{2\pi}\ln\left[\left(\frac{\kappa_1}{G_1}+\frac{1}{G_2}\right)\Big/\left(\frac{\kappa_2}{G_2}+\frac{1}{G_1}\right)\right] \tag{1}$$

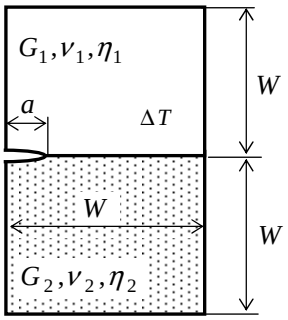

Fig. 1 Treated unknown problem of small edge interface crack under uniform temperature change

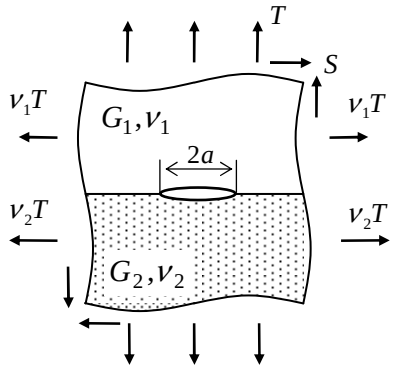

Fig. 2 Reference problem of an interface crack in bonded semi-infinite plates

In Eq.1, G_j is the shear modulus, $\kappa_j = 3-4\nu_j$ for plane strain, $\kappa_j = (3-\nu_j)/(1+\nu_j)$ for plane stress and ν_j is Poisson's ratio (j=1, 2). From Eq.1, SIFs may be separated as

$$K_1 = \lim_{r\to 0}\sqrt{2\pi r}\,\sigma_y\{\cos Q + (\tau_{xy}/\sigma_y)\sin Q\}, \quad K_2 = \lim_{r\to 0}\sqrt{2\pi r}\,\tau_{xy}\{\cos Q - (\sigma_y/\tau_{xy})\sin Q\}, \tag{2}$$

$$Q = \varepsilon \ln\{r/(2a)\}. \tag{3}$$

Here, r and Q can be chosen as constant values when the reference and unknown problems have the same crack length and the same material constants. If Eq.4 is satisfied, Eq.5 may be derived from Eqs.2.

$$\tau_{xy}{}^*/\sigma_y{}^* = \tau_{xy}/\sigma_y \tag{4}$$

$$K_1{}^*/\sigma_y{}^* = K_1/\sigma_y, \quad K_2{}^*/\tau_{xy}{}^* = K_2/\tau_{xy} \tag{5}$$

Here, σ_y*, τ_{xy}* are stresses of reference problem near the crack tip, and σ_y, τ_{xy} are stresses of unknown problem in Fig. 1. The asterisk means the value of reference problem. In the FEM analysis, the stresses at the crack tip node, $\sigma_{y0,FEM}$ and $\tau_{xy0,FEM}$, are obtained as the finite value. By using the stress values at the interface crack tip calculated by FEM under the same mesh pattern, the SIFs of the unknown problem can be determined by

$$K_1 = \frac{\sigma_{y0,FEM}}{\sigma_{y0,FEM}{}^*}K_1{}^*, \quad K_2 = \frac{\tau_{xy0,FEM}}{\tau_{xy,FEM}{}^*}K_2{}^* \tag{6}$$

When the single interface crack in a dissimilar bonded infinite plane subjected to the loads T and S shown in Fig. 2 is selected as the reference problem, the SIFs of the reference problem are evaluated by

$$K_1{}^* + iK_2{}^* = (T+iS)\sqrt{\pi a}(1+2i\varepsilon) \tag{7}$$

In order to determine the applied loads T and S in Eq.7, the reference problem is expressed by superposing the tension and shear problems [5, 6]. Then, the stresses at the interface crack tip of the reference problem are expressed by

$$\sigma_{y0,FEM}{}^* = T\cdot\sigma_{y0,FEM}^{T=1}{}^* + S\cdot\sigma_{y0,FEM}^{S=1}{}^*, \quad \tau_{xy0,FEM}{}^* = T\cdot\tau_{xy0,FEM}^{T=1}{}^* + S\cdot\tau_{xy0,FEM}^{S=1}{}^* \tag{8}$$

where $\sigma_{y0,FEM}^{T=1}$ stands for the stress σ_y at the crack-tip node calculated by FEM in the condition of T=1 and S=0. From the condition that the crack-tip-stresses between the unknown and the reference problems are the same, we obtain the applied loads T and S as follows,

$$T = \frac{\sigma_{y0,FEM} \cdot \tau_{xy0,FEM}^{S=1\ *} - \sigma_{y0,FEM}^{S=1\ *} \cdot \tau_{xy0,FEM}}{\sigma_{y0,FEM}^{T=1\ *} \cdot \tau_{xy0,FEM}^{S=1\ *} - \sigma_{y0,FEM}^{S=1\ *} \cdot \tau_{xy0,FEM}^{T=1\ *}}, \quad S = \frac{\sigma_{y0,FEM}^{T=1\ *} \cdot \tau_{xy0,FEM} - \sigma_{y0,FEM} \cdot \tau_{xy0,FEM}^{T=1\ *}}{\sigma_{y0,FEM}^{T=1\ *} \cdot \tau_{xy0,FEM}^{S=1\ *} - \sigma_{y0,FEM}^{S=1\ *} \cdot \tau_{xy0,FEM}^{T=1\ *}} \tag{9}$$

Since the applied loads T and S determined by Eq.9 satisfy the condition that $\sigma_{y0,FEM}^* = \sigma_{y0,FEM}$ and $\tau_{xy0,FEM}^* = \tau_{xy0,FEM}$, the SIFs of unknown problem are equivalent to that of reference problem. Therefore, we can obtain the SIFs of unknown problem from Eqs.7 and 9 by using the crack tip stress values calculated by FEM under the same mesh pattern.

3 NUMERICAL RESULTS AND DISCUSSION

In this analysis, eight-node-quadrilateral element is used and the FEM mesh near the crack tip is made fine systematically [3-6]. It should be noted that the same mesh size and pattern near the crack tip have to be used in the calculation of stress values for the unknown and reference problems.

3.1 Effect of singular stress field near the interface edge due to thermal stress

The SIF of the short interface crack is dominated by the singular stress field near the free edge. Figure 3 shows the normalized SIFs for small edge interface crack under uniform temperature change analysed by the crack tip stress method. Dimensionless factors, F_1 and F_2, are defined as follows in this study,

$$K_1 + iK_2 = (F_1 + iF_2)\sigma_0\sqrt{\pi a}(1 + 2i\varepsilon) \tag{10}$$

$$\sigma_0 = \frac{8G_1G_2(\eta_2^* - \eta_1^*)\Delta T}{G_1(\kappa_2 - 1) - G_2(\kappa_1 - 1) - 2(G_1 - G_2)} \tag{11}$$

Here, σ_0 is the equivalent tensile stress in tension problem which gives the same edge singularity, and $\eta_j^* = (1+\nu_j)\eta_j$ for plane strain, $\eta_j^* = \eta_j$ for plane stress (j=1, 2). As shown in Fig.3, the values of $F_{1,2}$ tend to increase or decrease markedly as the interface crack becomes short. This is the reflection of the free edge stress singularity caused by the thermal stress.

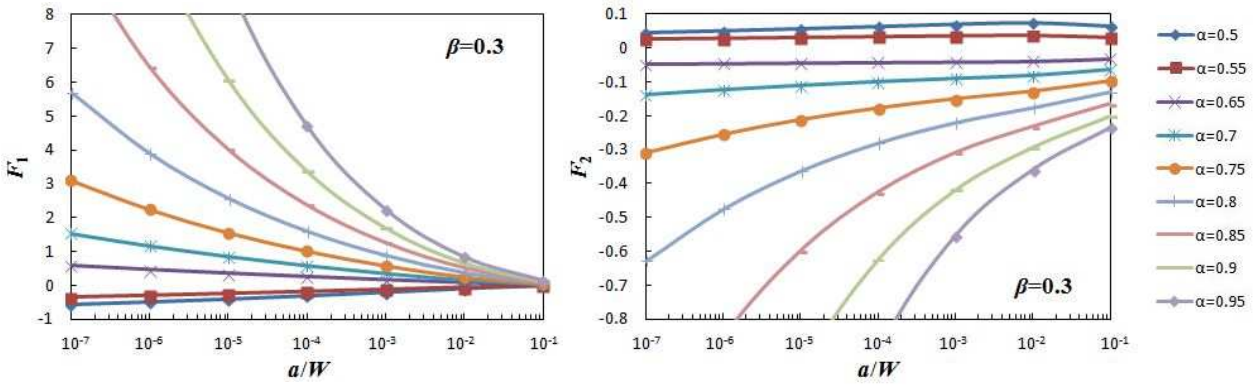

(a) F_1 vs a/W (b) F_2 vs a/W

Fig. 3 Relation between normalized SIFs and the relative crack length a/W when β=0.3

3.2 Superposition method to analyze a small edge interface crack problem under thermal stress

In this study, the problem of the small interface crack under thermal stress is represented by superposing two different problems as illustrated in Fig. 4. Fig. 4(b) is the small edge interface crack problem under tension in y-direction and Fig. 4(c) is the problem subjected to compression and uniform temperature change. The problem of Fig. 4(b) has the edge singularity and Fig. 4(c) has no edge singularity.

Figure 5 shows the stress distributions near the free edge in each problem without the crack. As shown in Figs. 5(a) and 5(b), the problem of Fig.4b has the same stress singularity as the thermal problem of Fig. 4(a) by using the tensile stress σ_0 in Eq.11. In Fig. 5(c), the problem of Fig. 4(c) has the uniform stress field along the interface because the singular stress due to the temperature change is counteracted by the singular stress due to the compressive stress σ_0. Noda et al [7, 8] have reported that the normalized SIFs for the small edge interface crack in the bonded plate subjected to uniaxial tension in y-direction become constant values by dividing by $(a/W)^{1-\lambda}$ when the relative crack length $a/W<10^{-2}$. Then, the normalized SIFs in Fig.1 can be expressed by the following definition.

$$F_1 = C_1 \cdot (W/a)^{1-\lambda} + D_1, \quad F_2 = C_2 \cdot (W/a)^{1-\lambda} + D_2 \tag{12}$$

Here, λ is the index of stress singularity at the interface edge without the crack and is given as the root of the eigenequation [8, 9]. In Eq.12, the factors $C_{1,2}$ and $D_{1,2}$ are obtained by analysing the problems of Fig.4b and Fig.4c, respectively.

Figures 6 and 7 show the relation between the normalized factors $C_{1,2}$ and $D_{1,2}$ and the relative crack length a/W when β=0.3. It is seen that the factors $C_{1,2}$ and $D_{1,2}$ become constant when $a/W<10^{-2}$.

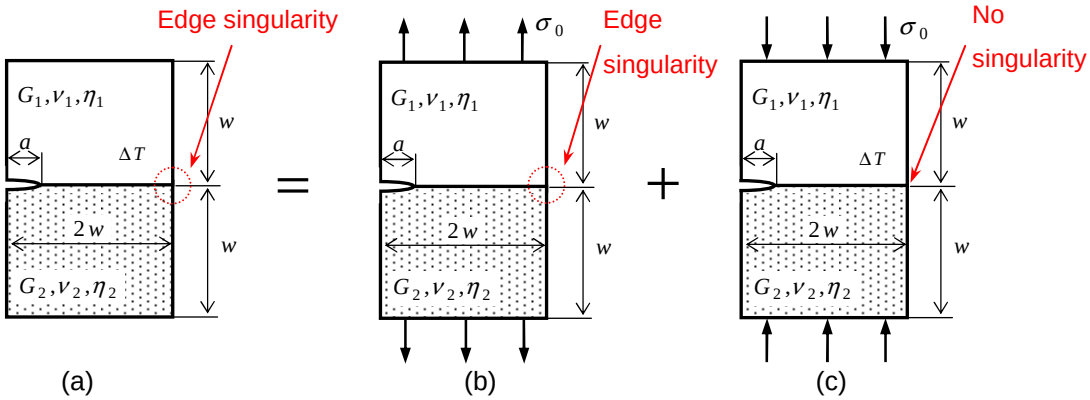

Fig. 4 Relation between normalized SIFs and the relative crack length a/W.

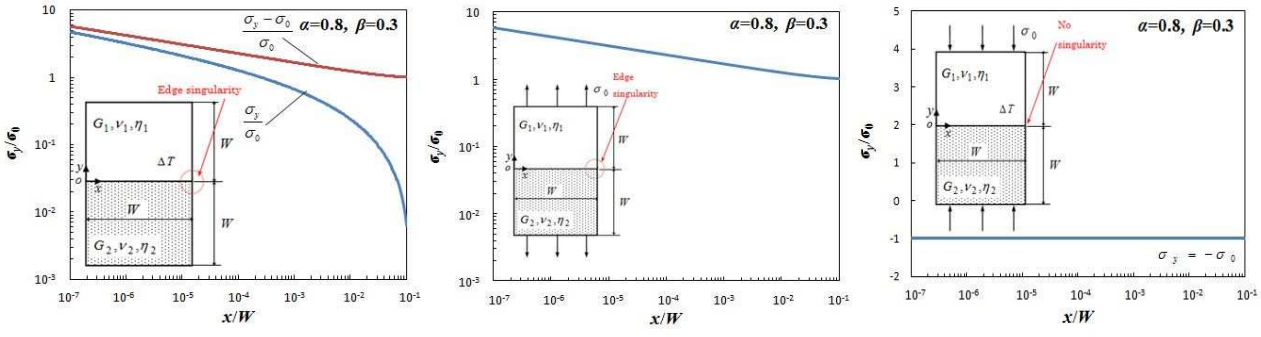

Fig. 5 Stress distribution near the interface edge in bonded dissimilar plates without the crack

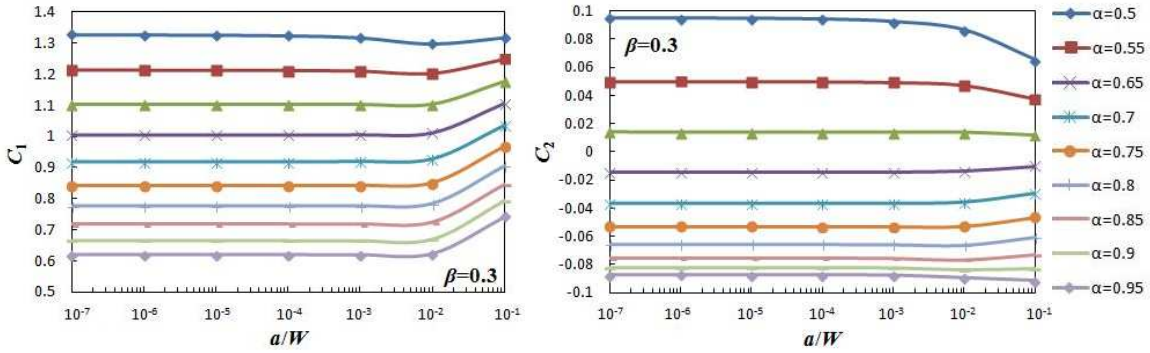

Fig. 6 Relation between $C_{1,2}$ (Fig. 4(b)) and the relative crack length a/W when β=0.3

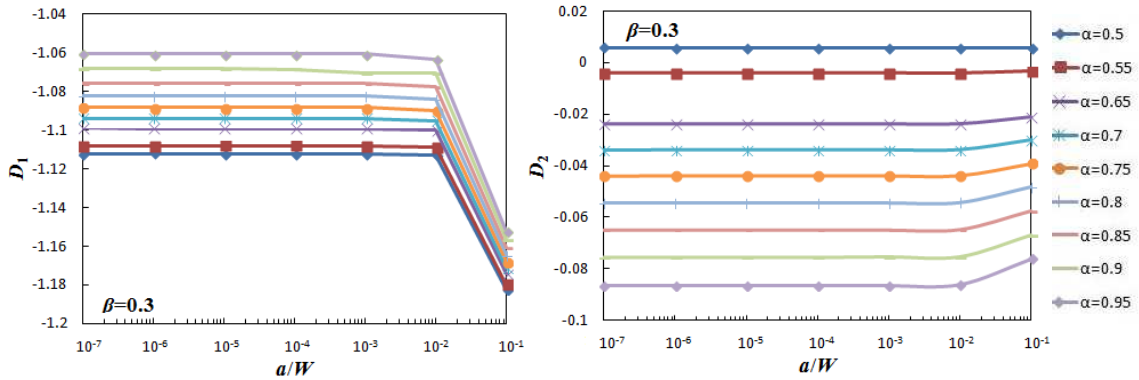

Fig. 7 Relation between $D_{1,2}$ (Fig. 4(c)) and the relative crack length a/W when β=0.3

The factors $C_{1,2}$ and $D_{1,2}$ for the small edge interface crack depend on the material combination. Since the factors C_1 and C_2 of Fig.4b have already been presented in Ref. [7, 8], Tables 1 and 2 show the values of D_1 and D_2 obtained from the problem of Fig.4c when Dundurs' parameters α and β are widely changed. In the case that α=2β, the factors $D_{1,2}$ cannot be determined by using the problem of Fig.4c because the thermal problem of Fig.4a has a logarithmic singularity at the free edge of interface between bonded dissimilar materials.

In Table 3, the dimensionless SIFs $F_{1,2}$ evaluated from Eq.12 are compared with the SIFs directly calculated by the crack tip stress method (CTSM). As shown in Table 3, both results are in good agreement with each other. Therefore, the SIFs of the small interface crack under the uniform temperature change can be easily evaluated by using C_1, C_2, D_1 and D_2 without FEM analysis for any material combinations.

Table 1 Values of D_1 for Fig.4c. [$K_1 + iK_2 = (F_1 + iF_2)\sigma_0\sqrt{\pi a}(1+2i\varepsilon)$, $F_1 = C_1 \cdot (W/a)^{1-\lambda} + D_1$, $F_2 = C_2 \cdot (W/a)^{1-\lambda} + D_2$]

α	β=-0.2	β=-0.1	β=0	β=0.1	β=0.2	β=0.3	β=0.4
0	-1.127	-1.123	-	-1.123	-1.127		
0.10	-1.128	-1.123	-1.121	-1.122	-1.126		
0.20		-1.122	-1.119	-	-1.123		
0.30		-1.120	-1.117	-1.117	-1.119	-1.125	
0.40		-1.117	-1.113	-1.112	-	-1.119	
0.50		-1.112	-1.108	-1.107	-1.108	-1.112	
0.60			-1.102	-1.099	-1.100	-	
0.70			-1.094	-1.091	-1.091	-1.094	-1.099
0.80			-1.085	-1.081	-1.080	-1.082	-
0.90			-1.074	-1.070	-1.068	-1.069	-1.072

Table 2 Values of D_2 for Fig.4c. [$K_1 + iK_2 = (F_1 + iF_2)\sigma_0\sqrt{\pi a}(1+2i\varepsilon)$, $F_1 = C_1 \cdot (W/a)^{1-\lambda} + D_1$, $F_2 = C_2 \cdot (W/a)^{1-\lambda} + D_2$]

α	β=-0.2	β=-0.1	β=0	β=0.1	β=0.2	β=0.3	β=0.4
0	-0.0647	-0.0318	-	0.0318	0.0647		
0.10	-0.0828	-0.0497	-0.0179	0.0139	0.0466		
0.20		-0.0677	-0.0358	-	0.0283		
0.30		-0.0857	-0.0538	-0.0222	0.0100	0.0441	
0.40		-0.1038	-0.0736	-0.0405	-	0.0251	
0.50		-0.1221	-0.0902	-0.0590	-0.0274	0.0058	
0.60			-0.1089	-0.0778	-0.0465	-	
0.70			-0.1278	-0.0970	-0.0660	-0.0338	0.0009
0.80			-0.1472	-0.1166	-0.0860	-0.0544	-
0.90			-0.1671	-0.1368	-0.1066	-0.0756	-0.0425

4 CONCLUSIONS

In this paper, the bonded dissimilar plates with a single-edge interface crack subjected to the uniform temperature change were analyzed with varying the relative crack length and material combinations systematically. The stress intensity factors of interface crack were evaluated by using the ratio of crack-tip stress values between the reference and target unknown problems. In this study, the small edge interface crack problem under thermal stress was solved by superposing the uniaxial tension problem with edge singularity and the problem subjected to temperature change and uniaxial compression with no edge singularity. The calculation showed that the stress intensity factors of the small edge interface crack under thermal stress can be evaluated from the following definition with four factors when the relative crack length $a/W<10^{-2}$:

$F_1 = C_1 \cdot (W/a)^{1-\lambda} + D_1$, $F_2 = C_2 \cdot (W/a)^{1-\lambda} + D_2$.

In above definition, λ is the order of the stress singularity at the interface edge without the crack.

Table 3 Comparison of the normalized SIFs F_1 and F_2 calculated by CTSM and Eq.12.
[$K_1 + iK_2 = (F_1 + iF_2)\sigma_0\sqrt{\pi a}(1+2i\varepsilon)$, $F_1 = C_1 \cdot (W/a)^{1-\lambda} + D_1$, $F_2 = C_2 \cdot (W/a)^{1-\lambda} + D_2$]

a/W	F_1 (CTSM)		C_1		D_1		F_1 (Eq.12)	
	α=0.5	α=0.9	α=0.5	α=0.9	α=0.5	α=0.9	α=0.5	α=0.9
10^{-6}	-0.4989	10.38	1.326	0.666	-1.1122	-1.0689	-0.499	10.38
10^{-5}	-0.4150	6.058	1.326	0.666	-1.1122	-1.0689	-0.415	6.059
10^{-4}	-0.3206	3.367	1.326	0.666	-1.1122	-1.0689	-0.319	3.368
a/W	F_2 (CTSM)		C_2		D_2		F_2 (Eq.12)	
	α=0.5	α=0.9	α=0.5	α=0.9	α=0.5	α=0.9	α=0.5	α=0.9
10^{-6}	0.0497	-1.491	0.089	-0.083	0.0058	-0.0756	0.0493	-1.486
10^{-5}	0.0556	-0.956	0.089	-0.083	0.0058	-0.0756	0.0552	-0.953
10^{-4}	0.0621	-0.624	0.089	-0.083	0.0058	-0.0756	0.0620	-0.622

5 REFERENCES

[1] F. Erdogan, Stress Distribution in Bonded Dissimilar Materials with Cracks, *Journal of Applied Mechanics*, Vol.32, pp.403–410, 1965.

[2] T. Ikeda, T. Sun, Stress Intensity Factor Analysis for an Interface Crack between Dissimilar Isotropic Materials under Thermal Stress, *International Journal of Fracture*, Vol. 111, pp.229-249, 2001.

[3] H. Nisitani, T. Kawamura, W. Fujisaki, T. Fukuda, Determination of Highly Accurate Values of Stress Intensity Factor or Stress Concentration Factor of Plate Specimen by FEM, *Transactions of the Japan Society of Mechanical Engineering (JSME)*, Vol. 65A, No. 629, pp. 26-31, 1999 (in Japanese).

[4] H. Nisitani, T. Teranishi, K. Fukuyama, Stress Intensity Factor Analysis of a Bimaterial Plate Based on the Crack Tip Stress Method, *Transactions of the JSME*, Vol. 69A, No. 684, pp. 1203-1208, 2003 (in Japanese).

[5] K. Oda, N.-A. Noda, S.N. Atluri, Accurate Determination of Stress Intensity Factor for Interface Crack by Finite Element Method, *Key Engineering Materials*, Vols. 353-358, pp.3124-3127, 2007.

[6] K. Oda, K. Kamisugi, N.-A. Noda, Stress Intensity Factor Analysis of Interface Crack by Proportional Method, *Transactions of the JSME*, Vol. 75A, No. 752, pp. 476-482, 2009 (in Japanese).

[7] N.-A. Noda, X. Lan, K. Michinaka, Y. Zhang. K. Oda, Stress Intensity Factor of an Edge Interface Crack in a Bonded Semi-Infinite Plate, *Transactions of the JSME*, Vol. 76A, No. 770, pp. 1270-1277, 2010 (in Japanese).

[8] K. Oda, X. Lan, N.-A. Noda, K. Michinaka, Effect of Arbitrary Bi-material Combination and Bending Loading Conditions on Stress Intensity Factors of an edge Interface Crack, *International Journal of Structural Integrity*, Vol. 3, No. 4, pp.457-475, 2012.

[9] D.-H. Chen, H. Nisitani, Intensity of Singular Stress Field near the Interface Edge Point of a Bonded Strip, *Transactions of the JSME*, Vol. 59A, No. 567, pp. 2682-2686, 1993 (in Japanese).

Proceedings of the 3rd International Conference on
Fracture Fatigue and Wear, pp. 70-74, 2014

A VIRTUAL JOINT ELEMENT METHOD FOR NUMERICAL SIMULATION OF QUASI-BRITTLE MATERIAL FAILURE PROCESS

Chunhui Xu and Mingrui Li

College of Science, China Agricultural University, Beijing 100083, China

Abstract: The combination of finite deformation element and virtual joint element is introduced to simulate the failure process of quasi-brittle materials. For planar problem, the so called virtual joint element is a 4-nodes quadrilateral element, which is add between two 3-nodes triangle finite elements. Based on accurate finite deformation theories and the Total Lagrangian formulation (T.L.), tangent stiffness matrix of the virtual joint element is derived, where the second Piola-Kirchhoff stress and Green-Lagrange strain are chosen as the energy conjugate stress and strain. According to numerical results, the relationship between virtual joint element size and calculation error are discussed. As verification, the numerical example is illustrated, which shows that this method has a promising future and is suitable for modelling failure process of quasi-brittle materials.

Keywords: quasi-brittle; finite deformation; virtual joint element; failure; numerical simulation

1 INTRODUCTION

Quasi-brittle materials include rock, concrete and ceramics and thereby constitute a significant proportion of our immediate structural environment. Numerical modelling constitutes a powerful and relatively inexpensive tool for obtaining invaluable insight into complex system responses. The ability to accurately model quasi-brittle systems is of great importance in assessing (amongst other applications) the feasibility, including safety and serviceability, of concrete structures and mining excavations in rock.

One method is based on discrete bodies system (such as DEM): firstly, generating a group of discrete bodies; secondly, using some kind of mechanism to bond or "weld" them together; finally, the external forces are loaded. Once the structure reaches the failure criterion, the bonds are broken. The key to the success of this method is to the extend of approximation of the bond mechanism to physical nature. Comparison with the solutions of typical problem and experiments is the way to ensure the equivalency [1-4].

Another important method is based on continua system (such as FEM). After defining the continuum, a reasonable fracture criterion is set, and then external force is enforced to the structure. Once the criterion is attained, the continua become discontinuous. Owen [5,6] and Munjiza [7] have made innovative contributions to address the failure process of quasi-brittle materials. In their study, rules of the DEM are introduced when handling interaction between the sub-block and the remaining main block or between sub-blocks. The method is called the coupled finite element and discrete element method or finite element - discrete element method (FE / DE).

For planar problems, the so called virtual joint element method is to add a 4-nodes quadrilateral element between two 3-nodes triangle finite elements. The tangent stiffness matrix of the virtual joint element is derived using finite deformation theories and T.L. formulation, where the 2nd Piola-Kirchhoff stress and Green-Lagrange strain are chosen as the energy conjugate stress and strain; The concept of softening of quasi-brittle material is introduced when handling the brittle failure. For homogeneous materials, its material properties are set to be same with surrounding medium without any additional material parameters, which differs from artificially “weld” finite elements together. As verification, two numerical examples are illustrated, which shows that this method has a promising future and is suitable for modelling failure process of quasi-brittle materials.

2 TANGENT STIFFNESS MATRIX

The process of fracture in quasi-brittle materials involves relatively small strains and large displacements and rotations. In the presentence of large rotations, the small deformation element with updated displacement algorithm will result additional stress and strain and cannot be employed to solve such problems while the algorithm based on finite deformation theory can obtain the same exact solutions with the theoretical solutions. Therefore, the design of the virtual joint element is based on accurate finite deformation theory. Fig. 1(a) shows the 3- node triangle finite element and Fig. 1(b) shows the virtual joint element 4 between the triangle elements. For general problems, the joint element can be added in global scope; for large scale problems, the joint element can be added only in possible fracture areas in order to save calculation time and enhance efficiency.

(a) Triangle element (b) virtual joint element

Fig. 1 Joint Element

Joint element in local coordinates is illustrated in Fig. 2, where b is the side length of the triangle elements, and h is the height of joint element. In this section, the integral expressions of tangent stiffness matrix of the joint element are derived.

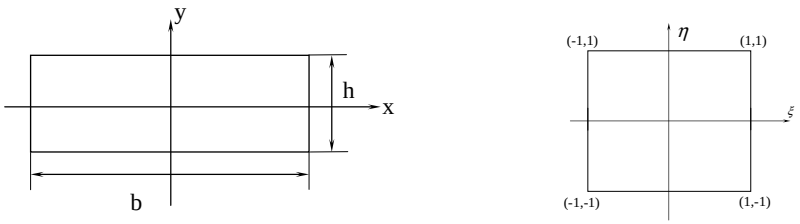

(a) Virtual joint element in x-y coordinates (b) Virtual joint element in $\xi-\eta$ coordinates

Fig. 2 Virtual joint element in local coordinates

The total Lagrangian formulation (T.L.) is used in calculation, which adopts the initial material (undeformed) configuration as the reference configuration. The 2nd Piola-Kirchhoff stress S and Green-Lagrange strain E are chosen as the energy conjugate stress and strain.

The definition of Green-Lagrange strain as show as.

$$E = (F^T F - I)/2 \tag{1}$$

By using (1), the variation of Green-Lagrange strain can be found as

$$\delta E = \begin{Bmatrix} \delta E_{xx} \\ \delta E_{yy} \\ \delta E_{xy} \end{Bmatrix} = \begin{bmatrix} 1+u_{,x} & v_{,x} & 0 & 0 \\ 0 & 0 & u_{,y} & v_{,y} \\ u_{,y} & 1+v_{,y} & 1+u_{,x} & v_{,x} \end{bmatrix} \begin{bmatrix} \delta u_{,x} \\ \delta v_{,x} \\ \delta u_{,y} \\ \delta v_{,y} \end{bmatrix} = L\delta e\,. \tag{2}$$

Assume

$$e = [u_{,x} \quad v_{,x} \quad u_{,y} \quad v_{,y}]^T, q = [u_1 \quad v_1 \quad u_2 \quad v_2 \quad u_3 \quad v_3 \quad u_4 \quad v_4]^T = [q_1 \quad q_2 \quad q_3 \quad q_4]^T \tag{3}$$

then

$$\delta e = \begin{bmatrix} N_{1,x} & 0 & N_{2,x} & 0 & N_{3,x} & 0 & N_{4,x} & 0 \\ 0 & N_{1,x} & 0 & N_{2,x} & 0 & N_{3,x} & 0 & N_{4,x} \\ N_{1,y} & 0 & N_{2,y} & 0 & N_{3,y} & 0 & N_{4,y} & 0 \\ 0 & N_{1,y} & 0 & N_{2,y} & 0 & N_{3,y} & 0 & N_{4,y} \end{bmatrix} \begin{Bmatrix} \delta u_1 \\ \delta v_1 \\ \delta u_2 \\ \delta v_2 \\ \delta u_3 \\ \delta v_3 \\ \delta u_4 \\ \delta v_4 \end{Bmatrix} = H \delta q \tag{4}$$

where

$$N_{i,x} = \frac{\xi_i}{8b}(1+\eta_i\eta)\,,\ N_{i,y} = \frac{\eta_i}{8h}(1+\xi_i\xi) \tag{5}$$

The strain variation can be expressed as

$$\delta E = LH\delta q = \overline{B}\delta q \tag{6}$$

The constitutive law of elastic planar problem is given by

$$S = DE \tag{7}$$

where ***D*** is constitutive matrix.

According to the principle of virtual work, the expressions of external virtual work and internal virtual work are given by

$$\delta W^{(e)} = \delta q^T P \tag{8}$$

$$\delta W^{(i)} = t\int_A \delta E^T S = t\delta q^T \int_A \overline{B}^T S dA \tag{9}$$

where P is equivalent node force and t is element thickness.

The arbitrariness of node virtual displacements yields the following equilibrium formulation

$$F(q) = P - N = 0 \tag{10}$$

where N is internal nodes force vector, and

$$N = t\int_A \overline{B}^T S dA \tag{11}$$

In static problems, linear algebraic equations are derived using Newton iteration method

$$K_T \Delta q = \Delta r \tag{12}$$

The tangent stiffness matrix K_T for planar problems can be expressed as follows

$$K_T = t\int_A \overline{B}^T \Delta S dA + t\int_A \Delta\overline{B}^T S dA = K_u + K_\sigma \tag{13}$$

Where K_u and K_σ are called displacement stiffness matrix and geometry stiffness matrix respectively.

Combining Eq. (4), Eq. (6) and Eq. (7) yields

$$K_u = t\int_A H^T L^T DLH dA \tag{14}$$

$$K_\sigma = t\int_A H^T G H dA \tag{15}$$

Where

$$G=\begin{bmatrix} S_{xx} & 0 & S_{xy} & 0 \\ 0 & S_{xx} & 0 & S_{xy} \\ S_{xy} & 0 & S_{yy} & 0 \\ 0 & S_{xy} & 0 & S_{yy} \end{bmatrix} \tag{16}$$

3 DETERMINE THE ELEMENT SIZE

When the finite deformation element and virtual joint element are combined to simulate damage or failure of quasi-brittle materials, it should ensure that, before the structure meets its failure criteria, the results are not affected whether the joint element exists or not. As illustrated beam in Fig. 3(a), impact on the calculation results is studied with different virtual joint element height h. Corner points of the bottom edge are restrained both in x and y directions. Mesh is shown in Fig. 3(b). In simulation, the concrete density, Young's modulus and Poisson's ratio are set at $3400kg/m^3, 39GPa$ and 0.2 respectively. The tensile strength $f_t = 3.15\text{MPa}$. Material parameters for the virtual joint element are consistent with the surrounding medium. The concentrated load is enforced on the top mid-point of the beam, and P=10KN.

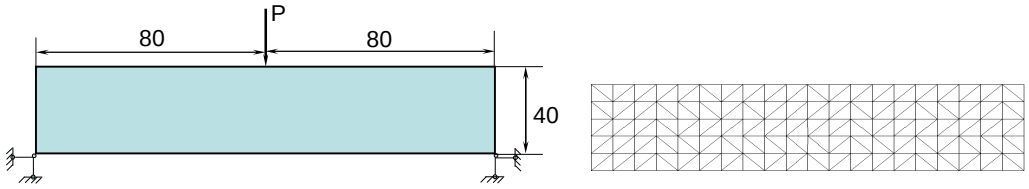

(a) Geometry of the beam (b) Mesh of the beam

Fig. 3 Geometry and mesh of beam model

Table 1 compares the stress and displacement (mid-point in the bottom edge) results for different height h with that of no virtual joint element and the relative error is shown. It can be seen from Table1 (a) that, the relative error is 3% when $h/b = 1.e-2$ and 0.01% when $h/b = 1.e-4$. Therefore, under normal circumstances, when $h/b \le 1.e-2$, the presentence of virtual joints element has little effect on the results and the calculation accuracy can be satisfied.

Table 1 Comparison of Static Calculation Results

Virtual joint element	h/b	σ_x (relative error)	σ_1 (relative error)	σ_2 (relative error)	u_y (relative error)
no		.6376e+05	.6451e+05	-.7162e+04	-.5119e-03
	1.e-1	.5210e+05(19.7%)	.1050e+06(62.7%)	-.9775e+04(36.5%)	-.5262e-03(2.8%)
	1.e-2	.6244e+05(2.1%)	.6313e+05(2.1%)	-.6851e+04(4.3%)	-.5134e-03(0.3%)
yes	1.e-3	.6363e+05(2.0%)	.6437e+05(0.2%)	-.7130e+04(0.4%)	-.5121e-03(0.04%)
	1.e-4	.6375e+05(0.01%)	.6450e+05(0.01%)	-.7158e+04(0.05%)	-.5119e-03(0)
	1.e-5	.6376e+05(0)	.6451e+05(0)	-.7162e+04(0)	-.5119e-03(0)

4 NUMERICAL EXAMPLE

Geometry, boundary conditions, loading, and materials parameters of the three-point bending beam are the same as shown in Fig. 3(a). The tensile strength $f_t = 3.15\text{MPa}$, and fracture energy $G_f = 69N/m$. Material parameters for the virtual joint element are consistent with the surrounding medium. In this simulation, the unstructured mesh is employed as shown in Fig. 4(a). The results indicate that, the crack starts at the lower midpoint, where tensile stress reaches maximum. With the gradual increased loading, the crack begins to propagate upward. The crack propagations at various time steps after failure are shown in Fig.4 (b)-(d).

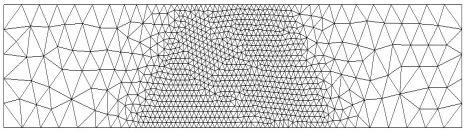

(a) Unstructured mesh of beam model

(b) Time step=20 (c) Time step=40 (d) Time step=60

Fig. 4 Crack propagation

5 CONCLUSIONS

In this paper, a virtual joint element method for simulate the failure of quasi-brittle materials is presented. The regular finite deformation element and the virtual joint element are combined to simulate the failure processes of structures. The main conclusions are drawn as follows:

1) The second Piola-Kirchhoff stress S and Green-Lagrange strain E are chosen as the energy conjugate stress and strain. The total Lagrangian formulation (T.L.) is used in calculation, which adopts the initial material (undeformed) configuration as the reference configuration.
2) The precise tangent stiffness matrix of the virtual joint element is derived using finite deformation theories. According to numerical results, numerical accuracy depends on the ratio of *h/b*, and the ratio can be set at 0.01 in most cases.
3) As verification, the failure processes of concrete beams under concentrated force loading are simulated. The results are consistent with that of other documents. The combination of virtual joint element and finite deformation element is a new and feasible method to simulate the failure process of quasi-brittle materials.

6 ACKNOWLEDGEMENT

The authors acknowledge the support from the National Natural Science Foundation of China(Grant No. 11272341，No.11072260)

6 REFERENCES

[1] K Iwashita, M. Oda, Micro-deformation mechanism of shear banding process based on modified distinct element method, Powder Technology, 109,192-205, 2000.
[2] K D Kafui, C Thornton, Discrete particle-continuum fluid modelling of gas–solid fluidised beds, Chemical Engineering Science, 57(13), 2395-2410, 2002.
[3] C Thornton , L F Liu, How do agglomerates break? Powder technology, 143-144,110-116, 2004,
[4] E Oňate, J Rojek, Combination of discrete element and finite element methods for dynamic analysis of geomechanics problems. Computer methods in applied mechanics and engineering. 193(27-29): 3087~3128, 2004.
[5] D R J Owen, Y T Feng, Parallelised finite/discrete element simulation of multi-fracturing solids and discrete systems. Engineering computations. 18(3,4), 557–576,2001.
[6] P A Klerck, E J Sellers, D R J Owen, Discrete fracture in quasi-brittle materials under compressive and tensile stress states. Computer methods in applied mechanics and engineering.193(27-29): 3035–3056,2004,
[7] T Munjiza, N Bangash, W M John, The combined finite-discrete element method for structural failure and collapse, Engineering Fracture Mechanics, 71,469–483, 2004.

Proceedings of the 3rd International Conference on
Fracture Fatigue and Wear, pp. 75-79, 2014

OBSERVING THE FREQUENCY ANALYSIS OF ACOUSTIC EMISSION PATTERN DURING TENSILE TEST OF SAE 1045 STEEL

M.Mohammad[1], S.Abdullah[2] , J.Ganesh[1], N.Jamaludin[2] and O.Innayatullah[3]

[1]Department of Mechanical Engineering, Faculty of Engineering, Universiti Selangor, Bestari Jaya Campus, Jln Timur Tambahan, 45600 Bestari Jaya, Selangor, Malaysia
[2]Department of Mechanical and Materials Engineering, Faculty of Engineering and Built Environment, Universiti Kebangsaan Malaysia , 43600 UKM Bangi, Selangor, Malaysia
[3]Department of Mechanical and Manufacturing Engineering, Faculty of Engineering, Universiti Putra Malaysia, 43400 UPM Serdang, Malaysia

Abstract: This study presents the observation of acoustic emission (AE) signal behavioural pattern for SAE 1045 steel under a tensile test condition. This study was meant to observe the failure signal pattern that can be seen in the elastic and plastic region when the specimen exposed to tensile tests at the specific strain rate of 1.2 mm/min . In order to achieve the goal, the designated specimen of SAE 1045 steel has been loaded to the tensile loading using the Universal Testing Machine (UTM) by following the ASTM E8. The specific data acquisition systems were used to collect the AE signatures. The AE signals were then compared to the stress-strain curves in order to verify the elastic and plastic region. For the purpose of analysis, the time series waveform will be transformed to the Fast Fourier Transform and the Wavelet transform to monitor the frequency difference between the elastic and plastic region during the test. These results can be used as a basic baseline in order to monitor the component condition under tensile loading.

Keywords: AE; elastic; plastic; spectrum; signal analysis

1 INTRODUCTION

Acoustic Emission is an advanced non-destructive technique (NDT) that is widely used in field monitoring and indicate great potentials as an effective tool for condition monitoring assessment [1]. AE is used to monitor rolling contact fatigue of contact surface and subsurface of rotating components. The damage stages are defined through AE amplitude and counts [2]. Previous study by Omer et al. [3] showed that the fatigue damage of 304L stainless steel was monitored by AE in order to identify specific damage mode through signal processing approach. In addition, the AE technique also has been used to detect and locate the early stages of steel wire corrosion and macro cracks in pre-stressed concrete structure using the statistical analysis approach [4].

This technique has also been used to detect and monitor the internal structural changes such as crack initiation and growth in the material during tensile test. A group of researcher has been using the AE technique to monitor the tensile loading of thermoplastic composites material using the peak amplitude, duration, and energy of AE [5]. Junichiro et al. [6] used AE to detect internal cracks of sealing rubber material by high pressure hydrogen during tensile test by showing the relationship of AE cumulative count to the crack length. In other study, these methods succeed to identify the characterization of crack during tensile test of methyl methacrylate specimen. The statistical parameters such as duration, rise time and amplitude were used as to identify the characteristic of the crack meanwhile the crack length was determined by signal Fourier spectrum [7]. However, most of the research analyses are based on common AE parameter or statistical approach analysis.

Since most of the researches successfully use this technique to monitor the material behaviours during tensile test by the statistical parameters, it is inspired the authors to work for the monitoring procedure on the issue of material changes using signal processing approach [8,9]. Therefore, it is worth to suggest for working on the signal processing investigation and identification of the elastic and plastic regions observed during the tensile test of SAE1045 steel specimens. The collected AE signals from the tensile test will then be analysed using the Fast Fourier Transform (FFT) and the Wavelet transform. The frequency spectrum

determined from the analysis will be used as a baseline data for determining the condition of the material during the test.

2 METHODOLOGY

2.1 Experimental Procedure

The material that has been used in this study is SAE 1045 medium carbon steel because it is widely used in heavy machinery industries such as oil and gas piping, power plant, and automotive components. In this research, a flat type specimen was used throughout the test as the surface can be attached softly to the AE sensor. The specimen geometry in Fig. 1 has been designed according to the ASTM E8 standard with the dimension of 146 mm, 20 mm and 7 mm for the respective of length, width and thickness. The specimen was polished using silicon carbide abrasive paper in order to obtain a smooth surface finish, hence to remove the residual stress.

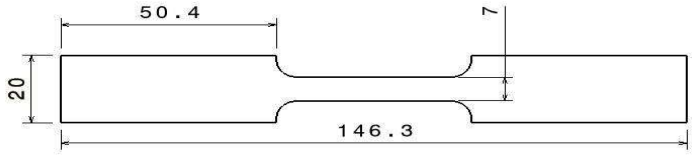

Fig. 1 Drawing of SAE 1045 medium carbon steel flat type geometry (Unit in mm)

The tensile test was performed using 100 kN Zwick-Roell type universal testing machine with a cross speed head of 1.2 mm/min and pre-load of 30 kN in reference with ASTM E8 standard. Mechanical wedge is used to grip the flat type specimen. The specimen is vertically aligned to avoid torsional force react during the test. For collecting the AE signatures, the AE sensor type SE2MEG-P231 (100 – 2000 kHz) was mounted on the specimen by applying couplant on the sensor to avoid air present between surface of specimen and sensor. The sensor was then connected to the specific data acquisition system of AMSY-5 to store the collected signal (Fig. 2). The threshold was set at 40 dB to avoid noise from the environment. Before collecting the data, the sensor has been calibrated by using pencil lead brake test. The value of the amplitude during the test should be in the range of 90-100 dB every time the test is repeated. The collected signals were then analysed using the signal processing approach.

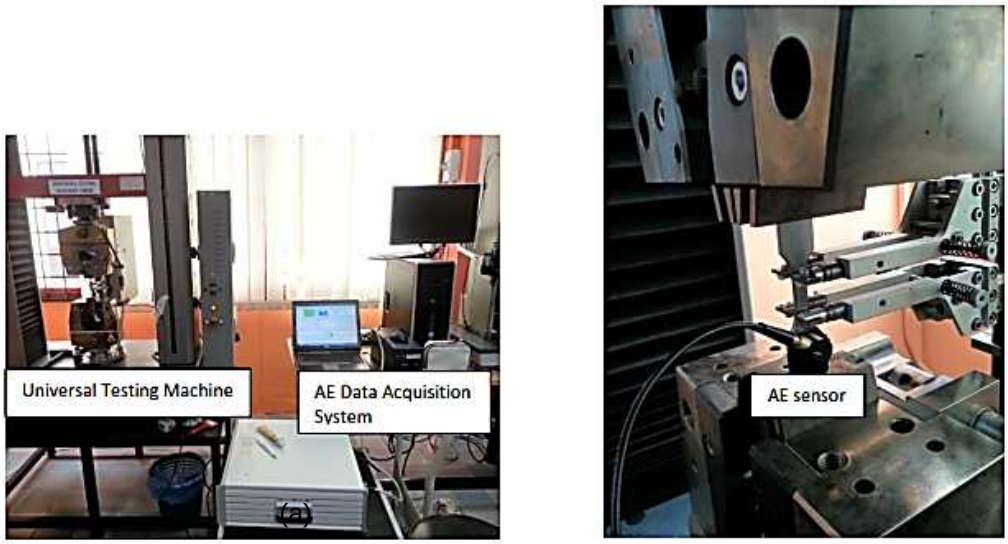

Fig. 2 (a) Experiment set-up and (b) Position of AE sensor on the specimen gripped to the Universal Testing Machine

2.2 Signal Processing Approach

There are many techniques has been used in order to interpret the AE signals. The signals collected can be analysed using either the statistical and signal processing approach to obtain the acquired result. Signal processing approaches such as fast Fourier transform (FFT), short time Fourier transform (STFT) and wavelet has been used widely to reflect the AE behaviour of various applications [10] .

Fast Fourier Transform is calculated from the data collected through AE technique. Each region, elastic and plastic two data were collected. Then the waveforms that generated through FFT are compared between both regions. Discrete Fourier Transform (DFT) is a common use form of Fast Fourier Transform. This algorithm transforms a time-domain sample sequence into a frequency-domain sequence to discover the spectral content of the signal. DFT is defined as in eq. 1:

$$Xk = 1/(N\ ) \quad \sum\_(t=0)^(N-1)xj\ e\text{-}i(2\pi kt/N) \qquad j,k = 0,1,2,3,4,5\ldots\ldots, (N-1) \tag{1}$$

where X_k is the amplitude of discrete Fourier Transform, x_j is the value in time series (mm, microstrain, etc), N is number of sample in time series, k is the number of repetition in discrete Fourier transform and t represents time in seconds [10].

The wavelet transform is applied to analysis the AE signals that collected at the two different regions. The frequency by time is defined from the pattern of the wavelet that transformed from the Vallen wavelet that actually falls into the Daubechies family. Wavelet can be described as an oscillating function of short duration, which temporarily localized around the centre t=1/2.The displacement generates the function with localization in time-frequency. Eq. 2 shows the standard equation of Daubechies wavelet:

$$D_j s(t) = \sum_k d_{j,k}\, g(m-2k) \tag{2}$$

3 RESULT AND DISCUSSION

Figure 3 shows the stress strain curve with overall AE signal hits until the specimen fractured. It is clearly stated that the elastic region happened before reached the first 50 sec and followed by the plastic region until the specimen fractured. The figure shows that the density of AE hits are higher in elastic rather than in plastic region during tensile test. In elastic region, 39 hits appeared in less than 60 s, meanwhile 131 hits appeared in 320 s. As average, in elastic region, 0.65 hits/s appeared compared to elastic with only 0.41 hits/s in plastic region. This result shows that elastic region produce more energy that emitted in this region is more in order to break the atomic bonding in the microstructure of the material. Meanwhile, less energy is produced in the plastic region as the internal crack has been proposed to the materials at early stage.

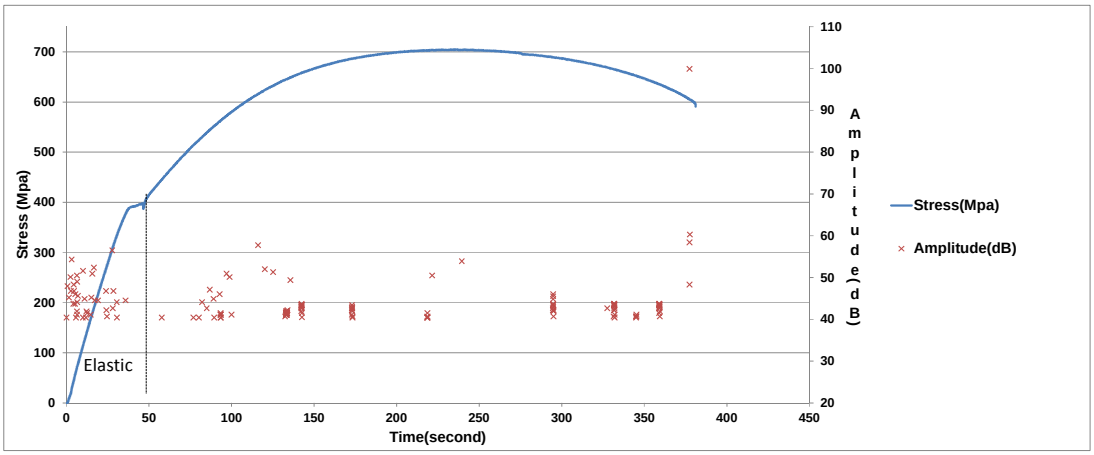

Fig. 3 Stress strain curve compared with AE signal

Figure 4 shows the plots of FFT features and wavelet pattern for the elastic region. The plots has been analysed for a hit at 11.8 sec and 12.2 sec. From the plots, it shows that the maximum frequency occurred from 100 kHz to 200 kHz during the elastic region. Low frequency usually indicates low percentage of failure experienced by the material. In tensile test, it is known that if the load has been released from the material, the material will be backed to its original form. It is contradicted to the materials that already having the plastic deformation where the material nearly reached the failure zone. Thus, a higher value of

frequency has been shown by the FFT and wavelet transformation in this region as plotted in Fig. 5. Frequency of 300 to 800 KHz has been analysed from hits at 89.1 sec and 100 sec, respectively where this hits are fell in the plastic region during the test. Higher frequencies always give an indication that the material is experienced higher damage. In this stage the AE activity increases due to crack initiation activity that lead the material break when the stress is beyond the ultimate tensile stress of the material.

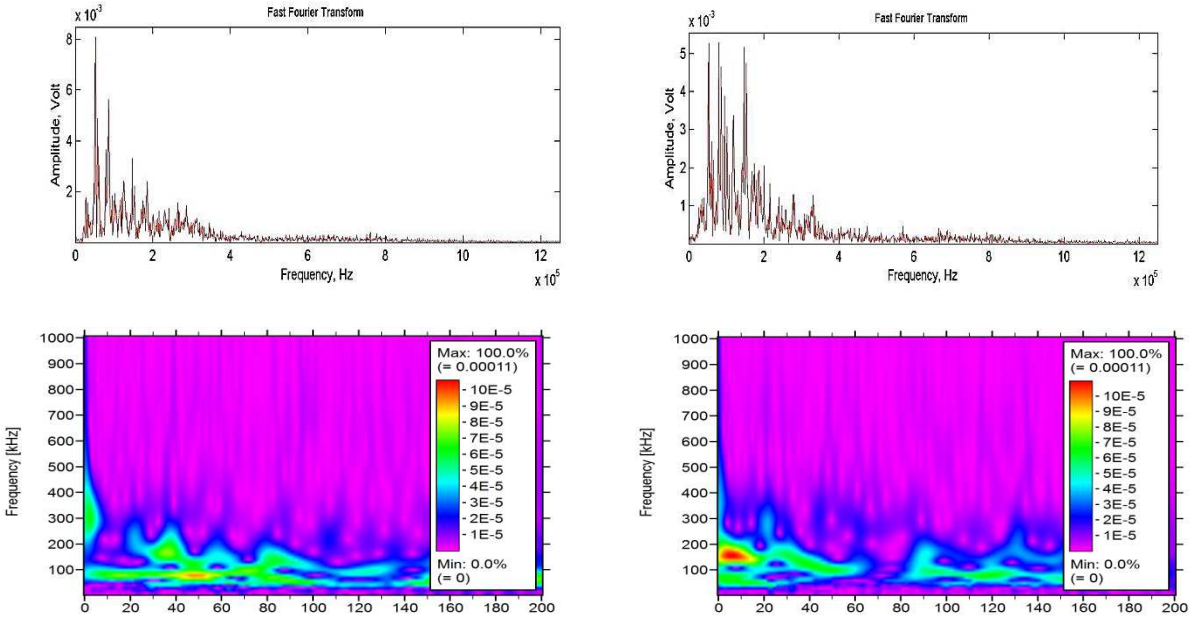

Fig. 4 FFT and wavelet plot for elastic region a) at 11.8 s and b) at 12.2 s

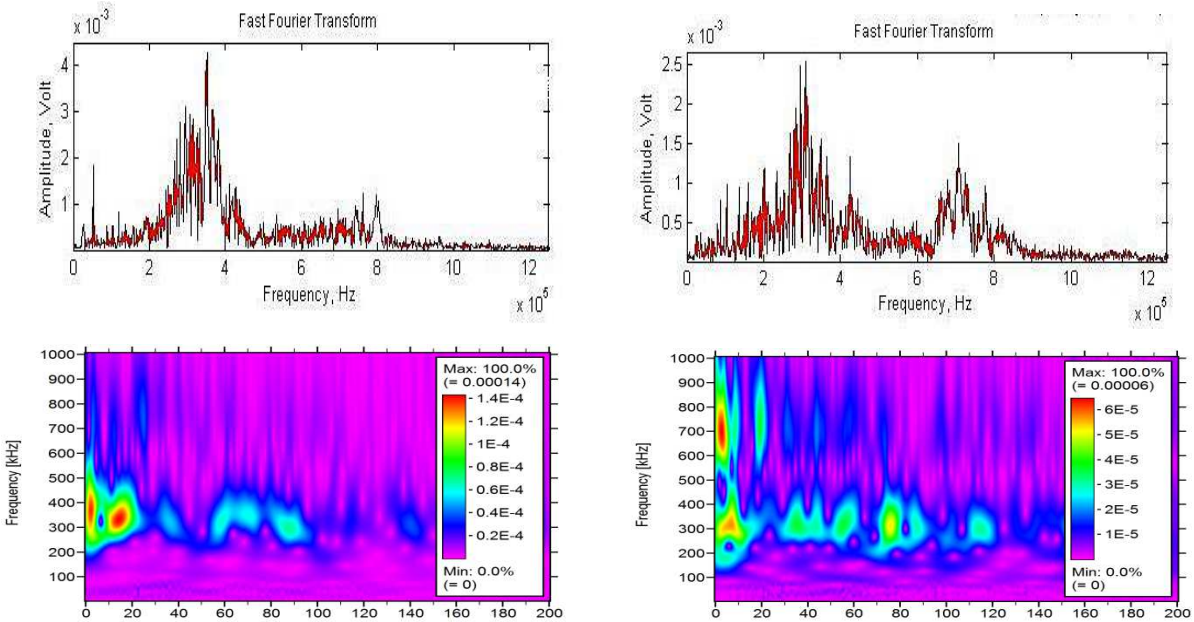

Fig. 5 FFT and wavelet plot for plastic region a) at 89.1 s and b) at 99.9 s

4 CONCLUSIONS

This paper presents the AE technique capability in detecting and monitoring the signals emitted during the tensile test in SAE 1045 medium carbon steel. Using the signal processing approach technique, the trends of the signal collected in elastic and plastic region detected by sensor were determined and monitored. A range of frequency between 100 kHz to 200 kHz has been found during the elastic stage. Meanwhile the plastic region showed a frequency range between 300 kHz to 800 kHz. Higher frequency shows that the materials were experienced more damage and can lead to the failure.

5 REFERENCES

[1] P.F.Liu, J.K.Chu, Y.L.Liu and J.Y.Zheng, "A study on the failure mechanisms of carbon fiber/epoxy composite laminates," Materials and Design, vol. 37, p. 228–235, 2011.

[2] L. Guo-lu, Zhang Zhi-qiang, Wang Hai-dou, Xu Bin-shi, Piao Zhong-yu and Zhu Li-na, "Acoustic emission monitoring and failure mechanism analysis of rolling contact fatigue for Fe-based alloy coating," Tribology International, vol. 61, pp. 129-137, 2013.

[3] A. O. AMER, A-L.GLOANEC, S.COURTIN and C.TOUZE, "Characterization of fatigue damage in 304L steel by an acoustic," Procedia Engineering, vol. 66, pp. 651-660, 2013.

[4] H. A. Elfergani, Rhys Pullin and Karen M. Holford, "Damage assessment of corrosion in prestressed concrete by acoustic emission," Construction and Building Materials, vol. 40, pp. 925-933, 2013.

[5] A.Laksimi, S.Benmedakhene and L.Bounouas, "MONITORING ACOUSTIC EMISSION DURING TENSILE LOADING OF THERMOPLASTIC COMPOSITES MATERIALS".

[6] Y. Junichiro, T. Matsumoto and S. Nishimura, "Application of acoustic emission method to detection of internal fracture of sealing rubber material by high-pressure hydrogen decompression," Polymer Testing, vol. 30, p. 76–85, 2011.

[7] D. Filipussia, Rosa Piotrkowski and José Ruzzantea, "Characterization of a crack by the acoustic emission signal generated during propagation," Materials Science, p. 266 – 272, 2012.

[8] K.Barat, H.N.Bar, D.Mandal, H.Roy, S.Sivaprasad and S.Tarafder, "Low temperature tensile deformation and acoustic emission signal characteristics of AISI 304LN stainless steel," Materials Science & Engineering A, vol. 597, pp. 37-45, 2013.

[9] J.Bohlen, F.Chmelik, P. Dobroˇn, D. Letzig, P. Lukác and K.U.Kainer, "Acoustic emission during tensile testing of magnesium AZ alloys," Journal of Alloys and Compounds, vol. 378, pp. 214-219, 2003.

[10] C. Lu, Peng Ding and Zhenhua Chen, "Time-frequency Analysis of Acoustic Emission Signals Generated by Tension Damage in CFRP," Procedia Engineering, vol. 23, pp. 210-215, 2011.

Proceedings of the 3rd International Conference on
Fracture Fatigue and Wear, pp. 80-86, 2014

THERMOELECTROMECHANICAL RESPONSE OF A FUNCTIONALLY GRADED PIEZOELECTRIC MATERIAL STRIP WITH TWO PARALLEL CRACKS IN ARBITRARY POSITIONS

S. Ueda and T. Kishimoto

Department of Mechanical Engineering, Osaka Institute of Technology, 5-16-1 Omiya, Asahi-ku, Osaka, 535-8585, Japan

Abstract: In this paper, thermo-electro-elastic fracture behaviour of two parallel cracks in arbitrary positions of a FGPM strip under thermo-electric loadings is considered. The crack faces are supposed to remain thermally and electrically insulated. We assume that all material properties depend only on the coordinate z (perpendicular to the crack faces) in such a way that properties are some exponential functions of z. Fourier transform techniques are used to reduce the mixed boundary value problems to two systems of singular integral equations. Numerical calculations are carried out, and detailed results are presented to illustrate the influence of the geometric and material parameters on the stress and electric displacement intensity factors. The results for the temperature and electro-elastic field are also included.

Keywords: thermo-electro-elasticity; fracture mechanics; functionally graded piezoelectric material; arbitrary position; two parallel cracks; integral transform

1 INTRODUCTION

Piezoelectric materials widely have been used as sensors and actuators in smart or intelligent systems to sense thermally induced distortions and to adjust for adverse thermo-mechanical conditions [1,2]. The requirements of structural strength, reliability and lifetime of these structures call for a better understanding of the mechanics of fracture in piezoelectric materials under thermal loading.

Recently, functionally graded piezoelectric materials (FGPMs) have been developed to improve their reliability [3], and the electromechanical fracture of the FGPM under mechanical and electrical loadings has received much attention [4-6]. Thus, it is also important to investigate the fracture behaviour of FGPMs under thermal load, and some interesting results have been reported [7-12]. While the fact that piezoelectric materials involve multiple cracks, most of the existing contributions are concerned with the fracture behaviour of a single crack. Then some thermal fracture problems of homogeneous piezoelectric strips with two dimensional cracks, such as two coplanar cracks [13], two parallel cracks [14], parallel multi cracks [15] and a T-shaped crack [16], have been treated. Although the present authors investigated the thermo-electro-mechanical interaction between two parallel axisymmetric cracks in an FGMP strip [17,18], one of the remaining problems that need to be fully understood is that of interaction between cracks in arbitrary positions of FGPMs under thermal loading.

In this study, thermo-electro-elastic fracture behaviour of two parallel cracks in arbitrary positions of a FGPM strip under thermo-electric loadings is considered. The crack faces are supposed to remain thermally and electrically insulated [9]. We assume that all material properties depend only on the coordinate z (perpendicular to the crack faces) in such a way that properties are some exponential functions of z. Fourier transform techniques are used to reduce the mixed boundary value problems to two systems of singular integral equations [19,20]. Numerical calculations are carried out [21], and detailed results are presented to illustrate the influence of the geometric and material parameters on the stress and electric displacement intensity factors. The results for the temperature and electro-elastic field are also included.

2 FORMULATION OF THE PROBLEM

Consider an infinite FGPM strip of thickness $h = h_1 + h_2$ containing two parallel through cracks of different length $2c_k (k = 1,2)$ being spaced at distances $2d$ in the x-direction and $2h_0$ in the z-direction as shown Fig. 1. The rectangular coordinates x, y and z are coincident with the principle axes of material. It is assumed that uniform temperatures T_{10}, T_{20} and a uniform electric displacement D_0 are maintained over the stress-free boundaries, and the crack faces remain thermally and electrically insulated [9]. The piezoelectric strip is poled in the z-direction and is in the plane strain conditions perpendicular to the y-axis. In the following, the subscripts x, y and z will be used to refer to the direction of coordinates.

The material properties, such as the elastic stiffness constants c_{kl}, the piezoelectric constants e_{kl}, the dielectric constants ε_{kk}, the stress-temperature coefficients λ_{kk}, the coefficients of heat conduction κ_x, κ_z and the pyroelectric constant p_z are one-dimensionally dependent as

$$\left.\begin{aligned} (c_{kl},\ e_{kl},\ \varepsilon_{kk}) &= (c_{kl0},\ e_{kl0},\ \varepsilon_{kk0})\exp(\beta z) \\ (\lambda_{kk},\ p_z) &= (\lambda_{kk0},\ p_{z0})\exp\left[(\beta+\omega)z\right] \\ (\kappa_x,\ \kappa_z) &= (\kappa_{x0},\ \kappa_{z0})\exp(\delta z) \end{aligned}\right\} \tag{1}$$

where β, ω, and δ are positive or negative constants, and the subscript 0 indicates the properties at the plane $z = 0$.

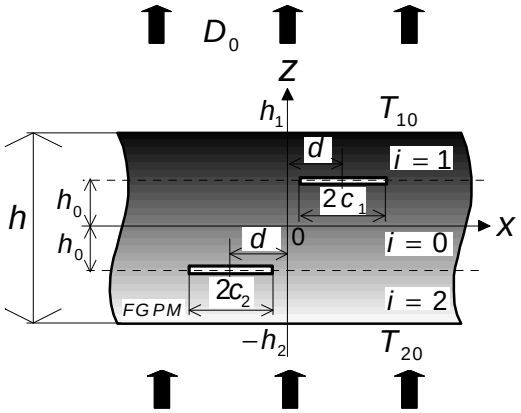

Fig. 1 Geometry of the crack problem in a functionally graded piezoelectric material strip

The constitutive equations for the elastic field are

$$\left.\begin{aligned} \sigma_{xxi} &= c_{11}\frac{\partial u_{xi}}{\partial x} + c_{13}\frac{\partial u_{zi}}{\partial z} + e_{31}\frac{\partial \phi_i}{\partial z} - \lambda_{11}T_i \\ \sigma_{zzi} &= c_{13}\frac{\partial u_{xi}}{\partial x} + c_{33}\frac{\partial u_{zi}}{\partial z} + e_{33}\frac{\partial \phi_i}{\partial z} - \lambda_{33}T_i \\ \sigma_{zxi} &= c_{44}\left(\frac{\partial u_{xi}}{\partial z} + \frac{\partial u_{zi}}{\partial x}\right) + e_{15}\frac{\partial \phi_i}{\partial x} \end{aligned}\right\} \quad (i = 0, 1, 2), \tag{2}$$

where $T_i(x,z)$ is the temperature, $\phi_i(x,z)$ is the electric potential, $u_{xi}(x,z)$ and $u_{zi}(x,z)$ are the displacement components, and $\sigma_{xxi}(x,z)$, $\sigma_{zzi}(x,z)$, and $\sigma_{zxi}(x,z)$ $(i = 0, 1, 2)$ are the stress components. The subscript $i = 0, 1, 2$ denotes the thermo-electro-elastic fields in $-h_0 \le z \le h_0$, $h_0 \le z \le h_1$, $-h_2 \le z \le -h_0$, respectively.

For the electric field, the constitutive relations are

$$\left.\begin{aligned} D_{xi} &= e_{15}\left(\frac{\partial u_{xi}}{\partial z}+\frac{\partial u_{zi}}{\partial x}\right)-\varepsilon_{11}\frac{\partial \phi_i}{\partial x} \\ D_{zi} &= e_{31}\frac{\partial u_{xi}}{\partial x}+e_{33}\frac{\partial u_{zi}}{\partial z}-\varepsilon_{33}\frac{\partial \phi_i}{\partial z}+p_z T_i \end{aligned}\right\} \quad (i=0,1,2), \tag{3}$$

where $D_{xi}(x,z)$, $D_{zi}(x,z)$ $(i=0,1,2)$ are the electric displacement components.

The temperature is assumed to satisfy the Fourier heat conduction equation:

$$\kappa^2\frac{\partial^2 T_i}{\partial x^2}+\frac{\partial^2 T_i}{\partial z^2}+\delta\frac{\partial T_i}{\partial z}=0 \quad (i=0,1,2), \tag{4}$$

where $\kappa^2=\kappa_x/\kappa_z$. The equations of equilibrium and electrostatics are

$$\left.\begin{aligned} &c_{110}\frac{\partial^2 u_{xi}}{\partial x^2}+c_{440}\frac{\partial^2 u_{xi}}{\partial z^2}+(c_{130}+c_{440})\frac{\partial^2 u_{zi}}{\partial x\partial z}+(e_{310}+e_{150})\frac{\partial^2 \phi_i}{\partial x\partial z} \\ &\quad+\beta\left[c_{440}\left(\frac{\partial u_{xi}}{\partial z}+\frac{\partial u_{zi}}{\partial x}\right)+e_{150}\frac{\partial \phi_i}{\partial x}\right]=\lambda_{110}\exp(\omega z)\frac{\partial T_i}{\partial x} \\ &c_{440}\frac{\partial^2 u_{zi}}{\partial x^2}+c_{330}\frac{\partial^2 u_{zi}}{\partial z^2}+(c_{130}+c_{440})\frac{\partial^2 u_{xi}}{\partial x\partial z}+e_{150}\frac{\partial^2 \phi_i}{\partial x^2}+e_{330}\frac{\partial^2 \phi_i}{\partial z^2} \\ &+\beta\left[c_{130}\frac{\partial u_{xi}}{\partial x}+c_{330}\frac{\partial u_{zi}}{\partial z}+e_{330}\frac{\partial \phi_i}{\partial z}\right]=\lambda_{330}\exp(\omega z)\left\{\frac{\partial T_i}{\partial z}+(\beta+\omega)T_i\right\} \\ &e_{150}\frac{\partial^2 u_{zi}}{\partial x^2}+e_{330}\frac{\partial^2 u_{zi}}{\partial z^2}+(e_{150}+c_{310})\frac{\partial^2 u_{xi}}{\partial x\partial z}-\varepsilon_{110}\frac{\partial^2 \phi_i}{\partial x^2}-\varepsilon_{330}\frac{\partial^2 \phi_i}{\partial z^2} \\ &+\beta\left[e_{310}\frac{\partial u_{xi}}{\partial x}+e_{330}\frac{\partial u_{zi}}{\partial z}-\varepsilon_{330}\frac{\partial \phi_i}{\partial z}\right]=-p_{z0}\exp(\omega z)\left[\frac{\partial T_i}{\partial z}+(\beta+\omega)T_i\right] \end{aligned}\right\} i=(0,1,2) \tag{5}$$

If the electrically impermeable boundary is chosen as an idealized crack face electric boundary conditions [9], the boundary conductions for the temperature field can be written as:

$$\left.\begin{aligned} &\frac{\partial T_0(x,\theta_{0i})}{\partial z}=0 \qquad (a_i<x<b_i) \\ &T_0(x,\theta_{0i})=T_i(x,\theta_{0i}) \quad (-\infty<x\le a_i,b_i\le x<\infty) \end{aligned}\right\} \quad (i=1,2), \tag{6}$$

$$\left.\begin{aligned} &\frac{\partial T_0(x,\theta_{0i})}{\partial z}=\frac{\partial T_i(x,\theta_{0i})}{\partial z} \quad (-\infty<x<\infty) \\ &T_i(x,\theta_{1i})=T_{i0} \qquad (-\infty<x<\infty) \end{aligned}\right\} \quad (i=1,2), \tag{7}$$

for thermal loading condition and

$$\left.\begin{aligned} &\sigma_{zz0}(x,\theta_{0i})=0 \qquad (a_i<x<b_i) \\ &u_{z0}(x,\theta_{0i})=u_{zi}(x,\theta_{0i}) \quad (-\infty<x\le a_i,b_i\le x<\infty) \end{aligned}\right\} \quad (i=1,2), \tag{8}$$

$$\left.\begin{aligned} &\sigma_{zx0}(x,\theta_{0i})=0 \qquad (a_i<x<b_i) \\ &u_{x0}(x,\theta_{0i})=u_{xi}(x,\theta_{0i}) \quad (-\infty<x\le a_i,b_i\le x<\infty) \end{aligned}\right\} \quad (i=1,2), \tag{9}$$

$$\left.\begin{aligned} &D_{z0}(x,\theta_{0i})=-D_0 \qquad (a_i<x<b_i) \\ &\phi_0(x,\theta_{0i})=\phi_i(x,\theta_{0i}) \quad (-\infty<x\le a_i,b_i\le x<\infty) \end{aligned}\right\} \quad (i=1,2), \tag{10}$$

$$\left.\begin{aligned} &\sigma_{zz0}(x,\theta_{0i})=\sigma_{zzi}(x,\theta_{0i}) \quad (-\infty<x<\infty) \\ &\sigma_{zx0}(x,\theta_{0i})=\sigma_{zxi}(x,\theta_{0i}) \quad (-\infty<x<\infty) \\ &D_{z0}(x,\theta_{0i})=D_{zi}(x,\theta_{0i}) \quad (-\infty<x<\infty) \end{aligned}\right\} \quad (i=1,2), \tag{11}$$

$$\left.\begin{array}{ll}\sigma_{zzi}\left(x,\theta_{1i}\right)=0 & \left(-\infty<x<\infty\right)\\ \sigma_{zxi}\left(x,\theta_{1i}\right)=0 & \left(-\infty<x<\infty\right)\\ D_{zi}\left(x,\theta_{1i}\right)=D_0 & \left(-\infty<x<\infty\right)\end{array}\right\}\quad (i=1,2), \tag{12}$$

for the electro-elastic conditions. In Eqs. (6)-(12), θ_{0i}, θ_{1i}, a_i and $b_i\,(i=1,2)$ are given by

$$\left(\theta_{0i},\theta_{1i},a_i,b_i\right)=\left\{\begin{array}{ll}\left(h_0,h_1,d-c_1,d+c_1\right) & (i=1)\\ \left(-h_0,-h_2,-d-c_2,-d+c_2\right) & (i=2)\end{array}\right\}. \tag{13}$$

3 STRESS AND ELECTRIC DISPLACEMENT INTENSITY FACTORS

The stress and electric displacement intensity factors may be, respectively, evaluated as:

$$\left.\begin{array}{l}K_{\mathrm{IA}}^{(k)}=-(\pi c_k)^{1/2}\left[Z_{1k11}^{\infty}\Phi_{k1}(a_k)+Z_{1k31}^{\infty}\Phi_{k3}(a_k)\right]\\ K_{\mathrm{IIA}}^{(k)}=-(\pi c_k)^{1/2}Z_{2k21}^{\infty}\Phi_{k2}(a_k)\\ K_{\mathrm{DA}}^{(k)}=-(\pi c_k)^{1/2}\left[Z_{3k11}^{\infty}\Phi_{k1}(a_k)+Z_{3k31}^{\infty}\Phi_{k3}(a_k)\right]\end{array}\right\}\quad (k=1,2), \tag{14}$$

$$\left.\begin{array}{l}K_{\mathrm{IB}}^{(k)}=(\pi c_k)^{1/2}\left[Z_{1k11}^{\infty}\Phi_{k1}(b_k)+Z_{1k31}^{\infty}\Phi_{k3}(b_k)\right]\\ K_{\mathrm{IIB}}^{(k)}=(\pi c_k)^{1/2}Z_{2k21}^{\infty}\Phi_{k2}(b_k)\\ K_{\mathrm{DB}}^{(k)}=(\pi c_k)^{1/2}\left[Z_{3k11}^{\infty}\Phi_{k1}(b_k)+Z_{3k31}^{\infty}\Phi_{k3}(b_k)\right]\end{array}\right\}\quad (k=1,2), \tag{15}$$

where Z_{jkm1}^{∞} $(k=1,2,\ j,m=1,2,3)$ are known constants and the functions $\Phi_{km}(\xi)$ $(k=1,2,m=0,1,2,3)$ are given by:

$$G_{km}(\xi)=\frac{c_k}{\left[(\xi-a_k)(b_k-\xi)\right]^{1/2}}\Phi_{km}(\xi)\quad (k=1,2,\ m=0,1,2,3). \tag{16}$$

The functions $G_{km}(\xi)$ $(k=1,2,\ m=0,1,2,3)$ are the solutions of the following system of six singular integral equations obtained from the first boundary conditions (8) - (10) with Eqs. (11) and (12).

$$\int_{a_1}^{b_1}\left\{\left[\frac{Z_{1111}^{(1)\infty}}{\xi-x}+M_{111}^{(1)}(\xi,x)\right]G_{11}(\xi)+M_{112}^{(1)}(\xi,x)G_{12}(\xi)+\left[\frac{Z_{1131}^{(1)\infty}}{\xi-x}+M_{113}^{(1)}(\xi,x)\right]G_{13}(\xi)\right\}d\xi$$
$$+\int_{a_2}^{b_2}\sum_{m=1}^{3}M_{12m}^{(1)}(\xi,x)G_{2m}(\xi)\,d\xi=\pi\sigma_{zz0}^{T}(x,h_0)\quad (a_1<x<b_1), \tag{17}$$

$$\int_{a_1}^{b_1}\left\{M_{211}^{(1)}(\xi,x)G_{11}(\xi)+\left[\frac{Z_{2121}^{(1)\infty}}{\xi-x}+M_{212}^{(1)}(\xi,x)\right]G_{12}(\xi)+M_{213}^{(1)}(\xi,x)G_{13}(\xi)\right\}d\xi$$
$$+\int_{a_2}^{b_2}\sum_{m=1}^{3}M_{22m}^{(1)}(\xi,x)G_{2m}(\xi)\,d\xi=\pi\sigma_{zx0}^{T}(x,h_0)\quad (a_1<x<b_1), \tag{18}$$

$$\int_{a_1}^{b_1}\left\{\left[\frac{Z_{3111}^{(1)\infty}}{\xi-x}+M_{311}^{(1)}(\xi,x)\right]G_{11}(\xi)+M_{312}^{(1)}(\xi,x)G_{12}(\xi)+\left[\frac{Z_{3131}^{(1)\infty}}{\xi-x}+M_{313}^{(1)}(\xi,x)\right]G_{13}(\xi)\right\}d\xi$$
$$+\int_{a_2}^{b_2}\sum_{m=1}^{3}M_{32m}^{(1)}(\xi,x)G_{2m}(\xi)\,d\xi=\pi D_{z0}^{T}(x,h_0)\quad (a_1<x<b_1), \tag{19}$$

$$\int_{a_2}^{b_2}\left\{\left[\frac{Z_{1211}^{(2)\infty}}{\xi-x}+M_{121}^{(2)}(\xi,x)\right]G_{21}(\xi)+M_{122}^{(2)}(\xi,x)G_{22}(\xi)+\left[\frac{Z_{1231}^{(1)\infty}}{\xi-x}+M_{123}^{(2)}(\xi,x)\right]G_{23}(\xi)\right\}d\xi$$
$$+\int_{a_1}^{b_1}\sum_{m=1}^{3}M_{11m}^{(1)}(\xi,x)G_{1m}(\xi)\,d\xi=\pi\sigma_{zz0}^{T}(x,-h_0)\quad(a_2<x<b_2),\tag{20}$$

$$\int_{a_2}^{b_2}\left\{M_{221}^{(2)}(\xi,x)G_{21}(\xi)+\left[\frac{Z_{2221}^{(2)\infty}}{\xi-x}+M_{222}^{(2)}(\xi,x)\right]G_{22}(\xi)+M_{223}^{(2)}(\xi,x)G_{23}(\xi)\right\}d\xi$$
$$+\int_{a_1}^{b_1}\sum_{m=1}^{3}M_{21m}^{(2)}(\xi,x)G_{1m}(\xi)\,d\xi=\pi\sigma_{zx0}^{T}(x,-h_0)\quad(a_2<x<b_2),\tag{21}$$

$$\int_{a_2}^{b_2}\left\{\left[\frac{Z_{3211}^{(2)\infty}}{\xi-x}+M_{321}^{(2)}(\xi,x)\right]G_{21}(\xi)+M_{322}^{(2)}(\xi,x)G_{22}(\xi)+\left[\frac{Z_{3231}^{(1)\infty}}{\xi-x}+M_{323}^{(2)}(\xi,x)\right]G_{23}(\xi)\right\}d\xi$$
$$+\int_{a_1}^{b_1}\sum_{m=1}^{3}M_{31m}^{(1)}(\xi,x)G_{1m}(\xi)\,d\xi=\pi D_{z0}^{T}(x,-h_0)\quad(a_2<x<b_2),\tag{22}$$

In these integral equations, $M_{jkm}^{(n)}(\xi,x)\ \ (k,n=1,2,j,m=1,2,3)$ are the known kernel functions. The functions $\sigma_{zx0}^{T}(x,\pm h_0)$, $\sigma_{zz0}^{T}(x,\pm h_0)$ and $D_{z0}^{T}(x,\pm h_0)$ in the right hand side are the stress and electric displacement components, and they contain the solutions of the system of the singular integral equations that are obtained in the temperature analysis using Eq. (4) with the boundary conditions (6) and (7).

4 NUMERICAL RESULTS AND DISCUSSION

For the numerical calculations, the thermo-electro-elastic properties of cadmium selenide with the following properties [2] are used as the properties of the FGPM plate at the plane $z=0$. The normalized non-homogeneous parameters $\beta h, \omega h$ and δh are assumed to be $\beta h=\omega h=\delta h$. Figures 2, 3 and 4 show the effect of the material non-homogeneity and the crack distance d/h on the normalized stress intensity factors $(K_{\eta A}^{(1)},K_{\eta B}^{(1)})/\lambda_{330}T_0(\pi c_1)^{1/2}\ \ (\eta=I,II)$ and the normalized electric displacement intensity factors $\left(K_{DA}^{(1)},K_{DB}^{(1)}\right)/p_{z0}T_0(\pi c_1)^{1/2}$ for βh = -1.0, 0.0, 1.0 with $h_0/h=0.3$ and $c_1/h=c_2/h=0.5$. The results for the cases of $d/h\to\infty$ and $\beta h=0.0$ coincide with the results of single parallel crack [8] and with the results for the homogeneous case [14], respectively. The values of the intensity factors tend to increase/decrease at first, reach maximum/minimal values and then decrease/increase with increasing d/h. The interaction between the two cracks may vanish for the range $3c_1/h<d/h$. Moreover, it is evident that the intensity factors can be reduced by increasing the material property gradient of functionally graded piezoelectric materials under the thermal load.

5 CONCLUSIONS

The mixed-mode thermo-electro-elastic fracture problem of two parallel cracks in arbitrary positions of a functionally graded piezoelectric material strip under thermo-electric loadings is studied. For the special cases of symmetrical geometry $(h_2/h=0.5, c_1/h=c_2/h)$, the effects of the crack distance (d/h) and the material parameter βh on the stress and electric displacement intensity factors are clarified. The following facts can be found from the numerical results. Firstly, the normalized intensity factors are under the great influence of the geometric and material parameters d/h and βh. Secondly, the interaction between two parallel cracks in arbitrary positions is more complicated than the interaction between two parallel cracks of

$d / h = 0.0$. Thirdly, the absolute peak values of the intensity factors tend to occur at about $c_1 / h = d / h$, and the interaction between the two cracks becomes zero at about $3c_1 / h = d / h$. Finally, the increase of the material parameter is beneficial for reducing the intensity factors.

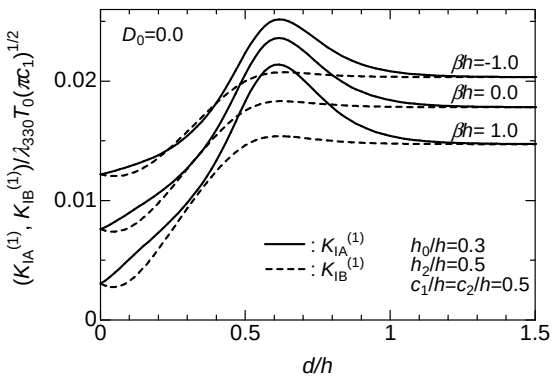

Fig. 2 The effect of the material non-homogeneity and the crack distance d on the stress intensity factors $K_{IA}^{(1)}$ and $K_{IB}^{(1)}$ under pure thermal load.

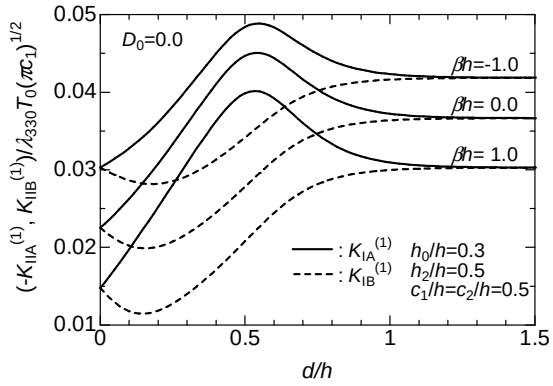

Fig. 3 The effect of the material non-homogeneity and the crack distance d on the stress intensity factors $K_{IIA}^{(1)}$ and $K_{IIB}^{(1)}$ under pure thermal load.

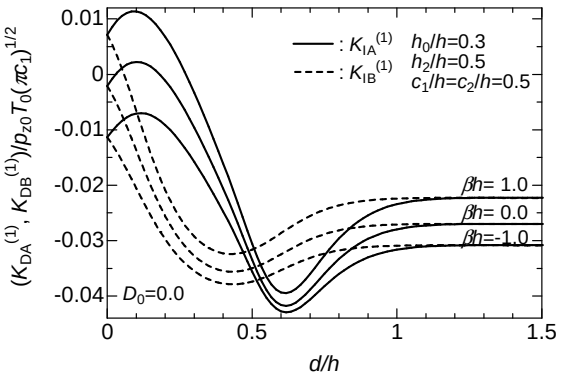

Fig. 4 The effect of the material non-homogeneity and the crack distance d on the electric displacement intensity factors $K_{DA}^{(1)}$ and $K_{DB}^{(1)}$ under pure thermal load.

6 REFERENCES

[1] S.S. Rao, M. Sunar, Piezoelectricity and Its Use in Disturbance Sensing and Control of Flexible Structures: A Survey, Applied Mechanics Review, 47(4), 113-123, 1994.

[2] F. Ashida, T.R. Tauchert, Transient Response of a Piezothermoelastic Circular Disk under Axisymmetric heating, Acta Mechanica, 128(1-2), 1-14, 1998.

[3] C.M. Wu, M. Kahn, W. Moy, Piezoelectric Ceramics with Functionally Gradients : A New Application in Material design, Journal of American Ceramics Society, 79(3), 809-812, 1996.

[4] J. Chen, Z.X. Liu, Z.Z. Zou, Electromechanical Impact of a Crack in a Functionally Graded Piezoelectric Medium, Theoretical and Applied Fracture Mechanics, 39(1), 47-60, 2003.

[5] B.L. Wang, X.H. Zhang, A Mode III Crack in Functionally Graded Piezoelectric Material Strip, Transactions of the ASME, Journal of Applied Mechanics, 71(3), 327-333, 2004.

[6] S. Ueda, A Finite Crack in a Semi-Infinite Strip of a Grade Piezoelectric Material under Electric Loading, European Journal of Mechanics A/Solids, 25, 250-259, 2006.

[7] S. Ueda, A Cracked Functionally Graded Piezoelectric Material Strip under Transient Thermal Loading, Acta Mechanica, 199(1-4), 53-70, 2008.

[8] S. Ueda, Thermal Intensity Factors for a Parallel Crack in a Functionally Graded Piezoelectric Strip. Journal of Thermal Stresses, 30(4), 321-342, 2007.

[9] S. Ueda, Effects of Crack Surface Conductance on Intensity Factors for a Cracked Functionally Graded Piezoelectric Material under Thermal Load. Journal of Thermal Stresses, 30(7), 731-752, 2007.

[10] S. Ueda, A Penny-Shaped Crack in a Functionally Graded Piezoelectric Strip under Thermal Loading, Engineering Fracture Mechanics, 74(8), 1255-1273, 2007.

[11] S. Ueda, Transient Thermo-electro-elastic Response of a Functionally Graded Piezoelectric Strip with a Penny-Shaped Crack, Engineering Fracture Mechanics, 75(5), 1204-1222, 2008.

[12] S. Ueda and N. Nishimura, An Annular Crack in a Functionally Graded Piezoelectric Strip under Thermoelectric Loadings, Journal of Thermal Stresses, 31(11), 1079-1098, 2008.

[13] S. Ueda and S. Tani, Thermal Stress Intensity Factors for Two Coplanar Cracks in a Piezoelectric Strip, Journal of Thermal Stresses, 31(5), 406-415, 2008.

[14] S. Ueda and H. Nishikohri, Two Parallel Cracks in Arbitrary Positions of a Piezoelectric Material Strip under Thermo-Electric Loadings, Journal of Thermal Stresses, 36(5), 480-500, 2013

[15] S. Ueda and Y. Uemura, Thermo-electro-mechanical Interaction among Multi Parallel Cracks in a Piezoelectric Material, Journal of Thermal Stresses, 32(10), 1005-1023, 2009.

[16] S. Ueda and H. Hatano, T-Shaped Crack in a Piezoelectric Material Thermo-electro-mechanical Loadings, Journal of Thermal Stresses, 35(1-3), 12-29, 2012.

[17] S. Ueda and T. Logawa, Two Parallel Penny-Shaped or Annular Cracks in a Functionally Graded Piezoelectric Strip under Electric Loading, Acta Mechanica, 210(1-2), 57-70, 2010

[18] S. Ueda and T. Ueda, Transient Thermoelectroelastic Response of a Functionally Graded Piezoelectric Strip with Two Parallel Axisymmetric Cracks, Journal of Thermal Stresses, 36(10), 1027-1055, 2013.

[19] I.N. Sneddon and M. Lowengrub, Crack Problems in the Classical Theory of Elasticity, John Wiley & Sons, Inc., New York, 1969.

[20] F. Erdogan and B.H. Wu, Crack Problems in FGM Layers under Thermal Stresses, Journal of Thermal Stresses, 19(3), 237-265, 1996.

[21] F. Erdogan, G.D. Gupta, and T.S. Cook, Methods of Analysis and Solution of Crack Problems (Edited by G.C. Sih), Noordhoff, Leyden, 1972.

Proceedings of the 3rd International Conference on
Fracture Fatigue and Wear, pp. 87-93, 2014

APPLICATION OF SINGULAR INTEGRAL EQUATIONS TO TRANSIENT ELASTODYNAMIC CRACK FOR PIEZOELECTRIC SOLIDS

P. Zhao[2], T.Y. Qin[1] L.N. Zhang[1] and X.B. Feng[1]

[1] College of Science, China Agricultural University, 100083, P. R. China
[2] College of Engineering, China Agricultural University, 100083, P.R. China

Abstract: A time-domain singular integral equation method for transient elastodynamic crack analysis in two-dimensional piezoelectric solids is presented in this paper. Based on the time-domain boundary integrate equation method, a set of singular integral equations for a straight crack in an infinite piezoelectric solid under impacted loading is obtained. By use of Laplace transform, time domain Green's functions for the infinite plane are split into singular plus regular terms, the singular ones coinciding with the static Green's function. A convolution quadrature formula is applied for temporal discretization, while Gauss-Chebyshev method is adopted for the spatial integrate. Finally, numerical examples are presented and discussed to show the effects of the mechanical and the electrical loading on the dynamic intensity factors.

Keywords: dynamic fracture; piezoelectric material; singular integral equations; intensity factor

1 INTRODUCTION

Due to coupling effects between the mechanical and the electrical fields, piezoelectric materials are widely applied in transducers, actuators, and many other smart devices and structures. Dynamic crack analysis in piezoelectric solids is an important issue in fracture and damage mechanics as well as non-destructive testing. It is very useful to characterize and evaluate the mechanical and the electrical integrity, the reliability and the durability of piezoelectric devices and structures. As to the complexity of the corresponding initial-boundary value problems, many numerical methods have been applied. Enderlein [1] and Enderlin et al. [2] have applied Finite element method for 2-D dynamic crack analysis in piezoelectric solids. Dziatkiewicz and Fedelinski [3], Gaul et al [4] have developed dual reciprocity BEM to avoid the difficulty to get Green's functions. Time-domain BEM for transient dynamic crack analysis in piezoelectric solids has been present in[5-6]. Meshless methods for piezoelectric solids have been implemented by Liu et al. [7] and Sladek et al. [8]. For temporal discretization, the quadrature formula of Lubich [9,10] is adopted for approximating the Riemann convolution integrals. For spatial integral, Gauss-Chebyshev method is implemented. A special feature of present time-domain BEM is that it requires only Laplace-domain instead of time-domain dynamic piezoelectric fundamental functions. Cauchy principal boundary integrals arising in the present time-domain BEM are computed by using Gauss-Chebyshev method. A basic function is multiplied, to describe the local behaviour of the displacement density functions properly.

2 BASIC EQUATIONS

A homogenous and linear piezoelectric solid containing a finite crack is considered. In the absence of body forces and under the quasi-electric assumption, the cracked solid satisfies the equations of motion and the Gauss's law [11]:

$$\sigma_{ij,j} = \rho \ddot{u}_i \ , \qquad D_{i,i} = 0 \tag{1}$$

where $\ddot{u}_i$ and σ_{ij} represent the displacement and the stress components, ρ is the mass density, and D_i denotes the electric displacements. The piezoelectric solid satisfies the following constructive equations:

$$\sigma_{ij} = c_{ijkl}u_{k,l} - e_{ijk}E_k \ , \quad D_i = e_{kli}u_{k,l} + \varepsilon_{ik}E_k \tag{2}$$

in which c_{ijkl} is elasticity tensor, e_{ijk} is the piezoelectric tensor, ε_{ik} is the dielectric permittivity tensor, and E_k represents the components of electrical field. Under quasi-electrostatic assumption, the electrical field components E_k and the electrical potential ϕ are related by:

$$E_i = \phi_{,i} \tag{3}$$

For convenience, the generalized displacements, the generalized stresses, and the generalized elasticity tensor are introduced as follows:

$$U_I = \begin{cases} u_I & I = 1,2 \\ \phi & I = 3 \end{cases}, \quad \Sigma_{iJ} = \begin{cases} \sigma_{iJ}, & J = 1,2 \\ D_i, & J = 3 \end{cases} \tag{4}$$

Thus, the equations of motion and constitutive equations can be rewritten as:

$$\Sigma_{iJ,i} = \rho\delta^*_{JK}\ddot{U}_K \ , \quad \Sigma_{iJ} = C_{iJKl}U_{K,l} \tag{5}$$

In Eq.5, d^*_{JK} is the generalized Kronecker delta defined by:

$$\delta^*_{JK} = \begin{cases} \delta_{JK}, & J,K = 1,2 \\ 0, & otherwise \end{cases} \tag{6}$$

3 SINGULAR INTEGRAL EQUATIONS

An infinite piezoelectric solid containing a straight crack under impact mechanical loading is considered. Initial conditions and boundary conditions are prescribed:

$$U_I(\mathrm{x},t) = \dot{U}_I(\mathrm{x},t) = 0, \quad \text{for} \quad t=0 \tag{7}$$

$$P_I(\mathrm{x},t) = P^*_I(\mathrm{x})H(t) \tag{8}$$

where the $P^*_I(\mathrm{x})$ represents the amplitude of the impact loading, $H(t)$ denotes the Heaviside step function.

By using the generalized Betti-Rayleigh reciprocity theorem, the formula for the extended displacements can be obtained:

$$U_J(\mathrm{x},t) = -\int_{\Gamma_{c^+}} T^G_{IJ}(\mathrm{x},\mathrm{y},t) * \tilde{U}_I(\mathrm{y},t)\mathrm{d}\Gamma_{\mathrm{y}} \tag{9}$$

By substituting the Eq.7 into the constitutive relations Eq.2, taking the limit process $\mathrm{x} \to \Gamma_{C^+}$, and considering the boundary conditions, traction BIEs can be obtained:

$$\oint_{\Gamma_{c^+}} -n_i(\mathrm{x})C_{iJKl}\frac{\partial T^G_{KM}(\mathrm{x},\mathrm{y},t)}{\partial x_l} * \tilde{U}_M(\mathrm{y},t)\mathrm{d}\Gamma_{\mathrm{y}} = P_J(\mathrm{x},t) \tag{10}$$

where $T^G_{IJ}(\mathrm{x},\mathrm{y},t)$ are the traction fundamental solutions, asterisk '*' denotes the Riemann convolution, and $\tilde{U}_M(\mathrm{y},t)$ is defined by:

$$\tilde{U}_M(\mathrm{y},t) = U_M(\mathrm{y} \in \Gamma_{C^+},t) - U_M(\mathrm{y} \in \Gamma_{C^-},t) \tag{11}$$

Using the relations

$$\frac{\partial T^G_{IJ}(\mathrm{x},\mathrm{y},t)}{\partial x_1} = -\frac{\partial T^G_{IJ}(\mathrm{x},\mathrm{y},t)}{\partial y_1} \tag{12}$$

$$\frac{\partial T^G_{IJ}(\mathrm{x},\mathrm{y},t)}{\partial x_2} = -\frac{\partial \sigma^G_{1IJ}(\mathrm{x},\mathrm{y},t)}{\partial y_1} + \rho\delta^*_{IK}\ddot{U}^G_{KJ} \tag{13}$$

and integration by parts, the hypersingular traction integral equations (10) can be degenerated into Cauchy integral equations:

$$n_i(\mathrm{x})\int_{\Gamma_{\varepsilon^+}}\left(C_{iJK1}T^G_{KM}(\mathrm{x},\mathrm{y},t)+C_{iJK2}\sigma^G_{1KM}(\mathrm{x},\mathrm{y},t)+C_{iJK2}\int_{y_1}^{a}\rho\delta^*_{KP}\ddot{U}^G_{PM}\mathrm{d}\Gamma_{\mathrm{y}}\right)*f_M(\mathrm{y},t)\mathrm{d}\Gamma_{\mathrm{y}}=P_J(\mathrm{x},t) \tag{14}$$

where $f_M(\mathrm{y},t)=\partial\tilde{U}_M(\mathrm{y},t)/\partial y_1$ are the basic unknown functions.

4 TEMPORAL AND SPATIAL PROCEDURE

4.1 Time discretization

To solve the Riemann convolution, the convolution quadrature formula of Lubich[9,10] is applied for temporal discretization. As the convolution quadrature formula of Lubich, the integral equations are turned into:

$$n_i(\mathrm{x})\int_{\Gamma_{\varepsilon^+}}\sum_{m=0}^{M}\omega(x,y,m\Delta t)\times\frac{\partial\tilde{U}_M(\mathrm{y},(M-m)\Delta t)}{\partial y_1}\mathrm{d}\Gamma_{\mathrm{y}}=P_J(\mathrm{x},M\Delta t) \tag{15}$$

where the time t is divided into M equal time-steps Δt, and the weights $\omega(x,y,m\Delta t)$ are determined by:

$$\omega(x,y,m\Delta t)=\frac{r^{-m}}{Q}\sum_{q=0}^{Q-1}\left(C_{iJK1}\tilde{T}^G_{KM}(\mathrm{x},\mathrm{y},s_q)+C_{iJK2}\tilde{\sigma}^G_{1KM}(\mathrm{x},\mathrm{y},s_q)+C_{iJK2}\int_{y_1}^{b}\rho s_q^2\delta^*_{KP}\tilde{U}^G_{PM}\mathrm{d}\Gamma_{\mathrm{y}}\right)e^{-2\pi i\cdot mq/Q} \tag{16}$$

in which $\hat{T}$, $\hat{\sigma}$, $\hat{U}$ are Laplace transform of the function T, σ, U, and

$$s_q=\delta(\zeta_q)/\Delta t,\delta(\zeta_q)=\sum_{j=1}^{2}\frac{(1-\zeta_q)^j}{2},\zeta_q=re^{i\bullet 2\pi q/Q},r=\varepsilon^{1/(2Q)} \tag{17}$$

with ε being the numerical error in computing the Laplace transform.

4.2 Spatial approximate

Time-domain and Laplace-domain dynamic fundamental solutions for homogenous and linear piezoelectric solids have been derived in[12,13]. Unfortunately, they can not be given in closed forms, but they can be represented by line-integrals over a unit-circle in 2-D case. Though time-domain BEM formulation presented in this paper, only the Laplace-domain fundamental solutions are needed in temporal discretization. Note here that the tractions BIEs are Cauchy singular and should be understood in sense of Cauchy-principal value integrals.2-D Laplace-domain displacement fundamental solution can be expressed as [12,13]

$$\hat{U}_{IJ}(\mathbf{x},\mathbf{y},s)=\frac{1}{8\pi^2}\int_{|\eta|=1}\sum_{m=1}^{2}\frac{\gamma^m_{IJ}}{\rho c_m^2}\Psi(s|\boldsymbol{\eta}\cdot(\mathbf{y}-\mathbf{x})|/c_m)\mathrm{d}S_\eta \tag{18}$$

in which γ^m_{IJ} and ρc_m^2 are determined by wave propagation vector $\boldsymbol{\eta}=(h_1,h_2)$ and material constants. The function $\Psi(z)$ is defined by

$$Y(z)=-[e^{-z}\mathrm{Ei}[z]+e^{z}\mathrm{Ei}(-z)] \tag{19}$$

with Ei[z] being the exponential integral and z a complex variable. The function $\Psi(z)$ has a logarithmic singularity when integration is taken over the collocation point.

The displacement fundamental solution can be decomposed into regular and singular static parts as

$$\hat{U}_{IJ}(\mathbf{x},\mathbf{y},s)=\hat{U}^R_{IJ}(\mathbf{x},\mathbf{y},s)+\hat{U}^S_{IJ}(\mathbf{x},\mathbf{y}) \tag{20}$$

where the regular dynamic part is given by

$$\hat{U}^R_{IJ}(\mathbf{x},\mathbf{y},s)=\frac{1}{8\pi^2}\int_{|\eta|=1}\sum_{m=1}^{2}\frac{\gamma^m_{IJ}}{\rho c_m^2}\Psi^R(s|\boldsymbol{\eta}\cdot(\mathbf{y}-\mathbf{x})|/c_m)\mathrm{d}S_\eta \quad , \tag{21}$$

$$\Psi^R(a,b)=\Psi(ab)+2\log b$$

while the singular static part has the following form:

$$\hat{U}_{IJ}^{S}(\mathbf{x},\mathbf{y})=\frac{1}{8\pi^2}\int_{|\eta|=1}\sum_{m=1}^{2}\frac{\gamma_{IJ}^{m}}{\rho c_m^2}\log\left(\left|\boldsymbol{\eta}\cdot(\mathbf{y}-\mathbf{x})\right|\right)\mathrm{d}S_{\eta} \tag{22}$$

The static displacement fundamental solution can be reduced to an explicit form as [14]:

$$\hat{U}_{IJ}^{S}(\mathbf{x},\mathbf{y})=-\frac{1}{\pi}\mathrm{Re}\left[\sum_{M=1}^{3}P_{JM}Q_{MI}\ln\left(z_M-z_M^0\right)-\ln\left(i+\mu_M\right)\right] \tag{23}$$

where

$$z_M=y_1+\mu_M y_2,\quad z_M^0=x_1+\mu_M x_2,\quad M=1,2,3 \tag{24}$$

are the counterpart of the collocation and the integration point.

By the constructive equations, the corresponding can be obtained as

$$\hat{T}_{IJ}^{R}(\mathbf{x},\mathbf{y},s)=\frac{1}{8\pi^2}\int_{|\eta|=1}\sum_{m=1}^{2}\frac{R_{IJ}^{m}}{\rho c_m^2}\cdot\frac{s}{c_m}\cdot\Psi'\left(s\left|\boldsymbol{\eta}\cdot(\mathbf{y}-\mathbf{x})\right|/c_m\right)\times\mathrm{sign}\left[\boldsymbol{\eta}\cdot(\mathbf{y}-\mathbf{x})\right]\mathrm{d}S_{\eta} \tag{25}$$

$$\hat{T}_{IJ}^{S}(\mathbf{x},\mathbf{y},s)=\frac{1}{\pi}\mathrm{Re}\left[\sum_{M}^{3}L_{JM}Q_{MI}\frac{\mu_M n_1(\mathbf{y})-n_2(\mathbf{y})}{z_M-z_M^0}\right] \tag{26}$$

$$\hat{\sigma}_{1IJ}^{R}(\mathbf{x},\mathbf{y},s)=\frac{1}{8\pi^2}\int_{|\eta|=1}^{}\sum_{m=1}^{2}\frac{C_{1IKl}\gamma_{JK}^{m}\eta_l}{\rho c_m^2}\cdot\frac{s}{c_m}\cdot\Psi'\left(s\left|\boldsymbol{\eta}\cdot(\mathbf{y}-\mathbf{x})\right|/c_m\right)\times\mathrm{sign}\left[\boldsymbol{\eta}\cdot(\mathbf{y}-\mathbf{x})\right]\mathrm{d}S_{\eta} \tag{27}$$

$$\hat{\sigma}_{1IJ}^{S}(\mathbf{x},\mathbf{y})=\frac{1}{\pi}\mathrm{Re}\left[\sum_{M=1}^{3}L_{JM}Q_{MI}\frac{\mu_M}{z_M-z_M^0}\right] \tag{28}$$

By Substituting Eq.21, Eq.22, and Eq. 25-28 into Eq. 15-16, and after normalized the limits of integration, the singular integral equations can be rewrite as

$$\sum_{j=0}^{N}\left(\int_{-1}^{1}\alpha_{iJ}^{M}\frac{f_M(\xi,j\Delta t)}{\xi-\eta}+\beta_{iJ}^{M}(\xi,\eta,(N-j)\Delta t)f_M(\xi,j\Delta t)\mathrm{d}\xi\right)=P_J(\eta,N\Delta t) \tag{29}$$

Dealing with the Cauchy Integration, Gauss-Chebyshev method is applied. $f_M(x,t)$ can be approximated by a series Chebyshev polynomial multiplied a weight function as

$$f_M(x,t)=w(x)F_M(x,t) \tag{30}$$

where the weight function $w(\xi)$ is determined by from the singular index, and the function $F_M(\xi,t)$ are unknown bounded functions.

$$w(\xi)=(1-\xi)^{-1/2},\qquad F_M(\xi,t)=\sum_{n=1}^{\infty}C_M(t)T_n(\xi) \tag{31}$$

By using the relation of Chebyshev polynomial [15]

$$\frac{1}{\pi}\int_{-1}^{1}\frac{\phi(\xi)}{\xi-\eta_j}\mathrm{d}\xi=\frac{1}{\pi}\int_{-1}^{1}\sum_{i=1}^{n}\frac{(1-\xi^2)^{1/2}T_n(\xi)}{\xi-\eta_j}\mathrm{d}\xi=\sum_{i=1}^{n}\frac{F(\xi_i)}{n(\xi_i-\eta_j)} \tag{32}$$

where

$$\xi_i=\cos\left[\frac{(2i-1)\pi}{2n}\right],\ i=1,\cdots,n;\quad \eta_j=\cos\left[\frac{j}{n}\pi\right],\ j=1,\cdots,n-1 \tag{33}$$

The integral Eq. 29 can be reduced to the following system of linear algebraic equations

$$\sum_{j=0}^{N}\left(\sum_{i=1}^{n}\frac{\pi}{n}F_M(\xi_i,j\Delta t)\left[\frac{\alpha_M}{\xi_i-\eta_k}+\beta_M(\xi_i,\eta_k,(N-j)\Delta t)\right]\right)=P_J(\eta_k,N\Delta t) \tag{34}$$

To solve the equations, supplementary equations are needed. Duo to CODs at the crack tip are zero, the supplementary equations are

$$\int_{-1}^{1}f_M(\xi,j\Delta t)\mathrm{d}\xi=0 \tag{35}$$

Using the same scheme, the above integral equations can be reduced as

$$\sum_{i=1}^{n}\frac{\pi}{n}F_M(\xi_i, j\Delta t)=0 \tag{36}$$

Solving Eq.34 and Eq.36, the unknown functions $F_M(x_i,t)$ can be computed, then by interpolating , $f_M(x,t)$ can be obtained.

4.3 Computation of dynamic intensity factors

Since the $F_M(x_i, jDt)$ have been solved, $\partial\tilde{U}_M(\xi, j\Delta t)/\partial\xi$ can be approximated by Lagrange interpolation. The generalized stress intensity factors *K* can be computed as

$$K_{\mathrm{I}}(j\Delta t)=\lim_{r\to 0}\sqrt{2r}\Sigma_{22}=\sqrt{2}\sum_{M=1}^{\tilde{}}\alpha_{12}^{M}F_M(1,j\Delta t),$$

$$K_{\mathrm{II}}(j\Delta t)=\lim_{r\to 0}\sqrt{2r}\Sigma_{12}=\sqrt{2}\sum_{M=1}^{3}\alpha_{22}^{M}F_M(1,j\Delta t),$$

$$K_{\mathrm{IV}}(j\Delta t)=\lim_{r\to 0}\sqrt{2r}\Sigma_{23}=\sqrt{2}\sum_{M=1}^{3}\alpha_{23}^{M}F_M(1,j\Delta t) \tag{37}$$

where α_{ij}^{M} are determined by material constants.

5 NUMERICAL EXAMPLES

5.1 Impact mechanical loading

The intensity factors are normalized as

$$K_{\mathrm{I}}^{*}(t)=\frac{K_{\mathrm{I}}(t)}{K_{\mathrm{I}}^{st}},\qquad K_{\mathrm{IV}}^{*}=\frac{K_{\mathrm{IV}}(t)}{K_{\mathrm{IV}}^{st}} \tag{38}$$

where $K_{\mathrm{I}}^{st}=s_0\sqrt{a}$, a is the semi-length of the crack.

To examine this method's accuracy, numerical calculations are carried out for piezoelectric material PZT-5H, which has a mass density of ρ=7500 kg/m^3 and the following material constants c_{11}=117.0 GPa, c_{12}=84.1 GPa, c_{22}=117.0 GPa, c_{66}=23.0 GPa, e_{21}=-6.5 C/m^2, e_{22}=23.3 C/m^2, e_{16}=17.0 C/m^2, ε_{11}=15.04 C/(GVm), ε_{22}=13.0 C/(GVm). The numerical results for $K_{\mathrm{I}}^{*}(t)$ and $K_{\mathrm{IV}}^{*}(t)$ have been given in Figs.1 and Figs.2 versus the time dimensionless time tc_T/a where $c_T=\sqrt{c_{66}/r}$. Comparison the results with that obtained by Garcia et al. [5] is shown a good agreement between both results.

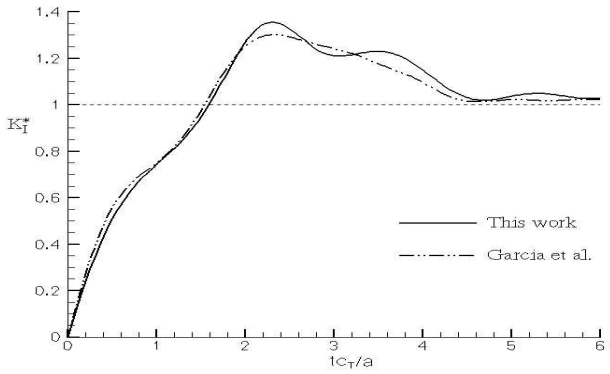

Fig. 1 Normalized mode-I stress intensity factor versus time for impact mechanical loading.

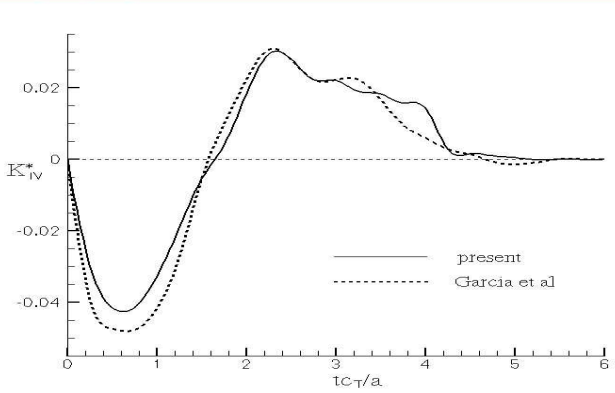

Fig. 2 Normalized electrical displacement intensity factor versus time for impact mechanical loading.

5.2 Infuluence of piezoelectric constants

As we know that the electric field doesn't contribute to K_I under static loading. In order to find out the influence of piezoelectric effect, numerical caculations are carried out for two different piezoelectric materials PZT-6B. Corresponding results for the normalized dynamic intensity factors are presented in Fig. 3. It shows that stress intensity factor K_I is significiantly affected by piezoelectric effect. Without considering the piezoelectric effect, $K_I^*(t)$ is larger at the begining, and reaches the maximun value earlier, but the peak value is much smaller.

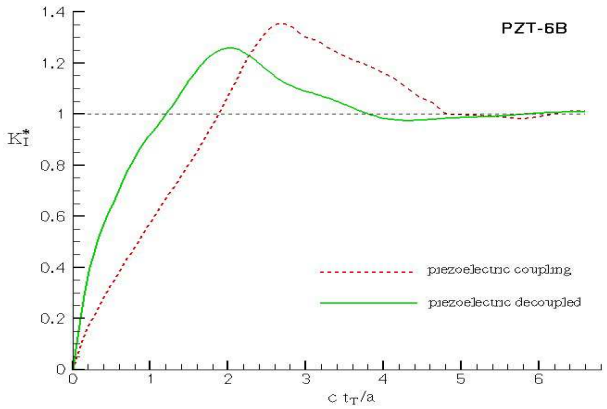

Fig. 3 Normalized mode-I stress intensity factor versus time for impact mechanical loading

6 CONCLUSIONS

Transient dynamic crack analysis in two-dimensional, homogenous and linear piezoelectric solids is presented in this paper. A Cauchy singular time-domain traction BEM is developed for this purpose. By using Lubich quadrature formula, Laplace-domain instead of time-domain dynamic fundamental solutions are applied, which is much more stable. By using the properties of straight crack and relations of fundamental solutions, the hypersingular integral equations are converts to Cauchy singular equations. Then, the singular integrals are treated by Gauss-Chebyshev method. Since the weight functions fully reflect the crack front singularity, dynamic intensity factors can be computed directly from the Displacement Discontinuity density functions, which is very accurate and easy. From the engineering points of view, the results presented here are useful to gain a better understanding of piezoelectric effect under impact loading conditions. The results show that in dealing with dynamic problems, piezoelectric effect must be considered, which has significiant influence.

7 ACKNOWLEDGEMENTS

The project was supported by the National Natural Science Foundation of China (No. 11172320), which is gratefully acknowledged.

8 REFERENCES

[1] M. Enderlein, FEM-analysis of cracks in piezoelectric structures under dynamic electromechanical loading, in: F. Nilsson (Ed.), Proceedings of the 15th European Conference on Fracture, Stockholm, Sweden, 2004, pp.

[2] M. Enderlein, A. Ricoeur, M. Kuna, Finite element techniques for dynamic crack analysis in piezoelectrics, International Journal of Fracture, 134, 191-208, 2005.

[3] G. Dziatkiewicz, P. Fedelinski, Dynamic analysis of piezoelectric structures by the dual reciprocity boundary element method, in: B. Gatmiri, A. Sellier, M. H Aliabadi, (Eds.), Advances in Boundary Element Techniques □. EC Ltd., UK, 2006, pp. 121-126.

[4] L. Gaul, M. Kögl, M. Wagner, Boundary Element Methods for Engineers and Scientists, Springer, Berlin, 2003.

[5] F.García-Sánchez, Ch. Zhang, J. Sladek, V. Sladek, 2-D transient dynamic crack analysis in piezoelectric solids by BEM, Comput. Mater. Sci. 39,179-186, 2007.

[6] F.García-Sánchez, Ch. Zhang, A. Sáez, 2-D transient dynamic analysis of cracked piezoelectric solids by a time-domain BEM, Comput. Methods Appl. Mech. Engng. 197, 3108-3121, 2008.

[7] G.R. Liu, K.Y. Dai, K.M. Lim, Y.T. Gu, A point interpolation mesh free method for static and frequency analysis of two-dimensional piezoelectric structures, Comput. Mesh. 29, 510-590, 2002.

[8] J. Sladek, V. Sladek, Ch. Zhang, F. García-Sánchez, M Wüunche, Meshless local Petrov-Galerkin method for plane piezoelectricity, Comput. Mater. Continua. 4, 109-118, 2002.

[9] C. Lubich, Convolution Quadrature and Discretized Operational Caculus.I. Numer. Math. 52, pp. 129~145, 1988.

[10] C. Lubich, Convolution Quadrature and Discretized Operational Caculus.II. Numer. Math. 52, 413~425, 1988.

[11] W.G. Cady, Piezoelectricity, Dover Publishers, New York, 1964.

[12] C.Y. Wang ,Ch. Zhang, 2D and 3D dynamic Green's functions and time –domain BIE formulations for piezoelectric solids, in: Z.H. Yao, M.W. Yuan, W.X. Zhong (Eds.), Proceedings of the WCCM Ⅵ in Conjuction with APCOM'04, September 5-10, 2004, Tsinghua University Press & Springer Verlag, Beijing, China, 2004.

[13] C.Y. Wang, Ch. Zhang, 3-D and 2-D dynamic Green's functions and time-domain BIEs for piezoelectric solids, Engng. Anal. Bound. Elem. 29, 454-465, 2005.

[14] E. Pan, A BEM analysis of fracture mechanics in 2-D anisotropic piezoelectric solids, Engng. Anal. Bound. Elem. 23, 67-76, 1999

[15] A.C. KAYA, F. Erdogan, On the solution of integral equations with strongly singular kernels, Quart. App. Math. April. 105-122, 1987.

Proceedings of the 3rd International Conference on
Fracture Fatigue and Wear, pp. 94-100, 2014

ONE-DIMENSIONAL GENERALIZED THERMOELASTIC ANALYSIS OF AN ELECTRICAL CONDUCTIVE THIN FILM SUBJECTED TO A MAGNETIC FIELD

F. Ashida[1], T. Morimoto[1] and Y. Suzuki[2]

[1] Shimane University, Matsue, Japan
[2] Mitsubishi Motors Cooperation, Tokyo, Japan

Abstract: This paper deals with a one-dimensional generalized thermoelastic problem of an electrical conductive thin film subjected to a thermal shock and a magnetic field intensity. This problem is formulated based on Lord and Shulman's generalized thermoelastic theory and analyzed by applying the Laplace transform technique. The analytical solution is obtained in the Laplace transform domain. The inversion of the Laplace transforms is performed numerically using Korrektur's method. Numerical calculations have been carried out for copper, nickel, and steel thin films. Numerical results show that the applied magnetic field intensity has little influence on the stress oscillation in the copper thin film, but it exerts a considerable influence on the stress oscillations in the nickel and steel thin films.

Keywords: magneto-thermo-elasticity; Lord and Shulman's theory; electrical conductive thin film

1 INTRODUCTION

Studies on magneto-electronics have been actively carried out and magnetic materials thin films have recently attracted considerable attention for application to new electronic devices. When magnetic and thermal loads act on an electrical conductive thin film, a stress wave propagates in the thin film and it may cause the stress concentration. Concerning dynamic magneto-thermo-elasticity, Kaliski [1] and Paria [2] derived basic equations. Since then, many papers on magneto-thermo-elastic problems of various solids have been published. For related papers recently published, Higuchi et al. analyzed a one-dimensional quasi-static problem of a plate [3] and a one-dimensional dynamic problem of a hollow circular cylinder [4] subjected to time-varying magnetic fields. Kawamura et al. studied a two-dimensional quasi-static problem of a conducting rectangular cylinder subjected to a sinusoidal time variation of magnetic field [5]. In these papers, quasi-stationary electric current fields were assumed and the Joule heating was taken into account, but a displacement current induced by a coupling effect between the displacement velocity and the magnetic filed intensity was neglected.

Now, in the case of a wave propagation problem, namely a generalized magneto-thermoelastic problem, the response within a very short time duration is necessary to be revealed, because it changes drastically with time. For that, the displacement current should be considered in the analysis of the problem, but the Joule heating induced by the quasi-stationary electric current can be neglected because there is little effect within the time duration.

The present paper deals with a one-dimensional generalized thermoelastic problem of an electrical conductive thin film when a constant heating temperature acts on one surface of the thin film and a time-varying magnetic filed intensity acts on both surfaces. This problem is analyzed based on Load and Shulman's theory which involves one relaxation time. In the analysis of the problem, the displacement current is considered, but the Joule heating is neglected. Applying the Laplace transform technique with respect to a time variable, the temperature change, displacement, and stress, which satisfy governing equations for the temperature and elastic fields as well as initial and boundary conditions, are obtained in the Laplace transform domain. The inversion of Laplace transforms has been carried out numerically by employing Korrektur's method [6]. Numerical results obtained for copper, nickel, and steel thin films are presented in graphical form in order to illustrate the effect of the displacement current on the thermo-

magneto-elastic field. The figures show that the applied magnetic field intensity has little influence on the stress oscillation in the copper thin film, but it exerts a considerable influence on the stress oscillations in the nickel and steel thin films.

2 PRESENTATION OF PROBLEM

2.1 Initial and boundary conditions

Let us consider an electrical conductive thin film of the thickness h as illustrated in Fig. 1.

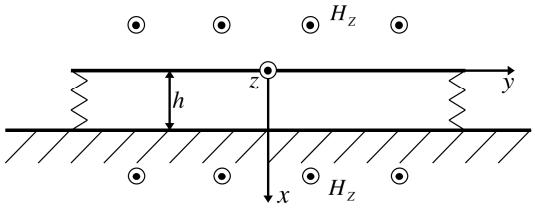

Fig. 1 An electrical conductive thin film

The thin film is considered to be initially at the reference temperature T_0 and free of displacement and stress. In the temperature filed, it is assumed that the top surface of the thin film is suddenly subjected to a thermal shock, while the bottom surface is thermally insulated. Then, the initial and boundary conditions are expressed by

$$\frac{\partial T}{\partial t} = 0,\ T = 0 \ \text{at}\ t = 0, \tag{1}$$

$$T = T_c \hat{H}(t) \ \text{on}\ x = 0, \tag{2}$$

$$\frac{\partial T}{\partial t} = 0 \ \text{on}\ x = h, \tag{3}$$

where T is the temperature change from the reference temperature T_0, t is time, and $\hat{H}(t)$ is Heaviside's unit step function. In the elastic filed, it is assumed that the top surface is stress free and the bottom surface is fixed to a flat rigid body:

$$\frac{\partial u_x}{\partial t} = 0,\ u_x = 0 \ \text{at}\ t = 0, \tag{4}$$

$$\sigma_x = 0 \ \text{on}\ x = 0, \tag{5}$$

$$u_x = 0 \ \text{on}\ x = h, \tag{6}$$

where u_x and σ_x are the displacement and stress in the x direction. It is considered that both surfaces are subjected to a time-varying magnetic field intensity:

$$H_Z = H_0 \sin(\omega t) \ \text{on}\ x = 0, h, \tag{7}$$

where H_Z is the magnetic field intensity in the z direction, H_0 is a constant magnetic field intensity, and ω is an angular velocity.

2.2 Basic equations

Applying Lord and Shulman's generalized thermoelastic theory, the equation of motion is:

$$\rho\frac{\partial^2 u_x}{\partial t^2}=(\lambda+2\mu)\frac{\partial^2 u_x}{\partial x^2}-\gamma\frac{\partial T}{\partial x}-\frac{k\mu_r^2\mu_0^2}{LT_0}H_Z^2\frac{\partial u_x}{\partial t}, \tag{8}$$

where ρ is density, λ and μ are Lamé's constants, $\gamma=(3\lambda+2\mu)\alpha_t$, α_t is the coefficient of thermal expansion, k is the thermal conductivity, μ_r is the relative permeability, μ_0 is the magnetic permeability of vacuum, and L is Lorenz's number. The heat conduction equation based on Lord and Shulman's theory is

$$k\frac{\partial^2 T}{\partial x^2}=\left(1+\tau_0\frac{\partial}{\partial t}\right)\left(\rho c\frac{\partial T}{\partial t}+\gamma T_0\frac{\partial^2 u_x}{\partial x\partial t}\right), \tag{9}$$

where c is the specific heat and τ_0 is the relaxation time. The constitutive equation for the elastic field is

$$\sigma_{xx}=(\lambda+2\mu)\frac{\partial u_x}{\partial x}-\gamma T. \tag{10}$$

The magnetic field intensity is governed by

$$\frac{\partial^2 H_Z}{\partial x^2}=\frac{k\mu_r\mu_0}{LT_0}\frac{\partial H_Z}{\partial t}. \tag{11}$$

3 ANALYSIS

The following dimensionless quantities are introduced:

$$\left.\begin{aligned}&\bar{x}=\frac{x}{h},\ \bar{t}=\frac{v_s}{h}t,\ \bar{\tau}_0=\frac{v_s}{h}\tau_0,\ \bar{\omega}=\frac{h}{v_s}\omega,\ \bar{T}=\frac{T}{T_C},\\&\bar{u}_x=\frac{(\lambda+2\mu)}{h\gamma T_C}u_x,\ \bar{\sigma}_x=\frac{\sigma_x}{\gamma T_C},\ (\bar{H}_0,\bar{H}_Z)=\frac{\sqrt{L}}{\gamma\alpha_t v_s h T_C}(H_0,H_Z)\end{aligned}\right\}, \tag{12}$$

where v_s is the velocity of elastic wave propagation. Application of Eq. (12) to Eqs. (8) ~ (11) yields

$$\frac{\partial^2\bar{u}_x}{\partial\bar{t}^2}=C_p^2\frac{\partial^2\bar{u}_x}{\partial\bar{x}^2}-C_p^2\frac{\partial\bar{T}}{\partial\bar{x}}-N\bar{H}_z^2\frac{\partial\bar{u}_x}{\partial\bar{t}}, \tag{13}$$

$$C_k^2\frac{\partial^2\bar{T}}{\partial\bar{x}^2}=\left(1+\bar{\tau}_0\frac{\partial}{\partial t}\right)\left(\frac{\partial\bar{T}}{\partial\bar{t}}+\varepsilon\frac{\partial^2\bar{u}_x}{\partial t\partial x}\right), \tag{14}$$

$$\bar{\sigma}_{xx}=\frac{\partial\bar{u}_x}{\partial\bar{x}}-\bar{T}, \tag{15}$$

$$\frac{\partial^2\bar{H}_z}{\partial\bar{x}^2}=P\frac{\partial\bar{H}_z}{\partial\bar{t}}, \tag{16}$$

where

$$C_p^2=\frac{\lambda+2\mu}{\rho v_s^2},\ C_k^2=\frac{k}{h\rho c v_s},\ \varepsilon=\frac{T_0\gamma^2}{\rho c(\lambda+2\mu)},\ N=\frac{k\mu_r^2\mu_0^2\gamma^2T_C^2\alpha_t^2v_s h^3}{L^2T_0\rho},\ P=\frac{k\mu_r\mu_0 h v_s}{LT_0}. \tag{17}$$

Applying the Laplace transform technique with respect to the time variable, the solution to Eq. (16) which satisfies the boundary conditions (7) is given by

$$\bar{H}_z=2\bar{H}_0\left(a_1\sin\bar{\omega}\bar{t}+a_2\cos\bar{\omega}\bar{t}\right), \tag{18}$$

where

$$\left.\begin{aligned} a_1 &= \frac{\cos\alpha\cosh\alpha\cos\beta\cosh\beta}{\cos 2\beta+\cosh 2\beta}+\frac{\sin\alpha\sinh\alpha\sin\beta\sinh\beta}{\cos 2\beta+\cosh 2\beta}, \\ a_2 &= -\frac{\cos\alpha\cosh\alpha\sin\beta\sinh\beta}{\cos 2\beta+\cosh 2\beta}+\frac{\sin\alpha\sinh\alpha\cos\beta\cosh\beta}{\cos 2\beta+\cosh 2\beta}, \\ \alpha &= \beta(1-2\bar{x}),\ \beta=\frac{\sqrt{\bar{\omega}P}}{2\sqrt{2}} \end{aligned}\right\}. \tag{19}$$

Applying the Laplace transform to Eqs. (13) ~ (15), the following equations are obtained:

$$s^2\bar{u}_x^* = C_p^2\frac{\partial^2\bar{u}_x^*}{\partial\bar{x}^2}-C_p^2\frac{\partial\bar{T}^*}{\partial\bar{x}}-NH_A\left(a_5 s-a_3 s^2+4a_3\bar{\omega}^2-4a_4 s\bar{\omega}\right)\bar{u}_x^*, \tag{20}$$

$$C_k^2\frac{\partial^2\bar{T}^*}{\partial\bar{x}^2} = \left(1+\bar{\tau}_0 s\right)\left(s\bar{T}^*+\varepsilon s\frac{\partial\bar{u}_x^*}{\partial\bar{x}}\right), \tag{21}$$

$$\bar{\sigma}_x^* = \frac{\partial\bar{u}_x^*}{\partial\bar{x}}-\bar{T}^*, \tag{22}$$

where s is the Laplace parameter and $\bar{T}^*$, $\bar{u}_x^*$, and $\bar{\sigma}_x^*$ are Laplace transforms of $\bar{T}$, $\bar{u}_x$, and $\bar{\sigma}_x$.

The solution to Eq. (20) can be taken to be

$$\bar{u}_x^* = D_1 e^{-\frac{s}{V_1}\bar{x}}+D_2 e^{\frac{s}{V_1}\bar{x}}+D_3 e^{-\frac{s}{V_2}\bar{x}}+D_4 e^{\frac{s}{V_2}\bar{x}}, \tag{23}$$

where D_i are unknown coefficients to be determined from the boundary conditions. Substituting Eq. (23) into Eq. (21), the temperature change in the Laplace transform domain is expressed as:

$$\begin{aligned}
\bar{T}^* = {} & \left(\frac{sV_1}{C_p^2}-\frac{s}{V_1}\right)\left(D_1 e^{-\frac{s}{V_1}\bar{x}}-D_2 e^{\frac{s}{V_1}\bar{x}}\right)+\left(\frac{sV_2}{C_p^2}-\frac{s}{V_2}\right)\left(D_3 e^{-\frac{s}{V_2}\bar{x}}-D_4 e^{\frac{s}{V_2}\bar{x}}\right) \\
& -\frac{NH_A}{C_p^2}\left[D_1V_1 e^{-\frac{s}{V_1}\bar{x}}b_{10}\left[-\frac{b_6}{s}+b_7\left(-\frac{e^{-2\beta+4\beta\bar{x}}}{s-4\beta V_1}-\frac{e^{2i\beta(-1+2\bar{x})}}{s-4i\beta V_1}-\frac{e^{(2-4\bar{x})\beta}}{s+4\beta V_1}-\frac{e^{-2i\beta(-1+2\bar{x})}}{s+4i\beta V_1}\right)\right.\right. \\
& \left.+e^{(-2-2i)(-1+2\bar{x})\beta}\left\{b_9\left(-\frac{e^{4\beta(-1+2\bar{x})}}{s-(4-4i)\beta V_1}-\frac{e^{4i\beta(-1+2\bar{x})}}{s+(4-4i)\beta V_1}\right)+b_8\left(-\frac{e^{(4+4i)(-1+2\bar{x})\beta}}{s-(4+4i)\beta V_1}-\frac{1}{s+(4+4i)\beta V_1}\right)\right\}\right] \\
& +D_2V_1 e^{\frac{s}{V_1}\bar{x}}b_{10}\left[\frac{b_6}{s}+b_7\left(\frac{e^{(2-4\bar{x})\beta}}{s-4\beta V_1}+\frac{e^{-2i\beta(-1+2\bar{x})}}{s-4i\beta V_1}+\frac{e^{(-2+4\bar{x})\beta}}{s+4\beta V_1}+\frac{e^{2i\beta(-1+2\bar{x})}}{s+4i\beta V_1}\right)\right. \\
& \left.+e^{(2-2i)(-1+2\bar{x})\beta}\left\{b_9\left(\frac{e^{(-4+4i)(-1+2\bar{x})\beta}}{s-(4-4i)\beta V_1}+\frac{1}{s+(4-4i)\beta V_1}\right)+b_8\left(\frac{e^{4\beta(1-2\bar{x})}}{s-(4+4i)\beta V_1}+\frac{e^{4i\beta(-1+2\bar{x})}}{s+(4+4i)\beta V_1}\right)\right\}\right] \\
& +D_3V_2 e^{-\frac{s}{V_2}\bar{x}}b_{10}\left[-\frac{b_6}{s}+b_7\left(-\frac{e^{-2\beta+4\beta\bar{x}}}{s-4\beta V_2}-\frac{e^{2i\beta(-1+2\bar{x})}}{s-4i\beta V_2}-\frac{e^{(2-4\bar{x})\beta}}{s+4\beta V_2}-\frac{e^{-2i\beta(-1+2\bar{x})}}{s+4i\beta V_2}\right)\right. \\
& \left.+e^{(-2-2i)(-1+2\bar{x})\beta}\left\{b_9\left(-\frac{e^{4\beta(-1+2\bar{x})}}{s-(4-4i)\beta V_2}-\frac{e^{4i\beta(-1+2\bar{x})}}{s+(4-4i)\beta V_2}\right)+b_8\left(-\frac{e^{(4+4i)(-1+2\bar{x})\beta}}{s-(4+4i)\beta V_2}-\frac{1}{s+(4+4i)\beta V_2}\right)\right\}\right] \\
& +D_4V_2 e^{\frac{s}{V_2}\bar{x}}b_{10}\left[\frac{b_6}{s}+b_7\left(\frac{e^{(2-4\bar{x})\beta}}{s-4\beta V_2}+\frac{e^{-2i\beta(-1+2\bar{x})}}{s-4i\beta V_2}+\frac{e^{(-2+4\bar{x})\beta}}{s+4\beta V_2}+\frac{e^{2i\beta(-1+2\bar{x})}}{s+4i\beta V_2}\right)\right. \\
& \left.\left.+e^{(2-2i)(-1+2\bar{x})\beta}\left\{b_9\left(\frac{e^{(-4+4i)(-1+2\bar{x})\beta}}{s-(4-4i)\beta V_2}+\frac{1}{s+(4-4i)\beta V_2}\right)+b_8\left(\frac{e^{4\beta(1-2\bar{x})}}{s-(4+4i)\beta V_2}+\frac{e^{4i\beta(-1+2\bar{x})}}{s+(4+4i)\beta V_2}\right)\right\}\right]\right],
\end{aligned} \tag{24}$$

where

$$\left.\begin{aligned} &V_1 = \sqrt{\frac{2A}{B+\sqrt{B^2-4AE}}}, \quad V_2 = \sqrt{\frac{2A}{B-\sqrt{B^2-4AE}}}, \\ &A = C_k^2, \quad B = \frac{C_k^2\left(s^2 + NH_A b_1\right)}{C_p^2 s^2} + \frac{1+\bar{\tau}_0 s + \varepsilon + \varepsilon\bar{\tau}_0 s}{s}, \quad E = \frac{s^2 + NH_A b_1 + \bar{\tau}_0 s^3 + \bar{\tau}_0 NH_A s b_1}{C_p^2 s^3} \end{aligned}\right\}, \tag{25}$$

and b_i are known coefficients, but they are omitted here for brevity. Substituting Eqs. (23) and (24) into Eq. (22), the stress in the Laplace transform domain is obtained, but the equation is omitted here.

Inversion of the Laplace transforms has been performed numerically by employing Korrektur's method [6] and the temperature, displacement, and stress in the physical domain are obtained.

4 NUMERICAL RESULTS

Numerical calculations have been carried out for copper:

$$\left.\begin{aligned} &\rho = 8954 \text{ kg/m},\ k = 386 \text{ W/mk},\ c = 380 \text{ J/kgK},\ \alpha_t = 1.75\times10^{-5} \text{ 1/K}, \\ &\lambda = 7.76\times10^{10} \text{ Pa},\ \mu = 3.86\times10^{10} \text{ Pa},\ v_s = 4157 \text{ m/s},\ \gamma = 5.518\times10^{6} \text{ Pa/K}, \\ &\mu_0 = 1.26\times10^{-6} \text{ H/m},\ \mu_r = 0.999,\ L = 2.45\times10^{-8} \text{ W½/K}^2,\ \tau_0 = 2.7\times10^{-14} \text{ s} \end{aligned}\right\}, \tag{26}$$

nickel:

$$\left.\begin{aligned} &\rho = 8908 \text{ kg/m},\ k = 90.9 \text{ W/mk},\ c = 440 \text{ J/kgK},\ \alpha_t = 1.34\times10^{-5} \text{ 1/K}, \\ &\lambda = 1.26\times10^{11} \text{ Pa},\ \mu = 7.60\times10^{10} \text{ Pa},\ v_s = 5589 \text{ m/s},\ \gamma = 7.11\times10^{6} \text{ Pa/K}, \\ &\mu_0 = 1.26\times10^{-6} \text{ H/m},\ \mu_r = 600,\ L = 2.45\times10^{-8} \text{ W½/K}^2,\ \tau_0 = 2.97\times10^{-12} \text{ s} \end{aligned}\right\}, \tag{27}$$

and steel:

$$\left.\begin{aligned} &\rho = 7800 \text{ kg/m},\ k = 43 \text{ W/mk},\ c = 465 \text{ J/kgK},\ \alpha_t = 1.18\times10^{-5} \text{ 1/K}, \\ &\lambda = 1.08\times10^{11} \text{ Pa},\ \mu = 8.00\times10^{10} \text{ Pa},\ v_s = 5864 \text{ m/s},\ \gamma = 5.72\times10^{6} \text{ Pa/K}, \\ &\mu_0 = 1.26\times10^{-6} \text{ H/m},\ \mu_r = 5000,\ L = 2.45\times10^{-8} \text{ W½/K}^2,\ \tau_0 = 1.6\times10^{-12} \text{ s} \end{aligned}\right\}. \tag{28}$$

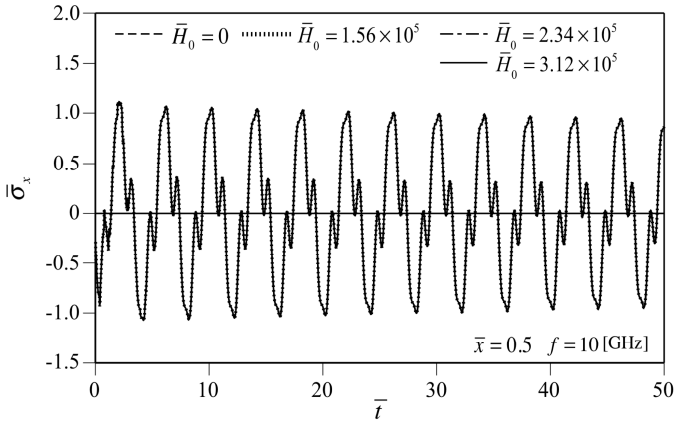

Fig. 2 Time histories of stresses in the copper thin film

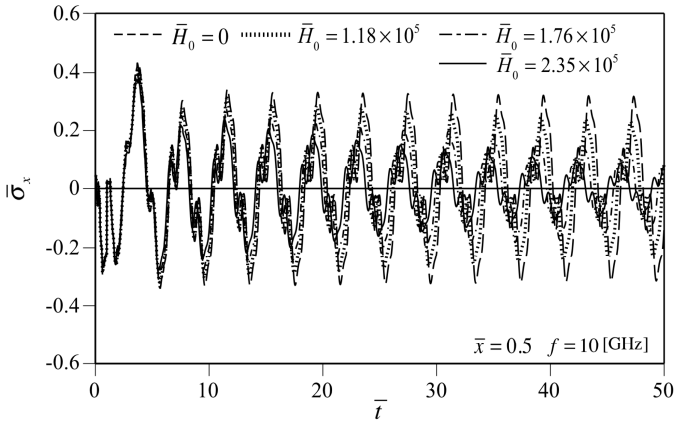

Fig. 3 Time histories of stresses in the nickel thin film

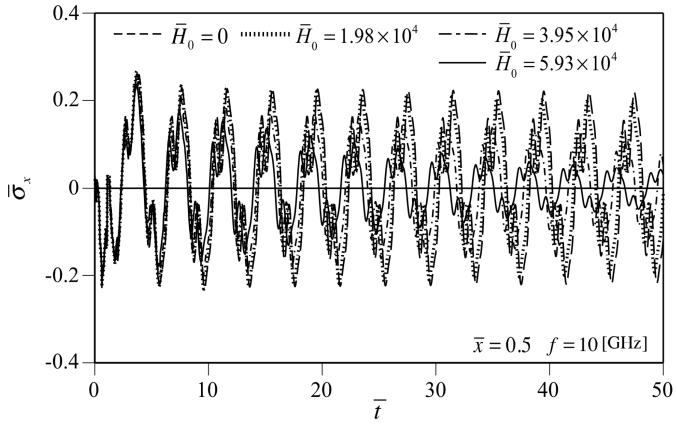

Fig. 4 Time histories of stresses in the steel thin film

Effects of the applied magnetic field intensity $\bar{H}_0$ of $f = 10$ GHz on the stresses at the middle positions ($\bar{x} = 0.5$) of the copper, nickel, and steel thin films are illustrated in Figs. 2 ~ 4. The nondimensional values of the applied magnetic field intensities shown in the figures are respectively corresponding to $H_0 = 4$ MN/Wb, $H_0 = 6$ MN/Wb, and $H_0 = 8$ MN/Wb for the cases of the copper and nickel thin films as well as to $H_0 = 0.5$ MN/Wb, $H_0 = 1$MN/Wb, and $H_0 = 1.5$ MN/Wb for the case of the steel thin film.

From Fig. 2, the applied magnetic field intensity has little influence on the stress oscillation in the copper thin film. In contrast, Figs. 3 and 4 show that it exerts a considerable influence on the stress oscillations in the nickel and steel thin films and the attenuation of the stress oscillations increases with increasing the applied magnetic field intensity. It is seen from Eq. (8) that the last term of the right-hand side represents the effect of damping, in which case the damping coefficient depends on the relative permeability μ_r only. From Eqs. (26) ~ (28), the relative permeability increases in the order of copper, nickel, and steel. It bears out the fact that the effect of the applied magnetic field intensity on the stress oscillation is hardly observed in the case of the copper thin film, whereas it appears considerably in the case of the steel thin film.

5 CONCLUSIONS

In this paper, a one-dimensional generalized thermoelastic problem of an electrical conductive thin film subjected to a constant heating temperature and a time-varying magnetic filed intensity is analyzed, based on Load and Shulman's theory. Applying the Laplace transform technique with respect to the time variable, the temperature change, displacement, and stress, which satisfy the governing equations of the temperature and elastic fields as well as the initial and boundary conditions, are obtained in the Laplace transform domain. The inversion of Laplace transforms has been carried out numerically by employing Korrektur's method. It is seen from the numerical results that the applied magnetic field intensity has little influence on the stress oscillation in the copper thin film, but it exerts a considerable influence on the stress oscillations in the nickel and steel thin films.

6 REFERENCES

[1] S. Kaliski, Wave equations of thermo-electro-magneto-elasticity, Proceedings of Vibration Problems, 6, 231-265, 1965.

[2] G. Paria, Magneto-elasticity and magneto-thermo-elasticity, Advances in Applied Mechanics, 10, 73-112, 1966.

[3] M. Higuchi, R. Kawamura, Y.Tanigawa, Magneto-thermo-elastic stresses induced by a transient magnetic field in an infinite conducting plate, Journal of Mechanics of Materials and Structures, 2 (1), 113-130, 2007.

[4] M. Higuchi, R. Kawamura, Y.Tanigawa, Dynamic and quasi-static behaviours of magneto-thermo-elastic stresses in a conducting hollow circular cylinder subjected to an arbitrary variation of magnetic field, Journal of Mechanical Sciences, 50 (3), 365-379, 2008.

[5] R. Kawamura, H. Fujita, Y. Ootao, Y. Tanigawa, K. Ikeda, H. Kinoshita, Magneto-thermo-elastic problem of a conducting rectangular cylinder subjected to sinusoidal change in time of magnetic field, Acta Mechanica, 214 (1-2), 133-144, 2010.

[6] G. Hoing, U. Hirdes, A method for the numerical inversion of Laplace transforms, Journal of Computation and Applied Mathematics, 10 (1), 113-132, 1984.

Proceedings of the 3rd International Conference on
Fracture Fatigue and Wear, pp. 101-107, 2014

THE SPREAD OF YIELD ZONE AT A NOTCH ROOT AND ITS NOTCH SIZE DEPENDENCE

H. Matsuno

Sojo University, Kumamoto, Japan

Abstract: The spread of the yield zone ahead of a notch root is analyzed under plane stress/strain and axi-symmetric conditions by finite element method (FEM). A model for predicting the yield zone size is devised by utilizing Dugdale expression. The model explained successfully the results of FEM. Notch size effect is considered based on the model proposed and formulated.

Keywords: stress concentration; yield zone size; dugdale model; notch behaviour map; notch size effect

1 INTRODUCTION

A stress concentration of notch, hole, slit, etc. often causes fracture and strength reduction of material and the processes are strongly controlled by the size of the stress concentration, as well known as a notch size effect. The elucidation of a yield phenomenon of notched material is helpful for understanding the fracture process and strength reduction of notched material by relating with theoretical stress concentration factor. If a uni-axial stress state is assumed, the nominal stress initiating the yield at a notch root is equal to the value, which is obtained by dividing the yield stress peculiar to material by theoretical stress concentration factor. As the average stress in the notch root section is increased, the yield zone spreads gradually from a notch root. Then, the yield zone size is influenced not only by the average stress but also by the scale of a notch, whose scale is expressed by the square root of the product of the notch depth and the notch root radius. In the present study, the growth behaviour of a yield zone ahead of a notch root, whose stress concentration factor is changed under a plane stress/strain and an axi-symmetric condition, is traced by finite element method (FEM). On the other hand, a model, which is named as a notch root yield zone model, is devised for the purpose of predicting the size of the yield zone growing ahead of the notch root by utilizing Dugdale model [1], and the validity of the model will be proved by the result of FEM analysis. Further, notch size effect on the yield phenomenon of material will be formulated concretely based on the Notch Root Yield Zone Model (NRYZM) newly proposed. It is expected that the acquired expression can be applied to explaining the notch size effect on the fatigue strength of notched material as it is.

2 PROCEDURE OF FEM ANALYSIS

Two-dimensional (plane stress/strain) and axial symmetric elastic-plastic FEM programs are prepared so as to cope with large deformation problems. They are applied to circular-holed/double edge-notched plates and spherical-cavity/circumferential-notched round bars subject to uni-axial tension loads. The longitudinal 1/4-sectional geometries of objective bodies for FEM analyses are shown in Fig. 1. In order to make influence of finite width and length as small as possible, the effective width and length of objects are set to 8 times the size of notch depth. This means that the nominal stresses, which are expressed by net-/gross-sectional average stresses, are nearly equal. The objective bodies are set up as elastic-perfectly plastic solids (yield stress: $S_Y = 250\,\mathrm{MPa}$). The objects are divided into eight-node iso-parametric quadrilateral elements, which include Gaussian integrating points of n=3. Number of elements is 115 to 217 and that of nodes is 386 to 708. Advance of the step of calculation is performed by R_{min} method proposed by Yamada. For every step, the size of yield zone is outputted as ω_{x0}, ω_{x1}, ω_{y1} and $\sqrt{\omega_{area}}$, which are defined in Fig. 2 where ω_{area} shows the area of the longitudinal section of yield zone. Distributions of axial stress and Mises'

equivalent stress components of notch root sections in the initial stage, σ_y and σ_{eq}, are approximated as follows, respectively.

$$\frac{\sigma_y}{\bar{\sigma}_y} = C_{y1} + \frac{C_{y2}}{\left(1+\frac{\chi}{\rho}\right)^2} + \frac{C_{y3}}{\left(1+\frac{\chi}{\rho}\right)^4}. \quad (1)$$

$$\frac{\sigma_{eq}}{\bar{\sigma}_{eq}} = C_{eq1} + \frac{C_{eq2}}{\left(1+\frac{\chi}{\rho}\right)^2} + \frac{C_{eq3}}{\left(1+\frac{\chi}{\rho}\right)^4}. \quad (2)$$

In Eq. 1 and Eq. 2, χ is a distance from a notch root, $\bar{\sigma}_y$ and $\bar{\sigma}_{eq}$ are sectional averages of σ_y and σ_{eq} respectively, and C_{yi} and C_{eqi} $(i=1:3)$ are coefficients. Theoretical stress concentration factor, K_t and K_{teq}, are determined by the following expressions respectively, and their values are summarized in Table 1.

$$K_t = \frac{\sigma_{yNR}}{\bar{\sigma}_y} = C_{y1} + C_{y2} + C_{y3}. \quad (3)$$

$$K_{teq} = \frac{\sigma_{eqNR}}{\bar{\sigma}_{eq}} = C_{eq1} + C_{eq2} + C_{eq3}. \quad (4)$$

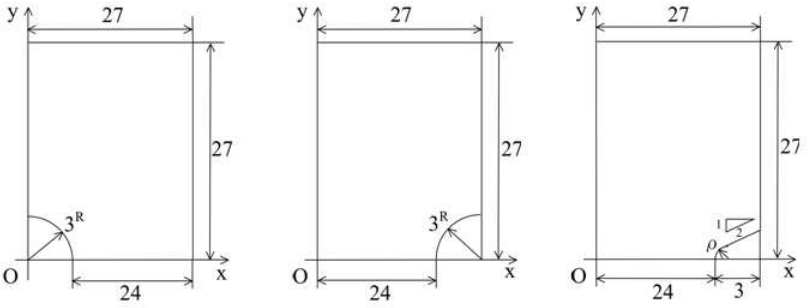

Fig. 1 Geometries of longitudinal 1/4-section of objective body for FEM.

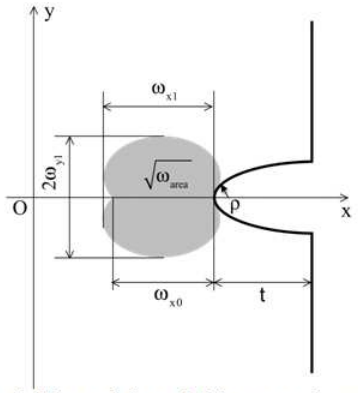

Fig. 2 Definition of the yield zone sizes ω_{x0}, ω_{x1}, ω_{y1} and $\sqrt{\omega_{area}}$.

Figure No.	ρ [mm]	t [mm]	t/ρ	√tρ	Plane stress condition		Plane strain condition		Axi-symmetric condition	
					K_t	K_{teq}	K_t	K_{teq}	K_t	K_{teq}
1 - a	3.00	3	1.00	3.000	2.69	2.78	2.69	2.90	2.01	1.95
1 - b	3.00	3	1.00	3.000	2.71	2.86	2.71	3.06	2.55	2.78
1 - c	1.00	3	3.00	1.732	4.18	4.43	4.18	4.92	3.94	4.48
	0.50	3	6.00	1.225	5.66	5.97	5.69	6.76	5.35	6.19
	0.25	3	12.0	0.866	7.62	8.10	7.61	9.37	7.18	8.62
	0.10	3	30.0	0.548	11.5	12.2	11.5	14.6	10.9	13.5

Table 1 Summary of K_t and K_{teq}.

3 RESULTS AND DISCUSSION

3.1 Reference equation for estimating the yield zone size ahead of a notch root

Based on Dugdale model known well [1], the model for predicting the yield zone size ahead of a notch root is newly constituted. The model is named as the Notch Root Yield Zone Model (NRYZM) in order to distinguish from the Crack Tip Yield Zone Model (CTYZM). Although the rationale of the model is not clear, it is very powerful as an empirical model for comparing and characterizing the results analyzed by FEM, as described in the following section 3.2. The CTYZM (Dugdale model) is expressed as Eq. 5. Eq. 6 and Eq. 7

are constituted by multiplying a right term of Eq. 5 by K_t or 1.12 K_t (a coefficient 1.12 means a surface factor) and by substituting $(\bar{\sigma}/S_Y - 1/K_t)$ for $\bar{\sigma}/S_Y$ of the right term of Eq. 5, respectively. The NRYZM is expressed as a geometric average of the right terms of Eq. 6 and Eq. 7 as shown in Eq. 8. In Eq. 8, $\sqrt{t\rho}$ represents the scale of the notch. The diagram obtained from the NRYZM with K_t changed is illustrated in Fig. 3, and it is compared with the diagram obtained from the CTYZM, whose diagram is approximated by two straight lines C_1D_1F and FH_1R_1. As shown in Fig. 3, the diagrams are classified into two groups, the diagrams intersecting the line of the CTYZM and those not intersecting. For the diagram belonging to the former group, the view of replacing a notch by a crack is materialized as described later.

$$\bar{\omega}_{CT} = \frac{\omega}{a} = \sec\left(\frac{\pi}{2}\frac{\bar{\sigma}}{S_Y}\right) - 1. \tag{5}$$

$$\bar{\omega}' = K_t\left\{\sec\left(\frac{\pi}{2}\frac{\bar{\sigma}}{S_Y}\right) - 1\right\} \quad \text{or} \quad \bar{\omega}' = 1.12K_t\left\{\sec\left(\frac{\pi}{2}\frac{\bar{\sigma}}{S_Y}\right) - 1\right\}. \tag{6}$$

$$\bar{\omega}'' = \sec\left\{\frac{\pi}{2}\left(\frac{\bar{\sigma}}{S_Y} - \frac{1}{K_t}\right)\right\} - 1. \tag{7}$$

$$\bar{\omega}_{NR} = \frac{\omega}{\sqrt{t\rho}} = \sqrt{\bar{\omega}' \cdot \bar{\omega}''}\ . \tag{8}$$

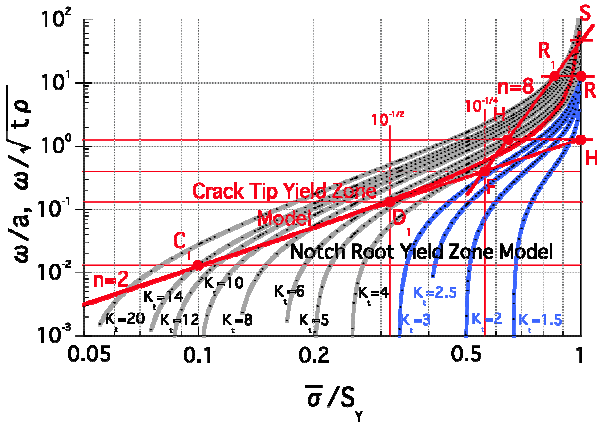

Fig. 3 Relation between the yield zone size ω and the average stress $\bar{\sigma}$ in CTYZM & NRYZM.

3.2 Growth behaviour of the yield zone ahead of a notch root

The results of FEM analyses on the spread of local yield zone ahead of a notch root under plane stress, plane strain and axi-symmetric conditions are shown in Figs.4-6. Figure (a) and (b) show the case that the stress parameter for arrangement is axial stress $\bar{\sigma}_y$ and Mises' equivalent stress $\bar{\sigma}_{eq}$, respectively. In all figures, the expression of the NRYZM is referred in order to make characterization and comparison of FEM results easy. The size of ω_{x1} is adopted as a most leading representative parameter expressing the size of

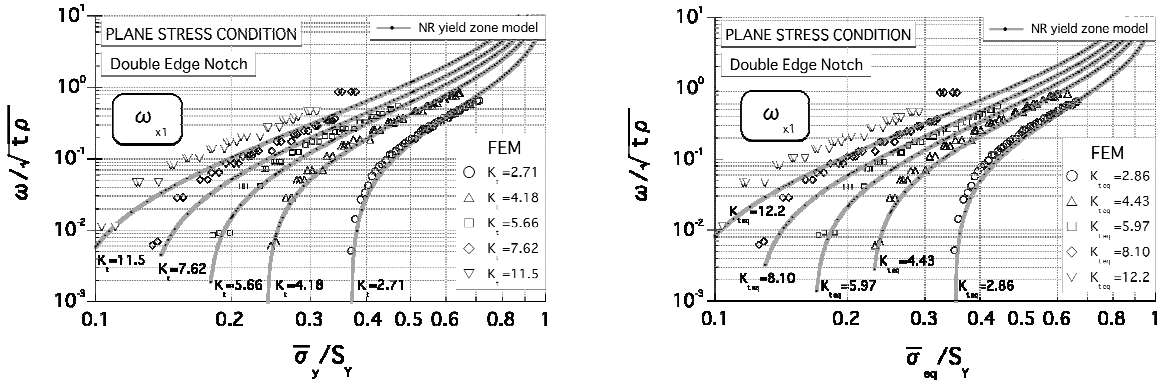

(a) Axial average stress $\bar{\sigma}_y$. (b) Mises' equivalent average stress $\bar{\sigma}_{eq}$.

Fig. 4 Change of a yield zone size ω_{x1} in a double edge notch plate under plane stress condition.

the yield zone. In the $\bar{\sigma}_{eq}$-based diagram of Figure (b), the influence of the multi-axial stress state on the growth behavior of the yield zone can be taken into account, as shown by comparison of Fig. 5 (a) and (b) for the plane strain condition, and by that of Fig. 6 (a) and (b) for the axi-symmetric condition. The behavior of other sizes ω_{x0}, ω_{y1} and $\sqrt{\omega_{area}}$ is shown in Fig. 7 (a), (b) and (c), respectively. Figure shows the case of the plain strain condition as an example. In an initial stage of local yield, the size ω_{x0} increases like the size ω_{x1}, maintaining the value equal to the size ω_{x1}. However, in the later stage of local yield, the increase in the size ω_{x0} stagnates on account of an elastic core, which is formed in the center of the solid with a double edge and circumferential notch. The size ω_{y1} presents a rapid increase in the initial stage of local yield. In a subsequent stage, the increase in the size ω_{y1} becomes loose and, in a final stage of local yield, the size ω_{y1} increases rapidly again. The behavior of the size $\sqrt{\omega_{area}}$ reflects remarkably the behavior of the size ω_{y1} in the initial stage of local yield. It turns out that the NRYZM explains very well the relation between the yield zone size ω_{x1} and Mises' equivalent stress $\bar{\sigma}_{eq}$ obtained by FEM analysis. In addition, since the mesh of models was very disorderly in the present study, the unnatural discontinuity was seen at some places in the plot of the result of FEM analysis.

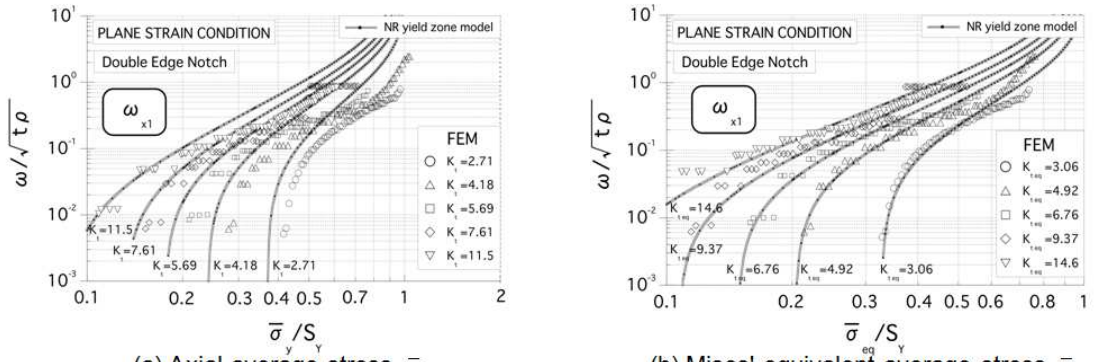

(a) Axial average stress $\bar{\sigma}_y$. (b) Mises' equivalent average stress $\bar{\sigma}_{eq}$.

Fig. 5 Change of a yield zone size ω_{x1} in a double edge notch plate under plane strain condition.

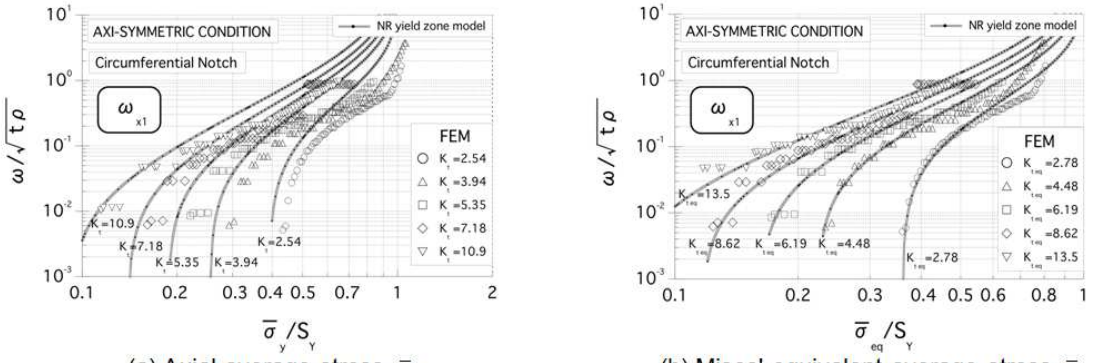

(a) Axial average stress $\bar{\sigma}_y$. (b) Mises' equivalent average stress $\bar{\sigma}_{eq}$.

Fig. 6 Change of a yield zone size ω_{x1} in a circumferential notch round bar under axi-symmetric condition.

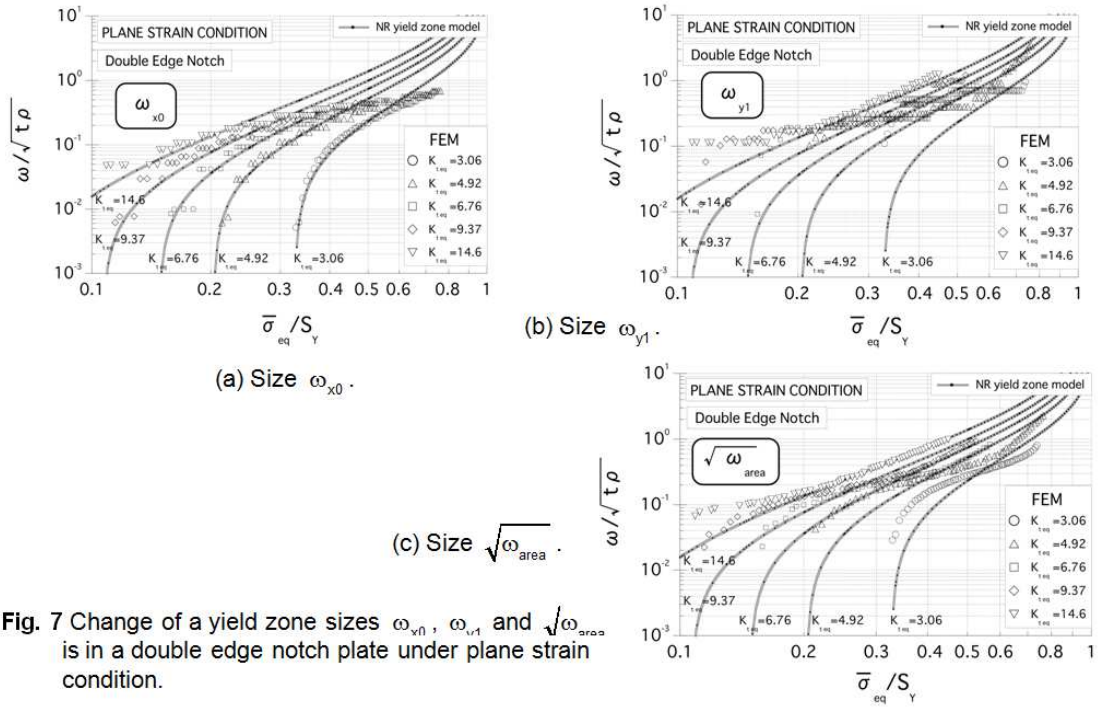

Fig. 7 Change of a yield zone sizes ω_{x0}, ω_{y1} and $\sqrt{\omega_{area}}$ is in a double edge notch plate under plane strain condition.

3.3 Notch size effect on yield phenomenon at a notch root

The author pointed out that a Notch Behavior Map had an important role in considering the size effect of the fatigue strength of notched material [2]. In the map, the notch is characterized by two parameter of t/ρ, which represents sharpness of a notch, and $\sqrt{t\rho}/L_0$, which represents a scale of the notch, where ρ is notch root radius, t is notch depth and L_0 is a referential size for judging whether a scale of the notch is large or small. The theoretical stress concentration factor K_t corresponding to the parameter t/ρ is calculated approximately by using Eq. 9 under the shallow notch condition.

$$K_t = 1 + 2\sqrt{\frac{t}{\rho}}\,. \tag{9}$$

The character of notch behaviour is classified into four type; (I) Blunt notch, (II) Prototype (archetype) notch, (III) Crack-like notch and (IV) Short notch. More importantly, two types of strength distributions reflecting notch size effect are drawn qualitatively on the map (and not quantitatively). The one is the strength distribution peculiar as notched material (whose prototype case is a circular hole in a plate or a spherical cavity inside a solid) and the other is the strength distribution of material whose notch is replaced by a crack (as the distribution is simulated by Kitagawa-Takahashi diagram [3]). The former is formulated concretely by using the NRYZM as shown in Fig. 8 following the notch behaviour map. The latter is formulated by relating the NRYZM with the CTYZM (Dugdale model) as shown in Fig. 9 following the map. The diagrams are created as follows. First, an x-axis and a y-axis are replaced in the diagram, Fig. 3, relating between the normalized yield zone size $\omega/\sqrt{t\rho}$ and the normalized average stress $\bar{\sigma}/S_Y$. Next, Scale 1 of a new x-axis ($\omega/\sqrt{t\rho}$) is converted into Scale 2 ($\sqrt{t\rho}/\omega$), further again into Scale 3 ($\sqrt{t\rho}/L_0$ in Fig. 8(b) and t/L_0 in Fig. 9(b)). As a result, both NRYZM and CTYZM can be linked with the Notch Behaviour Map. The boundary line between large and small size notch, D_1DQBB_1, is mutually common in Fig. 8(a) and (b). From Fig. 8(b), the strength distribution, that is, notch size effect is formulated as follows.

For the large size notch: $$\frac{\bar{\sigma}}{S_Y} = \frac{1}{K_t}\,. \tag{10}$$

For the small size notch: $\dfrac{\bar{\sigma}}{S_Y} = \dfrac{1}{K_t}\left(\dfrac{\sqrt{t\rho}}{L_0}\right)^{-1/n}$. (11)

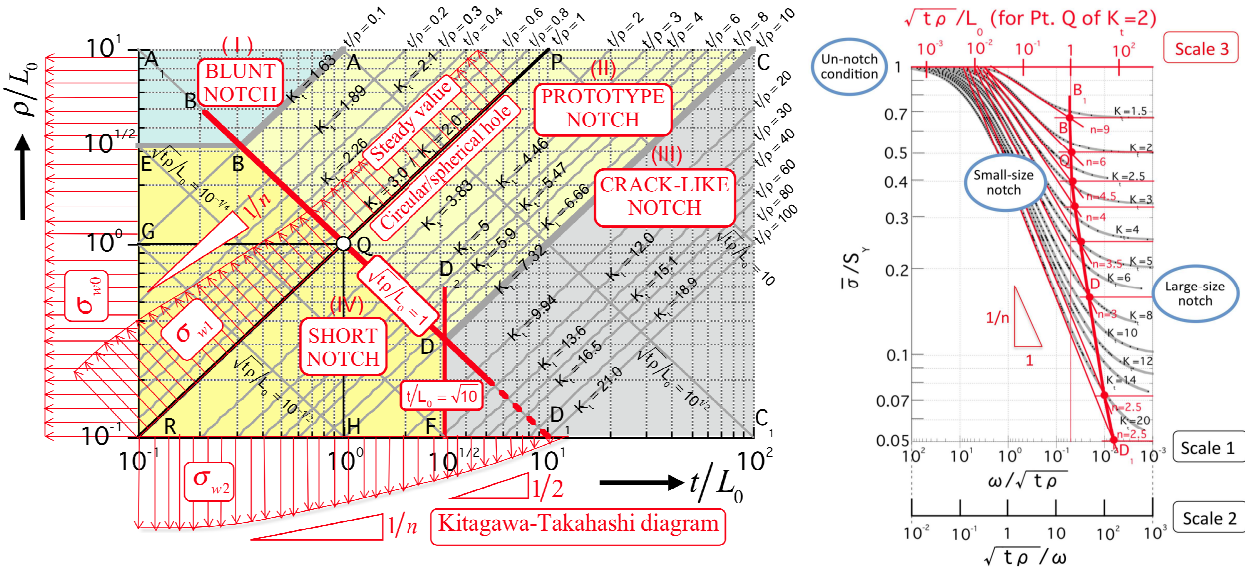

(a) Notch behavior map. (b) Diagram for predicting size effect.

Fig. 8 Notch behavior map and size effect diagram peculiar to a notch.

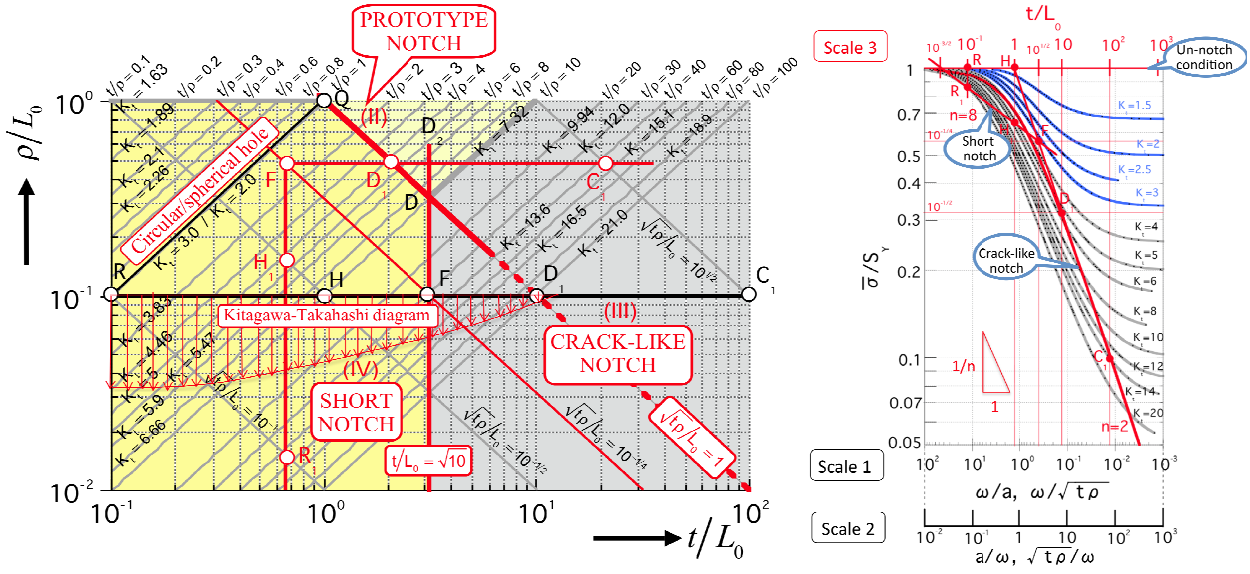

(a) Notch behavior map. (b) Diagram for predictng size effect.

Fig. 9 Notch behavior map and size effect diagram where a notch is replaced by a crack

For the un-notch condition: $\dfrac{\bar{\sigma}}{S_Y} = 1.$ (12)

The line on the crack-like notch, C_1D_1F, and the line on the short notch, FH_1R_1, is mutually common in Fig. 9(a) and (b). From Fig. 9(b), the strength distribution, that is, size effect of a notch replaced by a crack is formulated as follows.

For the crack-like notch: $\frac{\bar{\sigma}}{S_Y} = \left(\frac{t}{L_0}\right)^{-1/2}$. (13)

For the short notch: $\frac{\bar{\sigma}}{S_Y} = 10^{-3/16}\left(\frac{t}{L_0}\right)^{-1/8}$. (14)

4 CONCLUSIONS

1) The behavior of a yield zone size developing ahead of a notch root, whose stress concentration factor is changed under a plane stress/strain and an axi-symmetric condition, is traced by FEM.
2) A model is devised for the purpose of predicting the size of the yield zone growing ahead of the notch root by utilizing Dugdale model. The model is named as Notch Root Yield Zone Model so as to distinguish from Crack Tip Yield Zone Model (Dugdale model).
3) The Notch Root Yield Zone Model explains very well the relation between the maximum yield zone size ahead of the notch root and the sectional average of Mises equivalent stress, which are obtained by FEM analyses.
4) By relating Notch Root Yield Zone Model with the Notch Behavior Map, the notch size effect on the yield phenomenon of material is formulated concretely from two viewpoints; the original size effect of a notch, whose prototype case is a circular hole in a plate or a spherical cavity inside a solid, and the size effect of the case where a notch is replaced by a crack.

5 NOMENCLATURE

FEM	Finite element method
CTYZM	Crack tip yield zone model (Dugdale model)
NRYZM	Notch root yield zone model
S_Y, S_U	Yield/tensile strength of material
σ, σ_y, σ_{eq}	Stress; general term and y-axial/Mises equivalent stress
$\bar{\sigma}$, $\bar{\sigma}_y$, $\bar{\sigma}_{eq}$	Sectional average of stress; general term and y-axial/Mises equivalent stress
K_t, K_{teq}	Stress concentration factor; normal (y-axial)/Mises equivalent stress (defined theoretically)
t, ρ	Notch depth, notch root radius
ω	Yield zone size; general term
ω_{x0}, ω_{x1}, ω_{y1}	Yield zone size, length on an x-axis, maximum length, half width
$\sqrt{\omega_{area}}$	Yield zone size; Square root of yield zone area defined specially in FEM analyses
$\bar{\omega}_{CT}$, $\bar{\omega}_{NR}$	Normalized yield zone size predicted by CTYZM/NRYZM
C_{yi}, C_{eqi}	Coefficients in an approximate expression of stress distribution (i=1-3)

6 REFERENCES

[1] D. S. Dugdale, Yielding of Steel Sheets Containing Slits, J. Mech. Phys. Solids, Vol.8, 100–104, 1960.
[2] H. Matsuno, Formulation and Characterization of Fatigue Strength Diagrams of Notched Specimens Based on Equivalent Cyclic Stress Ratio, Attending Especially to Material Dependence and Notch Size Effects, Proc. 13th International Conference on Fracture, June 16-21, 2013,Beijing, China.
[3] H. Kitagawa and S. Takahashi, Applicability of Fracture Mechanics to Very Small Cracks or the Cracks in the Early Stage, Proc. Second International Conference on Mechanical Behaviour of Materials, August 16-20, 1976, Boston, MA, 627-631.

Proceedings of the 3rd International Conference on
Fracture Fatigue and Wear, pp. 108-113, 2014

MAKING SMART PHONE APPLICATIONS IN ORDER TO HAVE EXPERIENCE OF MECHANICS OF MATERIALS

T. Tsuji

Chuo University, Tokyo, Japan

Abstract: In resent year, students have a little experience of destructions. They have not know how materials to break and where forces to concentrate. It is important to have the experiences as strain measurement, pulling test, destruction test and so on in order to recognize the mechanics of materials. Thus, we have been making the desktop experiment kits by which students can proceed to do the experiments. But, it is difficult to make the experiment in the lecture room for more than 100 students. On the other hand, smart phones such as iPhone are developed and interactive operation is easily carried out. In this study, we propose the some applications for a smart phone, which is interactive and similar to the real experiment. By the proposed applications, a student can apply the force, displacement and temperature to the materials by moving their fingers and can observe the extension, internal force, stress, strain, and stress concentration of the materials.

Keywords: smart phone; application; mechanics of materials; stress concentrate; education

1 INTRODUCTION

In resent year, real experiences, which are related to the mechanics of material, are decreasing. Thus, the mechanics of material is one of the difficult subjects to understand for resent students in a faculty related to the mechanical engineering. In order to make the best instruction of the Strength of Materials, authors have been trying many methods by using multimedia [1,2]. In our lectures, we have met serious problems coursed from character of the recent students. "They dislike to think.", "They can not concentrate.", "They have not reality.", "They can not think theoretically.", "They have no applicability.", "They are not actively." and so on. When a human makes something, he uses his hands, thinks by his brain, makes mistake, and creates. Accordingly, we think that the main reason of such the changing of the students' character depends on the decreasing of the total time for the lectures, which are related to creation. The new curriculum in JAPAN, the total time for such the lectures decreases 1/4 in junior high school and 0 in high school [3]. Then, there are some attempts, such as "Design lecture" and "Problem oriented lecture", in order to think students by themselves. For example, in engineering division of Tokyo Institute of Technology, they have been made the robot contest for all new students (200 persons). We think such the attempts must be effective, but it takes large cost and voluntary effort by many staffs. It is difficult to precede such the lecture in our division. Thus, we constructed virtual pulling machine for the instruction of the strength of materials[2,4].

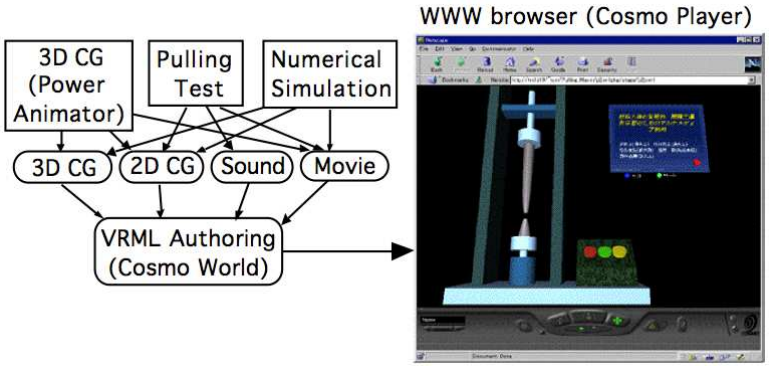

Fig. 1 How to make the Virtual Pulling Test Machine

Figure 1 shows the main view of the virtual machine constructed by the VRML system. But, it is very complicate to make the virtual machine, which can simulate like the real experiences as the real machine does, and the operator push the buttons on the screen with no idea. Thus, we have been making the desktop experiment kit by which students can proceed to do the experiments and learn the mechanics of material [5]. Some examples of these experiments are shown in Fig. 2. But, It is difficult to make the experiment in the lecture room for more than 100 students. And, it is also difficult to prepare all experiment which is related each category of the lecture. Moreover, it takes at least one hour to complete each experiment including prepare and cleaning up. On the other hand, the tablet computer such as iPad is developed and interactive operation is easily carried out. Some applications for iPad are available related to the mechanics of materials [6,7]. For example, "Truss Me!" is a truss simulator. User can make truss construction by dragging many parts and simulate. These applications are very easy to use and match interactive, but are not real as same as our virtual machine. We made the some applications, which is more interactive than the virtual machine and similar to the real experiment [8]. Unfortunately, a few students in my class have iPad, although almost all students have iPhone. Moreover, iPhone is easier than iPad to handle.

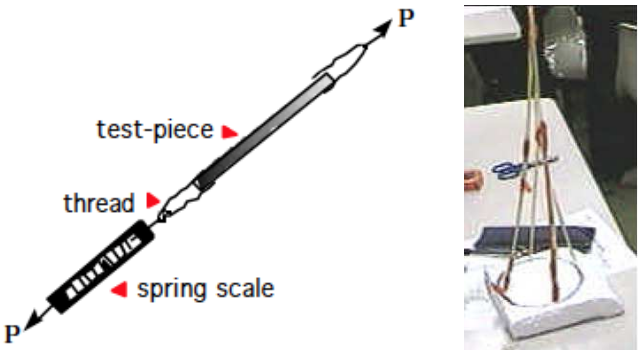

(a) Pulling test (b) Making tower

Fig. 2 Some examples of the desktop experiments

Therefore, in this study, I made the several applications in order to assist students to understand the basic phenomena related to the mechanics of materials. By the proposed applications, a student can apply the force, displacement and temperature to the materials by moving their finger and can observe the deformation, internal force, stress, strain, thermal stress and stress concentration of the materials.

2 THE METHOD TO DEVELOP AN APPLICATION FOR THE IPHONE

The target smart phone is iPhone or IPod Touch. IPod Touch and the computer screen are shown in Fig. 3. The screen size and resolution of iPhone are 88.5x50.0 mm and 1136x640 pixels respectively. The MacMini (Apple) is used to develop the application by using Xcode5.0. Xcode is the software environment in order to make an application for the iPad, iPhone and computers by Apple. The iPhone is connected to the iMac through the USB cable. The developed applications can be tested on time. The application can be made graphically. Buttons, figures and texts can be set by dragging them using a mouse. For example, Fig. 4 shows the method to make the slider bar by which user can move object. By connecting these objects to the program code, the application is given. Thus, it is very easy to make an application for iPad and/or iPhone.

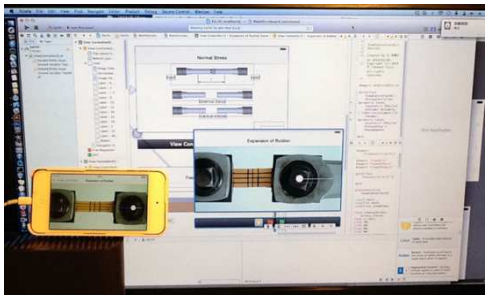

Fig. 3 iPod touch and computer display

An application is constructed from the Storyboard, the ViewController and the View. The storyboard is such as a container of figures, buttons, labels and texts. We can add and change the layout of these objects by dragging a mouse. The hierarchy through the main menu to each application can be made by the storyboard as shown in Fig. 5. The transition from the storyboard to the other storyboard can be easily made by connecting each storyboard to the others.

The ViewController is the program, which controls the objects, events and the views of the iPad. For example, if a user moved the finger at an object, the property such as placement of the finger is sent automatically to the ViewController. According to this information, we can write the program, which deform the object. The V any ready-made command eady-made systems, the ma buttons and making a code to

The applications distribution system. It is pos the teacher makes applicatio .

(a) Sele lication

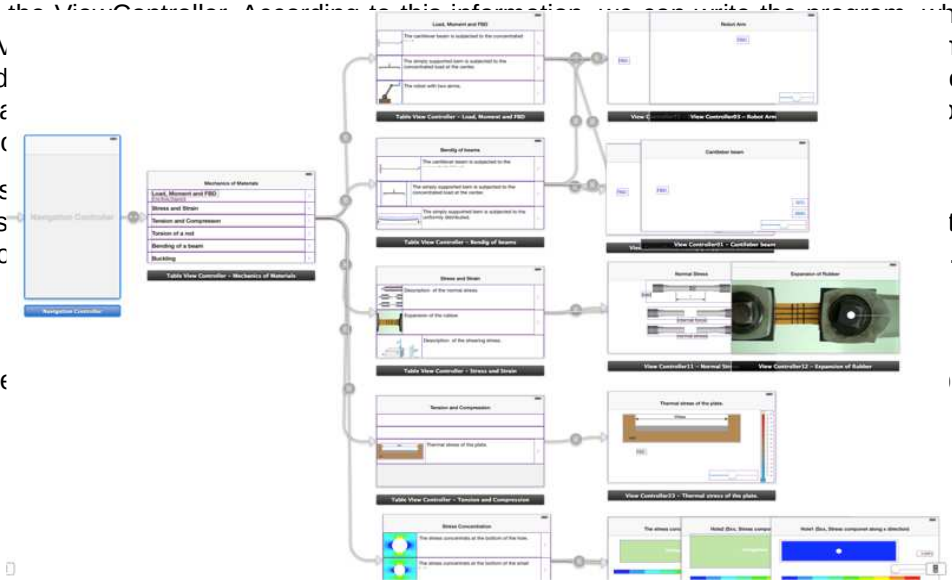

Fig. 5 The hierarchy of the main menu, the sub menu's and the applications

3 THE APPLICATION FOR THE MECHANICS OF MATERIALS

I started to make applications for iPad [3] instead of iPhone, since the screen size of iPad is bigger than the one of iPhone. However, the number of students who are using iPad is very small. Almost all students have iPhone in my class. Therefore, I had been started to make application for iPhone. Many applications had been made for iPad. Thus I intended to translate them into the iPhone. The translation from iPad to iPhone is easy, but the iPhone's size is small and we can't see and manipulate application, which are made for iPad's screen size. Thus, I intended to make simple applications, which can instinctively manipulate. At this time, 11 applications as listed in Table 1 are made. Three of them will be explained in the following sections.

Table 1 Lists of applications

Main menu	Sub Menu
Load, Moment and FBD	Cantilever beam. Simply supported beam. Robot Arm.
Stress and Strain	Description of the normal stress. Expansion of the rubber.
Tension and Compression	Thermal stress.
Bending of a beam	Cantilever beam subjected to the concentrated load. Simply supported beam subjected to the concentrated load. Simply supported beam subjected to the uniformly distributed load.
Stress Concentration	The stress concentration at the bottom of the small hole. The stress concentration at the bottom of the large hole. The stress concentration at the crack tip.

3.1 Expansion of the rubber plate

This application is translated from iPad's application. Students can observe the experiment, which is the expansion of the rubber as shown in Fig. 6(a). The photo of the rubber plate which is set to the pulling machine is seen. This picture is changing sequentially by dragging the bolt of the picture. The number of pictures is 36. These pictures are made from the movie by taking pictures at every five seconds. Students can carry out the expansion of the rubber plate. By touching two figures at screen and elongating distance of these fingers, user can observe the magnified view as show in Fig. 6(b). The only 15 lines are taken for the main program as shown in Fig. 7. If we have a movie of an experiment, this kind of application can be made during less than half hour.

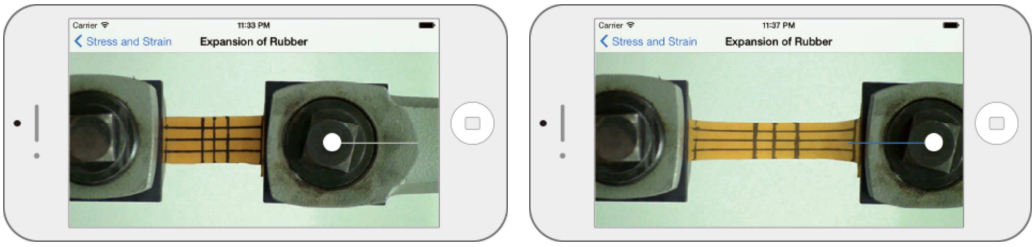

(a) Snapshots of the iPhone when the rubber is extended through 0 to 30 mm

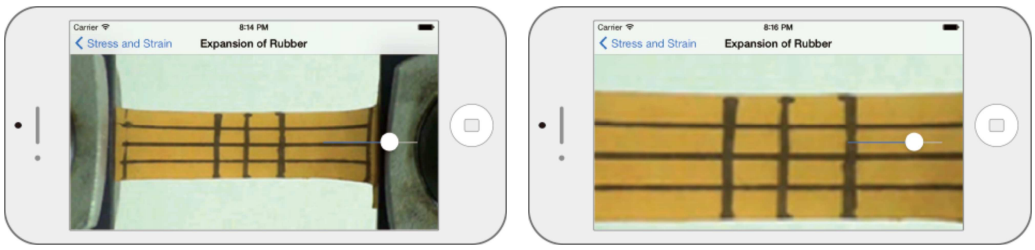

(b) Magnified view of the rubber. By using fingers, the photo is magnified to five times

Fig. 6 The expansion of the rubber plate

```
// attached by the moving of the slider bar
- (IBAction)slider1:(id)sender {
    [self readImage];
}

// read photo files and change size.
- (void)readImage{
    myWidth=576,myHight=324;
    float sld = [_slider1 value];
    int sldi = sld;
    NSString *myStr = [NSString stringWithFormat:@"%02i",sldi];
    NSString *fName = [NSString stringWithFormat:@"S12%@.png",myStr];
    _v1.image = [UIImage imageNamed:fName];
    UIGraphicsBeginImageContext(CGSizeMake(myWidth, myHight));
    [_v1.image drawInRect:CGRectMake(0, 0, myWidth, myHight)];
    _v1.image = UIGraphicsGetImageFromCurrentImageContext();
    _v1.frame=CGRectMake(250*(1-magFactor),_slider1.frame.origin.y*(1-magFactor),myWidth*
        magFactor,myHight*magFactor);
    UIGraphicsEndImageContext();
}
```

Fig. 7 Main program (about 15 lines) of "the expansion of the rubber"

3.2 The stress concentration at the crack tip

This application is newly made for iPhone. Students can observe the stress distributions of the plates containing a hole or a crack. These pictures are made from the result by the FEM simulations. It is difficult for inexperience to image the real object, understand constrains and applied loads from a common FEM application. In this application, the constrain and the load is graphically shown as Fig. 8(b). By moving the slider, the load arrows are increasing and the contour of the stress is changing. Moreover stress distribution

along the cross section including the crack tip is given as shown in Fig. 8(c). These figures can be magnified to five times larger as shown in Fig. 8(d) by the finger action.

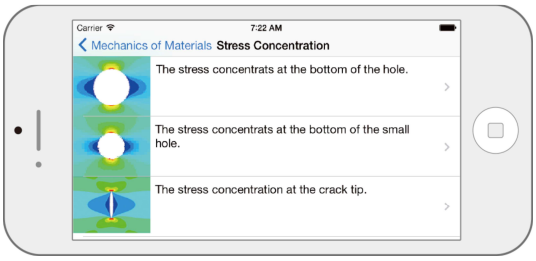

(a) The sub menu for the stress concentration

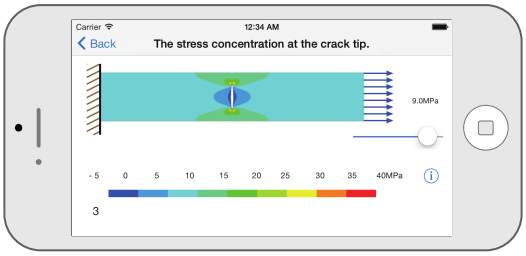

(b) The stress distribution can be shown by increasing load at the free end of the plate using the slider bar

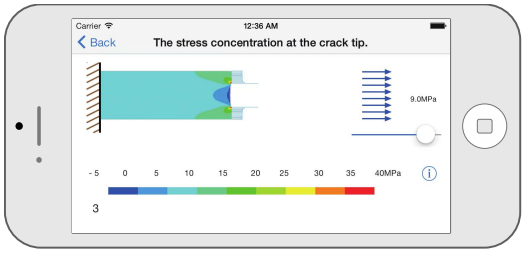

(c) The stress distribution along the cross section including the crack tip can be shown

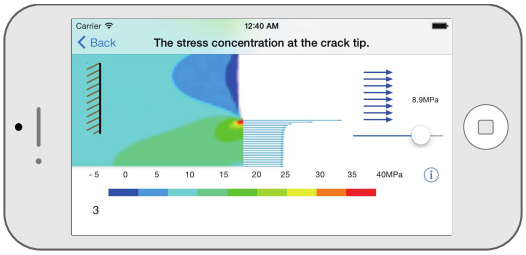

(d) The picture is magnified through one to five time by the finger action

Fig. 8 IPhone application "The stress concentration at the crack tip"

3.3 The simply supported beam subjected to the uniformly distributed load

As shown in Fig. 9, the bending of the simply supported beam subjected to the uniformly distributed load can be simulated by this application. By touching the finger on the beam and moving up and down, the beam is bending. The free body diagram of the beam is shown in Fig. 9(a). The reaction force by the support is increasing related to the increasing of the applied uniform load. By touch the button, FBD (Free Body Diagram) and SFD (Shearing Force Diagram) can be shown along the bar as shown in Fig. 9(b).

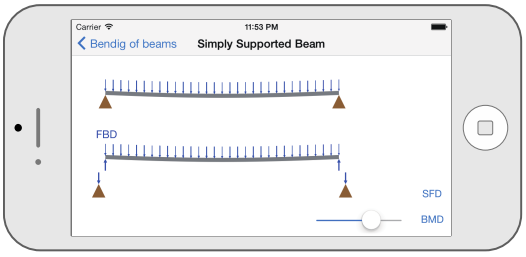

(a) The deformation and FBD

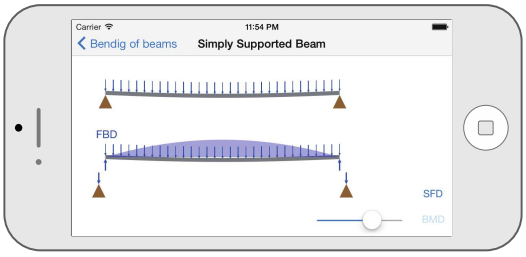

(b) BMD is shown in the FBD

Fig. 9 The simply supported beam subjected to the uniformly distributed load

Table 2 Desktop experiments vs. Smart Phone (iPhone)

	Desktop Experiments	Smart Phone and Tablet Computer
Preparation time	Less than a day	Half day
Initial Cost	≅ 5$	≅ 2,000 $
Running Cost	≅ 1$ for each	≅ 100$/year(#1)
Handling	Fair	Excellent
Accuracy	Poor	Good
Efficient	Good	Unknown

Initial Cost: equipment, computer, material, software Running cost: material, software, #1: license

4 EPILOG

In 1998, we took a huge cost and effort to make the application as same as the present applications [1]. But now, it is very cheap and takes a little effort. Moreover, it is very easy to use and much more interactive. On the other hand, we made some equipment in order to carry out experiments on desktop[2]. The comparison between the desktop experiment and the present applications for iPhone as a smart phone is listed at Table 2. The desktop experiments are useful in order to recognize the phenomenon, but it takes more than an hour for each time including the preparation and the clean up. The iPhone and iPad applications take a few minutes for each lecture. Moreover distribution is very easy and we can distribute worldwide at once and students can use at everywhere. We wish that the student understand the phenomenon of the mechanics of material exactly by himself.

5 REFERENCES

[1] T. Tsuji, H. Kimura, N. Noda, Some Challenges on Lecture of Strength of Materials by using Multimedia, JSME (Ser.A), Vol.61, 2514-2519, 1995.

[2] T. Tsuji, Y. Matsunaga, K. Fukui, N. Noda, F. Sunada, The Active and Problem Oriented Education in the Strength of Materials by using Multimedia, JSME, No.97-44, 75, 1997

[3] N. Ookouchi, JSME, No.99-4, 3-6, 1999

[4] T. Tsuji, The Virtual Machine for the Education of the Strength of Materials by using VRML, *JSSUME'98*, ISBN 89-7581-073-9 93550, 53-56, 1998.

[5] T. Tsuji and N. Noda, The Desktop Experiments for Education of Strength of Materials to Improve Motivation of Students, JSSUME 2000 (Joint Symposium between Sister Unv. In Mech. Eng.), 83-86, 2000.

[6] Information on http://www.scientificmonkey.com/software.html

[7] Information on http://products.wolframalpha.com/courseassistants/mechanics-of-materials.html

[8] T. Tsuji and Y. Matsuzawa, Making Applications for Education of Mechanics of Materials by using a Tablet Computer, 10th International Congress on Thermal Stresses (TS-2013), 2013.

Proceedings of the 3rd International Conference on
Fracture Fatigue and Wear, pp. 114-120, 2014

A FINITE ELEMENT SUB-PARTITION METHOD FOR SIMULATING CRACK PROPAGATION

C. W. Zhou* and Y. L. Sun

State Key Laboratory of Mechanics and Control of Mechanical Structures, Nanjing University of Aeronautics and Astronautics, Nanjing, China

*Corresponding author: zcw@nuaa.edu.cn

Abstract: Finite element method (FEM) has been widely employed to study fracture in structures or solids. Crack extending process simulation will bring re-meshing of FE model which usually be inefficient. Extended finite element method (XFEM) which developed in recent two decades can simulate crack growth efficiently. It possesses merits of free from re-meshing and well representing singularity at crack tip without local mesh refining. However, current XFEM faces big difficulty in formulating singular function at crack tip for nonlinear fracture problem. In this study, a new methodology for simulating crack propagation based on methods of element sub-partition and substructure was suggested. It keeps the merits of current XFEM while can be conveniently developed to deal with nonlinear problems in traditional FEM frame. This new XFEM was used to calculate the stress intensity factors of central crack in infinite plane to validate its accuracy. It was further used in in-homogenous material to demonstrate its adaptability for simulating of complex path cracking.

Keywords: extended finite element method; sub-partition; substructure; crack propagation

1 INTRODUCTION

Finite element method (FEM) is the most widely used numerical simulation method in engineering and science. For traditional FEM continuous shape functions are employed, therefore they intrinsically have continuous deformations in elements. Crack is a strong discontinuity in solid. To represent such strong discontinuity, FE mesh should be discretized complying with the crack configuration. Refined mesh or singular elements are usually arranged around crack tip in order to represent the singularity there. Crack propagation simulating in traditional FEM frame will lead to re-meshing [1] or node splitting [2] which usually to be complicated and inefficient. Eliminating element [3] and reducing element stiffness [4] are also the often used alternative ways to represent crack. Though easy to implement in the traditional FEM frame, they could not well represent the singularity at crack tip, hereby K criterion which has sound experiment support could not be employed. Crack zone model (CZM) is another often employed technology to simulate crack extend. It has been used to represent quasi-static [5], dynamic [6] and fatigue [7] fracture processes. Its attraction limits in scenario of crack path predictable, e.g. interface fracture. Virtual crack closure technology (VCCT) [8] characterizes similarly to CZM. Extended finite element method (XFEM) [9,10] is the most attractive numerical method to deal with discontinuous mechanics problems. Through enriching displace jump across crack face and singular asymptotic function near crack tip, crack is capable of being well represented by original continuous elements. In other word, crack can nucleate and propagate independent to original element mesh in XFEM frame. However, current XFEM faces a great challenge when formulating singular asymptotic field for nonlinear problems. In this study, a novel XFEM has been suggested. This new XFEM based upon ideas of sub-partition and substructure and could be further developed to simulate various nonlinear fracture process in convenient.

2 SUB-PARTITION AND SUBSTRUCTURE OF A CRACKED BODY

As demonstrated in Fig. 1, all the elements in a cracked structure (or solid) are clarified to three types, i.e. element split by the crack (bright grey colour, also named split element), element enveloping crack tip (dark

grey colour, also named crack tip element) and virgin element (white colour). The first two elements group a substructure. For the elements split by crack, crack could go through their two opposite sides or two adjacent sides, which corresponding to different sub-partition patterns. The element enveloping crack tip is sub-partitioned to several triangle shape singular elements around crack tip. The dashed lines denote the sides of sub-partitioned elements. The interior degree of freedom (DOF) of substructure relating to interior nodes (small solid round dot) is introduced by sub-partition and could be condensed to the boundary DOF (relating boundary nodes denoted by bold open circle) of the substructure. The later actually just are the freedoms in original FE model. The equilibrium equation of substructure is written as

$$\boldsymbol{K}_{\text{sst}} \cdot \boldsymbol{u}_{\text{sst}} = \begin{pmatrix} \boldsymbol{K}_{\text{out}} & \boldsymbol{K}_{\text{out-in}} \\ \boldsymbol{K}_{\text{in-out}} & \boldsymbol{K}_{\text{in}} \end{pmatrix} \begin{pmatrix} \boldsymbol{u}_{\text{out}} \\ \boldsymbol{u}_{\text{in}} \end{pmatrix} = \begin{pmatrix} \boldsymbol{f}_{\text{out}} \\ \boldsymbol{f}_{\text{in}} \end{pmatrix}. \tag{1}$$

In which $\boldsymbol{K}_{\text{sst}}$, $\boldsymbol{u}_{\text{sst}}$ are the stiffness matrix and nodal displacement vector of the substructure respectively. Block matrix $\boldsymbol{K}_{\text{out}}$, $\boldsymbol{K}_{\text{in}}$, $\boldsymbol{K}_{\text{out-in}} = \boldsymbol{K}_{\text{in-out}}^{T}$ relate to boundary DOF, interior DOF and cross phase of them. $\boldsymbol{u}_{\text{out}}$, $\boldsymbol{u}_{\text{in}}$ are the boundary DOF vector and interior DOF vector, and $\boldsymbol{f}_{\text{out}}$, $\boldsymbol{f}_{\text{in}}$ are the nodal load vectors of the substructure corresponding to boundary nodes and interior nodes. When crack surface is free from load, the interior nodal vector will be a zero vector as $\boldsymbol{f}_{\text{in}} = \boldsymbol{0}$. The interior DOF can be condensed to boundary DOF with below expression as

$$\boldsymbol{u}_{\text{in}} = -\boldsymbol{K}_{in}^{-1}\boldsymbol{K}_{\text{in-out}}\boldsymbol{u}_{\text{out}}. \tag{2}$$

Substituting Eq. (2) to Eq. (1), equilibrium equation expressed by equivalent stiffness matrix of the substructure can be obtained as

$$\left[\boldsymbol{K}_{\text{out}} - \boldsymbol{K}_{in}^{-1}\boldsymbol{K}_{\text{in-out}}\boldsymbol{u}_{\text{out}}\right]\boldsymbol{u}_{\text{out}} = \boldsymbol{f}_{\text{out}}. \tag{3}$$

On account of that the interior DOF of a substructure are condensed to boundary DOF which are just the DOF of ordinary mesh, no matter how a crack propagates or how many new cracks nucleate, DOF for the whole structure analysis is invariable and the re-meshing in global level is not needed. The substructure is dynamic for its size expands with the crack extend.

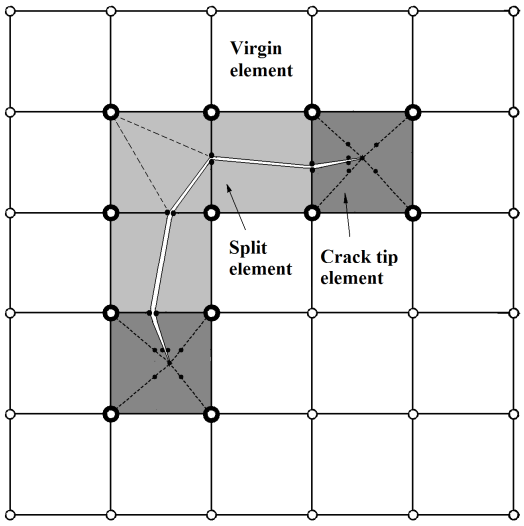

Fig. 1 Three types of element in a cracked solid

3 CRITERIA OF CRACK NUCLEATION AND PROPAGATION

The maximum stress (or strain) law are often employed to predict crack nucleation in brittle materials. Here, if the average maximum principal stress over a virgin element has reached a critical value, a crack which perpendicular to the stress direction is assumed emerge. It goes though the gravity centre of this element and split the element to two separated parts. Meanwhile, the crack tips are supposed have entered the adjacent elements. In this way, a substructure which grouped with one split element and two (or one) crack tip element(s) generates. For avoiding mal-mesh in sub-partition, the crack tracks in both split element and crack tip element will be adjusted if it too close to the element corner nodes. Crack propagation is determined with stress intensity factor (SIF) law in this study. SIF is obtained by interactive integral as

$$K_{\mathrm{I}} K_{\mathrm{I}}^{*} + K_{\mathrm{II}} K_{\mathrm{II}}^{*} = \frac{E^{*}}{2} \int_{A} \left[\sigma_{ij} \frac{\partial u_i^{*}}{\partial x_1} - \sigma_{ij}^{*} \frac{\partial u_i}{\partial x_1} - \sigma_{ij}^{*} \varepsilon_{ij} \delta_{1j} \right] \frac{\partial q(x_1, x_2)}{\partial x_j} dA , \tag{4}$$

$$W^{*} = \sigma_{ij}^{*} \varepsilon_{ij} = \sigma_{ij} \varepsilon_{ij}^{*} . \tag{5}$$

Where K_{I} and K_{II} are the SIFs wanted, σ_{ij} and u_i are the stress and displacement in crack tip region which could be obtained from FE model. K_{I}^{*}, K_{II}^{*}, σ_{ij}^{*}, u_i^{*} are the SIFs, stress and displacement for auxiliary fracture model respectively. To determine the two unknown SIFs via Eq. (4, 5), two auxiliary models are in need and here they are chosen solutions of central crack in infinite plane under pure tension and pure shear respectively. The value of weight function $q(x_1, x_2)$ keeps unit on interior integral loop while be zero on outer integral loop. In this study the outer loop is chosen the four sides of crack tip element and interior loop contract to crack tip point. The crack kick angle is determined by maximum circumference stress law as

$$\theta_{\mathrm{c}} = 2 \arctan \frac{1}{4} \left(K_{\mathrm{I}} / K_{\mathrm{II}} \pm \sqrt{\left(K_{\mathrm{I}} / K_{\mathrm{II}} \right)^2 + 8} \right). \tag{6}$$

Here crack extending is indicated by a simplified engineering law as

$$f(K_{\mathrm{I}}, K_{\mathrm{II}}) = \left(K_{\mathrm{I}} + K_{\mathrm{II}} \right) / K_{\mathrm{IC}} \geq 1. \tag{7}$$

Where K_{IC} is the toughness of material. This new XFEM methodology has been implemented in commercial FE package of ABAQUS as its user element (UEL) and the calculation result is post processed by software of TECPLOT.

4 EXAMPLES AND DISCUSSION

In the following example models, four-node plane iso-parameter element were used for virgin elements and the sub-partitioned elements in split element, a six-node plane iso-parameter singular element [11] was used for the sub-partitioned elements in crack tip element. All the calculations were limited in elastic state. Firstly, the XFEM developed in this study was used to calculate the crack tip filed of central crack in infinite plane. For its not practical for a FE model with infinite dimension, here the width and length of the plane are 20 and 26 times of crack length (denoted as $2a$) respectively. Modulus, Poisson ratio and fracture toughness are supposed as $E = 240\mathrm{GPa}$, $\upsilon = 0.33$ and $K_{\mathrm{IC}} = 15\mathrm{MPa}\sqrt{\mathrm{m}}$, which characterise the material constants of typical steel with middle or low strength. Three combinations of far field uniform tension ($\bar{\sigma}$) and shearing ($\bar{\tau}$) are applied, i.e. $\bar{\sigma} = 10\mathrm{MPa}$ and $\bar{\tau} = 0$ (mode I); $\bar{\sigma} = 0$ and $\bar{\tau} = 10\mathrm{MPa}$ (mode II); $\bar{\sigma} = 10\mathrm{MPa}$ and $\bar{\tau} = 10\mathrm{MPa}$ (mixture of mode I and mode II). For each load mode, crack with three lengths, i.e. $2a = 0.06\mathrm{m}$, $0.12\mathrm{m}$ and $0.18\mathrm{m}$ are considered. The comparisons of SIFs and crack kick angle obtained analytically and from this XFEM are listed in Table 1. The crack extending indicator is also listed in the same Table. Local stresses at crack domain ($2a$=0.06 m) are shown in Fig. 2.

In order to validate the ability of this approach to represent complicated path cracking process, nucleation and propagation of micro cracks in a unidirectional glass fibre/epoxy matrix composite under transverse loading are simulated. Fig. 3 is the micro scale representative volume element (RVE) of the composite. The modulus and Poisson ratio for fibre are $E_{\mathrm{f}}=73\mathrm{GPa}$ and $\upsilon_{\mathrm{f}}=0.20$, those for matrix material are $E_{\mathrm{m}}=3.5\mathrm{GPa}$ and $\upsilon_{\mathrm{m}}=0.35$. Under transverse load, the dominated damage in fibre reinforced composites is matrix cracking. Here, the tensile strength for brittle matrix is $\sigma_{\mathrm{m}}=100\mathrm{MPa}$, i.e. a virgin element will be transmuted to split element so as its average maximum principal stress reach this critical value. The toughness of matrix material is assumed as $K_{\mathrm{IC}}^{\mathrm{m}}=150\mathrm{MPa}\sqrt{\mathrm{m}}$. This example is stressed to exam adaptability of this XFEM for in-homogenous in general, thus the strength and crack resistance toughness of matrix were chosen fictionally in reasonable range instead of from experiment measure. The RVE is applied gradually increasing uniform tensile load (y direction) and the process of micro crack initiation and developing as well as the local stress distribution are illustrated in Fig. 3. One can find the cracks nucleate in high stress spots, and then move forward progressively round fibres. The local unloading can be observed in regions where crack tracks pass. The prediction well represents the general feature of micro scale damage evolution in composite. Fibre/matrix interfacial deboning is also a main damage in fibre composites. Interfacial progressive fracture simulation by this method is being studied and will be reported in future. Under transverse load, fibre usually will not fail, so the failure of fibre has not been considered here.

Table 1 SIF, kick angle and fracture indicator for infinite plane CCT

load	$a\,[\mathrm{m}]$	$K_{\mathrm{I}}\ [\mathrm{MPa}\sqrt{\mathrm{m}}]$		$K_{\mathrm{II}}\ [\mathrm{MPa}\sqrt{\mathrm{m}}]$		$\theta_{\mathrm{c}}\ [\mathrm{degree}]$		f
		XFEM	Analytical	XFEM	Analytical	XFEM	Analytical	
$\bar{\sigma}=10\mathrm{MPa}$ $\bar{\tau}=0$	0.03	2.86	3.07	0.11	0	4.39	0	0.20
	0.06	4.25	4.34	0.10	0	2.69	0	0.29
	0.09	5.23	5.32	0.08	0	1.75	0	0.35
$\bar{\sigma}=0$ $\bar{\tau}=10\mathrm{MPa}$	0.03	0.13	0	2.89	3.07	69.7	70.5	0.20
	0.06	0.15	0	4.60	4.34	69.9	70.5	0.32
	0.09	0.11	0	5.71	5.32	70.2	70.5	0.39
$\bar{\sigma}=10\mathrm{MPa}$ $\bar{\tau}=10\mathrm{MPa}$	0.03	3.28	3.07	3.18	3.07	52.7	53.1	0.43
	0.06	4.69	4.34	4.51	4.34	52.5	53.1	0.61
	0.09	5.58	5.32	5.47	5.32	52.8	53.1	0.74

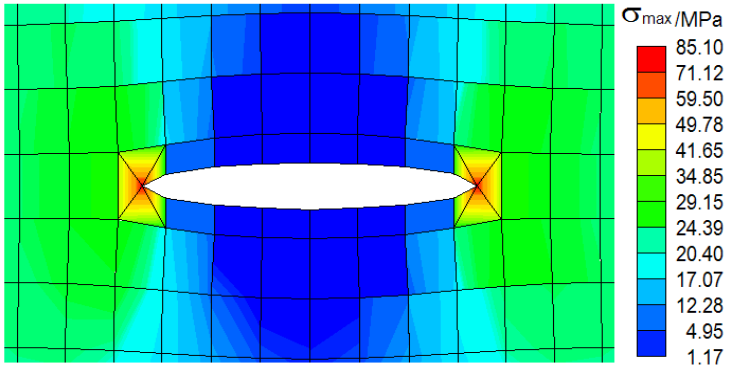

(a) Distribution of σ_{max} for mode I crack

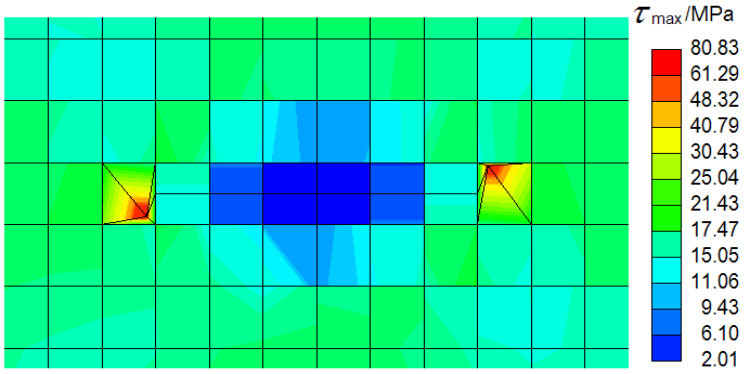

(b) Distribution of τ_{max} for mode II crack

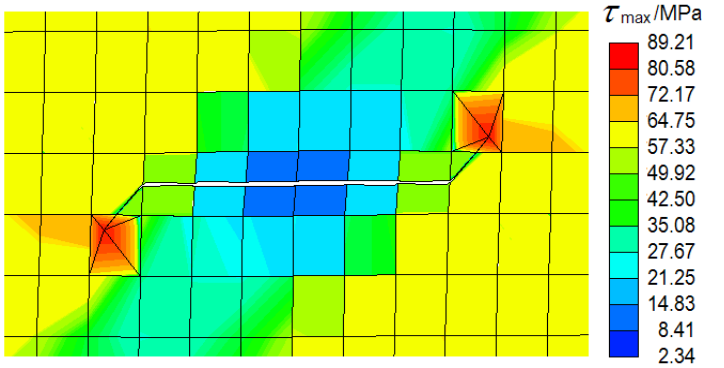

(c) Distribution of τ_{max} for mixture I and II crack mode

Fig. 2 Local stress distributions around cracks with various fracture modes

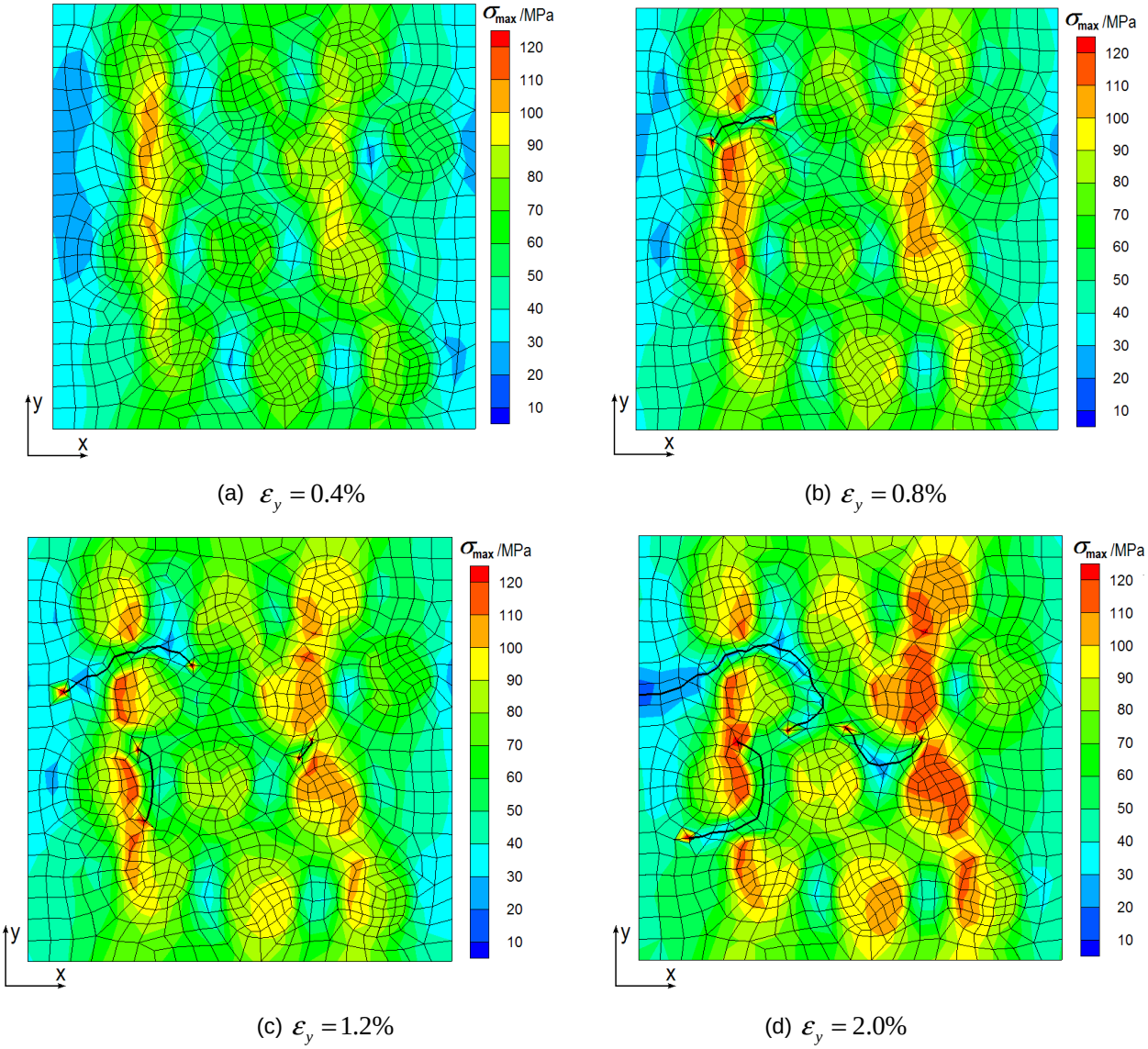

(a) $\varepsilon_y = 0.4\%$ (b) $\varepsilon_y = 0.8\%$

(c) $\varepsilon_y = 1.2\%$ (d) $\varepsilon_y = 2.0\%$

Fig. 3 Micro crack expanding and distribution of $\sigma_{\max}$ in RVE of unidirectional composite

5 CONCLUSIONS

A novel methodology, which combines element sub-partition and substructure, was suggested for simulating crack propagation in this study. The model suggested herein maintains the main merits of currant XFEM, i.e. crack extending path is free from global mesh and global re-mashing is not needed when crack moves forward. Further, the total DOF in this methodology is invariant no matter how crack propagates and nucleates. The most potential attraction is that in this way singularity at crack tip region is represented via singular element instead of formulating singular asymptotic function which is a big challenge for nonlinear fracture problems. Therefore, this approach could be further developed to deal with various nonlinear fracture problems via employing existing nonlinear FEM models corresponded in nearly direct way. The well prediction of singularities of central crack in infinite plane has proven the accuracy of this method. The simulating of micro scale crack propagation in inhomogeneous material demonstrated the validity of it to tracking crack propagation along complicated path.

6 ACKNOWLEDGEMENTS

The authors would like to acknowledge the support of the National Natural Science Foundation of China (Grant No. 11272147, 10772078), Chinese Aviation Science Fund (2013ZF52074) , SKL Open Fund (IZD13001-1353) and Priority Academic Program Development of Jiangsu Higher Education Institutions.

7 REFERENCES

[1] Q. Yang, W. Yang, Finite Element Simulation Of Fracture Process. Chinese Journal of Computational Mechanics, 14(4), 407–412, 1997.

[2] K. Komori, Ductile Fracture Criteria For Simulating Shear By Node Separation Method. Theoretical and Applied Fracture Mechanics, 43, 101–114, 2005.

[3] C. Zhou, W. Yang, D. Fang, Meso-Fracture Of Metal Matrix Composites Reinforced By Particles Of Large Volume Fraction, Theoretical and Applied Fracture Mechanics, 41, 311–326, 2004.

[4] Z. Xia, Y. Chen, F. Ellyin, A Meso/Micro-Mechanical Model For Damage Progression In Glass-Fibre/Epoxy Cross-Ply Laminates By Finite-Element Analysis, Composites Science and Technology, 60, 1171–1179, 2000.

[5] K. Gordnian, H. Hadavinia, P. Mason, E. Madenci, Determination Of Fracture Energy And Tensile Cohesive Strength In Mode Delamination Of Angle-Ply Laminated Composites, Composite Structures, 82(4), 577–586, 2008.

[6] X. Xu, A. Needleman, Numerical Simulations Of Fast Crack Growth In Brittle Solids. Journal of the Mechanics and Physics of Solid, 42, 1397–1434, 1994.

[7] M. Spandan, H. Philippe, A Cohesive Model For Fatigue Failure Of Polymers, Engineering Fracture Mechanics, 72 (5), 691 708, 2005.

[8] Q. Qian, D. Xie, Analysis of Mixed-Mode Dynamic Crack Propagation By Interface Element Based On Virtual Crack Closure Technique, Engineering Fracture Mechanics, 74, 807–814, 2007.

[9] T. Belytschko, T. Black, Elastic Crack Growth In Finite Elements With Minimal Remeshing, International Journal for Numerical Methods in Engineering, 45, 601–620, 1999.

[10] X. Liu, Q. Xiao, B. Karihaloo, XFEM For Direct Evaluation Of Mixed Mode SIFs In Homogeneous And Bi-materials, International Journal for Numerical Methods in Engineering, 59, 1103–1118, 2004.

[11] H. Shen, C. Zhou, Study On The Accuracy Of Plane Six-Node Isoparametric Stress Singular Element, Journal of Mechanical Strength, 34(3), 410–414, 2012. (In Chinese)

Proceedings of the 3rd International Conference on
Fracture Fatigue and Wear, pp. 121-126, 2014

STRESS INTENSITY FACTOR ANALYSIS DURING THE PROPAGATION OF A CRACK IN A BRITTLE MATERIAL

H. HamliBenzahar and M. Chabaat

BuiltEnv. Res. Lab., Civil Engineering Faculty, U.S.T.H.B., B P. 32.ElAlia, BabEzzouar, Algiers 16111, Algeria

Abstract: The present study evaluates the stress field and the mode I Stress Intensity Factor (SIF) during the cracking caused by applying pressure loading to a brittle material such as a glass. In this research study, the problem is formulated using complex potentials of Muskelishvili to establish analytical stress field which lead us to determine the SIF. This latest can be analyzed by a Finite Element Method (FEM) using the Software (ABAQUS). Experimentally, semi-infinite thin rectangular elements containing an edge crack and having various cracks lengths are considered. For each crack's length, stress fields characterized by the SIF have been determined. Obtained results are compared and agreed with those of other researchers.

Keywords: stress, crack; stress intensity factor; finite element; brittle-material

1 INTRODUCTION

Microscopic observations of cracks propagation in brittle materials [1,2] show that a damage zone develops in the vicinity of crack tips. This zone can be identified in certain cases like an intensive area of micro-crack. These micro-cracks can have a significant influence on the propagation of the main crack. They can either cause crack amplification or crack shielding. Crack shielding reduces stress intensity factors of the main crack while crack amplification increases those values. These effects have been investigated by several researchers using exact analytical methods for some particular cases [3], and with analytical approximations under certain assumptions [4]. Because this damage can constitute an important toughening mechanism, problems dealing with crack propagation have received considerable research attention since they were introduced to fracture mechanics. As a result, a wide body of literature, on this topic, exists [5]. Solutions obtained are mostly based on the complex variable technique [6], or on numerical procedures [7], or asymptotic estimates for remotely located cracks [8]. Those techniques are usually different to a degree, but the basic principles remain the same.

The ideal model is proposed by Chudnovsky and co [9] known as a crack layer where a crack and its surroundings micro-cracks are considered as an entity. This theory considers the process of propagation of the crack as being a development and a subsequent coalescence of the micro-defects in the vicinity of the crack tip. During the formation of a crack, a high concentration of stress fields takes place around the crack tip where a zone called zone with strong disturbance is formed. For this research work, a standard specimen is chosen so that one can evaluate easily stress fields and corresponding SIF during the crack propagation.

Brittle fracture is influenced in most cases by the micro-structural composition of the material. In general, the materials are considered heterogenic. Their behaviour is either ductile or brittle. In this case the main crack is represented like a semi-infinite crack subjected to a stress field under the first mode of fracture.

Fracture mechanics studies the interaction between a geometrical discontinuity and neighbouring continuous medium and analyzes the evolution of this discontinuity. From a mechanical point of view, one can distinguish schematically, in a medium fissured three successive zones:

- A zone of development (zone 1); this zone is at the point of the crack and in the wake left by the crack during its propagation. The study of this zone is very complex because of significant constraints in a strongly damaged material. The size of this zone is very small; it is specific from a mechanical point of view.

- A singular zone (zone 2); in which the fields of displacements, deformations and stresses are continuous and have a formulation independent of the remote geometry of the structure. It is shown that in this zone, the components of the stress fields are infinite in the vicinity of the face of the crack (r→0). The singularity is in ($r^{-\frac{1}{2}}$) in linear elastic medium.
- An external zone (zone 3)**;** this external zone includes the far fields being connected on one hand, at the singular zone, and on the other hand in the boundary conditions in loads and displacements. In this zone, fields of displacements, deformations and stresses vary very little.

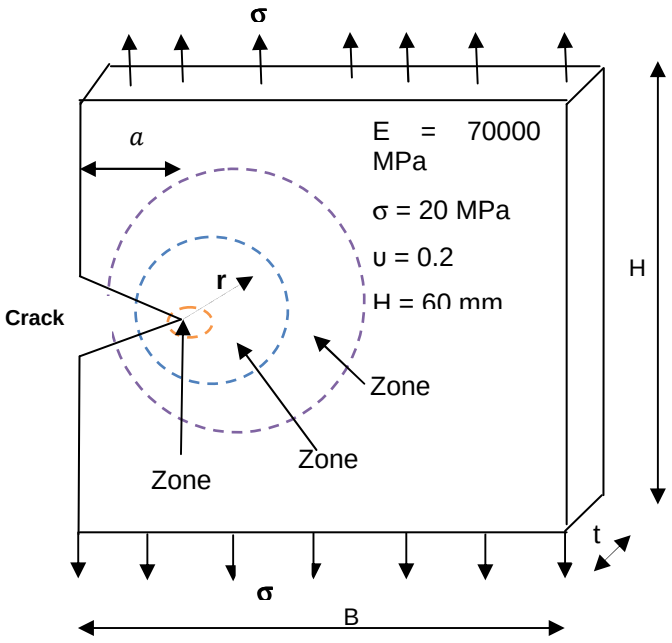

Fig. 1 Schematization of the proposed model

2 STRESS FIELD

During the formation of a crack, a zone surrounding the initial crack is formed and where, a strong concentration of stress takes place. This zone is considered as being a zone with strong disturbance and commonly called a damage zone or fracture process zone. A great number of researchers admit nowadays that the extension of a crack is considered in a small zone close to the face of the crack in which, it exists high stress and separations where the mechanics of continuous mediums does not admit. On the other hand, around this zone, the remainder of the body whose behaviour is elastic or plastic concerns the mechanics of the continuous mediums.

2.1 Problem formulation

The problem is formulated in terms of complex potentials [10] using complex variable functions in plane elasticity, The stresses (σ_x, σ_y, σ_{xy}) are expressed in terms of the complex potentials ϕ(z) and ω (z) such that;

$$\sigma_x - \sigma_y + 2i\sigma_{xy} = 2\left(\overline{\phi(z)} - (z-\bar{z})\overline{\phi'(z)} - \omega'(\bar{z})\right) \quad (1)$$

$$\sigma_x + i\sigma_{xy} = \Phi(z) + 2\overline{\phi(z)} - (z-\bar{z})\overline{\phi'(z)} - \omega'(\bar{z}) \quad (2)$$

where; $\phi(z)$, $\omega(z)$ are complex potentials used in the representation of an elastic field zand $\sigma_x, \sigma_y, \sigma_{xy}$ are the stress components. Then, the stress distribution near a crack tip under the traction free crack face can be expressed as [11]:

$$\begin{bmatrix}\sigma_x & \sigma_{xy}\\ \sigma_{xy} & \sigma_y\end{bmatrix}=\frac{K_I}{\sqrt{2\pi r}}\begin{bmatrix}f_{11}(\theta) & f_{12}(\theta)\\ f_{21}(\theta) & f_{22}(\theta)\end{bmatrix}+\frac{K_{II}}{\sqrt{2\pi r}}\begin{bmatrix}g_{11}(\theta) & g_{12}(\theta)\\ g_{21}(\theta) & g_{22}(\theta)\end{bmatrix}+\begin{bmatrix}T & q_c\\ q_c & p_c\end{bmatrix} \quad (3)$$

where the first two terms in the expansion form are singular at the crack tip, K_I, K_{II} denote the mode I and mode II stress intensity factors, respectively. Functions $f_{ij}(\theta)$,$g_{ij}(\theta)$ represent the angular distributions of the crack tip stresses. In Eq. (3), the third term is finite and bounded. The term T is denoted as the T-stress and can be regarded as the stress acting parallel to the crack flanks where q_c, p_c two regular stresses at vicinity of crack tip. Besides, the term $O(r^{1/2})$ has been neglected for clarity. For a crack loaded in mode I under a remote external stress σ, the elastic stress field around the crack tip equal [12]; the second and the third term can be neglected.

$$\begin{bmatrix}\sigma_x & \sigma_{xy}\\ \sigma_{xy} & \sigma_y\end{bmatrix}=\frac{K_I}{\sqrt{2\pi r}}\begin{bmatrix}f_{11}(\theta) & f_{12}(\theta)\\ f_{21}(\theta) & f_{22}(\theta)\end{bmatrix} \quad (4)$$

The angular distribution can be expressed as [13]

$$\begin{Bmatrix}f_{11}(\theta)\\ f_{12}(\theta)\\ f_{22}(\theta)\end{Bmatrix}=\cos(\theta/2)\begin{Bmatrix}1-\sin(\theta/2)\sin(3\theta/2)\\ \sin(\theta/2)\cos(3\theta/2)\\ 1+\sin(\theta/2)\sin(3\theta/2)\end{Bmatrix} \quad (5)$$

2.1 Proposed model

The proposed model is a square plate from where the height equals the width H = B = 60mm with a thickness of *t* =1 mm. The problem is analyzed by the Finite Element Method while using software (ABAQUS). The model is mashed per square finite element where a = b = 2 mm. The chosen material can be a composite material who is considered as an heterogeneous brittle material where the equivalent elasticity modulus is E = 70000 n/mm^2 and a Poisson's ratio $\upsilon = 0.2$ corresponding to a glass. Taking into account boundary conditions, the proposed model is set along the y-axis which allows us to open the crack according to the first mode of rupture (Mode I). Using numerical analysis, the stress fields are shown in the following cartographic figures.

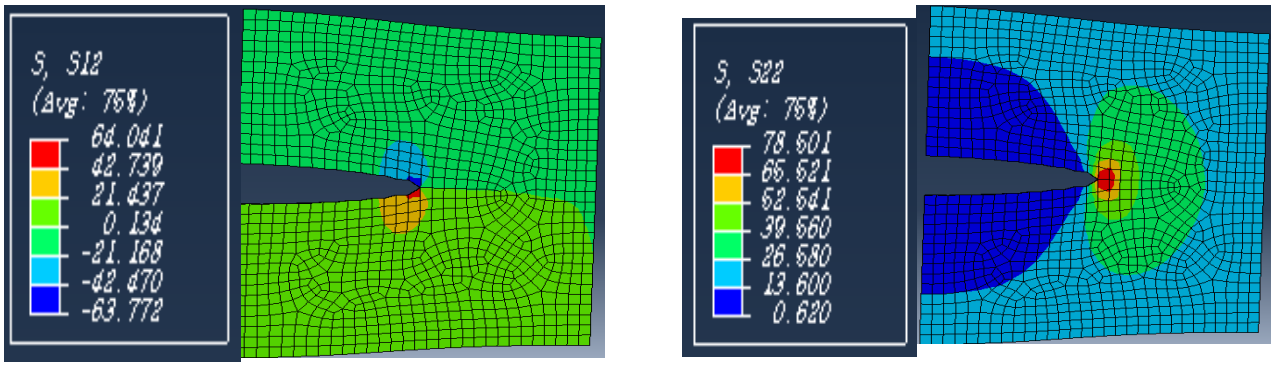

Fig. 2 Cartographic of values of stress fields; a) values of stress σ_{12}, b) values of stress σ_{22}.

Obtained results of stress field versus various crack's lengths are given in the following Table 1.

Table 1 Numerical results of stress field function crack's length.

Crack's length a(mm) / $Stress$ (N/mm2)	0	5	10	15	20	25	30
σ_{11}	5.00	7.94	10.1	12.98	14.82	17.49	19.63
σ_{12}	0	18.13	26.91	38.21	46.09	56.34	64.04
σ_{22}	20	30.97	40.4	51.92	59.27	69.96	78.5

Stress fields plots for various crack's length are represented in the following Fig. 3.

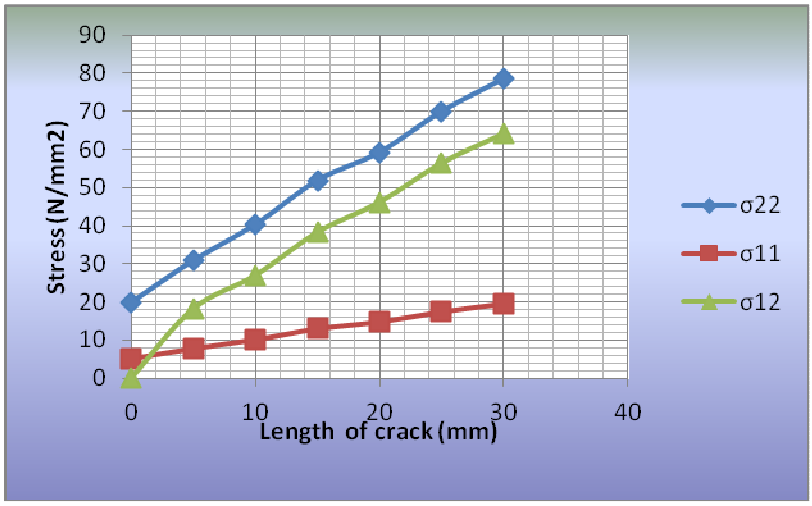

Fig. 3 Variation of stress field $\boldsymbol{\sigma_{ij}}(\mathbf{N/mm^2})$ versus crack's length $\boldsymbol{a}$ $(\mathbf{mm})$.

3 STRESS INTENSITY FACTOR

Stress fields found previously are characterized by SIF. These factors are considered as essential parameters for the evaluation of the strength fracture of materials. They give information on the evolution of the crack propagation in materials through the state of the various stress fields generated during the cracking. Irwin [14] was first who considered the local stress state around a crack tip for establishing a crack propagation criterion. From then, stress fields near crack tips are divided into three basic types: Mode I (Opening), Mode II (Sliding) and Mode III (Tearing). These SIF can be expressed by using Eq. (4) and Eq. (5) as follows;

$$K_I = \sigma_{yy}\sqrt{2\pi r}\ /cos(\theta/2)\{1+\sin(\theta/2)\sin(3\,\theta/2)\} \quad (6)$$

Stresses are concentrated at the tip of crack. For a point located at a position (r, θ) from the tip, one obtain SIF for various crack's length. These values are given in Table 2.

3. 1 Stress intensity factor by Irwin

Let consider a straight, two-dimensional crack occupying the segment of the x –axis $0 \leq x \leq a$ and assume that the y-axis is the free boundary of a semi -infinite plate. The elastic stress fields at the main crack are $\sigma_y = \sigma$, $\sigma_x = 0$, $\sigma_{xy} = 0$, From previous comment, the k is not altered if the remote stresses are all taken as zero and that a uniform pressure, σ, is assumed acting inside of the crack. Thus approximate estimate of k is given by [12].

$$K_I = \sigma\sqrt{\pi a} \tag{7}$$

Table 2 gives numerical results and theoretical values of SIF found by Irwin.

Table 2 Numerical results of the stress intensity factor (SIF) according the crack's length.

Crack's length (mm)	0	5	10	15	20	25	30
SIF (N/mm $^{3/2}$) numerical results	0	77.61	101.24	130.11	148.59	175.32	196.72
SIF (N/mm $^{3/2}$) given by Irwin	0	79.25	112.07	137.26	158.5	177.2	194.11

Previous results and values of Mode I stress intensity factors are shown in Fig. 4.

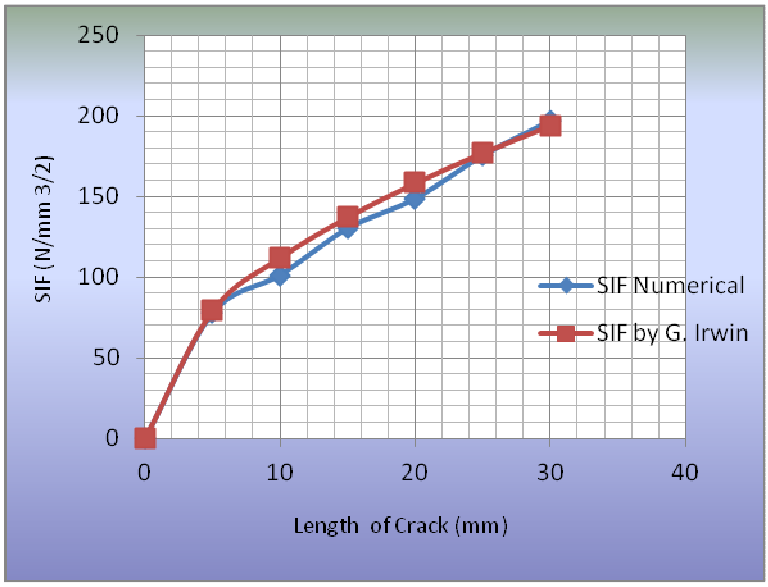

Fig. 4 Variation of Stress Intensity Factor (SIF) versus the crack's length.

3. 2 Discussion and analysis

Values of stress fields found in Table 2 and curves of SIF's variation versus crack's length shown in Fig. 3 are similar to those found by Irwin. It is proven also that SIF (numerical and theoretical) increase at the same rate with respect to the crack's length. Plotted curves are collinear in the intervals of a crack's length a ϵ $[0, 4]$ mm and a ϵ $[24, 30]$ mm. On the other hand, for an interval of a crack's length a ϵ $[4, 24]$, there is a small shift between points of two curves. This latest is generated by the effect to the thickness of 1mm. Then, the theoretical analysis of Irwin considers the model in 2-D meaning no thickness is taken into consideration.

4 CONCLUSIONS

In this research work, stress fields and stress intensity factors are determined during the propagation of a crack in a brittle material. These Stress fields and SIF's are obtained for the case of cracked models having different crack's lengths. It is shown that stress field maximum are found about the point of the crack and that for each crack's length stress field are plotted and their values are compared to the ones obtained by Irwin meaning for $\sigma_{22} > \sigma_{12} > \sigma_{11}$. Besides, one can notice that the stress fields increase at the same rate depending on the loading and the crack length. According to Irwin, the value found for a maximum stress σ_{22} did not exceed the elastic stress of the material itselfσ_{e}. For our case, the elastic stress for glass

$\sigma_{\mathrm{e}} = 70000\ \mathrm{N/mm^2}$ is much lower than the maximum stress $\sigma_{22} = 78.5\ \mathrm{N/mm^2}$.

5 NOMENCLATURE

$\Phi\,(\mathrm{z}), \omega(z)$	Complex potentials
Z	Complex number
$\sigma_x, \sigma_y, \sigma_{xy}$	Stress components
K_I, K_{II}	Mode I and II stress intensity factors.
$f_{\mathrm{ij}}(\theta)$, $\mathrm{g_{ij}}(\theta)$	Functions representing angular distributions of crack tip stresses
θ	Angular orientation of r with respect to the crack tip
r	Limiting length zone of disturbance
T	T-stress
q_c, p_c	Regular stresses in the vicinity of a crack tip
a	Crack's length
H, B	Dimensions of the model
E	Young's modulus
σ	Remote stress field
t	Thickness of the model
υ	Poisson's ratio

6 REFERENCES

[1] M. Chabaat, "*Comparisons of minimal principal stress with crazes trajectories in a brittle Material*". International Journal of fracture, 1988.

[2] D. Hull, "*Effect of Crazes on the propagation of cracks in polystyrene*". Journal of Materials Sciences" 357-363,1970.

[3] A. Chudnovsky and M. Kachanov, "*Interaction of a crack with a field of micro-cracks*". International Journal of Engineering Sciences. **21**, 1009-1018,1983.

[4] K. K. Lo, *Journal of Applied Mechanics*, **45**, 797-802, 1978.

[5] M. Denda and P. Quick, *Electronic Journal of Boundary Element*, **2**, 2004.

[6] A. A. Rubinstein, *International Journal of Fracture,* 2**7**, 113-119, 1985.

[7] S. Shiue and A. Lee, *International Journal of Fracture*, **28**,1985

[8] L. R. F. Rose, *International Journal of Fracture*, **31***,* 1986.

[9] A. Chudnovsky, *Crack Layer Theory*, NASA report Cleveland, Ohio USA, 1984.

[10] N. F. Muskhelishvili. "*Some basic problem of the mathematical theory of elasticity".* The Netherlands: Noordhoof,1953.

[11] M. L. Williams, "On the Stress at the Base of a Stationary Crack," Journal of Applied Mechanics, Transactions ASME, Vol. **24**, pp.109-114, 1957.

[12] M. Chabaat and, H. Ayas, Complex variable Green's functions for crack-microcracks interactions", Key Engineering Materials, Vol. **465** pp 123-128, 2011.

[13] H. Seddiki and M. Chabaat, Crack crazing patterns interactions based on damage criteria, International Journal of Advanced Research Materials, trans tech. publishing, Vol. **79-82**, pp. 135-138, 2009.

[14] H. Tada, P. C. Paris and G. R. Irwin. The stress analysis of cracks, Handbook Del Res. Corporation, Hellertown. 1973.

Proceedings of the 3rd International Conference on
Fracture Fatigue and Wear, pp. 127-133, 2014

VIBRATION ANALYSIS OF CRACKED PLATE USING HIGHER-ORDER SHEAR DEFORMATION THEORY

Loc V. Tran[1], P. Phung-Van[1,3], Vinh Phu Nguyen[2], M. Abdel Wahab[3] and H. Nguyen-Xuan [1]

[1] Division of Computational Mechanics, Ton Duc Thang University Ho Chi Minh City, Vietnam
[2]Cardiff University, Queen's Buildings, The Parade, Cardiff CF24 3AA, Wales, UK
[3]Department of Mechanical Construction and Production, Faculty of Engineering and Architecture, Ghent University, Belgium

Abstract: A novel and effective formulation that combines the eXtended IsoGeometric Approach (XIGA) and Higher-order Shear Deformation Theory (HSDT) is proposed to study the free vibration of cracked plates. XIGA utilizes the Non-Uniform Rational B-Spline (NURBS) functions with their inherent arbitrary high order smoothness, which permit the C^1 requirement of the HSDT model. Two numerical examples are provided to show excellent performance of the proposed method compared with other published solutions in the literature.

Keywords: cracked plate; non-uniform rational b-spline; isogeometric analysis; higher-order shear deformation theory

1 INTRODUCTION

Plate structures play an increasing important role in engineering applications. They thus were researched since long time from static to dynamic and buckling analysis [1-5]. From the literature, these works are carried out for designing the plate structures without the presences of cracks or flaws. It is known that in service, the cracks are generated and grown when subjected to large cyclic loading. They lead to a reduction of the load carrying capacity of the structures. To clearly understand the dynamic behaviour of plate with initial cracks is hence too necessary. This problem has been interesting by many scientists with various methods: Stahl and Keer [6] and Liew et al. [7] with analytical solutions, Finite Element Method (FEM) [9], eXtended Finite Element Method (XFEM) [8,10], etc. Among them, XFEM is known as a robust numerical method, which uses enrichment functions to model discontinuities independent of the finite element mesh. Recently, Natarajan et al. [11] extended this method for dynamic analysis of FGM plate based on the FSDT model. This model is simple to implement and is applicable to both thick and thin FGM plates. However, the accuracy of solutions will be strongly dependent on the Shear Correction Factors (SCF) of which their values are quite dispersed through each problem.

In this paper, we develop the Higher-order Shear Deformation Theory (HSDT) model that includes higher-order terms in the approximation of the displacement field for modelling the plates. It is worth mentioning that this model requires C^1-continuity of the generalized displacements leading to the second-order derivative of the stiffness formulation which causes some obstacles in standard C^0 finite formulations. Fortunately, it is shown that such a C^1-HSDT formulation can be easily achieved using a NURBS-based isogeometric approach [12]. In addition, to capture the discontinuous phenomenon in the cracked plates, the enrichment functions is incorporated with NURBS basic functions to create a novel method as so-called eXtended Isogeometric Analysis (XIGA) [13]. Herein, our study focuses on investigating the vibration of the cracked plates with an initial crack. Two numerical examples are given to show the performance of the proposed method and results obtained are compared to other published methods in the literature.

2 GOVERNING EQUATIONS FOR PLATES

To consider the effect of shear deformation directly, the five-parameter displacement field based on higher-order shear deformation theory is defined as

$$\begin{aligned} u(x,y,z) &= u_0 - zw_{,x} + \left(z - \tfrac{4}{3h^2}z^3\right)\beta_x \\ v(x,y,z) &= v_0 - zw_{,y} + \left(z - \tfrac{4}{3h^2}z^3\right)\beta_y \quad , \quad \left(\frac{-h}{2} \le z \le \frac{h}{2}\right) \\ w(x,y) &= w_0 \end{aligned} \tag{1}$$

where u_0, v_0, w are the axial displacements and β_x, β_y are the rotations in the *x* and *y* axes, respectively.

The strains of the mid-surface deformation are given by

$$\begin{Bmatrix} \boldsymbol{\varepsilon} \\ \boldsymbol{\gamma} \end{Bmatrix} = \begin{Bmatrix} \boldsymbol{\varepsilon}_0 + z\boldsymbol{\kappa}_1 + \left(z - \tfrac{4}{3h^2}z^3\right)\boldsymbol{\kappa}_2 \\ \left(1 - \tfrac{4}{h^2}z^2\right)\boldsymbol{\beta} \end{Bmatrix} \tag{2}$$

Using the Hamilton principle, the weak form for free vibration analysis of a plate can be expressed as:

$$\int_\Omega \delta\boldsymbol{\varepsilon}^T \mathbf{D}^b \boldsymbol{\varepsilon} \mathrm{d}\Omega + \int_\Omega \delta\boldsymbol{\gamma}^T \mathbf{D}^s \boldsymbol{\gamma} \mathrm{d}\Omega = \int_\Omega \delta\tilde{\mathbf{u}}^T \mathbf{m}\ddot{\tilde{\mathbf{u}}} \mathrm{d}\Omega \tag{3}$$

where $\mathbf{D}^b$ and $\mathbf{D}^s$ are the material matrices

Herein, the mass matrix **m** is calculated according to consistent form as follow

$$\mathbf{m} = \begin{bmatrix} I_1 & I_2 & I_4 \\ I_2 & I_3 & I_5 \\ I_4 & I_5 & I_6 \end{bmatrix} \text{ with } I_i = \int_{-h/2}^{h/2} \rho_e \left(1, z, z^2, \left(z - \tfrac{4}{3h^2}z^3\right), z\left(z - \tfrac{4}{3h^2}z^3\right), \left(z - \tfrac{4}{3h^2}z^3\right)^2\right) \mathrm{d}z \tag{4}$$

and

$$\tilde{\mathbf{u}} = \begin{Bmatrix} \mathbf{u}_1 \\ \mathbf{u}_2 \\ \mathbf{u}_3 \end{Bmatrix}, \quad \mathbf{u}_1 = \begin{Bmatrix} u_0 \\ v_0 \\ w \end{Bmatrix}; \mathbf{u}_2 = -\begin{Bmatrix} w_{,x} \\ w_{,y} \\ 0 \end{Bmatrix}; \mathbf{u}_3 = \begin{Bmatrix} \beta_x \\ \beta_y \\ 0 \end{Bmatrix} \tag{5}$$

3 AN EXTENDED ISOGEOMETRIC CRACKED PLATE FORMULATION

3.1 A brief of B-spline/NURBS functions

A knot vector $\Xi = \{\xi_1, \xi_2, ..., \xi_{n+p+1}\}$ is defined as a sequence of knot value $\xi_i \in R$, $i = 1, ...n + p$. If the first and the last knots are repeated *p*+1 times, the knot vector is called an open knot. Through open knot, the B-spline basis functions $N_{i,p}(\xi)$ are defined by the following recursion formula

$$\begin{aligned} N_{i,p}(\xi) &= \frac{\xi - \xi_i}{\xi_{i+p} - \xi_i} N_{i,p-1}(\xi) + \frac{\xi_{i+p+1} - \xi}{\xi_{i+p+1} - \xi_{i+1}} N_{i+1,p-1}(\xi) \\ \text{as } p = 0,\ N_{i,0}(\xi) &= \begin{cases} 1 & if \quad \xi_i < \xi < \xi_{i+1} \\ 0 & \text{otherwise} \end{cases} \end{aligned} \tag{6}$$

To present exactly some curved geometries (e.g. circles, cylinders, spheres, etc.) the Non-Uniform Rational B-Splines (NURBS) functions are used. Be different from B-spline, each control point of NURBS has additional value called an individual weight w_i [12]. Then the NURBS functions can be expressed as

$$R_i(\xi, \eta) = \frac{N_i w_i}{\sum N_i(\xi, \eta) w_i} \tag{7}$$

3.2 Cracked plate formulation eXtended IsoGeometric Analysis (XIGA)

To capture the local discontinuous and singular fields, the new enriched functions are added according to idea of XFEM as follow:

$$\mathbf{u}^h(\mathbf{x}) = \sum_{I\in S} R_I(\boldsymbol{\xi})\mathbf{q}_I^{std} + \sum_{J\in S^{enr}} R_J^{enr}(\boldsymbol{\xi})\mathbf{q}_J^{enr} \tag{8}$$

Here, the NURBS basis functions are utilized instead of the Lagrange polynomials to create a new numerical procedure – so-called eXtended IsoGeometric Analysis (XIGA) [13,14]. R_J^{enr} are the enrichment functions associated with node J located in enriched domain S^{enr} which is splitted up two parts including: a set S^c for Heaviside enriched control points and a set S^f for crack tip enriched control points as shown in Fig. 1.

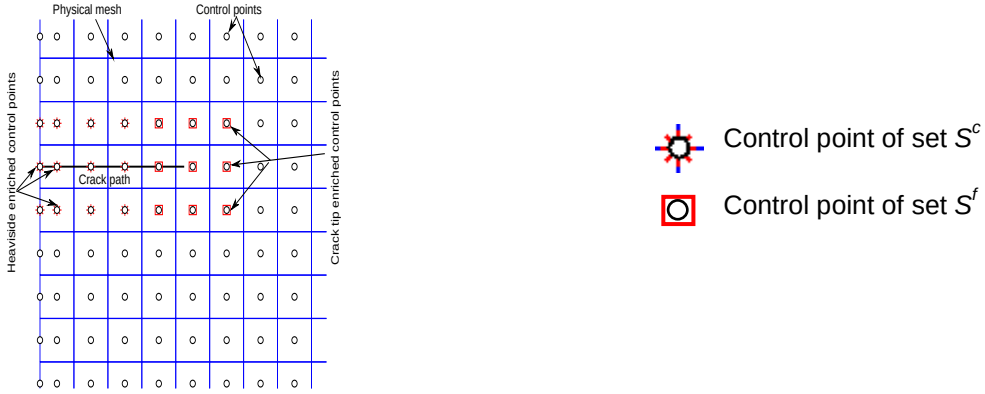

Fig. 1 Illustration of the nodal sets S^c, S^f for a quadratic NURBS mesh

To describe the discontinuous displacement field, the enrichment function is given by

$$R_J^{enr}(\boldsymbol{\xi}) = R_J(\boldsymbol{\xi})\left(H(\mathbf{x}) - H(\mathbf{x}_J)\right), \quad J \in S^c \tag{9}$$

where $H(\mathbf{x})$ is the Heaviside function and the singularity field near crack tip is modified by the branching functions (see more details in Ref [10]) as follow

$$R_J^{enr}(\boldsymbol{\xi}) = R_J(\boldsymbol{\xi})\left(\sum_{L=1}^{4}\left(G_L(r,\theta) - G_L(r_J,\theta_J)\right)\right), \quad J \in S^f \tag{10}$$

where

$$G_L(r,\theta) = \begin{cases} r^{3/2}\left[\sin\dfrac{\theta}{2} \quad \cos\dfrac{\theta}{2} \quad \sin\dfrac{3\theta}{2} \quad \cos\dfrac{3\theta}{2}\right] & \text{for } u_0,\ v_0,\ w \text{ variables} \\ r^{1/2}\left[\sin\dfrac{\theta}{2} \quad \cos\dfrac{\theta}{2} \quad \sin\dfrac{\theta}{2}\sin\theta \quad \cos\dfrac{\theta}{2}\cos\theta\right] & \text{for } \beta_x,\ \beta_x \text{ variables} \end{cases} \tag{11}$$

in which r and θ are polar coordinates in the local crack tip coordinate system.

3.3 Cracked plate formulation based on HSDT

Now, using the displacement field approximated in Eq. (8), the strain matrices including in-plane and shear strains can be rewritten as:

$$\left[\boldsymbol{\varepsilon}_0^T \ \boldsymbol{\kappa}_1^T \ \boldsymbol{\kappa}_2^T \ \boldsymbol{\varepsilon}_s^T\right]^T = \sum_{I=1}^{m\times n}\left[\left(\mathbf{B}_I^m\right)^T \ \left(\mathbf{B}_I^{b1}\right)^T \ \left(\mathbf{B}_I^{b2}\right)^T \ \left(\mathbf{B}_I^s\right)^T\right]^T \mathbf{q}_I \tag{12}$$

in which the unknown vector **q** contains both displacements and enriched DOFs, and

$$\mathbf{B} = \left[\mathbf{B}^{std} \middle| \mathbf{B}^{enr}\right] \tag{13}$$

where $\mathbf{B}^{std}$ and $\mathbf{B}^{enr}$ are the standard and enriched strain matrices of $\mathbf{B}$.

Substituting Eq. (2) with relation in Eq. (12) into Eq. (3), the formulations of free vibration problem can be rewritten as follow:

$$\left(\mathbf{K}-\omega^2\mathbf{M}\right)\mathbf{d}=\mathbf{0} \tag{14}$$

where $\omega \in \mathrm{R}^+$ are the natural frequency and the global stiffness matrix **K** is given by:

$$\mathbf{K}=\int_\Omega \left\{\mathbf{B}^m \;\; \mathbf{B}^{b1} \;\; \mathbf{B}^{b2}\right\}\mathbf{D}^b\left\{\mathbf{B}^m \;\; \mathbf{B}^{b1} \;\; \mathbf{B}^{b2}\right\}^T+\mathbf{B}^{sT}\mathbf{D}^s\mathbf{B}^s \mathrm{d}\Omega \tag{15}$$

4 NUMERICAL RESULTS

First, let study the natural frequencies of a thin isotropic cracked plate (ν=0.3) with dimension $L\times W\times h$ has an initial crack at center as shown in Fig. 2a.

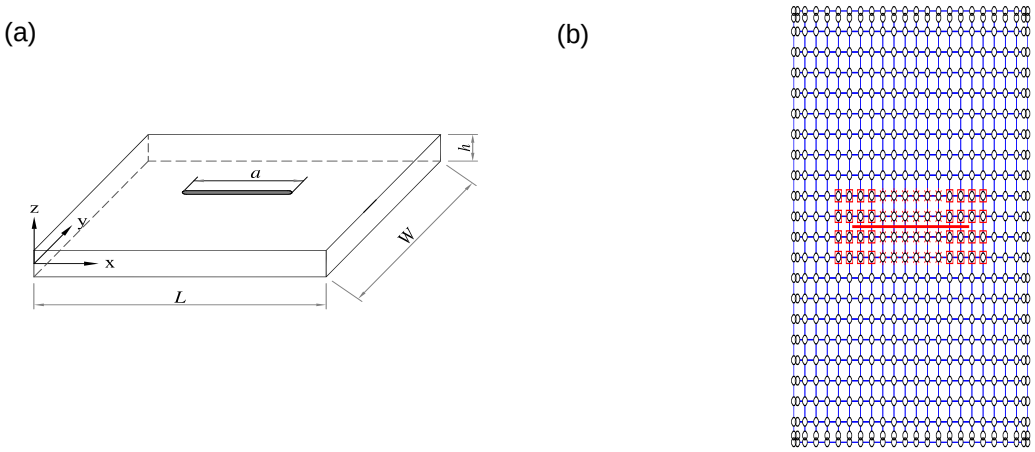

Fig. 2 The plate with a center crack: (a) model; (b) mesh of 21x21 cubic NURBS elements

The relation between non-dimension frequencies $\hat{\omega}=\omega L^2\sqrt{\rho h/D}$ and crack length ratio according to mesh 21x21 as shown in Fig2b is reported in Table1. The obtained results from XIGA are in good agreement compared to both analytical solution [6,7] and XFEM [8] using 20x20 nine-node Lagrange elements. For clearer vision, the comparison of first five frequencies between the present result and that of Stahl [6] and Liew [7] is depicted in Fig.3. It is revealed that the frequencies decrease via increase in crack length ratio. For example, the values of frequency according to change of mode from 1 to 5 drop up to 18.3%, 67.3%, 5.3%, 40.8% and 23.7% of its initial values corresponding to an intact plate, respectively. It is concluded that the magnitude of the frequency according to anti-symmetric modes through the y-axis, which is perpendicular with cracked path (e.g. mode 2, mode 4, shown in Fig. 4), is much more affected by the crack length. Here, the discontinuous displacement is shown clearly along crack path.

Table 1 Non dimensional natural frequency of an isotropic square plate with central crack *L/h*=1000

Mode Number	Source	Crack length ratio *a/L*						
		0	0.2	0.4	0.5	0.6	0.8	1
1	Stahl [6]	19.7390	19.3050	18.2790	17.7060	17.1930	16.4030	16.1270
	Liew [7]	19.7400	19.3800	18.4400	17.8500	17.3300	16.4700	16.1300
	XFEM [8]	19.7390	19.3050	18.2780	17.7070	17.1800	16.4060	16.1330
	XIGA	19.7392	19.3846	18.4617	17.8989	17.3576	16.5157	16.1345
2	Stahl [6]	49.3480	49.1700	46.6240	43.0310	37.9780	27.7730	16.1270
	Liew [7]	49.3500	49.1600	46.4400	42.8200	37.7500	27.4300	16.1300
	XFEM [8]	49.3480	49.1810	46.6350	43.0420	37.9870	27.7530	17.8260
	XIGA	49.3501	49.1906	47.1197	44.7124	39.3469	29.1186	16.1345
3	Stahl [6]	49.3480	49.3280	49.0320	48.6970	48.2230	47.2560	46.7420
	Liew [7]	49.3500	49.3100	49.0400	48.7200	48.2600	47.2700	46.7400
	XFEM [8]	49.3480	49.3240	49.0320	48.6850	48.2140	47.2010	46.7340
	XIGA	49.3501	49.3292	49.0903	48.6328	48.3547	47.3448	46.7376
4	Stahl [6]	78.9570	78.9570	78.6020	77.7330	75.5810	65.7320	46.7420
	Liew [7]	78.9600	78.8100	78.3900	77.4400	75.2300	65.1900	46.7400
	XFEM [8]	78.9550	78.9450	78.6000	77.7100	75.5790	65.7150	49.0990
	XIGA	78.9589	78.9452	78.6507	77.6642	76.0779	67.2308	46.7376
5	Stahl [6]	98.6960	93.9590	85.5100	82.1550	79.5880	76.3710	75.2850
	Liew [7]	98.7000	94.6900	86.7100	83.0100	80.3200	76.6000	75.2800
	XFEM [8]	98.6980	93.8930	85.4500	82.1080	79.5560	76.3510	75.2750
	XIGA	98.7292	94.5834	86.6987	82.7347	80.3835	76.7866	75.2823

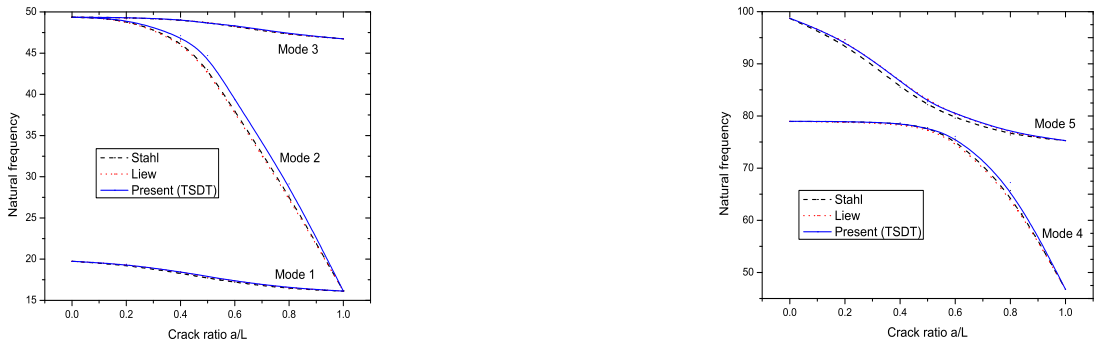

Fig. 3 Variation of first five mode frequencies via length crack ratio

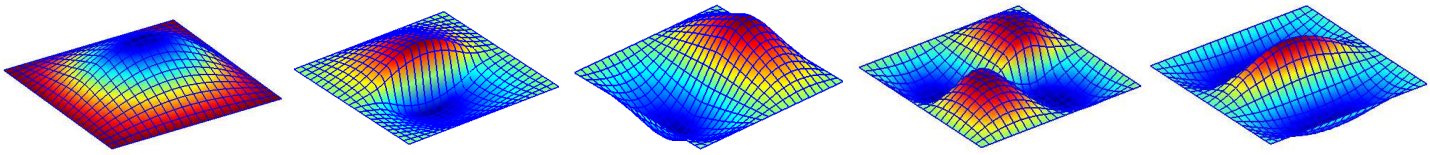

Mode 1 Mode 2 Mode 3 Mode 4 Mode 5

Fig. 4 The first five mode shapes of simply supported plate having center crack with *a/L* =0.8

Next, an annular plate with uniform thickness *h*, outer radius *R* and inner one *r* as shown in Fig. is studied. The plate is made of Al/Al_2O_3 FGM with properties : E_c=70 GPa , E_m=380 GPa , $\nu_c=\nu_m$=0.3, ρ_c=2707 kg/m^3, ρ_m=3800 kg/m^3. The FGM is homogenized according to the Mori-Tanaka scheme with the effective values of Young's modulus *E* and Poisson's ratio ν are calculated from the effective bulk and shear modulus [4] as below :

$$E_e = \frac{9K_e\mu_e}{3K_e+\mu_e}, \qquad \nu_e = \frac{3K_e-2\mu_e}{2(3K_e+\mu_e)} \tag{16}$$

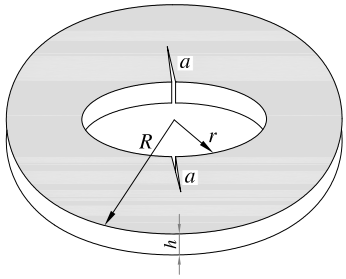

Fig. 5 The model of annular plate.

Table 2 tabulates the frequency parameter of the annular Al/Al_2O_3 plates via outer radius to inner radius ratio *R/r* and radius to thickness ratio *R/h* according to *n*=1. It is concluded that the frequency parameters decrease sequentially following to increase in inner radius to outer radius ratio *r/R*. To enclose this section the first four mode shapes of annular FGM plate are depicted in Fig. 6.

Table 2 The frequency parameter $\tilde{\omega} = \omega(R-r)^2 / h\sqrt{\rho_c / E_c}$ of an annular pate via inner radius to outer radius ratio *r/R* and radius to thickness ratio *R/h* according to *n*=1.

R/h	*r/R*	Mode number				
		1	2	3	4	5
2	0	1.2786	1.7682	2.3336	2.7352	2.8058
	0.2	0.8438	1.0109	1.7316	1.8588	1.9021
	0.5	0.5516	0.5896	0.7308	0.8458	0.9817
	0.8	0.2760	0.2771	0.2800	0.2896	0.2905
10	0	1.8480	3.5185	4.0473	5.9916	6.3512
	0.2	1.1563	1.5352	3.1932	4.1404	4.8849
	0.5	0.8621	0.9560	1.3533	1.6388	2.3101
	0.8	0.6470	0.6540	0.6730	0.6975	0.7545
20	0	1.8379	3.1941	4.1533	6.1526	6.4956
	0.2	1.1793	1.598	3.3309	4.4139	5.2045
	0.5	0.8877	0.9954	1.4507	1.7937	2.5902
	0.8	0.7279	0.7371	0.7655	0.7999	0.8775
100	0	1.8649	3.3264	4.2398	6.3270	6.7435
	0.2	1.1922	1.6442	3.4202	4.6187	5.3415
	0.5	0.8973	1.0154	1.5007	1.8656	2.6187
	0.8	0.7646	0.7753	0.8124	0.8567	0.9362

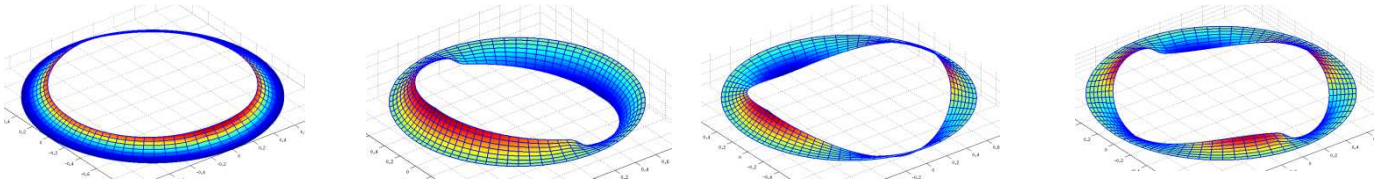

Mode 1 Mode 2 Mode 3 Mode 4

Fig. 6 The first four mode shapes of the annular plate with r/*R*=0.8, *R/h*=10.

5 CONCLUSIONS

In this paper, a novel and effective formulation based on combining XIGA and HSDT has been applied to dynamic analysis of the cracked plates. The present method, utilizing NURBS basis functions, allows us to achieve easily the smoothness with arbitrary continuity order compared with the traditional FEM. Consequently, it naturally fulfills the C^1-continuity of HSDT model. Furthermore, the special enrichment functions are applied for describing the singularity behaviors along the crack. The obtained results are in excellent agreement with others in the literature.

6 REFERENCES

[1] J.N. Reddy, Analysis of functionally graded plates. International Journal for Numerical Methods in Engineering 47, 663–684, 2000.

[2] S.V. Senthil, R.C. Batra, Exact solution for thermoelastic deformations of functionally graded thick rectangular plates. AIAA Journal 40,1021–1033, 2002.

[3] H. Nguyen-Xuan, Loc V. Tran, T. Nguyen-Thoi, H.C. Vu-Do, Analysis of functionally graded plates using an edge-based smoothed finite element method. Composite Structures 93, 3019-3039, 2011.

[4] Loc V. Tran, A.J.M. Ferreira, H. Nguyen-Xuan, Isogeometric approach for analysis of functionally graded plates using higher-order shear deformation theory. Composite Part B: Engineering 51, 368-383, 2013.

[5] Loc V. Tran, Chien H. Thai, H. Nguyen-Xuan, An isogeometric finite element formulation for thermal buckling analysis of functionally graded plates, Finite Element in Analysis and Design 73, 65-76, 2013.

[6] B. Stahl, L. Keer, Vibration and stability of cracked rectangular plates. Int J Solids Struct 8, 69–91,1972.

[7] K.M. Liew, K.C. Hung, M.K. Lim, A solution method for analysis of cracked plates under vibration, Engineering Fracture Mechanics 48, 393–404, 1994.

[8] M. Bachene, R. Tiberkak, S. Rechak, Vibration analysis of cracked plates using the extended finite element method**,** Archive of Applied Mechanics 79, 249-262, 2009.

[9] G. Qian, S. Gu, J. Jiang, A finite element model of cracked plates and application to vibration problems. Comput Struct 39, 483–487, 1991.

[10] J. Dolbow, N. Moës, T. Belytschko, Modeling fracture in Mindlin–Reissner plates with the extended finite element method. Int J Solids Struct 37, 7161–7183, 2000.

[11] S.Natarajan, P.M. Baiz, S.Bordas, T.Rabczuk, P. Kerfriden, Natural frequencies of cracked FGM plates by the extended finite element method, Composite Structures 93, 3082–3092, 2011.

[12] T.J.R. Hughes, J.A. Cottrell, and Y. Bazilevs, Isogeometric analysis: CAD, finite elements, NURBS, exact geometry and mesh refinement, Computer Methods in Applied Mechanics and Engineering 194, 4135–4195, 2009.

[13] S.S. Ghorashi, N. Valizadeh, and S. Mohammadi, Extended isogeometric analysis for simulation of stationary and propagating cracks. International Journal for Numerical Methods in Engineering, 89, 1069–1101, 2012.

[14] E. De Luycker, D.J. Benson, T. Belytschko, Y. Bazilevs, and M.C. Hsu, X-FEM in isogeometric analysis for linear fracture mechanics. International Journal for Numerical Methods in Engineering 87,541–565,2011.

Proceedings of the 3rd International Conference on
Fracture Fatigue and Wear, pp. 134-140, 2014

Buckling analysis of piezoelectric composite plates using NURBS-based isogeometric finite elements and higher-order shear deformation theory

P. Phung-Van[1,2,*], M. Abdel-Wahab[2], Loc V. Tran[1] and H. Nguyen-Xuan[3]

[1]Division of Computational Mechanics, Ton Duc Thang University, Vietnam
[2]Department of Mechanical Construction and Production, Faculty of Engineering and Architecture, Ghent University, Belgium
[3]Department of Mechanics, University of Science, VNU - HCMC, Vietnam
*Corresponding author: phuc.phungvan@ugent.be

Abstract: This paper further exploits the utility and robustness of Isogeometric Analysis (IGA) together with Higher-order Shear Deformation Theory (HSDT) for buckling analysis of piezoelectric composite plates. In the composite plates, the mechanical displacement field is approximated according to the HSDT model using NURBS-based isogeometric elements. These achieve naturally any desired degree of continuity through the choice of the interpolation order, so that the method easily fulfils the C^1-continuity requirement of the HSDT model. The electric potential is assumed to vary linearly through the thickness for each piezoelectric sub-layer. The accuracy and reliability of the proposed method is verified by comparing its numerical predictions with those of other available numerical approaches.

Keywords: Isogeometric Analysis (IGA); composite plates; piezoelectricity; sensors and actuators

1 INTRODUCTION

The integration of composite plates with piezoelectric materials to obtain active lightweight smart structures has attracted a considerable interest for various applications such as automotive sensors, actuators, transducers and active damping devices. Due to the attractive properties of piezoelectric composite structures, various numerical methods have been proposed to model and simulate their behaviour. For static and free vibration analysis, Yang and Lee [1] showed that the early work on structures with piezoelectric layers could lead to substantial errors in the natural frequencies and mode shapes. Kim et al. [2] validated the Finite Element (FE) model of a smart cantilever plate through comparison with experiments. Willberg et al. [3] studied a three-dimensional piezoelectric solid model using isogeometric finite elements. For vibration control, some theories integrated with various numerical methods have been proposed and the three most popular theories are the Classical Lamination Theory (CLT), the First-order Shear Deformation Theory (FSDT), and the Higher-order Shear Deformation Theory (HSDT). In the CLT, which is based on the assumptions of Kirchhoff's plate theory, the interlaminar shear deformation is neglected. Hwang and Park [4], Lam et al. [5] reported control algorithms based on classical negative velocity feedback control and the FE method which were formulated based on the discrete Kirchhoff quadrilateral element. In the FSDT, a constant transverse shear deformation is assumed through the entire thickness of the laminate and hence stress-free boundary conditions are violated at the top and bottom surfaces of the panel. Milazzo and Orlando [6] studied free vibration analysis of smart laminated thick composite plates. Phung-Van et al. [7] extended the cell-based smoothed discrete shear gap method to static, free vibration and control of piezoelectric composite plates. In both CLT and FSDT theories, a shear correction factor is required to ensure the stability of the solution. In order to improve the accuracy of transverse shear stresses and to avoid the introduction of shear correction factors, the HSDT based on the FE method has been proposed to study piezoelectric plates [8,9]. It is worth mentioning that the HSDT requires at least C^1-continuity of generalized displacements due to the presence of their second-order derivatives in the stiffness formulation. This is a source of difficulty in standard finite elements featuring C^0 inter-element continuity. As it emerges from the above review, the available studies have focused on the dynamic analysis of piezoelectric composite plates using the FE method, the smoothed FE method, etc. This paper aims at further contributing to the dynamic analysis of piezoelectric composite plates using an

isogeometric approach based on Non-Uniform B-Spline (NURBS) basis functions. In particular, we show that a HSDT formulation fulfilling C^1-continuity requirements is easily achieved in the isogeometric framework. Isogeometric analysis (IGA) has been recently proposed by Hughes et al. [10] with the original objective to tightly integrate Computer Aided Design (CAD) and FE analysis. IGA makes use of the same basis functions typically used in the CAD environment (most notably NURBS or T-Splines) to describe the geometry of the problem exactly as it is produced from CAD as well as to approximate the solution fields for the analysis.

This paper exploits further the advantages of a NURBS-based isogeometric approach for buckling analysis of laminated composite plates integrated with piezoelectric sensors and actuators using the HSDT theory. In the composite plates, the mechanical displacement field is approximated according to the HSDT model using NURBS-based isogeometric elements. These achieve naturally any desired degree of continuity through the choice of the interpolation order, so that the method easily fulfils the C^1-continuity requirement of the HSDT model. The electric potential is assumed to vary linearly through the thickness for each piezoelectric sub-layer. The accuracy and reliability of the proposed method is verified by comparing its numerical predictions with those of other available numerical approaches.

2 WEAK FORM AND FEM FORMULATION FOR PIEZOELECTRIC COMPOSITE PLATE

2.1 Linear piezoelectric constitutive equations

The linear piezoelectric constitutive equations can be expressed as

$$\begin{bmatrix} \boldsymbol{\sigma} \\ \mathbf{D} \end{bmatrix} = \begin{bmatrix} \mathbf{c} & -\mathbf{e}^T \\ \mathbf{e} & \mathbf{g} \end{bmatrix} \begin{bmatrix} \boldsymbol{\varepsilon} \\ \mathbf{E} \end{bmatrix} \tag{1}$$

where $\boldsymbol{\sigma}$ and $\boldsymbol{\varepsilon}$ are the stress and strain vectors; **D** and **E** are dielectric displacement and electric vectors; **c** is the elasticity matrix; **e** is the piezoelectric constant matrix and **g** denotes the dielectric constant matrix.

The Galerkin weak form of the governing equations of piezoelectric structures can be derived by using Halminton's variational principle [4], which can be written as

$$L = \int \left(\tfrac{1}{2} \rho \dot{\mathbf{u}}^T \dot{\mathbf{u}} - \tfrac{1}{2} \boldsymbol{\sigma}^T \boldsymbol{\varepsilon} + \tfrac{1}{2} \mathbf{D}^T \mathbf{E} + \mathbf{u} \mathbf{f}_s - \boldsymbol{\phi} \mathbf{q}_s \right) \mathrm{d}\Omega + \sum \mathbf{u}^T \mathbf{F}_p - \sum \boldsymbol{\phi} \mathbf{Q}_p = 0 \tag{2}$$

where $\mathbf{u}$ and $\dot{\mathbf{u}}$ are the mechanical displacement and velocity; $\boldsymbol{\phi}$ is the electric potential; $\mathbf{f}_s$ and $\mathbf{F}_p$ are the mechanical loads and point loads; $\mathbf{q}_s$, $\mathbf{Q}_p$ are the surface charges and point charges.

2.2 Approximations on the mechanical displacement field

2.2.1 Governing equations for a third-order shear deformation theory model

According to the third-order shear deformation theory proposed by Reddy [11], the displacements of an arbitrary point in the plate are expressed by

$$u = u_0 + z\beta_x + cz^3 \left(\beta_x + w_{,x} \right); \; v = v_0 + z\beta_y + cz^3; \; w = w_0 \tag{3}$$

where t is the thickness of the plate; $c = 4/3t^2$ and the variables $\mathbf{u}_0 = \left[u_0 \; v_0 \right]^T$, w_0 and $\boldsymbol{\beta} = \left[\beta_x \; \beta_y \right]^T$ are the membrane displacements, the deflection of the mid-plane and the rotations of the mid-plane around y-axis and x–axis, respectively.

The strains are thus expressed by the following equation

$$\boldsymbol{\varepsilon}=\begin{bmatrix}\varepsilon_{xx}\\ \varepsilon_{yy}\\ \gamma_{xy}\end{bmatrix}=\begin{bmatrix}u_{0,x}\\ v_{0,y}\\ u_{0,y}+v_{0,x}\end{bmatrix}+z\begin{bmatrix}\beta_{x,x}\\ \beta_{y,y}\\ \beta_{x,y}+\beta_{y,x}\end{bmatrix}+z^3c\begin{bmatrix}\beta_{x,x}+w_{0,xx}\\ \beta_{y,y}+w_{0,yy}\\ \beta_{x,y}+\beta_{y,x}+2w_{0,xy}\end{bmatrix}=\boldsymbol{\varepsilon}_0+z\boldsymbol{\kappa}_1+z^3\boldsymbol{\kappa}_2 \tag{4}$$

$$\boldsymbol{\gamma}=\begin{bmatrix}\gamma_{xz}\\ \gamma_{yz}\end{bmatrix}=\begin{bmatrix}\beta_x+w_{0,x}\\ \beta_y+w_{0,y}\end{bmatrix}+z^2 3c\begin{bmatrix}\beta_x+w_{0,x}\\ \beta_y+w_{0,y}\end{bmatrix}=\boldsymbol{\varepsilon}_s+z^2\boldsymbol{\kappa}_s \tag{5}$$

From Hooke's law and the linear strains given by Eqs. (4) and (5), the stress is computed by

$$\boldsymbol{\sigma}=\begin{bmatrix}\boldsymbol{\sigma}_p\\ \boldsymbol{\tau}\end{bmatrix}=\begin{bmatrix}\bar{\mathbf{D}} & \mathbf{0}\\ \mathbf{0} & \bar{\mathbf{D}}_s\end{bmatrix}\begin{bmatrix}\boldsymbol{\varepsilon}\\ \boldsymbol{\gamma}\end{bmatrix}=\mathbf{c}\boldsymbol{\varepsilon} \tag{6}$$

where $\boldsymbol{\sigma}_p$ and $\boldsymbol{\tau}$ are the in-plane stress component and shear stress; $\bar{\mathbf{D}}$ and $\bar{\mathbf{D}}_s$ are material constant matrices given in the form of

$$\bar{\mathbf{D}}=\begin{bmatrix}\mathbf{A} & \mathbf{B} & \mathbf{E}\\ \mathbf{B} & \mathbf{D} & \mathbf{F}\\ \mathbf{E} & \mathbf{F} & \mathbf{H}\end{bmatrix},\ \bar{\mathbf{D}}_s=\begin{bmatrix}\mathbf{A}_s & \mathbf{B}_s\\ \mathbf{B}_s & \mathbf{D}_s\end{bmatrix},\quad \begin{matrix}(\mathbf{A},\mathbf{B},\mathbf{D},\mathbf{E},\mathbf{F},\mathbf{H})=\int_{-h/2}^{h/2}\left(1,z,z^2,z^3,z^4,z^6\right)\bar{Q}_{ij}\mathrm{d}z\ \ (i,j=1,2,6)\\ (\mathbf{A}_s,\mathbf{B}_s,\mathbf{D}_s)=\int_{-h/2}^{h/2}\left(1,z^2,z^4\right)\bar{Q}_{ij}\mathrm{d}z\qquad i,j=4,5\end{matrix} \tag{7}$$

2.2.2 NURBS-based novel composite plate formulation

Using the NURBS basis functions [10], the displacement field **u** of the plate is approximated as

$$\mathbf{u}^h(\xi,\eta)=\sum_{I}^{m\times n}N_I(\xi,\eta)\mathbf{d}_I \tag{8}$$

where $\mathbf{d}_I=\begin{bmatrix}u_{0I} & v_{0I} & w_{0I} & \beta_{xI} & \beta_{xI}\end{bmatrix}^T$ is the vector of degrees of freedom associated with the control point *I*.

Substituting Eq. (8) into Eqs. (4) and (5), the in-plane and shear strains can be rewritten as:

$$\begin{bmatrix}\boldsymbol{\varepsilon}_0^T & \boldsymbol{\kappa}_1^T & \boldsymbol{\kappa}_2^T & \boldsymbol{\varepsilon}_s^T & \boldsymbol{\kappa}_s^T\end{bmatrix}^T=\sum_{A=1}^{m\times n}\begin{bmatrix}\left(\mathbf{B}_I^m\right)^T & \left(\mathbf{B}_I^{b1}\right)^T & \left(\mathbf{B}_I^{b2}\right)^T & \left(\mathbf{B}_I^{s0}\right)^T & \left(\mathbf{B}_I^{s1}\right)^T\end{bmatrix}^T\mathbf{d}_I \tag{9}$$

where

$$\mathbf{B}_I^m=\begin{bmatrix}N_{I,x} & 0 & 000\\ 0 & N_{I,y} & 000\\ N_{I,y} & N_{I,x} & 000\end{bmatrix},\ \mathbf{B}_I^{b1}=\begin{bmatrix}000 & N_{I,x} & 0\\ 000 & 0 & N_{I,y}\\ 000 & N_{I,y} & N_{I,x}\end{bmatrix},\quad \mathbf{B}_I^{b2}=c\begin{bmatrix}00 & N_{I,xx} & N_{I,x} & 0\\ 00 & N_{I,yy} & 0 & N_{I,y}\\ 002 & N_{I,xy} & N_{I,y} & N_{I,x}\end{bmatrix},$$
$$\mathbf{B}_I^{s0}=\begin{bmatrix}00 & N_{I,x} & N_I & 0\\ 00 & N_{I,y} & 0 & N_I\end{bmatrix},\ \mathbf{B}_I^{s1}=3c\begin{bmatrix}00 & N_{I,x} & N_I & 0\\ 00 & N_{I,y} & 0 & N_I\end{bmatrix} \tag{10}$$

2.3 Approximation of the electric potential field

In each sub-layer, a linear electric potential function is assumed through the thickness as [12]:

$$\phi^i(z) = \mathbf{N}_\phi^i \boldsymbol{\phi}^i \tag{11}$$

where $\mathbf{N}_\phi^i$ is the vector of the shape functions for the electric potential, and $\boldsymbol{\phi}^i$ is the vector containing the electric potentials at the top and bottom surfaces of the *i*-th sub-layer.

For each piezoelectric sub-layer element, the electric field **E** in Eq. (1) can be rewritten as [13]:

$$\mathbf{E} = -\nabla \mathbf{N}_\phi^i \boldsymbol{\phi}^i = -\mathbf{B}_\phi \boldsymbol{\phi}^i \tag{12}$$

2.4 Elementary governing equation of motion

The final form of equation of buckling is written in the following form

$$(\mathbf{K} - \omega^2 \mathbf{M})\mathbf{u} = 0 \quad \text{and} \quad (\mathbf{K} - \lambda_{cr} \mathbf{K}_g)\mathbf{u} = 0 \tag{13}$$

where

$$\mathbf{M} = \begin{bmatrix} \mathbf{M}_{uu} & 0 \\ 0 & 0 \end{bmatrix}, \mathbf{K} = \begin{bmatrix} \mathbf{K}_{uu} & \mathbf{K}_{u\phi} \\ \mathbf{K}_{\phi u} & \mathbf{K}_{\phi\phi} \end{bmatrix}, \mathbf{u} = \begin{bmatrix} \mathbf{d} \\ \boldsymbol{\phi} \end{bmatrix} = \begin{bmatrix} \mathbf{F} \\ \mathbf{Q} \end{bmatrix} \tag{14}$$

in which

$$\mathbf{K}_{uu} = \int_\Omega \mathbf{B}_u^T \mathbf{c} \mathbf{B}_u \mathrm{d}\Omega \; ; \; \mathbf{K}_{u\phi} = \int_\Omega \mathbf{B}_u^T \mathbf{e}^T \mathbf{B}_\phi \mathrm{d}\Omega ; \; \mathbf{K}_{\phi\phi} = -\int_\Omega \mathbf{B}_\phi^T \mathbf{p} \mathbf{B}_\phi \mathrm{d}\Omega \; ; \; \mathbf{M}_{uu} = \int_\Omega \mathbf{N}^T \mathbf{m} \mathbf{N} \mathrm{d}\Omega \tag{15}$$

which $\mathbf{B}_u = [\mathbf{B}^m \; \mathbf{B}^{b1} \; \mathbf{B}^{b2} \; \mathbf{B}^{s0} \; \mathbf{B}^{s1}]^T$; **m** is defined by

$$\mathbf{m} = \begin{bmatrix} \mathbf{I}_0 & 0 & 0 \\ 0 & \mathbf{I}_0 & 0 \\ 0 & 0 & \mathbf{I}_0 \end{bmatrix} \text{where } \mathbf{I}_0 = \begin{bmatrix} I_1 & I_2 & cI_4 \\ I_2 & I_3 & cI_5 \\ cI_4 & cI_5 & c^2 I_7 \end{bmatrix}$$
$$(I_1, I_2, I_3, I_4, I_5, I_7) = \int_{-h/2}^{h/2} \rho \left(1, z, z^2, z^3, z^4, z^7\right) \mathrm{d}z \tag{16}$$

and

$$\mathbf{K}_g = \int_\Omega \left(\mathbf{B}_g\right)^T \mathbf{N}_0 \mathbf{B}_g \mathrm{d}\Omega \quad \text{where } \mathbf{B}_g = \begin{bmatrix} 0\,0\,N_{I,x}\,0\,0 \\ 0\,0\,N_{I,y}\,0\,0 \end{bmatrix}, \mathbf{N}_0 \begin{bmatrix} N_x^0 & N_{xy}^0 \\ N_{xy}^0 & N_y^0 \end{bmatrix} \tag{17}$$

and ω, λ_{cr} are the natural frequency and the critical buckling value, respectively.

In this work, the constant gain G_d of the displacement feedback control is used to couple the input actuator voltage vector $\boldsymbol{\phi}_a$ and the output sensor voltage vector $\boldsymbol{\phi}_s$ as $\boldsymbol{\phi}_a = G_d \boldsymbol{\phi}_s$

The global stiffness matrix can be rewritten [7]:

$$\mathbf{K}^{*} = \mathbf{K}_{uu} + G_d \left[\mathbf{K}_{u\phi}\right]_s \left[\mathbf{K}_{\phi\phi}^{-1}\right]_s \left[\mathbf{K}_{\phi u}\right]_s \tag{18}$$

3 NUMERICAL RESULTS

In this section, first, we verify the accuracy and efficiency of the proposed isogeometric element for analyzing the natural frequencies of the piezoelectric composite plates. We consider a square five-ply piezoelectric laminated composite plate [*pie*/0/90/0/*pie*] in which *pie* denotes a piezoelectric layer. The plate is simply supported and the thickness to length ratio of each composite ply is *t/a* = 1/50. The laminate configuration includes three layers of Graphite/Epoxy (*Gp/Ep*) with fiber orientations of [0/90/0]. Two continuous PZT-4 piezoelectric layers of thickness 0.1*t* are bonded to the upper and lower surfaces of the laminate. Two sets of electric boundary conditions are considered for the inner surfaces of the piezoelectric layers including: (1) a closed-circuit condition in which the electric potential is kept zero (grounded); and (2) an open-circuit condition in which the electric potential remains free (zero electric displacements). Table 1 shows the dimensionless first natural frequency of the piezoelectric composite plate with meshing of 8×8. In this study, the isogeometric elements use the HSDT with only 5 dofs per control point while Ref [15] uses the layerwise theory and Ref [8] uses HSDT with 11 dofs per node. It is seen that the results given by the isogeometric formulation are slightly lower than the analytical solution [16], however the errors are less than 5%. We observe that the isogeometric results are stable in both a closed-circuit condition and an open-circuit condition similarly to the analytical solution [16], while those of Refs [15,8] are very different for a closed-circuit condition and an open-circuit condition.

Table 1 Dimensionless first natural frequency of the piezoelectric composite plate [*pie*/0/90/0/*pie*]

Method	Meshing	Degrees of freedom (DOFs)	$\overline{f} = \omega_1 a^2 / \left(10000t\sqrt{\rho}\right)$	
			Closed circuit	Open circuit
IGA (5 dofs per control point)	8×8	500	235.900	236.100
FE layerwise [15]	12×12	2208	234.533	256.765
Q9 - HSDT (11 dofs per node) [8]	-	-	230.461	250.597
Q9 - FSDT (5 dofs per node) [8]	-	-	206.304	245.349
Ref [16]			245.941	245.942

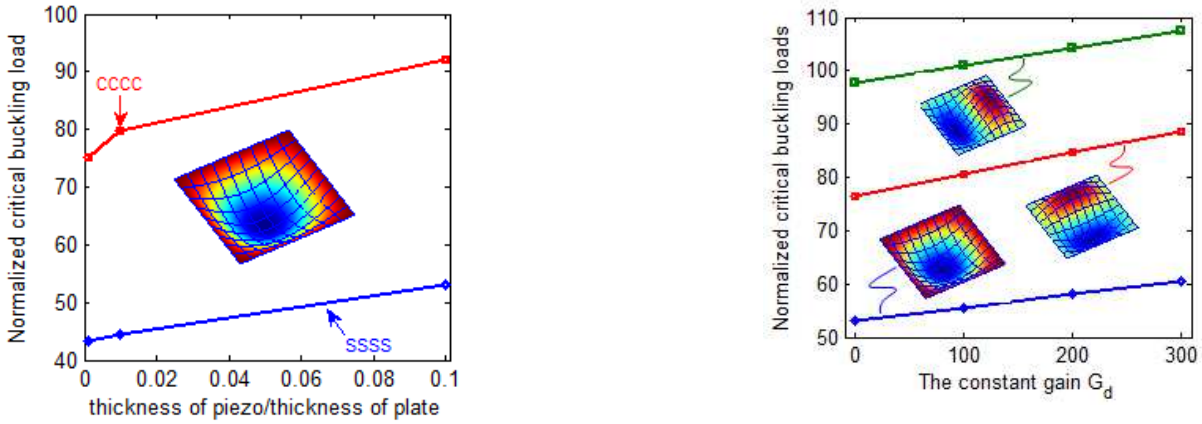

(a) The buckling loads (b) First three buckling mode

Fig. 1 Model of a 5-ply piezoelectric composite plate

Next, we consider a piezoelectric composite plate under axial compression. The buckling load parameter $\overline{\lambda}_{cr} = \lambda_{cr} a^2 / \left(10000 t\sqrt{\rho}\right)$ of piezoelectric with boundary condition: simply supported and clamped is plotted in Fig. 1a. It can be seen that the buckling load for clamped plate is higher than that for simply supported plate, as expected. This is because the stiffness of the clamped plate is stiffer. Next, the effect of the constant gain of the displacement to the buckling loads is displayed in Fig. 1b. The results show that the buckling load increases when the constraint gain increases.

4 CONCLUSIONS

This paper presents a simple and effective approach based on the combination of IGA and HSDT for the buckling analyses of composite plates integrated with piezoelectric sensors and actuators. In the piezoelectric composite plates, the mechanical displacement field is approximated according to the HSDT using isogeometric elements based on NURBS and featuring at least C^1-continuity, whereas the electric potential is assumed to vary linearly through the thickness for each piezoelectric sub-layer. The accuracy and reliability of the proposed method is verified by comparing its numerical predictions with those of other available numerical approaches.

5 REFERENCES

[1] S.M. Yang, Y.J. Lee, Interaction of structure vibration and piezoelectric actuation, Smart Materials and Structures, 3, 494–500, 1994.

[2] J. Kim, V.V. Varadan, V.K. Varadan, X.Q. Bao, Finite element modelling of a smart cantilever plate and comparison with experiments, Smart Materials and Structures, 5, 165–170, 1996.

[3] C. Willberg, U. Gabbert, Development of a three-dimensional piezoelectric isogeometric finite element for smart structure applications, Acta Mechanica, 223(8), 1837-1850, 2012.

[4] W.C. Hwang, H.C. Park, Finite element modelling of piezoelectric sensors and actuators, AIAA Journal, 31, 930-937, 1993.

[5] K.Y. Lam, X.Q. Peng, G.R. Liu, J.N. Reddy, A finite-element model for piezoelectric composite laminates, Smart Materials and Structures, 65, 83–91, 1997.

[6] A. Milazzo, C. Orlando, An equivalent single-layer approach for free vibration analysis of smart laminated thick composite plates, Smart Material and Structures, 21, 075031, 2012.

[7] P. Phung-Van, T. Nguyen-Thoi, T. Le-Dinh, H. Nguyen-Xuan, Static and free vibration analyses and dynamic control of composite plates integrated with piezoelectric sensors and actuators by the cell-based smoothed discrete shear gap method (CS-FEM-DSG3), Smart Materials and Structures, 22, 095026, 2013.

[8] M.F.C. Victor, A.A.G. Maria, S. Afzal, M.M.S. Cristóvão, A.M.S. Carlos, C.V.M. Franco, Modelling and design of adaptive composite structures, Computer Methods in Applied Mechanics and Engineering, 185, 325-346, 2000.

[9] J.N. Reddy, On laminated composite plates with integrated sensors and actuators, Engineering Structures 21, 568–593, 1999.

[10] T.J.R. Hughes, J.A. Cottrell, Y. Bazilevs, Isogeometric analysis: CAD, finite elements, NURBS, exact geometry and mesh refinement, Computer Methods in Applied Mechanics and Engineering, 194(39-41), 4135–4195, 2005.

[11] J.N. Reddy, A simple higher-order theory for laminated composite plates, Journal of Applied Mechanics, 51, 745–752, 1984.

[12] S.Y. Wang, A finite element model for the static and dynamic analysis of a piezoelectric bimorph, International Journal of Solids and Structures, 41, 4075-4096, 2004.

[13] S.Y. Wang, S.T. Quek, K.K. Ang, Vibration control of smart piezoelectric composite plates, Smart Materials and Structures, 10, 637-644, 2001.

[14] M.F.C. Victor, A.A.G. Maria, S. Afzal, M.M.S. Cristóvão, A.M.S. Carlos, C.V.M. Franco, Modelling and design of adaptive composite structures, Computer Methods in Applied Mechanics and Engineering, 185, 325-346, 2000.

[15] D.A. Saravanos, P.R. Heyliger, D.A. Hopkins, Layerwise mechanics and finite element for the dynamic analysis of piezoelectric composite plates, International Journal of Solids and Structures, 34, 359-378, 1997.

[16] P. Heyliger, D.A. Saravanos, Exact free-vibration analysis of laminated plates with embedded piezoelectric layers, Journal of the Acoustical Society of America, 98, 1547-1557, 1995.

Proceedings of the 3rd International Conference on
Fracture Fatigue and Wear, pp. 141-147, 2014

MULTI-PHASE RANDOM MEDIUM BASED FAILURE SIMULATION OF CONCRETE

Liang Shixue[1,2], Ren Xiaodan[1] and Li Jie[1,3]

[1] School of Civil Engineering, Tongji University, Shanghai 200092, P.R.China
[2] Department of Civil and Environmental Engineering, UCLA, Los Angles 90095, CA, USA
[3] The State Key Laboratory on Disaster Reduction in Civil Engineering, Tongji University, Shanghai 200092, P.R.China

Abstract: In this paper, the concrete is defined as a kind of multi-phase random medium with micro-cracks. At first, the concrete is randomly discretized by the non-uniform finite elements and the cohesive elements are inserted in the adjacent finite elements as the potential cracking paths. The randomness of material properties is modelled by the random field theory. The stochastic harmonic function is used for the simulation the Gaussian random field and the Nataf transformation based method is used in turning the Gaussian random field to the multi-phase random field. Finally, 300 sample specimens are simulated to describe the failure modes and the random stress-strain relationship of concrete. The effectiveness and efficiency of the proposed model can be testified both in the sample level and the collection level.

Keywords: cohesive elements; multi-phase random field; failure simulation; concrete

1 INTRODUCTION

Concrete, as the most widely used construction material for infrastructures, is featured by its stochastic nonlinearities due to the random distribution of the multiple phases and defects [1]. Therefore, getting better understandings of the random nature of the concrete and representation for its random micro-structures provide a potential direction to solve the complex problems such as the random cracking processes, the stochastic damage evolution law which induces the stochastic stress-strain relationship and so on.

To represent the randomly heterogeneous micro-structures of concrete, two different methods are developed: the statistical image based method [2, 3] and the random field based method [4, 6]. In the former method, the matrix of the concrete is defined as a homogeneous material, and the inclusions such as the aggregates and the sands are modelled explicitly based on the photos or CT scans of concrete, while the randomness is introduced by the random material properties of the inclusions. However, is annoying to generate all shapes and positions of the inclusions based on the statistical images, especially the highly irregular inclusions in concrete.

Meanwhile, some researchers turn to the random field representation of material properties in avoiding the intricate generation of each phase in the composite materials. Within the framework of the random field modelling, the Gaussian random field is generated beforehand by variety of methods, such as the Karhunen-Loeve expansion [4] and linear path functions [5]. Then, to capture the material properties in more complex materials, the non-Gaussian random fields, mostly the lognormal distribution and the Weilbull distribution random field, are reconstructed and put into the simulation of the fracture of concrete structures [6]. However, when comparing with the other composite materials, the micro-structure of concrete has its own features: the cracks often happen at the interface due to the dramatic strength difference between the aggregates and the mortar. Thus, the simulation of multi-phase random field will enable us to obtain more realistic micro-structure of concrete.

In the present paper, the randomly distributed finite elements and the cohesive elements are developed in the first step to introduce the possible cracking paths. Then, the concrete is considered as a two-phase random medium. We start with the 2-D Gaussian random field which is generated by the newly developed stochastic harmonic function. Then, the Nataf's transformation is introduced to convert Gaussian random

field into the target two phase random field. The two phase random field samples are used to model the spatial variation of fracture energy. At last, 300 samples of the concrete specimens under the uniaxial tensile loading are simulated to testify the failure modes and stress-strain behaviours of the proposed method.

2 RANDOM COHESIVE MODEL

2.1 Cohesive crack method

Consider a solid Ω, in which contains a series of zero-thickness cracks or shear bands. Herein, we denote the two sides of interface S by S^+ and S^-; and the two parts of solid Ω by Ω^+ and Ω^-.

Fig. 1 Solid with interfaces

According to the equilibrium of surface tractions $\boldsymbol{T} = \boldsymbol{T}^+ = -\boldsymbol{T}^-$, we can formulate the functional equation as

$$\int_{\Omega} \boldsymbol{\sigma}(\boldsymbol{u}) : \boldsymbol{\varepsilon}(\boldsymbol{v}) d\Omega + \int_{S} \boldsymbol{T} \cdot \boldsymbol{w}(\boldsymbol{v}) d\Gamma = \int_{\partial\Omega} \boldsymbol{t} \cdot \boldsymbol{v} d\Gamma \tag{1}$$

where $\boldsymbol{u}$ is the displacement and $\boldsymbol{v}$ is the trial function. $\boldsymbol{T}[\boldsymbol{w}(\boldsymbol{u})]$ in Eq. 1 is the cohesive stress, which can be deemed as the function of COD (crack opening displacement) and $\boldsymbol{w}(\boldsymbol{v})$ is deemed as $\boldsymbol{w}(\boldsymbol{v}) = \boldsymbol{v}^- - \boldsymbol{v}^+$.

Aiming at solving the interfacial stress $\boldsymbol{T}[\boldsymbol{w}(\boldsymbol{u})]$ in Eq. 1, a nonlinear zone is introduced between the real crack and the non-cracking area. In this paper, the following stress-COD relationship expressions [7] as

$$f = f_t - kw \tag{2}$$

where $f = \boldsymbol{T} \times \boldsymbol{n}$ denotes the normal cohesive stress; $w = \boldsymbol{w} \times \boldsymbol{n}$ denotes the crack width; $\boldsymbol{n}$ is the normal unit vector; and k is the strength intensity factor. As for the linear decay relationship between $f - w$ which suggested by Hillerborg [7], the fracture energy G_c can be expressed as $G_f = f_t \times w_1 / 2$.

It could be noted in Eq. 1 that the presence of a cohesive surface results in the addition of a new term to the functional equation of the finite element [8]. Thus, the finite elements and the cohesive elements are compatible in a unified model.

2.2 Random cohesive model

As discussed in section 2.1, the cohesive elements give the potential crack paths when connecting the finite elements. As we know, the cracks in concrete are highly irregular and randomly oriented. Thus, the irregular elements are developed to model the random distributed initial micro cracks within concrete. The irregular cohesive model [9] is established as follows:

1) Generate the set of random points in the domain and boundary.
2) Decompose the domain by the Delaunay triangulation scheme.
3) Contract the triangles to gain the cohesive elements that connect the adjacent finite elements.

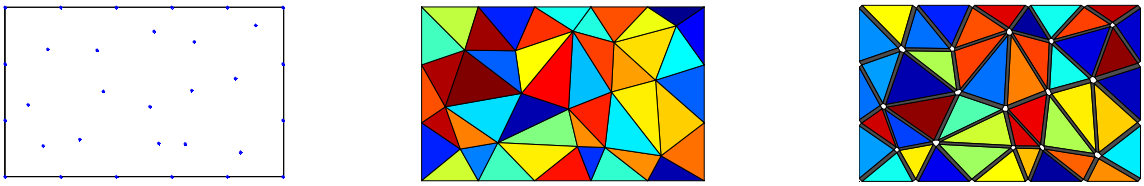

Fig. 2 Generation of the irregular cohesive elements

3 MULTI-PHASE RANDOM FIELD MODELING

To start with, we consider the concrete as a two phase random field: the strong phase which indicates the aggregates in it and the weak phase which indicates the mortar and other components. Thus, the 0-1 discrete valued random field can be demonstrated below to simulate the concrete as:

$$Z_0(\boldsymbol{u}) = \begin{cases} 1 & if \quad \boldsymbol{u} \quad is \quad in \quad the \quad strong \quad phase \\ 0 & if \quad \boldsymbol{u} \quad is \quad in \quad the \quad weak \quad phase \end{cases} \tag{3}$$

where $\boldsymbol{u}$ is a 2-D special vector.

We define the probability of the strong phase as ρ and the weak phase as 1- ρ, respectively. Considering the numerical characteristics, one can easily obtain that the mean value $E(Z_0) = \rho$ and the variance $D(Z_0) = E(Z_0^2) - E^2(Z_0) = \rho - \rho^2$. Normalize the random field $Z_0(\boldsymbol{u})$ into the zero mean and unit variance and define the random field $Z(\boldsymbol{u})$ as follows [12]

$$Z(\boldsymbol{u}) = \begin{cases} \dfrac{\rho - 1}{\sqrt{\rho(1-\rho)}} & if \quad \boldsymbol{u} \quad is \quad in \quad the \quad strong \quad phase \\ \dfrac{\rho}{\sqrt{\rho(1-\rho)}} & if \quad \boldsymbol{u} \quad is \quad in \quad the \quad weak \quad phase \end{cases} \tag{4}$$

Establish the correlation function $R_Z(\boldsymbol{u}_1, \boldsymbol{u}_2)$ of the normalized random field as

$$R_Z(\boldsymbol{u}_1, \boldsymbol{u}_2) = E[Z(\boldsymbol{u}_1) Z(\boldsymbol{u}_2)] \tag{5}$$

3.1 Gaussian random field generation

Chen et al [10] originally represent the stochastic process by the combination of finite stochastic harmonic functions. In characterizing the 2-D Gaussian, homogeneous random field, Liang et al [11] give the formulation based on the stochastic harmonic function with the form

$$Y(x_1, x_2) = \sqrt{2} \sum_{n_1=1}^{N_1} \sum_{n_2=1}^{N_2} \left[A_{n_1 n_2} \cos(K_{1n_1} x_1 + K_{2n_2} x_2 + \Phi_{n_1 n_2}^{(1)}) + \tilde{A}_{n_1 n_2} \cos(K_{1n_1} x_1 - K_{2n_2} x_2 + \Phi_{n_1 n_2}^{(2)}) \right] \tag{6}$$

Where $A_{n_1 n_2}$, $\tilde{A}_{n_1 n_2}$ refer to the amplitude; K_{1n_1}, K_{2n_2} refer to the n_1- , n_2- random wave numbers respectively; $\Phi_{n_1 n_2}^{(1)}$, $\Phi_{n_1 n_2}^{(2)}$ refer to the random phase and N_1, N_2 are the number of the components. Introduce the different inner point $K_{1n_1}^p$ which should meet that $0 \le K_{11}^p \le K_{12}^p \le \cdots \le K_{1N_1-1}^p \le K_{1u}$ and $0 \le K_{21}^p \le K_{22}^p \le \cdots \le K_{2N_2-1}^p \le K_{2u}$, where K_{1u} and K_{2u} are the cut-off wave numbers. The PDF of K_{1n_1} and K_{2n_2} are uniformly distributed in $\left(K_{1n_1-1}^p, K_{1n_1}^p\right]$ and $\left(K_{2n_2-1}^p, K_{2n_2}^p\right]$, respectively.

The amplitude $A_{n_1 n_2}$ and $\tilde{A}_{n_1 n_2}$ are the function of the random wave number which can be defined as follow

$$A_{n_1 n_2} = \sqrt{2 S_{Y_0 Y_0}(K_{1n_1}, K_{2n_2}) \Delta K_{1n_1} \Delta K_{2n_2}} \tag{7}$$

$$\tilde{A}_{n_1 n_2} = \sqrt{2 S_{Y_0 Y_0}(K_{1n_1}, -K_{2n_2}) \Delta K_{1n_1} \Delta K_{2n_2}} \tag{8}$$

where $S_{Y_0 Y_0}$ is the target power spectrum density function. The relation of $R_{Y_0 Y_0}$ and $S_{Y_0 Y_0}$ hold:

$$S_{Y_0Y_0}(K_1,K_2)=\frac{1}{(2\pi)^2}\int_{-\infty}^{\infty}\int_{-\infty}^{\infty}R_{Y_0Y_0}(\xi_1,\xi_2)e^{-i(K_1\xi_1+K_2\xi_2)}d\xi_1 d\xi_2 \tag{9}$$

It is proved that the mean value of $Y(x_1,x_2)$ is equal to zero and the variance is equal to one. According to the mathematical manipulations [11], the random field based on the stochastic harmonic functions is homogeneous and asymptotic Gaussian.

3.2 Nataf transformation of the correlation function

With the two-phase random field definition and the Gaussian random field aforementioned, we choose the Nataf's transformation in transforming the Gaussian random field Y to the target two-phase random field Z. The target Z and the original one Y both have the same cumulative distribution functions (CDF) as

$$F_Z(z)=F_Y(y) \tag{10}$$

where $F_Z(z)$ refers to the CDF of the target two-phase random field and $F_Y(y)$ refers to the Gaussian random field.

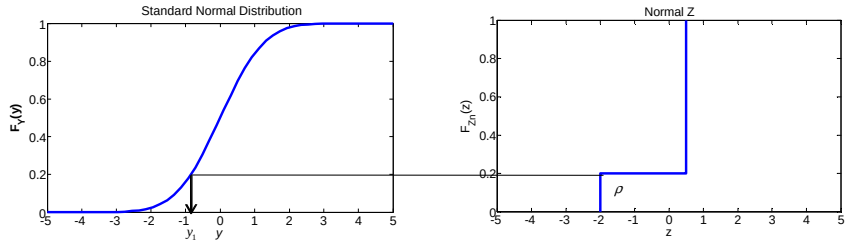

Fig. 3 Nataf's transformation

As depicted in cumulative distribution functions between Y and Z in Fig. 3, the situation that $\boldsymbol{u} < \boldsymbol{u}_1$ and $\boldsymbol{u}^3\ \boldsymbol{u}_1$ can be mapped to the normalized random field by the Nataf's transformation function as

$$z=t(\boldsymbol{u})=\begin{cases}\dfrac{\rho-1}{\sqrt{\rho(1-\rho)}} & if \quad \boldsymbol{u}\le\boldsymbol{u}_1\\ \dfrac{\rho}{\sqrt{\rho(1-\rho)}} & other\end{cases} \tag{11}$$

Eq. 12 can be understood that if $\boldsymbol{u}\,£\,\boldsymbol{u}_1$ the value in the original two-phase random field is $Z_0 = 1$ and if $\boldsymbol{u} > \boldsymbol{u}_t$ the value in the same way is $Z_0 = 0$. It is equal to say that the relationship between is:

$$Z(\boldsymbol{u})=t(Y(\boldsymbol{u})) \tag{12}$$

Considering the relationship in Eq. 5 and Eq. 12, the correlation function of the two-phase random field can be defined as

$$R_{ZZ}(\boldsymbol{u}_1,\boldsymbol{u}_2)=E(t(Y(\boldsymbol{u}_1))\cdot t(Y(\boldsymbol{u}_2))=\int_{-\infty}^{\infty}\int_{-\infty}^{\infty}t(\boldsymbol{u}_1)t(\boldsymbol{u}_2)p_{tt}(\boldsymbol{u}_1,\boldsymbol{u}_2)d\boldsymbol{u}_1 d\boldsymbol{u}_2 \tag{13}$$

where $p_{zz}(z_1,z_2)$ refers to the second order probability density function; z_1 represents the value of normalized two phase random field at the point $\boldsymbol{u}_1$; z_2 represents the value of normalized two phase random field at the point $\boldsymbol{u}_2$ in the same way.

Ilango et al [12] applied the Hermite polynomials expansion in solving this integral equation which is essential in determining the relationship between correlation functions.

The probabilistic Hermite polynomials is chosen, herein, as

$$H_m(x)=(-1)^m e^{x^2/2}\frac{d^m}{dx^m}(e^{x^2/2}) \tag{14}$$

It is noteworthy to demonstrate the most important property of the probabilistic Hermite polynomials that

$$\frac{1}{\sqrt{2\pi}}\int_{-\infty}^{\infty} H_m(x)H_n(x)e^{x^2/2}dx = n!\delta_{mn} \tag{15}$$

Then, introducing the orthogonal condition of the Hermite polynomials to solve the double integral, Eq. 15 can be solved and simplified as:

$$R_{ZZ} = \sum_{m=0}^{\infty}\frac{K_m^2}{m!}R_{YY}^m \tag{16}$$

where the parameters

$$K_m = \int_{-\infty}^{\infty} t(\boldsymbol{u})H_m(\boldsymbol{u})\phi(\boldsymbol{u})d\boldsymbol{u} \tag{17}$$

To sum up the aforementioned sections, a sample of two-phase random media could be generated by the following procedures:

(1) Indentify the ratio of each phase to attain the ρ and the correlation function R_{ZZ} .
(2) Compute the R_{YY} based on Eq. 16.
(3) Utilize the stochastic harmonic functions of Eqs. 6 – 9 and the R_{YY} in step (2) in generating the Gaussian random field.
(4) Transform the Gaussina random field into the two-phase random field by Eq. 11.

4 NUMERICAL EXAMPLES

A series of simulations for the tensile failure of concrete are carried out based on the proposed methods in the former sections. The geometric sizes of the numerical specimens are $b = 150mm$, $h = 150mm$. Due to the strong nonlinearities induced by the cracking process, we choose the explicit solution algorithm to get the integration of the crack process. And the numerical specimen is developed by using the finite element package ABAQUS. Based on the previous irregular discretization method, more than 20,000 finite elements and 30,000 cohesive elements are generated. The numerical specimen and its boundary conditions are given in Fig. 4.

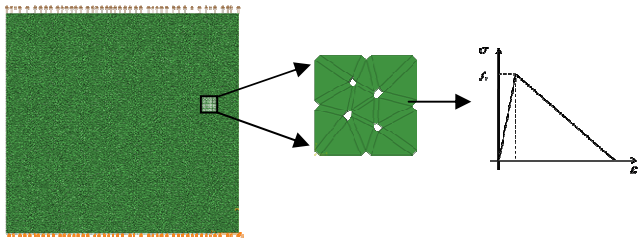

Fig. 4 The numerical model

According to the test results which proposed by Ren et al [13], the material parameters are taken to be $E = 37559MPa$ and $\nu = 0.2$. The mean value of the tensile strength of concrete is $f_t = 3.25MPa$ .The random field of fracture energy is introduced based on the methods proposed in the Section 3. With the concrete mix proportion in the test of Ren et al [13], we can back-calculate the ratio of the aggregates ρ as $\rho = 0.451$.

The autocorrelation function of the fracture energy random field $Z(x_1, x_2)$ is adopted

$$R_{ZZ}(x_1, x_2) = \sigma^2 \exp\left[-\left(\frac{\xi_1}{b_1}\right)^2 - \left(\frac{\xi_2}{b_2}\right)^2\right], \quad -\infty < x_1 < \infty, -\infty < x_2 < \infty \tag{18}$$

where ξ_1 , ξ_2 are the separation distances along the x_1 and x_2 directions respectively; b_1 and b_2 are the correlation length with $b_1 = 1$ and $b_2 = 1$.

The correlation function of the Gaussian random field is gained by Eqs. 16 - 17, where the adaptive Simpson quadrature is used to get the K_m and polynomial terms is chosen as $m = 20$. Then, the Gaussian random field is generated from Eqs. 6 – 9. The cut-off wave numbers are chosen as K_{1u}=K_{2u} $= 10\text{rad/m}$, and the numbers of component are given as $N_1 \times N_2 = 8 \times 8$. As for the two-phase random field, the fracture emery of the strong phase is chosen as $G_{f_1} = 180N/\text{m}$ and the weak phase is $G_{f_1} = 60N/\text{m}$.

Figure 5 is the average PSD of 300 samples and Fig.6 is the target PSD. It should be noted that these 300 samples are used in the simulation below, thus the statistical information will all be included.

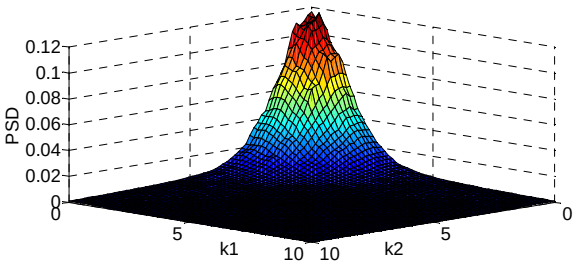

Fig. 5 Generated PSD

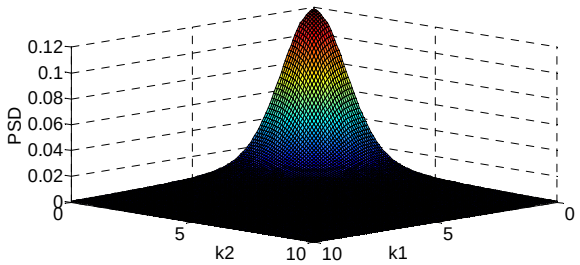

Fig. 6 Target PSD

Two concrete samples are shown in Fig. 7 to validate the procedure we present in this paper in a geometric level.

Fig. 7 Samples of the random field

Fig. 8 shows one of the random field sample (sample 112) and the corresponding simulation results. It is shown that with the multi-phase random field representation of the concrete specimens, one can clearly observe the cracks happen at the interface of each phase which is investigated by a plenty of test results.

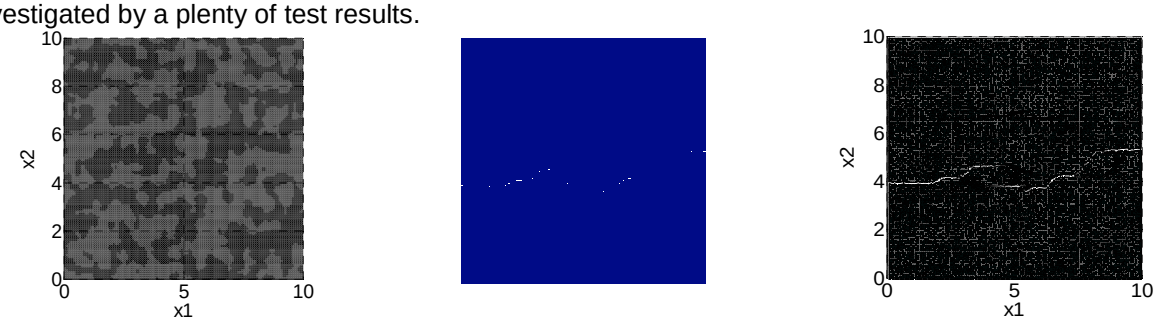

(a) Random field sample (b) Cracking process (c) cracking path at the interface

Fig. 8 Sample (sample 112) simulation result

As is illustrated in Fig. 9 the comparisons between the simulating results and the test results suggest the validation of the proposed model.

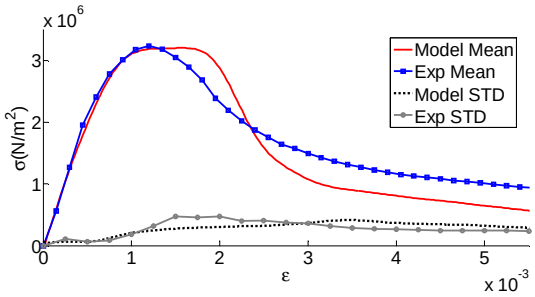

Fig. 9 Mean value and standard deviation curve for stress-strain

5 CONCLUSIONS

In this paper, the simulation of the concrete based on the multi-phase random medium model is presented. The randomness of concrete is considered in two aspects. On one hand, the random micro cracks are introduced by the irregular finite elements and cohesive elements. On the other hand, the 2-D random field of fracture energy is generated by the newly developed multi-phase stochastic harmonic functions. Then, the simulation the failure is given to testify the proposed model on the sample level and the mean and variance values of the stress-strain relationship are also given on the collective level. With the efforts of the present work, a new random medium base model for the accurate simulation of concrete is developed.

6 ACKNOWLEDGEMENT

The authors would like to acknowledge the support of National Natural Science Foundation of China (Grant Nos. 51261120374 and 51208374).

7 REFERENCE

[1] Li, J. and X. Ren, Stochastic damage model for concrete based on energy equivalent strain. International Journal of Solids and Structures, 46(11), 2407-2419, 2009.
[2] Masad, E., et al., Internal structure characterization of asphalt concrete using image analysis. Journal of computing in civil engineering, 13(2), 88-95, 1999.
[3] Garboczi, E.J., Three-dimensional mathematical analysis of particle shape using X-ray tomography and spherical harmonics: Application to aggregates used in concrete. Cement and Concrete Research, 32(10), 1621-1638, 2002.
[4] Xu, X.F. and L. Graham-Brady, A stochastic computational method for evaluation of global and local behaviour of random elastic media. Computer methods in applied mechanics and engineering, 194(42), 4362-4385, 2005.
[5] Quiblier, J.A., A new three-dimensional modelling technique for studying porous media. Journal of Colloid and Interface Science, 98(1), 84-102, 1984.
[6] Yang, Z.J., et al., Monte Carlo simulation of complex cohesive fracture in random heterogeneous quasi-brittle materials. International journal of Solids and Structures, 46(17), 3222-3234, 2009.
[7] Hillerborg, A., M. Modéer and P. Petersson, Analysis of crack formation and crack growth in concrete by means of fracture mechanics and finite elements. Cement and concrete research, 6(6), 773-781, 1976.
[8] Xu, X. and A. Needleman, Numerical simulations of fast crack growth in brittle solids. Journal of the Mechanics and Physics of Solids, 42(9), 1397-1434, 1994.
[9] Ren, X. and J. Li, Dynamic fracture in irregularly structured systems. Physical Review E, 85(5) 055102(1)-(4), 2012.
[10] Chen J B, Li J. Stochastic harmonic function and spectrum representations. Chinese Journal of Theoretical Applied Mechanics, 43(3), 505-513, 2011.
[11] Liang S X, Sun W L. Simulation of multi-dimensional random fields by stochastic harmonic functions. Journal of Tongji University (Natural Science), 40(7), 965-970(995), 2012.
[12] Jude Joseph Ilango, S., S. Sarkar and A. Sameen, Reconstruction of 2-D porous media using Karhunen-Lóeve expansion. Probabilistic Engineering Mechanics, 32(2013), 56-65, 2013.
[13] Ren X D, Yang W Z, Zhou Y, Li J. Behaviour of high-performance concrete under uniaxial and biaxial loading. ACI Material Journal, 105-M62, 548-557, 2009.

Proceedings of the 3rd International Conference on
Fracture Fatigue and Wear, pp. 148-154, 2014

BUCKLING OF FUNCTIONALLY GRADED CARBON NANOTUBE-FIBER REINFORCED PLATES UNDER MECHANICAL LOADS

B. Sobhani Aragh and M. Abdel wahab

Department of Mechanical Construction and Production, Faculty of Engineering and Architecture, Ghent University, Belgium

Abstract: Based on first-order shear deformation (FSDT), the mechanical buckling of a functionally graded nanocomposite rectangular plate reinforced by aligned and straight single-walled carbon nanotubes (SWCNTs) subjected to uniaxial and biaxial in-plane loadings is investigated. The material properties of the nanocomposite plate are assumed to be graded in the thickness direction and vary continuously and smoothly according to two types of the symmetric carbon nanotubes volume fraction profiles. The equilibrium and stability equations are derived using the Mindlin plate theory considering the FSDT effect and variational approach. A numerical study is performed to investigate the influences of the different types of compressive in-plane loadings, CNTs volume fractions, various types of CNTs volume fraction profiles, geometrical parameters and different types of estimation of effective material properties on the critical mechanical buckling load of functionally graded nanocomposite plates.

Keywords: functionally graded materials; mechanical buckling; first-order shear deformation; nanocomposite

1 INTRODUCTION

Functionally Graded Materials (FGMs) which are advanced multiphase composites and are engineered to have a smooth spatial variation of material constituents have attracted considerable attention recent years [1]. In most recent literature regarding FGM structures [2-3], the material properties are assumed having a smooth variation usually in one direction. In traditional nanocomposites, the resulting mechanical, thermal, or physical properties do not vary spatially at the macroscopic level since nanotubes distribute either uniformly or randomly in the composites. On the other hand, mechanical properties of nanotube-reinforced composites will deteriorate if the volume fraction of nanotubes arises beyond certain limit. Therefore, In the modelling of carbon nanotubes-reinforced composites (CNTRCs) the concept of FGM might be incorporated to effectively make use of the nanotubes. According to a comprehensive survey of literature, the authors found that there are few research studies on the mechanical behaviour of functionally graded carbon nonotube-reinforced composite (FGM-CNTRC) structures. Shen [4] studied the nonlinear bending of reinforced composite plate by SWCN under the sinusoidal loading in thermal environment. The results obtained indicated that the effect of FG distribution of CNTs causes increase in the moment and stress. Also Shen [5] investigated the thermal buckling of composite plate reinforced by CNT (FG distribution). The obtained results of the paper shown that the FG distribution of CNTs causes critical buckling temperature to be higher than the UD distribution of CNTs. Shen and Zhu [6] investigated the buckling and post-buckling of nanocomposite plates with functionally graded nanotube reinforcements subjected to uniaxial compression in thermal environments. The effective material properties of the nanocomposite plates were derived by the use of extended rule of mixture. They found that the linear functionally graded nano-reinforcement has a quantitative effect on the uniaxial buckling load as well as post-buckling strength of the plates.

The main objective of the present work is to investigate the buckling behaviour of the functionally graded nanocomposite rectangular plates reinforced by straight, single-walled CNTs subjected to uniaxial and biaxial in-plane loadings. The material properties of the nanocomposite plate are assumed to be graded in the thickness direction and vary continuously and smoothly according to two types of the symmetric carbon nanotubes volume fraction profiles. The equilibrium and stability equations are derived using the Mindlin plate theory considering the first-order shear deformation (FSDT) effect and variational approach. Resulting equations are employed to obtain the closed-form solution for the critical buckling load for each loading case. A detailed parametric study is carried out to investigate the influences of the different types of

compressive in-plane loadings, CNTs volume fractions, various types of CNTs volume fraction profiles, geometrical parameters and different types of estimation of effective material properties on the critical mechanical buckling load of functionally graded nanocomposite plates.

2 THEORETICAL FORMULATION

As shown in Fig. 1, a polymer rectangular plate with the length of *a*, width of *b* and the thickness of *t* reinforced by SWCNTs, graded distribution in the thickness direction, is assumed. It is also assumed that the mentioned nanocomposite plate is being influenced by plane forces N_x and N_y, which are in x and y direction respectively.

2.1 Mathematical modelling of FGM-CNTRC

In this paper, for the first time, two types of symmetric profiles for CNTs volume fractions are configurated. As can be seen from Fig. 2, for the first type, a mid-plane symmetric graded distribution of CNT reinforcements is achieved and both top and bottom surfaces are CNT-rich referred to as Type I FG. For the second type, the distribution of CNT reinforcements is inversed and both top and bottom surfaces are CNT-poor, whereas the mid-plane surface is CNT-rich, referred to as Type II FG. We assume the CNTs volume fraction for Type I FG follows as:

$$V_{CN} = \frac{4|z|}{h} V_{CN}^{*} \tag{1}$$

In which:

$$V_{CN}^{*} = \frac{w_{CN}}{w_{CN} + (\rho_{CN}/\rho_m) - (\rho_{CN}/\rho_m) w_{CN}} \tag{2}$$

Where w_{CN} is the mass fraction of nanotube [7], and ρ_{CN} and ρ_m are the densities of CNT and matrix, respectively. The CNTs volume fraction for Type II FG follows as:

$$\mathrm{V_{CN}} = 4\left(0.5 - \frac{|z|}{h}\right) V_{CN}^{*} \tag{3}$$

Note that $V_{CN} = V_{CN}^{*}$ corresponds to the uniformly distributed CNTR plate, referred to as UD. It should be mentioned that these two FG plates and the UD plate have the same CNT mass fraction.

In this paper, for estimating effective material properties of CNTRC two different methods including extended rule of mixture [7] and Eshelby-Mori-Tanaka approach [8] have been used.

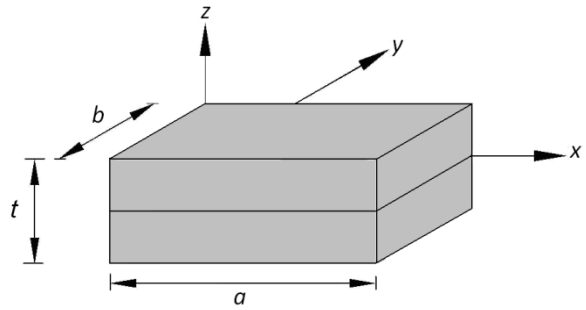

Fig. 1 Schematic of nanocomposite plate.

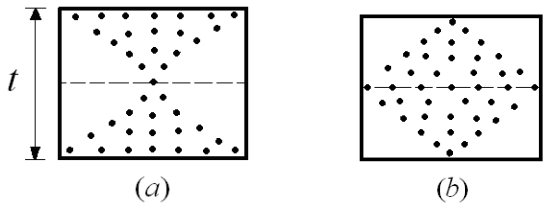

Fig. 2 Configurations of FG nanocomposite plate (Fig. (*a*): Type I FG, Fig. (*b*): Type II FG)

2.2 Equilibrium equations

According to the based on the FSDT of Mindlin [9], the displacement field of the rectangular plate is considered as

$$\begin{aligned} u(x,y,z) &= z\psi_x(x,y) \\ v(x,y,z) &= z\psi_y(x,y) \\ w(x,y,z) &= w(x,y) \end{aligned} \tag{4}$$

n which u, v and w are the displacement components in x, y and z directions respectively. ψ_x and ψ_y are also the neutral plate rotation around y and x axes, respectively.

In order to obtain the equilibrium relations, the energy method will be used. Therefore, the plate overall potential energy is written as follows:

$$V = U + \Omega \tag{5}$$

In which V is the overall potential energy, U is the elastic potential energy and Ω is work done by the external forces the relations of which are written as follows:

$$U = \frac{1}{2}\iint\int_{-t/2}^{t/2}\left(\sigma_x\varepsilon_x + \sigma_y\varepsilon_y + \sigma_z\varepsilon_z + \tau_{xy}\gamma_{xy} + \tau_{yz}\gamma_{yz} + \tau_{zx}\gamma_{zx}\right)dzdxdy \tag{6}$$

$$\Omega = \iint\left(\frac{1}{b}p_x u_{,x} + \frac{1}{a}p_y v_{,y} - p_n w\right)dxdy = \iint\left(\frac{1}{b}p_x\frac{\partial\psi_x}{\partial x} + \frac{1}{a}p_y\frac{\partial\psi_y}{\partial y} - p_n w\right)dxdy \tag{7}$$

By applying the Euler-Lagrange equations to the functional of energy, the equilibrium equations of the nanocomposite plate are obtained based on Midlin plate theory in the form below:

$$\begin{aligned} &M_{x,x} + M_{xy,y} - Q_x = 0 \\ &M_{y,y} + M_{xy,x} - Q_y = 0 \\ &\left(Q_{x,x} + Q_{y,y}\right) + \frac{\partial}{\partial x}\left(N_x\frac{\partial w}{\partial x} + N_{xy}\frac{\partial w}{\partial y}\right) + \frac{\partial}{\partial y}\left(N_{xy}\frac{\partial w}{\partial x} + N_y\frac{\partial w}{\partial y}\right) = 0 \end{aligned} \tag{8}$$

In which N_{ij} and M_{ij} are the forces and the resultant moments.

2.3 Stability equations

We give small increments to the displacement and rotation variables and examine the two adjacent configurations represented by the displacements and rotations before and after the increment, as follows:

$$\begin{aligned} \psi_x &\to \psi_{x0} + \psi_{x1} \\ \psi_y &\to \psi_{y0} + \psi_{y1} \\ w &\to w_0 + w_1 \end{aligned} \tag{9}$$

In which the subscript 0 indicates the equilibrium state and the subscript 1 expresses a minute change in the plate equilibrium condition.

By substituting the aforementioned relations into the equilibrium equations and applying the following assumptions; the linear stability equations will be obtained in the form of the Eq. (10).

1) w_0 and all its derivatives are zero.
2) The expressions conclude the N_{i0}, M_{i0} and Q_{i0} indicate the initial equilibrium condition and should be eliminated.
3) The expressions consists of multiplying the (Q_{i0}, M_{i0} and N_{i0}) in (w_{i0}, ψ_{x0} and ψ_{y0}) are negligible and should be eliminated.

$$M_{x1,x} + M_{xy1,y} - Q_{x1} = 0$$
$$M_{y1,y} + M_{xy1,x} - Q_{y1} = 0$$
$$\left(Q_{x1,x} + Q_{y1,y}\right) + \frac{\partial}{\partial x}\left(N_{x0}\frac{\partial w_1}{\partial x} + N_{xy0}\frac{\partial w_1}{\partial y}\right) + \frac{\partial}{\partial y}\left(N_{xy0}\frac{\partial w_1}{\partial x} + N_{y0}\frac{\partial w_1}{\partial y}\right) = 0 \quad (10)$$

It has been assumed that the forces are N_x and N_y in x and y directions respectively and their relation is $N_y=\gamma N_x$ (Fig. 3).By applying plate boundary condition and regarding that N_x and N_y are the plane forces per unit length applied on the plate edges one would get:

$$N_x = -\frac{p_x}{a} \qquad N_y = -\frac{p_y}{b} \quad (11)$$

$$-k\left(G_{12a} + G_{12d}\right)\left(\psi_{x1,x} + w_{1,xx} + \psi_{y1,y} + w_{1,yy}\right) - \frac{p_y}{a}w_{1,yy} - \frac{p_x}{b}w_{1,xx} = 0 \quad (12)$$

In which P_x and P_y are the total imposed forces on the plate in the direction of x and y respectively. By solving Eq. (12) the critical buckling can be obtained.

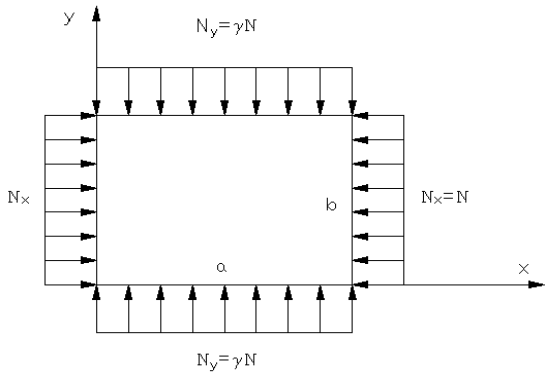

Fig. 3 Nanocomposite rectangular plate reinforced by SWCNTs under the plane forces in *x* and *y* directions ($N_x=N$, $N_y=\gamma N_x$)

3 RESULTS AND DISCUSSION

For more explanation we choose the loading of plate as follows:

1) Plane loading in the x direction.
2) Plane loading in the y direction.
3) Plane loading in the x and y directions.

For uniaxially compressed nanocomposite plate (sections 3.1 and 3.2), the extended rule of mixture is used for predicting the overall material properties and responses of the plate, while for the case of biaxial in-plane loadings (section 3.3), effective elastic moduli are computed by using Eshelby-Mori-Tanaka approach. The material properties and effective thickness of SWCNTs used for the present analysis properly are selected according to the MD simulation results of Shen [6].

3.1 Loading of plate only in *x* direction

In this section, nanocomposite rectangular plate is subjected to a uniform compressive load on edges $x=0$ and $x=a$. Figs. 4 shows the critical load versus the aspect ratio of *a/b* with different CNTs volume fractions and various types of CNTs volume fraction profiles. From Fig. 4, it is concluded that the critical buckling load of various types of CNTs volume fraction profiles become larger when the CNTs volume fraction increases. Another important result of Fig. 4 is that the influence of the CNTs volume fraction on the critical buckling load for different types of CNTs profiles is generally significant at high aspect ratio of *a/b*.

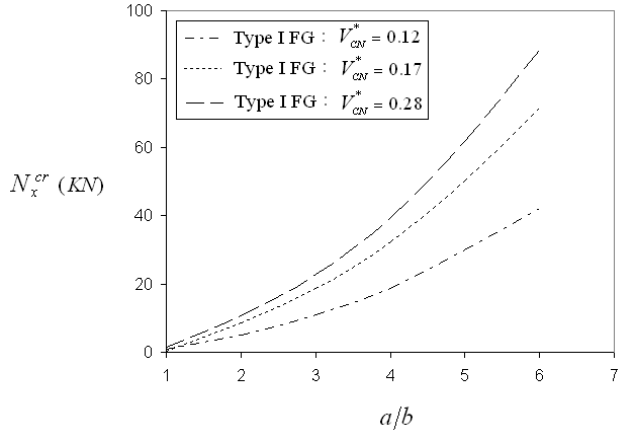

Fig. 4 Critical load $(N_x)_{cr}$ in the case of Type I FG distributed SWCNTs for various values of *a/b* (*t/b* =0.1, N_y=0)

3.2 Loading of plate only in the *y* direction

Critical buckling loads of the nanocomposite plates subjected to uniaxial in-plane loading ($N_x = 0$) are listed in Table 1 for various aspect ratio of *a/b*. It can be concluded from Table 1 that the increase of the CNTs volume fractions yields an increase in the critical buckling load. The variation of the critical buckling load versus the aspect ratio of t/b for various types of CNTs volume fraction profiles is shown in Fig. 5 for $V_{CN}^{*} = 0.12$. The results in Fig. 5 indicate that discrepancy among the various types of CNTs profiles increases with the increasing values of the aspect ratio of t/b.

Table 1 Critical buckling load N_y^{cr} (*KN*) for various types of CNTs volume fraction profiles versus *a/b* (*t*=5mm, N_x=0)

	Type I FG			**UD**			**Type II FG**		
a/b	V_{CN}^{*} =0.12	V_{CN}^{*} =0.17	V_{CN}^{*} =0.28	V_{CN}^{*} =0.12	V_{CN}^{*} =0.17	V_{CN}^{*} =0.28	V_{CN}^{*} =0.12	V_{CN}^{*} =0.17	V_{CN}^{*} =0.28
1	1.1034	1.4863	1.7067	0.9977	1.1573	1.5010	0.9011	1.0052	1.3893
2	1.2112	1.5258	1.8264	1.1143	1.2887	1.6999	1.0021	1.1362	1.6012
3	1.4396	1.8253	2.0875	1.2667	1.5014	1.9053	1.1743	1.3999	1.8111
4	1.7649	2.1002	2.3209	1.4909	1.8319	2.1876	1.5196	1.6243	1.9903
5	2.1574	2.5000	2.6999	1.8387	2.3190	2.4372	1.7784	2.1842	2.3732
6	2.5649	2.9742	3.2370	2.2989	2.6823	2.9074	2.1635	2.4987	2.8222

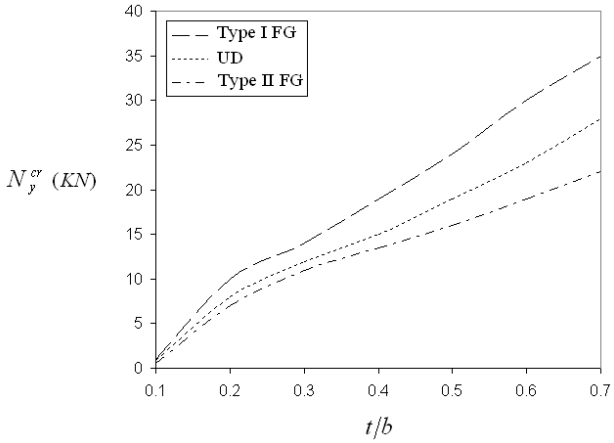

Fig. 5 Critical load $(N_y)_{cr}$ against the aspect ratio *t/b* for various types of CNTs volume fraction profiles (*a/b*=1, N_x=0, $V_{CN}^{*}=0.12$)

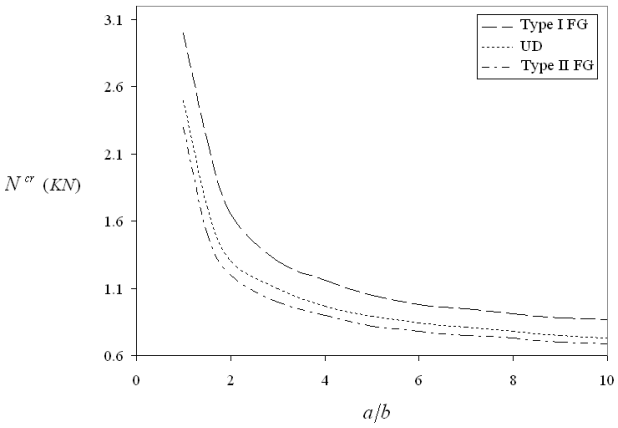

Fig. 6 Influence of different types of CNTs volume fraction profiles on critical buckling load against aspect ratio *a/b* (*t/b* =0.1, *γ*=1, $V_{CN}^{*}=0.12$)

3.3 Loading of plate in *x* and *y* directions

In this section we consider two axial loading of plate (N_x and N_y) and their relation is $N_x=\gamma N_y$. Also the material properties of the FGM nanocomposite plate are assumed to be graded in the thickness direction and estimated though the Eshelby-Mori-Tanaka approach. Influence of different types of CNTs volume fraction profiles on critical biaxial buckling load against aspect ratio *a/b* and *t/b* is presented in Figs. 6 and 7 for $V_{CN}^{*}=0.12$. It is worthy of mention that critical biaxial buckling load of the Type II FG nanocomposite plate is lower than that of one with symmetric profile (Type I FG) and close to that of the uniformly distributed CNTs. It is seen that as the aspect ratio *a/b* increases, the critical biaxial buckling load mainly decreases, while an inverse behaviour is experienced for critical uniaxial buckling load. In addition, it is found that the critical biaxial buckling load increases rapidly with increasing the aspect ratio *t/b* and then remains almost unaltered for $t/b>0.5$.

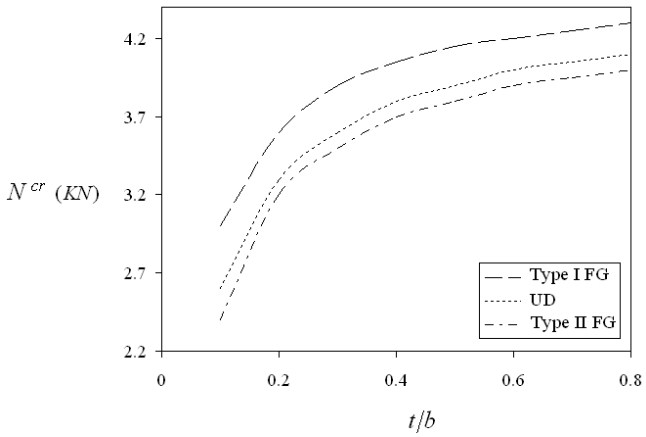

Fig. 7 Influence of different types of CNTs volume fraction profiles on critical buckling load against aspect ratio *t/b* (*a/b* =1, *γ*=1, $V_{CN}^{*} = 0.12$)

4 CONCLUSIONS

In this research work, buckling analysis of functionally graded nanocomposite rectangular plates reinforced by aligned and straight single-walled carbon subjected to uniaxial and biaxial in-plane loadings was investigated. In order to equilibrium and stability equations of the rectangular plate under in-plane load, the analysis procedure was based on the Mindlin plate theory considering the first-order shear deformation effect. Resulting equations were employed to obtain the closed-form solution for the critical buckling load for each loading case. The effective material properties of the nanocomposite plate were assumed to be graded in the thickness direction and estimated by either the Eshelby-Mori-Tanaka approach or the extended rule of mixture. Two types of the symmetric carbon nanotubes volume fraction profiles were presented in this paper. It is observed that as the aspect ratio a/b increases, the critical biaxial buckling load mainly decreases, while an inverse behaviour is experienced for critical uniaxial buckling load. Moreover, it is found that the critical biaxial buckling load increases rapidly with increasing the aspect ratio *t/b* and then remains almost unaltered for $t/b > 0.5$.

5 REFERENCES

[1] M. Koizumi, FGM activities in Japan. Compos Part B-ENG 28, 1997, 1–4.
[2] D.P.H. Hasselman, G.E. Youngblood, Enhanced Thermal Stress Resistance of Structural Ceramics with Thermal Conductivity Gradient, J. Am. Ceram. Soc. 61, 1978.
[3] Z.S. Shao, T.L. Wang, Three-dimensional solutions for the stress fields in functionally graded cylindrical panel with finite length and subjected to thermal/mechanical loads, Int. J. Solids Struct. 43, 2006, 3856–3874.
[4] H.S. Shen. Nonlinear bending of functionally graded carbon nanotube-reinforced composite plates in thermal environments. Composite Structures 2009;91:9-19.
[5] H.S. Shen, C.L. Zhang. Thermal buckling and post buckling behaviour of functionally graded carbon nanotube-reinforced composite plates. Materials and Design 2010;31:3403-11.
[6] H.S. Shen, Post-buckling of nanotube-reinforced composite cylindrical shells in thermal environments, Part II: Pressure-loaded shells. Composite Structures 93; 2011, 2496–2503.
[7] H.S. Shen and Z.H. Zhu, Buckling and Post-buckling Behaviour of Functionally Graded Nanotube-Reinforced Composite Plates in Thermal Environments, CMC 18, 2010:2;155-182.
[8] B. Sobhani Aragh, H. Hedayati, Eshelby-Mori-Tanaka approach for vibrational behaviour of continuously graded carbon nanotube-reinforced cylindrical panels. Composites: Part B 43, 2012, 1943–1954.
[9] R.D. Mindlin, Influence of rotatory inertia and shear on flexural motions of isotropic elastic plates, American Society of Mechanical Engineers Journal of Applied Mechanics:1951, 18:31-38.

Proceedings of the 3rd International Conference on
Fracture Fatigue and Wear, pp. 155-160, 2014

ANALYZING STRESS INTENSITY FACTOR AND T-STRESS BY STRESS DIFFERENCE METHOD (SDM) IN ARC OF GAS PIPELINE

Alfred Hasanaj*, Alvin Asimi and Mentor Balilaj

Polytechnic University of Tirana, Albania
*Corresponding author: alfred.hasanaj@yahoo.com

Abstract: In crack tips, corners and material interfaces are locations, where mostly singular stress occurs. In order to determine the evolution of T-stress for arc pipeline specimen with external surface crack, we use Finite Element Analysis (FEA). In order to calculate the T-stress near the crack tip, we use Stress Difference Method (SDM). Also, the other geometrical crack parameters are analyzed including length-to-thickness parameters. Measuring stress difference is the best method to be used in order to define the stress parameters near the arc of pipe.

Keywords: T-stress; stress intensity factor; stress difference method; finite element analysis

1 INTRODUCTION

In this paper, we analyze the T- stress as a fracture parameter to study the effects of different loading and structural configurations on the crack tip. This test can be concluded even if we do not know the significant physical parameters. Therefore, we need to simplify higher term parameters in order to correlate its effects on the appropriate physical parameter. This constant stress value acts in the same line with crack and its magnitude goes in proportion to the nominal stress. T- stress serves as a key element in defining and analyzing crack evaluation, its direction, stability and giving hints about the fracture toughness. Crack direction is becoming one of the most important points for studying, discussing and determining the path of a crack. With the identification of the path, we can take measures in advance to stop its evolution.

Plain strain crack is depended by the sign and magnitude of T-stress, when it is found under finite load levels. When we have $T > 0$, the crack will continue to diverge from its main direction. Also, the fracture toughness depends on the size and geometrical parameters of the cracked body. As we already have mentioned, T-stress is used to determine the arc tip direction on the pipe. In the arc, there are several methods, which can be applied to determine the T-stress. In order to determine the T-stress, we either use simple geometric methods or complicated mathematical numerical tests.

In this paper, we will use the Stress Difference Method (SDM), i.e. a numerical approach, to determine T-stress effectively and accurately, focusing on a point just in front of crack tip by evaluating (σ_{xx}-σ_{yy}). This difference should be as small as possible in order to eliminate in an effective way the errors, which may occur along the crack tip with a parameter denoted as r.

2 FINITE ELEMENT MODELING

In order to avoid miscalculation, we use a half arc tube as shown in Fig. 1. Dimensions of specimen are given in Table 1. This tile Roman structure is a symmetric one. In order to determine the evolution of T-stress and the intensity stress factor, Kρ, we use the Stress Difference Factor (SDM), at a distance r starting from the tip of the notch.

The variation of T-stress and Kρ, for a defect in external surface defect taken at the deepest point are obtained for different ratios (a/t). Geometrical parameters of the applied load and specimen dimensions are shown in Fig. 2.

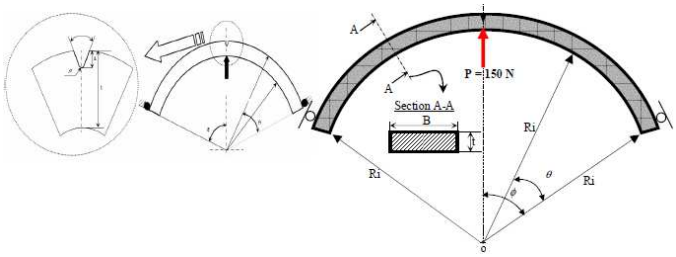

Fig. 1 Specimen in Arc Hose

Table 1 Dimensions of specimen

Ri (mm)	P (N)	Φ (°)	Θ (°)	φ (°)	ρ (mm)	a(mm)	t(mm)
163.5	150	60	60	45	0.15	1.22-4.88	8

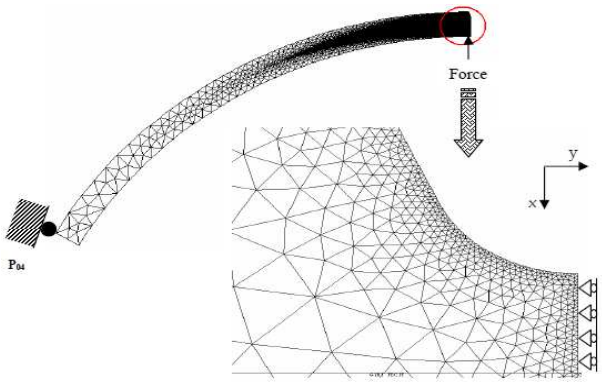

Fig. 2 Mesh specimen finite element (a) the expansion of mesh bottom of the notch and (b) full mesh structure

For the two main directions σ_{xx} and σ_{yy} the stress distribution is shown in Fig. 3(a). In this direction the opening stress σ_{yy} is the dominant one. In this figure we see two zones the first one is tension and the second is compression. In Fig. 3(b), the separation of these two zones by neutral axes is shown.

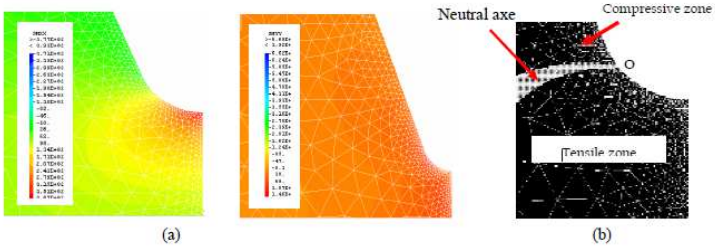

Fig. 3 Distribution of stresses σ_{xx} and σ_{yy} and identifying areas of compression and tension

3 RESULTS AND INTERPRETATIONS

For a three dimensional crack subjected to a symmetric loading, the stress can be written as William's development. Terms of higher order series developments near the crack tip due to constraints are negligible. The for the mode I can be written as follows:

$$\sigma_{xx} = \frac{K_I}{\sqrt{\pi r}} \cdot \cos\frac{\theta}{2}\left(1 - \sin\frac{\theta}{2}\sin\frac{3\theta}{2}\right) + T \qquad \sigma_{zz} = \frac{K_I}{\sqrt{\pi r}} \cdot 2\vartheta \cos\frac{\theta}{2} + E \cdot \varepsilon_{zz}$$

$$\sigma_{yy} = \frac{K_I}{\sqrt{\pi r}} \cdot \cos\frac{\theta}{2}\left(1 + \sin\frac{\theta}{2}\sin\frac{3\theta}{2}\right) + T \qquad \sigma_{Xy} = \frac{K_I}{\sqrt{\pi r}} \cdot \sin\frac{\theta}{2}\cos\frac{\theta}{2}\cos\frac{3\theta}{2}$$

$$\sigma_{Xz} = \sigma_{yz} = 0 \qquad (1)$$

Normal and share stress are localized at the tip notch stress with x,y and z suggest Cartesian coordinate stress, the symbols r and θ are local polar coordinates shown in Fig. 4 and E is Young's modulus.

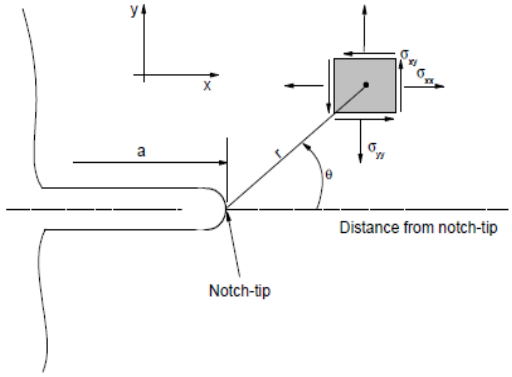

Fig. 4 Cartesian coordinates (x, y) and polar (r, q) to the tip of a notch

For a ratio a/t =2 shown in Fig. 5, T-stress is given as an example of the effect of the depth of the flaw. These results are influenced by errors provided by the finite element analysis, which are affected by the areas, which have high stress field. In the equation of Williams higher terms are found all over the ligament length. In Figs. 6 and 7 present T-stress and Kρ calculations, respectively. Each of the singular terms (a/t), which is fixed, vanishes, then begins to decrease as a fcuntion of the tip notch, after stabilization. Function of the flattering is the stabilization plate.

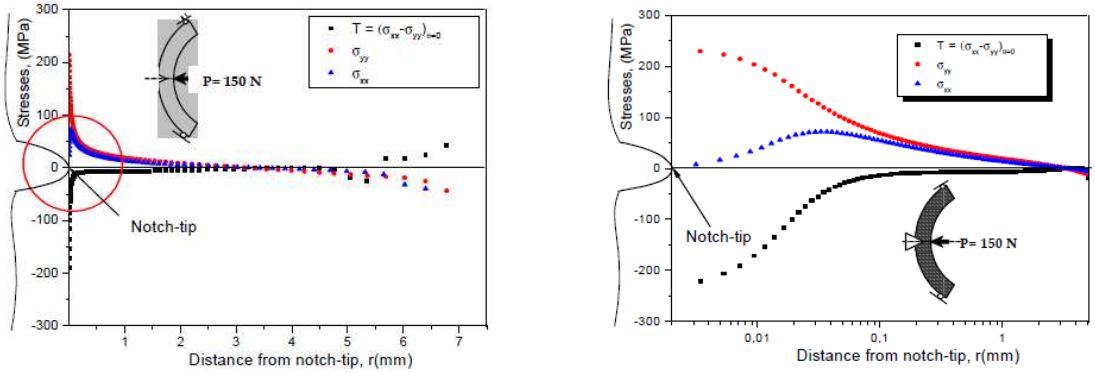

Fig. 5 Evolution of various constraints, (a) a / t = 0.2. (b) Details of (a)

When we have r <0.1 mm, T-stress increases as the ratio (a/t) increases to maximum value, and then decreases. Near the tip of the notch, the T-stress increases with the growth of ratio (a/t) to a maximum value and then decreases. The first singular term is a sensitive in all cases. In Fig. 6(a) and 6(b), the results for three most important key zones are given:

1) Zone I, difference constrain method gives a constant value of the constraint T (zone I). Tip of the notch is controlling this zone.
2) Zone II, the evolution of the T-stress is proportional to $r^{-0.5}$.

3) Zone III, T has a linear change with distance from the ligament. Distribution tends to give stable values for short slits a/t ≤ 0.2, found very close to the tip of the notch. In the situation where a/t> 0.2, the negative T-stress, is stabilized away from the tip of the notch.

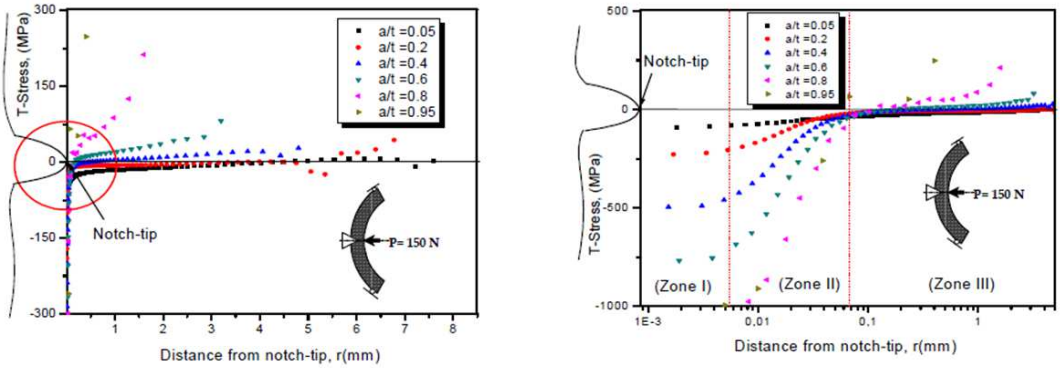

Fig. 6 evolution of the stress along the ligament T near the tip of the notch; (a) & (b) for different ratios (a/t)

In Fig. 7, the results of the intensity factor constraints (IFC) obtained from the three-point bending loading condition are shown. Variations of SIF demonstrate that changes with the length of the ligament are not monotonic. The analysis shows that this two-dimensional distribution can be characterized by three regions: the first is close to the tip of the notch (0 <r <r max), where the values are practically constant SIF (for the report / t = 0.2) and / or increases to a maximum value K_I^{max} (for a / t> 0.2); the second intermediate zone located between the first and the third is simulated with unknown constraints and can be described by an approximate linear dependence.

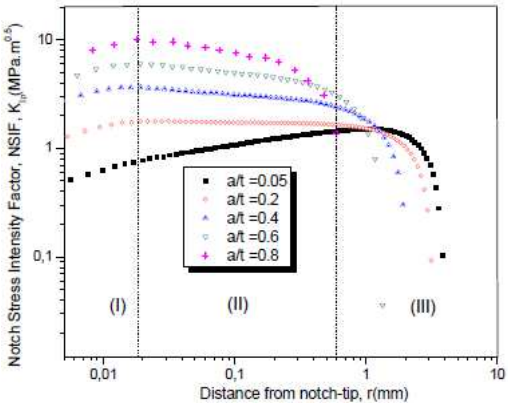

Fig. 7 Evolution of Stress Intensity Factor notch along the ligament for different depths

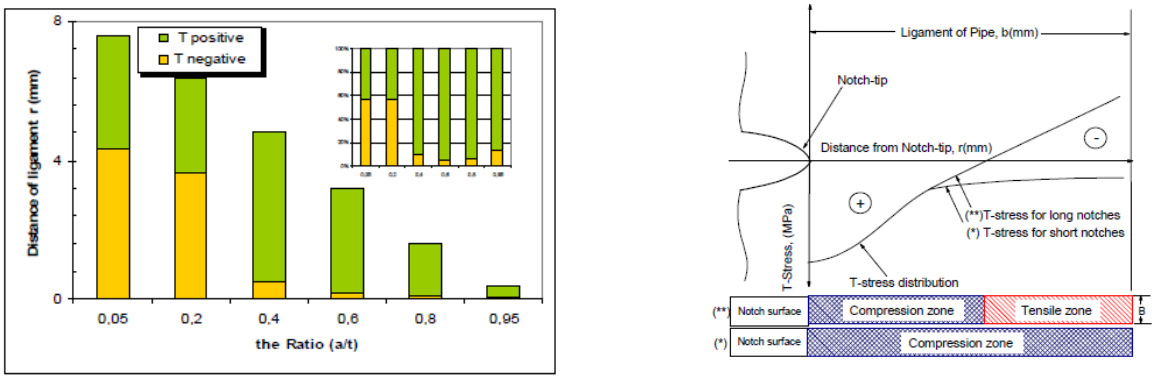

a) b)

Fig. 8 Diagram of sign change for different ratios (a/t)

Figure 8 shows that, for a short incision (a / t ≤ 0.2), in a dominant mode I loading, the T-stress is negative (compression under ligament). A crack, which starts from notch, normally evolves in the main direction. As a result, for the long cuts when a/t> 0.2, the transition from negative values to positive values changes quickly resulting in a crack deviation from its main direction. In such a case, the crack path is not a stable one. Change of the value of T-stress from negative to positive value can take a certain amount of time, depending on the size of crack, and time increases with the increase of the cut depth. As a result, the T changes with a notch depth under load bending, when it is in conditions of flexure.

When T-stress decreases slowly with the increase of the crack depth, it becomes positive afterwards. In the flat areas, values change rapidly from negative to highly positive. These results show that the characteristics of crack evolvement depend on the conditions of the geometric load of the test specimen. As a result, the stabilization phenomenon for the direction of the evolvement of the crack, is influenced by the overall situation of stresses in the specimen.

4 DISCUSSION

In order to analyze the T-stress distribution along the ligament we introduce three different zones: a) points near where T is the first constant region; b) points where T is proportional to $r^{-0.5}$ and c) a remote zone.

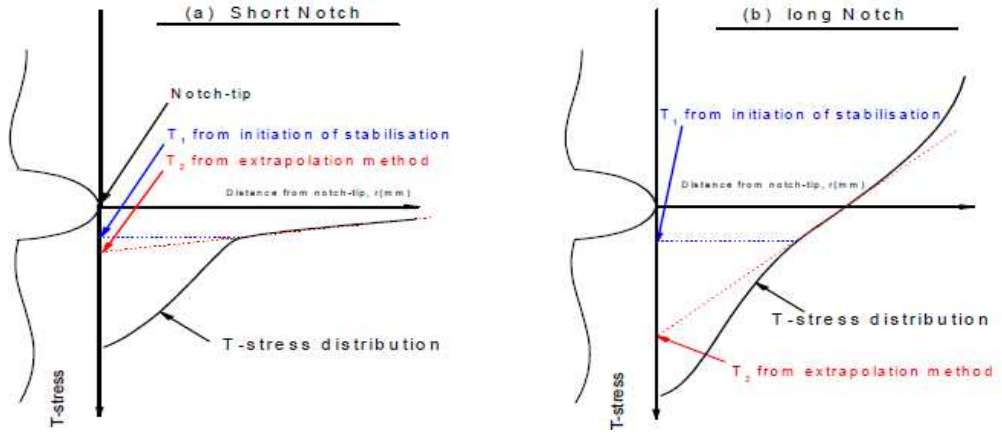

Fig. 9 T-stress versus disntance for short and long notches

For a distance of 0.25 mm, stress distribution acts in two ways. For short cuts, we have hidden stability, whereas for long distances this stability is not recognized. In Fig. 9, two methods to extract schematic constraints are shown with schematic representation. Stabilization of the first curve along the ligament is denoted as T1, and the second extrapolation curve is denoted as T2. Both methods show distinct values when the depth of the crack increases. These methods are demonstrated for short cuts and long cuts. Similar values are gained by both methods when we have short cuts, however for long cuts there are major differences in deviations.

The difference method is not the appropriate constraint method in the case of arc tube in three-point bending when we have a notch. This method is used to provide stabilization for certain distances from the tip, which cannot be the case for distances with different reference points. Further work will be continued to define T-stress distribution for other specimens and new methods will be used.

5 CONCLUSIONS

In conclusion, in order to define the impact of the t-stress on the crack tip, we have used finite element analysis, which suggest that with the increase of the stress, the crack direction increases. Also three zones near the crack tip show different results, when we analyze crack direction and crack depth. It is easy to predict the short cuts using t-stress analysis comparing to long cuts. For long cut, the direction of crack deviates from the point of the crack tip notch.

6 REFERENCES

[1] Adib. R. Theoretical and numerical aspects of the volumetric approach for fatigue life prediction in notched components, International Journal of fatigue 25, 2003, P: 67- 76.

[2] M. Hadj Meliani, H. Moustabchir, Z. Azari (2006). A modified stress difference method (MSDM) of T-stress on mode I loading. Séminaire EMMA 2006 "les nouveaux défies de la mécanique et desmatériaux". 11 May 2006, Université de Metz. France.

[3] Adib. R. Theoretical and numerical aspects of the volumetric approach for fatigue life prediction in notched components, International Journal of fatigue 25, 2003, P: 67- 76

[4] M. Hadj Meliani, H. Moustabchir, Z. Azari (2007). T-stress to predict the directional stability of crack propagation in arc of pipeline with internal pressure. Congrés Algérien de Mécanique de Construction (CAMC'07). Alger 29-30 Avril 2007.

[5] Williams JG. Ewing PD (1972). Fracture under complex stress—the angled crack problem. Int J Fract; 8(4): 416–41.

[6] Wang, X, Bell, R. Elastic T-stress solutions for semi-elliptical surface cracks infinite thickness plates subject to non-uniform stress distributions. Engng Fract Mech. 2004, 71, 1477.1496.

[7] Jayadevan, K.R, Thaulow, C, Østby, E, Berg, B, Skallerud, B, Holthe, K, and Nyhus, B. Structural integrity of pipelines: T-stress by line-spring. Fatigue Fract Engng Mater Struct 28, 2005, 467-488.

[8] Yang, B. Ravi-Chandar, K. Evaluation of elastic T-stress by the stress difference method. Engng Fract Mech. 1999, 64:589-605.

[9] Hutar P. Seitl S. K Knésl Z. Quantification of the effect of specimen geometry on the fatigue crack growth response by two-parameter fracture mechanics. Materials Science and Engineering A. 387-389 (2004) 491-494.

[10] R. M. Andrews “An analysis of fracture under biaxial loading using the non-singular T-stress.” Fatigue Fract. Eng. Mater. Struct. 23. 53–62 (2001).

[11] Parks. D.M. “Small-scale yielding analysis of mixed plane strain crack problem.” in: Fracture Analysis (ASTM STP 560). Philadelphia (1974). pp.

[12] Taylor D, Wang G. the critical volume method in fatigue analysis. Actes de ‘NATO Advanced Research Workshop on Notch Effects in Fatigue and Fracture. Pluvinage G., Gjonaj M. éditeurs, pp.187-205, Durres, Albania, 2000.

[13] Martin S. (2002) .The influence of the T -stress on the directional stability of cracks. Int J Fract; 114(3): 259 .65.

[14] k. Zerbst. Elastic-Plastic Mixed Mode Fracture Criteria and Parameters. Springer. Berlin (2003). ANSYS V5.4. User’s Manual. Swanson Analysis Systems Inc. USA (1994).

[15] Kujawski D. Estimation of stress intensity factors for small cracks at notches. Fatigue Fract Engng Mater Struct 1991;14:953–90.

Proceedings of the 3rd International Conference on
Fracture Fatigue and Wear, pp. 161-168, 2014

FATIGUE AND FRACTURE IN RAILROAD KEY PRODUCTS

H. Sakamoto

Kochi University of Technology, Japan

Abstract: Railroad products suffer fatigue since they are used in a condition of cyclic loading when railroad vehicles run. Key products are the most important mechanical parts, which are wheels, axles, discs, and truck frames. They are such failed-out components as can cause fatal failure of vehicles, when the components fail. Among such components, wheels and axles are the most critical railroad components, since they can cause derailment when fractured. Tremendous efforts have been devoted to research and development in the area of railroad industry. However, the accident of German railroad in 1998 clarified that we need to study more deeply. Fracture mechanics are now used as ordinary tools to apply to design products, and knowledge of fatigue characteristics is common. However, accidents seem to be never stopped. This paper summarizes how railroad products in Japan were developed using knowledge of fatigue characteristics and fracture mechanics, and considers the future research. The issues are whether fatigue limit exists based on scientific explanation, whether retardation of crack extension can happen with appropriate ground, and whether a crack extends under large compressive cyclic loading. The author had been engaged in this area for more than 40 years, and the summary adding such experience is explained.

Keywords: railroad vehicle products; fatigue; fracture mechanics; wheel; axle; disc; truck frame

1 INTRODUCTION

Railroad vehicle components are critically failed-out ones that may cause derailment. Especially, wheels, axles, discs, and truck frames need to be carefully designed and inspected. In the last quarter of 20th century, the aircraft, Boeing 747, accident caused more than 500 casualties in 1985 [1]. As for the case of aircrafts, design has been conducted by damage tolerance design philosophy. The cause of the accident was insufficient inspection. In 1998, German express train (ICE-Intercity Express) derailed [2], and brought death of more than 100 people. According to the report [3], the failed wheel tire (ring like part fitted outside of wheel centre) had not been inspected as for the tire inside. In order to avoid such an accident, critical vehicle components need to be carefully designed and inspected. Since such components suffer cyclic loading, state of the art in fatigue and fracture mechanics should be considered. Fracture mechanics have been a tool to evaluate causes and influencing factors for fracture. Today, fracture mechanics became to play an important role to design products. In this paper, examples of axle, truck frame, wheel, and disc are explained. Two cases are paid attention to fatigue and two to fracture. Since products produced by the knowledge of mechanical engineering are not almighty, inspection is highly important.

2 FATIGUE AND FRACTURE MECHANICS IN RAILROAD PRODUCTS AND DEVELOPMENT

2.1 Induction hardened axes for bullet trains

In 1964, bullet trains, Shinkansen, started the revenue service in Japan, and no fatal accidents have happened since then. Although the original induction hardened axles had been used since the inauguration, the method of induction hardening was changed from 10 kHz to 3 kHz hardening frequency in 1971. The author was the technical stuff at that time under the guidance of managers. The reason of induction hardening frequency change is to obtain deeper hardened layer and more safety. The method is induction heating by coils moving downward and water spray right after heating. Fig. 1 shows the facility, and explains the schematic method and hardened layer. The coils are multi-turn ones, and the axle is putted at the vertical position. The characteristic of the induction hardening is the high hardness and residual stress at the surface. Such a large compressive stress state of –500 to –600 MPa makes the crack propagation

rate greatly small, and it is expected that the crack will not propagate in such a layer. For the 200 mm diameter size axle such as the one of Shinkansen, the axle can possibly fracture when the crack depth deepens more than 100 mm. This is the estimated value from the fracture toughness of axle steel and assumed applied stress. The material for axles is medium carbon steel of about 0.40% carbon content. Japanese Railway companies apply a sever inspection system, and the crack depth of even 0.15mm, which is three order small depth, is not permitted. The inspection system[4)] for medium frequency induction hardened axles in Japanese Railway companies is as follows. General inspection is conducted monthly or after 30,000 km running ($1.05x10^7$ axle rotation). At the general inspection, cracks are detected by ultrasonic wave methods. Such inspection is made as the axles on the wheel seat, which means without removal of wheels from axles. The accuracy of detection is 3 mm for solid axles and 1 mm for hollow axles. According to the report [4], no cracks of the length 1-3 mm had been found in the past. More severely, axles are inspected by magnetic particle method [5,6] to detect around 0.15 mm depth crack. The inspection is conducted as truck inspection, which is every 18 months or after 600,000 km running ($2.1x10^8$ axle rotation). Moreover, the total inspection is made every 3 years or after 1,200,000 km running ($4.2x10^8$ axle rotation). The inspection is made by removing wheels from axles to detect very fine cracks of around 0.15 mm depth. When cracks of more than 0.15 mm depth are found, such axles are out of order. Such fatigue strength of axles is the issue of fretting fatigue. Regarding fretting fatigue, tremendous papers have been published, and still some issues such as crack propagation under large compressive load and threshold strength of crack initiation with statistical consideration are desired to be clarified.

The author wanted to describe the sever inspection by Japanese Railways to show how Japanese Railways are sensitive to maintain the security of railroad. This tells how the maintenance is of great importance. The cases of the crash of Boeing 747 and the German ICE accident are not well secured due to careless maintenance. The possibility of fine crack extension under large compressive stress state was studied. Using a rectangular specimen, compressive cyclic fatigue testing was conducted with exaggerated stress cycle. The normal stress cycle is ±60 MPa during one axle rotation. Counting the large compressive stress by induction hardening, the stress cycle for testing and analysis was decided to be 0~-500 MPa. Fig. 2 shows the specimen and fatigue test result, and Fig. 3 shows the result of calculation. This tells that large compressive stresses by induction hardening with ±60 MPa makes crack propagation extremely slow.

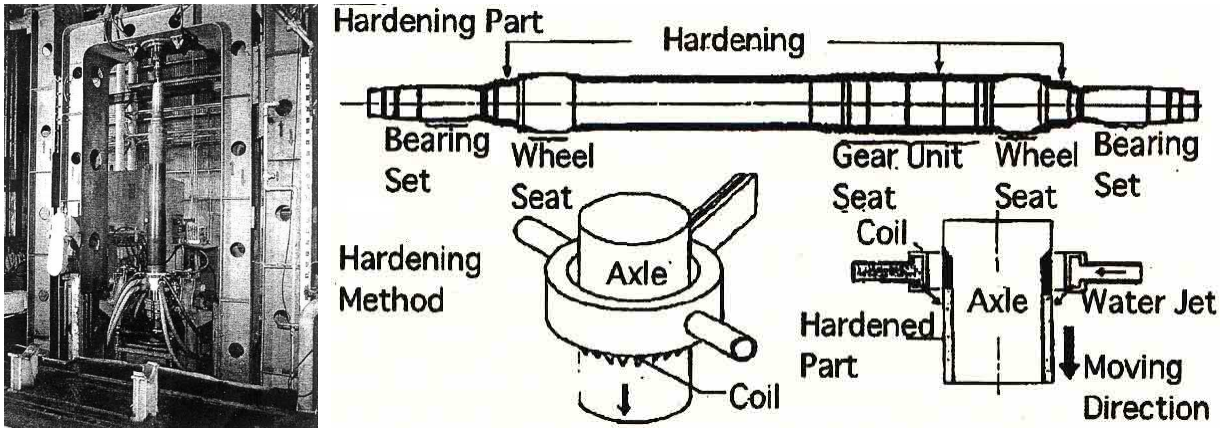

Fig. 1 Induction hardening for axles [4], facility (left), coil and hardened layer (right)

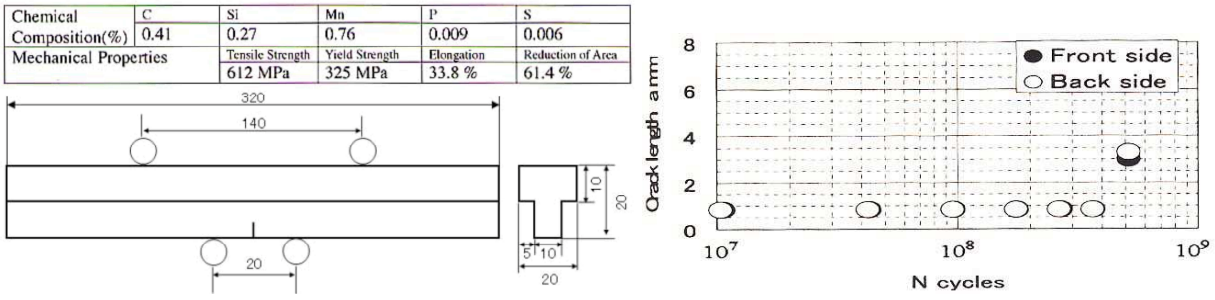

Fig. 2 Compressive cyclic fatigue testing, specimen (left), results for 0~-500 MPa cycle (right)

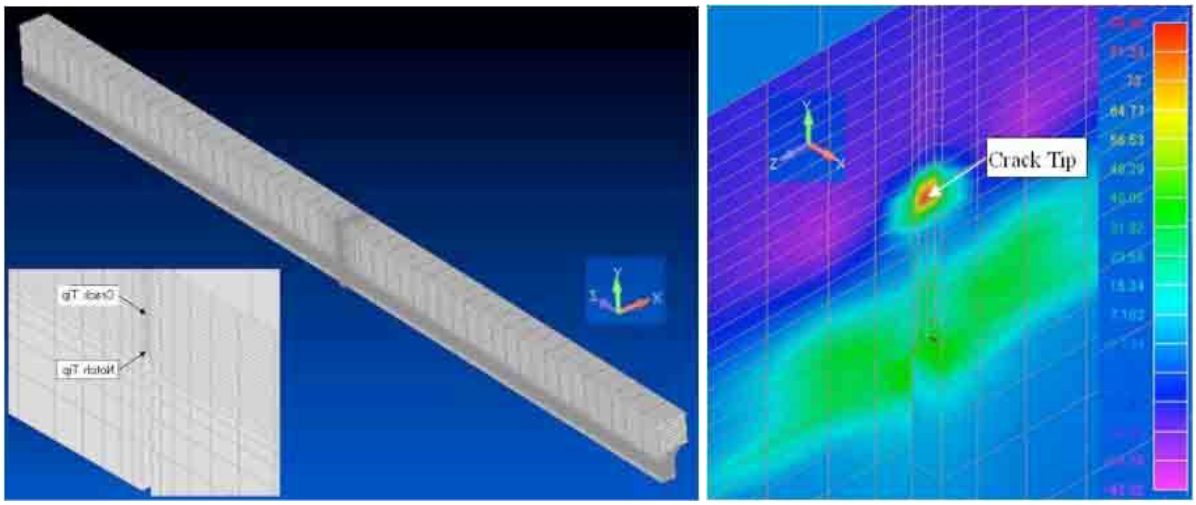

Fig. 3 Compressive stress analysis, mesh of 1/2model (left), result showing tensile stress (right)

2.2 Aluminium and FRP jointed truck frame

The conventional material of truck frame is a structural steel such as SS400 and SM 400 in Japan as the Japanese Industrial Standard [7]. For high-speed trains, light-weighted truck frames are of great importance. A trial truck frame of rectangular FRP tubes and aluminium fabricated structure was produced. FRP tubes used are pultruded ones considering the fabrication price for FRP products. The article [8] describes the design, analysis of beam theory and bolted aluminium joint, manufacture of the structure, and static and fatigue tests. The fatigue test was conducted using a test rig, and the result clarified that the fatigue crack originated and propagated at the location where it was not able to expect from the stress analysis. Fig. 4 left shows the fabricated truck frame consisting of rectangular FRP tubes and aluminium joint parts. The design of all aluminium truck frame was also tried to be made based on the fatigue design standard such as British Standard 8118 [9], which is shown in Fig. 4 right. However, as shown in Fig. 4 right, the categories consisting of 9 classes are complicated to judge the strength at each portion. As will be explained in the next chapter, categories should be preferably as few as possible like JIS 4207 [10] for the railroad truck frame design guidance. Fig. 5 shows the example of fatigue test result and failed part.

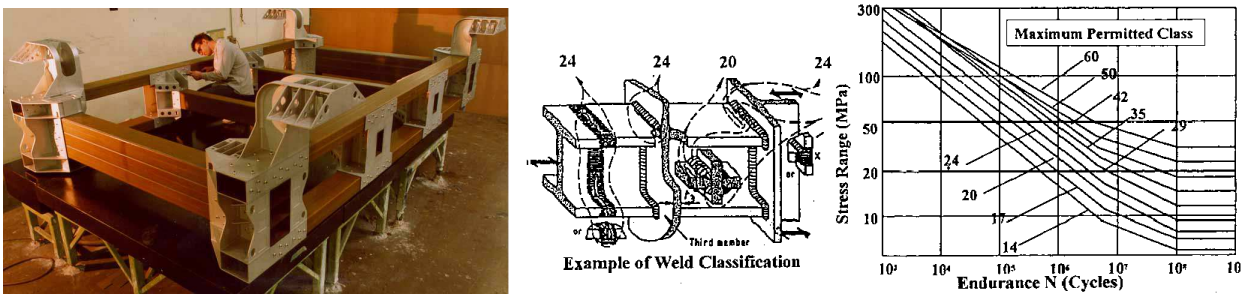

Fig. 4 Truck frame made of rectangular FRP tubes and aluminium joint parts [8] (left),

British standard 8118 fatigue design curves for aluminium structure [4] (right)

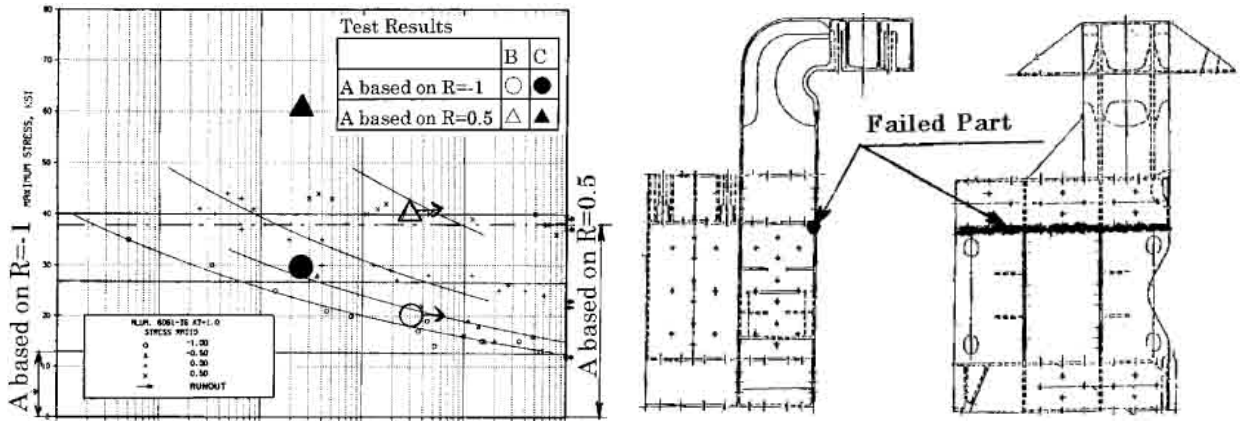

Fig. 5 Results of fatigue testing for rectangular FRP tubes and aluminium joint parts

2.3 Curved-plate anti-fracture wheels for freight cars

Goods transportation in the US is mainly conducted by freight cars. Energy in the US largely depends on coals, and coals are transported mainly by freight cars. In 1980 decade, a tremendous number of derailment happened only by wheel fracture [11]. Fig. 6 left shows how a wheel fracture looks like, which is the experimental result of an excessive drag brake application. The right hand in Fig. left shows the normal braking, and the left is the abnormal braking. The fracture of left hand figure can be easily understood how the fracture is dangerous. Fig. 6 right shows the examples of wheel fracture in the US. Three types of origin are from cracks at a stamp notch, flange tip, and tread. Because the initial residual stress in the rim of conventional wheels is compressive, tensile residual stress is considered to be converted due to an excessive drag brake condition [12]. From the obtained information, the countermeasures from the viewpoints of wheel modification are considered as follows:

1) Raise the fracture toughness by material modification.
2) Lower the tensile residual stress accumulation by configuration modification.

Herein, the first material countermeasure is described. In order to prevent the wheel fracture from the materials viewpoint, the material modification was considered. The material of railroad wheel has been medium-high carbon steel, mainly taking into consideration of wear characteristics. This is because railroad wheels in the US are used under a heavy loading condition for use of freight cars. For example, the load per wheel for the 100 tonnage freight car is 12.5 tonnage per wheel, whereas the one of Shinkansen in Japan is around 8 tonnage per wheel or less. High carbon steel for freight cars is desirable from the viewpoint of wear resistance, and has been used. However, the fracture morphology is brittle one as is shown in Fig. 6, and high carbon steel can cause brittle fracture. As a preliminary study, microstructure investigation using materials of martensitic and bainitic was conducted. They are considered to have higher fracture toughness than ferrite-pearlitic one in a medium-high carbon range. However, such materials can change their microstructure under a sever brake condition causing high temperature rise due to brake operation. The transformed microstructure is brittle ferrite-pearlite. As a result, materials of stable ferrite-pearlitic microstructure in an existing carbon range were studied to get the material of high fracture toughness. The effect of chemical composition of carbon and manganese as well as grain refinement on the fracture toughness was studied. A series of 8 materials without grain refinement and with grain refinement in a carbon range of 0.4-0.7%, was selected. As for the selected materials, the fracture toughness testing was conducted. The result is shown in Fig. 7 left [13]. The effect of prior-austinitic grain size on the fracture toughness depends on the carbon content. As volume of ferrite structure in the material increases, the effect of plastic work by tearing on the cleavage fracture strength is considered to be prominent. Surface energy of ferrite structure around a crack tip is proportional to $(\text{volume})^{2/3}$. Using the model by Smith [14], which was derived for cleavage fracture for ferrite structural material, the relation between fracture toughness and $(\text{ferrite volume})^{1/3} \times (\text{grain size})^{-1/2}$ was investigated. It can be concluded that the fracture toughness depends on the ferrite volume fraction and the prior austenitic grain size. From the study on the effect of manganese, the effect was found to be the same as in a low carbon range. Therefore, the followings are concluded:

1) Effect of grain size on wheel material fracture toughness depends on carbon content.
2) Fracture toughness is proportional to $(\text{ferrite volume fraction})^{1/3}/(\text{prior austenitic grain size})^{1/2}$.

Fig. 6 Example of wheel fracture, brake testing (left), categories from stamp, flange, tread (right)

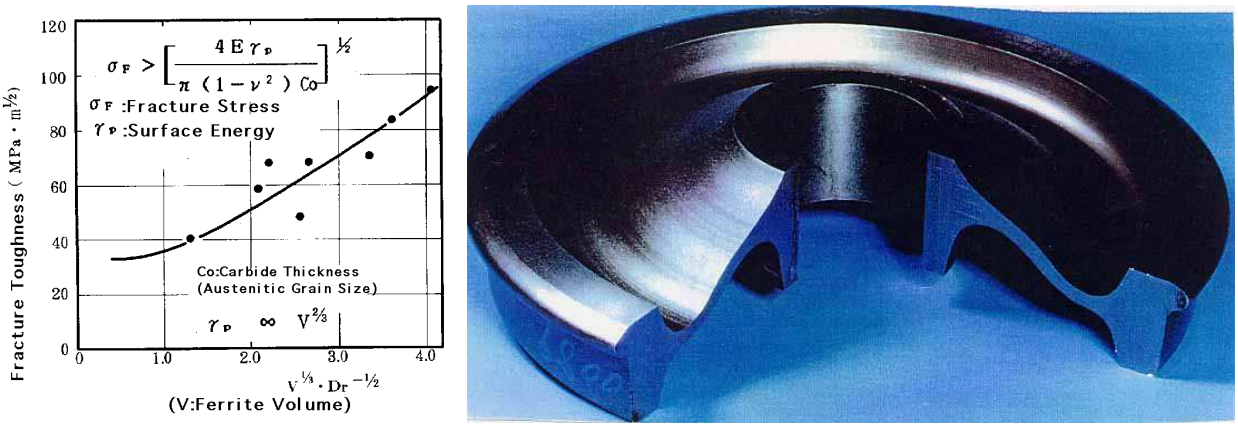

Fig. 7 New wheel, effect of ferrite volume and grain size (left), curved wheel plate (right)

The configuration modification was also studied. Since the tensile residual stress originates by an excessive brake heating resulting in rim part expansion, the plate part should not to be tightly constrained. Therefore, the effect of plate offset between at the rim and hub roots and plate thickness was studied. As a result, it was concluded that the large offset plate wheel reduces the residual stress even under an excessive brake heat condition. The new wheel is shown in Fig. 7 right. The idea was confirmed right and was supported by 3 dimensional FEM analysis[12)] and the experimental study. The effect of overhanging shoe location on the wheel fracture was also studied. Since the wheel fracture is caused by the tensile residual stress, non-destructive testing was also researched. The non-destructive testing was used by transverse ultrasonic waves, which can measure the stress in a solid. The research [15-17] had been conducted, and concludes that the tensile residual stress can be measured. Besides the wheel fracture issue, the thermal crack initiation and propagation and the shelling behaviour [18] were studied.

2.4 Forged steel brake discs with fins for bullet trains

When the Japanese bullet trains, Shinkansen, started their revenue service, brake discs [19] were made of cast iron with special metal materials such as Ni, Cr, and Mo. At that time, the running speed was 210 km/h (58.3 m/s). Since then, higher speed is demanded. When the discs are used in an emergency case like electricity fail, in which vehicles can not use the conventional electric braking, the absorbed energy for 300 km/h (83.3 m/s) initial brake speed is double as the one for 210 km/h. When such energy is absorbed, the discs need to have the double weight if the disc strength is the same. In around 1975, forged steel brake discs were considered as the one for next generation bullet trains. Instead of cast iron discs, the forged steel was selected, and the configuration was applied in such a manner to attach to the wheel. The shape is hat-like one as shown in Fig. 8 left. During the durability testing, the brake disc fractured. Fig. 8 righ [20] shows how it failed. The fracture morphology was (1) tortoise-like surface crack origination and (2) thermal crack propagation from tortoise-like crack. The scanning electron microscope observation on the failed surface clarified the fracture process. The countermeasure from the results was considered to be forged steel material to raise the fracture toughness. Since the material of hat-type disc material was medium carbon steel with the heat treatment of normalizing and tempering, the fracture toughness of the material is around 100 MPam$^{1/2}$. The improvement for the brake steel material was investigated. As a result, the steel material of Ni, Cr, and Mo addition with grain refinement was selected, as Fig. 9 left shows.

Although the material of around 220 MPam$^{1/2}$ fracture toughness was selected, the hat-type disc makes the width of bogie trucks larger than conventional ones. Instead of applying hat-type brake discs, the

conventional brake disc configuration was again studied. In order to apply the conventional brake disc configuration, the brake disc needs to have high heat convection to lower the brake heat accumulation [21]. The fin configuration was studied, and high technical issues for forging were required to be solved. The reason is the material of high toughness, which is hard to forge. From numerous experimental studies, the forged brake disc with fins was produced, and is shown in Fig. 9 right.

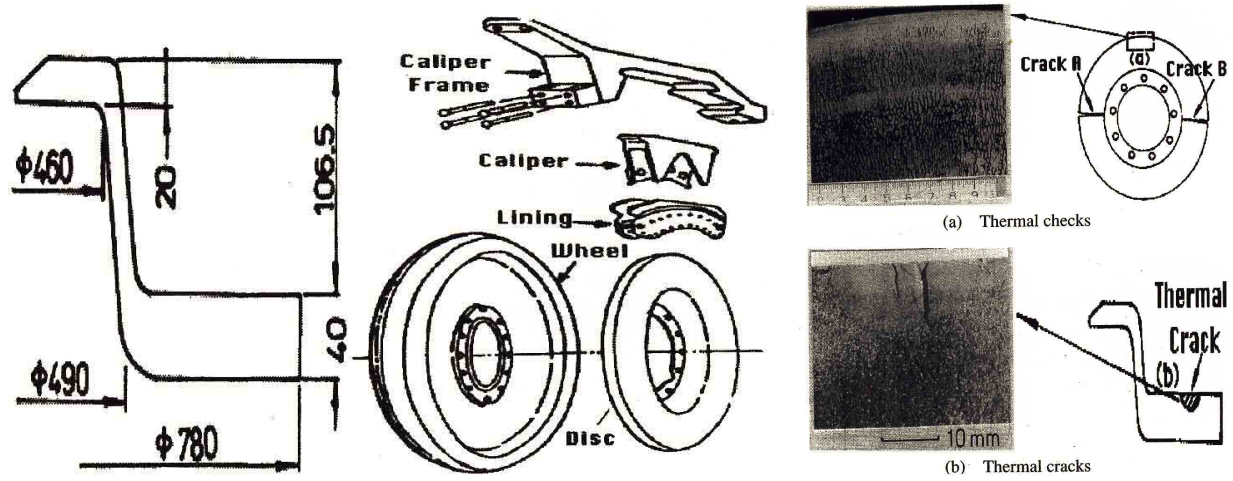

Fig. 8 Hat-like brake disc, attached to the side of wheel (left), observation on failed surface (right)

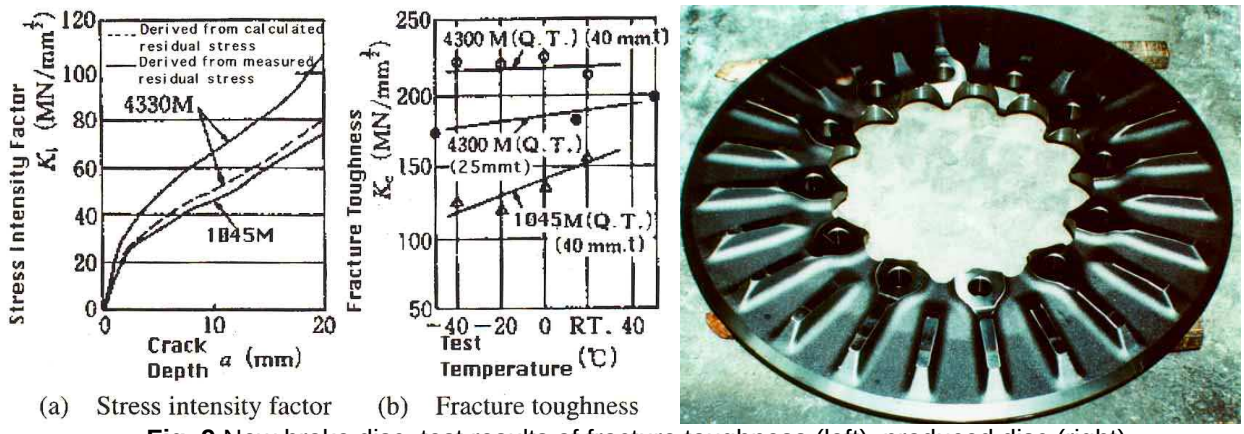

Fig. 9 New brake disc, test results of fracture toughness (left), produced disc (right)

3 DISCUSSION

3.1 Fracture resistance and inspection

A railroad accident can cause serious casualties, especially by the failure of failed-out components such as wheels and axles. Wheels are high carbon steel, and may cause brittle fracture depending on the service condition. Therefore, the most adequate material selection needs to be considered. The large ferrite volume and grain refined material was selected. Since wheels are failed-out components, the method of inspection is required to study. As for wheels that suffer excessive braking, the issue is the possibility of high tensile residual accumulation. In this report, the transverse ultrasonic wave measurement was reported, and the method is desired to put in reality by successive researches on the method. As far as axles are concerned, they are also failed-out components. Large compressive stress state on surface of medium frequency induction hardened axles can be expected to prevent crack extension even if the crack initiates.

Fracture mechanics are useful and now became to be a common technology as were shown in this report. Although the fracture events tend to be avoided through the knowledge of fracture mechanics today, the remained issues exist. They are whether fatigue limit exists based on scientific explanation, whether retardation of crack extension can happen with appropriate ground, and whether a crack extends under large compressive cyclic loading. From such issues that are not to be clarified yet, it is considered that the

inspection needs to be appropriately maintained for especially failed-out components. When an inspection is omitted, the strict reason needs to be explained.

3.2 Fatigue design for truck frame

In this report, an example of truck frame development is explained. The case was conducted by the stress analysis, and fatigue design guidance was not used. JIS 4207 [10] is the design guidance for railroad truck frames in Japan. As is shown in Table 1 left, the guidance is simple, in a sense of having only three categories compared to the other guidance such as British Standard 8118 [9] in Fig. 4 right. Among three fatigue limits, the fatigue limit for as-welded is 69 MPa. This value is reversal stress at zero mean stress. Compared to the JSSC (Japanese Structural Steel Construction) guidance, which is described by the stress range, it is concluded that 69 MPa is little high. The fatigue experiments for the welded structures resulted that the value of fatigue strength at 10^7 cycles is around 40-50 MPa as is shown in Table 1 right. The value is the fatigue strength, and not the allowable strength. Therefore, 69 MPa in Table 1 left is considered to be too high. However, JIS 4207 can be said to be simple. The further study is needed, regarding the validity and scattered data of JIS 4207 [10]. A paper on the research on fatigue design code for welded structure is referred [22].

Table 1 Design guidance of JIS 4207 (left) and test results for three type specimens (right)

Material Category / Strength (MPa)	G3101,SS400 G3106,SM400	G3114, SMA490
Tensile (σ_B)	402	490
Fatigue Limit for Base Metal (σ_{w1})	137	157
Fatigue Limit for As-Welded (σ_{w2})	69	
Farigue Limit for Ground Weldment (σ_{w3})	108	

Welded Joints Category	Test Specimen, Method	Fatigue Strength at 10^7
Cruciform Joints	Plate, One-side Tensile	60 MPa
Side and Bolster Frames	Box Type, One-side Bending	55 MPa
Joints of Side and Bolster	Joints, Reversible Bending	40-45 MPa

4 CONCLUSIONS

The research on fatigue and fracture mechanics for railroad key product development is reported. The research of the past 40 years has been conducted by the author in the company and the university. The summary of this report is as follows:

1) Fracture mechanics are useful for development of railroad vehicle products, and two examples of wheels and discs are explained. Two examples of fatigue, axle and truck frame, are also explained. Since the railroad vehicle products are highly important key components, the security should be maintained. Especially, wheels and axles are failed-out components, and need security to be maintained by the appropriate inspection system.

2) Further research on the following issues is desired. The issues are whether fatigue limit exists based on scientific explanation, whether retardation of crack extension can happen with appropriate ground, and whether a crack extends under large compressive cyclic loading. After the evidence of such issues is obtained, the inspection system can be re-considered.

3) Regarding the existing truck frame fatigue design guidance of JIS (Japanese Industrial Standard) 4207, the allowable stress is considered to be high. The fatigue data to obtain the scatter for non-fracture probability is required. Design guidance is considered to be simple with not many design curves, and many guidance such as BS 8118 and JSSC fatigue design are considered to be complex for designer to design.

5 ACKNOWLEDGMENT

The author greatly acknowledges the cooperated people of Sumitomo Metal Industries (at present Shin-nittetsu Sumikin) Co., and helpful discussion by researchers in Technical Railway Institute and Japanese Railways.

6 REFERENCES

[1] H. Kobayashi, Cause of Aircraft Boeing 747 Crash, Zairyo, 36-409, 1084-1089, 1987, (in Japanese)

[2] Bild am Sonntag, German Newspaper, 7, Juni, 1998

[3] K. Hirakawa, Truth of German Super Express Railroad Derailment Accident, Keibun Publish Co., 2006, (In Japanese)

[4] H. Ishiduka, High Frequency Induction Hardened Axes, Railway Research Report (RRR), 34-35, 2005 (In Japanese)

[5] H. Ishizuka and Y. Sato, Fretting Fatigue Strength of Axles of Bullet Train and Their Maintenance, Proc. of the 10th International Wheelset Congress, 195-199, 1992

[6] H. Ishizuka, Thirty Years of Axles Maintenance for Japanese Bullet Train-Shinkansen, Proc. of the 11th International Wheelset Congress, 43-46, 1995,

[7] Japanese Industrial Standard, G 3101, 3106 (in Japanese)

[8] H. Sakamoto, B. Jones B, R. Bank, S. Mcleskey, and Y. Kishi, Design and Durability Assessment on a Train Chassis with Pultruded FRP Tubes and Aluminium Joints, Proc. of International Conference on Materials and Mechanics, JSME (Japanese Society of Mechanical Engineers), 713-718, 1997

[9] British Standard 8118, Design Standard for Aluminium Structure.

[10] Japanese Industrial Standard, Design Standard for Railway Truck Frame, (in Japanese)

[11] D. H. Stone, 8th Wheelset Congress, V-4/1, 1985

[12] H. Sakamoto and K. Hirakawa, Prevention of Railroad Wheel Fracture, JSME International Journal, Series A, Vol, 46, No.4, 613-619, 2003

[13] H. Sakamoto, K. Toyama, and K. Hirakawa, Fracture Toughness of Medium High Carbon Steel for Railroad Wheel, Material Science and Engineering-A (MSE-A), A285, 288-292, 2000

[14] K. F. Knott, Fundamentals of Fracture Mechanics, 204, Nutterworths, 1973

[15] H. Fukuoka, H.Toda, K. Hirakawa, H. Sakamoto, Y. Toya, Acoustoelastic Measurement of Residual Stress in the Rim of Railroad Wheels, Trans. ASME (American Society of Mechanical Engineers) AMD (Applied Mechanics Division), 62, 185-193, 1993

[16] K. Fujisawa, R. Murayama, H. Sakamoto, S. Yonehara, Nondestructive Measurement of Residual Stress in Railroad Wheel by EMAT, 3rd. Int. Conf. On Residual Stress Measurement (ICRS 3), 328-333, 1991

[17] H. Fukuoka, H. Toda, K. Hirakawa, H. Sakamoto, Y. Toya, Nondestructive Assessment of Residual Stress in Railroad Wheel Rim by Acoustoelasticity, Trans. ASME, Ser. B, 281-287, 1978

[18] H. Sakamoto, Fundamental Evaluation of Thermal Crack Resistance for Wheel Fracture Prevention, ASME Int., IMECE 2002-30604, 1-6, 2002

[19] J. Hamazaki, S. Nishimura, H. Sakamoto, Disc Brake for Shinkansen Vehicles, I Mech E (Institution of Mechanical Engineers), Int. Conf. On Railway Technology, 1-7, 1980

[20] H. Sakamoto, and K. Hirakawa, “Fracture Analysis and Product Development of Brake Disc,” JSME, International Journal, Series A, Vol. 48, No.4, Nov., 458-464, 2005

[21] Sakamoto H., Heat Convection and Design of Brake Discs, Proc. I Mech E, Vol. 218, 2004

[22] H. Sakamoto, Codes and Practice of Fatigue Design for Welded Structure, ASME, DE (Design Engineering) -Vol.,102, 91-96, 1999

Proceedings of the 3rd International Conference on
Fracture Fatigue and Wear, pp. 169-174, 2014

STRESS ANALYSIS OF STEAM GENERATOR TUBESHEET AND MAIN FACTORS AFFECTING FATIGUE AND FRACTURE FAILURE

Hao Qian*, Chang Liu, Xingyun Liang, Jingjing Deng, Yongcheng Xie and Shaoxuan Lin

Department of Component Research and Design,
Shanghai Nuclear Engineering Research and Design Institute, Shanghai 200233, China
*Corresponding author: qianhao@snerdi.com.cn

Abstract: The steam generator (SG) serves as the primary means for removing the heat generated within the reactor core. The tubesheet is the boundary of the primary side and second side of Nuclear Power Plant (NPP) and is the thickest forging among the NPPs' components. Stress analysis of SG tubesheet is performed to ensure the 60 years lifetime of the component, with the FEM model of channel head, tubesheet, and lower shell complex. The fatigue analysis and the fracture mechanics calculation with evaluation are performed per ASME B&PVC III-1 Subsection NB and Appendix G. The results of fatigue usage factors and critical defect size are shown. Moreover, the main factors affecting fatigue failure and non-ductile failure are proposed, which is significant for the design and fabrication of SG.

Key words: steam generator (SG), tubesheet, fatigue usage factors, non-ductile failure

1 INTRODUCTION

Steam generators are heat exchangers used to convert water into steam from heat produced in a nuclear reactor core. They are used in pressurized water reactors (PWR) between the primary and secondary coolant loops. That water flowing through the steam generator boils water on the shell side to produce steam in the secondary loop that is delivered to the turbines to generate electricity. The tubesheet of steam generator is the thickest forging among the NPPs' components. It plays an important safety role because it constitutes the primary barrier between the radioactive and non-radioactive sides of the plant as the primary coolant becomes radioactive from its exposure to the core.

About 50% new NPPs are being built in China now. Safety is one of the most important issue for Nuclear Power Plant (NPP), especially for post-Fukushima ages. The radioelement should always be restricted in the Reactor Coolant System (RCS) safely.

Stress analysis of SG tubesheet is performed to ensure the 60 years lifetime of the component, with the FEM model of channel head, tubesheet, and lower shell complex. There are many failure reasons for SG, such as corrosion, wear, fatigue and fracture. Fatigue and fracture are two main failure reasons for tubesheet. In this paper, the fatigue analysis and the fracture mechanics calculation with evaluation are performed per ASME B&PVC III-1 Subsection NB and Appendix G [1]. The fatigue analysis and analysis of protection against nonductile failure is essential, together with strength analysis. ASME B&PVC III-1 NB-3222.4 provides the requirement and method to perform the fatigue analysis. And there are some requirements of material's fracture toughness and fracture mechanics analysis in ASME code, such as ASME B&PVC III-1 NB-2300 Fracture Toughness Requirements for Material, NB-3200 Design by Analysis, Appendix G Protection Against Nonductile Failure, etc. The results of fatigue usage factors and critical defect size are shown in this paper. Moreover, the main factors affecting fatigue failure and non-ductile failure are proposed, which is significant for the design and fabrication of SG.

2 GEOMETRY AND MATERIAL OF COMPONENTS

The geometry of Steam Generator tubesheet is illustrated in Fig. 1. The material of the components is SA-508, Grade 3 Class 2 per ASME code. The material strengths and physical properties can be obtained from the ASME Code [2].

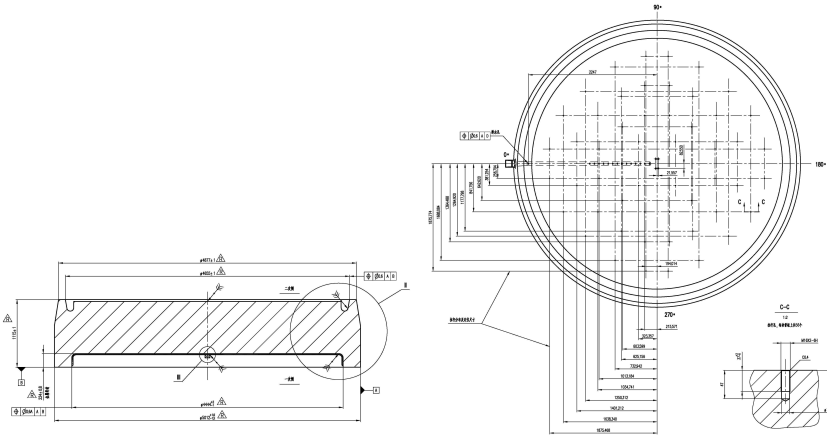

Fig. 1 Structure drawing of Steam Generator tubesheet

3 ANALYSIS METHODS AND MODELS

The analysis employs finite element methods using the ANSYS computer program for stress analysis. The structural, fatigue and non-ductile failure analyses were performed in accordance with the ASME Boiler and Pressure Vessel Code, Section III, Rules for Construction of Nuclear Power Plant Components [1].

The tubesheet connects channel head and lower shell. The model of channel head, tubesheet, and lower shell complex is created herein. The stresses in the channel head, tubesheet and lower shell due to the pressure loads, thermal loads and the external mechanical loads are obtained using finite element analysis. Thermal loads are temperature gradients (distributions) due to the thermal transients in the components and are also obtained using finite element analysis.

ANSYS PLANE83 two-dimensional, axisymmetric-harmonic 8-node structural solids are used to construct the structural model of the channel head, tubesheet, and lower shell in structural analysis. The equivalent solid plate method is applied per ASME for the perforated region of the tubesheet which has more than 24 thousand holes. The equivalent solid plate procedure greatly simplifies the structural analysis of a perforated plate, for the explicit modelling of each penetration is not necessary. The perforated plate is treated as an orthotropic homogeneous material with effective elastic constants E, v and G, which are used to account for the effect of the holes on the stiffness of the plate by the method of ASME B&PVC III-1 Appendix A [1]. In the perforated region of the tubesheet, the finite element stresses represent the stresses in the equivalent solid plate, and are adjusted by stress multipliers in order to obtain the ligament stress in the perforated plate. Specifically, the linearized membrane and the linearized membrane plus bending stress components are divided by the ligament efficiency (η). This analysis method for perforated plate is similar to Slot's method [3].

Finite element analyses were performed to obtain the temperature distributions in the channel head, tubesheet, and lower shell. The thermal analysis model is constructed of the PLANE77 elements and SURF151 elements. The PLANE77 element type is a 2-D, 8-node thermal solid. The SURF151 element type is a 2-D thermal surface element. The model is run using the axisymmetric option for these element types. On the primary surfaces, a clad layer is modelled by the thermal surface elements and loaded with the bulk temperatures on the surfaces. Heat transfer coefficients are important input in this model.

Analysis model of channel head, tubesheet, and lower shell assembly and the limiting stress locations are shown in Fig. 2. The calculation and analysis are performed for design, normal, upset, emergency, faulted and test condition.

The fatigue evaluation is performed per ASME B&PVC III-1 NB-3222.4(e). The primary plus secondary plus peak stresses (total stresses) are used in determining the fatigue usage factor for each of the limiting locations. The design fatigue curves of ASME B&PVC III-1 Appendix I is applied.

Non-Ductile failure evaluation is performed per ASME B&PVC III-1 NB-3211(d) and Appendix G to prevent form brittle fracture of components. WRCB 175 [4] “PVRC Recommendations on Toughness Requirements for Ferritic Materials” is applied by the guidance of ASME B&PVC III-1 Appendix G. And KIC, the lower bound static initiation critical KI value, is applied for the evaluation of the postulated flaw size to ensure non-ductile failure does not occur.

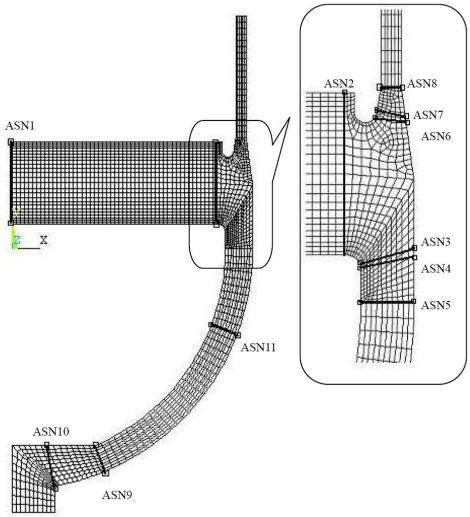

Fig. 2 Analysis Model and Limiting Stress Locations in Channel Head, Tubesheet, and Lower Shell Assembly (ASN = Analysis Section Number)

4 ANALYSIS AND EVALUATION RESULTS FOR STRENGTH, FATIGUE AND FRACTURE

The Steam Generator channel head, tubesheet, and lower shell complex are analyzed in accordance with Section III of the ASME Boiler and Pressure Vessel Code. The calculated stress intensities, the ASME Code allowable stress limits, the ratios of the stress intensities to the allowable limits, and the calculated fatigue usage factors for each of some locations are listed in Table 1. Herein, the results of two typical locations ASN 2 and ASN 4 are shown, where P_m is general primary membrane stress, P_b is primary bending stress, and Q is secondary stress.

Table 1 Stress Analysis Results and Evaluation for Tubesheet

Loading Condition	Stress Category	ASN 2			ASN 4		
		Stress (MPa)	Allow (MPa)	Ratio	Stress (MPa)	Allow (MPa)	Ratio
Design	P_m	105.71	207	0.51	65.41	207	0.32
	P_m+P_b	243.89	310	0.79	234.89	310	0.76
	Triaxial σ	114.44	827	0.14	95.75	827	0.12
Level B (Upset)	P_m	123.51	228	0.54	78.55	228	0.35
	P_m+P_b	299.91	341	0.88	269.34	341	0.79
	Triaxial σ	128.44	827	0.16	109.01	827	0.13
Level A, B & Test (Normal, Upset & Test)	P_m+P_b+Q	396.45	740	0.54	662.86	740	0.90
	Fatigue Usage	/	1	0.83	/	1	0.15
Level C (Emergency)	P_m	141.70	335	0.42	88.35	334	0.26
	P_m+P_b	340.83	557	0.61	288.02	557	0.52
	Triaxial σ	135.48	827	0.16	92.05	827	0.11
Level D (Faulted)	P_m	151.71	434	0.35	96.84	434	0.22
	P_m+P_b	365.07	652	0.56	300.25	652	0.46
Test	P_m	185.64	373	0.50	109.71	373	0.29
	P_m+P_b	441.56	560	0.79	368.20	560	0.66
	Triaxial σ	167.10	827	0.20	105.57	827	0.13

Moreover, the results from the fracture mechanics assessment are shown in Table 2. The results of the most rigorous transient of typical locations ASN 4 are shown herein, where N19 is primary to secondary side leak test, and T01 is primary side hydro test. The lowest temperature is chosen for evaluation. In primary side hydro test, the method of WRCB 175 is applied, and the critical flaw size 17.78 mm is obtained which is detectable by inspection.

Table 2 Non-Ductile Failure Evaluation Results for Tubesheet

ASN Number	Section Thickness T(mm)	Transient No.	Transient Temperature (□)	K_I	K_{IC}	K_I/K_{IC}	Postulated Flaw Size a (mm)
ASN 4	290.87	N19(Normal)	8	89.76	111.23	0.81	T/4
		U05-B(Upset)	215.01	155.27	219.78	0.71	T/4
		E06(Emergency)	170.33	178.99	219.78	0.81	T/4
		F02(Faulted)	127.50	157.17	219.78	0.72	T/4
		T01(Test)	8	-	-	0.99	17.78

Tables 1 and 2 indicate that all the results (stress, cumulated fatigue usage factors and fracture results) are below the limit of 1.0 and meet the ASME Code requirement. As an example, the temperature distribution and total stress intensity (with thermal stress) plots for the Inadvertent Safeguards Actuation Transient at 1810 second are shown in Fig. 3 and Fig. 4 herein.

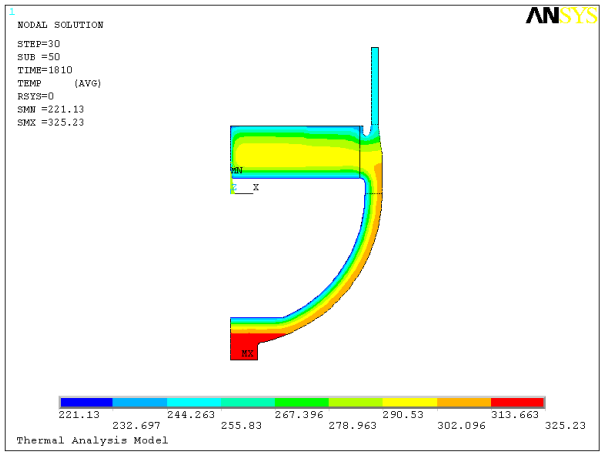

Fig. 3 Body Temperature Plot for Inadvertent Safeguards Actuation Transient at 1810 second

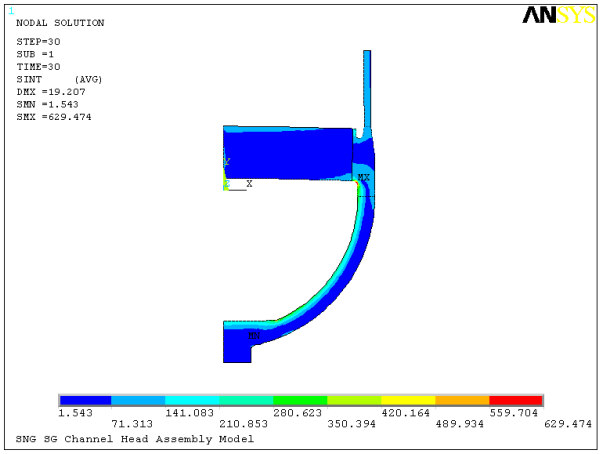

Fig. 4 Total Stress Intensity Plot for Inadvertent Safeguards Actuation Transient at 1810 seconds (Combined Pressure and Thermal Loads)

5 MAIN FACTORS AFFECTING FATIGUE FAILURE

The design basis of the Steam Generator is 60 years with 90 percent availability over the design life. The fatigue analysis and evaluation is performed per ASME B&PVC III-1 NB and the design fatigue curves of ASME B&PVC III-1 Appendix I. The main factors affecting fatigue failure is as follows:

1) The cycles of transients. Generally the equipment with 60 years design life endures more cycles of transients than the equipment with 30~40 years design life.

2) Stress of components. It depends on the structure design, load condition, and method of calculation.

3) Fatigue parameters of material. The design fatigue curves for carbon, low alloy, and high tensile steels for metal temperatures not exceeding 370□ of ASME B&PVC III-1 Appendix I is applied.

The information indicates that some certain methods can be attempted to solve the problem if the structure cannot meet the fatigue requirement of ASME, which are elaborated as follows:

1) Improvement of component structure. For example, if the support column is designed in channel head like NPP System 80, the stress of tubesheet can be reduced obviously [5].

2) More accurate transients, which may decrease the peak stress of components.

3) More accurate analysis method. For example, Equation (21) of ASME B&PVC III-1 Appendix A-8142.2 can be applied to calculate peak stress intensity and fatigue usage factor instead of Equation (20). Even if NCR occurs, Equation (21) can also be used for a special perforated plate which has been wrong drilled and has a ligament deviation. There is a small clerical error in ASME B&PVC III-1 Appendix A-8143.

6 MAIN FACTORS AFFECTING FRACTURE FAILURE

ASME B&PVC III-1 Appendix G with postulated defect, such as 1/4 section thickness, prevents the structure from brittle fracture. Certain locations which are discontinuous regions, i.e. highly stressed regions, generally cannot be expected to meet the proposed rules if a quarter-thickness is assumed [4]. The smaller defects can be assumed if nondestructive examination methods can be sufficiently reliable and sensitive to detect these smaller defects. The relationship between reference nil ductility temperature, fracture toughness and defect size (a ~ KI ~ KIR or KIC ~ RTNDT) is summarized in Fig.5 [6].

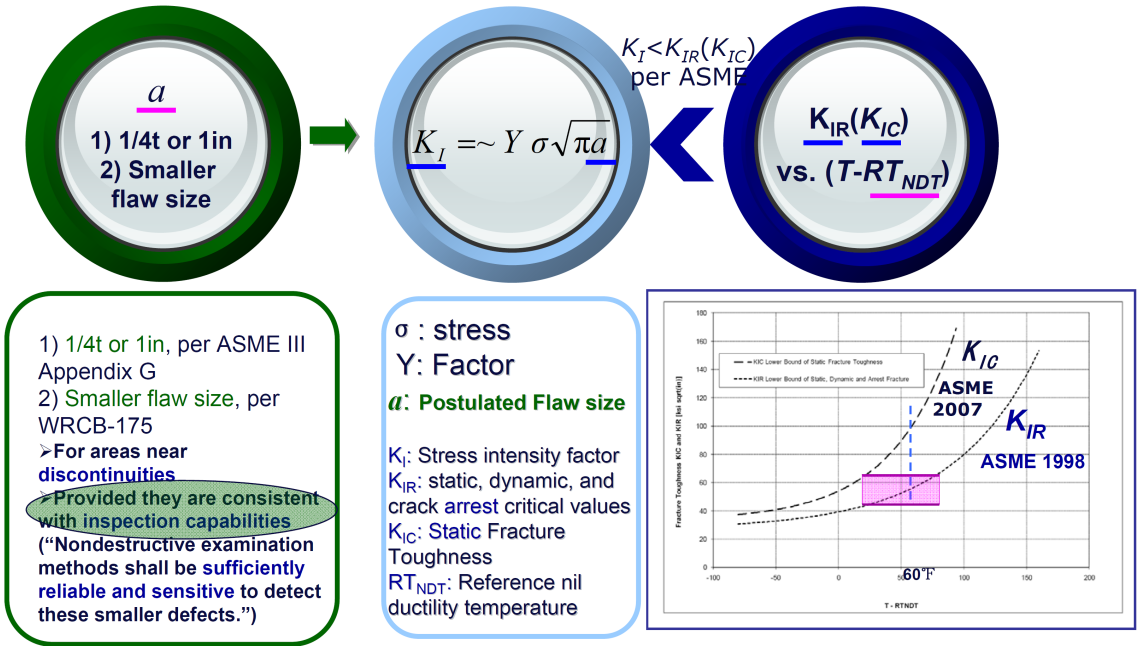

Fig. 5 Relationship of the fracture toughness parameter

Figure 5 indicates that there are some parameters affect the effects of protection against nonductile failure, which are as follows:

1) Reference nil ductility temperature (RT_{NDT}) of ferritic pressure retaining materials. It depends on the experience, technic level and process control ability of industry. And more lower RT_{NDT}, more expensive the material is.

2) Stress intensity factor (K_I). It depends on the structure design, load condition, and method of calculation.

3) Critical stress intensity factor (K_{IR}, or K_{IC}). It depends standards or the editions of ASME code, service temperature, and materials' RT_{NDT}. For more attention, data of ASME B&PVC III-1 Appendix G's figure may be used for ferritic steels, which have a specified minimum yield strength at room temperature of 50.0 ksi (345 MPa) or less. For materials which have specified minimum yield strengths at room temperature greater than 50 ksi (345 MPa) but not exceeding 90 ksi (620 MPa), such as SA-508 Gr.3 Cl.2 whose yield strength is 65 ksi (448 MPa), fracture mechanics data should be obtained on at least three heats of the material on a sufficient number of specimens to cover the temperature range of interest, including the weld metal and heat affected zone.

4) Postulated defect size or maximum possible defect size. It depends on the capabilities of nondestructive examination (NDE).

The information indicates that some ways can be attempted to solve the problem if non-conformance case occurs by the reason of manufacture capacity limit, such as RT_{NDT}. The ways to solve the problem are listed as follows:

1) To modify and control the service temperature to avoid the component works on low temperature and high pressure, such as the hydrostatic tests' water temperature.
2) To apply some more accurate analysis method.
3) To confirm and improve the capabilities of nondestructive examination. Some tests, research and statistic should be performed.

7 CONCLUSIONS

The stress analysis of the tubesheet of NPP's Steam Generator is performed by finite element methods using the ANSYS computer program. The structural, fatigue and non-ductile failure analyses with evaluation are performed in accordance with the ASME B&PVC and WRCB 175. The pressure loads, thermal loads and external mechanical loads of all the Reactor Coolant System Design Transients are considered. All the results (stress, cumulated fatigue usage factors and fracture results) indicate that the component meets the ASME Code requirement. Moreover, the main factors affecting fatigue failure and fracture failure are proposed, which is significant for the design and fabrication of SG. Some methods can be applied to deal with the problem of Non Conformity Report (NCR) that occurs in fabrication of equipments.

8 REFERENCES

[1] ASME Boiler and Pressure Vessel Code. Section III. Rules for Construction of Nuclear Facility Components [S]. New York, 2007 Edition with Addenda through 2008

[2] ASME Boiler and Pressure Vessel Code. Section II. Materials [S]. New York, 2007 Edition with Addenda through 2008

[3] Thomas Slot, Stress analysis of thick perforated plate. New York, Technomic publication, 1972

[4] WRCB 175 (Welding Research Council Bulletin 175), PVRC Recommendations on Toughness Requirements for Ferritic Materials [S], 1972.8

[5] Qian Hao, Liang Xingyun, Zhou Quan, He Yinbiao, Lin Shaoxuan, Jing Yi, Stress Analysis of Steam Generator Channel Head, Tubesheet, Lower Shell Complex and Comparison Study of Design Schemes. The Chinese Congress of Theoretical and Applied Mechanics (CCTAM 2013), 2013.8

[6] QIAN Hao, ZHANG Kefeng, ZHU Yizhou, LIANG Xingyun , HE Yinbiao, YAO Weida, Fracture Toughness Requirements of Steam Generator Channel Head and Disposition Methods of Non-conformance Case. 2012 International Symposium on Structural Integrity, From Failure to Better Design , Manufacture and Construction, 2012

Proceedings of the 3rd International Conference on
Fracture Fatigue and Wear, pp. 175-181, 2014

NUMERICAL INVESTIGATION OF FATIGUE PERFORMANCE OF BUTT WELDED JOINT WITH UNDERCUT

Ezzarhan Abdullah[1,2] and Koji Gotoh[3]

[1]Dept. of Civil and Structural Engineering, Kyushu University, Japan
[2]Dept. of Occupational Safety and Health, Malaysia
[3]Dept. of Marine Systems Engineering, Kyushu University, Japan

Abstract: Undercut is a defect which mostly found in welded joint. In many cases, undercut near the weld to become a stress concentrator. The numerical investigation was performed to evaluate the performance of fatigue at different type of geometrical parameter which includes the shape of undercut and the effect of the undercut ratio to plate thickness. In this study, stress distribution along undercut root will be defined in numerical procedure for fatigue performance calculation. Next, the difference of geometrical shape as U and V-shape of undercut will be discussed. In addition, the importance of stress concentration factor (SCF) and stress gradient (χ) in the evaluation of fatigue strength will be highlighted with various geometrical parameters. Re-tensile plastic zone generation (RPG) stress criterion by Toyosada will be used in order to estimate fatigue life. Furthermore, the study will be useful in improving of the Japan Shipbuilding and Quality Standard (JSQS) which emphasis on the undercut geometrical parameter. Then, such shape factor can be ignored by considering undercut breadth and depth.

Keywords: undercut; fatigue strength; butt welded joint; RPG stress criterion

1 INTRODUCTION

Throughout the years, codes and standards become as first referral documents in industrial practise in order to ensure the structural integrity and safety performance. As material, design methodology and fabrication technique getting improved with rapid growth in development, some of allowable parameter in such code and standard is suggested to be revised. Furthermore, in order to achieve a good structural design with safety, integrity and cost optimization, fundamental way by mathematical calculation can be done. As an example, nowadays many methods found great agreement which can be used in the calculation. In the evaluation of fatigue strength, such method like S-N curve based on the nominal stress range is very popular. Nevertheless, another method also available in order to analyse the fatigue strength of welded joint like nominal stress approach, hot spot stress method, notch stress approach and notch stress intensity [1].

There are many codes available for welded structure. However, not many codes presents allowable parameters for welding defects such as undercut. Table 1 shows several codes in considering undercut depth. Here, only the Japan Shipbuilding and Quality Standard (JSQS) code did not consider plate thickness as a parameter in order to limit the undercut on welded structure. The study will focus on the effect of notch shape and undercut depth towards fatigue performance. In general, many researchers [2-5] studied the importance of geometrical parameter and defect for welded joint which is affecting the fatigue performance.

2 THEORETICAL BACKGROUND

2.1 Stress concentration factor, K_t

Stress concentration factor (SCF) is defined as the ratio of maximum stress and nominal stress at undercut root. SCF expressed by $K_{t(net)}$ indicate how stress amplified at undercut root net ligament area and is calculated based following definition:

$$\boldsymbol{K_{t(net)} = \sigma_{max}/\sigma_{nominal}} \quad (1)$$

Here; $\boldsymbol{\sigma_{nominal} = F/a}$, *a = s(t-d); s* = plate length*; a* = net area thickness*; t* = plate thickness*; d* = undercut depth.

Table 1 Available standard for welded structure with undercut

No.	Standard	For Strength Member	Other Member
1.	American Welding Society, AWS D1.1/D1.1M:2006	*d* ≤ 0.25 mm *d* ≤ 1 mm – other cases	If thickness (t) ≤ 25mm, *d* ≤ 1 mm
			If thickness (t) > 25mm, d ≤ 2 mm
2.	JSQS / IACS	*d* ≤ 0.5 mm	*d* ≤ 0.8 mm
3.	ISO 5817 :2003	If thickness (t) : 0.5 to 3mm – Undercut, d is not permitted If thickness (t) > 3mm, undercut, *d* ≤ 0.05t or maximum of 0.5mm	

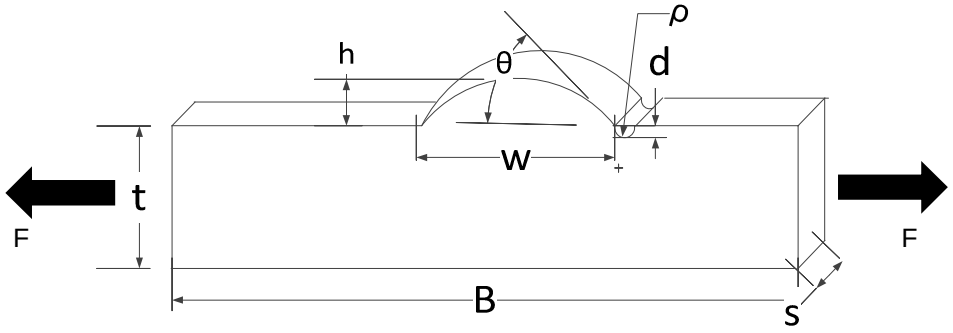

Fig. 1 Definition of butt welded joint (here, *h* = weld bead height; *w* = weld bead width; *d* = undercut depth; *ρ* = undercut root radius; *Θ* = flank angle; *B* = plate width; *s* = plate length and *t* = plate thickness

2.2 Stress gradient, χ

Stress gradient can be simply described as how fast the stress decreases along the extension of the undercut. The stress gradient at the notch root gives an indication of the volume of highly stressed material which is significant for the geometrical effect on fatigue limit [6]. In other words, how fast the decrement of stress from undercut root gives an important indicator on the fatigue performance. Below is the definition of stress gradient, χ:

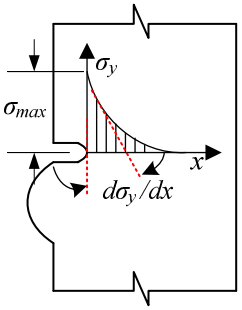

$$\sigma_y(x) = \sigma_{max} + \chi x \quad (2)$$

Stress gradient;

$$\chi \equiv \left(\frac{d\sigma_y}{dx}\right)_{x=0} < 0 \quad (3)$$

Fig. 2 Definition of stress gradient, *χ* [6]

2.3 Fatigue life

In this study, fatigue life is calculated based on the retensile plastic zone's generated (RPG) stress criterion as proposed by Toyosada et. al [7,8] based on Paris law.

$$da/dN = C(\Delta K_{RPG})^m \quad (4)$$

here; ΔK_{RPG}= effective stress intensity factor based on the RPG stress*; C,m*=material constant

2.4 Residual stress

The inherent stress method is used to estimate the residual stress distribution for the butt welded joint. The following equation established by Matsuoka et. al [9] is used in order to calculate the residual stress:

$$\sigma_1(x,y:T) = \alpha\sigma_y \exp\left(-\pi(x/B)^2\right) f(y;T) \quad (5)$$

Where; $f(y;T) = \sum_{n=0}^{\infty} \exp(-\pi(\lambda y_n/B)^2)$, $y_n = |y + \{(-1)^n(n+0.5) - 0.5\}T|$, $B = \beta(F/\sigma_y)$, $F = \gamma Q$

Here; Heat input, Q=1300 J/mm [10], T=plate thickness, non-dimensional coefficient, β=1.357, γ =0.16, α=1.942 and λ=1.788, σ_y=300 MPa.

3 ANALYSIS

Finite element analysis (FEA) has been carried out in this study by commercial finite element software, MSC Marc Mentat 2011. Geometrical condition used in the study is tabulated in Table 2. Type of undercut notch is illustrated in Fig. 3. Next, fatigue crack growth calculation was done by the numerical simulation code developed by Toyosada et. al [7-8] which is based on the RPG stress criterion and enables to describe the fatigue crack opening/closing behaviour. Harada and Gotoh [11] improved the simulation code by considering work hardening effect on the material. Stress distribution data from FEA is used in order to calculate the fatigue life. In this case, the model is treated as a plane stress condition and approximated as the single edge notch tension (SENT) type specimen.

Table 2 Model dimension

Type of specimen	U-type undercut			V-type undercut	
Plate thickness (mm)	10	25	30		
Weld bead height, *h* (mm)	0	2.5	5	7.5	10
Flank angle, θ^o	0	75	90		
Weld bead width, 2Bw (mm)	10	16	20		
Root radius, *ρ* (mm)	0.25	0.5	1		
Undercut depth, *d* (mm)	0.25	0.5	1		
Shape ratio *b/d*	2	3	4		

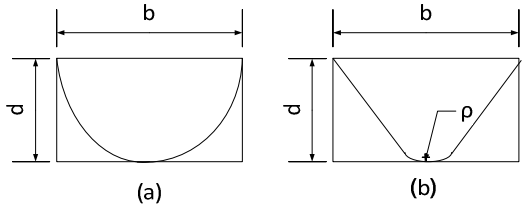

Fig. 3 Type of notch (a) U-Notch (b) V-notch

This study will be focusing on tension cases. Past studies by author presents stress distribution of tension cases is higher compared to bending cases. In other words, results obtain from this analysis, which will be used in the improvement of the code is considered higher side of the calculation where can be translated as a safety concern. Tension force will be applied at one edge and fixed at another edge (see Fig. 1). In FEA work, 4-node quadrilateral element type will be used with a minimum mesh size of 0.1 and maximum mesh size of 0.3. For mechanical properties, modulus of elasticity will be set to 210 GPa, yield strength of 300 MPa and Poisson's ratio, *v* is 0.3. In calculating fatigue performance, material constant, *C* and *m* is set according to the reference [7-8]. Fatigue life is calculated based on constant amplitude with the stress ratio, *R* = 0.

4 RESULT AND DISCUSSION

4.1 Effect of notch shape

Figure 4 shows fatigue life calculation results for the selected cases as stated in table 2. As can be seen, all V-notch type shows higher fatigue life compare to the U-notch type. This can be explained by referring to the stress distribution for each model. Even though higher stress concentration factor present for the V - notch model (see Fig. 5b), the stress gradient plays important role in reducing the stress along undercut root. It shows vital information related to the effect of stress gradient to fatigue strength. As we can see at Fig.6, stress distribution rapidly decreases by a V - notch model while differing behaviour found at U-notch model. At the distance point of about 0.07mm from undercut root, both stress distributions for V and U-

notch are at the same level. Next, the stresses keep decreasing for V-notch model and finally to the end of the plate thickness. This means that stress found higher in V-notch model up to distances of about 0.07 mm and then maintains low compare to the U - notch model. This phenomenon also occurred for the other shape ratio. The effect of shape ratio, b/d significantly found in the V - notch model (see Fig. 4) where higher fatigue life presents by higher shape ratio, b/d=4. Fig. 5 (b) presents stress distribution for the V - notch model with different shape ratio, *b/d*. Based on this figure, even though V-notch model with higher ratio *b/d* gives lower *SCF* but there is no significant effect by stress gradient. In the other hand, there are no significant differences in fatigue life for U-notch model with different shape ratio, *b/d* even though significant stress gradient effect is shown in Fig. 5(a).

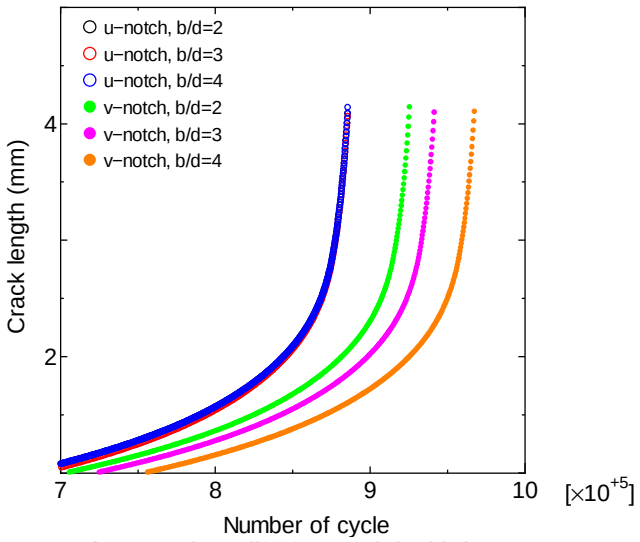

Fig. 4 Fatigue life for model with h=5mm

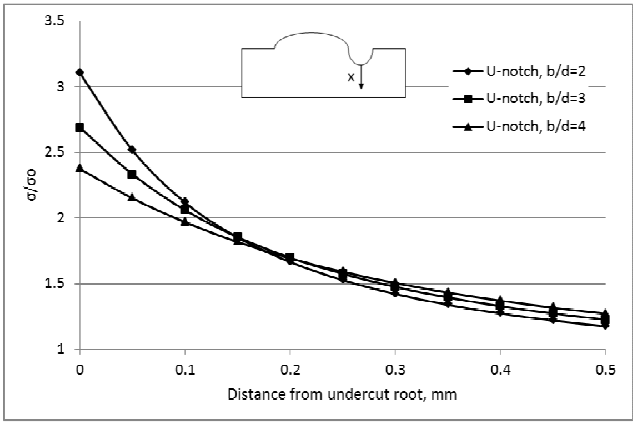

(a) U-notch

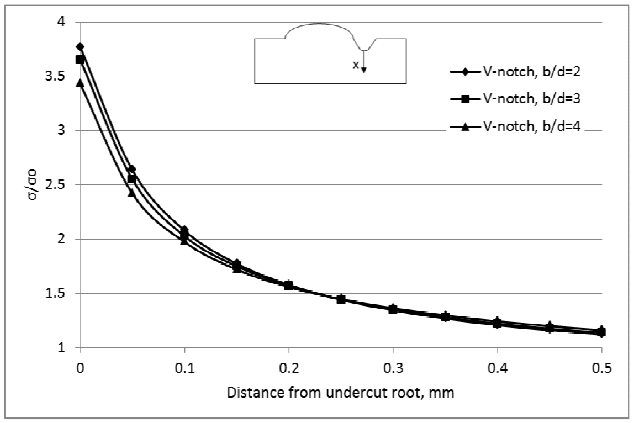

(b) V-notch

Fig. 5 Stress distribution of model with h=5mm, Θ=90°

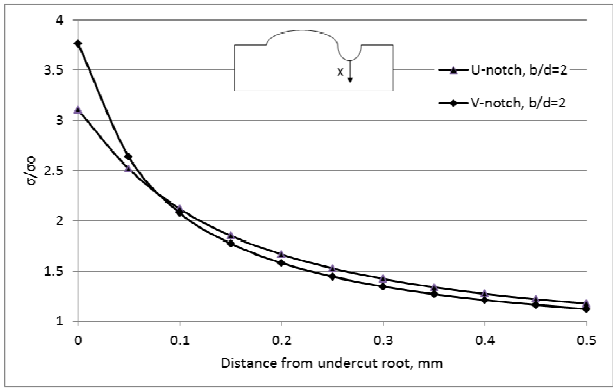

Fig. 6 Comparison of stress distribution

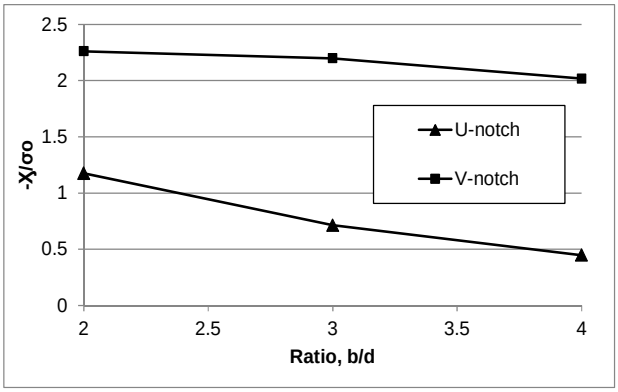

Fig. 7 Stress gradient based on shape ratio

4.2 Effect of undercut depth

The most important factor which effecting fatigue life is undercut depth. N.T Nguyen [2] suggests three types of crack which are curve, crack-like and micro flaw. In this case, the study focuses to the curve and crack-like type. Fig. 8 illustrates selected cases for fatigue life at different weld bead height and undercut depth. As can be seen, model with no reinforcement with lower undercut depth shows higher fatigue life compare to others. Next, model with weld bead height of 2.5mm with undercut depth of 1mm present lower fatigue life. Here, the result confirms deeper undercut depth will reduce the fatigue life of any welded joint structures. However, this case shows the stress concentration factor has significant effect even though stress gradient at higher side for deeper undercut depth (see Fig. 9).

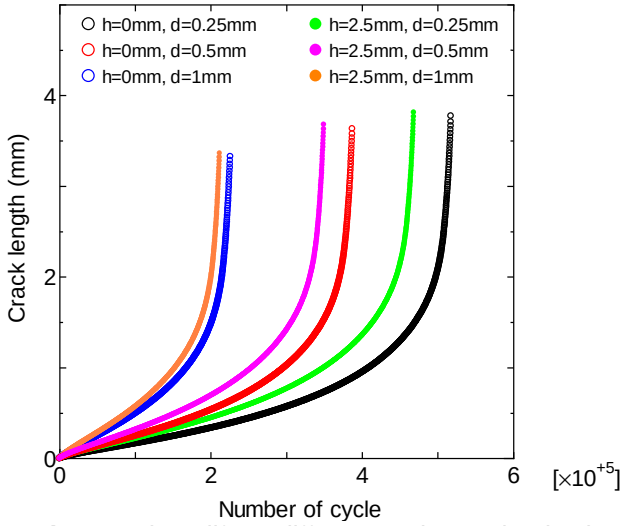

Fig. 8 Fatigue life at different undercut depth, *d*

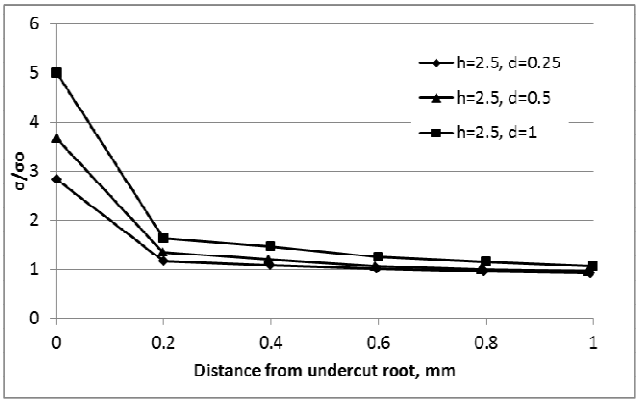

Fig. 9 Stress distribution for *h*=2.5mm at different undercut depth

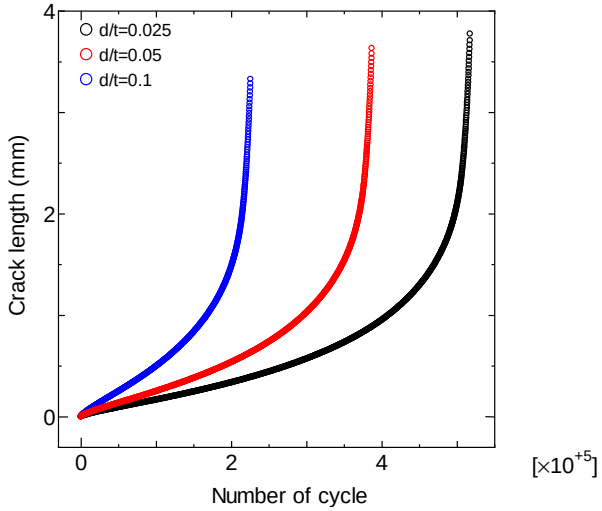

Fig. 10 Fatigue life at different *d/t*

The relationship between undercut depth and the plate thickness is vital in order to estimate the fatigue life. Fig. 10 shows fatigue life at higher d/t present lower fatigue life. The undercut over plate thickness ratio can be considered in the improvement of the JSQS code. The figure presents a significant effect of different ratio where the different fatigue life at d/t=0.05 and 0.1 is about 300,000 cycles. Comparison between different type of notch shape at same shape ratio, b/d=4 shows about 80,000 cycles. Therefore, undercut depth, especially d/t ratio plays more significant effect in contributing to the fatigue performance on welded structure.

5 CONCLUSIONS

Numerical investigation shows the importance of geometrical parameters of welded joint in order to specify undercut limit. The study is limited to the effect of notch shape and undercut depth. However, other geometrical parameter such as flank angle and weld bead width is not discussed. The outcome of the study will be beneficial in order to improve JSQS code which emphasis only undercut limit without considering the plate thickness. Most of the codes and standards mention about the limitation of undercut depth related to plate thickness but in very small tolerance. Therefore, the study suggests the improvement of undercut limit with consideration of the plate thickness. In addition, several conclusions can be drawn are as follows:

a) The study found the V-notch undercut type gives higher fatigue life compared to the U-notch at the constraint of same shape ratio, *b/d.*
b) Stress gradient, χ is the important criteria in assessing fatigue strength for different shape of the notch of the butt welded structure. However, it is not significant when investigating the effect of undercut depth.
c) Undercut over plate thickness ratio, *d/t* was introduced to consider plate thickness in evaluating fatigue performance of welded structure.

6 ACKNOWLEDGEMENTS

The first author gratefully acknowledged the Malaysian Government (Public Service Dept.) especially Dept. of Occupational Safety and Health Malaysia for their supports through scholarship provided. The authors also acknowledge FFWP Lab members especially Mr. K. Murakami, Mr. K. Matsuda and Mr. K. Yamashita for their help during simulation work.

7 REFERENCES

[1] W. Fricke, Fatigue Analysis of Welded Joints: State of Development, Marine Structures 16, pp 185-200, 2003.

[2] N.T Nguyen and M.A Wahab, The Effect of Undercut and Residual Stresses on Fatigue Behaviour of Misaligned Butt Joints, Engineering Fracture Mechanics, vol. 55, no. 3, pp 453-469, 1996.

[3] S.M.I. Mahmud and Y. Sumi, Thickness Effect on Fatigue Strength of Plates with Semi-Elliptical Side Notches and Weld Joints, *Journal* of *JASNAOE* 14, pp.19-26, 2011.

[4] M.Cerit, O.Kokumer and K.Genel, Stress Concentration Effects of Undercut Defect and Reinforcement Metal in Butt Welded Joint, Engineering Failure Analysis 17, pp 571-578, 2010.

[5] Hobbacher, Problem of Effect of Weld Imperfections on Fatigue and Their Consideration in Design Codes, Steel Structures 6, 289-298, 2006.

[6] M. Fillippini, Stress Gradients Calculations at Notches, International Journal of Fatigue 22, pp 397-409, 2000.

[7] M. Toyosada, K. Gotoh and T. Niwa, Fatigue Crack Propagation for a Through Thickness Crack: A Crack Propagation Law Considering Cyclic Plasticity Near the Crack Tip, International Journal of Fatigue 26, Issue 9, pp 983-992, 2004.

[8] M. Toyosada, K. Gotoh and T. Niwa, Fatigue Life Assessment for Welded Structures without Initial Defects: An Algorithm for Predicting Fatigue Crack Growth from a Sound Site, International Journal of Fatigue, 2004.

[9] K. Matsuoka, I. Takahashi, T. Yoshii, H. Iidaka and Fujii, Effects of Plate Thickness and Heat Input of Fatigue Strength of Non-Load-Carrying Fillet Welded Joints, IIW Doc. XIII-1407-91, 1991.

[10] K. Harada and K. Gotoh, Improvement of the Strip Yield Model Considering the Work Hardening Effect of Materials, Journal of the Japan Society of Naval Architects and Ocean Engineers, 2011 (in-press), (in-Japanese).

[11] K.Yuan and Y.Sumi, Welding Residual Stress and Its Effect on Fatigue Crack Propagation After Overloading, Analysis and Design of Marine Structures, Taylor and Francis Group, London, 2013.

Proceedings of the 3rd International Conference on
Fracture Fatigue and Wear, pp. 182-188, 2014

EVALUATION OF SMALL-CRACK GROWTH RATE IN ULTRAFINE GRAINED COPPER

M. Goto[1], N. Teshima[2], S.Z. Han[3], J.H. Ahn[3], J. Kitamura[1] and S. Kim[4]

[1]Oita University, Department of Mechanical Engineering, Oita, Japan
[2]Oita National College of Technology, Oita, Japan
[3]Korea Institute of Materials Science, Changwon, Republic of Korea
[4]Gyeongsang National University, Chinju, Republic of Korea

Abstract: In order to evaluate the crack growth rate (CGR) of ultrafine grained copper processed by equal channel angular pressing (ECAP), high-cycle fatigue tests of smooth specimens were conducted. Prior to fatigue tests, some ECAPed specimens were annealed at 160 °C to reduce the microstructural instability. The CGR of small cracks in non-annealed specimens could not be treated by the stress intensity factor range (ΔK), but it was uniquely determined by the term $\sigma_a{}^n l$ for all stress amplitudes examined, with $\sigma_a \geqq 90$ MPa. For annealed specimens, the growth law of small cracks was divided into two types according to the magnitude of applied stress amplitudes: the CGR was estimated by ΔK for $\sigma_a \leqq 120$ MPa and by $\sigma_a{}^n l$ for $\sigma_a \geqq 160$ MPa. The effect of post-ECAP annealing on the crack growth behaviour is discussed from the viewpoints of the microstructural evolution during stressing.

Keywords: copper; ECAP; high-cycle fatigue; crack propagation; stress intensity factor

1 INTRODUCTION

Ultrafine grained (UFG) and nano-crystalline materials have gained remarkable attention due to their extraordinary properties [1,2]. The severe plastic deformation (SPD) technique, such as the equal channel angular pressing (ECAP), has been used to obtain UFG materials in bulk size. Until recently, most studies on UFG materials have focused on optimizing processing conditions, underlying microstructural mechanisms, or attainable post-ECAP strength levels. For envisaged structural applications of UFG metals, attention has been paid to fatigue performance regarding cyclic properties, S-N characteristics, and formation of shear bands (SBs). Many investigators have reported that high-cycle fatigue (HCF) tests of UFG copper generally exhibits enhanced fatigue life in an S-N plot, whereas when low-cycle fatigue (LCF) life was plotted in a Manson-Coffin plot , the fatigue life is known to decrease [3,4]. Recently, the effects of post-SPD annealing on LCF have been studied. Mughrabi et al. [5] reported that after optimized annealing, UFG ECAP copper exhibits enhanced Manson-Coffin fatigue life, and is superior to conventional-grain-size copper. However, study on fatigue properties in the HCF regime of post-SPD annealed copper has been relatively rare, and only a few reports can be found.

On the other hand, it has been shown that the crack growth life from an initial size to 1 mm accounted for about 70% of the fatigue life of plain specimens of many conventional grain-sized metals. Therefore, the growth behaviour of small cracks must be clarified to estimate the fatigue life of smooth members.

In this study, the evaluation of small-crack growth rate was discussed for UFG copper samples having different microstructures; ECAPed microstructure with 300nm grain size, and post-ECAPed bi-modal microstructure.

2 EXPERIMENTAL PROCEDURES

Pure oxygen-free copper (99.99 wt% Cu) was used in the experiment. Prior to ECAP processing, the materials were annealed at 500°C for 1 hr (average grain size, 100 μm). The die used for the ECAP processing had a 90° angle between intersecting channels. The angles at the inner and outer corners of the channel intersection were $\Phi = 90°$ and $\Psi = 45°$, respectively. Repetitive ECAP was accomplished according to the Bc route (after each pressing, the billet bar was rotated 90˚ around its longitudinal axis). Each rod was subjected to 4 sequential passes of pressing at room temperature. After the ECAP processing, some of the samples were annealed at a temperature of 160 ˚C in an oil bath for 3 min. The UFG copper

processed through 4 ECAP passes, and the post-ECAP annealed UFG copper are referred to hereafter as UFG4 and UFG4A, respectively.

Round bar specimens 5 mm in diameter were machined from their respective processed bars. Although the specimens had a shallow circumferential notch (20-mm notch radius and 0.25-mm notch depth), the fatigue strength reduction factor for this geometry was close to 1, meaning that they could be considered plain. The fatigue specimens were electrolytically polished (≈ 25 μm from the surface layer) prior to mechanical testing to remove any preparation-affected surface layer. Polishing was carried out at 25°C using an electrolyte consisting of 600 mL of phosphoric acid, 300 mL of distilled water, and 100 mL of sulphuric acid. All fatigue tests were performed at room temperature using a rotating-bending fatigue machine (constant bending-moment type) operating at 50 Hz. The fatigue damage on the specimen surface was observed using optical microscopy and scanning electron microscopy (SEM). The crack length, l, is a length measured along the circumferential direction of the surface. The crack length measurements were conducted by using a plastic replication technique. The stress value referred to is that of the nominal stress amplitude, σ_a, at the minimum cross-section (5-mm diameter).

The cross-section perpendicular to the press direction was observed in electron backscatter diffraction (EBSD) analyses. EBSD mappings were executed using a Tescan Mira II SEM incorporating an EDAX-TSL Hikari EBSD detector. Orientation imaging microscopy (OIM) analysis software version 5.3 was used. The degree of non-equilibrium state in the microstructures was measured using differential scanning calorimetry (DSC). All of the experiments were performed using nitrogen atmosphere in a DSC chamber with continuous heating and ramp rate of 10°C/min up to 450°C.

3 EXPERIMENTAL RESULTS AND DISCUSSION

Figure 1 shows image quality (IQ) maps and grain boundary (GB) maps of the (a) ECAP processed and (b) post-ECAP annealed samples. The IQ maps represent the strain distribution; the bright and dark areas in the maps indicate less strained and highly strained regions with higher dislocation density, respectively. The GBs in GB maps are denoted either by red lines corresponding to low-angle GBs (LAGBs) where the misorientation, θ, is between 2° and 15°, or by black lines corresponding to high-angle GBs (HAGBs) with θ > 15°. The GB maps of UFG4 exhibit inhomogeneous microstructures including fine equiaxed grains and large elongated grains. This map indicates the development of subgrains within elongated grains, isolated with LAGBs. In addition, there is contrast that arises from a variety of strain distribution in the IQ map. Considering IQ and GB maps together, high-strained microstructures revealed as dark areas in the IQ map correspond to areas filled with many defects (dislocations/LAGBs) meaning non-equilibrium state. Thus, the microstructure in UFG4 has enhanced strain energy due to the redundant defect structure, meaning that the microstructure is in the process of evolving to equiaxed grains isolated with HAGBs. The average grain/cell size (d) of UFG4 was measured as 411 nm for elongated grains; their thicknesses were measured as grain size instead of the diameter of equiaxed grains. For the microstructure of UFG4A, the fraction of dark areas in the IQ map was drastically reduced compared to UFG4. The GB map of UFG4A showed larger grains with few defects in their interior due to short-term annealing. These larger grains had sizes ranging from a few to a few tens of micrometers, and were surrounded by fine grains with HAGBs and bimodal microstructure. Microstructure of UFG4 can be regarded as some of bimodal grain mixture in the form of patches of elongated larger grains next to regions with the UFG microstructure. In UFG4A, larger grains were embedded in the original UFG structure, resulting in a developed bimodal structure. The annealing treatment led to the development of a bimodal grain size distribution [5,6]. The ECAP deformed Cu microstructure contains a high dislocation density and comprises a high fraction of LAGBs as any typical structure does. In post-ECAP annealed UFG copper, recrystallized grains appear to grow by consuming deformed microstructure with high density of defects, shown as dark areas in the IQ map of UFG4, and the recrystallization process should still be in progress. Thus, the large grains appeared as a result of discontinuous recrystallization. The decreased strain energy due to annealing should affect microstructural evolution during cyclic stressing.

The differences in the heat-flow (HF) values measured by DSC were 0.85 and 0.27 J/g for UFG4 and UFG4A, respectively. As might be expected, the HF values of the fully annealed copper were almost zero. The large HF value for UFG4 means that the strain energy related to defect structure is stored in the microstructure. The HF for UFG4A reduced to about one third that of UFG4, but it was larger than that of fully annealed copper, indicating that the matrix still had appreciable strain energy and was microstructurally unstable in comparison with perfect polycrystalline structure.

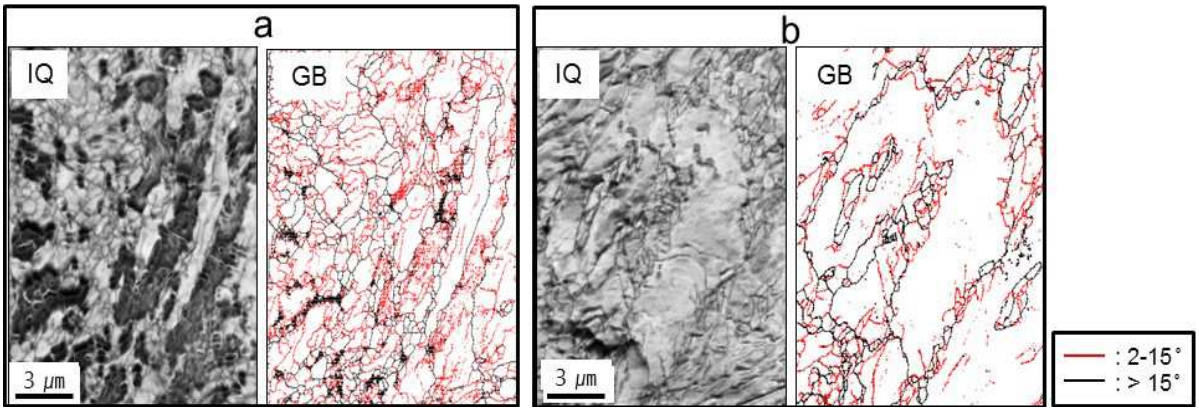

Fig. 1 The IQ and GB maps for ECAPed copper: (a) as received; (b) with post-ECAP annealing at 160 ˚C in an oil bath for 3 min

The tensile strength, σ_u, of fully annealed copper is enhanced by ECAP processing (σ_u = 232 → 413 MPa). Conversely, this processing method also causes a large drop in tensile elongation, (ϕ = 65 → 21 %). Post-ECAP annealing leads to the recovery of elongation (ϕ = 42 %), whereas the tensile strength decreases to σ_u = 334 MPa.

With regard to the crack initiation, a major crack, which led to the final fracture of the specimen, was initiated from SBs/slip bands at an early stage of cycling (N/N_f < 0.3). Figs. 2a and b show the initial growth behaviour of major cracks in UFG4 (σ_a = 120 MPa) and UFG4A (σ_a = 85 MPa), respectively. The intermittent monitoring showed that a 15 μm-length crack in UFG4 was monitored at N = 3.9x10^5 (N/N_f = 0.17). Here, the specialization of crack initiation time/length was unclear, and the initiation length was likely to depend on applied stress amplitudes. On the other hand, the major crack in UFG4A started from long damaged traces with 40 μm length (Fig. b). Major crack initiation sites in UFG4A were slip bands and boundaries of coarse grains formed due to pre-annealing.

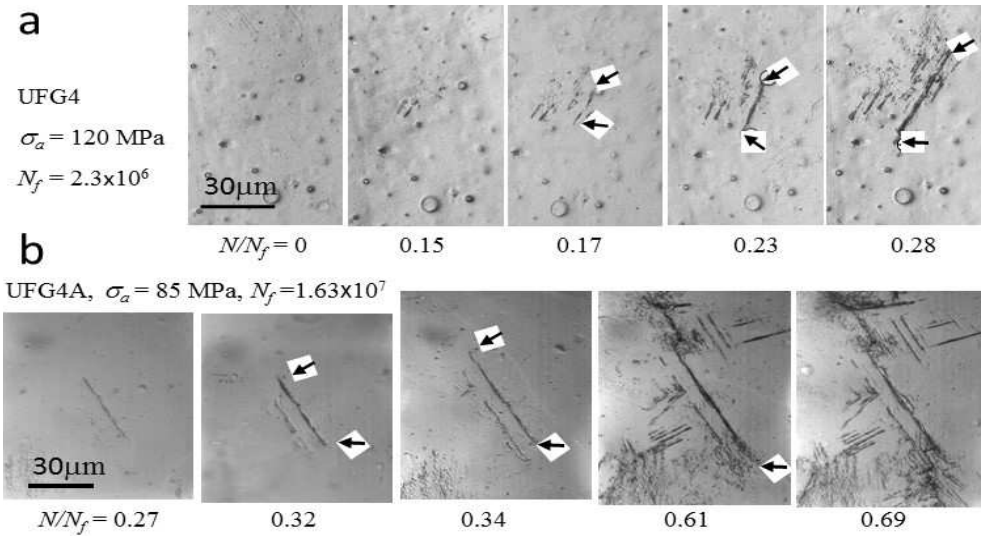

Fig. 2 Changes in the surface state around major-crack initiation sites during repeated stressing: (a) UFG4 (σ_a = 120 MPa), and (b) UFG4A (σ_a = 85 MPa)

The growth behaviour of surface cracks was monitored by a plastic replication technique. Fig. 3 shows the growth curves (ln$l$ vs. N) of the major cracks that led to the final specimen fracture. The crack growth life from an initial size (e.g. 30 μm) to fracture accounted for about 60% of the fatigue life of the UFG4 specimens. Like the UFG4 specimens, the crack growth life from initial size to fracture accounted for 80% of the fatigue life of UFG4A. However, the shapes of the growth curves were clearly differentiated between the UFG4 and UFG4A specimens. The growth curve for UFG4 can be approximated by a linear relationship. The linearity of growth curve indicates that CGR is proportional to the crack length. For the

UFG4A, the relationship can be divided into two types: linear and concave upward lines, according to the magnitude of applied stress. This means that the measure to evaluate the CGR is changed by applied stress amplitudes.

To qualitatively study the growth behaviour of both copper samples, the CGR (*dl/dN*) was calculated based on the raw growth data. Fig. 4 shows the *dl/dN* vs. *l* correlation, showing a linear relation for UFG4 copper with the exception of threshold regions (*dl/dN* < 10^{-7} mm/cycle). That is, the CGR of UFG4 copper was proportional to the crack length. For UFG4A copper, the linear correlation with slope of 1 nearly held at high stress amplitudes, but the correlation at low stress amplitudes exhibited the linear relation with slope larger than 1 with the exception of threshold regions (*dl/dN* < 5x10^{-7} mm/cycle).

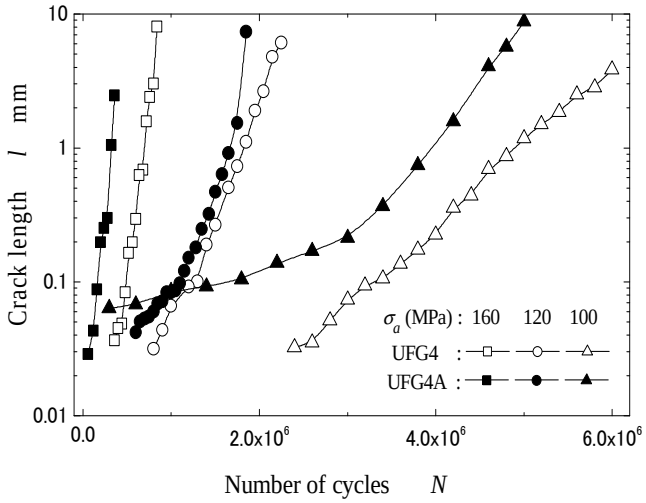

Fig. 3 Crack growth curves (ln*l* vs. *N*)

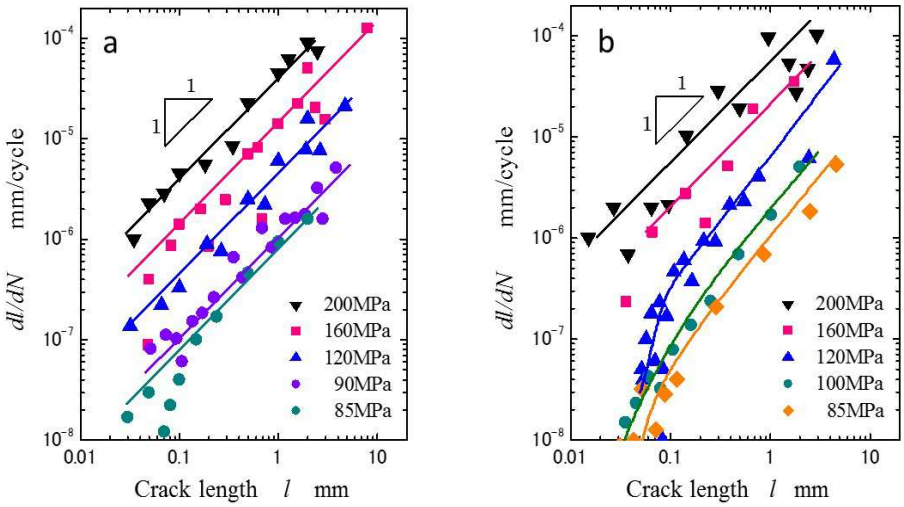

Fig. 4 The *dl/dN* vs. *l* relationship: (a) UFG4; (b) UFG4A

With regard to the linear elastic fracture mechanics (LEFM) approach in UFG materials, the propagation for a long (millimeter-range) crack for intermediate ΔK magnitudes is controlled by the Paris law [7]:

$$dl/dN = C\,\Delta K^m \quad (1)$$

where *C* and *m* are material constants. Figs. 5 a and b show the *dl/dN* vs. ΔK correlation for UFG4 and UFG4A, respectively. The solution for ΔK is taken from Fonte and Freitas [8] for semi-elliptical surface cracks in round bars under bending. The CGR of UFG4 cannot be determined by ΔK, showing a stress dependency of the *dl/dN*-ΔK relation. For UFG4A, the CGR at high stress amplitudes ($\sigma_a \geqq 160$ MPa) cannot be estimated by ΔK like UFG4. At low stress amplitudes ($\sigma_a \leqq 120$ MPa), however, the relationship,

except for the threshold range $dl/dN < 10^{-6}$ mm/c, can be represented by a linear relation, indicating the validity of LEFM approach for estimating CGR of small surface cracks. Nisitani and Goto [9] proposed Eq. (2) for determining the CGR at high stress amplitudes:

$$dl/dN = D\,\sigma_a^n l \qquad (2)$$

where D and n are material constants. The growth data of small cracks in various conventional-grain-size metals indicated that dl/dN of a mechanically small crack is uniquely determined by the term: $\sigma_a^n l$ and not by ΔK. Here, Eqs. (1) and (2) structurally contradict each other except when $m = n = 2$ (m can be ≤ 4 and n

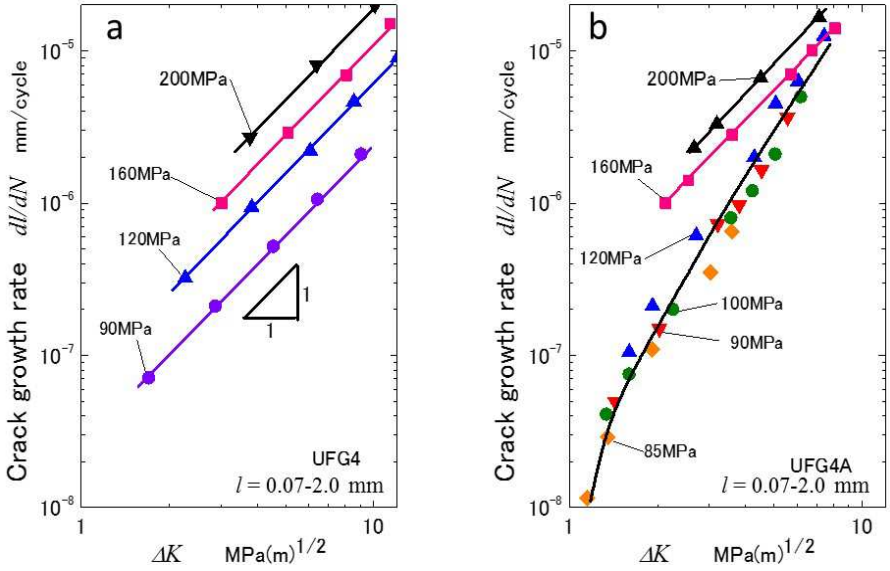

Fig. 5 Growth data of small cracks (dl/dN vs. ΔK correlation) in (a) UFG4 and (b) UFG4A

is usually > 2). But, it has been shown that these two equations can be consistently deduced from the same physical basis that the CGR is proportional to the reversible plastic zone (RPZ) size, and can successfully

deal with the variation in crack closing behaviours between long and short cracks [9]. Fig. 6 shows the growth data of a small crack with the dl/dN vs. $\sigma_a^n l$ correlation. The values of n in Eq. (2) were 4.4 for the ECAP-processed copper samples regardless of post-ECAP annealing. Although Eq. (1) failed to represent the growth rate of a small crack other than for cracks growing under low stress amplitudes for UFG4A, the plots of all growth data based on Eq. (2) produced a straight line in each sample. Thus the CGR of small cracks propagating at $\sigma_a \geqq 90$ MPa for UFG4 and $\sigma_a \geqq 160$ MPa for UFG4A can be approximately estimated by Eq. (2).

To investigate the effect of post-ECAP annealing on the microstructural evolution during long-term stressing, the specimen surfaces were studied after 2×10^7 repetitions of $\sigma_a = 80$ MPa, through observations of microstructure revealed by etching after polishing off a few μm surface layer. Figs. 7a and b show the UFG4 microstructure of pre- and post-stressing, respectively. After the stressing, large grains with sizes in excess of 100 μm embedded in fine microstructures were formed. Dynamic recovery/recrystallization process is very likely to be responsible for the cyclic grain coarsening [10]. Figs. 7c and d show the UFG4A microstructure of pre- and post-stressing, respectively. Fig. 7c reveals the annealed UFG microstructure consisting of recrystallized grains with diameters up to a few tens of micrometers. The grain coarsening due to post-ECAP annealing was a result of discontinuous recrystallization. Fig. 7d shows the surface microstructure after the stressing. There are no significant differences in coarse grain sizes between pre- and post-stressing, suggesting less driving force for dynamic recrystallization because of a release of high strain energy due to the post-ECAP annealing.

Figure 8 shows SEM micrographs of crack tip areas taken at the state of unloading. The cracks were formed under repetitions of $\sigma_a = 120$ MPa and the crack tip areas were observed when the CGR reached about $dl/dN \approx 10^{-6}$ mm/cycle. It is evident that the crack tip for UFG4 exhibits an opening state, whereas crack closure appears to occur for UFG4A. The opened crack tip in the unloaded state suggests constant U-values close to 1 under applied stress amplitudes, leading to
applicability of Eq. (2) for CGR estimation [9]. The failed small scale yielding (SSY) condition in UFG4, in spite of relatively lower applied stress amplitudes in comparison with its original high tensile strength, is mainly attributed to softening of matrix derived from the occurrence of larger grains as a result of dynamic

recrystallization. On the other hand, Eq. (1) can be applicable to cracks in UFG4A at a stress range $\sigma_a \leqq$ 120 MPa where the SSY condition holds, in spite of the CGR of UFG4 at the same stress range having been evaluated by Eq. (2). This applicability of Eq. (1) in UFG4A is attributed to the bimodal microstructure. For UFG4A, since no further grain coarsening due to dynamic recovery/recrystallization occurred, the bimodal microstructure consisting of both moderately coarse and fine grains still remains during stressing, and is likely to be convenient for the suppression of reversible plastic deformation at crack tips. Thus, fatigue cracks in UFG4A could satisfy the SSY condition at the stress amplitudes ranging from 90 to 120 MPa.

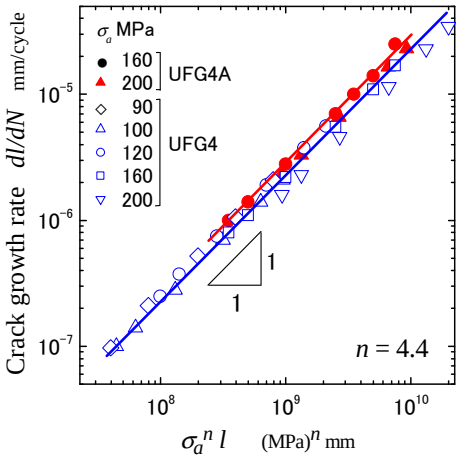

Fig. 6 Growth data of small cracks (*dl/dN* vs. $\sigma_a^n l$ correlation: n = 4.4) in UFG4 and UFG4A .

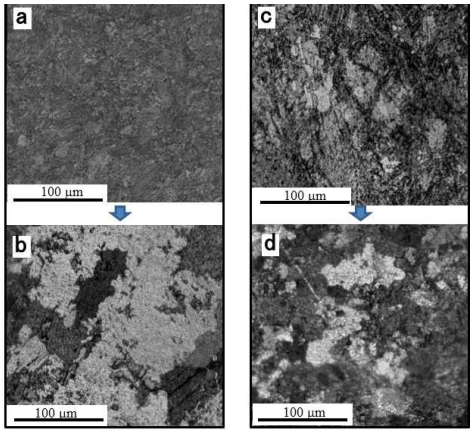

Fig. 7 Evolution of microstructures in (a, b) UFG4A and (c, d) UFG4A before and after N = 2x10^7 of σ_a = 80 MPa: (a,c) pre-stressing; (b,d) post-stressing.

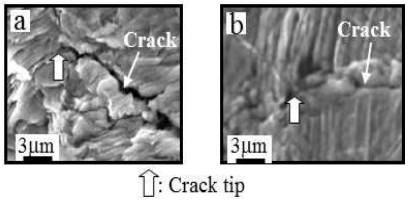

Fig. 8 SEM micrographs of crack tip areas (*dl/dN* ≈ 10^{-6} mm/c) taken at an unloading state (the cracks were initiated and propagated at σ_a = 120 MPa); (a) UFG4; (b) UFG4A.

4 CONCLUSIONS

The CGR of small cracks in UFG4 could not be treated by ΔK because of a failure to satisfy the SSY condition, but it was uniquely determined by the term $\sigma_a^n l$ for all stress amplitudes examined, with $\sigma_a \geqq$ 90 MPa. For UFG4A, the growth law of small cracks was divided into two types according to the magnitude of applied stress amplitudes: CGR was estimated by ΔK for $\sigma_a \leqq$ 120 MPa and by $\sigma_a^n l$ for $\sigma_a \geqq$ 160 MPa. The expanded applicability of ΔK in UFG4A was attributed to an extended coverage of SSY condition, which resulted from the suppressed RPZ caused by the dynamically stable bimodal microstructure with large grains ranging from a few to a few tens of micrometers embedded in the UFG microstructure

5 ACKNOWLEDGEMENTS

This study was supported by a Grant-in-Aid (23560093) for Scientific Research (C) from the Ministry of Education, Science and Culture of Japan as well, as the National Research Foundation of Korea (NRF) grant funded by the Korea government (MEST) (No. 2011-0030801), and by a grant from the Integrated Technology of Industrial Materials funded by the Ministry of Knowledge Economy, Republic of Korea.

6 REFERENCES

[1] V.M. Segal, Materials processing by simple shear, Mater Sci Eng, A197, 157-164, 1995.

[2] R.Z. Valiev, Structure and mechanical properties of ultrafine-grained metals, Mater Sci Eng, A 234-236, 59-66, 1997.

[3] A. Vinogradov, S. Hashimoto, Multiscale phenomena in fatigue of ultra-fine grain materials-an overview, Mater Trans, 42, 74-84, 2001.

[4] V. Patlan, A. Vinogradov, K. Higashi, K. Kitagawa, Overview of fatigue properties of fine grain 5056 Al-Mg alloy processed by equal-channel angular pressing, Mater Sci Eng, A300, 171-182, 2001.

[5] H. Mughrabi, H.W. Höppel, M. Kautz, Fatigue and microstructure of ultrafine-grained metals produced by severe plastic deformation, Scripta Mater, 51, 807-812, 2004.

[6] H.W. Höppel, M. Kautz, C. Xu, M. Murashkin, T.G. Langdon, R.Z. Valiev, H. Mughrabi, An overview: fatigue behaviour of ultrafine-grained metals and alloys, Int J Fatigue, 28, 1001-1010, 2006.

[7] A. Vinogradov, S. Nagasaki, V. Patlan, K. Kitagawa, M. Kawazoe, Fatigue properties of 5056 Al-Mg alloy produced by equal-channel angular pressing, NanoStruct Mater, 11, 925-934, 1999.

[8] M da. Fonte, M de. Freitas, Stress intensity factors for semi-elliptical surface cracks in round bars under bending and torsion, Inter J Fatigue, 21, 457-463, 1999.

[9] H. Nisitani, M. Goto, A small-crack growth law and its application to the evaluation of fatigue life, The Behaviour of Short fatigue Cracks, Edited by Miller KJ, de los Rios ER. EGF-Pub 1, MEP, 461-78, 1988.

[10] M. Goto, K. Kamil, S.Z. Han, K. Euh, S.S. Kim, J. Lee, Fatigue-induced grain coarsening and crack growth behaviour in ultrafine grained copper under different loading histories, Int J Fatigue, 51, 57-67, 2013.

Proceedings of the 3rd International Conference on
Fracture Fatigue and Wear, pp. 189-194, 2014

GENERATION OF SIMULATED ACCELERATION AND STRAIN SIGNALS AS THE RESPONSES OF A CAR COIL SPRING

S. Abdullah[1], T.E. Putra[1], D. Schramm[2], M.Z. Nuawi[1] and T. Bruckmann[2]

[1]Department of Mechanical and Materials Engineering, Universiti Kebangsaan Malaysia, Malaysia
[2]Departmental Chair of Mechatronics, Universität Duisburg-Essen, Germany

Abstract: This study aims to develop fatigue-based acceleration and strain signals using simulations. Acceleration and strain signals of a coil spring were undertaken from data acquisition experiments involving car movements on highway road surface at constant speeds. The measured acceleration and strain data then were used as input for the simulations in order to obtain simulated acceleration and strain signals. The results showed that there is a significant correlation between acceleration and strain data responses.

Keywords: acceleration; strain; simulation; statistics

1 INTRODUCTION

Control and stability of a car entirely depend on the contact between the road surface and the tires [1]. The contact gives a certain amount of vibration contributing to mechanical failure of car components due to fatigue as the components are subjected to cyclic loadings. The vibration causes problems with respect to the car components and the ride quality since the vibration interfaces the function of the car suspension system because the suspension components are directly exposed to variable amplitude loadings and gives a great impact on the performance of the car [2-5].

The tire forces cannot be measured directly with a high degree of accuracy especially during normal driving and they are mostly estimated using tire models and auxiliary sensors. Currently, the force is measured during the prototype phase, where this process is very expensive and intrusive. This measurement involves a lot of sensors to be placed in many orientations since the tire force does not always flow in the same way for different manoeuvres. As real testing of cars is proving to be exorbitant expensive, this study replicates these problem scenarios using simulation. Many problems arising in the automotive area have been solved using simulation methods in order to provide convenience to passengers and ensure driving safety. Thus, this study aims to develop fatigue-based acceleration and strain signals utilizing computers-based simulations. The acceleration signals are predicted to show similar behaviour to the strain signals in terms of the statistics.

2 LITERATURE OVERVIEW

2.1 The mass-spring-damper system

A method used to classify vibration is based on degree of freedom which is number of independent kinematic variables to describe the movement of a system. Fig. 1 shows an example for system with two degrees of freedom. Two degrees of freedom system were considered in this study with the assumption that that vibration acts in each tire, without affecting other tires. A mass-spring-damper system could be characterized by the mass m, the spring stiffness k, the damping coefficient c, the displacement x, the velocity $\dot{x}$ and the acceleration $\ddot{x}$. Then, the equation of motion of the system is obtained as follows:

$$m\ddot{x} + c\dot{x} + kx = F_0 \sin \omega t \quad (1)$$

In this study, forces induced from engine operation and alike are not considered, so the equation becomes the equation of motion for damped free vibration, as follows:

$$m\ddot{x} + c\dot{x} + kx = 0 \quad (2)$$

From the equation, the vibration is generated by:

$$\ddot{x} = -\frac{c}{m}\dot{x} - \frac{k}{m}x \tag{3}$$

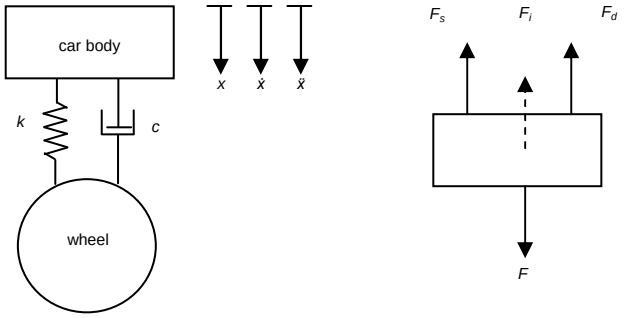

Fig. 1 A mass-spring-damper system and its free body diagram

It was hypothesized that the displacement has a strong relationship to the strain axially loaded. Strain ε is expressed as the change in length ΔL per unit of the original length L of the coil spring:

$$\varepsilon = \frac{\Delta L}{L} = \frac{\ell - L}{L} = \frac{x}{L} \tag{4}$$

where ℓ is the final length.

2.2 Global signal statistical parameters

Statistical parameters are used for random signal classification and pattern monitoring. The standard deviation (SD) measures the distribution of data based on the mean value. The SD for a number of sampling data that exceed 30 could be expressed as follows:

$$SD = \left\{ \frac{1}{n} \sum_{j=1}^{n} \left(x_j - \bar{x} \right)^2 \right\}^{1/2} \tag{5}$$

where n is the number of data, $\bar{x}$ is the mean value and x_j is the amplitude of the signal. The root-mean square (r.m.s.) is the 2nd statistical moment used for determining the total energy contained in a signal. The r.m.s. of signals with zero mean value is equal to the SD. The r.m.s. of discrete data could be calculated as follows:

$$r.m.s. = \left\{ \frac{1}{n} \sum_{j=1}^{n} x_j^{\,2} \right\}^{1/2} \tag{6}$$

In addition, the kurtosis is the 4th statistical moment that is very sensitive to spikes and it represents the continuation of peaks in a time series loading. The kurtosis for a set of discrete data is formulated as:

$$K = \frac{1}{n(SD)^4} \sum_{j=1}^{n} \left(x_j - \bar{x} \right)^4 \tag{7}$$

3 METHODOLOGY

The coil spring of a sedan car of 1,300 cc was used as a case study in this work with the values of the spring stiffness k and the damping coefficient c were 18,639 N/m and 15,564 Ns/m, respectively. The specifications were from the original sources that cannot be publically revealed. The mass m of 3,600 N was applied on the surface of the coil spring. The car was driven on highway road surface in Malaysia at velocities of 70 km/h to 80 km/h. Fig. 2 shows the general process for generating simulated strain signals.

4 RESULTS AND DISCUSSION

The Dymola® (Dynamic Modeling Laboratory) software package [6,7] was used for the multi-body dynamic simulations yielding the simulated strain signals and a MATLAB (Matrix Laboratory) Simulink®-based model [8] was developed to obtain the acceleration signals. The data acquisition experiment conducted in the current study was undertaken on highway road surface. The experiment provided vibration and strain data

received by the coil spring in accordance with the road surface profile. From the data acquisition, four acceleration signals and four strain signals were obtained. The data were time domain signals sampled at 500 Hz for the total record lengths were 15 and 10 seconds for the acceleration and the strain, respectively. Furthermore, the acceleration data were the input for the Dymola® while the strain data were the input for the MATLAB Simulink®. The simulation models, the measured acceleration data and the measured strain data are shown in Figs. 3 - 5, respectively. The 2D strain and acceleration profile graphs for each data time series are shown in Figs. 6 - 7, respectively. All accelerations occur around a fixed point and have a zero mean over time.

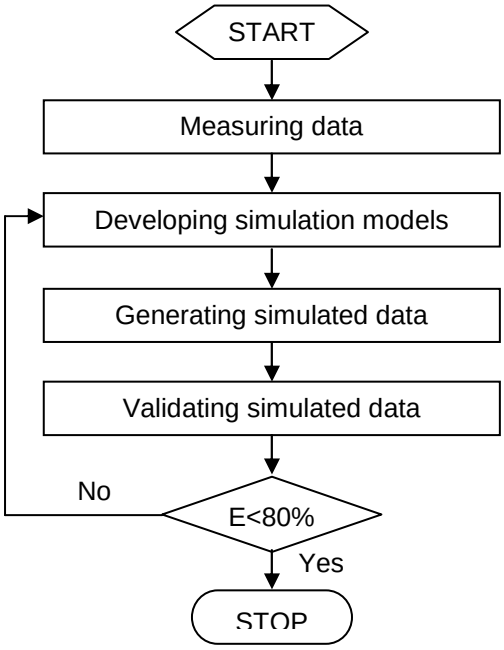

Fig. 2 Simplified flowchart of the developed simulations

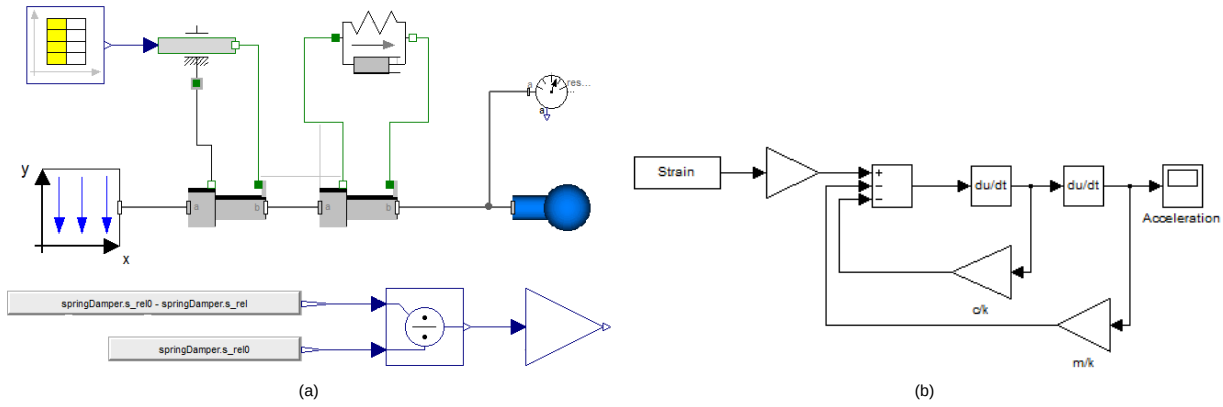

Fig. 3 The simulation models: (a) Dymola® and (b) MATLAB Simulink®

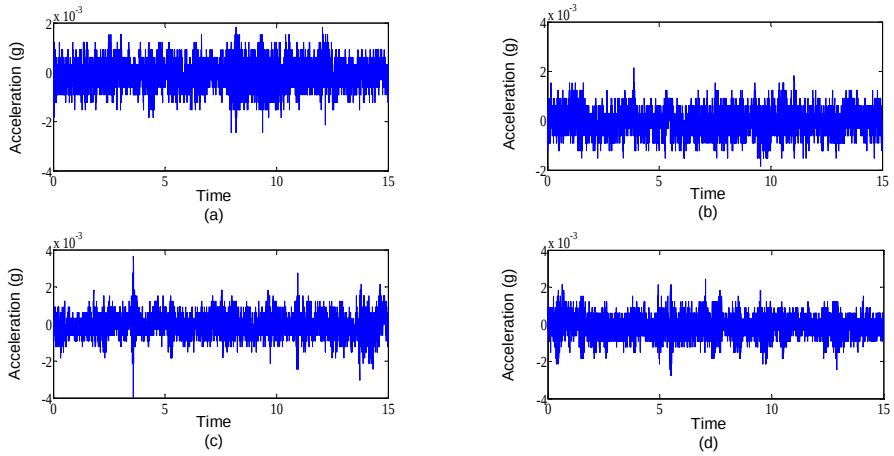

Fig. 4 The measured acceleration data

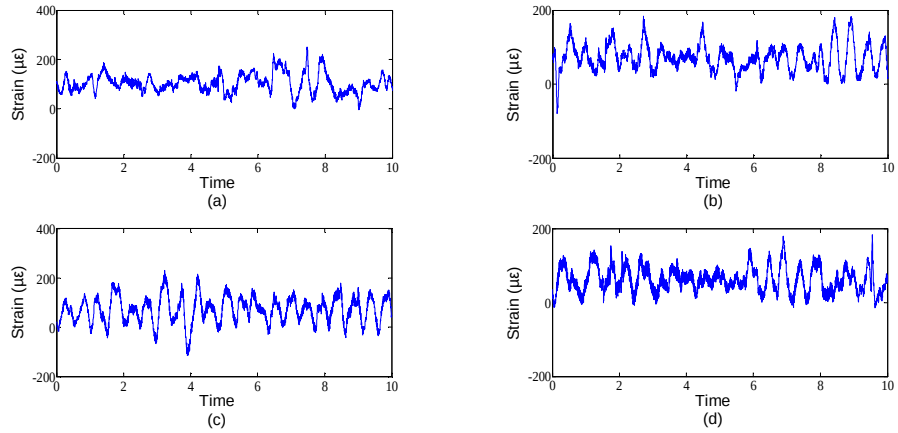

Fig. 5 The measured strain data

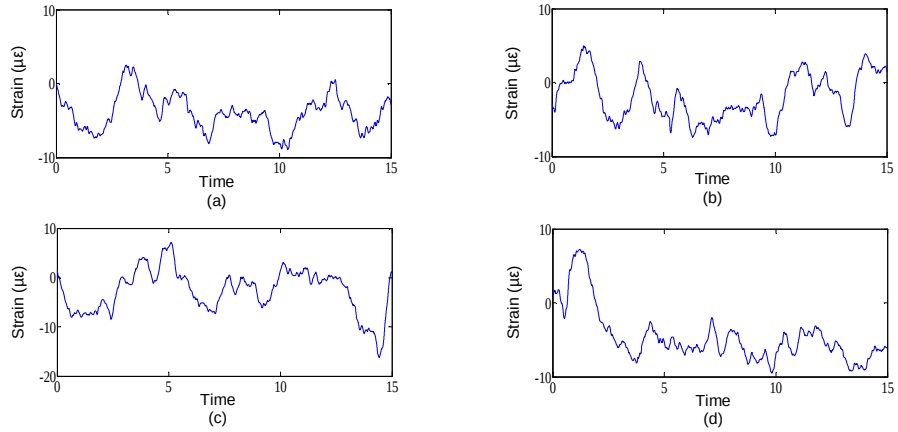

Fig. 6 The simulated strain data

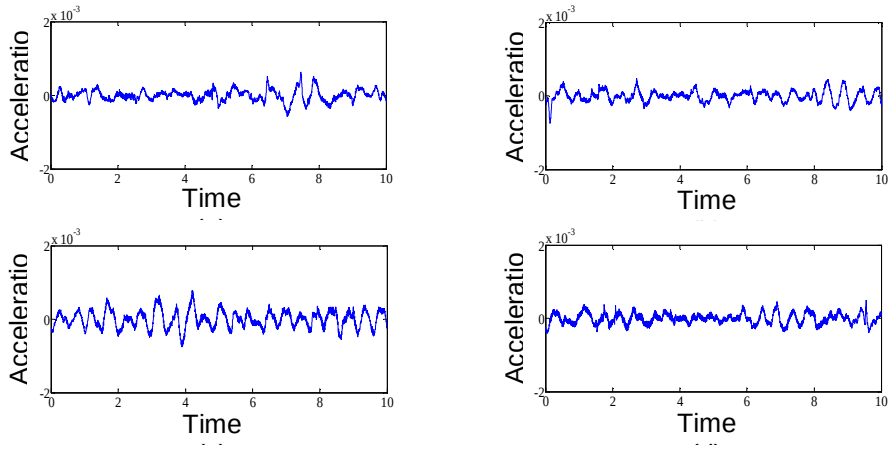

Fig. 7 The simulated acceleration data

Furthermore, the statistical parameter values for each signal were determined and scattered to observe the correlations. Fig. 8 shows the correlations between measured strain and simulated acceleration. The results show that the SD gave the highest correlation, which was 98 %, followed by the r.m.s. and the kurtosis, which were 96 % and 84 %, respectively. Then, Fig. 9 shows the correlations between measured acceleration and simulated strain. The results gave the highest correlation of 96 % for the kurtosis, followed by the r.m.s. and the SD which were 84 % and 80 %, respectively. Statistical parameters have emerged as good indicators of the fatigue life assessments. The SD measures the distribution of data based on the mean value. Higher SD shows each point in one data set is far from the mean value and gives higher fatigue damage. The r.m.s. used for determining the total energy contained in a signal. Higher energy also gives higher fatigue damage. The last one, the kurtosis is very sensitive to spikes and it represents the continuation of peaks in a time series loading. Higher kurtosis indicates higher fatigue damage.

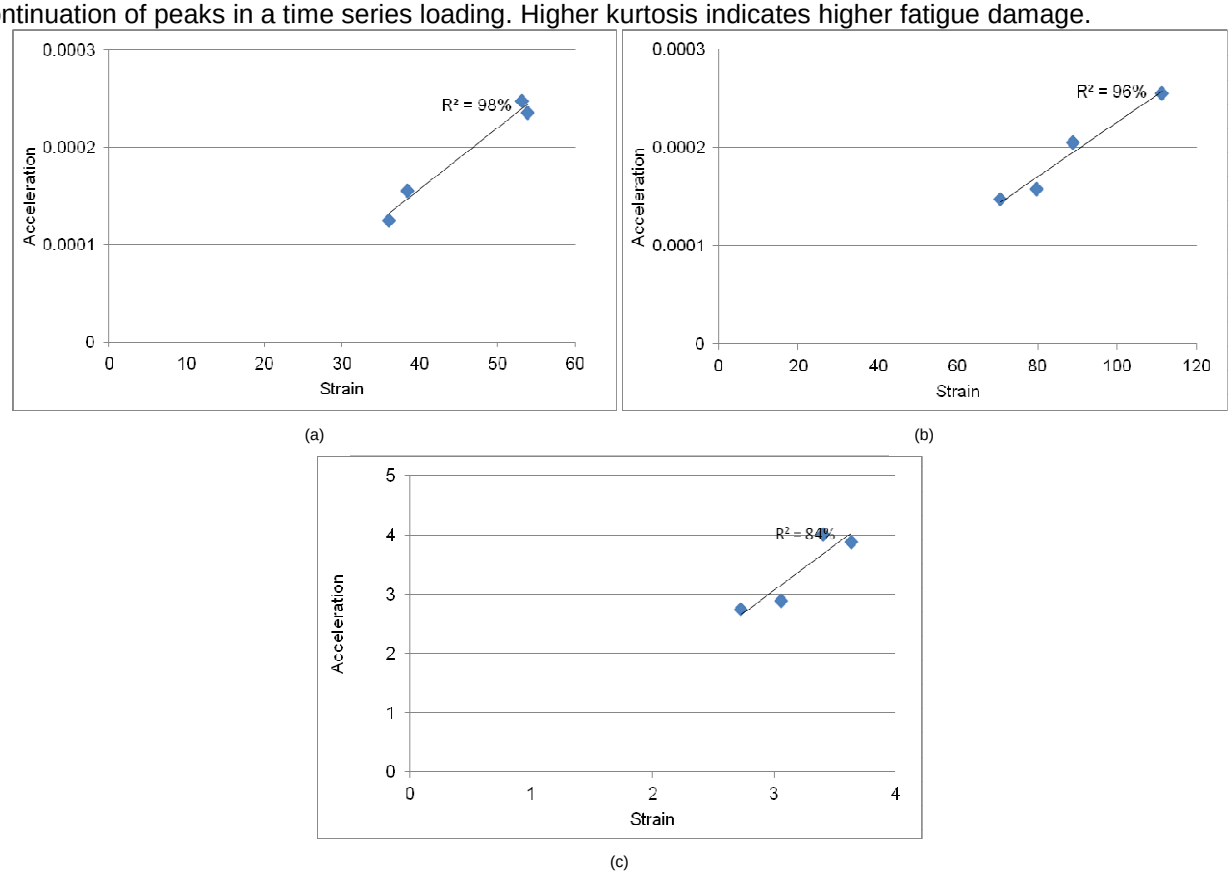

Fig. 8 Correlations between measured strain and simulated acceleration: (a) SD, (b) r.m.s. and (c) kurtosis

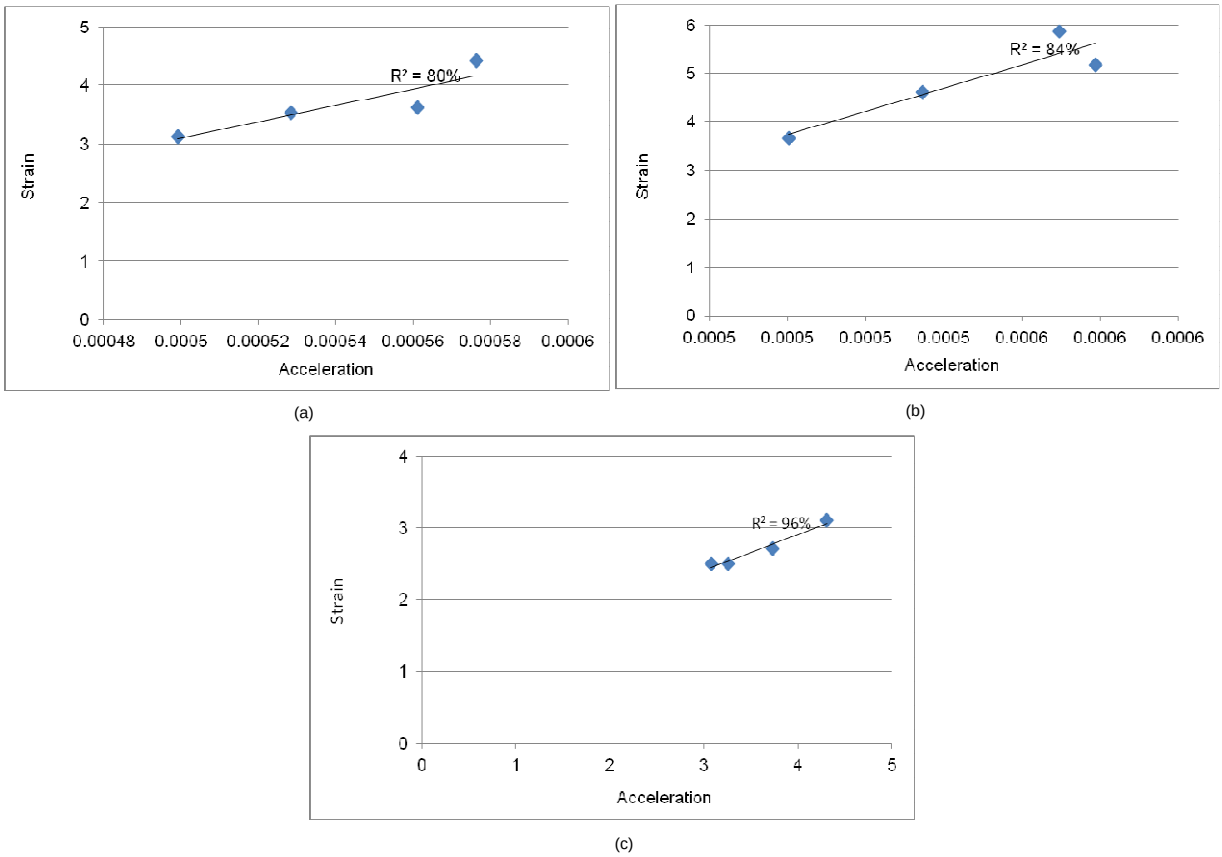

Fig. 9 Correlations between measured acceleration and simulated strain: (a) SD, (b) r.m.s. and (c) kurtosis

5 CONCLUSSION

Fatigue-based acceleration and strain signals were developed in this study using simulations. Four acceleration and strain data were measured on highway road surface as the input for the simulations. Based on the statistical parameters, each data gave high correlations, more than 80 %. It shows that simulations developed were able to produce simulated acceleration and strain data. This work will help engineers of automotive industry involved in collecting actual road surface profiles which are main input signals for the vehicle structures.

6 REFERENCES

[1] C. Ferreira, P. Ventura, R. Morais, A. L. G. Valente, C. Neves, M. C. Reis, Sensing Methodologies to Determine Automotive Damper Condition Under Vehicle Normal Operation, Sensors and Actuators A: Physical, 156, 237-244, 2009.

[2] S. Narayanan, S. Senthil, Stochastic Optimal Active Control of a 2-DOF Quarter Car Model with Non-linear Passive Suspension Elements, Journal of Sound and Vibration, 211, 495-506, 1998.

[3] V. Yildirim, Free Vibration Characteristics of Composite Barrel and Hyperboloidal Coil Springs, Mechanics Composite Materials and Structures, 8, 205-217, 2001.

[4] L. Sun, Optimum Design of ‘‘Road-Friendly’’ Vehicle Suspension Systems Subjected to Rough Pavement Surfaces, Applied Mathematical Modelling, 26, 635-652, 2002.

[5] V. Yildirim, A Parametric Study on the Natural Frequencies of Unidirectional Composite Conical Springs, Communications in Numerical Methods in Engineering, 20, 207-227, 2004.

[6] Dymola, User Manual, vol. 1, Dassault Systèmes AB, Lund, Sweden, 2011.

[7] Dymola, User Manual, vol. 2, Dassault Systèmes AB, Lund, Sweden, 2011.

[8] Simulink, User’s Guide, The MathWorks, Inc., MA, 2013.

Proceedings of the 3rd International Conference on
Fracture Fatigue and Wear, pp. 195-200, 2014

EXPERIMENTAL INVESTIGATION ON THE SUITABLE PITCH DIFFERENCE IMPROVING THE FATIGUE STRENGTH SIGNIFICANTLY FOR HIGH STRENGTH BOLTS AND NUTS

X. Chen[1], N.-A. Noda[1], H. Maruyama[1], H. Wang[1], Y. Sano[1] and Y. Takase[1]

[1] Kyushu Institute of Technology, Kitakyushu, Japan

Abstract: The high strength bolts and nuts are widely used in various fields. To ensure the structure safety, a lot of special bolts and nuts were studied previously. In this paper, a slight pitch difference is considered between the bolt and nut. Here, the pitch of the nut is α μm larger than the pitch of the bolt. The fatigue experiment is performed for three kinds of specimens with different levels of pitch difference. The obtained S-N curves show that the fatigue life is extended by about 1.5 times by introducing the suitable pitch difference especially under the high stress amplitude. According to the detail investigation on the fractured specimens, it is found that the fractured positions and the crack configuration are totally different by introducing the pitch difference. To find out the mechanism of the improvement of the fatigue strength, the finite element method is also applied to calculate the stress amplitude and mean stress at each bottom of bolt threads.

Keywords: bolted joint; pitch difference; fatigue strength; crack; finite element method

1 INTRODUCTION

The bolts and nuts are important joining elements widely used in various engineering fields. To ensure the structure safety, the high fatigue strength has been required as well as the anti-loosening performance. However, because high stress concentration factors always occur at the root of bolt thread and it is not easy to improve the fatigue strength for normal bolt and nut. A previous study indicated that the fatigue strength may be improved depending on the pitch error [1]. The effect of the thread shape on the fatigue life of bolt has also been investigated [2]. The tapered bolts named CD bolts (Critical Design for Fracture) are widely used because they showed higher fatigue strength experimentally [3,4]. Hua Zhao analyzed the stress concentration factors within bolt-nut connectors [5].

In this study, in order to improve the fatigue strength, a slight pitch difference is considered between the bolt and nut. The authors' previous study shows that the pitch difference improves the bolt fatigue life [6]. In this paper, more detailed fatigue experiment is conducted systematically under various stress amplitudes for three types specimens having different pitch difference. Then the S-N curves and fatigue life will be discussed under these conditions. To clarify the effect of pitch difference, the finite element method will be applied to analyze the stress amplitude and mean stress at the thread bottoms. The fatigue life improvement mechanism will be considered by comparing the experimental results and the finite element analysis.

2 RESEARCH METHOD

2.1 Experimental Materials

The Japanese Industrial Standard (JIS) M16 bolts and nuts are employed, and the fatigue experiment is conducted by using the 392kN Servo Fatigue Testing Machine. Table 1 and Table 2 show the JIS standard and the material properties of the bolt and nut. The normal M16 bolt and nut have the same pitch dimension 2000μm, here, the nut pitch is assumed to be equal or slightly larger than the bolt pitch. Three types of pitch difference α=0, α=15μm and α=33μm are considered. The clearance between bolt and nut is assumed as a standard dimension 125μm. The schematic diagram of bolt and nut is shown as Fig. 1. Figure 2 shows the contact status between bolt and nut when a large pitch difference is introduced.

Table 1 JIS Standard of Bolt and Nut

	Strength grade	Yield strength (MPa)	Tensile strength (MPa)
Bolt	8.8	660	830
Nut	8	-	-

Table 2 Material Properties of Bolt and Nut

	Young's modulus (GPa)	Poison's ratio	Yield strength (MPa)	Tensile strength (MPa)
SCM435 (Bolt)	206	0.3	800	1200
S45C (Nut)	206	0.3	530	980

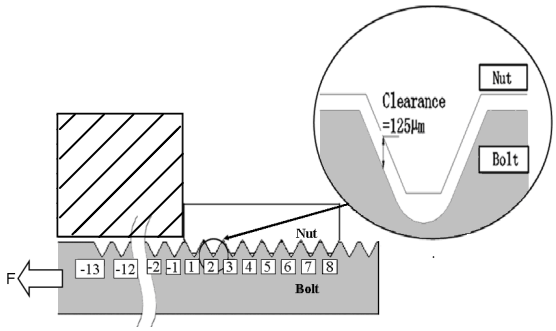

Fig. 1 Schematic diagram of bolt joint

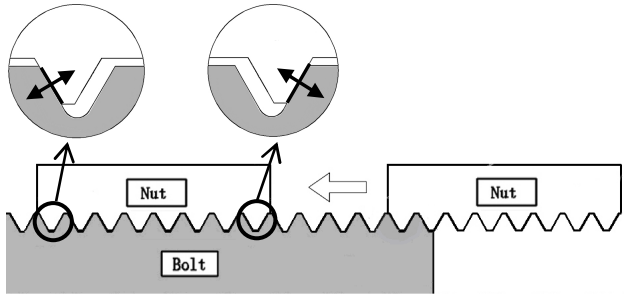

Fig. 2 Contact status between bolt and nut considering pitch difference

2.2 Experimental Conditions

The experimental device is shown in Fig.3. The bolt specimens are subjected to a series repeated loadings. Table 3 shows the experimental loading conditions and the corresponding stress according to the bottom cross sectional area of the bolt A_R=141 mm^2. The cycling frequency of the loadings is 8Hz. The stress amplitude that the specimen sustains 2×10^6 stress cycles before failure occurs is considered as the fatigue limit.

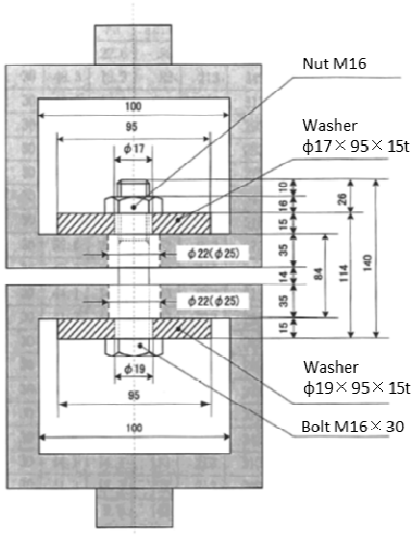

Fig. 3 Experimental device

Table 3 Experimental conditions

Load (kN)		Stress (MPa)	
Mean load	Load amplitude	Mean stress	Stress amplitude
30	22.6	213	160
30	18.3	213	130
30	14.1	213	100
30	11.3	213	80
30	8.5	213	60
30	7.1	213	50

3 THE FATIGUE EXPERIMENT RESULTS

Figures 4 to 6 show the fractured specimens subjected the stress amplitude σ_a=100MPa. For the normal bolts and nuts, it is confirmed that the fracture always occurs at the first thread bottom as shown in Fig.4. For the specimens of α=15μm and α=33μm, the fracture position is between the No.1 thread and No.3 thread of bolt. The fracture surfaces also show obviously different characteristics as varying the pitch difference.

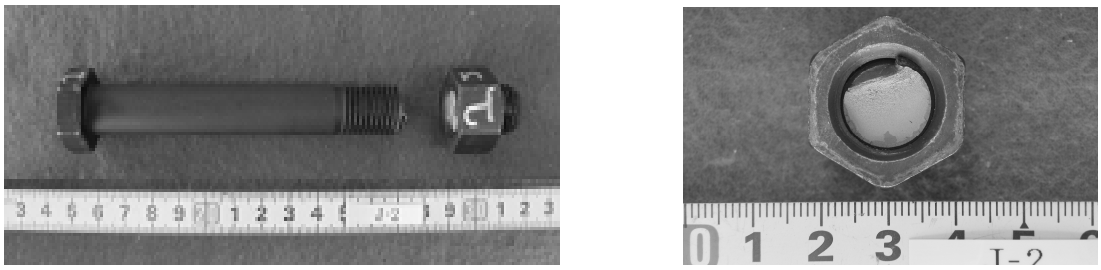

Fig. 4 Specimen (α=0 μm, σ_a=100 MPa)

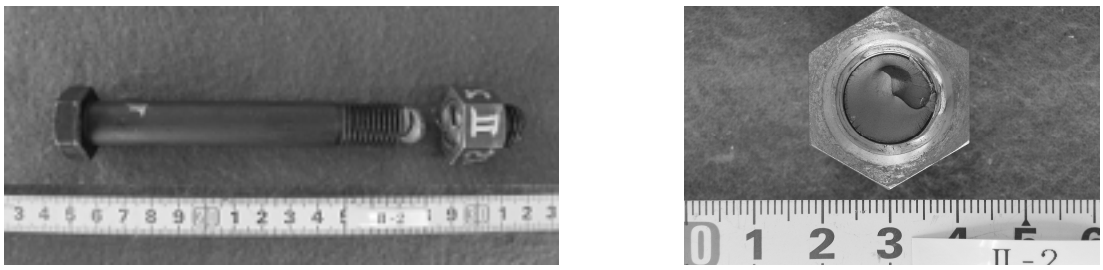

Fig. 5 Specimen (α=15 μm, σ_a=100 MPa)

Fig. 6 Specimen (α=33 μm, σ_a=100 MPa)

The S-N curves with fatigue limit at $N=2\times10^6$ stress cycles are obtained as shown in Fig. 7. It is found that the fatigue lives are clearly different depending on the three levels of pitch difference. Table 4 shows the comparison between the fatigue life normalized by the results of α=0. When the stress amplitude is above 80 MPa, the fatigue life for α=15μm is about 1.5 times larger and the fatigue life for α=33μm is about 1.2 times larger than the normal bolt and nut of α=0. However, near the fatigue limit, the fatigue life of three types specimens is not very different, and the fatigue limit remains the same value of 60 MPa for three cases of pitch difference.

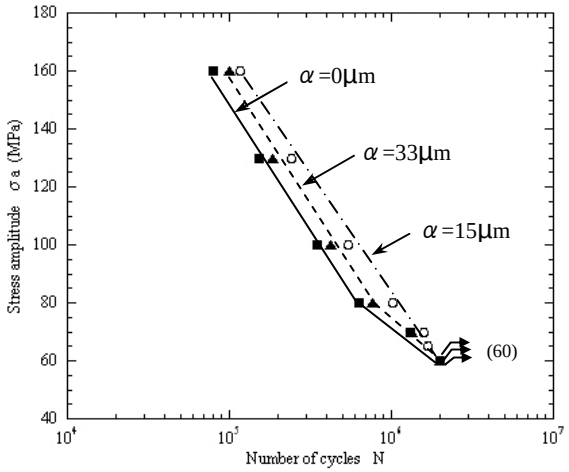

Fig. 7 S-N curves

Table 4 Comparison between the fatigue life

Pitch difference	Stress amplitude σ_a (MPa)				
	160	130	100	80	70
α=0μm	1	1	1	1	1
α=15μm	1.49	1.60	1.53	1.61	1.21
α=33μm	1.26	1.22	1.20	1.21	1.02

4 THE CRACK OBSERVATION

Figures 8-10 show the observed cracks distribution with the longitudinal cross section of the specimens under the stress amplitude σ_a=100MPa. For the specimen α=0μm, there is no crack observed. For the specimen α=15μm, a large crack occurs at No.5 thread with also small cracks between No.5 thread and No.2 thread where the fracture occurs. For the specimen α=33μm, a large crack occurs at No.6 thread with small cracks between No.6 thread and No.1 thread where the fracture occurs.

Crack observation in Fig.8 shows that for the normal bolt and nut, the crack occurs at No.1 thread causing finial fracture. However, for the specimens α=15μm and α=33μm in Fig.9, 10, the initial crack starts at No.5 thread or No.6 thread extending toward No.1 thread and finally fracture happens nearby No.1 thread. Therefore, the fatigue life of the bolt may be extended by introducing the pitch difference.

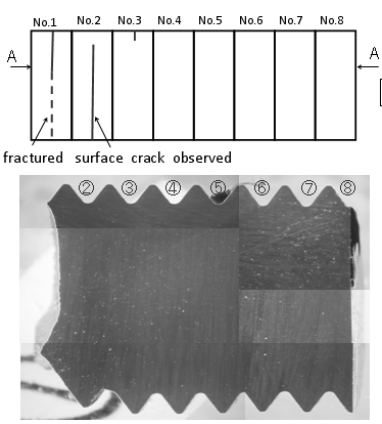

Fig. 8 Crack observation (α=0 μm, σ_a=100 MPa)

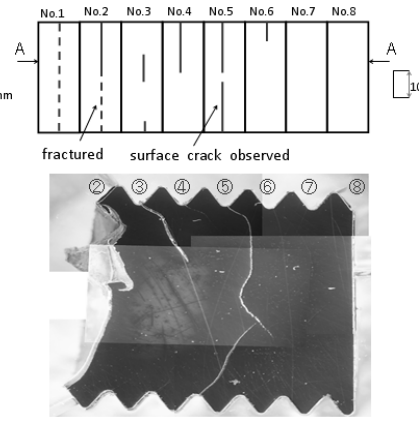

Fig. 9 Crack observation (α=15 μm, σ_a=100 MPa)

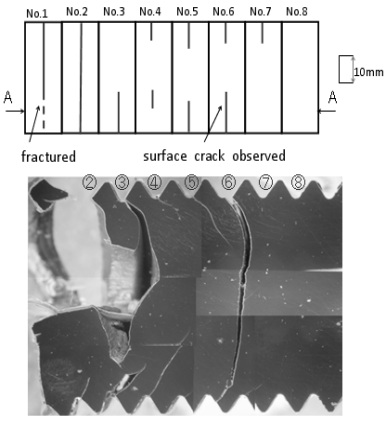

Fig. 10 Crack observation (α=33 μm, σ_a=100 MPa)

5 THE FINITE ELEMENT ANALYSIS

To analyze the stress status at the bottom of the bolt threads, the finite element models are created by using FEM code MSC.Marc/Mentat 2007. Three models have the different pitch difference of α=0, α=15μm and α=33μm in according with the experimental specimens. Figure 11 shows the axisymmetric model of the bolt, nut and clamped plate. The elastic-plastic analysis is performed for three models under the same load F=30±14.1kN. The material properties listed in Table 2 are used in the calculation. For each thread bottom from No.-3 to No.8, the stress status where the maximum stress amplitude occurs is considered, and the mean stress and the stress amplitude at that node are calculated to obtain the endurance limit diagrams as shown in Fig.12-14. The fatigue limit σ_N of the material SCM435 is 420 MPa.

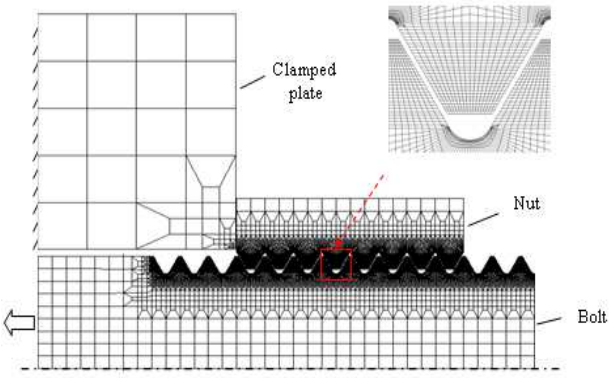

Fig. 11 Axi-symmetric finite element model

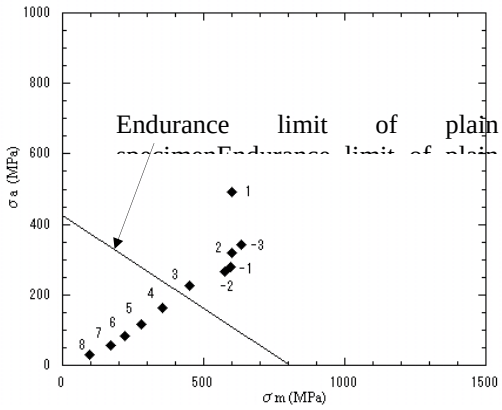

Fig. 12 Endurance limit diagram (α=0 μm, σ_a=100 MPa)

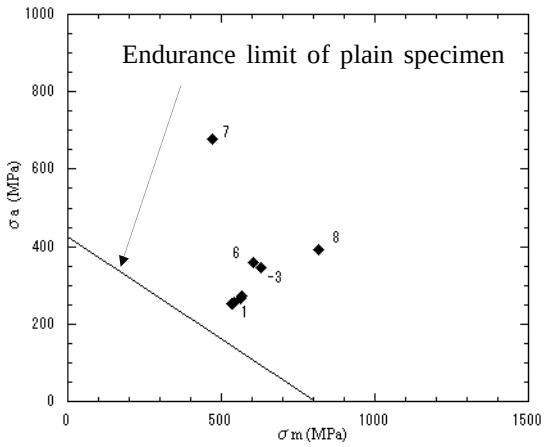

Fig. 13 Endurance limit diagram (α=15 μm, σ_a= 100 MPa)

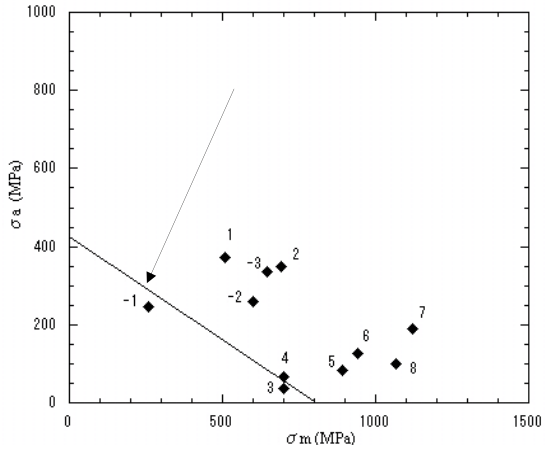

Fig. 14 Endurance limit diagram (α= 33μm, σ_a=100 MPa)

From Fig.12 we can see that for the normal bolt and nut, the No.1 thread bottom has the highest stress amplitude, which corresponds to the fracture position in the fatigue experiment as shown in the section 3. In Fig. 13, when a pitch difference of α=15μm is introduced, the stress amplitude decreases at the No.1 thread bottom. On the other hand, the stress amplitude at No.6, No.7 and No.8 increases significantly. For α=33μm, the severe stress status occurs nearby No.1 thread and No.7 thread as shown in Fig.14.

6 CONCLUSIONS

In this study, a slight pitch difference is designed between bolt and nut. The fatigue experiment have been performed, and the effect of pitch difference on the stress status of the bolt thread bottom has been numerically analyzed by using the finite element method. The conclusions can be summarized as follows:

1) It is found that α=15μm is the most desirable pitch difference to extend the fatigue life of the bolt and nut. Compared with the normal bolt and nut, the fatigue life for α=15μm can be extended by about 1.5 times.

2) It is found that the stress amplitude at the No.1 thread bottom decreases significantly when the pitch difference is introduced. For α=15μm, the FEM analysis result shows that high stress

amplitude occurs at No.6, No.7 and No.8 thread bottom, which almost corresponds to the experimental observation.

3) For the specimens α=15μm, the fatigue life improvement mechanism is considered. It is found that the crack occurs at No.5 thread in the first place, then it extends toward No.1 thread and finally fracture happens nearby No.1 thread. Therefore, the fatigue life of the bolt is extended compared with the normal bolt and nut.

7 REFERENCES

[1] K. Maruyama, Stress Analysis of a Bolt-Nut Joint by the Finite Element Method and the Copper-Electroplating Method, Trans Jpn Soc Mech Eng. 19, 360–368, 1976.

[2] S.-I. Nishida, Failure analysis in Engineering Applications, Butterworth Heinemann, Oxford, 1994.

[3] S.-I. Nishida, Screw Connection Having Improved Fatigue Strength, United States Patent 4,189,975. 1980.

[4] S.-I. Nishida, A Manufacturing Method of the Bolt Fastener, Japan Patent 2009-174564, 2009.

[5] H. Zhao, Stress concentration factors within bolt-nut connectors under elasto-plastic deformation, Int J Fatigue. 20, 651-659, 1998.

[6] Y.-I. Akaishi, X. Chen, Y. Yu, H. Tamasaki, N.-A. Noda, Y. Sano and Y. Takase, Fatigue Strength Analysis for Bolts and Nuts Which Have Slightly Different Pitches Considering Clearance, Transactions of Society of Automotive Engineers of Japan, 44(4), 1111-1117, 2013 (In Japanese).

Proceedings of the 3rd International Conference on
Fracture Fatigue and Wear, pp. 201-206, 2014

ROLLING CONTACT FATIGUE SIMULATION USED FOR FULL-OPEN TYPE GREENHOUSE

Luyu Wang,Nao-Aki Noda, Qifeng Luo, Hiroyuki Nagatomo, Yoshikazu Sano And Yasushi Takase

Kyushu Institute of Technology, Kitakyushu, Japan

Abstract: The green house is often used to add the quality and value of agricultural products. Newly developed full open type green house has a lot of attracted attention whose roof opens and closes automatically in order to control the temperature. However, since the roof opens and closes very often, the cover sheet can be used only for 3-4months. This is because the plastic film is damaged between the support pipe and rolling pipe during opening-closing affected by fatigue and wear. In this study, the damage mechanism is investigated for the several plastic films used for the full open type green house. In the first place, FEM analysis is performed to evaluate the damage of plastic film between pipes under different film materials. Here, the maximum contact pressure and thickness reduction are analysed under static contact analysis and rolling contact analysis as the most important factors. Finally, rolling fatigue experiment is performed to investigate the damage with changing plastic films. Then, the results are compared with the FEM analysis.

Keywords: contact problem; finite element method; polymer materials

1 INTRODUCTION

The new full-open type greenhouse is a building in which plants are grown at all season. It is a structure consisting of plastic roof and walls as shown in Fig. 1. To control room temperature, the plastic roof open and close frequently and automatically, which leads to the tear of the roof in short periods. In this study, FEM analysis is performed to evaluate the damage of plastic film between pipes under different film materials. Here, thickness reduction is analyzed under static contact analysis and rolling contact analysis as the most important factor. Moreover, rolling fatigue experiment has been done to simulate the real damage in plastic film and investigate the effect with changing plastic films.

2 OBSERVATION ON DAMAGED PLASTIC FILM

To find the out the possible reasons that cause the fracture, we observed several pieces of damaged plastic film by using optical microscope and scanning electron microscope. Figure 2 (a) shows the surface tear of damaged piece. We found that due to the rolling squeezing between two pipes, plastic film extends and that some creases cause on it. Figure 2 (b) shows a line scar on the flaky surface, which is caused by the cycle action of friction and pressure between pipe and plastic film or between plastic films.

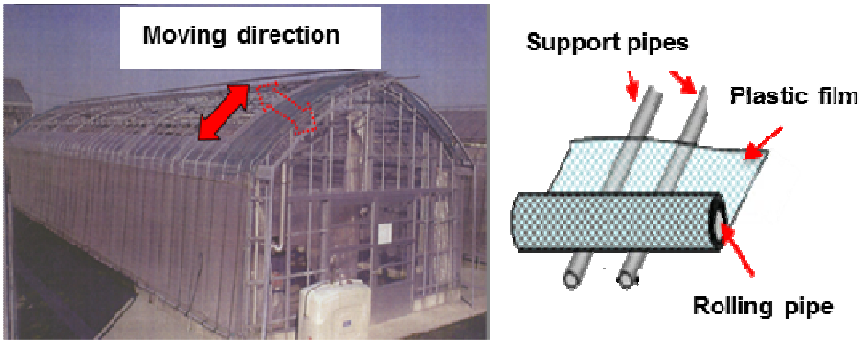

Fig. 1 Full-open greenhouse

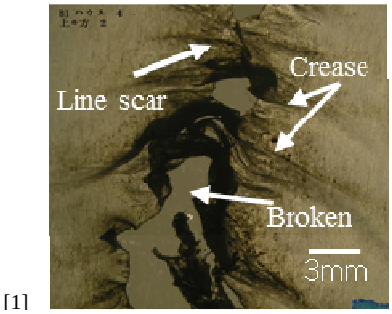

[1]

(a) Surface tear

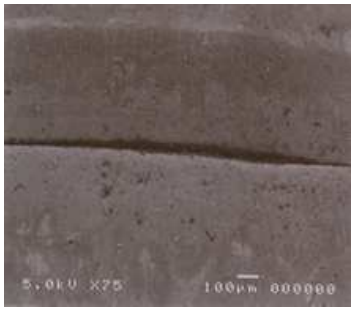

[2]

(b)Line scar

Fig. 2 Damaged plastic film

3 FEM MODEL AND RESULTS FOR STATIC CONTACT ANALYSIS

Figure 3 (a) shows the stress-strain diagram of plastic film which is used for FEM analysis. Because polymer material strength decreases with increasing the temperature [1], the ambient temperature for tensile test is assumed to be 70°C which equals to the highest temperature on pipes of greenhouse in summer. The product names of plastic film used for greenhouse are called “T”, “D”, “So”, “Su” for short.

FEM mesh for standard model is shown as Fig. 3(b), which is used to evaluate the contact pressure and thickness reduction of plastic film between pipes. The dimension of the model is consistent with the actual dimension on full-open greenhouse. Both support pipe and rolling pipe have the same diameter d_1=d_2=38mm, and thickness of plastic film is 0.15mm. The number of elements is 1.5×10^5 and the smallest element size is 0.1mm×0.1mm×0.375mm which may provide high accuracy without large calculation time. The friction coefficient between pipe and plastic film is assumed as 0.15 [2], and the load is 75N. It is known that each support pipe may carry 15N on average, however due to the manufacturing error we assume the largest load may be 75N.

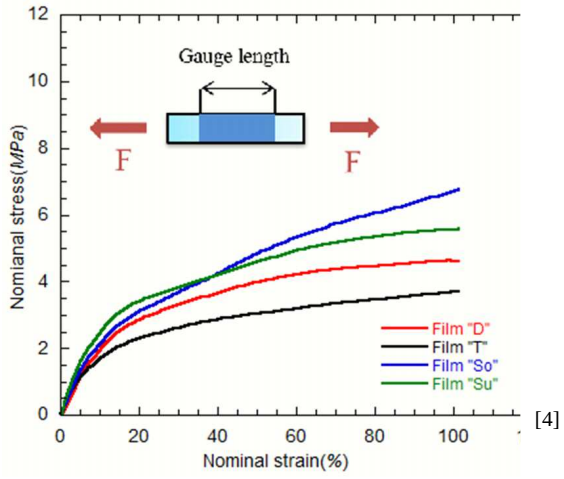

[3]

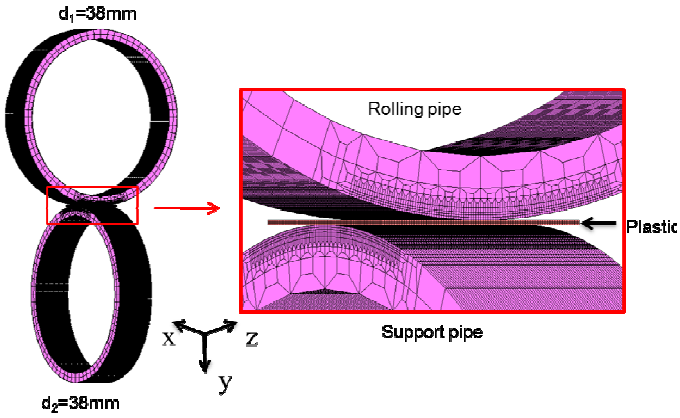

[4]

(a) S-S diagram at temperature 70°C (b) FEM mesh for standard model under static contact analysis

Fig. 3 FEM mesh for standard model and S-S diagram of different material

Various contact stresses are investigated in Ref. [3], However there is no results available for the plastic film between the two pipes. Figure 4(a) shows profiles for stress along the y-axis for plastic film D and the maximum stress along the y-axis p_{max}=17.54 MPa appears at the centre of plastic film. Figure 4(b) shows profile of thickness reduction under stress distribution of Figure 4(a). According to the results, the maximum thickness reduction appears at the centre of the plastic film (Δt/2=0.04 mm) and the reduction of the upper and lower surface is the same.

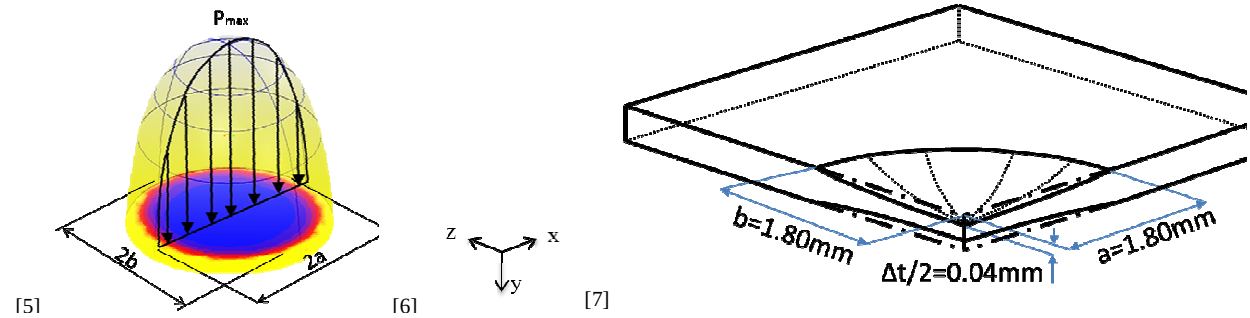

(a) Profiles for stress σ_y (b) Profile of Thickness reduction (quarter model)

Fig. 4 Profiles of stress and thickness reduction for plastic film “D”.

Table 1 shows the thickness reduction and maximum contact pressure of four kinds of materials. According to the results, the maximum contact pressure of plastic film “So” is the largest, and thickness reduction of plastic film “T” is the largest among four kind of materials.

Table 1 Results for different materials

Plastic film	Film “T”	Film “D”	Film “So”	Film “Su”
p_{max}[MPa]	16.0	17.5	19.5	18.0
Contact area[mm^2]	11.1	10.2	8.87	8.7
Maximum thickness reduction Δt_{static} [mm]	0.090	0.080	0.074	0.072

4 FEM MODEL AND RESULTS FOR ROLLING CONTACT ANALYSIS

Static contact analysis was performed, and the maximum contact pressure and thickness reduction between pipes was discussed. However, in fact the rolling pipe rolls up the plastic film as a rolling action in full-open greenhouse. It is necessary to investigate the effect of rolling action compared with the static analysis. FEM mesh for standard model is shown as Fig.5, which is used for rolling contact analysis. Both support pipe and rolling pipe have the same diameter d_1=d_2=38mm for the perpendicular contact model. The number of elements is 6.2×10^4 and the smallest element size is 0.09 mm X 0.09 mm X 0.375 mm which may provide high accuracy without large calculation time. Because Young's modulus of iron is much larger than the plastic film (about 420 times), in order to simplify the model, the models of pipes are regarded as rigid models for rolling contact analysis. The rolling speed for rolling pipe is 8.38rad/min and rolling time is 1.3s in FEM simulation. The load is 75N which is the same as the one of static contact analysis.

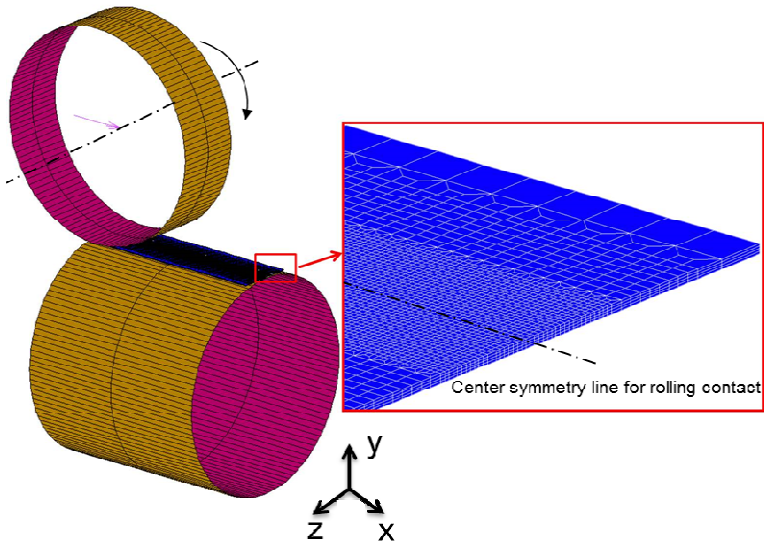

Fig. 5 FEM mesh for standard model under rolling contact analysis.

Figure 6 shows the thickness reduction Δt of y-direction on the plastic film. According to Figure 7, the red line shows the contact result of the static contact analysis and the blue line shows the contact result of the rolling contact analysis. The initial thickness of plastic film is t_0=0.15 mm. The notations Δt and t represent thickness reduction and final thickness of plastic film. Moreover, the relation between thickness reduction and final thickness of plastic film is $\Delta t + t = t_0$ =0.15 mm. According to these results, the maximum thickness reduction does not appear at the original point. Table 2 shows the data of thickness reduction on four kinds of material under static contact analysis and rolling contact analysis. According to the result, thickness reduction of plastic film "T" is larger than that of other materials in steady state under rolling contact analysis. The results in thickness reduction in rolling contact analysis are found to be nearly equal or larger than the ones in static contact analysis by 10%.

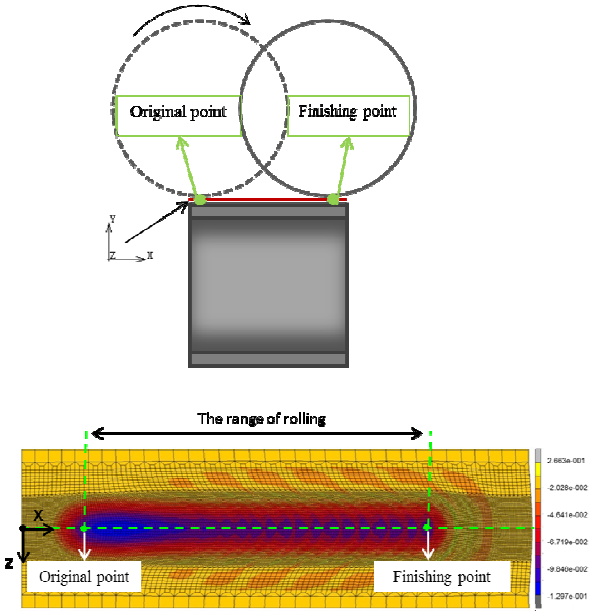

Fig. 6 Typical thickness reduction Δt distribution map

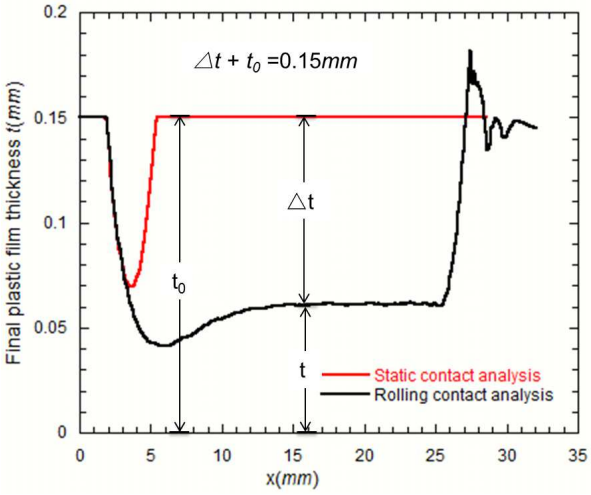

Fig. 7 The final thickness of plastic film in static contact analysis and rolling contact analysis

Table 2 Thickness reduction Δt for static contact analysis and rolling contact analysis

Plastic film	Film "T"	Film "D"	Film "So"	Film "Su"
Maximum thickness reduction Δt_{static} [mm] under static contact analysis	0.0897	0.0804	0.0744	0.0719
Thickness reduction $\Delta t_{rolling}$ [mm] in steady state under rolling contact analysis	0.108	0.0889	0.0708	0.0748
$\Delta t_{rolling} / \Delta t_{static}$	1.20	1.10	0.95	1.04

Figure 8 shows the final elongation of plastic film in x direction for plastic film "T". The original length and elongation are represented by l and Δl. Table 3 shows the data of thickness reduction and elongation under rolling contact analysis. It is found that elongation is increasing when thickness reduction increases. Since the both sides of rolling indentation are constrained, only the central part of the rolling indentation is elongated during rolling, thus the stretched portion at the central film leads to crease. Therefore formation of crease is closely relative to elongation, and crease is considered as the early damage before line scar.

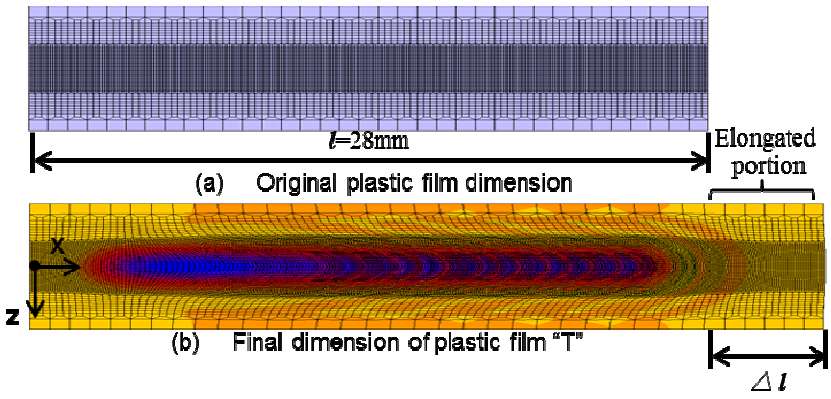

Fig. 8 The final elongation of plastic film in x direction for plastic film "T".

Table 3 The final elongation of plastic film Δl and the thickness reduction Δt for steady state

Plastic film	Film "T"	Film "D"	Film "So"	Film "Su"
Final elongation Δl [mm]	5.12	3.71	2.64	2.83
Thickness reduction $\Delta t_{rolling}$ [mm]	0.109	0.089	0.070	0.075
$\Delta l / l$	0.183	0.133	0.094	0.101
$\Delta t_{rolling} / t_0$	0.727	0.593	0.467	0.500

5 ROLLING CONTACT EXPERIMENT RESULTS

Rolling contact experiment has been done to simulate the real damage in plastic film. The temperature on support pipe is assumed as 70°C which equals to the highest temperature on pipes of greenhouse in summer. The load is 75N which is same as contact analysis. It is known that each support pipe may carry 15 N on average, however due to the manufacturing error we assume the largest load may be 75 N. To control room temperature, the plastic roof open and close 10 times for one day. In order to simulate damage of plastic film which has used for one month, cycles for rolling action are assumed as 300 times. Figure 9 shows damage of test piece which is taken by optical microscope. Four line scars are seen on the Fig. 9. Table 4 shows the results of rolling contact experiment and analysis. According to the results, elongation ratio is related to the reduction ratio under rolling contact analysis. Elongation ratio increases with increasing reduction ratio. Figure 10 shows the relationship between number of line scar n and reduction ratio $\Delta t_{rolling} / t_0$. From the comparison between the results of rolling contact experiment and the results of rolling contact analysis, the number of line scar under rolling contact experiment increases with increasing the reduction ratio under rolling contact analysis.

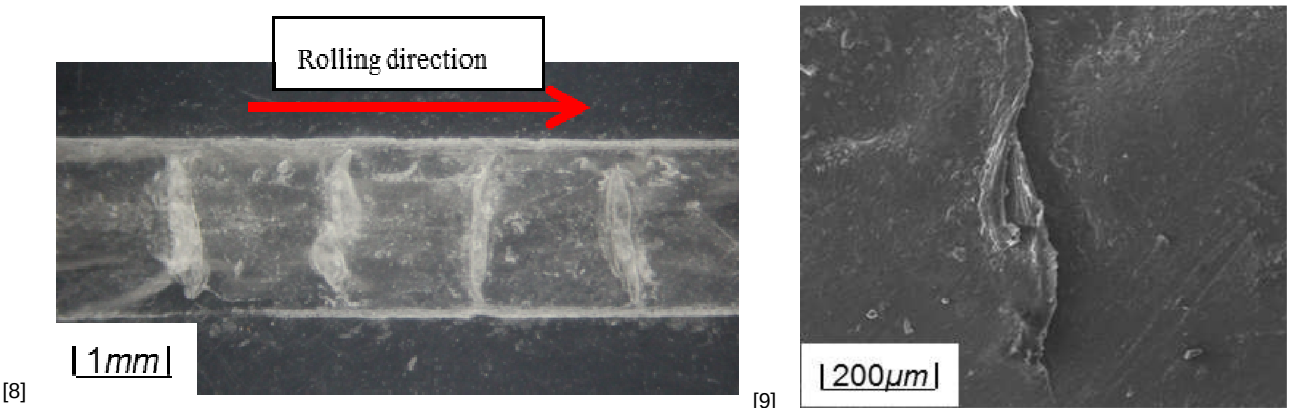

[8] [9]

Fig. 9 Microscopic photo of film rolled 300 times at 70℃ (film "D")

Table 4 Number of line scar per centimeter for four kinds of plastic film

Plastic film	Film “T”	Film “D”	Film “So”	Film “Su”
Number of line scar n under rolling contact experiment	3.85	2.95	1.2	0.15
Elongation ratio $\Delta l / l$ under rolling contact analysis	0.183	0.133	0.094	0.101
Reduction ratio $\Delta t_{rolling} / t_0$ under rolling contact analysis	0.727	0.593	0.467	0.500

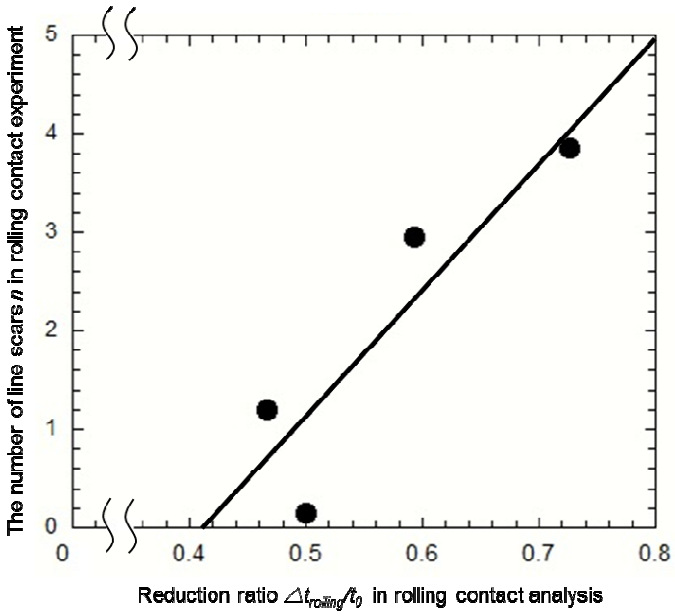

Fig. 10 Relationship between number of line scar n and $\Delta t_{rolling} / t_0$

6 CONCLUSION

In this study, the damage mechanism is investigated for four kinds of plastic films used for the full open type greenhouse. From the FEM analysis and rolling experiment, the following results can be obtained.

1) From the comparison between the results of rolling experiment and the results of rolling contact analysis, the number of line scar in rolling tests increases with increasing the reduction ratio in rolling contact analysis.
2) The results in thickness reduction in rolling contact analysis are found to be nearly equal or larger than the ones in static contact analysis by 10%.
3) According to the results of rolling contact analysis, it is found that elongation is increasing when thickness reduction increases. Since the both sides of rolling indentation are constrained, only the central part of the rolling indentation is elongated during rolling, thus the stretched portion at the central film leads to crease. Therefore formation of crease is closely relative to elongation, and crease is considered as the early damage before line scar.

7 REFERENCES

[1] A.T.Hiroe, Introduction to material properties of plastic, third ed., Nikkan Kogyo Shimbun, Tokyo, 1996.
[2] S.S.L.Yamakuchi, Lubricity of the plastic material: Application to the sliding portion and its characteristics, Nikkan Kogyo Shimbun, Tokyo, 1981.
[3] K. L. Johnson, Contact mechanics, Cambridge University Press, Cambridge, 2003.

Proceedings of the 3rd International Conference on
Fracture Fatigue and Wear, pp. 207-213, 2014

FATIGUE LIFE PREDICTION OF COMPOSITE RISERS DUE TO VORTEX-INDUCED VIBRATION (VIV)

X.S. Sun, V.B.C. Tan*, L.B. Tan, Y. Chen, R.K. Jaiman and T.E. Tay

Department of Mechanical Engineering, National University of Singapore, Singapore
*Corresponding author: mpetanbc@nus.edu.sg

Abstract: Risers are vertical pipelines connecting the platform on water surface to well bores at the seabed in offshore oil production. Composite risers consist of multiple coaxial layers of different materials including metals and composites. The riser system usually experiences vortex-induced vibration (VIV) which produces cyclic variable-amplitude loads acting on risers in seawater environment. The VIV loads can cause fatigue damage and failure of the riser system and therefore VIV fatigue life prediction of composite risers is one of particular concerns in the design. This paper presents a fatigue life prediction method of composite risers due to VIV in seawater environment. This method is based on the overall S-N curves of the composite risers. Multiaxial fatigue failures of metals and composites are determined by von Mises and Hashin criteria, respectively, with the degraded fatigue strengths in the layer level obtained from fatigue master curves. The overall S-N curves are then obtained from a layer-by-layer progressive failure analysis with the fatigue strengths of each layer. The fatigue master curves are generated with limited uniaxial fatigue tests and can be applied to fatigue loading conditions with various frequencies and stress ratios. The VIV loads are obtained from a global analysis of the riser system under a typical seawater current profile. The rainflow counting technique is adopted to count the cycle numbers of the VIV loads with variable amplitudes. Miner's rule is used to account for the damage accumulation during the variable VIV fatigue loads. Finally, an example of fatigue life prediction of a composite riser is presented to demonstrate the application of the proposed method.

Keywords: composite riser; vortex-induced vibration (VIV); variable-amplitude load; fatigue life prediction; multiaxial fatigue failure; overall S-N curve

1 INTRODUCTION

Risers are typical pipelines used in the offshore oil and gas industry, which connect the platform on water surface to well bores at the seabed. With the modern offshore oil production moving to seawaters deeper than 1500 meters, risers made of metals such as steel or titanium have reached their design limits because of their extra weight in deep seawaters. Light materials such as composites with the advantage of better mechanical performances are therefore increasingly considered to use in offshore risers. Risers usually experience vortex-induced vibration (VIV) in seawater environment [1]. The VIV can produce series of variable-amplitude cyclic loads on the riser system, which often causes fatigue damage on risers. Hence the concerned fatigue problem on risers is typically the fatigue analysis of riser structures under fatigue loads with variable amplitudes [1, 2]. For composite risers with multiple coaxial layers of different materials including metals and composite plies, the fatigue analysis with variable amplitudes may be complicated because of the material anisotropy and heterogeneity in the riser structure. In order to present reasonable fatigue life predictions on composite risers, proper fatigue models for all materials of the composite risers and fatigue analysis methods for the whole riser structure need to be exploited.

This paper presents a fatigue analysis method for the fatigue life prediction of multilayered composite risers due to VIV in seawater environment. This method is based on the overall S-N curves of composite risers. Fatigue strengths of each layer are obtained from fatigue master curves of the material in this layer. The overall fatigue strengths or overall S-N curves can be obtained from a layer-by-layer progressive failure analysis with the degraded fatigue strengths of each layer. Fatigue failure analyses for both metals and composites are based on fatigue master curves and failure criteria. Multiaxial fatigue failures of metals and composites are determined by von Mises and Hashin criteria, respectively. The fatigue master curves are generated with limited uniaxial fatigue tests and can be applied to fatigue loads with various frequencies and stress ratios. The VIV loads are obtained from a global analysis of the riser system under a typical seawater current profile. The cycle numbers of the VIV loads with variable amplitudes is counted by the

rainflow counting method. The damage accumulation during the variable VIV fatigue loads is determined by Miner's rule. An example of fatigue life prediction of a 22-layer composite riser is presented to demonstrate the application of the proposed method.

2 VORTEX-INDUCED VIBRATION (VIV) AND VARIABLE-AMPLITUDE FATIGUE LOADS

Vortex-induced vibration (VIV) is a kind of off-axis oscillation of a cylindrical structure caused by fluctuating forces due to current impacts in fluid environment [2]. Generally, the VIV can produce cyclic loads with variable amplitudes on risers in seawaters. The VIV cyclic loads can be obtained from a global analysis of the riser system under a typical seawater current profile. A cycle counting method is usually required to count the number of cycles through the loading history with variable amplitudes. Among different cycle counting methods, it has been shown that the rainflow counting method is more suitable for complex fatigue loadings and it is popular in applications of fatigue analysis with variable-amplitude cyclic loads [3]. For a VIV fatigue loading history, the numbers of cycles, maximum stresses, stress ratios and frequencies can be recorded by the rainflow counting method. Then the VIV fatigue loads are divided into series of cyclic loadings by different amplitudes, stress ratios and frequencies, with constant amplitude, stress ratio and frequency in each cyclic loading. These fatigue load data are input into a fatigue damage model to carry out the fatigue analysis or fatigue life prediction under the VIV fatigue loads.

3 FATIGUE LIFE PREDICTION METHOD BASED ON THE OVERALL S-N CURVE

3.1 Layer-level fatigue master curves and S-N curves

Fatigue master curves for composites are usually established by an accelerated testing methodology (ATM) with unidirectional laminates under constant-amplitude fatigue loads [4]. The fatigue master curves are obtained by the Time-Temperature Superposition Principal (TTSP) in ATM under ply-level uniaxial loadings. With fatigue master curves, the long-term fatigue life of composites can be described in wide ranges of loading and environmental conditions. The normalized fatigue master curve in the ply or layer level can be written as [5]:

$$M_f = \frac{1+c_0}{(2N_f)^{c_1} + c_0(2N_f)^{c_2}}, \tag{1}$$

where N_f is the number of cycles to failure which has a relationship with the time to failure t and frequency f as N_f=ft; c_0, c_1 and c_2 are parameters defined as:

$$c_0 = g_f \big/ (2ft_1)^{n_r}, \quad c_1 = g_f n_f, \quad c_2 = g_f n_f + n_c, \tag{2}$$

and t_1 is the transient reduced time which denotes a time when the material turns to a glassy phase.

The parameters n_r, n_f and n_c in Eq. 2 are determined from fitting test data under reference loadings, and g_f is a function of the stress ratio R defined as [5]:

$$g_f = \begin{cases} (1-r^2)\big/(1-r_0^2), & \text{if } r \geq 0, \\ \left[1-r(|r|+r_0)/2\right]\big/(1-r_0^2), & \text{if } r < 0, \end{cases} \tag{3}$$

where r and r_0 are the amplitude ratios under the present and reference loadings, respectively, which is defined as:

$$r = \begin{cases} R, & \text{if } -1 \leq R < 1, \\ 1/R, & \text{if } |R| > 1. \end{cases} \tag{4}$$

From Eq. 1, the layer-level S-N curves for composites can be obtained as:

$$\sigma_f = \sigma_0 M_f = \frac{\sigma_0(1+c_0)}{(2N_f)^{c_1} + c_0(2N_f)^{c_2}}, \tag{5}$$

where σ_f and σ_0 are the fatigue failure stress and initial static strength, respectively.

There are generally different fatigue master curves and S-N curves for composites depending on the material directions and loading conditions. Usually, test data of tension-tension fatigue ($0 \le R < 1$) and compression-compression fatigue ($R > 1$) along longitudinal and transverse directions are used to generate the layer-level fatigue master curves and S-N curves for unidirectional laminates [5]. For metals, the S-N curves can also be obtained by Eq. 5 from fitting test data in literature. As metals are isotropic materials, the coefficient parameter g_f in Eq. 3 can be set as $g_f = 1$, and therefore only one fatigue master curve is required for a metal under a specified condition.

3.2 Fatigue damage accumulation model

There are a number of different formulations of fatigue damage rules or models accounting for damage accumulation for fatigue loads with variable amplitudes in literature [6]. Among these damage models, a simple and popular formulation is the Palmgren-Miner damage rule, or Miner's rule [7], where fatigue damage accumulation is determined from a non-dimensional damage factor which is related to the life amount a structure has used. Miner's rule can be written as:

$$D_m = \sum_{i=1}^{m} D_i = \sum_{i=1}^{m} \frac{n_i}{N_i}. \tag{6}$$

where m is the total number of cyclic loadings counted; D_i and n_i are the non-dimensional damage factor and number of cycles in the ith cyclic loading, respectively; N_i is the number of cycles to failure in the ith cyclic loading, which is determined from the corresponding constant-amplitude S-N curve.

Miner's rule is a linear damage model independent of loading history, and it requires no additional material parameters except for those in the S-N curve.

3.3 Fatigue life prediction method

The basic idea of the fatigue life prediction method is based on a fatigue failure analysis with overall S-N curves of composite risers, which are to be determined from the layer-level S-N curves of both metals and composites as well as corresponding failure criteria through a layer-by-layer multiaxial failure analysis. Due to the material anisotropy and global loads applied on the composite risers, each layer of the risers is under a multiaxial stress state $\boldsymbol{\sigma}^{(k)}$ (the local stress in the kth layer). The local stress $\boldsymbol{\sigma}^{(k)}$, which is usually discontinuous through different layers due to the material heterogeneity, can be determined from the global loads through the homogenization stress analysis method [8, 9]. Consider three basic and important loads on risers, i.e., external pressure q by seawater, axial tension T_a by riser weight and bending moment M_b by VIV loads, with $q \ge 0$, $T_a \ge 0$ and M_b positive or negative. For a specified deep position in the seawater, q and T_a are constant, while M_b is a kind of cyclic loads with variable amplitudes. Therefore, q and T_a result in mean stresses and M_b causes stress amplitudes in the composite risers due to the VIV cyclic loads. Furthermore, the maximum stresses and the stress ratios in the composite risers will be different through layers and also vary with the cycles of the VIV loads. Define three global averaged stresses Σ_1, Σ_2 and Σ_3 which correspond to the loads q, T_a and M_b, respectively, as:

$$\Sigma_1 = \frac{qb^2}{b^2 - a^2}, \quad \Sigma_2 = \frac{T_a}{\pi(b^2 - a^2)}, \quad \Sigma_3 = \frac{2M_b(b+a)}{\pi(b^4 - a^4)}, \tag{7}$$

where a and b are inner and outer radii of risers, respectively; and the global stress vector $\boldsymbol{\Sigma}$ and load ratios λ_i (i=1,2) are then defined respectively as:

$$\boldsymbol{\Sigma} = [\Sigma_1 \quad \Sigma_2 \quad \Sigma_3]^T = \Sigma_3 [\lambda_1 \quad \lambda_2 \quad 1]^T, \tag{8}$$

$$\lambda_i = \Sigma_i / \Sigma_3, \quad i = 1,2. \tag{9}$$

The local stress $\sigma_j^{(k)}$ (j=1,2,…,6) in the kth layer of the composite risers can be determined from the global load Σ_3 as:

$$\sigma_j^{(k)} = \Sigma_3 \left[\frac{(b^2 - a^2)}{b^2} \lambda_1 \Psi_{jq}^{(k)} + \pi(b^2 - a^2) \lambda_2 \Psi_{jT_a}^{(k)} + \frac{\pi(b^4 - a^4)}{2(b+a)} \Psi_{jM_b}^{(k)} \right], \tag{10}$$

where $\Psi_{jq}^{(k)}$, $\Psi_{jT_a}^{(k)}$ and $\Psi_{jM_b}^{(k)}$ are components of the coefficient matrix $\boldsymbol{\Psi}^{(k)}$ determined from the geometrical parameters and material properties of the composite risers [9].

Then the local stress ratio $R_j^{(k)}$ (j=1,2,…,6) of the jth local stress component in the kth layer can be calculated as:

$$R_j^{(k)} = \begin{cases} (C_j^{(k)} + \Psi_{jM_b}^{(k)} R)/(C_j^{(k)} + \Psi_{jM_b}^{(k)}), & \text{if } M_{b,max}(C_j^{(k)} + \Psi_{jM_b}^{(k)} R) < M_{b,max}(C_j^{(k)} + \Psi_{jM_b}^{(k)}), \\ (C_j^{(k)} + \Psi_{jM_b}^{(k)})/(C_j^{(k)} + \Psi_{jM_b}^{(k)} R), & \text{if } M_{b,max}(C_j^{(k)} + \Psi_{jM_b}^{(k)} R) > M_{b,max}(C_j^{(k)} + \Psi_{jM_b}^{(k)}), \end{cases} \quad (11)$$

with

$$C_j^{(k)} = \frac{2(b+a)}{\pi(b^2+a^2)}\left(\lambda_{1,max}\Psi_{jq}^{(k)}/b^2 + \pi\lambda_{2,max}\Psi_{jT_a}^{(k)}\right), \quad (12)$$

where $R=\Sigma_{3,min}/\Sigma_{3,max}=M_{b,min}/M_{b,max}$ is the global VIV stress ratio, and $\lambda_{i,max}= \Sigma_i/\Sigma_{3,max}$ (i=1,2).

It can be seen that the local stress ratios vary with the local stress components and the global load ratios due to the constant pressure and axial tension. Therefore, the stress ratio in the layer-level composite fatigue master curve and S-N curve defined in Eq. 1 and Eq. 5 should be replaced with the local stress ratio defined in Eq. 11 in the VIV fatigue analysis. By defining an equivalent global stress Σ_{eq} as:

$$\Sigma_{eq} = \sqrt{\boldsymbol{\Sigma}^T\boldsymbol{\Sigma}} = |\Sigma_3|\sqrt{\lambda_1^2+\lambda_2^2+1}, \quad (13)$$

the overall static strength $\Sigma_{eq,0}$ of the composite risers under a specified group of global load ratios (λ_1, λ_2) can be determined from a layer-by-layer progressive failure analysis [9].

This static failure analysis method can be extended to fatigue failure analysis. In the fatigue failure analysis, the material strengths used in the static analysis are replaced with degraded fatigue strengths in each layer obtained from the corresponding layer-level S-N curves. Then multiaxial fatigue failures of metals and composites are determined by corresponding failure criteria, e.g. von Mises and Hashin criteria [10], respectively, with the material fatigue strengths. Similar to the static analysis case, the overall fatigue strength $\Sigma_{eq,f}$ of the composite risers under a specified group of global load ratios (λ_1, λ_2) can be obtained from the fatigue strengths of layer materials under a specified number of cycles to failure. Then the overall S-N curve, or Σ_{eq}-N curve, of the composite risers under the same group of global load ratios can be obtained. The Σ_{eq}-N curve may vary with the global load ratios and stress ratios. With the Σ_{eq}-N curves, the number of cycles to failure corresponding to the maximum stress in each cyclic load can be determined, and the fatigue life of the composite risers under VIV loads can be predicted from Miner's rule in Eq. 6.

4 EXAMPLE OF FATIGUE LIFE PREDICTION OF A 22-LAYER COMPOSITE RISER

The example will show the application of the abovementioned fatigue life prediction method to a 22-layer composite riser under VIV fatigue loads. The composite riser consists of a liner (Titanium), twenty composite layers (carbon/epoxy) and an outer layer (polymer). The inner and outer radii are a=140 mm and b=160.335mm, respectively. More details on the riser geometry and material properties are presented in the references [9,11]. The VIV response of the composite riser system with a total length of 1500 meters in the seawater is shown in Fig. 1(a), which is obtained from the global analysis of the riser system under the Gulf of Mexico current profile [11]. The VIV response is transformed to a fatigue loading history based on the bending-equivalent stress Σ_3 defined in Eq. 7. The load-equivalent stresses Σ_1 and Σ_2 are calculated with the maximum designed values of q=15 MPa and T_a=375 kN, respectively, which are extracted from the global analysis of the composite riser system [11]. The fatigue loading history is simplified as repeated block loads and the loads in one block are shown in Fig. 1(b). The fatigue master curves and S-N curves of Titanium and the carbon/epoxy composite material are shown in Fig. 2 and Fig. 3, respectively. For the carbon/epoxy composite material, the fatigue master curves are fitted from test data along the fibre direction, and the same fatigue master curves are assumed for the transverse and shear directions.

The maximum stress and stress ratios of each cycle sequence in one load block shown in Fig. 1(b) is counted by the rainflow method and the results are listed in Table 1, where the number of cycles of each cycle sequence is n_i=1. The load ratios corresponding to the maximum stress state ($\lambda_{1,max}$, $\lambda_{2,max}$) are also calculated for each cycle sequence in Table 1. The number of cycle to failure $N_{f,i}$ of each cycle sequence is obtained from the corresponding Σ_{eq}-N curve which is determined from the maximum stress, stress ratio

and load ratios in the cycle sequence through the layer-by-layer fatigue failure analysis. The damage factor in one load block can be calculated from Eq. 6 as $D_m=1.454\times10^{-11}$, and the total number of blocks for the final fatigue failure of the composite riser is $B=1/D_m=6.875\times10^{10}$. With the loading time $t_0=31$s in one block shown in Fig. 1(b), the fatigue life t_f of the composite riser is $t_f=B\times t_0/3600/24/365=6.758\times10^4$ years.

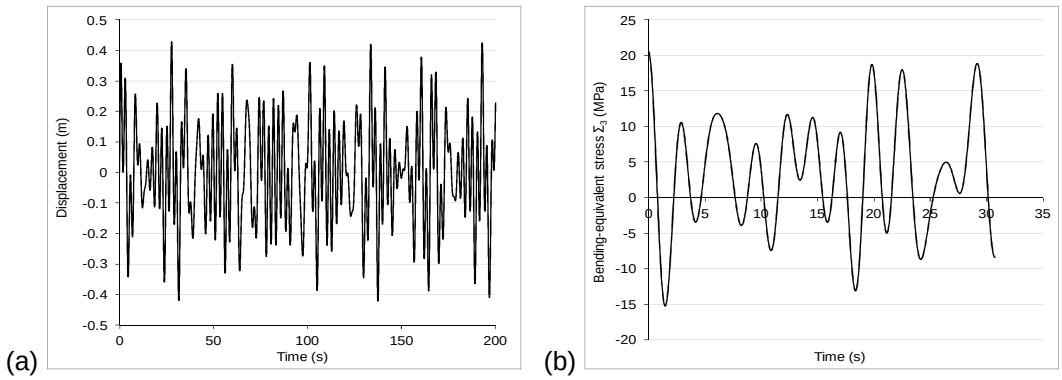

Fig. 1 VIV fatigue loads: (a) VIV response (b) fatigue loads from the VIV (one block)

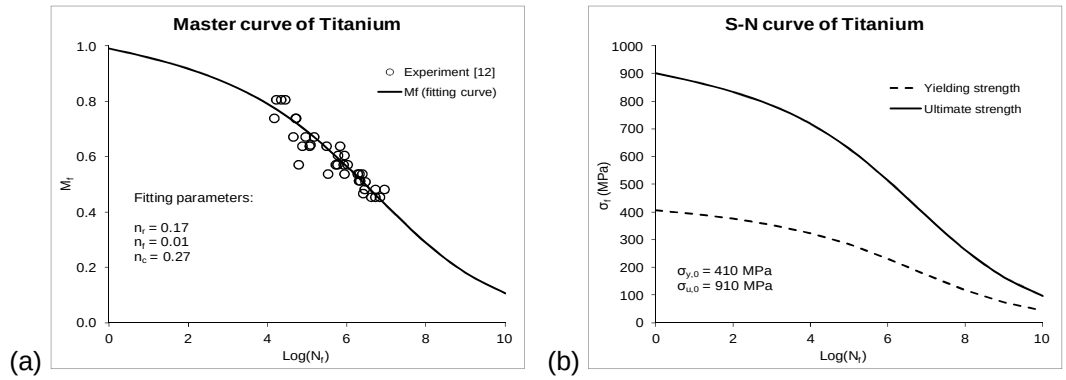

Fig. 2 S-N curve of Titanium: (a) fatigue master curve and (b) S-N curve

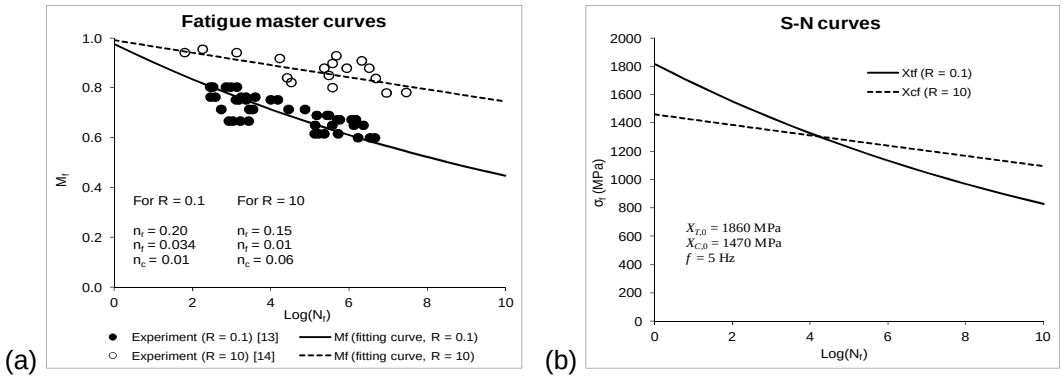

Fig. 3 S-N curves of the carbon/epoxy composite: (a) fatigue master curves and (b) S-N curves

Table 1 VIV fatigue load information in one block

Cycle sequence i		1	2	3	4	5	6	7	8	9	10	11
Maximum stress $\Sigma_{3,max,i}$ (MPa)		10.61	7.65	11.32	9.23	11.75	11.87	18.05	5.02	18.79	18.93	20.61
Stress ratio R_i		-0.326	-0.514	0.217	-0.372	-0.635	-1.107	-0.277	0.117	-0.463	-0.471	-0.742
Load ratios	$\lambda_{1,max,i}$	5.949	8.254	5.578	6.840	5.375	5.319	3.498	12.586	3.360	3.335	3.063
	$\lambda_{2,max,i}$	1.842	2.555	1.727	2.117	1.664	1.646	1.083	3.896	1.040	1.032	0.948
Number of cycles to failure $N_{f,i}$ ($\times 10^{10}$)		90	200	90	100	90	90	50	1000	50	50	40

5 CONCLUSIONS

A fatigue analysis method is presented in this paper for fatigue life prediction of multilayered composite risers due to VIV in seawater environment. This method is based on the overall S-N curves of composite risers, which are obtained from the degraded fatigue strengths of each layer through a layer-by-layer progressive failure analysis. The fatigue strengths of each layer are determined from the layer-level S-N curves which are obtained from fatigue master curves generated with limited uniaxial fatigue tests. In the fatigue analysis, layer-based multiaxial fatigue failures of metals and composites are determined by von Mises and Hashin criteria, respectively. Both the constant loads and the variable VIV loads are considered in the fatigue analysis. The VIV loads are obtained from a global analysis of the riser system under a typical seawater current profile, and the rainflow counting method is used to count the cycle numbers of the variable-amplitude VIV fatigue loads. The damage accumulation during the variable VIV fatigue loads is determined by Miner's rule. The application of the proposed fatigue life prediction method is demonstrated with an example of a 22-layer composite riser under VIV fatigue loads. This method provides a feasible solution for fatigue assessment on multilayered composite risers in the offshore oil and gas industry.

6 ACKNOWLEDGEMENTS

The authors would like to acknowledge the support of Singapore A*STAR (Agency for Science, Technology and Research) through the project No. 1123004033 for MIMO (Materials Innovation for Marine & Offshore Applications).

7 REFERENCES

[1] M.S. Pantazopoulos, Vortex-Induced Vibrations Parameters: Critical Review, in: Proceedings of the 17th International Conference on Offshore Mechanics and Arctic Engineering, Osaka, Japan, 1994, pp. 199–255.

[2] C. Le Cunff, F. Biolley, E. Fontaine, S. Étienne, M.L. Facchinetti, Vortex-Induced Vibrations of Risers: Theoretical, Numerical and Experimental Investigation, Oil & Gas Science and Technology – Rev. IFP, 57(1), 59–69, 2002.

[3] Y.L. Lee, J. Pan, R.B. Hathaway, M.E. Barkey, Fatigue Testing and Analysis: Theory and Practice, Elsevier Butterworth-Heinemann, Oxford, 2005.

[4] Y. Miyano, M. Nakada, H. Cai, Formulation of Long-Term Creep and Fatigue Strengths of Polymer Composites Based on Accelerated Testing Methodology, Journal of Composite Materials, 42(18), 1897–1919, 2008.

[5] X.S. Sun, A. Haris, V.B.C. Tan, T.E. Tay, S. Narasimalu, C.N. Della, A Multi-Axial Fatigue Model for Fibre Reinforced Composite Laminates Based on Puck's Criterion, Journal of Composite Materials, 46(4), 449–469, 2012

[6] N.L. Post, S.W. Case, J.J. Lesko, Modeling the Variable Amplitude Fatigue of Composite Materials: A Review and Evaluation of the State of the Art for Spectrum Loading, International Journal of Fatigue, 30(12), 2064–2086, 2008.

[7] DNV-OS-F101, Submarine Pipeline Systems, Section 5, D808, 2012.

[8] X.S. Sun, V.B.C. Tan, Y. Chen, L.B. Tan, R.K. Jaiman, T.E. Tay, Stress Analysis of Multi-Layered Hollow Anisotropic Composite Cylindrical Structures Using the Homogenization Method, Acta Mechanica, to appear, 2014.

[9] X.S. Sun, V.B.C. Tan, Y. Chen, R.K. Jaiman, T.E. Tay, An Efficient Analytical Failure Analysis Approach for Multilayered Composite Offshore Production Risers, in: Proceedings of the 1st International Conference on Advanced Composites for Marine Engineering (ICACME 2013), Beijing, China, 2013, ICACME2013-004.

[10] Z. Hashin, Failure Criteria for Unidirectional Fibre Composites, Journal of Applied Mechanics, 47(2), 329–334, 1980.

[11] L.B. Tan, Y. Chen, R.K. Jaiman, X.S. Sun, V.B.C. Tan, T.E. Tay, Coupled Fluid-Structure Simulations for Evaluating a Performance of Full-scale Deepwater Composite Riser, Ocean Engineering, submitted, 2014.

[12] W. Illg, C.B. Castle, Fatigue of Four Stainless Steels and Three Titanium Alloys before and after Exposure to 550° F (561° K) up to 8800 Hours, NASA Technical Note, NASA-TN-D2899, 1965.

[13] G.D. Sims, A VAMAS Round-Robin on Fatigue Test Methods for Polymer Matrix Composites. Part 1 - Tensile and Flexural Tests of Unidirectional Material, NPL Report DMA(A)180, 1989.

[14] L.M. Lifshitz, Compressive Fatigue and Static Properties of a Unidirectional Graphite/Epoxy Composite, Journal of Composites Technology & Research, 10(3), 100–106, 1988.

Proceedings of the 3rd International Conference on
Fracture Fatigue and Wear, pp. 214-219, 2014

CRACK NUCLEATION AT INCUBATION AND EARLY STAGES OF WATER DROPLET EROSION IN TI-6AL-4V

P. Bocher[1], N. Kamkar[1], F. Bridier[1] and P. Jedrzejowski[2]
[1]Mechanical Engineering Department, École de technologie supérieure, University of Quebec,
1100 Notre-Dame Ouest, Montreal, Quebec, H3C 1K3, Canada
[2]Rolls-Royce Canada Ltd. 9545 Cote-de-Liesse, Dorval, Quebec, H9P 1A5, Canada

Abstract: Identifying the mechanisms of water droplet erosion of Ti-6Al-4V parts is a critical issue encountered in many situations from aircraft body exposed to rain during flight to steam turbine blade. The present work focuses on the early damage stages of forged Ti-6Al-4V parts exposed to high-speed water impact erosion. Qualitative observations and quantitative measurements were done both on and below the surfaces that are undergoing deformation due to water droplet impingements. Progressive cross-sectional polishing revealed both surface and sub-surface damage features. Microplasticity phenomena including micro-cracks have been reported. Microcracks have intergranular features at surface and present transgranular characteristics below the surface. From these observations a damage mechanism was proposed to explain the early stages of water erosion. These observations, together with information gathered from more advanced erosion stages tend to prove that the mechanisms typical of low cycle fatigue may control the nucleation and early growth of cracks below the surface of the parts subjected to high-speed water droplet impingement.

Keywords: Titanium; water erosion; crack nucleation; transgranular; incubation time

1 INTRODUCTION

Severe erosion may occur at the leading edge of compressor blade when inlet fogging system is used to improve the efficiency of gas turbines [1-3]. Even if a great extent of works has documented material response to water impingement erosion phenomena [4-6], the topic of material removal mechanism was mainly discussed at advanced erosion stages and the erosion rate was the parameter used to quantify the erosion resistance of the material to water droplet impacts. Attempts were made to correlate the erosion rate to water droplet speed and size and to the surface properties such as absorption hardness, toughness, elastic modulus, or ultimate tensile strength [4-7]. Lower erosion rates were documented for material with higher surface hardness and yield strength.

The cyclic nature of impact erosion has motivated the possibility that fatigue-like mechanisms may play an important role for this type of material degradation. In the mid-70s, Adler et al. [5,6] observed localized crack and reported similarities between fatigue and erosion mechanism for the Ti-6Al-4V alloy subjected to supersonic rain erosion. Almost at the same period Richman and McNaughton [7,8] introduced and discussed fatigue strength as an important parameter to be used to quantify the cavitation erosion resistance of a given material. Specifically for water droplet erosion, Robinson et al. [9] suggested also a link between erosion resistance and fatigue properties of laser surface treated and untreated Ti-6Al-4V samples, however, they did not provide clear evidence of fatigue features. Similarly, Mann et al. [10] did not report fatigue related damages for Ti-6Al-4V under cavitation and water jet impingement erosion. On the other hand, the cyclic nature of water droplet erosion damage was clearly identified through observation of trans-granular cracks and striation marks in Ti-6Al-4V [11], indicating that the material removal mechanisms are most likely based on crack propagation and related fatigue behaviours.

Limited studies have been carried out on the early stages of water erosion phenomena. The present work proposes to concentrate on these issues, covering the incubation and onset of material removal in a Ti-6Al-4V alloy (it should be noted that there are still some arguments about the presence of incubation period in Ti-6Al-4V alloy [9]). As early as 1970, several alloys (excluding Titanium alloys) have been studied by Thomas and Brunton [12] and they reported micro-scale surface plastic deformations as the first evidence of the erosion damage. On stainless steel 316SS, Futakawa and co-workers [13,14] have used mercury impact erosion tests to report plastic deformation on the surface and sharp edge protrusions and

depressions at the sample surface were proposed as the damage initiation mechanisms. Kong et al. [15] reported also plastic deformation followed by surface crack nucleation on gamma titanium aluminide impacted by high velocity water in plain water jet milling. Similar results were recently reported on titanium alloys. Based on hardness measurements, Chillman et al. [16] documented significant sub-surface plastic deformation in Ti-6Al-4V alloy subjected to plain water jet expose; however, no clear evidence of surface plastic deformation was reported. Huang et al. [17] also reported intergranular cracks at the initial stages of erosion on Ti-6Al-4V under plain water jet impingement and proposed intergranular damage as the dominant mechanism for erosion initiation. The conclusions drawn from all these investigations point out that damage in water droplet impingement initiates by localized plastic deformation at the sample surface leading to intergranular damage. On the other hand, evidence of transgranular cracks formations were reported on advance erosion stages for Ti-6Al-4V submitted to water droplet impact erosion test, suggesting the other degradation mechanism may participate in the crack formation and propagation during water impingements [11]. In this context, the objective of the present work is to investigate the early stages of material removal in conditions where water erosion takes place on a forged titanium alloy (Ti-6Al-4V). The surface features observed at what can be considered as the incubation period and the onset of material removal were studied using atomic force (AFM) and scanning electron microscope (SEM).

2 MATERIALS AND METHODS

Water droplet erosion tests were performed on bolt coupons of 45 mm length, 8 mm width, and 8mm thickness on a rig according to ASTM international G73 standard [18] at Alstom, Switzerland [19]. The impingement direction is noted ID in this paper. The linear impact speed was set to 350 m/s with the disk rotational speeding at 5500 RPM and an arm length of 60 cm. The test was performed at ambient temperature under 25 mbar pressure, and a mean droplet diameter of 0.6mm as measured by Phase Doppler Anemometry (PDA). A first set of tests were run up to some advance stage of erosion in order to obtain the erosion curve. An incubation period was observed and precisely determined. Two more tests were performed on new coupons up to the number of rotation corresponding to the incubation period and the onset of material removal (1000 and 20000 revolutions, respectively, as displayed in Fig. 1).

The microstructure of the Ti-6Al-4V consisted in a duplex microstructure as displayed in Fig. 2.

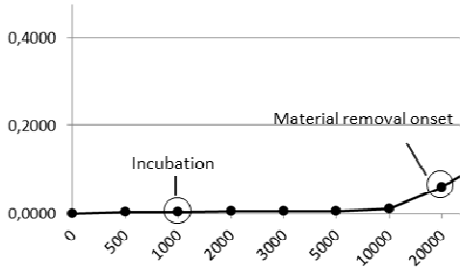

Fig. 1 Cumulative mass loss (in g) vs. number of jet impingements

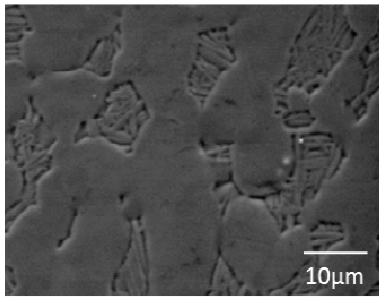

Fig. 2 Alloy microstructure as revealed after electropolishing of the surface before rig test

In order to better capture erosion features, the surface of the coupon was grounded with SiC papers, polished with monocrystalline diamond suspension and electrochemically-polished with refrigerated A3 solution under 30 Volt for 7 seconds before impingements. The electrochemical polishing process was performed on the surface to attain an unstressed surface as well as to perfectly reveal the microstructure so that after the erosion test, induced damage can be analyzed relative to the microstructure. The prepared surface and the eroded ones were examined by SEM and AFM to document slip activities and initial damage. The precise surface topographic scanning was realized thanks to a Di Enviroscope 5.30, Veeco AFM in tapping mode with a 0.2 Hz scanning frequency, a scan length of 97 µm and a Si cantilever. The data were processed via NanoScope Analysis 1.40 software. As in [11], progressive sectional polishing was also done along the erosion trace to better document some observed features using SiC papers and vibromet polisher with monocrystalline diamond suspension.

3 MICROSCOPIC OBSERVATION OF THE DAMAGE

3.1 Incubation surface features

At what was considered to be the incubation period on the cumulative mass lost curve shown in Fig.1 some subtle features were found on the surface. Typical examples of these features are shown in Fig. 3a. When observed at higher magnification, they appear micro-scale protrusions and can be considered as the first local damages to be generated on a water eroded surface (Fig. 7b). The damages are found spatially and

randomly in region receiving the water droplets. These isolated protrusions are out of plane about 1.5 micron high plat bumps. Actually, these features are in contradiction with the general understanding of the initial stage of erosion which is mostly described as surface depressions, micro-void or pit formation at the surface. These bumps were systematically documented using AFM and the results from the bumps found in region A in Fig. 3 are shown in Fig 4.

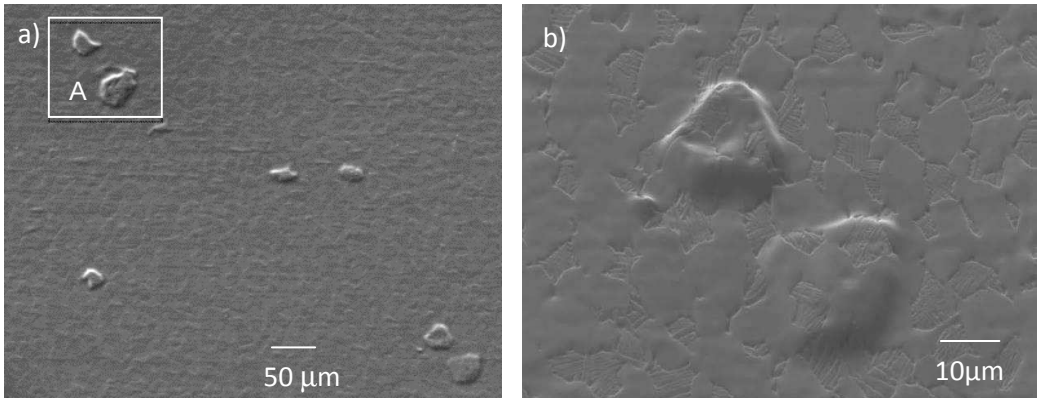

Fig. 3 SEM images of surface damages seen on the sample surface at the incubation of water erosion

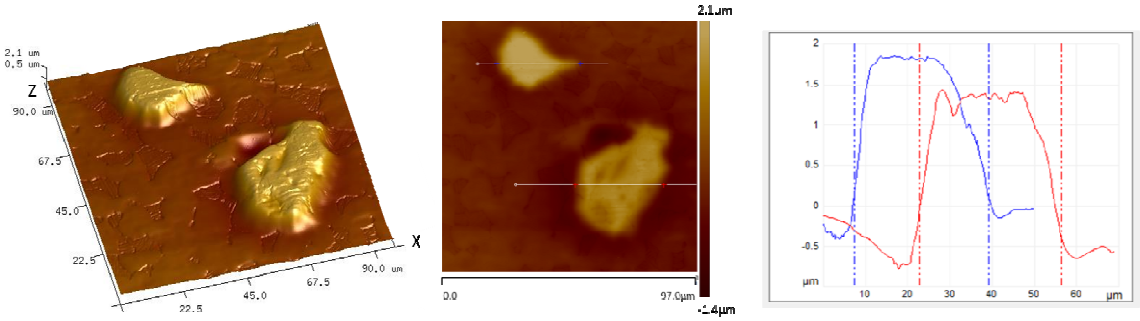

Fig. 4 AFM images and profile of surface damages found in the region A of Fig. 3 (incubation period)

The widths of the bumps are typically few tens of microns in width (10 to 50 µm) and less than two microns in height. They were observed on both α_p grains and α_s lamellae. They are associated with a slight surface depression observed around the edges of the protrusions as clearly seen in Fig.4b. The bumps are actually quite flat as only a microstructure contract coming from the initial electropolishing preparation of the sample can be seen.

The progressive cross sectional polishing performed on the sample along the erosion line revealed the existence of cracks below some of the investigated bumps (note that some bumps did not show any evidence of crack). Fig. 5 illustrates an example of such a crack found under a bump. The subsurface damage is actually a network of micro-cracks ranging from 13 µm to 28 µm (which is around the average α-grain size) that was observed at about 150 µm from the sample surface. The primary crack is inclined about 45° from the impinged surface plane while secondary cracks can be parallel to the surface. The observed cracks are mostly within α-grains in which they propagate in a transgranular manner up to the grain boundaries and the latters act as microstructure barriers, forcing the crack to deviate. When the crack becomes “long” they tend to propagate parallel to the surface. Some portions of the cracks also propagate in the lamellar matrix. At the surface of the bumps, other types of damage, micro-cracks, can be found but they do not seems to be the primary damage that would lead to the onset of material removal. The orientation of the primary cracks propagation (45° from the impinged surface plane) suggests that cracks have nucleated along a high shear stress plane of a properly oriented grain. Then, their propagation path will depend on either the local stress state or microstructure, both crystallographically and morphologically.

Evidence of significant plastic deformation under water impingement can be found in some regions of the surface where slip bands were observed in α-grains. This is true at the incubation stage but also at the onset of material as shown in Fig. 6. These slip lines were distributed sparsely over the surface at incubation stage and systematically found around the rim of craters at the stage of material removal (as discussed below). The presence of these slip bands suggests that an intense plastic activity is taking place at and below the surface of the impinged sample surface.

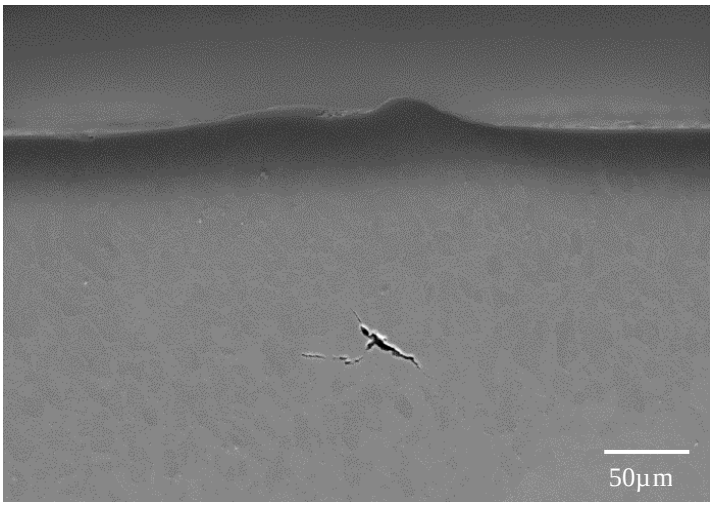

Fig. 5 45 degree tilted SEM image of the cross section of a surface damage observed on the sample surface at the incubation of water erosion

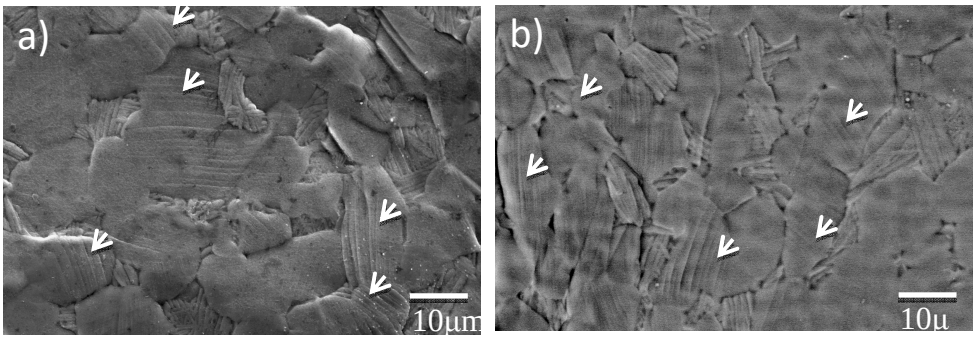

Fig. 6 SEM images of slip band marks at a) incubation and b) the onset of material removal

3.2 Onset of material removal features

As the erosion damage advances, the number of marks on the surface increase and the erosion lines are progressively revealed (Fig. 7). This provides the opportunity to document various degradation stages on a given sample. If one document the topography of undamaged surface (no visible crack) at the onset of material removal using AFM (obtained image not shown here), significant surface roughness and grain surface tilting up to 2.3° can be found with a mean value of 1.2±0.6°. Although the angles of grain tilting were relatively small, they are evidences of crystallographic rotation due to severe plastic deformation and they give rise to steps between the adjacent grains. Regions with more erosion marks on the surface will eventually present damage at grain boundaries due to strain incompatibility.

As the number of local impingements increases, the region below the sample surface gets cyclically plastified and the density of isolated bumps increases; resulting, ultimately, in significant grain tilting. The repetition of load (or strain) may generate cracks according to the low cycle fatigue strength of the used alloy and microstructure. Surface grain boundary damage may also appear due to strain incompatibility grain plasticity but they may not be the main degradation mechanism. Further on, the nucleated cracks will propagate subsurface (see striations marks figure 7c) and crater will be generated. Big fragment of material will be removed, resulting into a significant increase of the erosion rate. The higher the potential energy of the droplet (driven by the size and the square of droplet speed) the deeper and the sooner the crack will be generated, leading to faster erosion rates.

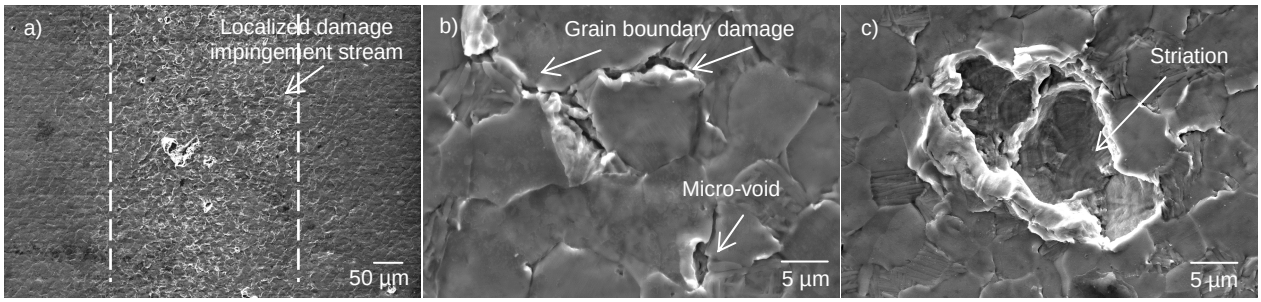

Fig. 7 SEM micrograph of erosion features at onset of material removal a) global view b) grain tilting and grain boundary damage c) striation marks below early formed craters

4 CONCLUSIONS

The onset of water erosion damage in forged Ti-6Al-4V was documented at the incubation and the onset of material removal. Sub-surface cracks resulting from severe cyclic local plastic deformation appears to be the major contributor to early erosion. Droplet impact pressure causes high local stress field underneath the surface resulting into dynamic LCF conditions capable of generating cracks. Cracks will grow forming a network of sub-surface cracks responsible for the material removal.

5 ACKNOWLEDGEMENTS

The authors would like to gratefully acknowledge the financial sponsorship from Rolls-Royce Canada Ltd., the Consortium for Research and Innovation in Aerospace in Quebec (CRIAQ) and the Natural Sciences and Engineering Research Council of Canada (NSERC). The authors wish to thank Alstom, Switzerland for the providing the help and support on doing the rig tests.

6 REFERENCES

[1] R.K. Bhargava, C.B. Meher-Homji, M.A. Chaker, B. Bianchi, F. Melino, A. Peretto, S. Ingistov, Gas turbine fogging technology: a state-of-the-art review-Part 1: Inlet evaporative fogging-Analytical and experimental aspects, Journal of engineering for gas turbines and power 129 (2007) 443-453.

[2] R.K. Bhargava, C.B. Meher-Homji, M.A. Chaker, B. Bianchi, F. Melino, A. Peretto, S. Ingistov, Gas turbine fogging technology: a state-of-the-art review-Part 3: Practical considerations and operational experience, Journal of engineering for gas turbines and power 129 (2007) 461-472.

[3] C. B. Meher-Homji, T. R. Mee, Gas Turbine Power Augmentation by Fogging of Inlet Air, Proceedings of the 28th Turbomachinery Symposium (1999) Houston, TX, Sept.

[4] N. Yasugahira, K. Namura, R. Kaneko, T. Satoh, Erosion resistance of titanium alloys for steam turbines blades as measured by water droplet impingement, in Titanium Steam Turbine Blading, Palo Alto, 2988, Pergamon, New York (1990) 385-401.

[5] W.F. Adler and R.F. Vyhnal, Rain erosion of Ti-6A1-4V, 4th International Conference on rain erosion and associated phenomena, Meersburg, Germany, May, 1974.

[6] W.F. Adler, Analysis of particulate erosion, Wear 37 (1976) 345-352.

[7] R.H. Richman, W.P. McNaughton, A metallurgical approach to improve cavitation-erosion resistance, J. Mater. Eng. Perform. 6 (5) (1977) 633–641.

[8] R.H. Richman, W.P. McNaughton, Correlation of cavitation erosion behaviour with mechanical properties of metals, Wear 140 (1990) 63–82.

[9] J.M. Robinson, R.C. Reed, Water droplet erosion of laser surface treated Ti-6Al-4V, Wear 186-187 (1995) 360-367.

[10] B.S. Mann, V. Arya, An experimental study to correlate water jet impingement erosion resistance and properties of metallic materials and coatings, Wear 253 (2002) 650-661.

[11] N. Kamkar, F. Bridier, P. Bocher, P. Jedrzejowski, Water droplet erosion mechanisms in rolled Ti-6Al-4V, wear 301 (2013) 442-448.

[12] G. P. Thomas, J. H. Brunton, Drop impingement erosion of metals, Proc. R. Soc. Lond. A. 314 (1970) 549-565.

[13] M. Futakawa, H. Kogawa, R. Hino, H. Date, H. Takeishi, Erosion damage on solid boundaries in contact with liquid metals by impulsize pressure injection, International Journal of Impact engineering 28 (2003) 123-135.

[14] H. Date, M. Futakawa, effect of tensile waves on impact erosion at solid/liquid interface, International Journal of Impact Engineering 32 (2005) 118-129.

[15] M.C. Kong, D. Axinte, W. Voice, Aspects of material removal mechanism in plain water jet milling on gamma titanium aluminide, Journal of Materials Processing Technology 210 (2010) 573-584.

[16] A. Chillman, M. Ramulu, M. Hashish, Waterjet peening and surface preparation at 600 MPa: A preliminary experimental Study, Journal of Fluids Engineering 129 (2007) 485-490.

[17] L. Huang, J. Folkes, P. Kinnel, P. H. Shipway, Mechanisms of damage initiation in a titanium alloy subjected to water droplet impact during ultra-high pressure plain waterjet erosion, Journal of Materials Processing Technology 212 (2012) 1906-1915.

[18] ASTM Standard G73, 2004 (2010), standard test method for liquid impingement erosion using rotating apparatus, ASTM International, West Conshohocken, PA, 2010, DOI: 10. 1520/C0033-03R06, www.astm.org.

[19] A. Uihlein, C. M. Maggi, I. Keisker, Water droplet erosion at steam turbines; testing method and validation, Proceeding of Milan international conference on solid particle and liquid droplet erosion: Part 2 (2012) 81-93.

Proceedings of the 3rd International Conference on
Fracture Fatigue and Wear, pp. 220-224, 2014

A UNIFIED FATIGUE THEORY BASED ON CHARACTERISTIC LENGTH

S.Q. Hou[1,2] and J.Q. Xu[1]

[1]Shanghai Jiaotong University, Shanghai, China
[2]Shandong Jiaotong University, Jinan, China

Abstract: Different approaches should be used to evaluate fatigue behaviours according to the geometric shape and size of defects in material till now, though it is well known that the fatigue properties of a material is intrinsic, and should be independent of geometric shape and size. By introducing the concept of fatigue characteristic length, a unified fatigue theory is proposed, which can deal with fatigue behaviours in the same way, no matter with or without stress concentration or even singularities (e.g., V-notches), for any shape of defects with macro or micro size. The unified theory can explain well the so called "size effect" of small defects on fatigue. Through the comparison with experimental results in literature, the validity of the unified theory is examined.

Keywords: Characteristic Length; Fatigue Limit; Threshold; Stress Concentration

1 INTRODUCTION

It is well-known that fatigue properties of smooth materials can be described by the S-N curve and the corresponding fatigue limit, while the fatigue properties of cracked materials should be described by the crack propagation curve and the corresponding threshold. This fact means that the evaluation method of fatigue problems, not only the fatigue property constants, in fact, is dependent of the geometric shape and size of materials. However, fatigue properties should be the intrinsic behaviours of a material, and thereby theoretically should be independent of geometric shape. Studies on fatigue limit and crack propagation threshold also indicated that they may be influenced greatly by the defect sizes [1-5]. Some experimental relationships between fatigue limit and defect size can be found in literature [6,7]. Murakami summarized the relationships between fatigue limit and defect sizes by tests of drilling various holes in a smooth material [8,9], and proposed empirical formula for threshold stress intensity factor range [10], Tanaka [11] also proposed a simple modified formula for the threshold of small cracks. However, even the relationship has been established, there remains the question that "Can such a fatigue limit or threshold be regarded as the intrinsic property of materials?

Based on the concept of characteristic fatigue length, a unified fatigue theory is proposed in this paper. By this theory, fatigue problems, with or without any defect, no matter what size the defect is, can be evaluated in the same way.

2 THE UNIFIED FATIGUE THEORY

Assumption: Fatigue is dominated by the average stress amplitude within the characteristic length of the material, not the maximum stress amplitude at a point. By the use of average stress amplitude, any fatigue problems with concentrated or even singular stress distribution can be evaluated in the same way as for smooth materials, by considering the characteristic length one by one, i.e., by considering the fatigue process step by step.

Equivalent stress amplitude formula:

$$\overline{\sigma}_a = \frac{1}{L_f}\int_0^{L_f} \sigma(x)\mathrm{d}x \tag{1}$$

here L_f is the characteristic length, a material constant. $\sigma(x)$ is the stress amplitude distribution, while the axis x concedes with the direction of maximum stress amplitude with its origin located at the singular point or stress concentrated point.

The characteristic fatigue length: Considering the case of a macro crack, the crack propagation condition is

$$\Delta K \geq K_{th} \tag{2}$$

Here K_{th} is the threshold for a macro crack, and is a material constant. While from the equivalent stress amplitude, the crack propagation condition is

$$\overline{\sigma}_a = \frac{1}{L_f}\int_0^{L_f} \frac{\Delta K}{2\sqrt{2\pi r}}\mathrm{d}r = \frac{\Delta K}{\sqrt{2\pi L_f}} \geq \sigma_{-1} \tag{3}$$

So easily we get

$$L_f = \frac{1}{2\pi}\left(\frac{K_{th}}{\sigma_{-1}}\right)^2 \tag{4}$$

Eq.4 means that among the three material constants σ_{-1}, K_{th}, L_f, only two are independent. However, K_{th} is a material constant only for macro crack problems, while L_f can be applied for any geometric shape and size of a defect, no matter it is a hole or a notch, no matter it is a micro or macro defect.

Application of the theory: By the use of equivalent stress amplitude, fatigue problems with any defect's geometric shape and size can be evaluated in the same way as that for smooth materials. For fatigue limit evaluation:

$$\overline{\sigma}_a = \sigma_r \tag{5}$$

Here σ_r is the fatigue limit for smooth materials, r denotes the cyclic property (for the simplicity, we illustrate $r = -1$ only in follows). For fatigue life evaluation for the characteristic length region:

$$\overline{\sigma}_a^m N_f = C \tag{6}$$

3 EXAMINATIONS

3.1 Theoretical examinations

Smooth materials: If there is no any stress concentration, then the equivalent stress amplitude is just the nominal stress amplitude, so the unified theory degenerates to that for smooth materials.

Small-defects: An initial micro defect in a material can be modeled as a spherical hole. From the knowledge of elasticity, the stress distribution is [12]:

$$\sigma(r) = \sigma_a\left[1 + \frac{1}{2(7-5\nu)}\frac{a^3}{r^3}\left(4 - 5\nu + 9\frac{a^2}{r^2}\right)\right] \tag{7}$$

Where ν is Poisson's ratio, a is the radius of spherical defect. Substituting Eq.7 into Eq.1, the fatigue limit condition can be represented as follows:

$$\overline{\sigma}_a = \sigma_a[1 - \frac{4-5\nu}{4(7-5\nu)}\rho^3\left(\frac{1}{(1+\rho)^2} - \frac{1}{\rho^2}\right) - \frac{9}{8(7-5\nu)}\rho^5\left(\frac{1}{(1+\rho)^4} - \frac{1}{\rho^4}\right)] = \sigma_{-1} \tag{8}$$

Where $\rho = a / L_f$ is the ratio of spherical defect radius and characteristic length, and σ_a is the nominal stress amplitude. According to Eq.8, the fatigue limit curve for various sizes of the hole defect can be obtained as shown in Fig.1. Some interesting results can be found. 1) When the defect size a / L_f is smaller than 1/100, then it will have no influence on fatigue, in other words, it can be regarded as the initial micro-defects in the material. This fact inversely means that the characteristic length shall be 100 times

larger than the initial micro-defects. 2) When the defect size a/L_f is larger than 100, then $\overline{\sigma_a} = k\sigma_a$, where $k = 3(9-5\nu)/[2(7-5\nu)]$ is the stress concentration coefficient for a macro hole, i.e., the equivalent stress amplitude can be simply determined by stress concentration. This fact inversely means that the size of a macro defect shall be 100 times larger than the characteristic length. 3) For small defects, which are between micro defects and macro defects, the fatigue stress limit described by the nominal stress amplitude σ_a, depends on the defect-size. However, this dependency does not means the fatigue property is dependent of defect-size, but indicates that the nominal stress is not the proper parameter of fatigue again. By the equivalent stress amplitude within the characteristic length, the fatigue limit can be evaluated in a unified way with the same material constants σ_{-1}, L_f. 4) If the defect size is in the order of characteristic length, then there is an approximate relationship of $\sigma_{af} \propto a^{-1/6}$, which agrees with Murakami's experimental results [8].

Small cracks: Complete stress distribution near a crack tip is [13].

$$\sigma(r) = \frac{\sigma_a(a+r)}{\sqrt{2ar+r^2}} \tag{9}$$

So the fatigue limit condition is

$$\overline{\sigma_a} = \frac{1}{L_f}\int_0^{L_f} \frac{\sigma_a(a+r)}{\sqrt{2ar+r^2}}dr = \sigma_a\sqrt{1+2\rho} = \sigma_{-1} \tag{10}$$

or

$$\overline{\sigma_a} = \frac{\Delta\sigma}{2}\sqrt{1+2\rho} = \frac{\Delta K}{2\sqrt{\pi L_f}}\sqrt{\frac{1+2\rho}{\rho}} = \sigma_{-1} \tag{11}$$

Where $\Delta\sigma$ is stress range, and ΔK is stress intensity factor range. Eq.10 degenerates into fatigue limit condition of smooth material when the crack is small enough (i.e., $\rho \to 0$). While if the crack is large enough ((i.e., $\rho \to \infty$), Eq.11 becomes $\Delta K = K_{th}$ by using Eq.4, which is just the condition for possible crack propagations. The relationship between stress intensity factor threshold and defect size for small cracks is shown in Fig.2. From Eq.11 and Fig.2, some interesting results can be obtained. 1) For small crack, the threshold described by stress intensity factor range can be deduced as

$$\Delta K_f = 2\sigma_{-1}\sqrt{\frac{\pi L_f \rho}{1+2\rho}} = \sqrt{\frac{a}{a_0+a}}\Delta K_{th} \tag{12}$$

here $a_0 = L_f/2$. Eq.12 agrees with Tanaka's result [11], but this dependency does not means the fatigue property changed with crack size, 2) If the crack length is around the order of one-tenth of characteristic length, then one has the relationship as $\Delta K_f \propto a^{1/3}$ approximately, which agrees with the Murakami's experimental law[8].

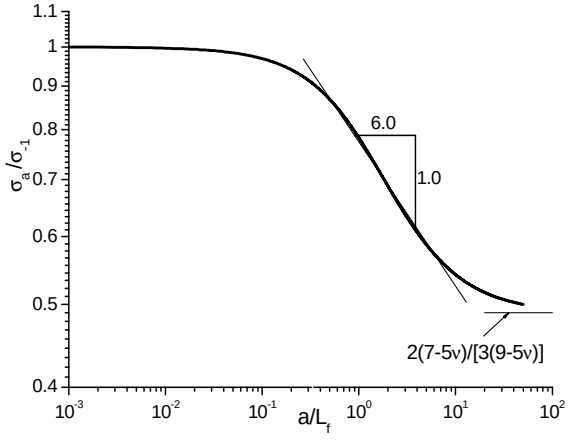

Fig. 1 Fatigue limit for various hole sizes

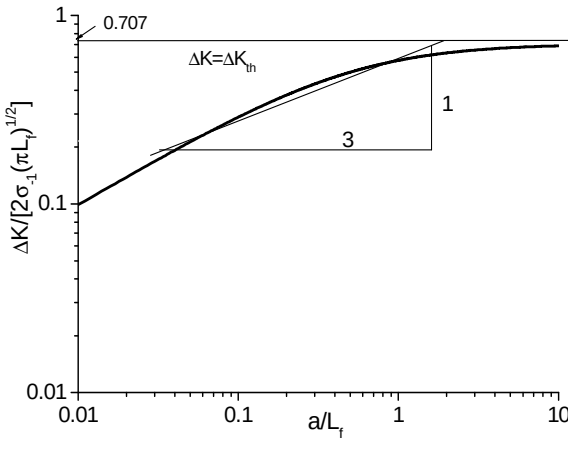

Fig. 2 Threshold for various crack sizes

3.2 Experimental examinations

Figure 3 compared the theoretical estimations of the nominal stress amplitude with the experimental data [8], and Fig.4 shows the comparison of Eq.12 with experimental results [8]. It can be seen that the theoretical estimations agree well with experiment data by new fatigue theory. From above examinations, it can be considered that the new fatigue theory is valid.

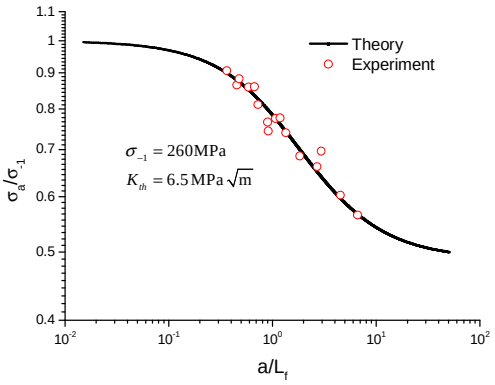

Fig. 3 Fatigue limit comparison

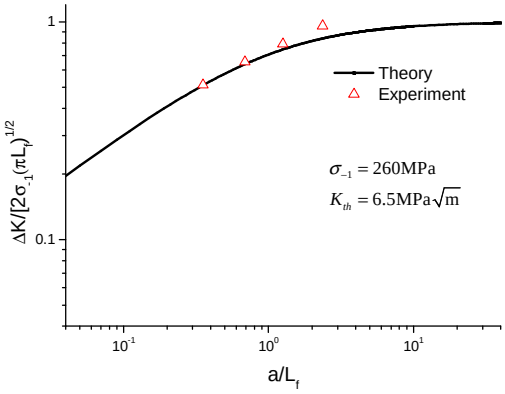

Fig. 4 Threshold comparison

4 DISCUSSIONS

For fatigue problems with distributed stress such as concentrated or singular stress etc., obviously, the unified fatigue theory is very useful.

This new theory can also explain the “wave shape” which can be usually observed from the fatigued sections, since the fatigue failure occurs for one characteristic length, from larger equivalent stress amplitude one to the lower one, step by step.

For the evaluation of fatigue limit condition, the new theory itself is enough to give the result, since only the first characteristic length near the stress concentrated point is needed to be considered. However, to evaluate the whole fatigue life of stress concentrated problems, the cumulative formula of fatigue damage is additionally necessary, because that multiple characteristic lengths should be considered step by step to follow the fatigue process. Though some empirical formula (e.g., Miner’s rule) may be useful, but generally such a cumulative law is unknown yet.

5 CONCLUSIONS

A new fatigue theory is proposed by introducing the concept of characteristic length. The main results obtained can be concluded as follows:

1) The new theory can deal with fatigue problems with any defect’s shape and size in a unified way.
2) The so-called “size effect”, which means the dependency of fatigue properties on defect’s size, is only the presentation due to improper evaluation parameters. All fatigue properties remain constants, if the equivalent stress amplitude is adopted as the evaluation parameter, for any geometric shape and size of defects.
3) The fatigue characteristic length is a material constant, among the three constants σ_{-1}, K_{th}, L_f , only two are independent. σ_{-1}, L_f can be used for any shape (notched or un-notched case) and any stress distribution, while K_{th} can be used only for crack problems.

6 REFERENCES

[1] N. Gubeljak, M.D. Chapetti, J. Predan, B. Sencic, Variation of Fatigue Threshold of Spring Steel with Pre-stressing, Procedia Engineering, 10, 3339-3344, 2011.

[2] M.D. Chapetti, Fatigue propagation threshold of short cracks under constant amplitude loading, International Journal of Fatigue, 25(12), 1319-1326, 2003.

[3] S. Beretta, M. Carboni, M. Madia, Modelling of fatigue thresholds for small cracks in a mild steel by "Strip-Yield" model, Engineering Fracture Mechanics, 76(10), 1548-1561, 2009.

[4] V. Chaves, A. Navarro, Fatigue limits for notches of arbitrary profile, International Journal of Fatigue, 48, 68-79, 2013.

[5] Y. Verreman, N. Limodin, Fatigue notch factor and short crack propagation, Engineering Fracture Mechanics, 75(6),1320-1335, 2008.

[6] N. E. Frost, A relation between the critical alternating propagation stress and crack length for mild steel, Proceeding Institute of Mechanical Engineering, 173(35), 811-827, 1959.

[7] H. Kobayashi, H. Nakazawa, The effects of notch depth on the initiation propagation and non-propagation of fatigue cracks, Transactions of the Japan Society of Mechanics Engineers, 35(277), 1856-1863,1969.

[8] Y. Murakami, Influence of minute defect and inclusion on fatigue, Yokendo, Tokyo, 1993.

[9] Y. Murakami, M. Endo, A geometrical parameter for the quantitative estimation of the effects of small defects on fatigue strength of metals, Transactions of the Japan Society of Mechanics Engineers, 49(438),127-136, 1983.

[10] Y. Murakami, K. Matsuda K, Dependence of threshold stress intensity factor range ΔK_{th} on crack size and geometry, and material properties, Transactions of the Japan Society of Mechanics Engineers, 52(478),1492-1499, 1986.

[11] K. Tanaka, Y. Nakai, M. Yamashita, Fatigue growth threshold of small cracks, International Journal of Fracture, 17(5), 519-533,1981.

[12] Y. R. Nakahara, Application of Elasticity, Jikyo Pub. Co.,Tokyo, 1977.

[13] H. Okamura, Linear fracture mechanics, Baifukan, Tokyo,1976.

Proceedings of the 3rd International Conference on
Fracture Fatigue and Wear, pp. 225-231, 2014

STUDY OF INDENTATION FATIGUE BEHAVIOR OF STEEL WELDMENT THROUGH CYCLIC BALL INDENTATION

S Arunkumar and Raghu V. Prakash*

Department of Mechanical Engineering, Indian Institute of Technology Madras, Chennai 600 036, India
*Corresponding author: raghuprakash@iitm.ac.in

Abstract: Fatigue resistance of base metal, heat affected zone and weld-nugget of steel is investigated by subjecting the material to cyclic ball indentation. An attempt has been made to study the effect of loading conditions viz. overloading and under-loading on the rate of plastic zone propagation beneath the indenter. The experimental results reveal that, overloading increases the resistance for plastic zone propagation and under-loading accelerates the rate of plastic zone propagation rate. Evidently, these observations are similar to the traditional fatigue crack propagation. The fatigue damage quantification in terms of hysteresis energy and loss of stiffness with subsequent cycles of indentation provides a means for evaluating the residual strength and quality of the weld-nugget, heat affected zone and parent metal for on field inspection.

Keywords: cyclic ball indentation; hysteresis energy; fatigue damage; steel weld; residual strength

1 INTRODUCTION

Indentation testing has been used widely for many years to measure the hardness of materials. With the development of sophisticated instruments and computational facility it has now become a ubiquitous tool among scientific and engineering community and in industry as well. As a result it is now possible to relate hardness to the more fundamental properties like young's modulus, yield stress, plastic, creep, fatigue and fracture properties.

The mechanical properties of components/structures degrade during service. To ensure safe and reliable operation, it is essential to obtain information about the extent of degradation of properties. The conventional tests in this regard may no longer be useful since they provide average/global response of entire material subjected to simple mechanical loading. Moreover conventional fatigue tests are expensive and labor intensive as they need to be operated over extended period of time [1]. The indentation testing thus becomes most promising in these situations for material property characterization. Different indenters like sharp, spherical and cylindrical flat-end have been used to study the fatigue properties of materials. Spherical indenters are ideal for the study of fatigue damage in materials as the presence of hydrostatic compressive stress postpones the fracture to larger strains as opposed to sharp/cylindrical flat-end indenters which might result in craking in the first contact due stress concentration [2-5].The present work exemplifies the viability of ball indentation testing in assessing the fatigue resistance in terms of loss of stiffness and hysteresis energy.

2 LITERATURE REVIEW

Several researchers have investigated the effect of cyclic indentation using flat end cylindrical indenters on different materials. For an elastic-perfectly plastic material both the amplitude and median of the load was observed to increase the rate of penetration of indenter and the rate of plastic zone propagation. However, for an elastic-plastic material, contradicting behavior was observed due to local strain hardening. The rate of penetration of indenter increased with indentation frequency due to the emission of negative dislocations during unloading and causes strain softening. The amplitude of the indentation load increases the size of the plastic zone and hence the average plastic energy dissipated per cycle. But, with larger mean indentation load the dissipation of plastic energy per cycle decreases due to strain hardening. Higher frequency of indentation, results in the reduction of resistance for plastic zone propagation and dissipates more plastic energy during each cycle [1,6].

Li et al. [4] demonstrated that the impression fatigue test may be used to understand the effect of variable amplitude load on fatigue crack growth. It was obsevered from experiments that the overloading and

underloading effects (the rate of plastic zone propagation retards with overload cycles due to strain hardening and underloading reduces the resistance for plastic zone propagation) are similar to that of conventional fatigue crack propagation. Nevertheless, the mechanism of deformation has not been investigated due to indentation fatigue. Xu et al. [7], found the similar overloading and underloading effects due to indentation fatigue in case of a polycrystalline copper; the authors investigated the deformation mechanism and observed the formation of shear bands which were piled-up around the indented area. In these shear bands cavities have nucleated and coalesced to form crack; as a result, the indenter continuously sinked into the material with the number of cycles. Another interseting feature reported was the existance of a gap between the piled-up shear band and the indenter. This ensured the constancy of contact area with the number of cycles which is conducive for creep and fatigue tests.

Prakash et al. [8-11] have investigated the material fatigue response through cyclic ball indentation on three different metallic materials; two aluminium alloys (2014-T651 and 7175-T7351) and a duplex stainless steel (2205). The load-displacement response was analyzed to obtain information about failure. The criterion chosen was unloading intercept (plastic depth of penetration) and was tracked continuously as a function of number of cycles and a change in its trend was interpreted as an indication material failure. The plastic strain value at this failure point was estimated using Haggag's formulation. To correlate these failure indications with fatigue data, conventional low-cycle fatigue experiments at a true strain amplitude as estimated from Haggag's formulation (on plain cylindrical specimens conforming to ASTM E-606 standard) were conducted. A good correlation was obtained between failure life data between conventional low cycle fatigue and cyclic ball indentation experiments. It was also demonstrated that cyclic ball indentation is capable of assessing the degradation in material property induced due to creep and creep-fatigue damage.

The review suggests that extensive study has been made on cyclic indentation using *flat end cylindrical indenter* to understand the effect of loading conditions and deformation mechanism. Whether the same loading-condition-effects manifest during cyclic indentation using a spherical indenter is a question. There is a need to investigate the trend of material property degradation and accumulation of damage during cyclic indentation for quality assessment of materials. Thus, the purpose of this research is to study the effect of loading conditions and assess the fatigue damage through cyclic ball indentation on steel weldment.

3 EXPERIMENTAL METHOD

3.1 Material

The material used in this work is a steel weldment whose base metal composition is presented in Table 1. The base metal, Heat Affected Zone (HAZ) and weld nugget were sawed separately from the weld plate (Fig. 1) and examined for microstructure under optical microscope (Fig. 2). The samples were given a light electrolyte etching using 2% Nital solution to reveal the microstructure. The average grain size of the base metal, HAZ and weld nugget were 0.085 mm, 0.076mm and 0.047 mm respectively. All the samples were polished with 800, 1000, and 1200 grit emery papers to diminish the influence of surface irregularities during indentation.

Table 1 Chemical composition of base metal

C	Mn	Si	S	P	Cr	Ni	Mo
0.084	0.556	0.289	0.005	0.009	0.792	0.205	0.438

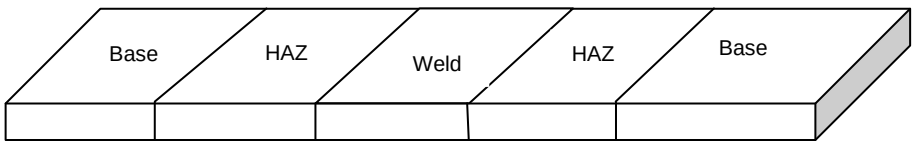

Fig. 1 Schematic of the Weld metal geometry

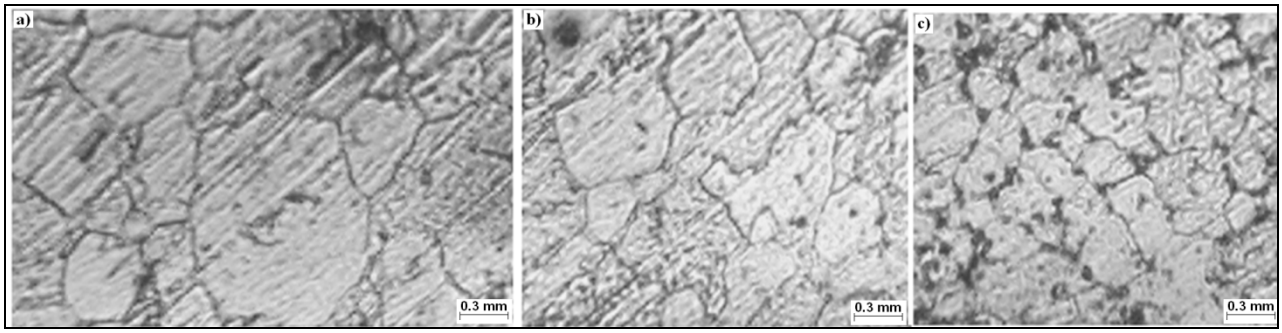

Fig. 2 Microstructures of a) Base metal b) HAZ and c) Weld nugget

3.2 Test system

Cyclic indentation experiments were performed using MTS 810 servo hydraulic test system with a 100 kN load cell. A PC was attached to the machine to control the test and store the digital data. A spherical ball of diameter 1.5875 mm made of tungsten carbide (WC) was used. A clip-on displacement gauge (full range - 3 mm) was mounted between the knife edges of the loading members to measure the displacement of the indenter. The force and displacement transducers were scaled downed to $1/10^{th}$ of its full range for cyclic indentation. The schematic of the fixture is shown in Fig.3a. The test was carried out under load control mode. The loading cycle was a typical sinusoidal waveform (Fig 3b and 3c). The test procedure was programmed in MultiPurpose Testware software. The load was applied with ramp waveform initially at a rate of 0.1 kN/s to achieve the peak load (0.5 kN in low-high block sequence and 0.8 kN in high-low block sequence) and then the load was cycled between 0.25 kN (compressive load) and peak load at a frequency of 1 Hz. The normal (N_0) and secondary (N_1) loading block consisted of 500 cycles each. The specimens were then subjected to fatigue loading with a minimum compressive load of 0.3 kN and maximum compressive load of 0.8 kN for 2500 cycles in order to assess the fatigue damage. The force-displacement was continuously tracked and acquired at a rate of 20 Hz. The test data was then analyzed for peak indentation depth, plastic zone propagation rate, and hysteresis energy with the number of cycles.

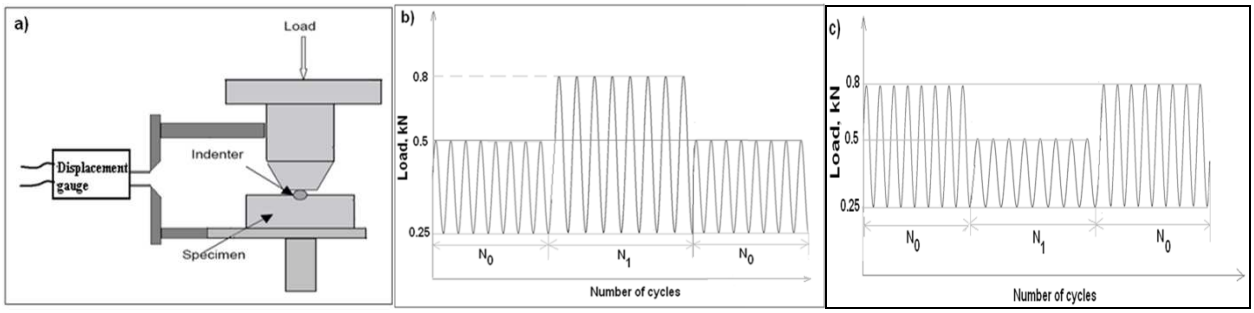

Fig. 3 a) Schematic of indentation fixture b) Low-High load sequence block, N_0 - Normal load block, N_1 - Over/Under load block c) High-Low load sequence block

3.3 Effect of loading frequency

The frequency of loading is found to influence on hysteresis energy significantly; assessing the fatigue behaviour at a randomly chosen frequency may not give accurate results. Experimental results reveal that, under constant load amplitude conditions hysteresis energy increases with frequency (Fig. 4a and 4c). A similar behaviour was also observed during cyclic indentation in aluminium [1]. In order to understand this, the indentation depth was continuously tracked for different frequencies with the number of cycles. The average indentation depth rate from 0.5 to 1.5 Hz is 2.17×10^{-6} mm/cycle and from 2 to 3 Hz is 1.51×10^{-5} mm/cycle (Fig. 4b). This increase in the penetration speed of the indenter by an order, results in dissipation of more plastic strain energy. The hysteresis loop is a combination of plastic and inelastic deformation. Only a portion of the applied load is used in plastically deforming the material and the rest is converted in to heat [12,13]. In order to separate the plastic portion of the hysteresis loop, indentation experiments were carried out at different frequencies and load levels. The hysteresis is nearly stable below 1.5 Hz indicating that the heat and inelastic effects become insignificant. From these results cyclic indentation experiments were conducted at a frequency of 1 Hz.

4 RESULTS AND DISCUSSION

4.1 Effect of overloading and underloading

Figures 5a and 5b show the effect of overload on the indentation depth and plastic zone propagation rate with the number of cycles on the base metal. The test specimen was cyclically penetrated with load amplitude of 0.125 kN for the first 500 cycles. The indentation depth rate decreases initially with number of cycles and attains a steady state value after around 250 cycles. The amplitude was then increased by 120% for the next 500 cycles. Soon after the change in load amplitude, the indentation depth rate (plastic zone propagation rate) becomes higher than the previous low amplitude block loading. In this case, the indentation depth rate decreases with the number of cycles till the end of high block loading without reaching a steady state value. This indicates that the overloading increases the resistance for plastic zone propagation and might take higher number of cycles to attain the steady state value. The introduction of the low load block soon after overloading resulted in a continuous decrease in the indentation depth rate (whose value is found to be less than that of first 0 to 500 cycles). This might be due to the strain hardening of the material beneath the indenter.

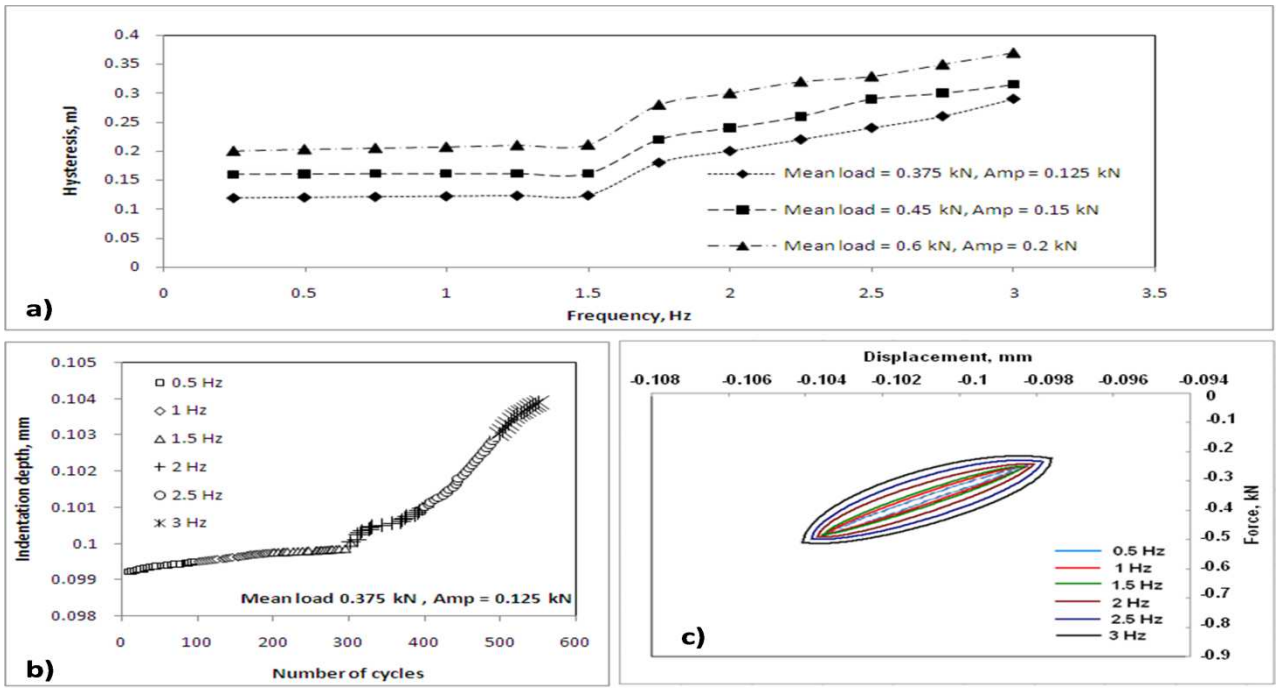

Fig. 4 a) Effect of frequency of loading on hysteresis energy, b) Indentation depth for different frequency of loading and c) Hysteresis loops for different test frequencies

Figures 6a and 6b show the effect of underloading on indentation depth and plastic zone propagation rate. In this case, the amplitude of the low block loading was reduced by 120%. After the under loading period of 500 cycles the indentation depth rate is higher than the previous high block loading and it takes fewer nubmer of cycles to attain the steady state value. This indicates that, underloading reduces the resistance for plastic zone propagation beneath the indenter. A similar behavior was also observed for a flat end cylindrical indenter [4,7]. All these effects are similar to that observed in traditional fatigue crack propagation.

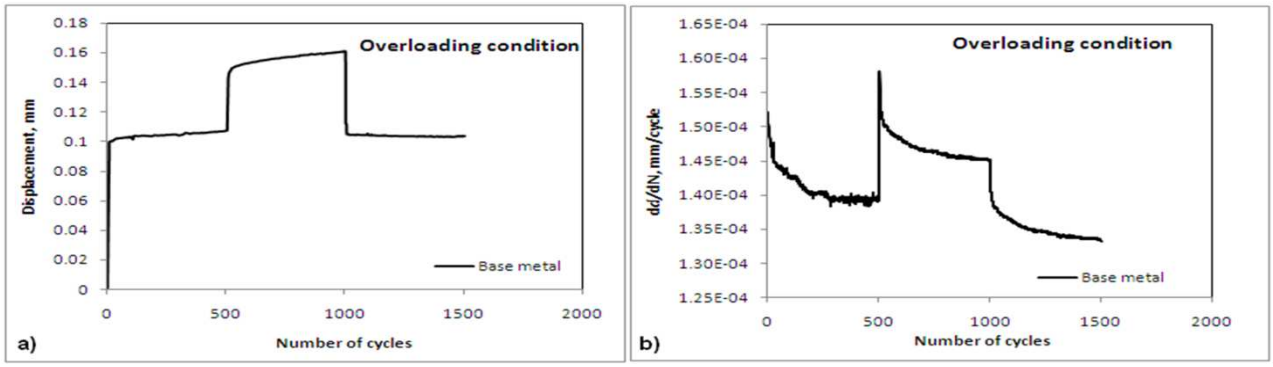

Fig. 5 a) Displacement of the indenter with number of cycles, b) Effect of overloading on the indentation depth rate with number of cycles

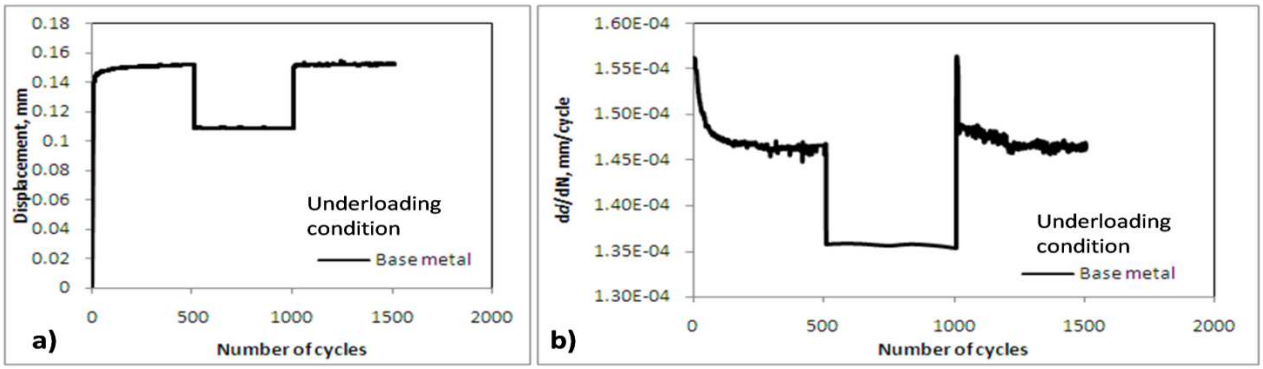

Fig. 6 a) Indentation depth – number of cycles curve, b) Effect of underloading on the indentation depth rate with number of cycles

4.2 Fatigue damage assessment

During cyclic indentation, the material is plastically deformed beneath the indenter. The plastic strain thus accumulates with the subsequent cycles of indentation and this phenomenon is termed as fatigue damage. The plastic strain involves the movement of dislocations and a part of the applied mechanical energy is dissipated during this process. The dislocation movement leads to breaking of atomic bonds and weakening of material stiffness. The plastic dissipation energy/hysteresis energy and loss of stiffness of material may thus be looked upon as a measure of fatigue damage.

The base metal, HAZ and weld nugget were subjected to cyclic indentation with a minimum compressive load of 0.3 kN and maximum compressive load of 0.8 kN for 2500 cycles. The force-displacement response was continuously monitored. The stiffness (S) of the material is then determined by estimating the slope of unloading curve (within the window of 95% to 60% of peak load) of the force-displacement response. The hysteresis energy (H) was also determined by measuring the area between the loading and unloading paths of the force-displacement response.

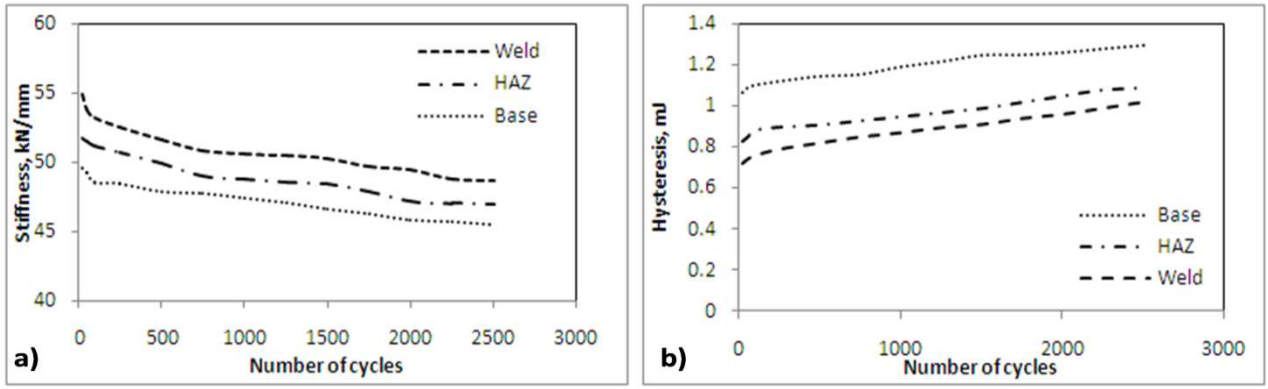

Fig. 7 a) Variation of stiffness (S) with number of cycles, b) Hysteresis energy (H) – number of cycles curve

Table 2

Material	Power law	R^2
Base	$S=52.661\ N^{-0.017}$	0.874
HAZ	$S=56.062\ N^{-0.021}$	0.905
Weld	$S=59.262\ N^{-0.023}$	0.960

Table 3

Material	Power law	R^2
Base	$H=0.916\ N^{0.040}$	0.891
HAZ	$H=0.688\ N^{0.051}$	0.853
Weld	$H=0.560\ N^{0.068}$	0.904

Figures 7a and 7b show the degradation of stiffness and accumulation of hysteresis in the test specimens. By fitting a power law between S and N (number of cycles) and H and N it is possible to assess the quality of the material being tested. The exponent in the power law indicates the rate at which the mechanical property degrades with the number of cycles. Thus from Table 2, for the weld the exponent value (0.023) is higher than the HAZ and base metal indicating that it loses its stiffness at a higher rate than the other two for the same number of cycles of loading. The rate at which hysteresis energy accumulates as a function of number of cycles for the weld metal (the exponent value is 0.068 from Table 3) is higher than HAZ and base metal. This suggests that the fatigue resistance of weld nugget is less than that of HAZ and the base metal. This is also evident from Fig. 8b which shows that the indenter penetrates into the weld at a faster rate than HAZ and base metal.

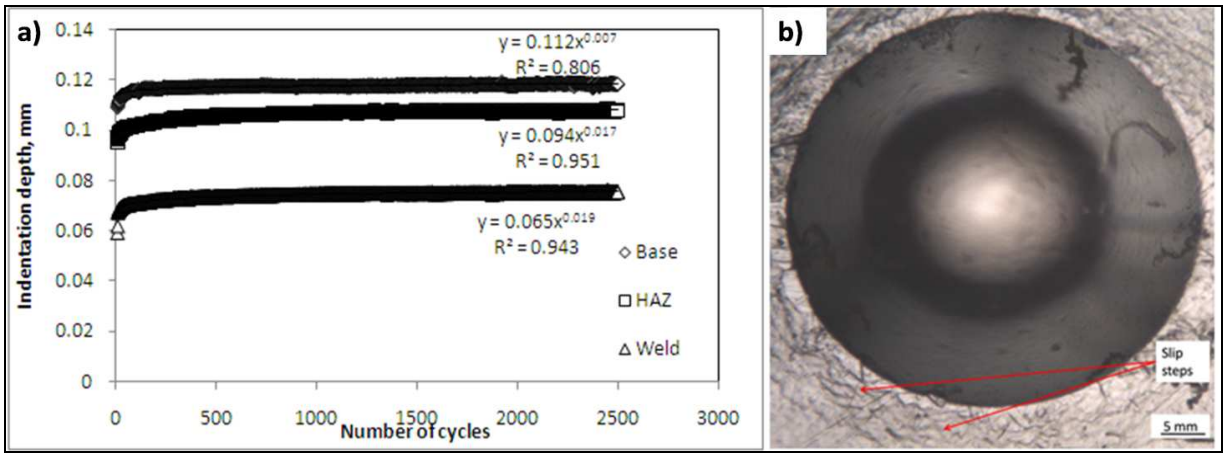

Fig. 8 a) Indentation depth versus number of cycles for all the test specimens b) Optical micrograph of indented area showing the slip steps

Figure 8b shows the optical micrograph image of indentation profile after fatigue loading. The image shows the pile up around the indented surface and layers of material overlapped one above the other. These overlapping layers represent the slip-steps around the indentation area. It may be inferred as the mechanism of deformation is due to the movement of dislocations.

5 CONCLUSIONS

Cyclic ball indentation experiments were conducted on base, HAZ and weld nugget of steel weldment to investigate the material fatigue behaviour. An optimum frequency level was found at which hysteresis was constant for cyclic indentation. The overloading and underloading effects observed during indentation are similar to that observed in conventional fatigue crack growth experiments. A methodology has been proposed to assess the material fatigue damage by continuously tracking the rate of stiffness degradation and rate of hysteresis energy accumulation. Based on these findings it is possible to assess the fatigue resistance of materials through cyclic indentation.

REFERENCES

[1] Fuqian Yang, Lingling Peng, Kenzi Okazaki, Cyclic indentation in aluminium, Journal of material science, 42:4513-4520, 2007.

[2] G. Sundararajan, Y. Tirupataiah, The hardness-flow stress correlation in metallic materials, Bull. Material Science, Vol. 7, pp. 747-770, 1994.

[3] A.E. Giannakopoulos, S. Suresh, Determination of elastoplastic properties by instrumented sharp indentation, Scripta materialia, Vol.40, No.10, pp.1191-1198, 1999.

[4] J.C.M. Li, S.N.G. Chu, (1979), Impression fatigue, Scripta Metallurgica, Vol.13, pp.1021-1026, 1979.

[5] Fernando Guiberteau, P. Nitin, Padture, Hongda Cai, Brian R. Lawn, (1993), Indentation fatigue: A simple cyclic Hertzian test for measuring damage accumulation in polycrystalline ceramics, Philosophical Magazine, Vol. 68, No. 5, pp. 1003-1016, 1993.

[6] Fuqian Yang, Aditi Saran, Cyclic indentation of elastic-perfectly plastic material, Journal of material science, 41:6077-6080, 2006.

[7] B.X. Xu, Z.F. Yue, J. Wang, Indentation fatigue behaviour polycrystalline copper, Mechanics of materials, Vol. 39, pp.1066-1080, 2007.

[8] Raghu V. Prakash, Prashant Bhokardole, Chow Shing Shin, Investigation of Material Fatigue Behaviour Through Cyclic Ball Indentation Testing, Journal of ASTM International, Vol. 5, No. 9, STP, pp.236-255, 2008.

[9] Raghu V Prakash, Evaluation of fatigue damage in materials using indentation testing and infrared thermography, Transactions of The Indian Institute of Metals, Vol. 63, Issues 2-3, pp.173-179, 2010.

[10] Raghu V. Prakash and Sabita Ghosh, "Creep, Creep-fatigue damage identification through monotonic and cyclic ABI testing, ASTM symposium on Creep, Creep-Fatigue Interactions, San Antonio, TX, USA, Nov. 2010

[11] Sabita Ghosh, Raghu V Prakash, Study of damage and fracture toughness due to influence of creep and fatigue of commercially pure copper by monotonic and cyclic indentation, Metallurgical and Materials Transactions A, Vol.44A, pp.224-234, 2012.

[12] J. Lanteigne, P. Nguyen-Duy, Energy Balance Approach to Low Cycle Fatigue, Journal of Fracture, Vol.23 - RI47-RI49, 1983.

[13] C. S. Chang, W. T. Pimbley, H. D. Conway, An Analysis of Metal Fatigue Based on Hysteresis Energy, Journal of Experimental Mechanics, Vol. 8, pp.133-137, 1968.

Proceedings of the 3rd International Conference on
Fracture Fatigue and Wear, pp. 232-238, 2014

A COMBINED *CRITICAL DISTANCE - STRESS GRADIENT* APPROACH TO PREDICT THE FRETTING FATIGUE CRACK NUCLEATION RISK: APPLICATION TO FEM ANALYSIS

S. Fouvry, C. Gandiolle and B. Berthel

Ecole Centrale de Lyon, LTDS, France

Abstract: Fretting-Fatigue problems are very complex to address due to the multi-axiality and the very sharp stress gradients imposed below the interfaces. Hence, multi-axial and non local fatigue approach must be considered. An experimental cylinder/plane fretting fatigue analysis of a 35NiCrMo16 low alloyed steel was performed to investigate the incipient crack nucleation response at 10^6 cycles for various stress gradient conditions. Imposing elastic stress conditions, the Crossland fatigue approach is applied to predict the crack nucleation risk. This analysis confirms that a local stress analysis at the “hot spot” stress located at surface trailing contact border is not suitable because it sharply overestimates the cracking risk. A non local “weight function” alternative approach based on the Papadopoulos theory is applied where the crack nucleation risk computed at the “hot spot” is weighted by a linear decreasing function of the surrounding hydrostatic stress gradient. This strategy is validated using an exact analytical surface stress analysis. However it is not suitable for FEM analyses due to a miss-estimation of surface stress fields: the larger the surface mesh size the smaller the “hot spot” stress value. To palliate such limitation an original “critical distance - weight function” approach is introduced. By only considering reliable subsurface stress values (i.e., second and third nodes below the surface), stable and consistent predictions can be achieved.

Keywords: fretting fatigue crack nucleation; stress gradient; non local fatigue approach; crossland; FEM analysis

1 INTRODUCTION

Fretting is a small amplitude oscillatory movement, which may occur between contacting surfaces subjected to vibration or cyclic stress. Combined with cyclic bulk fatigue loading, the so-called fretting-fatigue loading can induce catastrophic cracking phenomena reducing the contact assembly endurances [1,2]. The crack nucleation phenomenon is commonly addressed by transposing conventional multi-axial fatigue criteria [3] taking into account the stress gradient effects by considering non local fatigue stress analysis [4-6]. Stress averaging approaches [4,6], or equivalent critical distance methods [5] which consists in considering the stress state at a “critical distance” from the “hot spot” stress are commonly applied to capture the stress gradient effect. However, these approaches, which consider fixed length scale values are limited when large stress gradient fluctuations are operating [7]. An alternative strategy which consists to weight the prediction given at the “hot spot” through a linear decreasing function of the surrounding hydrostatic stress gradient is considered [8,9]. The purpose of this research work is to extend this approach for FEA partial slip fretting fatigue computation considering that FEA analyses are not able to provide an exact estimation of surface stress fields due to convergence aspects. A “critical distance- weight function” alternative strategy only involving reliable subsurface stress estimations, independent of the contact mesh size, is introduced and discussed.

2 MATERIALS AND EXPERIMENTAL PROCEDURE

2.1 Materials

The studied material is a tempered 35NiCrMo16 low alloyed steel displaying a tempered Martensitic structure. The original austenite grain size is about Ø =20 µm. The mechanical and fatigue properties of this steel, are summarized in table 1. Chromium 52100 steel was chosen for the cylindrical pads in order to maintain elastically similar conditions whilst simultaneously ensuring that cracks arose only in 35NiCrMo16 specimens. Both plane and cylindrical pad surfaces were polished to achieved a small Ra=0.05 µm surface roughness.

Table 1 Mechanical and fatigue properties of the studied 35NiCrMo16 low alloyed steel.

E(MPa)	ν	$\sigma_{y0.2\%}$ (MPa)	σ_u (MPa)	σ_d (MPa)	τ_d (MPa)	ΔK_{th} (MPa$\sqrt{m}$)
205000	0.3	950	1130	575	386	3.2

E: Young's modulus; ν: Poisson Coefficient, $\sigma_{y0.2\%}$: Yield stress (0.2%); σ_u: Ultimate Stress; σ_d : traction – compression fatigue limit ($R\sigma = \sigma_{min}/\sigma_{max}$=-1 for 10^7 cycles); τ_d : shear fatigue limit ($R\tau$=-1 for 10^7 cycles); ΔK_{th} : long crack threshold (R=-1).

2.2 Test procedures

Two different test apparatuses were used to quantify respectively the fretting and the fatigue influences in cracking processes. Plain Fretting tests were applied by imposing a nominally static normal force P, followed by an alternated cyclic displacement amplitude (δ∗), so that a cyclic tangential load amplitude Q* was generated on the contact surface (Fig. 1a). During a test, P, Q and δ are recorded, from which the δ - Q fretting loop can be plotted. The studied plane specimen is not subjected to any fatigue stress.

The fretting fatigue experiments were performed using a dual actuator device [7, 10] (Fig. 1b). This test system allows the separate application and control of fretting and fatigue loadings. Like for the plain fretting, the system is instrumented to measure the contact loading (P, Q*, δ*) but also the fatigue stress (σ, $R_\sigma=\sigma_{min}/\sigma_{max}$). Both fretting and fatigue loadings are in phase. All the tests were performed at a constant 13 Hz frequency.

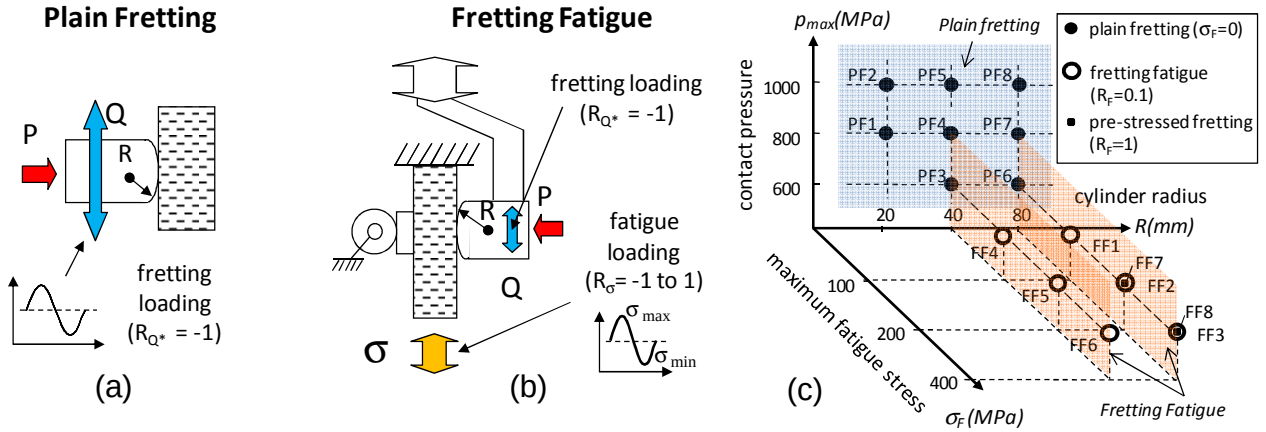

Fig. 1 Schematics of Plain Fretting (a) and Fretting Fatigue, (b) experiments and (c) Studied loading conditions

In order to analysis both contact pressure, fatigue stress and stress gradient effects, various cylinder radius from R= 20 to 80 mm, Hertzian contact pressures from p_{max}=600 to 1000 MPa and fatigue stress conditions from σ_{max}= 0 and 400 MPa considering two stress ratio Rσ=0.1 and 1.0 were investigated (Fig. 1c). The lateral width and thickness of cylinder and plane specimens were chosen to satisfy Hertzian plain strain hypothesis. Plain fretting tests were first performed to identify the coefficient of friction at the partial slip transition. An averaged μ_t=0.8 friction value was founded. This value was assumed representative of the friction coefficient operating in the sliding zones of partial slip interfaces. For each R, P and σ loading conditions, an iterative test procedure was applied to identify the threshold tangential force amplitude Q_{CN}* inducing a 10 µm crack length after 10^6 cycles. This crack nucleation investigation was performed applying destructive cross-section expertises. It confirms that the incipient crack nucleation was systematically observed at the surface trailing contact border.

3 STRESS AND MULTIAXIAL FATIGUE ANALYSES

All the crack nucleation conditions correspond to elastic loading conditions which permits a direct correlation between analytical and Finite Element stress modelling [7]. The analytical stress description was achieved coupling cylinder/plane Mindlin formalism with the McEven stress formulations thus to extract the stress path below and on the top surface of the studied contacts [7,11]. The fatigue stress effect on surface shear profile was considered coupling the Nowell's eccentricity formalism [12]. The major interests of such analytical formulation are the very fast computation and the exact stress estimation over the whole surface and subsurface contact like for instance at the trailing contact border where a singular "hot spot"

stress condition is operating. For more complex contact configurations, Finite Element Analyses are usually required. To evaluate the stability of such strategy, an equivalent FEM analysis was performed (Fig. 2a and 2b). The ABAQUS commercial code was used. The mesh is composed of triangular (CPE3) and quadratic (CPE4R) linear elements. Quadratic elements are used to define the contact zone in a square domain of about 500 µm in depth and from –2a to 2a in length where mesh size from 1 to 10 µm were compared. Outside the contact zone triangular elements are considered in order to reduce time costs. The contact is described by a master-slave algorithm and the tangential loading is determined by Lagrange multipliers though a constant friction coefficient (μ_t=0.8). Figure 2c compares the σ_{11max} stress profiles computed at the trailing contact border along the z for a given partial slip cylinder/plane condition. As previously underlined in [13], due to extrapolation approximations, the surface stresses provided by FEM computations are systematically under estimated. The 1st surface node displays a significant error which increases with the mesh size. This error can reach 30% for the studied 10µm mesh size contact. By contrast, the second and third subsurface stress values are nearly superimposed on the reference analytical profile. The error remains lower than 5 % and the computation is nearly not affected by the FEM mesh size. From this basic comparison, it can be concluded that under severe stress gradient conditions like imposed by fretting contacts, cautions must be taken regarding the surface FEM stress estimation. By contrast, reliable estimations are achieved below the surface which implies that consistent crack nucleation predictions can be obtained if the fatigue stress analysis exclusively involves subsurface stress components defined for instance at the second and third nodes below the surface [13].

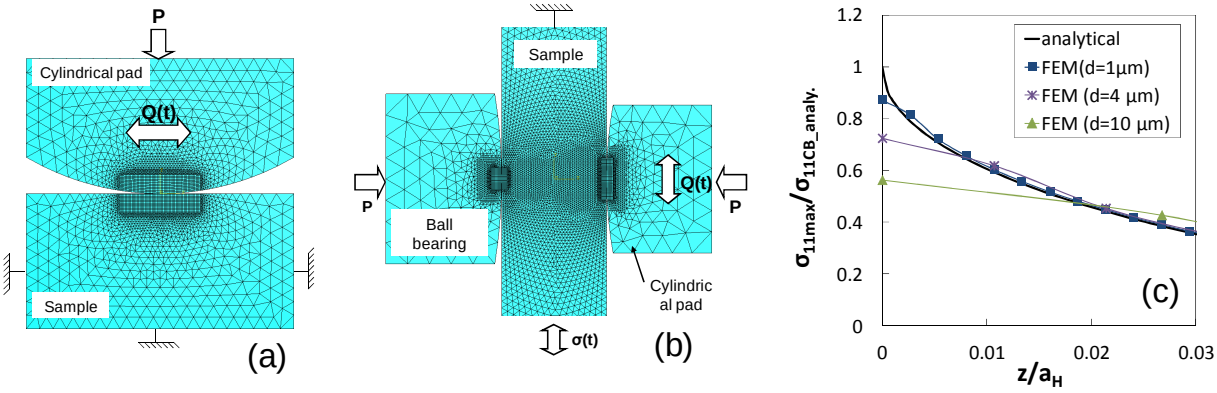

Fig. 2 (a) FEM model of Plain Fretting test; (b) FEM model of Fretting Fatigue test; (c) Comparison between analytical and FEM simulations of the σ_{11max} stress profile at the trailing contact border along the z axis as a function of the contact mesh size "d" (plain fretting, cylinder/plane contact, R=20 mm, p_{max} = 1000 MPa, a_H= 0.35 mm Q*/P =0.23)

4 CROSSLAND MULTIAXAIL FATIGUE ANALYSIS

The fretting stresses are very complexes and therefore a multiaxial fatigue analysis is required. The Crossland's multiaxial fatigue approach [14], well adapted to describe the fatigue response of the studied steel alloy, is considered. The crack risk is expressed as a linear combination of the maximum amplitude of the second invariant of the stress deviator $\sqrt{J_{2,a}}$, and the maximum value of the hydrostatic pressure ($\sigma_{H,max}$) (Fig. 3). The crack nucleation condition is verify if the maximum equivalent Crossland fatigue stress generated in the contact (i.e. hot spot) is becoming larger than the shear fatigue limit :

$$\sigma_C = \sqrt{J_{2,a}} + \alpha_C . \sigma_{H,max} \geq \tau_d \qquad (1)$$

with for the studied alloy $\alpha_C = 0.28$.

Figure 3b displays the Crossland's local stress distribution computed for a representative Fretting Fatigue crack nucleation condition (i.e. FF2, Fig.1). Confirming the expertises, the maximum crack nucleation risk is located at the surface trailing contact border displaying a discontinuous evolution. Very sharp stress gradients are indeed observed as well as a dissymmetry induced by the stick zone eccentricity [12].

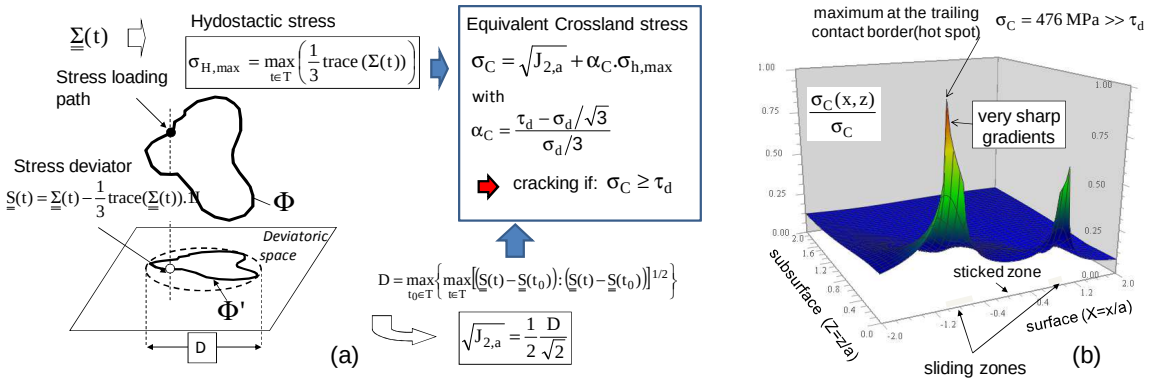

Fig. 3 (a) Illustration of the Crossland criterion – (b) Crossland distribution of the FF2 (Fig.1) condition using an analytical local stress analysis

5 RESULTS AND DISCUSSION

6.1 "Hot spot" stress analysis

A multi-axial fatigue analysis is first performed using analytical stress computations and a local "hot spot" fatigue stress approach (i.e., trailing contact border stress path). The analysis is performed for each plain fretting and fretting fatigue crack nucleation conditions and reported in a $\sqrt{J_{2,a}}$ - $\sigma_{H,max}$ diagram (Fig. 4).

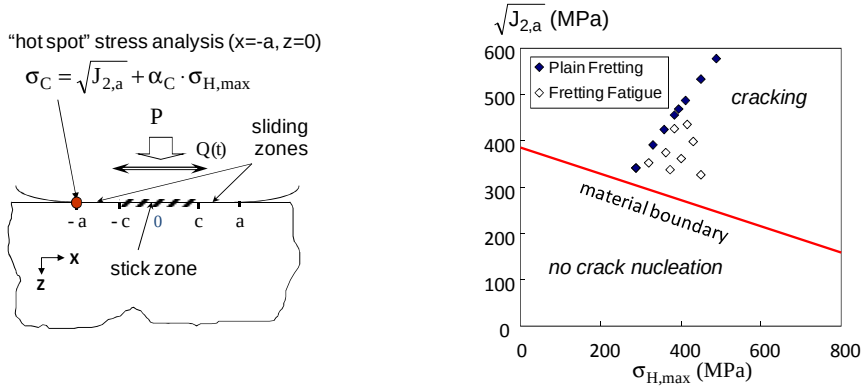

Fig. 4 Local Crossland analysis at the "hot spot" trailing contact border

As expected, the experimental data are highly dispersed and systematically above the material boundary. This local Crossland fatigue approach does not integrate the severe stress gradients operating next to the "hot spot" and therefore is not suitable to predict the fretting cracking risk. To quantify the stability of the prediction, the mean value and the square root variance of the equivalent Crossland stress obtained for the 16 test conditions, are computed.

$$\sigma_{C,m} = \frac{1}{N}\sum_{i=1}^{N}\sigma_C(i)\,,\quad V\sigma_C = \sqrt{\frac{\sum_{i=1}^{N}(\sigma_C(i)-\sigma_{C,m})^2}{N-1}}\,,\quad \%E\sigma_C = \left(\frac{\sigma_{C,m}-\tau_d}{\tau_d}\right)x100 \text{ and } \%V\sigma_C = \left(\frac{V\sigma_C}{\tau_d}\right)x100 \qquad (2)$$

The $\%E\sigma_C$ allows to estimate the global error of prediction versus the theoretical material prediction, whereas the $\%V\sigma_C$ variable provides a relative estimation of the dispersion. For the given local fatigue description, we found $\%E\sigma_C$ = +36 % and $\%V\sigma_C$ = 21% which corresponds to a critical overestimation and a high dispersion.

6.2 "Weight" function approach

An alternative strategy to consider the stress gradient effect consists in multiplying the "hot spot" fatigue stress by a weight function (w) expressed as a linear decreasing function of the hydrostatic stress gradient operating around the hot spot location [7,8,15] (Fig. 4a):

$$\sigma_C^* = \sigma_C.w\left(\left|\overline{\nabla}_\lambda(\sigma_{H,max})\right|\right) \text{ where } w = 1 - k.\left|\overline{\nabla}_\lambda(\sigma_{H,max})\right| \qquad (3)$$

With $\left|\overline{\nabla}_{\lambda}(\sigma_{H,max})\right|$ the mean stress gradient of the hydrostatic stress over a cubic volume defined by the length scale λ. Hence for plain strain conditions it leads to:

$$\left|\nabla(\sigma_{H,max}(x,z))\right| = \sqrt{\left(\frac{\partial\sigma_{H,max}}{\partial x}\right)^2 + \left(\frac{\partial\sigma_{H,max}}{\partial z}\right)^2} \quad (4)$$

which for the studied fretting conditions infers :

$$\left|\overline{\nabla}_{\lambda}(\sigma_{H,max})\right| = \sqrt{\left(\frac{\sigma_{H,max}(-a,0)-\sigma_{H,max}(-a,\lambda)}{\lambda}\right)^2 + \left(\frac{\sigma_{H,max}(-a,0)-\sigma_{H,max}(-a+\lambda,0)}{\lambda}\right)^2} \quad (5)$$

The length scale was arbitrary fixed at λ =10 µm which corresponds to the crack nucleation length and the half dimension of the grain size. This non local fatigue stress analysis is here applied considering analytical stress computations. By plotting the evolution of the τ_d/σ_C ratio versus the corresponding $\left|\overline{\nabla}_{\lambda}(\sigma_{H,max})\right|$ hydrostatic stress gradient, thus for each crack nucleation condition, a linear evolution can be observed allowing the determination of the "k" factor (Fig. 5b).

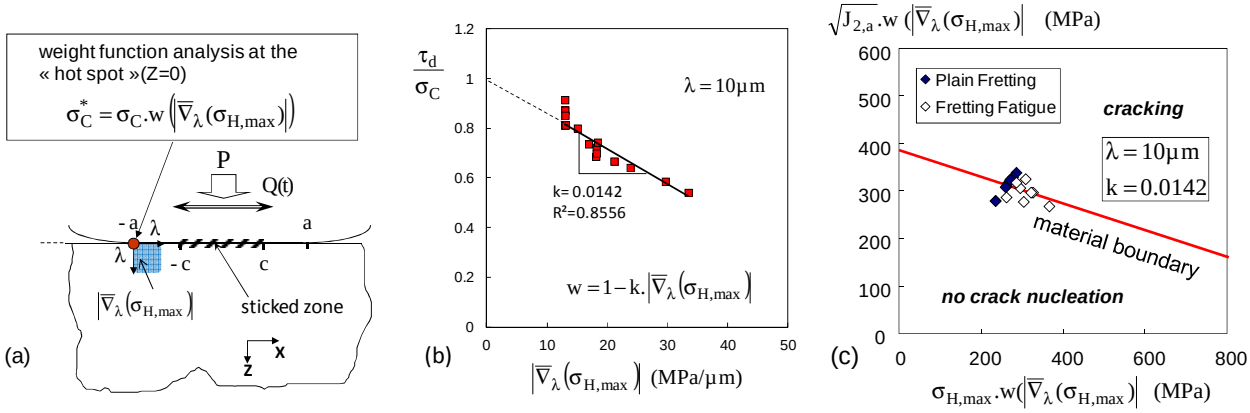

Fig. 5 Weight function approach: (a) illustration of the methodology; (b) reverse analysis of experimental results (Fig. 1) to establish the linear "w" weigh function (λ =10µm); (c) Application of the weight function approach to correct the "hot spot" crack nucleation predictions : plotting of the $w\sqrt{J_{2,a}}$ - $w\sigma_{H,max}$ diagram

For λ = 10 µm we fund k=0.0142 $(MPa/\mu m)^{-1}$. Using this weight function approach, the predictions are highly improved. Figure 5c compares the different crack nucleation conditions reported as a function of the corresponding $w\cdot\sqrt{J_{2,a}}$ and $w\cdot\sigma_{H,max}$ parameters where $\sqrt{J_{2,a}}$ and $\sigma_{H,max}$ are the "hot spot" values of the Crossland stress parameter (5.1). All the experimental results are aligned along the material boundary. The statistical analysis leads to $\%E\sigma_C^*$ = 1% and $\%V\sigma_C^*$ = 6%. The prediction is very good, equivalent to the experimental scattering.

6.3 Combined "Critical distance – Weight function" approach

The former weight function approach, by taking into account the stress gradient effect, provides reliable and stable predictions. However, involving surface stress components, it is restricted to analytical stress computations and can not be transposed in Finite Element analyses without an adequate correction of contact mesh size effect. This mesh size dependency is clearly detrimental for any engineering contact designing. To palliate such limitation, a "critical distance – weigh function" alternative approach, consisting in only considering the subsurface stress components is proposed: the equivalent Crossland stress is no more computed at the surface "hot spot" location but deeper below the surface at a ℓ critical distance. This subsurface stress field analysis is combined with an equivalent weight function approach to take into account the stress gradient effect (Fig. 6a). The hydrostatic stress gradient variable averaged over λ square volume is now computed from the ℓ subsurface position thus to avoid surface stress miss-estimation. The critical distance is assumed equal to the stress gradient length scale and the mesh size: d = ℓ = λ =10 µm. In addition to simplify the FEA implementation, it provides a mean description of the stress path operating in the material grain. The formulation of this non local fatigue alternative strategy is given by:

$$\sigma_C^*(\ell) = \sigma_C(\ell).w^*\left(\left|\overline{\nabla}_{\lambda,\ell}(\sigma_{H,max})\right|\right) \text{ where } w^* = w_0^* - k^*.\left|\overline{\nabla}_{\lambda,\ell}(\sigma_{H,max})\right| \quad (7)$$

With, $\left|\overline{\nabla}_{\lambda,\ell}(\sigma_{H,max})\right| = \sqrt{\left(\frac{\sigma_{H,max}(-a,\ell)-\sigma_{H,max}(-a,\lambda+\ell)}{\lambda}\right)^2+\left(\frac{\sigma_{H,max}(-a,\ell)-\sigma_{H,max}(-a+\lambda,\ell)}{\lambda}\right)^2}$ (8)

Plotting the $(\tau_d/\sigma_C(\ell),\ \left|\overline{\nabla}_{\lambda,\ell}(\sigma_{H,max})\right|)$ experimental crack nucleation data, a linear evolution is still observed (Fig. 6b) which allows us to extrapolate the modified w* weight function parameters. We found respectively w_0^*=1.3 and k*=0.062. Figure 6c compares the predictions provided by this "modified" weight function approach. All the experiments are now aligned along the material boundary. The statistical analysis leads to $\%E\sigma_C^*(\ell)$ = 1% and $\%V\sigma_C^*(\ell)$ = 6%. The stability of the predictions is equivalent to the former plain weight function analysis. However, the stress gradient correction can now be transposed to any FEA investigations according that such formulation does not imply the mis-estimated surface stress values.

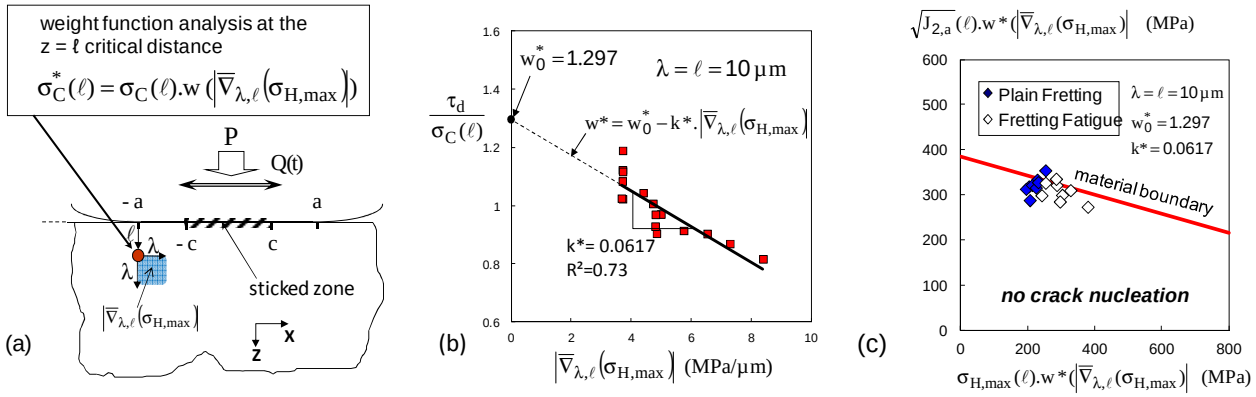

Fig. 6 Critical distance - Weight function approach: (a) illustration of the methodology; (b) reverse analysis to identify the linear "w*" weigh function (λ = ℓ =10µm); (c) Application of the method using the $w^*\sqrt{J_{2,a}}$ - $w^*.\sigma_{H,max}$ diagram

7 CONCLUSIONS

A combined experimental - Crossland modelling approach is developed to rationalise the crack nucleation risk induced by fretting fatigue loadings. It shows that due to the very important stress gradient imposed by the contact stressing, a local "hot spot" fatigue stress analysis is not suitable. The common non local "weight" function strategy provides stable and reliable predictions but it is restricted to analytical stress analysis. Indeed, a comparison between Finite Element computations and a reference analytical stress description shows that if the subsurface stresses are well predicted by FEM, it is not the case for the surface stresses. Such a mis-estimation decays the crack nucleation prediction and limits the application of FEA predictions. To palliate such limitation a combined "critical distance – weight function approach" is introduced. This original subsurface stress, non local formulation, provides stable and reliable predictions.

8 REFERENCES

[1] R.B. Waterhouse, Fretting Fatigue, Applied Science publishers, 1981.

[2] Y. Mutoh, M. Jayaprakash, Tangential stress range–compressive stress range diagram for fretting fatigue design curve, Tribology International, 44, 1394–1399, 2011.

[3] M.P. Szolwinski, T.N. Farris, Mechanics of fretting crack formation, Wear, 198, 93-107, 1996.

[4] S. Fouvry, Ph. Kapsa, L. Vincent, A multiaxial fatigue analysis of fretting contact taking into account the size effect, ASTM STP, 1367, 167-182, 2000.

[5] J.A. Araújo, D. Nowell, The effect of rapidly varying contact stress fields on fretting fatigue, Int. J. Fatigue 24(7), 763-775, 2002.

[6] R. Hojjati-Talemi, M. A. Wahab, Fretting fatigue crack initiation lifetime predictor tool: Using damage mechanics approach, Tribology International, 60, 176-186, 2013.

[7] S. Fouvry, H. Gallien, B. Berthel, From uni- to multi-axial fretting-fatigue crack nucleation: Development of a stress-gradient-dependent critical distance approach, Int. J. Fatigue, 62, 194–209, 2014.

[8] I.V. Papadopoulos, V. P. Panoskaltsis, Invariant formulation of a gradient dependant multiaxial high-cycle fatigue criterion, Eng Fract Mech, 55(4), 513–28, 1996.

[9] R. Amargier, S. Fouvry, L. Chambon, C. Schwob, C. Poupon. Stress gradient effect on crack initiation in fretting using a multiaxial fatigue framework, Int J. Fatigue, 32(12), 1904–1912, 2010.

[10] L.J. Fellows, D. Nowell, DA. Hills, On the initiation of fretting fatigue cracks, Wear, 205, 120–9, 1997.

[11] KL. Johnson, Contact Mechanics, Cambridge University Press, 1985.

[12] D. Nowell, D.A. Hills, Mechanics of fretting fatigue tests, Int. J. Mech. Sci., 29(5), 355-365, 1987.

[13] S. Heredia, S. Fouvry, B. Berthel, E. Greco, Introduction of a ‘‘principal stress–weight function’’ approach to predict the crack nucleation risk under fretting fatigue, Int. J. Fatigue, 61, 191–201, 2014.

[14] B. Crossland, Proc. of the Inter. Conf. on Fatigue of Metals, Inst. of Mech. Eng., Lond., 138-149, 1956.

[15] D.H. Luu, M.H. Maitournam, Q.S. Nguyen, Formulation of gradient multiaxial fatigue criteria, Int. J. Fatigue, 61, 170–183, 2014.

Proceedings of the 3rd International Conference on
Fracture Fatigue and Wear, pp. 239-245, 2014

INVESTIGATION OF RESIDUAL STRESS EFFECT ON FATIGUE CRACK INITIATION FOR 2024 T351 AL-ALLOY

M. Benachour[1], N. Benachour[1] and M. Benguediab[2]

[1]Tlemcen University, Laboratory of Mechanical Systems and Materials "IS2M", Faculty of Technology, Mechanical Engineering, BP 230 Tlemcen - 13000, Algeria
[2]Sidi Bel Abbes University, Laboratory of Materials and Reactive Systems "LMSR", Mechanical Engineering Department, Sidi Bel Abbes – 22000, Algeria

Abstract: The effect of residual stresses resulting from plastic beam bending technique on fatigue crack growth initiation was studied on 2024 aluminium alloy. The residual stresses were calculated analytically or numerically using finite element method. In the analytical calculation linear work-hardening behaviour were assumed. In the numerical calculations constitutive equations including isotropic work-hardening was introduced. Effect of applied bending load levels upper elastic behaviour generating residual stress field was studied on fatigue crack initiation. Fatigue initiation life was affected by compressive residual stress at small notch. Fatigue life was increased with increasing in levels of compressive residual stress at notch. Rubbed zone near notch was shown; this is due to compressive residual stress.

Keywords: compressive residual stress; fatigue crack initiation; aluminium alloy

1 INTRODUCTION

Research on the fatigue behaviour has shown that the life of a structure is divided into three stages [1]: fatigue crack initiation, stable crack propagation and unstable crack propagation. The most common site for fatigue crack initiation in structural components is at stress concentrators such as notches, holes or fillets. In order to increase fatigue resistance, compressive residual stresses are often purposely introduced around these concentrators through processes such as expanded hole [2,3], shot-peening [4,5], tensile pre-straining [6-9]. Given the importance of residual stresses, proper characterization of their values and effects on fatigue crack initiation and fatigue crack growth are vital. To assess the effects of notches on the behaviour of structures, the prediction of fatigue strength compared to the challenges of design and safety is relevant. Fatigue life prediction of structures with discontinuities has been extensively studied [10,11]. Fatigue crack initiation life has been estimated by many authors [12,13] when different approaches will be used, which is based on nominal stresses, stress concentration factor and local stress-strain concepts. Others researchers employed the equivalent strain-energy density method to predict fatigue crack initiation [11,14]. The cited works assumed that crack propagation part of fatigue life is small comparatively to the fatigue initiation life. Generally fatigue life of materials and structures depends on several parameters. Especially in initiation phase, fatigue life is linked strongly to metallurgical, geometrical and loading parameters. Compressive residuals stresses at notch offer beneficial effect on fatigue behaviour and consequently delay the initiation and propagation of fatigue crack [8,15]. The investigation conducted by Taghizadeh et al. [16] on 2024 T3 aluminium alloy plate shown that the initiation life in hole was affected by residuals stress dues to expansion process. The initiation life in expanded is important at low level of applied cyclic loading compared to the same plate without expansion. Contrarily at high level of applied cyclic loading, the initiation life is not affected. The effect of residuals stresses on fatigue crack initiation of X65 pipeline steel was studied by Mézière et al. [7]. These stresses were generated by mechanical preload (pre-straining process) in four-point bending. As shown in the studied endurance domain, the compressive residuals stresses lead to increase the initiation number of cycle. In contrast, the residual tensile stress does not change significantly the endurance curve compared to samples without residual stresses. The increasing in compressive residual stress levels lead to increase the fatigue initiation life [17].

Recently, in the investigation of Ranganathan et al. [18], crack initiation phase has been considered in the estimation of total fatigue life when short crack growth approach was used. The results on fatigue crack initiation of 2024 T351 aluminium alloy show an increasing in fatigue life initiation with increasing stress ratio and maximum remote stress in measured and predicted results. On other material (aluminium alloy 7449 T7951), the fatigue crack growth analysis show that for the test at 120 MPa the crack initiation period seems to be significant (30% of total life) comparatively to the test at 140 MPa when the initiation period is

negligible. In study conducted by Almer et al. [19], fatigue crack initiation behaviour was affected strongly by macro residual stress dues to pres-straining and press-fitting operations. The fraction of fatigue life taken up by initiation, N_i/N_f, was at least 0.44 in the specimens tested, and this ratio increased with decreasing applied stress amplitude. In this investigation, residual stresses resulting from plastic beam bending technique on fatigue crack growth initiation was investigated on 2024 T351 aluminium alloy. The crack was initiated through compressive residual stress face and tensile residual stress.

2 EXPERIMENTAL PROCEDURE

The fatigue experimentation was performed on 2024 T351 Al-alloy, widely used for aeronautical applications. This alloy was provided by the ALCAN Company of production of aluminium alloys to the profit of the Centre of Materials, School of Mines Paris, France. The chemical composition of different materials used in this study is listed in Table 1. The mechanical properties at room temperature are shown in Table 2 and the tensile stress-strain curve along L direction of studied material is shown in Fig. 1. The microstructure of aluminium alloy 2024 T351, respectively in (T-S) and (L-S) directions, is presented in other author's paper [20] where the size of the pancake shaped grains is significant (620 x 270 x 350 μm^3).

Table 1 Chemical composition of Aluminium 2024 T351

Si	Fe	Cu	Mn	Mg	Cr	Zn	Ti	Ni	Pb	Al
0.105	0.159	3.97	0.449	1.5	0.05	0.109	0.018	0.02	.056	Bal

Table 2 Chemical composition of Aluminium 2024 T351

E(GPa)	$\sigma_{Y0.2}$	UTS (MPa)	A%
74	363	477	12.5

Bars with a rectangular section 20x15 mm^2 were preloaded under four points bending as shown in Fig. 2. This preloading introduced residual stresses which can be either tensile or compressive depending on the position of the fatigue crack on the free surfaces. The specimens with tensile/compressive residual stresses are named TRS and CRS. A small notch with 45 degrees was machined in these bars as shown in Fig. 2. The depth of this notch was kept as small as possible to limit the importance of residual stresses redistribution after machining. These specimens were finally tested under fatigue conditions with a frequency of 10 Hz and a sinusoidal wave signal.

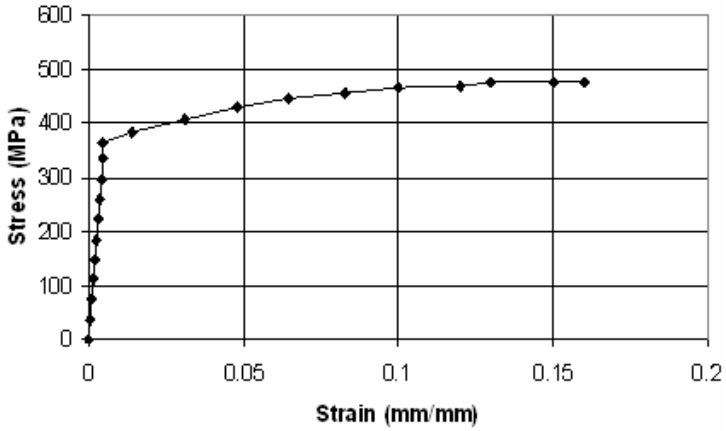

Fig. 1 Stress-Strain material properties for 2024 T351

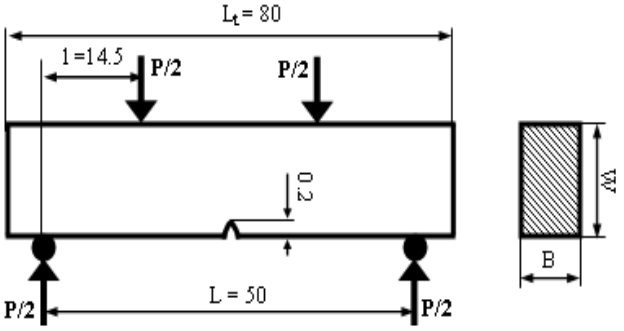

Fig. 2 V-notch specimen in four points bending test

3 EVALUATION OF RESIDUAL STRESSES IN FOUR POINTS BEND SPECIMENS

In order to assess the level of residual stresses introduced in four point bend specimens the applied preload was determined analytically and numerically. In analytical case, the distribution of residual stresses, σ_r, across the section is given by the following expressions which are valid only for perfectly plastic material:

$$\begin{cases} -h_e/2 \le y \le h_e/2 & \sigma_r = \sigma_Y . \dfrac{y}{h_e/2} - \dfrac{12M_a}{B(h)^3}.y \\ y \le h_e/2 & \sigma_r = \sigma_Y - \dfrac{12M_a}{B(h)^3}.y \\ y \ge h_e/2 & \sigma_r = -\sigma_Y - \dfrac{12M_a}{B(h)^3}.y \end{cases} \quad (1)$$

where “y” and “h_e” define respectively the variation through the height of specimen (W=h) and the size of the elastic core (see Figure 4 for example at α=1.40 PP)

In the present study three levels of residual stresses, denoted by the values of α parameter were investigated (Table 3). These values for α parameter were calculated using the engineering yield strength, $\sigma_{Y0.2}$ of studied material. These analytical expressions are based on the assumption that the bending bars are subjected to a pure moment, which is not necessary the case because they are not infinitely slender. This is the reason why the residual stresses were also calculated using finite element method.

Table 3 Applied preload for introducing residual stress in bending beams for 2024 T351 AL-alloy (σ_Y and σ_p indicate respectively the yield stress (MPa) and plastic stress above the yield stress)

Coefficient of preload α $\alpha = \sigma_p / \sigma_Y$	Applied preload (KN)
1.15	57.59
1.25	62.58
1.40	70.09

In numerical calculation of residual stress, finite element (FE) simulations were performed using the FE software Zebulon [21]. A fully implicit integration scheme was used to integrate the material constitutive equations. These FE calculations were performed using quadratic elements with reduced integration (8 nodes/4 Gauss points). The FE mesh used to model the specimens is given in Fig. 3, where only one half of the specimens is shown. FE simulations were carried out using 2D plane strain elements. The plastic behaviour of studied material was described using isotropic hardening based on classical potential constitutive model [22]. The isotropic work-hardening function is expressed as:

$$R_p = R_0 + Q_p\left(1 - e^{-b_p.p}\right) \quad (2)$$

where p is the accumulated plastic strain, R_0, Q_p and b_p are model’s coefficients.

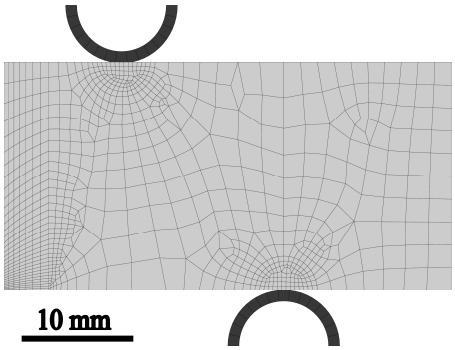

Fig. 3 Half-symmetry finite element model for 2024 Al alloy

In this material the constitutive equation was assumed to be isotropic. This constitutive equation involves three coefficients which are reported in Table 4.

Table 4 Parameters identified for elastic behaviour and work hardening of 2024 T351 Al-alloy

E (GPa)	ν	R_0 (MPa)	Qp	bp
74	0.33	336	270	10.55

The results of FE calculations of Al-alloy are reported in Fig. 4. Distribution of residual stress shown a strong asymmetry between the tensile and compressive residual stresses, which indicates that this specimen geometry is far from being subjected to a pure bending moment. The main explanation for this situation is in the fact that the aluminium alloy beam is not sufficiently slender. The comparison with the perfectly plastic (PP) model shown in Fig. 4 indicates that for a given load (α=1.40) the analytical results lead to values close to those of the FE simulation on the side with compressive residual stresses. It can be concluded that significant differences in the residual stresses distribution have been evidenced between analytical and numerical calculation, in particular in 2024 aluminium alloy.

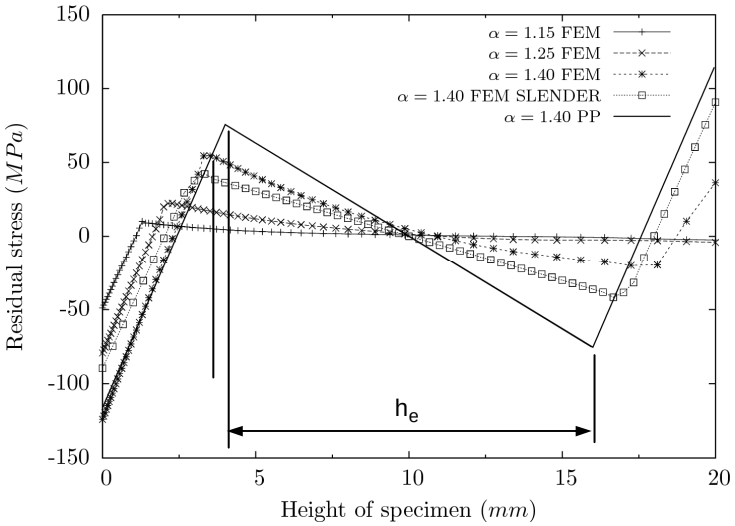

Fig. 4 Distribution of residual stress as a function of the preload coefficient, α, for 2024 T351 Al-alloy

4 EXPERIMENTAL RESULTS AND DISCUSSION

For the three levels of residual stress (Table 3), crack growth was initiated in a compressive residual stress field. Additionally, the crack growth was initiated on the tensile residual stress side at 1.25 of coefficients preload. This tensile stress is neglected, as shown previously (Fig. 4). The fatigue tests were carried out at a stress ratio R=0.1 and under a maximum load P_{max}=26.6 KN.

Figure 5 shows the effect of residual stress levels induced by preload on fatigue crack initiation at crack of 0.2 mm in length. An increasing in fatigue life initiation is shown with increasing of magnitude of

compressive residual stress at free surface. The maximum compressive residual stresses were about -125 and MPa for α=1.40; -80 MPa for α=1.25 and -50 MPa for α=1.15. It should be kept in mind that the fatigue life initiation obtained on TRS1.25 specimen can be considered as that of the as-received material (WRS : without residual stress) because of the absence of any significant tensile residual stresses in this specimen, as shown in Fig. 4. Preload level "α" is considered equal to "1" reported on Fig. 5.

Correlation in the evolution of initiation life is given by 2nd order of polynomial function. The fatigue life initiation under maximum compressive residual stress field (α=1.40) is approximately twice times larger than the fatigue life of lower compressive residual stress field (α=1.15) and is third times larger than the fatigue life under tensile residual stress field or WRS. At the same preload level (α=1.25), the fatigue life under compressive residual stress is 2.5 times larger than the fatigue life without residual stress (small tensile stress at notch). Table 5 presents the ratio of the initiation life N_i at 0.2 mm of crack to the total fatigue life N_f. CRS and TRS (WRS) denote respectively the compressive residual stress and the tensile residual stress. The analysis of the obtained results showed that initiation phase varies from 40% to 50% of total life under different levels of compressive residual stress. The fatigue fracture surfaces of 2024 T351 aluminium alloy specimens were examined by scanning electron microscopy (SEM). The fractured surfaces indicate rubbing effect near the notch and in initiation zone as illustrated in Fig. 6.

Table 5 Ratio of initiation to total fatigue life under residual stress field

Coefficient of preload α	Fatigue life initiation "N_i"	Total fatigue life "N_f"	Ratio "N_f/ N_i "
1.15 (CRS)	49500	100800	0.49
1.25 (CRS)	74570	148600	0.50
1.25 (TRS)	29364	64200	0.46
1.40 (CRS)	86600	219250	0.40

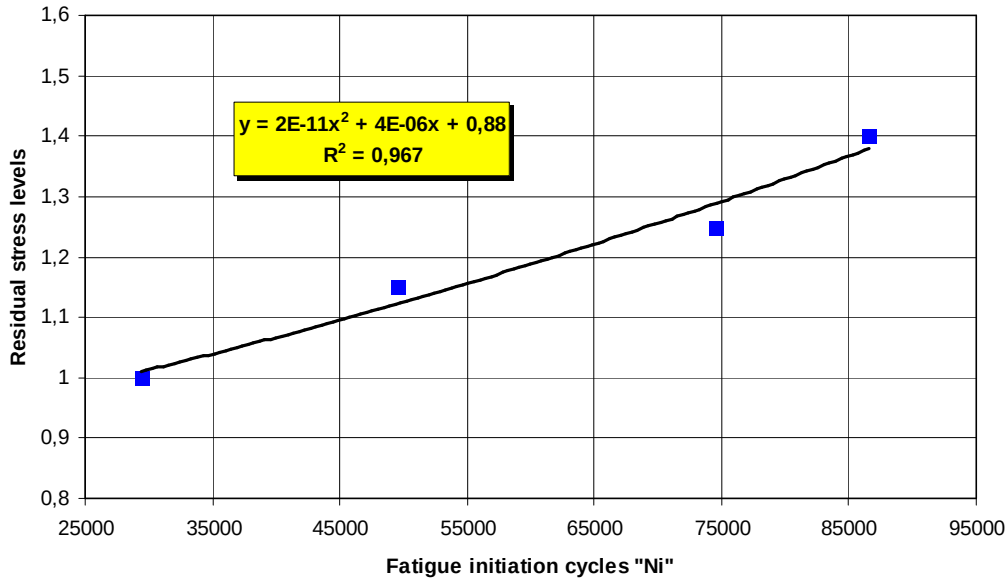

Fig. 5 Evolution of initiation life under compressive residual stress at notch for 2024 T351 Al-alloy

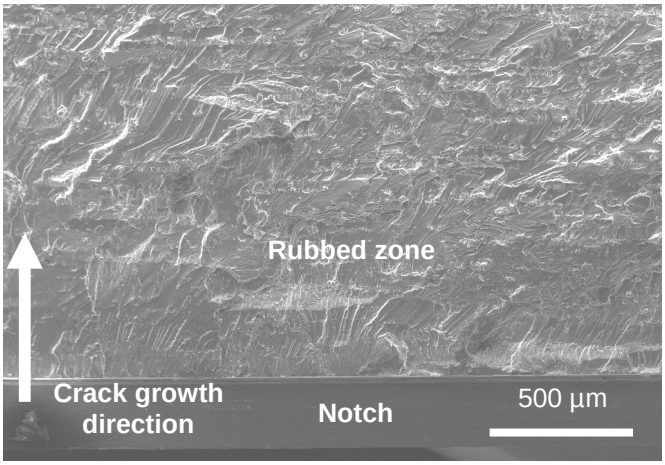

Fig. 6 Fracture surface through compressive residual stress (α=1.15)

5 CONCLUSIONS

The goal of this work is to study the effect of residual stress on fatigue initiation life in 2024 T3541 Al-alloy using four point bend specimens. Residual stress along path of crack was induced experimentally by plastic preload process. Evolution of residual stress fields under different levels of preload was predicted by finite element analysis considering isotropic hardening behaviour to this material. From the experimental results on fatigue initiation of crack, the following conclusions can be drawn:

- Level of compressive residual stress at free surface of specimen depends on applied preload.
- Numerical results has shown that the studied geometry specimen reveal that no significant tensile residual stress was produced in the other free surface (i.e. for α: 1.15 and 1.25)
- Fatigue crack initiation life is influenced by the level of compressive residual stress at notch. Increasing in compressive residual stress at notch increase the fatigue initiation life and consequently the fatigue crack growth life.
- Initiation phase varies from 40% to 50% of the total fatigue life considering different residual stress fields.
- At the same level of plastic preload, Fatigue initiation life through compressive residual stress at notch is about 2.55 times to fatigue initiation life through specimen without residual stress (neglected tensile residual stress).
- Fractured surface in compressive residual stress zone presents rubbing effect.

6 ACKNOWLEDGEMENTS

The authors gratefully acknowledge the technical support from the Centre des Matériaux – Ecole des Mines de Paris. The authors also with to express their gratitude to Professor emeritus A. Pineau and Dr. Y. Madi for fruitful discussions on residual stress effects and assistance in fatigue crack growth tests.

7 REFERENCES

[1] G. Glinka, Residual stress in fatigue and fracture: Theoretical analyses and experiments. In Niku-Lari A., Editor, Advances in Surfaces Treatments, Residual stresses, 4, 413-454, Pergamon Press, 1987.

[2] Z. Semari, A. Aid, A. Benhamena, A. Amrouche, M. Benguediab, A. Sadok, N. Benseddiq, Effect of residual stresses induced by cold expansion on the crack growth in 6082 aluminium alloy. Engng Fract. Mech., 99, 159-168, 2013.

[3] H.D. Gopalakrishna, H.N. Narasimha Murthy, M. Krishna, M.S. Vinod, A.V. Suresh, Cold expansion of holes and resulting fatigue life enhancement and residual stresses in Al 2024 T3 alloy: An experimental study, Engineering Failure Analysis, 17, 361-368, 2010

[4] C.A. Rodopoulos, S.A. Curtis, E.R. de los Rios, J. SolisRomero, Optimisation of the fatigue resistance of 2024-T351 aluminium alloys by controlled shot peening: methodology, results and analysis, Int. J. Fatigue, 26, 849-856, 2004.

[5] M. Benedetti, V. Fontanari, C. Santus, M. Bandini, Notch fatigue behaviour of shot peened high-strength aluminium alloys: Experiments and predictions using a critical distance method, Int. J. Fatigue, 32, 1600-1611, 2010

[6] J.E. LaRue, S.R. Daniewicz. Predicting the effect of residual stress on fatigue crack growth. Int. J. Fatigue, 29, 508–515, 2007.

[7] Y. Mézière, R. Champavère, R. Batisse, C. Mokhdani, A. Pineau, Fatigue crack initiation from notches in feritic-pearlitic steels. European Conference of Fracture: ECF 11- Mechanisms and Mechanics of Damage and Failure, Vol. II, 1996, Poitiers, France.

[8] K.W. Jones, M.L. Dunn, Fatigue crack growth through a residual stress field introduced by plastic beam bending, Fat. Fract. Engng Mat. Struct., 31, 863-875, 2008.

[9] M. Benachour, M. Benguediab, N. Benachour, Notch fatigue crack initiation and propagation life under constant amplitude loading through residual stress field. Advanced Materials Research, 682, 17-24, 2013.

[10] M. Truchon, Application of Low-Cycle Fatigue Test Results to Crack Initiation from Notches, Low-Cycle Fatigue and Life Prediction, ASTM STP 770, C. Amzallag, B. N. Leis, and P. Rabbe, (Eds.), American Society for Testing and Materials, pp. 254-268, 1982.

[11] G. Glinka, A notch stress-strain analysis approach to fracture crack growth. Engng. Fract. Mech., 21(2), 245-261, 1985.

[12] D.F. Socie, Fatigue-life prediction using local stress-strain concept, Experimental Mechanics, 17, 50-56, 1977.

[13] X. Zheng, On some basic problems of fatigue research in engineering, Int. J. Fatigue, 23, 751-66, 2001.

[14] Z. Khan, A Rauf, A. M. Younas, Prediction of fatigue crack propagation life in notched members under variable amplitude loading, Journal of Materials Engineering and Performance, 6(3), 365-373, 1997.

[15] D.L. Ball, D.R. Lowry, Fatigue and Fracture of Engineering Materials and Structures 21, 17-5, 1998.

[16] Hadi Taghizadeh, Tajbakhsh Navid Chakherlou, Afshin Babaei Aghdam, Prediction of fatigue life in cold expanded Al-alloy 2024-T3 plates used in double shear lap joints, Journal of Mechanical Science and Technology, 27(5), 1415-1425, 2013.

[17] M. Benachour, M. Dahaoui, N. Benachour, A. Cheikh, M. Benguediab. Effect of levels of residual stress at notch on fatigue crack growth. ICF13, June 16-21, 2013, Beijing, China

[18] N. Ranganathan, H. Aldroe, F. Lacroix, F. Chalon, R. Leroy, A. Tougui. Fatigue crack initiation at a notch, Int. J. Fatigue, 33, 492-499, 2011.

[19] J.D. Almer, J.B. Cohen, B. Moran, The effects of residual macrostresses and microstresses on fatigue crack initiation, Materials Science and Engineering A, 284, 268-279, 2000.

[20] M. Benachour, A. Hadjoui, M. Benguediab , N. Benachour, Effect of the amplitude loading on fatigue crack growth, Procedia Engineering, 2, 121-127, 2010.

[21] J. Besson, R. Foerch, Large scale object–oriented finite element code design, Comp. Meth. Appl. Mech. Engng, 142, 165–187, 1997.

[22] J. Lemaitre, J. Chaboche, Mechanics of solid materials, Cambridge University Press, UK, 1985.

Proceedings of the 3rd International Conference on
Fracture Fatigue and Wear, pp. 246-249, 2014

ON THE NEED OF THE WAVELET ANALYSIS FOR FATIGUE CONDITION MONITORING

N. Ismail[1], M.F.M. Yusof[1], C.K.E. Nizwan[1] and S. Abdullah[2]

[1]Faculty of Mechanical Engineering, Universiti Malaysia Pahang, 26600 Pekan, Pahang, Malaysia
[2]Department of Mechanical and Materials Engineering, Faculty of Engineering and Built Environment, Universiti Kebangsaan Malaysia, 43600 Bangi, Selangor, Malaysia

Abstract: Wavelet analysis has attracted attention for its ability to analyse rapidly changing transient signals. Based on that capability, it was then used in this study to detect high amplitude of strain signal of the coil spring. The signals were recorded at two different road profiles that are paved road and unpaved road. Wavelet analysis was then performed in order to obtain wavelet transform representation for each of the road. Fatigue damage assessment will be used to verify this finding. The obtained result shows that the time of peaks occurrence in wavelet transform representation is in line with the time of the high amplitude strain occurrence. It is true for all types of signal. It is also verified with the value of the fatigue damage. It is noticed that the value of the fatigue damage is higher at the similar time frame. The finding indicates that the wavelet analysis can be used as an alternative method for the fatigue condition monitoring cases.

Keywords: Strain signal; high amplitude; wavelet; fatigue damage; condition monitoring

1 INTRODUCTION

Currently, there are many conventional methods for faults identifying and diagnosis. Based on the representation of a signal during its processing, a method can be referred to as time-domain or frequency-domain [1].

Time domain methods are usually sensitive to impulsive oscillations. Characteristics arising from the defects being monitored, also known as features, of the raw time signal can be extracted from a machine. Typical features are the r.m.s. value, peak value, crest factor, kurtosis and the shape, size and orientation of a bearing locus derived from orbital analysis [2]. These features, once established to be related to the defect being monitored, often yield satisfactory results. However, if the signal generation mechanism is complex, time-domain methods are often not refined enough.

Frequency domain methods assume that the signal being analyzed has components that are periodic. Thus, a defect produces a periodic signal at the characteristic defect frequency. Examples of the frequency-domain methods include spectrum analysis, cepstrum analysis, high frequency resonance technique (HFRT) and holospectrum [3]. Among them, spectrum analysis seems to dominate the fault diagnosis scene. The main limitation of spectrum analysis is that although a local transient will contribute towards the overall frequency spectrum, its location on the time axis is lost. There is no way of knowing whether a particular frequency component exists throughout the life of the time signal or during just one or a few selected periods. Unfortunately, many monitoring situations demand knowledge of not just the frequency composition of a transient but also its time of occurrence [4].For instance, the coil spring will generates a transient signal when it is driven over a pithole or bump compared to the smooth surfaces. That situation will be detected in the measured time domain signal.

The continuous wavelet transform (CWT), a joint time- and frequency-domain technique, is proposed in this paper. CWT is capable of indicating abrupt changes in structure or system conditions [5]. In addition, it can give a better representation of the signal than conventional methods, providing fuller information on the machine operating condition. CWT is used here to produce a 3-D image from the measured signal.

CWT of a time series is defined as [6]

$$F_{\Psi}(a,b)=\frac{1}{\sqrt{a}}\int_{-\infty}^{\infty} f(t)\Psi\left(\frac{t-b}{a}\right)dt \qquad (1)$$

The quantity $\Psi_{a,b}(t)=\frac{1}{\sqrt{a}}\Psi\left(\frac{t-b}{a}\right)$ is referred to as the wavelet function. The position variable *b* shifts the wavelet function along the time axis *t* of *f(t)*while the scale variable *a* expands or compresses the wavelet function $\Psi_{a,b}(t)$. Compared to Fourier transform, the scale variable *a* is equivalent to the inverse of the frequency. The definition also suggests that $F_{\Psi}(a,b)$ is the correlation coefficient between the wavelet function $\Psi_{a,b}(t)$ and the time signal *f(t)* at the scale *a* and position *b* of $\Psi_{a,b}(t)$.

2 METHODOLOGY

The continuous wavelet transform was applied to the strain signals from two different road profiles that are paved and unpaved road. Samples of these signals are shown in Fig. 1a and 1b, respectively. Different types of road profile give different strain amplitude to the coil spring. Compared to unpaved road, paved road have smoother road surfaces. Thus, unpaved road exhibit higher amplitude rather than paved road. It is measured by using 1mm size of strain gauge which is fixed at a coil spring (refer to Fig 2). The strain signal was recorded in 60 seconds length and it was sampled at 500 Hz. Then the analysis was preceded with fatigue damage analysis in order to validate the obtained result from the wavelet analysis. This analysis was used the similar input signal for wavelet analysis.

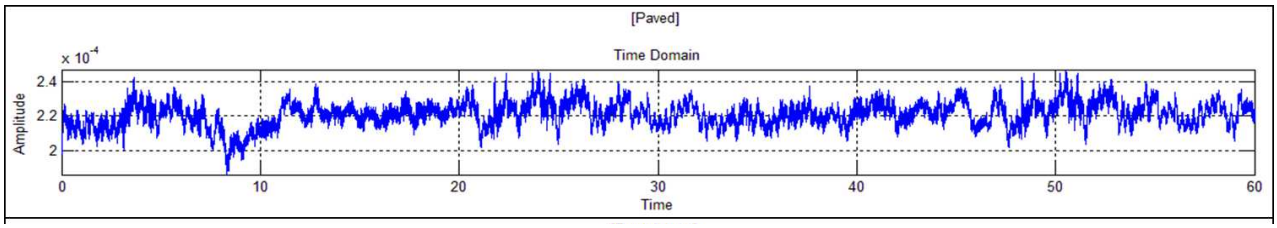

(a)

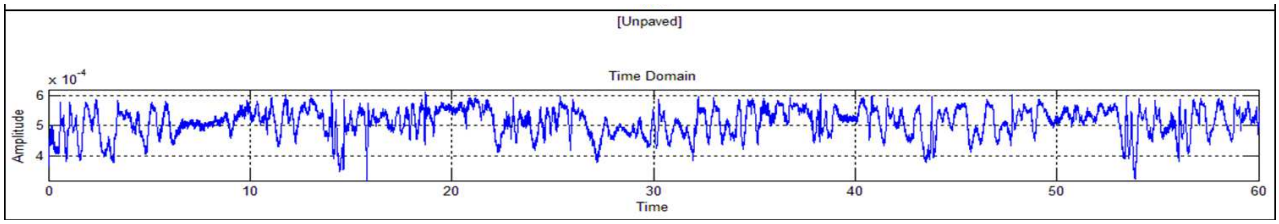

(b)

Fig. 1 Samples of wavelet transform signals

Fig. 2 1 mm size of strain gauge was used to record the strain signal

3 RESULT AND DISCUSSIONS

The measured strain signals were then analysed using continuous wavelet transform (CWT). The wavelet transform representation for unpaved road can be seen in Fig. 3b. It shows that the transient or high amplitude event of the strain signal can be detected using wavelet analysis. Based on Fig. 3a, the signal contains high amplitude approximately at 14s, 19s, 54s and 56s. These high amplitudes were also detected in the wavelet analysis at the similar time frame occurrence. The values of the frequency for these high

amplitudes were also provided. It seems that high amplitudes occur at frequency ranges from 40Hz to 90Hz. This indicates that the wavelet analysis is a good tool to monitor the condition of the structure due to fatigue failure since high amplitude strain will contribute to the fatigue damage.

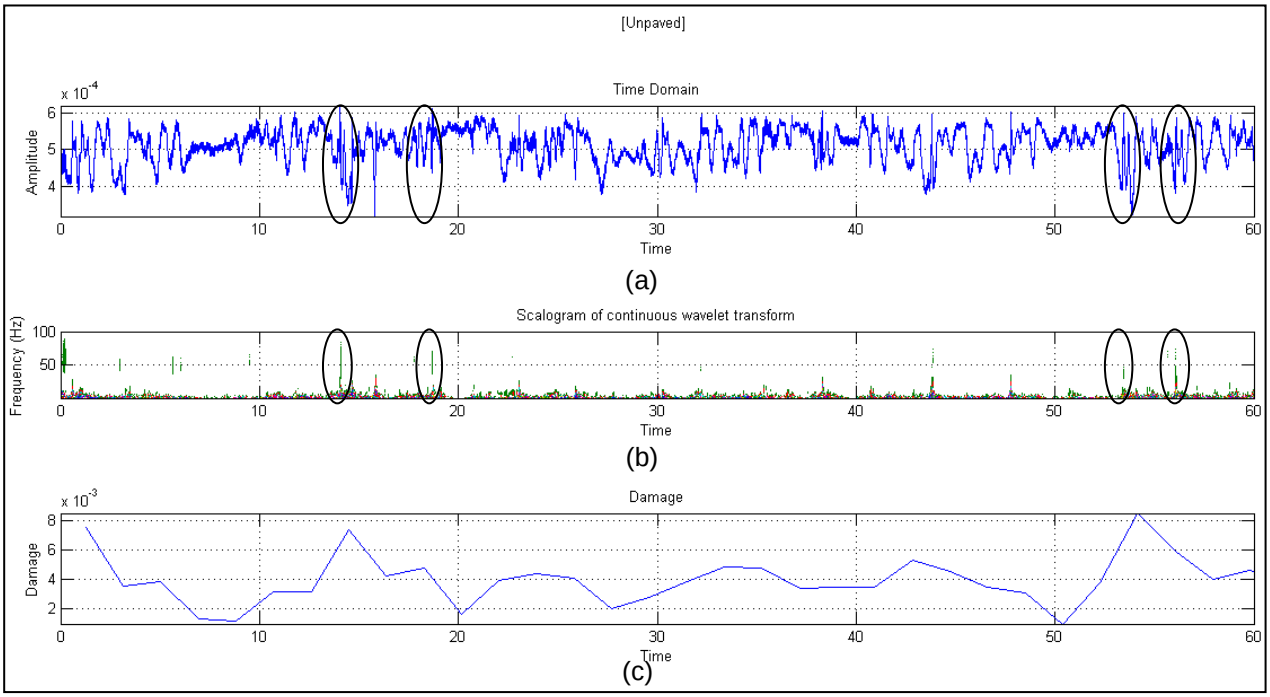

Fig. 3 a) Time domain signal for unpaved road, b) wavelet transform representation and c) fatigue damage value

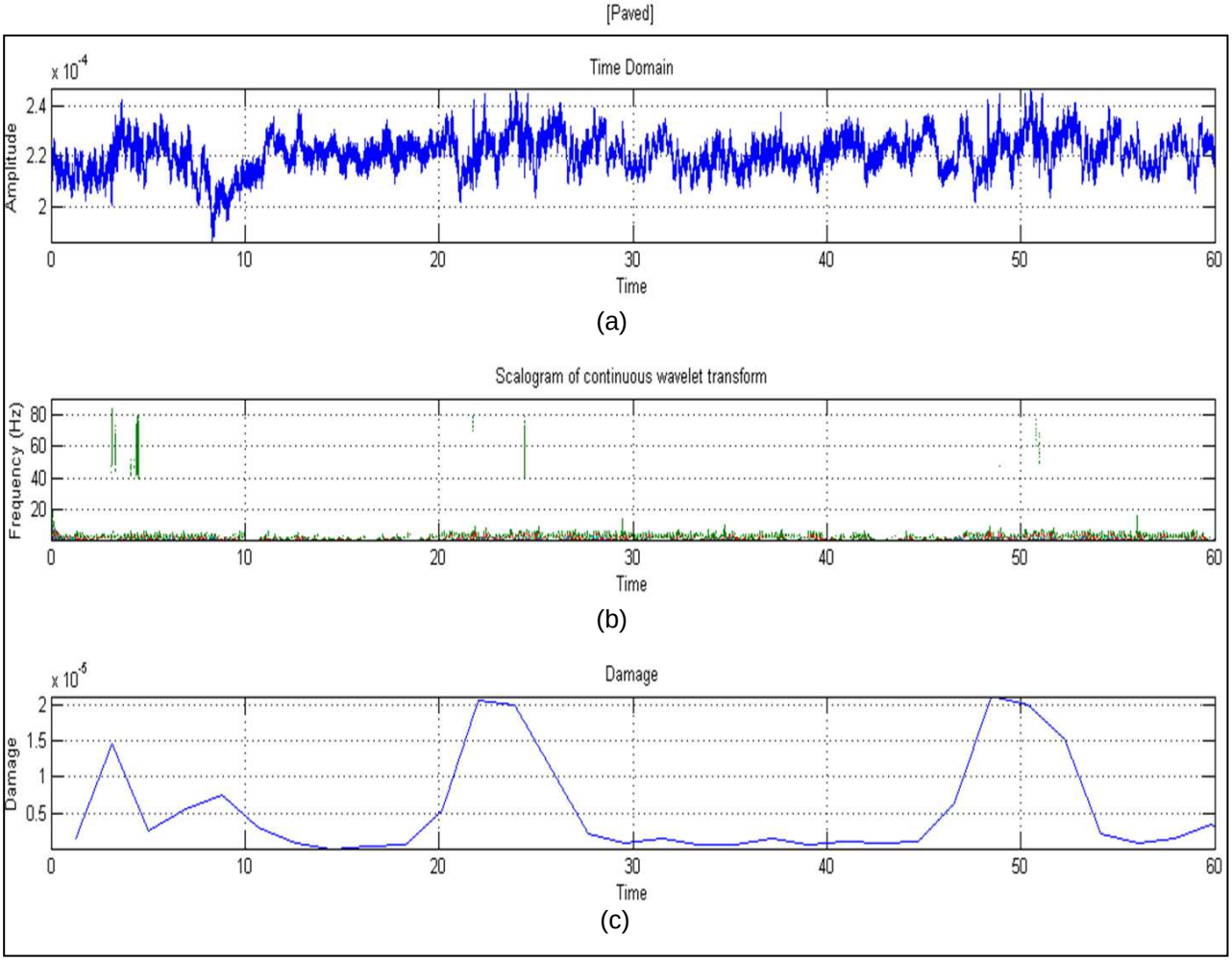

Fig. 4 a) Time domain signal for paved road, b) wavelet transform representation and c) fatigue damage value

Fatigue damage assessment has been performed in order to proof the result obtained from the wavelet analysis. The fatigue damage values were plotted against time. Based on Fig. 3c, the fatigue damage values were noticed going higher at the higher amplitude value that is $7.5x10^{-4}$ at 14s recorded time. The same case goes with 19s, 54s and 56s. They exhibit higher fatigue damage values compared to the other time occurrence. Another example of the analysis can be referred to Fig. 4 for paved road. The time occurrence of the high amplitude also detected in the wavelet transform representation and was proved by the existing of the high value of the fatigue damage.

4 CONCLUSIONS

Continuous wavelet transform was used to detect high amplitude strain signal. It is really important in monitoring condition due to fact the high amplitude strain will contribute to the fatigue damage. Fatigue damage assessment plays a vital role in supporting the obtained results.

5 ACKNOWLEDGEMENTS

The authors would like to express their gratitude to Universiti Malaysia Pahang especially Faculty of Mechanical Engineering through the fund of RDU130320, for supporting this research activity.

6 REFERENCES

[1] T. L. Daniel, A. Yamamoto, Wavelet Analysis: Theory and Applications, Hewlett-Packard Journal, December,1994.

[2] Chih-Chieh Chang, Shiuh-Ming Chand, Hsiao-Yi Huang, Jia-Yi Yeh, Application of The Wavelet Analysis To Strain Energy Damage Detection Method, Journal of Professional Mechanical Engineers, 1(1), 1- 4, 2008.

[3] C. Pachaud, R. Salvetat, C. Fray, Crest factor and kurtosis contributions to identify defects inducing periodical impulsive forces, Mechanical Systems and Signal Processing, 1(6), 903-916, 1997.

[4] T. Kaewkongka, Y. H. Joe Au, R. Rakowski, B. E. Jones, Continuous wavelet transform and neural network for condition monitoring of rotodynamic machinery, IEEE Instrumentation and Measurement, 1962-1966, 2001.

[5] H. Suzuki, T. Kinjo, Y. Hayshi, M. Takemoto, K. Ono, Wavelet transform of acoustic emission signals, Journal of Acoustic Emission, 14(2), 69-84, 1996.

[6] L. Gaul, S. Hurlebaus, Identification of the Impact Location on a Plate using Wavelets, Mechanical Systems and Signal Processing, 12(6), 783-795, 1997.

Proceedings of the 3rd International Conference on
Fracture Fatigue and Wear, pp. 250-256, 2014

FRACTO-METALLOGRAPHIC ANALYSIS OF FATIGUE CRACKING IN COLD DRAWN PEARLITIC STEEL

J. Toribio[1], B. González[1] and J.C. Matos[2]

[1]Department of Materials Engineering, University of Salamanca, E.P.S. Zamora, Spain
[2]Department of Computing Engineering, University of Salamanca, E.P.S. Zamora, Spain

Abstract: In this paper, a fracto-metallographic analysis was performed on the cracked samples of cold drawn pearlitic steel subjected to fatigue tests. Fatigue cracks are transcollonial and exhibit a preference for fracturing pearlitic lamellae, with non-uniform crack opening displacement values, micro-discontinuities, branchings, bifurcations and frequent local deflections that create microstructural roughness. At the micro-level, the cold drawn pearlitic steel exhibits higher micro-roughness than the hot rolled bar (consequence of the drawing process), so that the actual fractured surface in the cold-drawn wire is greater than that in the hot-rolled bar, due to the fact that the crack deflection events are more frequent and with higher angle in the former (the drawn material).

Keywords: cold drawn pearlitic steel; fatigue crack path; local mixed mode; locally multiaxial fatigue; micro-roughness

1 INTRODUCTION

The phenomenon of fatigue crack propagation in engineering materials is usually considered to be an issue requiring a two-parameter approach [1-3] involving at least two driving forces for crack propagation, e.g., ΔK and K_{max}, or ΔK and R. Following Kujawski [4], in the case of ductile materials, the crack driving force for fatigue is dominated by the ΔK parameter whereas in the case of brittle materials it is governed by K_{max}.

The fatigue cracking path is indeed determined by the microstructure. In ferritic-pearlitic steels the crack runs through the ferritic seam in the grain boundaries [5]. In steel with pearlite uniformly distributed in ferrite, the crack path is more tortuous than in those with isolated distribution, with larger angle deflections appearing along the cracking path [6]. In eutectoid steel with fully pearlitic microstructure, the crack has a preference for breaking the pearlite lamellae, producing a transcollonial fracture [7].

In banded ferritic-pearlitic steels, the bands of pearlite (oriented in preferential directions) decreases the rate of fatigue crack growth, since it causes a more tortuous crack path, with a greater number of branchings and deflections, which also have larger angles [8]. The tortuous path induces a frequent crack interlock and the crack branching reduces the local crack tip driving forces for its propagation [8].

The pearlite lamellar orientation in fully pearlitic steels produces a retardation in the crack growth rate because the lamellae behave as serious obstacles for the crack propagation [7,9]. Furthermore, an increase in surface roughness of the fracture is produced [7]. The non-linear crack configuration (crack morphology or crack morphological approach) should be taken into consideration in the framework of the fracture mechanics approach [10]. In addition, variations in crack morphology (degree and periodicity of crack deflections) influence considerably the fatigue crack propagation rates and threshold stress intensity range values [11,12].

2 EXPERIMENTAL PROCEDURE

A progressively drawn pearlitic steel (eutectoid chemical composition: 0.789 %C, 0.698 %Mn, 0.226 %Si, 0.078 %V, 0.071 %Cr, 0.011 %P, 0.005 %S, 0.003 %Al, balanced with Fe) was used in this work: from the hot-rolled bar (not cold drawn at all) to the prestressing steel wire (obtained after seven cold drawing steps and a stress-relieving treatment), as well as the intermediate steps. The fatigue tests were performed by applying a cyclic tensile load on the samples in axial direction. A sinusoidal wave was used with a frequency of 10 Hz and R-ratio ≈ 0. The maximum stress applied during the tests was always lower than the yield strength of the material. The fatigue fracture surfaces and the longitudinal cuts on the crack specimens, after its metallographic preparation and being etched with 4 % Nital (mixture of 4 ml of nitric

acid with 96 ml of ethanol) to reveal microstructure, they were examined by scanning electron microscopy (SEM). In all pictures shown, the crack propagation occurred from left to right.

3 EXPERIMENTAL RESULTS

3.1 Microstructure Analysis

Figs. 1 and 2 show the microstructure of both the hot rolled bar and the cold drawn wire, in their respective transverse and longitudinal sections. The horizontal axis of the micrograph corresponds to the radial direction in the cylinder, while the vertical axis of the micrograph is linked with the annular curvilinear coordinate in the transverse section of the cylinder and associated with the axial curvilinear coordinate in the longitudinal section of the cylinder. With regard to the first microstructural level of the pearlitic colony, it becomes progressively oriented and enlarged with cold drawing, i.e., an increasing drawing-induced slenderization is observed, together with a progressive orientation in the wire axis or cold drawing direction. In the matter of the second microstructural level associated with ferrite/cementite lamellae, they also become progressively oriented and more closely packed with cold drawing, i.e., a decreasing drawing-induced interlamellar spacing of pearlite is observed, together with a progressive orientation in the wire axis or cold drawing direction.

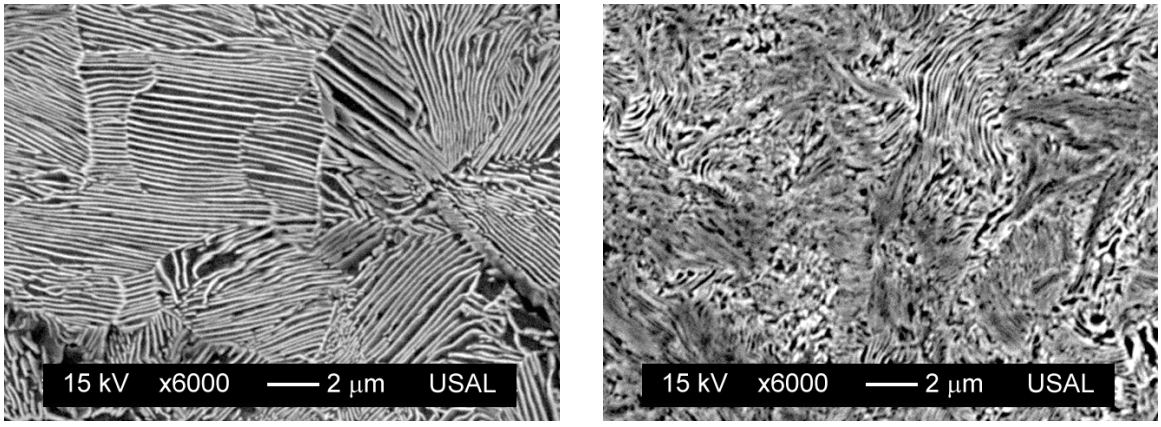

(a) (b)

Fig. 1 Microstructure of steel in transversal section: (a) hot rolled bar and (b) cold drawn wire

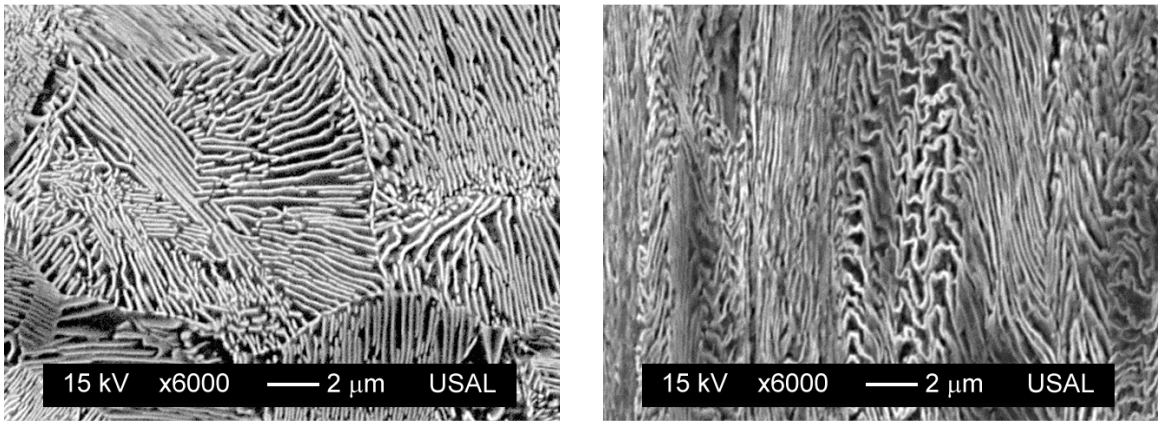

(a) (b)

Fig. 2 Microstructure of steel in longitudinal section: (a) hot rolled bar and (b) cold drawn wire

3.2 Fractographic Analysis

In pearlitic steels, subcritical propagation by fatigue shows fracture in global mode I, so that the crack runs macroscopically along the wire's cross section. At the microscopic level, the fatigue fracture surface shows ductile micro-tearing patterns (Fig. 3) corresponding to highly-localized plastic strains, which show no evidence of striation (characteristic of ductile metals and alloys). In the prestressing steel, the ductile microtears are of smaller size and with curvier geometry than in the hot rolled wire (Figs. 3a and 3b), due to the microstructural changes (mostly in the wire's cross section) produced by the high plastic strain undergone by the heavily cold-drawn steel. On the fatigue surface, microcracks with a perpendicular direction to the

advance of the crack are also observed, whose apparition frequency increases with a higher value for the SIF range Δ*K* or the *R*-ratio (Fig. 3c). The existence of inclusions (sulphides, oxides, silicates…) is also observed on the fatigue surface (Fig. 3d), although in many occasions only their trail is visible.

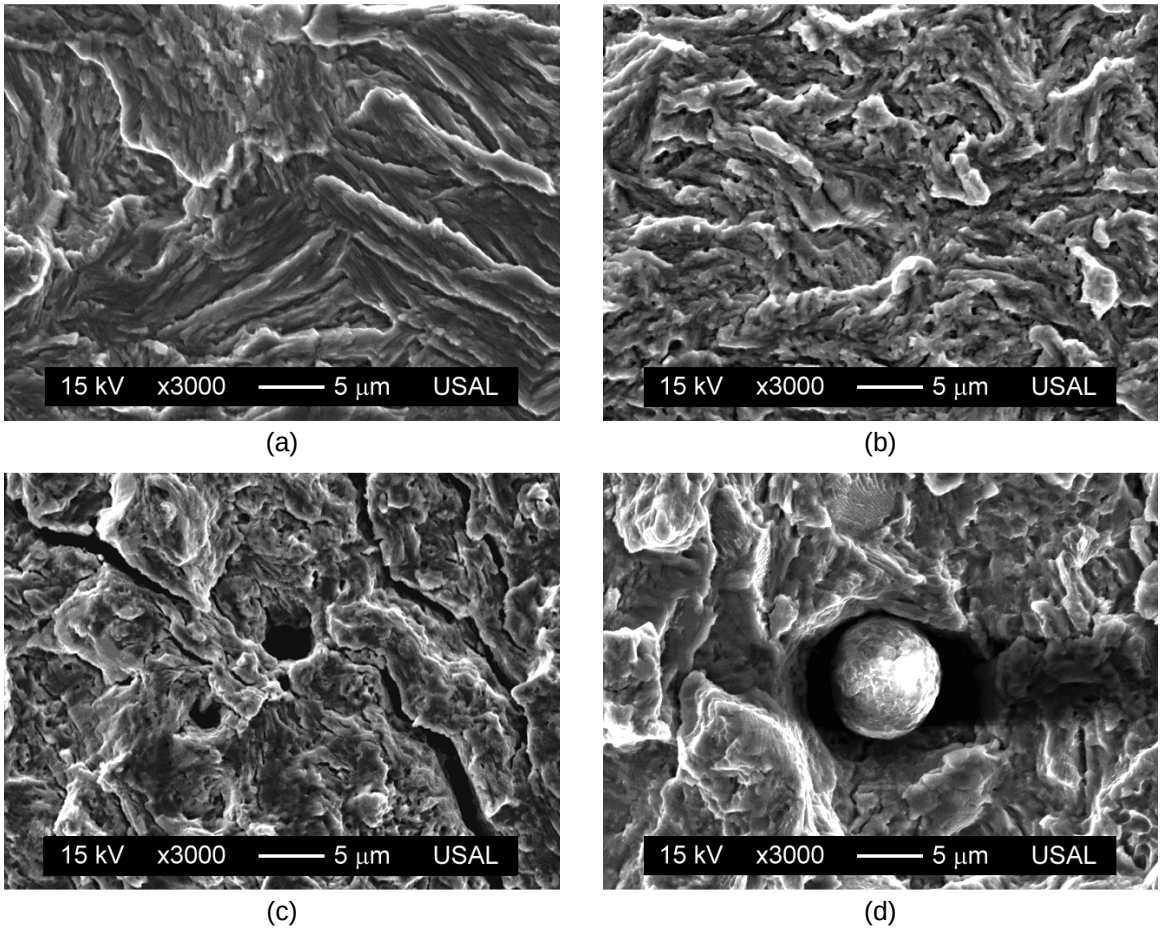

Fig. 3 Fatigue fracture surface: (a) hot rolled bar, (b) cold drawn wire, (c) micro-cracking and (d) particle

Figure 4 shows various longitudinal cuts of the crack path caused by fatigue in the steels studied. This crack is essentially transcollonial and translamellar, thereby tending to cross the pearlite colonies and to break the ferrite/cementite lamellae, showing very localized plastic damage (Fig. 4a). The crack propagation is tortuous, with frequent deflections (Fig. 4b) or changes in the direction of crack advance and evidence of branching (Fig. 4c), mainly bifurcations. Multicracking appears sometimes (see Fig. 4d). These events determine the existence of a heavy, local mixed mode fracture, so that fatigue cracking in steel may be considered locally multiaxial.

Sometimes, crack deflection appears next to a bifurcation, its appearance being more angular in this case. The crack branching shows the directionality of the fatigue advance, and are often in the form of branches on both sides of the macroscopic propagation plane, with an approximate angle between 45º and 90º, so that only one of the branches continues to grow and the other stops. These branches and bifurcations, observed in the longitudinal sections of the crack, correspond to the microcracks that appear on the metal surface fractured by fatigue (Fig. 3c). These phenomena, crack deflection and bifurcation, cause surface micro-roughness and decrease the driving force for fatigue, thereby slowing the fatigue crack advance [6,8].

The fatigue cracks show continuous variations in the crack opening displacement COD, although this opening generally decreases from the crack mouth (origin of crack initiation) to the crack tip (final crack front). Moreover, in some regions the crack shows local microdiscontinuities during its propagation (Fig. 4e). At the microscopic level, in the mixed mode crack advance (mode I + mode II), there are sections in which interlocking is observed [13], which corresponds to crack growth in the axial direction (mode II), resulting in a very small COD, which can even end up touching the fatigue fracture surfaces in a localized manner (Fig. 4f).

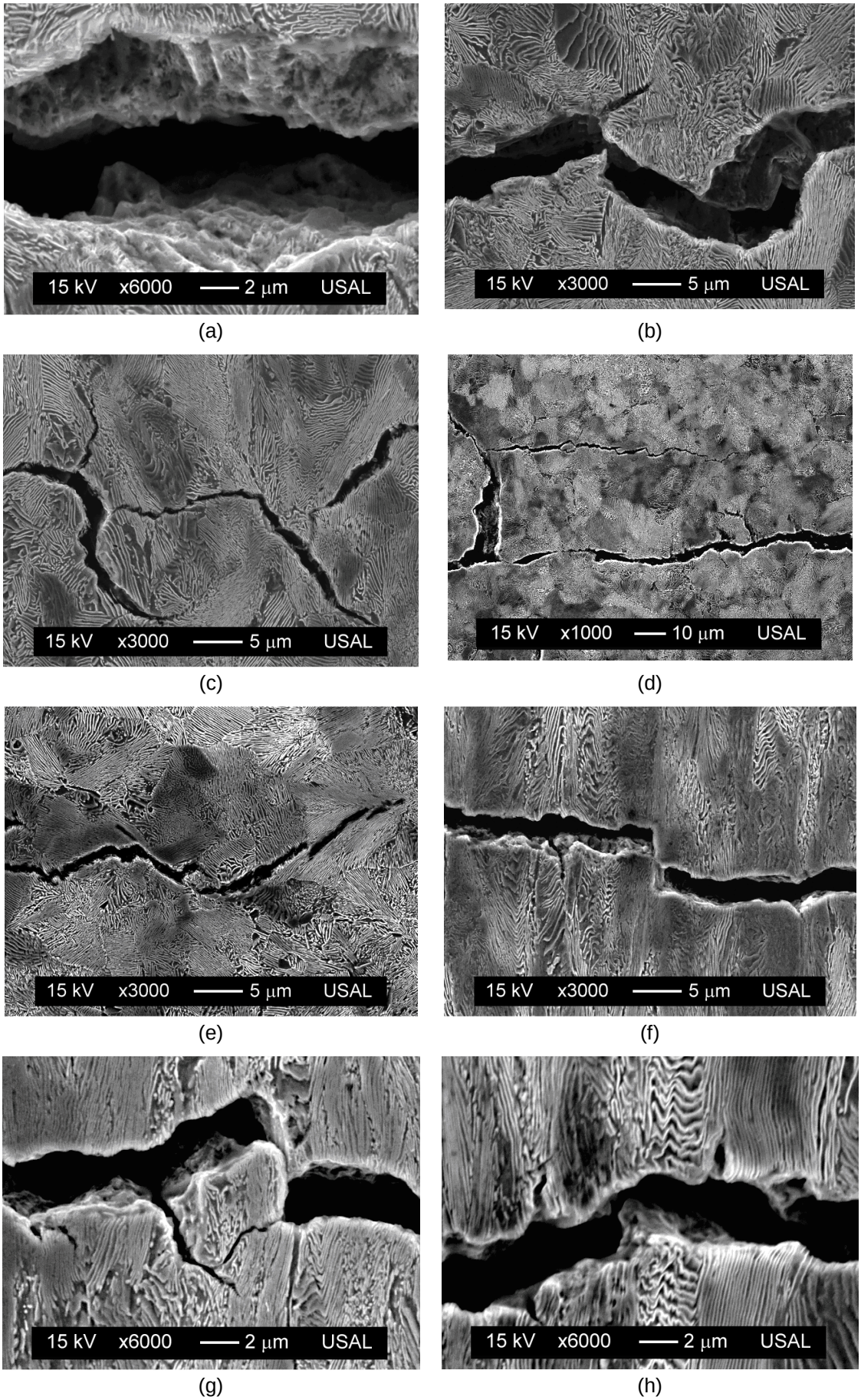

Fig. 4 Cracking paths: (a) micro-damage, (b) deflections, (c) branchings, (d) multi-cracking, (e) micro-discontinuities, (f) interlock, (g) debris particle and (h) pearlite pseudo-colonies

The existence of *debris* (small loose particles of material on the fracture surface arising from the fatigue phenomenon [14], which become detached during the test) was not found, so that this phenomenon, if it takes place, occurs sporadically (Fig. 4g). The presence of pearlite pseudo-colonies in strongly cold-drawn steel (colonies whose pearlite lamellae, oriented in a nearly perpendicular direction in relation to the direction of drawing, having an anomalously high interlamellar spacing and which are wavy and sometimes broken) does not produce fatigue crack deflection (Fig. 4h), unlike that which occurs in the fracture [15] of those steels subjected to a greater number of drawing steps..

4 DISCUSSION

The morphology of the crack path evolution during fatigue was analyzed for both the hot rolled bar and the prestressing steel wire. The fatigue cracks were characterized by means of the average angle (θ) and the average length between deflections (l), observing that a change of parameters with the drawing process does exist (Fig. 5). As the drawing degree rises, the average angle increases $\theta^{(7)} > \theta^{(0)}$ (this means that the net fatigue fracture surface is higher in the cold drawn steel wire than in the hot rolled bar) and the average length decreases $l^{(7)} < l^{(0)}$ (this implies more frequent deflections in the cold drawn steel wire than in the hot rolled bar). Both phenomena, probably associated with the orientation of the pearlite lamellae and the elongation of the colonies, produce a retardation of fatigue crack growth, thus indicating that the manufacturing process by cold drawing improves the behaviour of these steels.

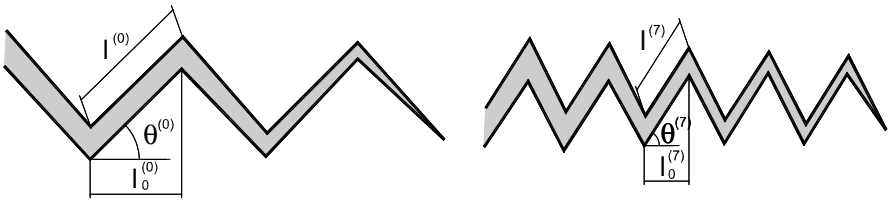

Fig. 5 Scheme of the fatigue crack: (a) hot rolled bar and (b) cold drawn wire.

For various ranges of the SIF, the profiles followed by the fatigue crack in the longitudinal sections of the specimen were drawn up. The profile length ratio λ –ratio of the actual length of the crack increment, l, to the length of its transverse projection, l_0– was calculated,

$$\lambda = \frac{l}{l_0}, \tag{1}$$

checking that its value increases with the SIF range, $\lambda=\lambda(\Delta K)$, as well as with the drawing process (Fig. 6). The SIF range ΔK and the R-ratio influence the aspect of the fatigue fracture surface. The increment of any of these parameters makes the typical micro-tearing features appearing in the fatigue surface more tortuous and pronounced [7]. Although the fatigue fracture surface of the hot-rolled bar exhibits, at the meso level, cracking with greater height variations than the cold-drawn wire, at a finer micro-level the latter exhibits higher micro-roughness, so that the actual fractured surface in the cold-drawn wire is greater than that in the hot-rolled bar, and the crack deflection events are more frequent and with higher angle in the former (the drawn material), so that an increment is observed of the level of kinking and tortuosity of the crack as it propagates, associated with the afore-said increase of the microcrack deviation angle in the cold drawn wire, the height of the deflection path in both materials (higher in the cold drawn wire), the number of deflections per projected length (more elevated in the plastically strained steel) and the general roughness of the fatigue fracture surface in the hot rolled bar and in the cold drawn wire.

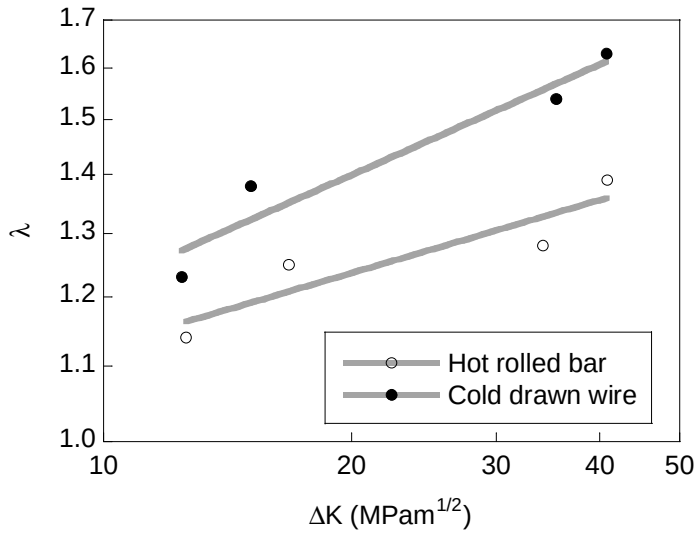

Fig. 6 Profile length ratio, *λ*

6 CONCLUSIONS

1) Microscopically the fractographic appearance of the pearlitic steel shows microplastic tearing, which is consistent with fatigue microdamage and crack growth by accumulation of localized plastic deformation. The cold drawn steel exhibits a pattern of micro-tearing events of lower size and more curved aspect than the hot rolled bar.

2) Fatigue cracks paths are trans-colonial and tend to fracture pearlitic lamellae. Fatigue crack propagation is tortuous, with micro-discontinuities, branchings, bifurcations and local deflections, thereby creating microstructural roughness, and even exhibiting non-uniform crack opening displacement values.

3) The fatigue fracture surface of the drawn steel shows micro-roughness with greater total surface than in the rolled material due to the fact that the deflections in the fatigue path are more frequent and with greater angle. The increase of the stress intensity range, Δ*K,* also produces higher micro-roughness.

7 ACKNOWLEDGEMENTS

The authors wish to acknowledge the financial support provided by the following Spanish Institutions: MICYT (Grant MAT2002-01831), MEC (Grant BIA2005-08965), MICINN (Grants BIA2008-06810 and BIA2011-27870), JCyL (Grants SA067A05, SA111A07 and SA039A08) and the steel supplied by TREFILERÍAS QUIJANO (Los Corrales de Buelna, Cantabria, Spain).

8 REFERENCES

[1] K. Sadananda, A.K. Vasudevan, Crack Tip Driving Forces and Crack Growth Representation under Fatigue, International Journal of Fatigue, 26, 39–47, 2004.

[2] S. Stoychev, D. Kujawski, Analysis of Crack Propagation Using ΔK and K_{max}, International Journal of Fatigue, 27, 1425–1431, 2005.

[3] J. Zhang, X.D. He, S.Y. Du, Analyses of the Fatigue Crack Propagation Process and Stress Ratio Effects Using the Two Parameter Method, International Journal of Fatigue, 27, 1314–1318, 2005.

[4] D. Kujawski, A Fatigue Crack Driving Force Parameter with Load Ratio Effects, International Journal of Fatigue, 23, S239–S246, 2001.

[5] F. Walther, D. Eifler, Local Cyclic Deformation Behaviour and Microstructure of Railway Wheel Materials, Materials Science and Engineering A, 387–389, 481–485, 2004.

[6] A.A. Korda, Y. Mutoh, Y. Miyashita, T. Sadasue, Effects of Pearlite Morphology and Specimen Thickness on Fatigue Crack Growth Resistance in Ferritic-Pearlitic Steels, Materials Science and Engineering A, 428, 262–269, 2006.

[7] J. Toribio, J.C. Matos, B. González, Micro- and Macro-Approach to the Fatigue Crack Growth in Progressively Drawn Pearlitic Steels at Different R-Ratios, International Journal of Fatigue, 31, 2014–2021, 2009.

[8] A.A. Korda, Y. Mutoh, Y. Miyashita, T. Sadasue, S.L. Mannan, In Situ Observation of Fatigue Crack Retardation in Banded Ferrite-Pearlite Microstructure Due to Crack Branching, Scripta Materialia, 54, 1835–1840, 2006.

[9] F. Wetscher, R. Stock, R. Pippan, Changes in the Mechanical Properties of a Pearlitic Steel Due to Large Shear Deformation, Materials Science and Engineering A, 445–446, 237–243, 2007.

[10] H. Kitagawa, R. Yuuki, T. Ohira, Crack-Morphological Aspects in Fracture Mechanics, Engineering Fracture Mechanics, 7, 515–529, 1975.

[11] S. Suresh, Crack Deflection: Implications for the Growth of Long and Short Fatigue Cracks, Metallurgical Transactions A, 14, 2375–2385, 1983.

[12] A. Carpinteri, A. Spagnoli, S. Vantadori, D. Viappiani, Influence of the Crack Morphology on the Fatigue Crack Growth Rate: A Continuously-Kinked Crack Model Based on Fractals, Engineering Fracture Mechanics, 75, 579–589, 2008.

[13] Y. Mutoh, A.A. Korda, Y. Miyashita, T. Sadasue, Stress Shielding and Fatigue Crack Growth Resistance in Ferritic-Pearlitic Steel, Materials Science and Engineering A, 468–470, 114–119, 2007.

[14] M. Okayasu, D. Chen, Z. Wang, Experimental Study of the Effect of Loading Condition on Fracture Surface Contact Features and Crack Closure Behaviour in a Carbon Steel, Engineering Fracture Mechanics, 73, 1117–1132, 2006.

[15] J. Toribio, E. Ovejero, M. Toledano, Microstructural Bases of Anisotropic Fracture Behaviour of Heavily Drawn Steel, International Journal of Fracture, 87, L83–L88, 1997.

Proceedings of the 3rd International Conference on
Fracture Fatigue and Wear, pp. 257-262, 2014

CRACK SHAPE EVOLUTION IN PLATES SUBJECTED TO CYCLIC LOADING

J. Toribio[1], J.C. Matos[2], B. González[1] and J. Escuadra[2]

[1]Department of Materials Engineering, University of Salamanca, E.P.S. Zamora, Spain
[2]Department of Computing Engineering, University of Salamanca, E.P.S. Zamora, Spain

Abstract: The aim of this paper is the numerical prediction of the cracking path followed by a surface crack front in plates constituted of different materials (determined by the exponent *m* of the Paris law), subjected to cyclic tension or cyclic bending loading. To this end, a numerical modelling was developed on the basis of a discretization of the crack front (characterized with elliptical shape) and the crack advance at each point perpendicular to such a front, according to a Paris law, using the stress intensity factor (SIF) calculated by Newman and Raju. Results show that the crack leads to a preferential crack path that corresponds to a very shallow initial crack with a quasi-circular crack front. The increase of the Paris exponent produces a quicker convergence during fatigue crack propagation from the different initial crack shapes.

Keywords: numerical modelling; cracked plate; Paris law; crack advance; crack aspect ratio

1 INTRODUCTION

The plate, a simple geometry of structural application, often presents cracks on its surface that can easily propagate due to fatigue, a reason why studying them is of great interest for Fracture Mechanics. The stress intensity factor (SIF) in a superficially cracked plate, subjected to tension or bending loads, has been calculated by several methods [1-8]. For tension loading the SIF increases with crack depth, showing its maximum value at the centre of the front for semi-elliptical cracks (with a ratio between semiaxes 0.2) and at the point of the surface for semicircular cracks [1,2]. For bending moment the SIF is highest at the crack surface from relative depths greater than or equal to 0.6, regardless of the geometry of the crack front [1].

The advance of the crack front in plates has been experimentally [1,8-13] and numerically [1,6-8,10-13] analyzed, applying the Paris Erdogan law [14]. Cracks try to grow so that the SIF remains constant along the front (iso-*K* condition of propagation), but the plate's free surfaces and the bending load prevent this [15]. Cracks asymptotically tend to a preferential propagation path [1,6-8,10-13], so that the larger the ratio of the bending loading to tension loading, the more intense the asymptotic tendency [12]. If the Paris exponent is greater, the change in the aspect ratio is more pronounced [12].

2 NUMERICAL MODELLING

A computer program in Java programming language was developed to study the propagation path of a symmetric surface crack on the cross section of a plate (Fig. 1a), subjected to fatigue (cyclic) loading in the form of remote uniform tension or pure bending moment (under Mode-I loading conditions).

The basic hypothesis of this modelling is the assumption that the crack front can be characterized as a semi-ellipse with its centre on the plate's surface and that fatigue propagation takes place in a direction perpendicular to such a front, following the Paris Erdogan Law [14]:

$$\frac{\mathrm{d}a}{\mathrm{d}N} = C\Delta K^{\mathrm{m}} \tag{1}$$

To discretize the crack front, modelled in a semi-elliptical way, the front was divided into *z* segments of equal length, using Simpson's rule. The point on the surface of the plate, where there is plane stress, was not taken into account. Subsequently, each of the points (*i*) was moved perpendicularly to the crack front, in accordance with the Paris Erdogan law, so that the maximum crack increases, $\Delta a(\max)$, corresponding to the point of the maximum SIF, $Y(\max)$, was kept constant. From this maximum increase and dimensionless SIF *Y* (where *K* is the SIF and σ remote tension stress or maximum remote bending stress):

$$Y = \frac{K}{\sigma\sqrt{\pi a}}, \tag{2}$$

The advance of each of the front points can be obtained Δa_i:

$$\Delta a_i = \Delta a(\max)\left[\frac{Y_i}{Y(\max)}\right]^m \tag{3}$$

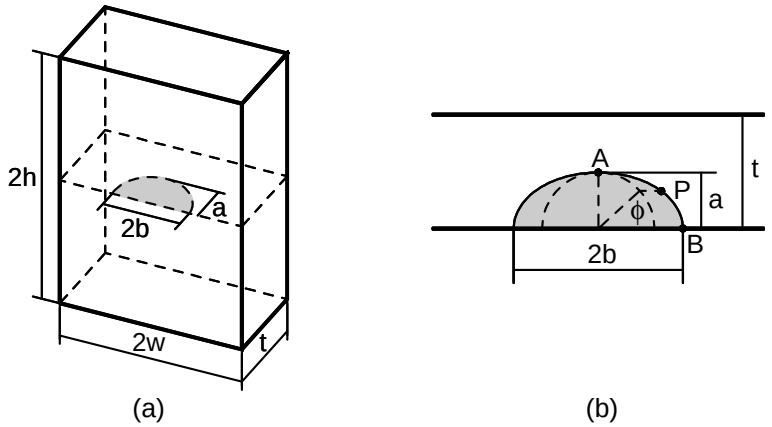

(a) (b)

Fig. 1 Surface crack in a plate.

The new points, fitted by the method of least squares, form a new semi-ellipse, so that the crack advancement progress is repeated iteratively. Due to the existing symmetry, only half of the problem was used in the calculations. The parameters z and $\Delta a(\max)$ were determined by a study of convergence.

The SIFs used were those obtained by Newman and Raju [1,2] by a 3D finite element analysis and the nodal-force method. These authors adjusted their results to an equation [1,13] that calculates the dimensionless SIF with parameters a/t, a/b, and ϕ, which characterizes each point of the crack front (Fig. 1b). This equation (valid for $0 < a/b \le 1.0$, $0 \le a/t < 1.0$, $0 \le \phi \le \pi$ and $b/w < 0.5$) has been tested experimentally and numerically by various methods [1,4,7-11,13,15]: measurements of K (photoelastic and numerical), the geometrical evolution of the front, the crack growth rate, failure stress, etc. Keeping in mind Newman and Raju's equation [1,13], the advancement at each point of the crack front can be calculated using the expression:

$$\Delta a_i = \Delta a(\max)\left[\frac{(Hf_\phi g)_i}{(Hf_\phi g)_{\max}}\right]^m \tag{4}$$

Where the parameters f_ϕ, g, and H are obtained by the following equations, ($H = 1$ in the case of tension loading):

$$f_\phi = \left[\left(\frac{a}{b}\right)^2 \cos^2\phi + \sin^2\phi\right]^{1/4} \tag{5}$$

$$g = 1 + \left[0.1 + 0.35\left(\frac{a}{t}\right)^2\right](1 - \sin\phi)^2 \tag{6}$$

$$H = H_1 + (H_2 - H_1)\sin^p\phi \tag{7}$$

$$p = 0.2 + \frac{a}{b} + 0.6\frac{a}{t} \tag{8}$$

$$H_1 = 1 - 0.34\left(\frac{a}{t}\right) - 0.11\left(\frac{a}{b}\right)\left(\frac{a}{t}\right) \tag{9}$$

$$H_2 = 1 + \left[-1.22 - 0.12\left(\frac{a}{b}\right) \right]\left(\frac{a}{t}\right) + \left[0.55 - 1.05\left(\frac{a}{b}\right)^{0.75} + 0.47\left(\frac{a}{b}\right) \right]^{1.5} \left(\frac{a}{t}\right)^2 \quad (10)$$

3 NUMERICAL RESULTS AND DISCUSSION

A convergence study was carried out in order to determine the number of parts in which each semi-ellipse is divided (crack front) and the maximum crack depth in the iterations, $z = 24$ and $\Delta a(\max) = 0.00005t$ or $0.00001t$ being chosen as was required by the calculation. Figs. 2 to 4 show how cracks propagate from distinctive initial geometry —relative crack depth $(a/t)_0$ and aspect ratio $(a/b)_0$— in plates of different materials (m = 2, 3 and 4), subjected to tension loading or bending moment. Fig. 2 shows the evolution of the aspect ratio a/b with relative depth a/t, and Figs. 3 and 4 the dimensionless advance of the crack front geometry in the form of a/t-b/t plot.

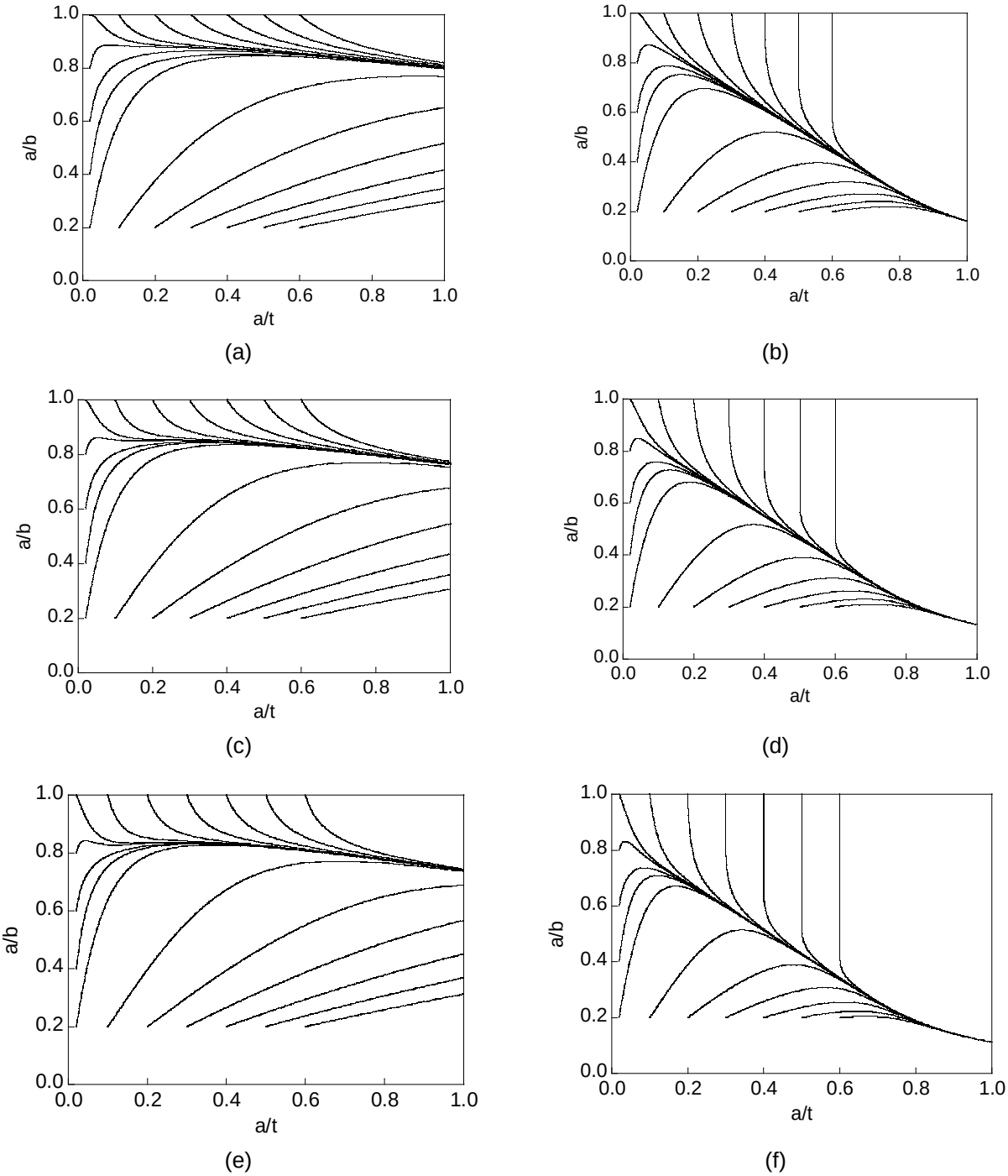

Fig. 2 Crack aspect ratio evolution for: (a) tension loading and m=2; (b) bending moment and m=2; (c) tension loading and m=3; (d) bending moment and m=3; (e) tension loading and m=4; (f) bending moment and m=4

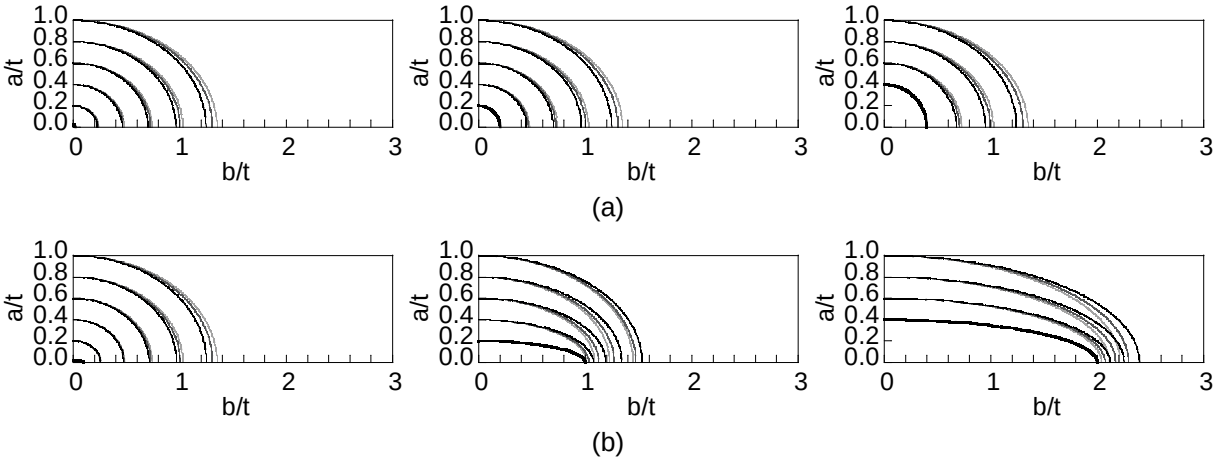

Fig. 3 Crack front advance for tension loading: (a) $(a/b)_0$=1.0 and (b) $(a/b)_0$=0.2

Initial crack front — m=2 — m=3 — m=4

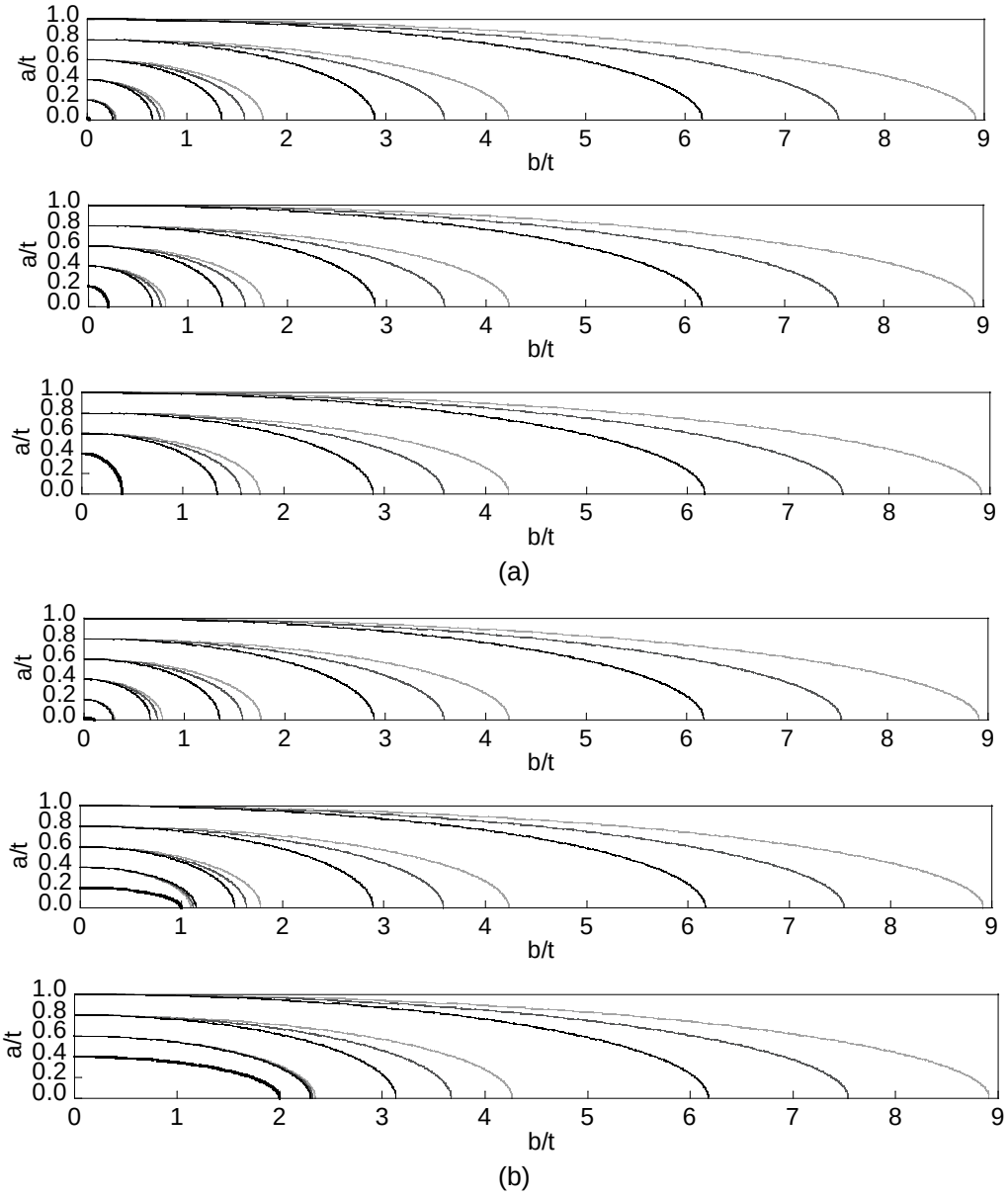

Fig. 4 Crack front advance for bending moment: (a) $(a/b)_0$=1.0 and (b) $(a/b)_0$=0.2

Initial crack front — m=2 — m=3 — m=4

The crack advance from different initial geometries (a/b-a/t curves) tends towards a preferential propagation path, which corresponds to that of an initial crack which is very shallow with a quasi-circular front. The convergence of the solution (approach between the curves corresponding to the propagation from the different initial geometries) is higher in the case of bending than in the situation of tension, and for a larger Paris exponent m (although this parameter has a weaker effect on the growth pattern). The convergence is greater as the initial crack gets closer to the geometry corresponding to the path of preferential propagation. The circular cracks with elevated relative crack depth for tension loading are those that show a lesser convergence. When the initial crack is circular $(a/b)_0$=1.0, a greater Paris coefficient m produces lower aspect ratios (that is, for the same crack depth a, bigger semi-axes b). Conversely, if the initial aspect ratio is quasi-straight $(a/b)_0$~0.2, the curves' behaviour with the Paris exponent m depends on the initial relative crack depth $(a/t)_0$ and the type of stress (tension loading or bending moment).

The preferential propagation path shows a slight decrease in the aspect ratio with the relative crack depth in tension and a marked decrease in bending (Fig. 5a). The Paris coefficient m reduces these curves slightly in an almost equidistant way along the whole path. The ratio between the minimum and the maximum SIF, Y_{min}/Y_{max}, in each crack front along the preferential propagation path shows high initial values that drop slowly for tension and sharply for bending (Fig. 5b). In tension, the preferential propagation path approaches the iso-K evolution (similar SIF between different points of the crack front, i.e., $Y_{min} \cong Y_{max}$) while in bending the increasing relative crack depth produces an appreciable separation of this iso-K evolution, so that, the higher the crack depth, the greater the difference between Y_{min} and Y_{max}. The increase of the Paris exponent m elevates the ratio between the minimum and maximum SIF, a generally weak effect except for bending loading and high relative crack depths.

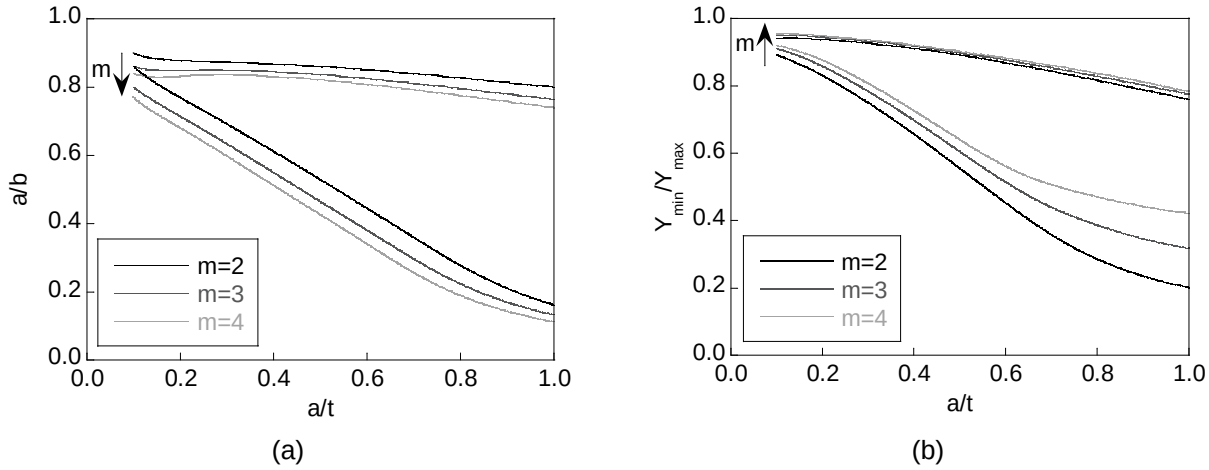

Fig. 5 Preferential cracking path: (a) crack aspect ratio and (b) minimum and maximum SIF ratio

A comparison was performed of the experimental results obtained by different authors [16,17] and the numerical modelling proposed in the present paper. It is shown in Fig. 6 that plots the fatigue crack propagation (evolution of the crack aspect ratio, a/b, *vs*. relative crack length, a/t) for both tension loading and bending moment. Both plots exhibit an excellent agreement between numerical predictions (solid lines) and experimental results (dotted lines), in spite of the inherent scattering of any fatigue phenomena.

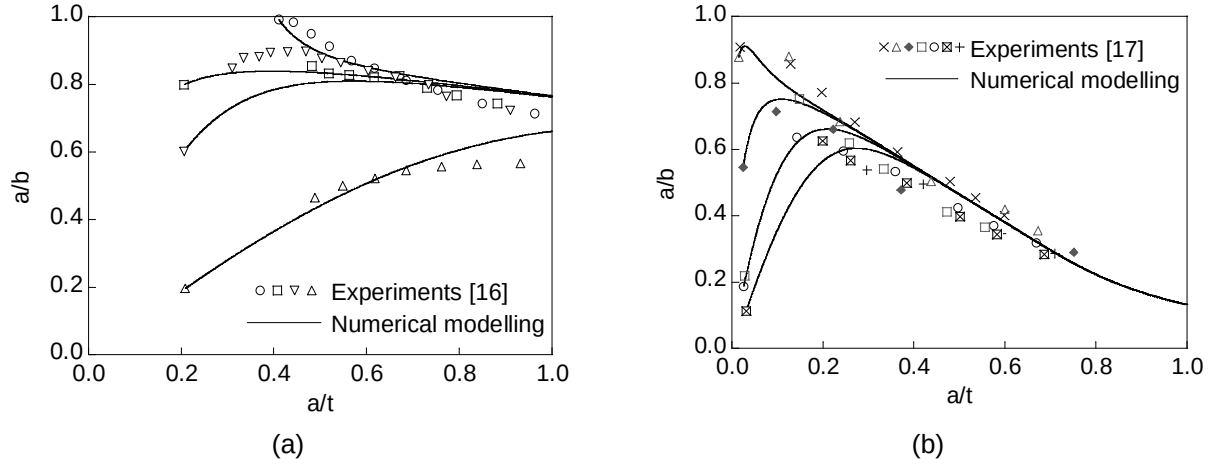

Fig. 6 Comparison between numerical and experimental results: (a) tension loading and (b) bending moment. The numerical results were computed using a Paris exponent m=3

4 CONCLUSIONS

1) The cracks in fatigue growth tend towards a preferential propagation path, which corresponds to that of an initial crack which is very shallow with a quasi-circular front.
2) The convergence, approaching between the propagation curves with different initial geometries, is higher for cyclic bending loading than for cyclic tension loading and for greater Paris exponent *m* (showing a weak effect on this parameter).
3) The crack aspect ratio and the relationship between the maximum and minimum stress intensity factors (SIF) for the preferential propagation path show initially high values that decrease slowly in the case of tension loading and sharply in the case of bending loading.
4) The increase of the Paris exponent *m* reduces the crack aspect ratio for the preferential propagation path, increasing the ratio between the minimum and maximum SIFs.

5 ACKNOWLEDGEMENTS

The authors wish to acknowledge the financial support provided by the following Spanish Institutions: MICYT (Grant MAT2002-01831), MEC (Grant BIA2005-08965), MICINN (Grants BIA2008-06810 and BIA2011-27870) and JCyL (Grants SA067A05, SA111A07 and SA039A08).

6 REFERENCES

[1] J.C. Newman Jr., I.S. Raju, Analyses of Surface Cracks in Finite Plates under Tension or Bending Loads, NASA TP-1578, USA, 1979.

[2] I.S. Raju, J.C. Newman Jr., Stress-Intensity Factors for a Wide Range of Semi-Elliptical Surface Cracks in Finite-Thickness Plates, Engineering Fracture Mechanics, 11, 817–829, 1979.

[3] S.J. Holdbrook, W.D. Dover, The Stress Intensity Factor for a Deep Surface Crack in a Finite Plate, Engineering Fracture Mechanics, 12, 347–364, 1979.

[4] M. Isida, H. Noguchi, T. Yoshida, Tension and Bending of Finite Thickness Plates with a Semielliptical Surface Crack, International Journal of Fracture, 26, 157–188, 1984.

[5] M. Isida, H. Noguchi, T. Yoshida, Oblique Semi-Elliptical Surface Crack in Semi-Infinite Solid Subjected to Tension, Engineering Fracture Mechanics, 36, 889–892, 1990.

[6] X.B. Lin, R.A. Smith, Finite Element Modelling of Fatigue Crack Growth of Surface Cracked Plates. Part I: The Numerical Technique, Engineering Fracture Mechanics, 63, 503–522, 1999.

[7] Z. Wu, The Shape of a Surface Crack in a Plate Based on a Given Stress Intensity Factor Distribution, International Journal of Pressure Vessels and Piping, 83, 168–180, 2006.

[8] Y. Peng, L. Tong, X.-L. Zhao, Z. Xiao, Modified Stress Intensity Factor Equations for Semi-Elliptical Surface Cracks in Finite Thickness and Width Plates, Procedia Engineering, 14, 2601–2608, 2011.

[9] O. Vosikovsky, A. Rivard, Growth of Surface Fatigue Cracks in a Steel Plate, International Journal of Fatigue, 3, 111–115, 1981.

[10] A. Hosseini, M.A. Mahmoud, Evaluation of Stress Intensity Factor and Fatigue Growth of Surface Cracks in Tension Plates, Engineering Fracture Mechanics, 22, 957–974, 1985.

[11] M.A. Mahmoud, A. Hosseini, Assessment of Stress Intensity Factor and Aspect Ratio Variability of Surface Cracks in Bending Plates, Engineering Fracture Mechanics, 24, 207–221, 1986.

[12] X.B. Lin, R.A. Smith, Finite Element Modelling of Fatigue Crack Growth of Surface Cracked Plates. Part II: Crack Shape Change, Engineering Fracture Mechanics, 63, 523–540, 1999.

[13] J.C. Newman Jr., I.S. Raju, An Empirical Stress-Intensity Factor Equation for the Surface Crack, Engineering Fracture Mechanics, 15, 185–192, 1981.

[14] P.C. Paris, F. Erdogan, A Critical Analysis of Crack Propagation Laws, Journal of Basic Engineering, 85D, 528–534, 1963.

[15] X.B. Lin, R.A. Smith, Finite Element Modelling of Fatigue Crack Growth of Surface Cracked Plates. Part III: Stress Intensity Factor and Fatigue Crack Growth Life, Engng Frac Mech, 63, 541–556, 1999.

[16] I.S. Putra, J. Schijve, Crack Opening Stress Measurements of Surface Cracks in 7075-T6 Aluminium Alloy Plate Specimen Through Electron Fractography. Fatigue & Fracture of Engineering Materials & Structures, 15, 323–338, 1992.

[17] N.B. McFadyen, R. Bell, O. Vosikovsky, Fatigue Crack Growth of Semielliptical Surface Cracks, International Journal of Fatigue, 12, 43–50, 1990.

Proceedings of the 3rd International Conference on
Fracture Fatigue and Wear, pp. 263-268, 2014

INFLUENCE OF FATIGUE LOADING ON THE RESIDUAL STRESSES INDUCED BY COLD DRAWING IN PRESTRESSING STEELS

J. Toribio, M. Lorenzo, D. Vergara and L. Aguado

Fracture of Materials and Structural Integrity Research Group, University of Salamanca, Spain

Abstract: Nowadays, cold drawing is the main conforming process used in industry for obtaining prestressing steel wires which are commonly subjected to fatigue loading during their life in-service. Plastic strain generated during wire drawing produces undesirable residual stresses which can affect the structural integrity of the material in both inert and aggressive environments. So, it seems to be interesting to analyse the evolution during several fatigue loading schemes of diverse residual stress states similar to the ones produced after a cold drawing process. To achieve this goal, numerical simulations by finite element method were carried out applying diverse fatigue loading schemes to several cold drawn prestressing steel wires. For each one of them a residual stress state was introduced, some of them with a tensile state at the wire surface and others with a compressive state. On one hand, numerical results reveal the key role of plastic strains produced by fatigue loading causing a *redistribution* of the wire residual stress when tensile stresses are placed at the wire surface. On the other hand, results show a negligible effect of fatigue loading on the residual stress state of those wires where a compressive residual stress was considered.

Keywords: Cold drawn steels; residual stresses; fatigue; stress redistribution

1 INTRODUCTION

Prestressing steel wires are commonly used in civil engineering as reinforcement elements for prestressed concrete structures which must bear fatigue loadings. Nowadays, cold drawing is the main conforming process used in industry for obtaining prestressing steel wires. Residual stresses appear in cold drawn wires due to the non-uniform distribution of plastic strain during the conforming process: wire drawing [1,2]. Briefly, this process consists in forcing to pass a hot rolled bar throughout diverse drawing dies where a progressive reduction of the wire cross sectional area is carried out [2]. As results, changes are produced at microstructural level causing a significantly increment of the cold drawn wire strength. Nevertheless, during drawing the wire undergoes a huge stress concentration over the vicinity of the contact zone between wire and die. Therefore, a non-uniform distribution of residual stress is produced in the wire section with a complex shape, with tensile stresses near the contact zone and compressive stresses near the wire core [2-4]. Residual stresses of tensile nature play a key role in surface crack initiation process [5,6]. It is well-know the industrial use of different surface treatments, e.g. shot peening, which provides compressive residual stress at the material surface, thus delaying the initiation and propagation of cracks [7-10]. In addition, the synergic action of non-uniform residual stress and strain states enhances environmental induced fracture such as hydrogen embrittlement (HE) to which prestressing steel wires are particularly susceptible [2,11]. The HE of prestressing steels has been analysed profusely [2] in terms of the main stage of such a process: the hydrogen diffusion that is strongly dependent of the stress and strain state fields inside the material.

Under in-service conditions, prestressing steels wires undergo fatigue loadings. Consequently, the variables affecting the damage and fracture processes in both inert and aggressive environments vary with time. Thus, the evolution with time of the residual stress state during fatigue loading is necessary for obtaining a better knowledge regarding to one of the factors involved in the damage processes and, therefore, to the determination of the optimal conditions for assessing the structural integrity of prestressing steel wires. So, the aim of this paper is to analyse the evolution during several fatigue loading schemes of diverse residual stress states similar to the ones produced after a cold drawing process and the implications of such states on HE susceptibility of wires. To achieve this goal, numerical simulations by the finite element (FE) method were carried out applying diverse fatigue loading schemes to several cold drawn wires. For each one of them, an idealized residual stress state was introduced not only with a tensile state at the wire surface but also with a compressive state in that location.

2 NUMERICAL MODELLING

Six different *fatigue loading schemes* were analysed. All of them with sinusoidal variation with time considering stress factor R = 0, as summarized in Table 1. This way, fatigue cycles oscillate between a null stress and a maximum stress of 1000 and 1200 MPa (i.e., about 75% and 90% of σ_Y=1300 MPa, 0% offset yield strength of a typical prestressing steel used in construction [12]). The effect of the number of cycles (N) was included in this analysis considering three loading sequences of 10, 20 and 100 cycles. Thus, the type I represents a fatigue loading of 10 cycles with a maximum stress level of $0.75\sigma_Y$ (1000 MPa), the type II and III reaches the same maximum stress but now considering 20 and 100 cycles respectively. The type IV consists of 10 cycles with a maximum stress level of $0.9\sigma_Y$ (1200 MPa) and, finally, the scheme V and VI has a maximum stress of 1200 MPa and 20 and 100 cycles respectively.

Table 1 Number of cycles and maximum stress level applied in the different fatigue loading considered.

Fatigue Loading Schemes	I	II	III	IV	V	VI
σ_{max} (MPa)	1000	1000	1000	1200	1200	1200
N	10	20	100	10	20	100

In addition, the *residual stress profiles* were idealized according to the values of the surface stresses obtained experimentally by the application of diverse techniques, such as Neutron or X-Ray diffraction [13-15]. Such techniques allow obtaining the stress state in samples only for a certain depth from surface. In this paper, the residual stress state after drawing was idealized considering two zones: (i) firstly a linearly decreasing stress from the wire surface up to a point whose depth from surface is equivalent to the one given by diffraction techniques, and, secondly a constant stress distribution up to the wire core. The value of the stress distribution over the second zone can be obtained applying the equilibrium condition to the stress state over the whole cross sectional area of the wire in terms of the second Pappus-Guldin Theorem [16]. This approach allows one to reproduce the general shape of the residual stresses profiles observed with the most commonly used measurement techniques without any loss of generality.

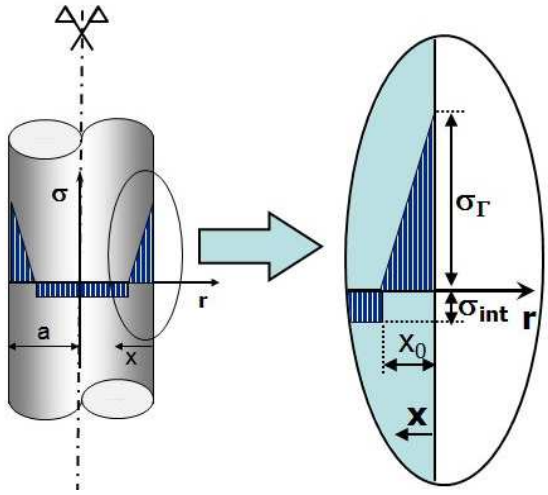

Fig. 1 Scheme of idealized residual stress profile

Thirteen residual stress profiles were analysed in the present study which can be divided, according to the nature of the surface wire stress, into tensile residual stress states (profiles 1, 3, 5, 7 and 9 to 13 in Table 2) and compressive residual stress states (profiles 2, 4, 6 and 8 in Table 2). The idealized residual stress profiles can be defined by using just two parameters: the maximum residual stress level at the surface, σ_Γ, and the depth x_0 (x being the distance from the wire surface) where the stresses reach a constant value, as depicted in Fig. 1.

Table 2 Parameters of the idealized residual stress profiles used in the computations

Profile	1	2	3	4	5	6	7	8	9	10	11	12	13
σ_Γ (MPa)	100	-100	200	-200	500	-500	800	-800	1200	1500	1700	2000	2500
x_0 (μm)	250	250	250	250	500	500	500	500	500	500	500	500	500

The simulation of the fatigue loading applied to the prestressing steel wire is carried out by FE using a commercial code (MSC.Marc). Due to the axisymmetric geometry of the wire, the three-dimensional (3D) case is simplified to an equivalent two-dimensional (2D) problem. In order to reproduce the idealized residual stress profile, the meshing of the wire was carried out considering progressively increased size of the elements with wire depth (Fig. 2) [17]. Thus, close to the wire surface, the profile exhibits the most significant variations and hence the mesh of the wire is more refined. On the contrary, out of this zone a constant distribution is considered and, therefore, a coarse mesh was applied. This way a more accurate approach to the theoretical stress profile can be achieved by assigning to each element an initial stress value which depends on the distance to the wire surface, as shown in Fig. 2 where these initial stress values (constant in each finite element) are plotted in comparison with the exact profile previously described. The meshing of the geometry is developed with four nodes quadrilateral elements due to the simple geometry of the wire. The constitutive model for the material was chosen to be elasto-plastic with isotropic strain hardening rule given by the master stress and strain curve obtained experimentally from a simple tensile test. Results provide the following material properties: Young modulus, E = 200 GPa and 0% offset yield stress, σ_Y = 1300 MPa.

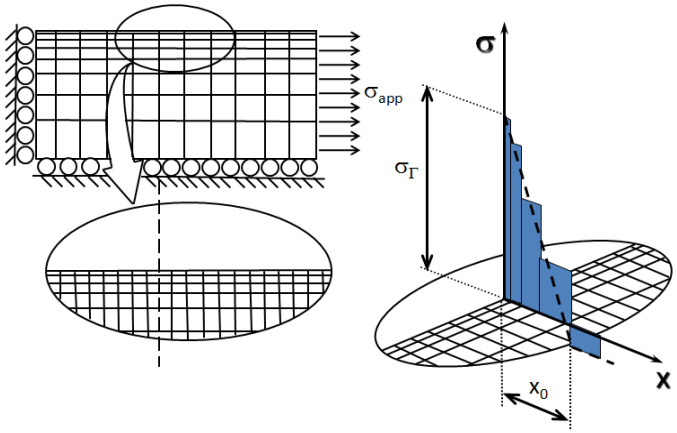

Fig. 2 Scheme of the meshing of the specimen and detail of the residual stress profile

3 INFLUENCE OF THE LOADING SCHEME

The evolution with time (simulation time t) of axial stress at two different depths was analysed. Each one of them represents the two zones in which the idealized residual stress profile was divided (cf. Fig. 1). Thus, the first one is placed at the wire surface where the maximum stress is located, and the second one is placed at the middle of the uniformly stress distributed zone (cf. Fig. 1). Due to a lack of space, only the evolutions of axial stress at the three last cycles for two wires are shown in Fig. 3: (i) profile 7 (σ_Γ = 800 MPa), representing the tensile residual profiles; (ii) profile 8 (σ_Γ = -800 MPa), representing the compressive stress profiles. In both cases t represents the dimensionless simulation time.

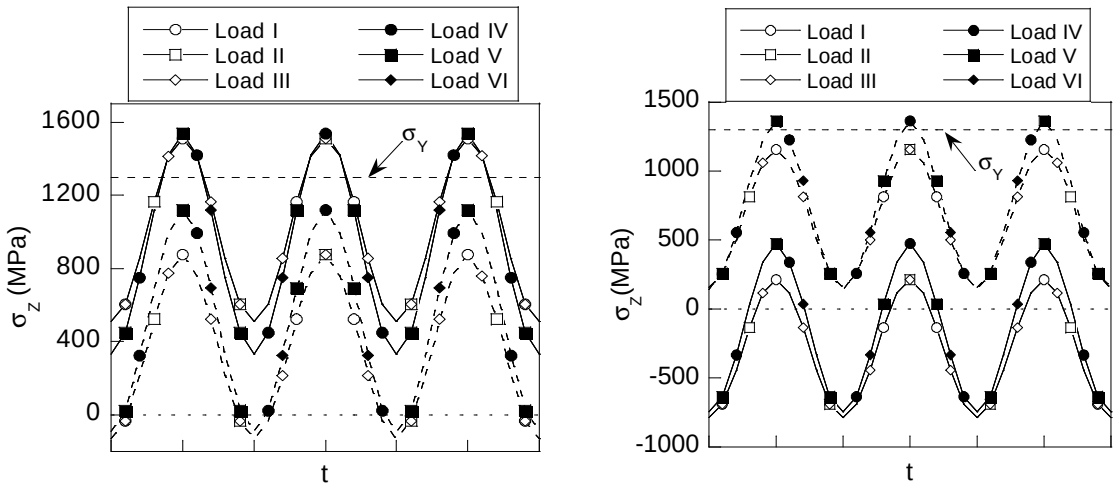

Fig. 3 Time evolution of the axial stress at the three last loading steps for the six loading schemes at external node (solid line) and internal node (dotted line): (a) residual stress profile 7 (σ_Γ = 800 MPa), and (b) residual stress profile 8 (σ_Γ = -800 MPa).

On one hand, the stress state of outer points of the residual stress profiles 3, 5 and 7 (Fig. 3a) overcomes the 0% offset yield stress during fatigue loading, whereas the residual stress profile 1 (corresponding to the lowest tensile residual stress state at surface) just scratch the material yield stress only when the maximum stress load is applied. However, for inner points the axial stress remains within the elastic regime and stress distribution does not significantly change. So, for those cases, the outer points of the wire undergo plastic strains that could modify the stress profile due to the constraining effect of the plastic zone. On the other hand, the evolution with time of the compressive residual stress profiles 2, 4, 6 and 8 reveals that only inner points of the wire (dashed lines in Fig. 3b) slightly overcome the 0% offset material yield stress. Consequently, the residual stress distribution must remain the same without changes during fatigue loading. In addition, results show the negligible effect of the number of cycles of the fatigue loading since the stress evolution is equivalent for fatigue loads with different number of cycles for a given maximum stress level (on one hand, loads I to III and on the other hand, for loads IV to VI, cf. Table 1). However, the influence of the maximum fatigue load does exists since it contributes, acting together with the residual stress, to overcome the material yield stress. So, taking this into account it seems to be interesting to analyse hereafter only those loading schemes where the maximum load is varied for a given number of cycles, i.e. load I and load IV according to Table 1.

Fig. 4a shows the distribution of the axial stress through wire radii when the load scheme IV is applied to residual stress profiles 7 (σ_Γ = 800 MPa) and 8 (σ_Γ = -800 MPa). In these graphs, the characteristic points of the loading history at the specific time instants are represented, namely at initial load, at minimum load, at final load and at maximum load with asterisk, which represents the maximum load with the shift factor (σ_{app}) applied according to the expression $\sigma_z^* = \sigma_z - \sigma_{app}$, where a new parameter called *effective stress* (σ_z^*) is defined and used throughout the present paper [17].

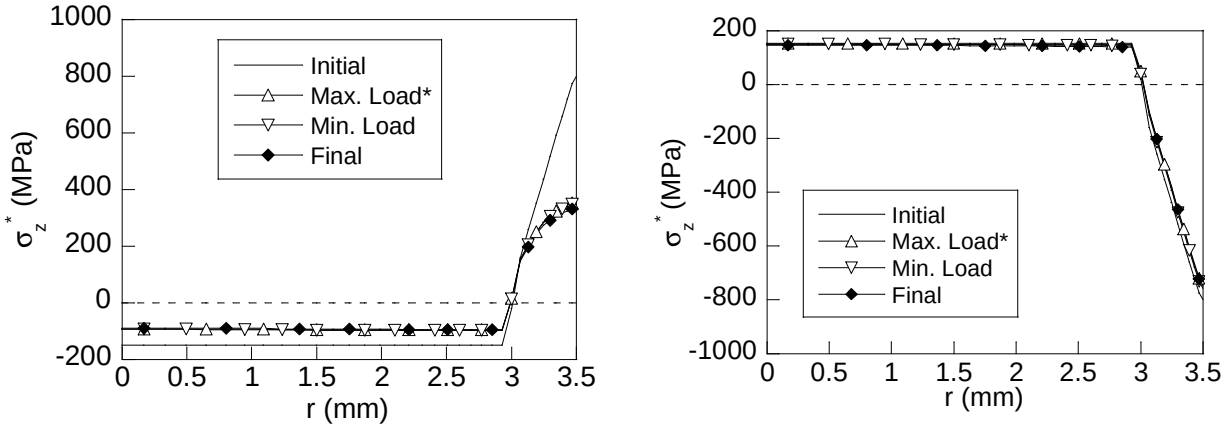

Fig. 4 Effective stress distribution through the wire radius at the characteristic fatigue loading instants of load IV for: (a) the residual stress profile 7 (σ_Γ = 800 MPa) and (b) the profile 8 (σ_Γ = -800 MPa)

On one hand, a huge reduction of the stress state (about 60%) at the wire surface vicinity is observed in the tensile residual stress cases (Fig. 4a), whereas only minor variations are observed for compressive stress profiles (Fig. 4b). The reduction generated at the maximum load instant remains during the rest of the fatigue loading. As a consequence of aforesaid reduction, a redistribution of the residual stress profile appears causing a reduction as well of the stress state at inner points. On the other hand, no significant differences can be observed regarding to the values of effective stress at the wire surface in the compressive stress state cases for the different characteristic loading instants (Fig. 4b). The same effect was observed for those tensile residual stresses in which the maximum stress does not exceeded 0% offset yield stress, i.e., profile 1 (σ_Γ = 100 MPa). Regarding the variable affecting the HE of prestressing steel wires, the hydrostatic stress, the same effect was observed.

4 DISCUSSION

To analyse variations of stress reduction at surface, the values of the dimensionless reduction of the residual stress at surface ($\Delta\sigma_\Gamma/\sigma_\Gamma$) were represented for both considered types of residual stress profiles (Fig. 5), according to the stress state at surface (tensile and compressive) corresponding to the fatigue loading schemes I and IV. A growing trend of stress reduction at surface ($\Delta\sigma_\Gamma$) with residual stress at surface (σ_Γ) is observed in Fig. 5a for residual stress profiles of tensile nature. Thus, for realistic residual stress profiles (3, 5 and 7) the variation of the stress reduction could be considered linear reaching significant reduction for the profiles 5 (σ_Γ = 500 MPa) and 7 (σ_Γ = 800 MPa). Thus, for the residual stress profile 5, stress reductions of 20% and 45% were obtained when fatigue loads I and IV are applied, whereas for stress profile 8 the stress

reductions reach the 30% and 60% for fatigue loading schemes I and IV respectively. For non-realistic residual stress profiles (stress profiles 9 to 13 in Table 2), a non-linear growing trend is observed reaching a maximum stress reduction of 80% for the residual stress profile 13 (σ_Γ = 2500 MPa) when the highest fatigue load (load IV) is applied. As observed in Fig. 5a, the stress reduction at wire surface depends on both maximum stress level of fatigue loading and surface residual stress. This way, results reveal the key role of residual stress at the wire surface in stress reduction. Therefore, the higher the boundary value of stress or the higher maximum fatigue load, the more pronounced the stress reduction that could be expected. This effect is clearly shown analysing the lower residual stress profiles. Thus, the variation of the stress state for the profile 1 (σ_Γ =100 MPa) is lower than 10% for both fatigue loads, whereas for the profile 3 (σ_Γ =200 MPa) a negligible change is observed for the lowest load (load I) but a notable stress reduction (about 30%) is observed when the fatigue loading IV is applied. With regard to the profiles with residual compressive stress at surface, a negligible reduction (always lower than 7%) is always obtained.

For a better understanding of the causes of such a residual stress reduction, the value of maximum stress reached during loading history for each one of the cases studied is represented (Fig. 5b) against the residual stress at surface. Thus, comparing the stress reductions plotted in Fig. 5a with the maximum stress reached during fatigue loading, it is clearly revealed the influence of plastic strain on stress reductions since this effect appears only if the maximum stress overcomes the material yield stress (dashed line in Fig. 5b), thereby generating plastic strains.

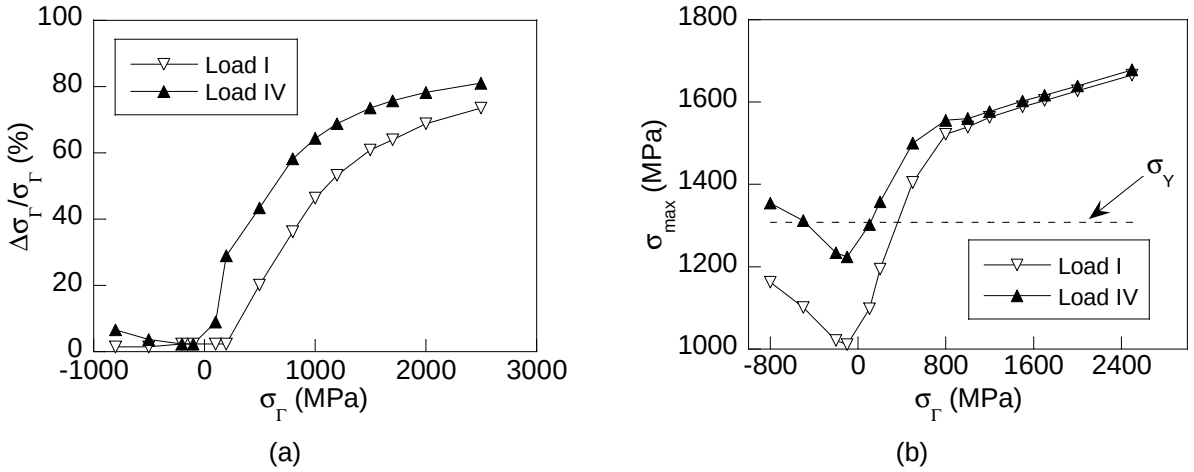

Fig. 5 (a) Variation of the stress reduction of the surface stress with residual stress at surface, and (b) evolution of the maximum stress during fatigue loading with residual stress at surface

Then, the cause of this macroscale stress reduction and subsequent stress redistribution is due to the changes at the microstructural level produced by plastic strains located near the wire surface. Thus, according to these results, the outer zone of the wire undergoes plastic strains while the rest of the section remains within elastic regimen. This way, elastic strains are vanished in the wire when load is removed, constraining the plastic zone which impedes the recovery of the initial geometry. However, if the maximum load does not reach the material yield stress and, consequently a plastic zone is not produced, the elastic strains return the wire to the original geometry without affecting the initial residual stress state. Therefore, low, or even negligible, stress reductions should be expected for residual stress of compressive nature at surface, since plastic strains only appear for very high external loads in these cases.

5 CONCLUSIONS

A reduction, and the consequent *redistribution,* of residual stresses in prestressing steel wires is produced during fatigue loading for those cases where the fatigue maximum stress overcome the material yield stress causing plastic strain at the vicinity of the wire surface. Results reveal a growing trend of the stress reduction with the residual stress at surface for profiles of tensile nature. Thus, the higher the residual stress at the surface, the higher the stress reduction. This reduction can be as high as 60% for common values of residual stresses due to wire drawing and up to 80% for non-realistic residual stress states. This reduction has a strong dependence of the value of maximum stress fatigue load and negligible dependence of number of cycles. However, for residual stress of compressive nature, a negligible reduction appears. The cause of the observed stress reduction is the constriction exerted by the plastic strain zone that impedes the elastic strain recovery during fatigue loading. Therefore, the stress reduction is only observed in those profiles where a localized plasticity is produced during fatigue loading. From these results it could be considered a theoretical way of reducing residual stresses generated by wire drawing. It consists of

applying a fatigue load with a maximum stress level that, together with the residual stresses generated during the process, produces plastic zones near the wire surface generating a constrain effect that leads to a stress reduction and redistribution through the wire radius.

6 ACKNOWLEDGEMENTS

The authors wish to acknowledge the financial support provided by the following Spanish Institutions: Ministry for Science and Technology (MICYT; Grant MAT2002-01831), Ministry for Education and Science (MEC; Grant BIA2005-08965), Ministry for Science and Innovation (MICINN; Grants BIA2008-06810 and BIA2011-27870), Junta de Castilla y León (JCyL; Grants SA067A05, SA111A07 and SA039A08).

7 REFERENCES

[1] P.J. Webster, G. Mills, Residual stresses in a steel strand, Physica B: Condensed Matter, 241-243, 1270–1273, 1997.

[2] J. Toribio, V. Kharin, M. Lorenzo, D. Vergara, Role of drawing-induced residual stresses and strains in the hydrogen embrittlement susceptibility of prestressing steels, Corrosion Science, 53, 3346–3355, 2011.

[3] M. de Giorgi, Residual stress evolution in cold-rolled steels, International Journal of Fatigue, 33, 507–512, 2011.

[4] H. Överstam, The influence of bearing geometry on the residual stress state in cold drawn wire analysed by the FEM, Journal of Materials Processing Technology, 171, 446–450, 2006.

[5] G.A. Webster, A.N. Ezelio, Residual stress distributions and their influence on fatigue lifetimes, International Journal of Fatigue, 23, S375–S383, 2001.

[6] J.D. Almer, J.B. Cohen, B. Moran, The effects of residual macrostresses and microstresses on fatigue crack initiation. Materials Science and Engineering, A284, 268–279, 2000.

[7] Y.M. Xing, J. Lub, An experimental study of residual stress induced by ultrasonic shot peening. Journal of Materials Processing Technology, 152, 56–61, 2004.

[8] H. Pron, J.F. Henry, B. Flan, J. Lu, S. Offermann, J.L. Beaudom, Estimation of residual stresses induced by shot-peening: Measurement of the thermal dissipation with an infrared camera, International Journal of Thermal Sciences, 41, 369–375, 2002.

[9] J.-Ch. Kim, S.-K. Cheong, H. Noguchi, Residual stress relaxation and low- and high-cycle fatigue behaviour of shot-peened medium-carbon steel, International Journal of Fatigue, 56, 114–122, 2013.

[10] J.-Ch. Kim, S.-K. Cheong, H. Noguchi, Evolution of residual stress redistribution associated with localized surface microcracking in shot-peened medium-carbon steel during fatigue test, International Journal of Fatigue, 56, 147–157, 2013.

[11] J. Toribio, M. Lorenzo, D. Vergara, V. Kharin, Hydrogen degradation of cold drawn wires: a numerical analysis of drawing-induced residual stresses and strains, Corrosion, 67, 5001–5009, 2011.

[12] J. Toribio, V. Kharin, F.J. Ayaso, B. González, J.C. Matos, D. Vergara, M. Lorenzo, Numerical and experimental analyses of the plasticity-induced fatigue crack growth in high-strength steels, Construction and Building Materials, 25, 3935–3940, 2011.

[13] M. Kuroda, S. Yamanaka, Y. Isobe, Detection of plastic deformation and estimation of maximum value of residual stress in low carbon steel by X-ray stress analysis using statistical techniques, NDT&E International, 36, 497–502, 2003.

[14] C.D.M. Liljedahl, O. Zanellato, M.E. Fitzpatrick, J. Lin, L. Edwards, The effect of weld residual stresses and their re-distribution with crack growth during fatigue under constant amplitude loading, International Journal of Fatigue, 32, 735–743, 2010.

[15] S. Sato, K. Wagatsuma, S. Suzuki, M. Kumagai, M. Imafuku, H. Tashiro, K. Kajiwara, T. Shobu, Relationship between dislocations and residual stresses in cold-drawn pearlitic steel analyzed by energy-dispersive X-ray diffraction, Materials Characterization, 83, 152–160, 2013.

[16] F.P. Beer, E.R. Johnston, R.E. Flori, Mechanics for Engineers. Statics. Ed. McGraw Hill, 2007, 5ºed.

[17] J. Toribio, M. Lorenzo, D. Vergara, Influence of fatigue loading on the residual stress distribution in prestressing steel wires, Journal of Civil Engineering and Architecture, 6(10), 1338–1344, 2012.

Proceedings of the 3rd International Conference on
Fracture Fatigue and Wear, pp. 269-274, 2014

ON FRETTING FATIGUE BEHAVIOUR OF SINGLE BOLTED LAP JOINT

R. Hojjati-Talmei[1,2], M.A. Wahab[1] T. Yue[1] and L. D'Alvise[2]

[1]Department of Mechanical Construction and Production, Faculty of Engineering and Architecture, Ghent University, Belgium
[2] Geonx Inc., Gosselies, Belgium

Abstract: Fretting fatigue failure mechanisms occurs between connected parts which are subjected to small oscillatory relative movement and bulk fatigue loading condition at the same time. In this study, fretting fatigue behaviour of single bolted lap joint connection is investigated by means of finite element modelling approach. To this end, a 3-D finite element model was developed to characterize behaviour of single bolted joint subjected to fretting fatigue loading conditions, which consists of initial crack site estimation, stress and slip distribution at contact interface.

Keywords: DIC; fretting fatigue; SBLJ; slip amplitude

1 INTRODUCTION

Fretting fatigue failure evolution is caused by combination of several parameters, which can be related to different mechanical response of material. These parameters can be divided into two sets of primary and secondary variables, which have more and less influence on fretting fatigue total lifetime. In general, fretting fatigue failure process is divided into two main phases, namely crack initiation and crack propagation. The fraction of fretting fatigue lifetime spent in crack initiation and in crack propagation depends on many factors, e.g. contact stresses, amount of slip, frequency, environmental conditions, etc., and varies from one practical application to another. Numerical modelling techniques are proper toolkits for analyzing fretting fatigue behaviour of contact problems subjected to fretting fatigue loading condition.

The early Finite Element Analysis (FEA) study of riveted joints dates back to mid-90's reported by Hoeppner et al. [1]. When a FEA based methodology was used to determine the stress state at rivet locations, where the fretting fatigue crack initiates. They used the FEA results as a valid baseline condition to apply the method for prediction of Coefficient of Friction (COF) during fretting process to a riveted joint. Szolwinski et al. [2] targeted at characterizing the conditions at/around the rivet/hole interface by means of FEA approach. They modelled both mechanics of load transfer in riveted joints and the residual stress field. A 3-D FEA of riveted joint was modelled by Guo et al. [3]. They have tried to study the mechanism of fretting fatigue crack formation in aluminium alloys, and the determination of the characteristic crack initiation sites by means of both experimental and numerical methods. Moreover, they investigated the influence of the contact COF and fastening forces on the initiation of cracks by means of the comparison of the different numerical results. Benhamena et al. [4] used 3-D FEA approach to analyses the effect of tightening torque on single bolted lap joint under fretting fatigue loading condition. In their work they also tried to monitor the contact status along with the potential location of fretting fatigue crack under different loading conditions. Chakherlou et al. [5] performed FE modelling of double shear lap joints subjected to cyclic load and compared with the experimental results under static loading condition in order to study the joints performance. In this paper fretting fatigue behaviour of SBLJ was monitored by developing a 3-D FE model, including location of initial crack, stress and slip distribution at contact interface between connected plates.

2 EXPERIMENTAL SET-UP

A SBLJ experimental specimen was configured by fastening two identical halves together through a single bolt, as schematically illustrated in Figure 1. Al 2024-T3 alloy panels of t= 4 mm thick were machined and cut to dimensions as described in the ASTM D5961/D5961M-01 standard, giving an overall length of 115 mm and a width of 40 mm, as shown in Figure 2. Circular fastener holes of 8.25 mm in diameter were drilled at the centre of the specimen width with a free edge distance of 15 mm. Socket head steel bolt (M8-8.8) was used to clamp the specimen halves and the tightening torque was applied with a calibrated torque

wrench. To avoid eccentricity in the applied load, which would lead to undesirable bending effects, end tabs of the same aluminium alloy 2024-T3 were bonded to each end of the test specimen as seen in Fig. 1.

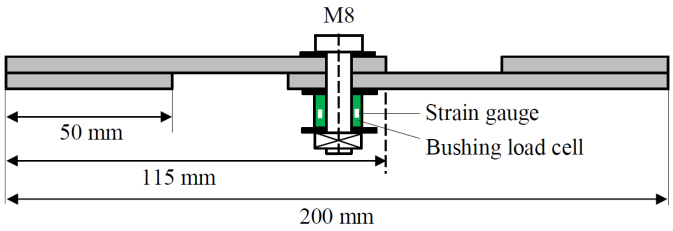

Fig. 1 Assembly view of the SBLJ specimen

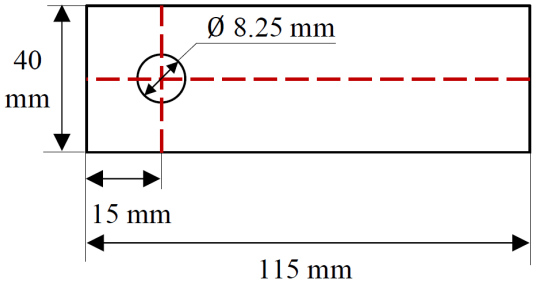

Fig. 2 Geometry of the SBLJ specimen

Specimens were prepared first by polishing lightly with sandpaper 800 grit followed by 1200 grit and finally cleaned with a pass by a cloth with acetone to remove all residual traces of debris remaining from this preparation process. Special care was taken for alignment of the specimens in the lower and upper grips as well as the relative alignment of the specimen halves to each other. For this purpose, a special fixture was used to assemble the SBLJ aiming to centring the bolt, load cell and plates to avoid having contact between inner side of the bolt hole and the bolt shank. The contact load was applied using a torque wrench after centring the Al plates, the load cell and the bolt using the special fixture.

Bolted joint specimens were tested with a servo hydraulic testing machine, according to the above-mentioned ASTM standard as depicted in Figure 3. In order to obtain experimentally the bolt clamping force in a bolted joint, there are different kinds of methods such as torque wrench method, angle control method and load cell strain gage method. In this research, the load cell and strain gage method was used, as it has better accuracy compared to other methods. The load cell comprised of a steel bush and two strain gauges positioned between the nut and the plate (see Fig. 1). This load cell was used to measure the compressive force due to the tightening torque. Two strain gauges were attached to the outer surface of the steel bush parallel to the bush axis as can be seen Fig. 3.

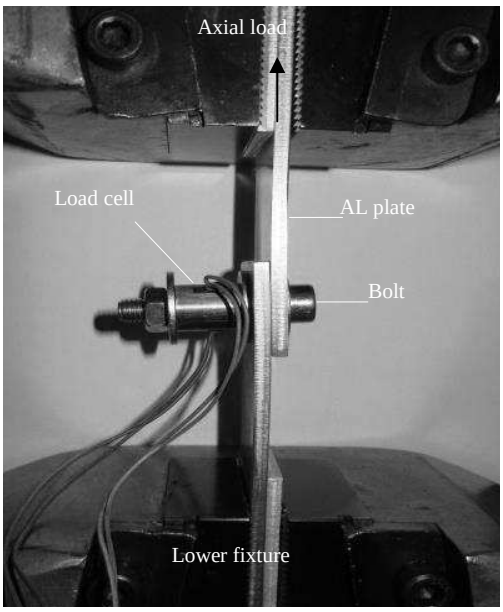

Fig. 3 SBLJ specimen mounted on universal servo-hydraulic fatigue machine

Figure 4 illustrates the variation of applied axial load versus displacement for SBLJ connection at F_{cl}= 14 kN clamping force. As shown in the figure, the elastic elongation of joint was used for validating FE model, which is elaborated later on. By increasing the axial load, the joint slips and eventually the bolt faces a shearing failure mode.

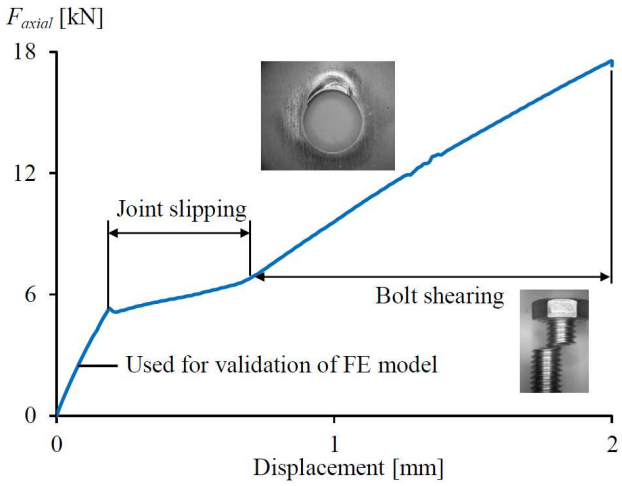

Fig. 4 Applied axial force versus displacement diagram for SBLJ

2.1 FE model

As mentioned earlier and shown above FE modelling approach is convenient methodology to investigate behaviour of fretting fatigue contact under different contact conditions. Therefore, using FE approach enhances the possibility to easily study more details compared to performed tests in a laboratory such as the distribution of slip at contact interface under different loading conditions. To this end, the preceding section focuses on characterizing fretting fatigue behaviour of SBLJ by means of 3-D FE modelling approach. In order to model SBLJ a few simplifications were made which may not cause any significant effect on the results. These simplifications can be listed as:

- A circular shape was used for the nut and bolt head. The socket shape of the bolt head was ignored.
- The washers were tied to the bolt head and nut because of having the same material elastic properties.
- Modelling of the bolt threads was ignored as there is no contact between threads and inner surface of hole.

A SBLJ model was generated using ABAQUS software. One half of experimental configuration needs to be model due to symmetry condition with respect to *x-y* plane in terms of both the geometry and loading. The model included two identical plates of Al 2024-T3, with a thickness of 4 mm and a 8.25 mm diameter hole as well as a M-8 steel bolt to clamp the plates. The dimensions of the modelled Al plates were the same as preformed SBLJ static test in Chapter 3. Isotropic material properties with elastic behaviour were defined to all components. Steel bolt, nut, load cell bush and washers with an elastic modulus of E= 210 GPa and a Poisson's ratio of ϑ = 0.33 and material properties with an elastic modulus of E= 72.4 GPa and a Poisson's ratio of ϑ = 0.33 was set for properties of the Al plates.

Figure 5 illustrates 3-D FE model of SBLJ along with the applied loading and boundary conditions, the same as static experimental set-up of SBLJ described in Chapter 3. The model consists of five different parts: two Al plates, three washers, bolt, nut and bushing load cell. Symmetric displacement boundary conditions were applied to the nodes on the symmetry planes. The loads were applied in two steps. Clamping contact load (F_{cl}) was applied in the first step to establish contact between contact pairs. In the second step axial stress was applied to the right side of Al plate. During the first step all three translational degrees of freedom (DOFs) at both left and right sides of the Al plates were restrained during applying clamping load. After applying clamping load the constraints at the right side of Al plate were removed and the axial load was applied instead as shown in Figure 5. 3-D structural 8-node linear brick, reduced integration, hourglass control (C3D8R) elements were used with the master-slave contact algorithm on the contact surface between Al plates interface, Al plates and the washers. The rest of contact pairs defined as a tie constant to reduce the computation time. As the vicinity of the bolt hole was the critical zone to be analyzed, density of the mesh was appropriately refined in this region as shown in Figure 5. The minimum mesh size at contact interface was 0.1 mm and increased gradually far from contact.

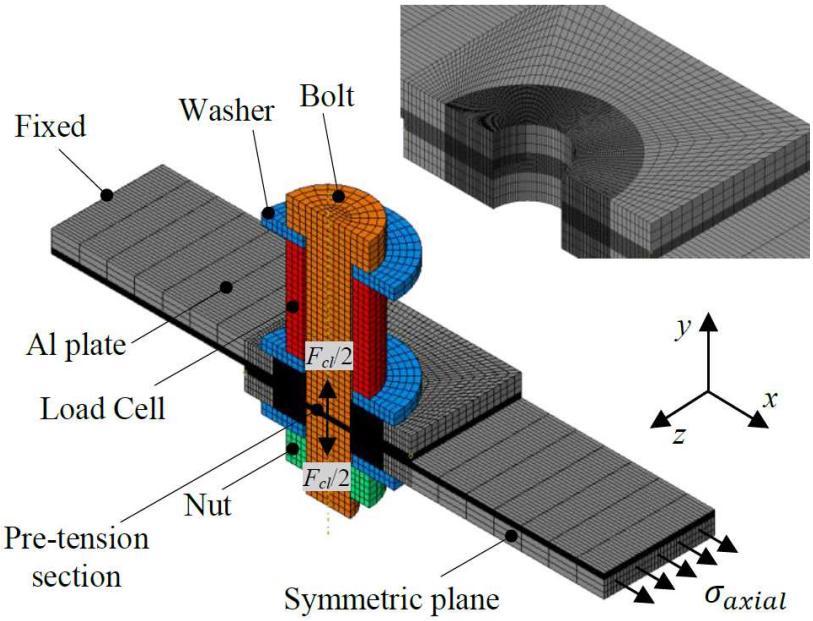

Fig. 5 FE model of SBLJ along with the applied loading and boundary conditions

A small sliding contact condition was used between the contact pair to transfer loads between the two bodies. The connecting contact surfaces were defined as a contact pair that enabled ABAQUS to determine if the contact pair was touching or separated. The contact region consisted of stick and slip regions under fretting fatigue loading condition. The stick region did not have a relative movement between contact surfaces. The slip region showed a small relative movement between contact surfaces on interface between two Al plates which is commonly observed in a fretting fatigue experiments. The penalty of friction was included in the contact pair to define the friction behaviour of the contact region as the Lagrange multiplier of friction did not converge in this particular SBLJ model. The coefficients of friction μ= 0.71 and μ= 0.2 were considered in this study for Al plates pairs and washer to Al plates, respectively.

In order to apply clamping load (F_{cl}) a pre-tension section in the bolt was defined as shown in Figure 5. When modelling the bolt with solid elements, the pre-tension section is defined as a surface in the bolt shank that effectively partitions the bolt into two regions. In continuum elements the pre-tension section is defined as a surface inside the fastener that “cuts” it into two parts. The pre-tension section can also be a group of surfaces for cases where a fastener is composed of several segments. Therefore, in the FE model the clamping load applied by applying a concentrated load, which is a self-equilibrating force carried across the pre-tension section in the bolt shank, to the pretension nodes.

3 FRETTING FATIGUE BEHAVIOUR OF SBLJ

Before investigation fretting fatigue behaviour of SBLJ it is essential to validate the FE model versus experimental results. Figure 6 illustrates the variation of axial load versus displacement for both FE model and static experimental test. Figures 7 (a) and (b) show the distribution of tangential and maximum principle stresses at contact interface between two Al plates. The high stress gradient is located at some distance from the hole near the contact edge (i.e. the side that the axial stress applied), which is also the potential location of initial crack in experimental results as reported in [9]. Figure 7 (c) indicates that the maximum frictional shear stress happens at almost the same distance as the maximum principle stress. Figure 7 (d) illustrates that the contact interface between two connected Al plates can be divided in three distinguished region namely, sticking, slipping and gapping.

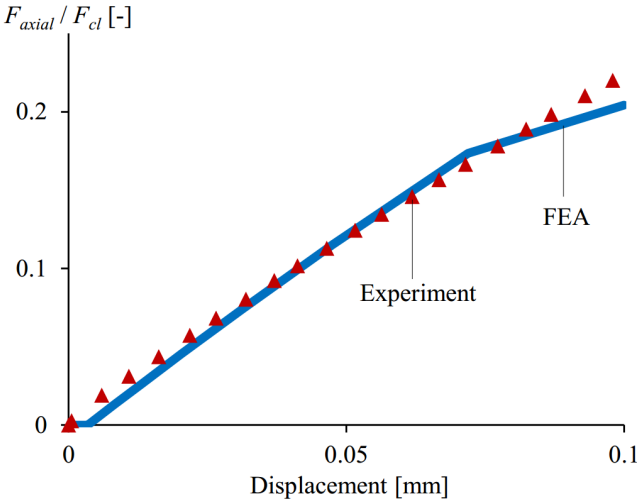

Fig. 6 Comparison between FE models and experimental results for F_{cl}= 14 kN

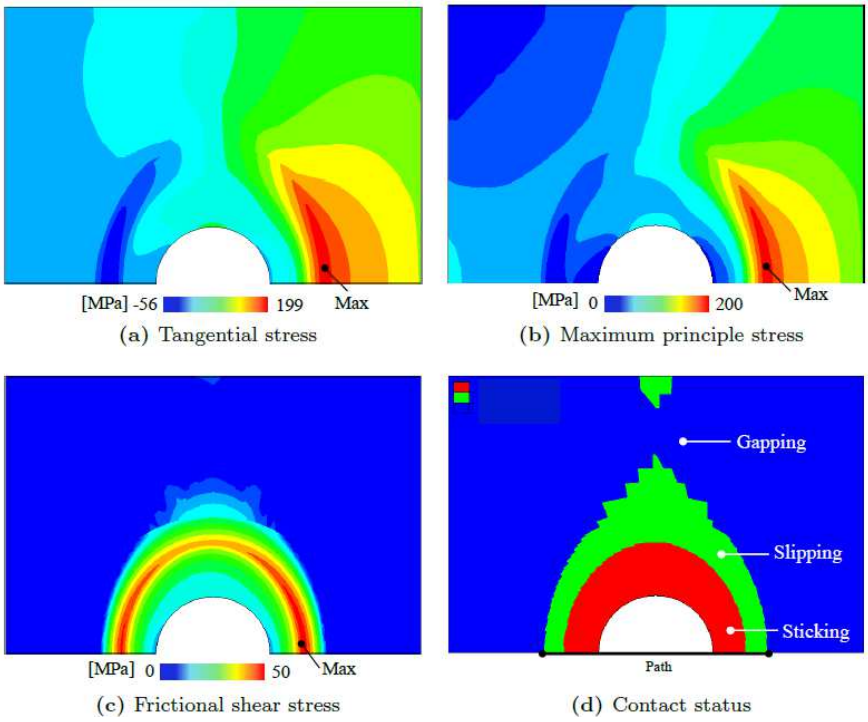

Fig. 7 Stress distribution at contact interface for SBLJ subjected to fretting fatigue loading condition at σ_{axial}= 20 MPa, F_{cl}= 14 kN and μ= 0.71

As investigated in author's' previous works the stress state is multiaxial for contact problems subjected to fretting fatigue loading condition. Therefore, by assuming that the damage causing stress is the equivalent multiaxial damage stress, the location of initial crack can be related to the location of maximum value of equivalent multiaxial damage stress (σ^*) at contact interface between two Al plates. More detailed information and validation of this criterion will be elaborated in [6-8].

Figures 8 (a) and (b) show the normalized equivalent multiaxial damage stress contour plot at contact interface between two Al plates and location of fretting fatigue crack initiation in SBLJ specimen for the same material taken from [9], respectively. As can be seen from Figures 8 (a), the maximum location of σ^* predicts the location of crack near the edge of contact, which is in good agreement with the experimental observation from literature [9]. Nonetheless, to find the exact location of initial crack the same loading and boundary conditions as the experimental test should be applied to the developed FE model for SBLJ.

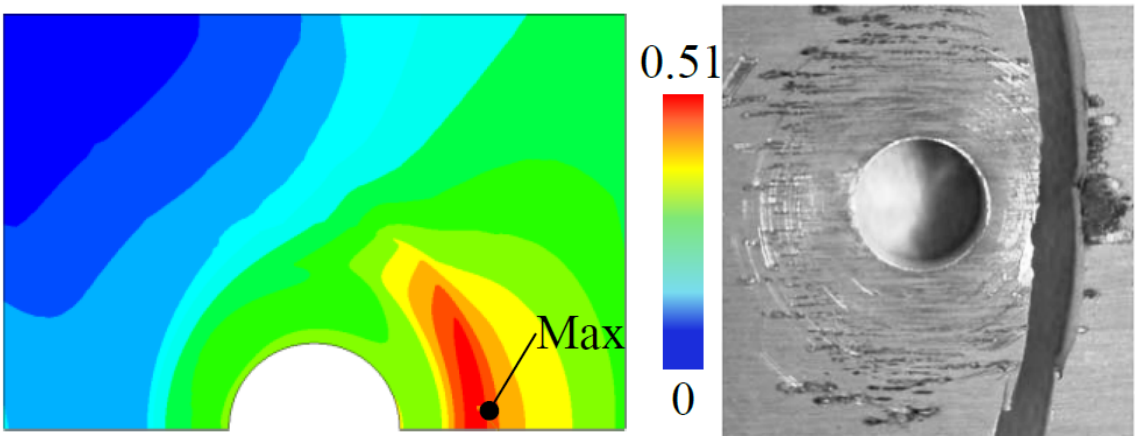

(a) σ^*/σ_{axial} (b)

Fig. 8 (a) Predicted location of initial crack in SBLJ connection subjected to fretting fatigue loading condition using FE approach at σ_{axial}= 20 MPa, F_{cl}= 14 kN and μ= 0.71, compared with the (b) experimental result

4 CONCLUSIONS

In this study, FE modelling approach was used to characterize fretting fatigue behaviour of SBLJ connection. It was found that FE modelling approach enhances the possibility to easily investigate more details compared to performed experimental tests in a laboratory and practical applications such as the distribution of relative slip amplitude, contact pressure or stresses at contact interfaces. It was shown that once the FE model is calibrated with help of experimental test or other calculation methods such as analytical one, it even offers the great capability of performing large parametric studies to check the influence of different parameters on behaviour of different structures subjected to fretting fatigue loading condition. To this end, using FE modelling approach the location of initial crack, stress and slip distribution at contact interface.

5 ACKNOWLEDGEMENTS

The authors wish to thank the Ghent University for the financial support received by the Special Funding, BOF (Bijzonder Onderzoeksfonds), in the framework of project (BOF 01N02410).

6 REFERENCES

[1] D. W. Heoppner, C. D. Elliot III, & M. W. Moesser, The role of fretting fatigue on aircraft rivet hole cracking, Technical report, DTIC Document, 1996.

[2] M. Szolwinski and T. Farris, Linking riveting process parameters to the fatigue performance of riveted aircraft structures, Journal of aircraft, 37(1), 130-137, 2000.

[3] R. Guo, R.C. Duan, G. Mesmacque, L. Zhang, A. Amrouche, Fretting fatigue behaviour of riveted al 6xxx components, Materials Science and Engineering: A, 483, 398-401, 2008.

[4] A. Benhamena, A. Talha, N. Benseddiq, A. Amrouche, G. Mesmacque and M Benguediab, Effect of clamping force on fretting fatigue behaviour of bolted assemblies: Case of couple steel aluminium. Materials Science and Engineering: A, 527(23), 6413-6421, 2010.

[5] T. Chakherlou and B. Abazadeh, Investigating clamping force variations in Al2024-T3 interference fitted bolted joints under static and cyclic loading, Materials & Design, 37,128-136, 2012.

[6] R. Hojjati-Talemi and M. A. Wahab, Fretting fatigue crack initiation lifetime predictor tool: Using damage mechanics approach, Tribology International 60(0), 176-186, 2013.

[7] R. Hojjati-Talemi and M. A. Wahab, Finite Element Analysis of Localized Plasticity in Al 2024-T3 Subjected to Fretting Fatigue, Tribology Transactions 55(6), 805-814, 2012.

[8] R. Hojjati-Talemi, M. A. Wahab, E. Giner, M. Sabsabi, Numerical estimation of fretting fatigue lifetime using damage and fracture mechanics, Tribology Letters, 52(1), 11-25, 2013.

[9] S. Wagle and H. Kato, Ultrasonic detection of fretting fatigue damage at bolt joints of aluminium alloy plates, International Journal of Fatigue, 31(8),1378-1385, 2009.

Proceedings of the 3rd International Conference on
Fracture Fatigue and Wear, pp. 275-280, 2014

WEAR OF ELECTRICALLY CONDUCTIVE SURFACES

Jian Song, Eugen Silbernagel, Liangliang Wang

Precision Engineering Laboratory, Ostwestfalen-Lippe University of Applied Sciences, Liebigstrasse 87, 32657 Lemgo, Germany

Abstract: Different materials are used for the coatings of electrical contacts. One of the most important factors, which determines the lifetime of electrical contacts is the tribological behaviour of the coating, which can be significantly influenced by both coating materials and the modification of coating materials. Electrical contacts are usually coated in order to protect them against corrosion. The lifetime, the electrical and wear properties of electrical contacts with different coating materials and different modifications of coating materials are investigated. Electrically conductive surfaces also experience wear due to the motion and the vibration of electrical contacts or due to different thermal expansions. Depending on the corrosion and oxidation resistance of coating materials, the wear of the coating of detachable electrical contacts can influence the lifetime of electrical contacts in a variety of ways. Our study shows the correlation between the wear behaviours of different coating materials and the lifetime of electrical contacts. The wear behaviours and the wear types of electrically conductive surfaces are analysed. The results form an important basis for the optimization of coatings for electrical contacts.

Keywords: coating; wear; electrical contacts

1 INTRODUCTION

The study of wear is mainly conducted for machine elements such as bearings and gears. Wear is also of great importance for electrical contacts. Since the base metals of electrical contacts such as copper and copper alloys are mostly not corrosion resistant, coatings are used. The wear properties of the coating determine the long-term stability of the basic functions of coatings such as the corrosion protection and the electrical conduction and therefore the lifetime of electrical contacts. Both the fundamentals of tribology and the physics of electrical contacts have to be considered in the investigation of wear of electrically conductive surfaces in addition to some special aspects of the wear of electrical contacts, these being as follows:

- The motion of electrical contacts is mostly oscillating and has a low amplitude of 10 to several hundred µm.
- Since the thickness of coatings is mostly between less than 1 µm and several µm, the progression of the wear lies between the primary stage or the run-in regime with a high wear rate and in the beginning of the secondary stage or the linear regime (also called normal wear) with a low and constant wear rate. The stages of wear will be described in detail later.
- Once the coating is worn through, the wear of the interlayer begins and the wear regime changes again. The wear through of the coating marks the end of corrosion protection for the base metal and a rapid change of the state of the surface due to corrosion and oxidation is then expected. Therefore the wear through can be considered as a turning point in the lifetime of electrical contacts.
- If there are ignoble metals in the coating, the oxidation products can change the progression of the wear significantly, especially with regard to the accumulation of oxides due to the fretting corrosion caused by the motion.
- The wear of the coating can result in a change in the electrical behaviour, however this mostly occurs with some delay. Therefore the wear can be used as an indicator for lifetime forecasting of electrical contacts.

1.1 Electrical Contacts

In order to provide a good electrical connection the electrical contacts should have a stable and low contact resistance. According to Holm the contact resistance R_C is proportional to the specific electrical resistance ρ and inversely proportional to the contact area [1-3]:

$$R_C = \rho / 2a \quad (1)$$

Where a is the radius of the contact area.

This means highly conductive materials have to be applied to the coatings, which is normally the case. However once the contact corrodes or oxidizes, the specific electrical resistance will increase markedly. Therefore coatings are used for corrosion and oxidation protection. There are basically two groups of coatings. One is made of ignoble materials such as tin or nickel and the other of noble materials such as gold or silver. The ignoble materials used have an almost gastight oxide layer, which protects the coating against corrosion and oxidation.

1.2 Wear

According to Archard, the total volumetric wear rate w_V, due to all asperity contacts, is the sum of all contributions over the total contact area [4]:

The total normal load is given by:

$$F = \sum \delta F = p^* \sum \pi a^2 \quad (2)$$

F is the normal force and p is the normal pressure.

And so the volumetric wear rate is

$$w_V = KF / H \quad (3)$$

This equation, which shows the relation between the wear volume per unit sliding distance and the normal force and indentation hardness H of the softer surface, is often called the „Archard Equation“. The constant, K, which is usually called the wear coefficient, is dimensionless, and always <1.

K/H [$mm^3N^{-1}m^{-1}$], sometimes called the “dimensional wear coefficient” is often used, especially in cases when the hardness is not easily definable (e.g. in the case of elastomers). K/H is the quantity of worn material [mm^3] per unit sliding distance [m] per unit of normal load [N]. The volumetric wear rate is, based on Archard’s assumptions, independent of the sliding speed and the apparent contact area. This assumption appears to hold in many situations.

It is more convenient to use the linear wear rate w_L for coatings of electrical contacts:

$$w_L = w_V / A \quad (4)$$

A is the contact area. Since the motion of electrical contacts is cyclical, the linear wear rate by cycle $w_{L,C}$, which is the linear wear rate per cycle, makes more sense:

$$w_{L,C} = w_L * 2 * s_0 \quad (5)$$

s_0 is the amplitude of the motion.

Wear takes place, even in properly lubricated mechanisms, according to a definite pattern as illustrated in Fig. 1. The initial wear rate (run-in) is relatively high because the microscopic surface asperities penetrate the lubricant film, particularly during the low speeds of start-up and shut-down. This rate is aggravated by oscillating motion and by increasing loads. If conditions are not sufficiently severe to cause scuffing in this stage, the wear rate is termed “mild”.

Normal wear begins when the true area of bearing contact (total asperity-contact area) has been substantially increased by plastic deformation and wear to the extent that the lubricant is fully able to support the load; there will then be only occasional metal-to-metal contacts. From this point onwards, wear occurs at a negligible rate, modified only by such events such as lubricant breakdown, sudden rises in temperature (which reduce oil viscosity), shock loads, or a significant reduction in speed.

Normal wear may proceed indefinitely, depending on the several controlling variables, until sufficient debris have accumulated to cause one of the following failure modes:

- Stress risers in the path of motion, ultimately initiating fatigue
- Abrasive wear sufficient to change surface roughness or dimensions appreciably

- Physical blockage

When severe wear or scuffing sets in, the system is so close to failure that the rates of wear are only of academic interest.

Electrical contacts are normally not lubricated and experience oscillating motions and the sliding of two surfaces across each other with low amplitude, which then causes the fretting wear. The accumulated debris of ignoble materials increase the specific electrical resistance of the surface and therefore the contact resistance (1), which in turn causes failures in the electrical function. In the case of noble coating materials, the electrical function can be ensured until the wear through of the coating. Electrical contacts obviously operate under hard conditions in terms of wear. If motion cannot be avoided and the results of the wear determine the functionality of contacts, a high wear resistance of the coating materials is beneficial for a long lifetime of electrical contacts. The hardness of coating materials is one of the key parameters for the wear resistance of coating materials [4-10].

2 EXPERIMENTAL WORK

The measurements were conducted with a tribological and fretting corrosion measurement rig (Fig. 2). The apparatus enables a small and precise displacement of fretting motion at the contact interface. A piezoelectrical actuator moving forwards and backwards generates the relative motion between the contacts. The travel of the motion, which is controlled during the measurement, can be adjusted between 10 and 400 µm. The duration of a cycle is 0.1 or 1 s. Shorter cycle duration is possible, but normally not advisable for electrical contacts. The duration of the cycle should be sufficiently long to enable the chemisorption of oxygen on the surface and sufficiently fast to enable an acceptable test time. The contact force is provided with a dead load. The normal force is between 2 and 4 N. The contacts are wired for a four-wire resistance measurement in order to observe the electrical functionality of the contacts. A computer controls the data acquisition system.

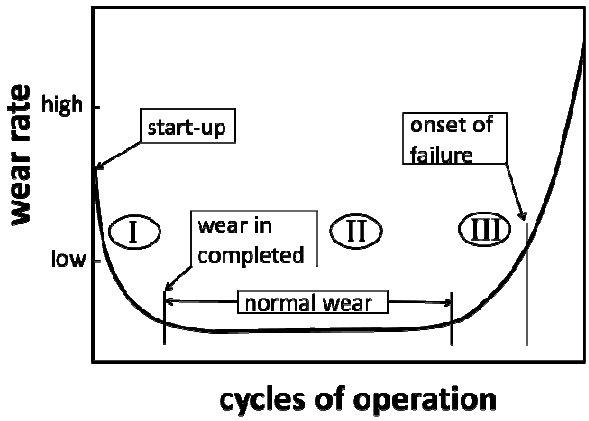

Fig. 1 Generalized pattern of the wear process [4, 11]

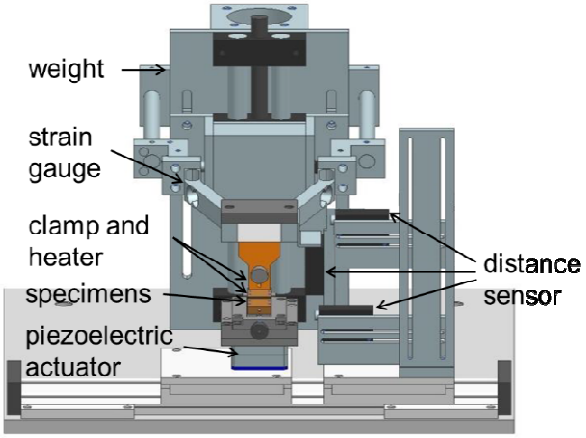

Fig. 2 Tribological and fretting corrosion measurement rig

Several criteria can be used to determine the lifetime of electrical contacts. The number of cycles to the rapid increase of contact resistance was used in this study as lifetime, since it has the strongest impact on the behaviour of electrical contacts. Two limits are set for the lifetime. Lifetime I is defined as the number of cycles which leads to a sharp increase in the contact resistance of 100% to 300% and lifetime II as the number of cycles when the contact resistance of 300 mΩ or more is measured. At the end of lifetime I initial damage on the surface material due to wear occurs and the contacts can usually still function properly. At the end of lifetime II a normal function of electrical contacts cannot be expected (Fig. 3). Lifetime II is a practical definition, but physically the definition is somewhat blurred. The degree of the electrical resistance increase depends partly on the distribution of debris in the contact zone, in the case of noble metals, and the distribution of oxidation products in the case of ignoble coating metals. In this phase both wear and transportation of debris play an important role in the electrical resistance.

Both the linear wear rate by cycle and the friction force were measured simultaneously to the contact resistance during the tests. The linear wear rate by cycle can be calculated from the wear curve – wear crater depth over number of cycles. There are typically two or three phases of wear, depending on the coating systems. The first phase is the wear of the surface material. The second phase is the wear of the

interlayer, if present, or the base metal, see Fig. 4. In the case of coating systems with an interlayer, there is a third phase of wear.

There is usually a very good correlation between phase I of wear and lifetime I of electrical contacts, since the instant of time of phase I of wear corresponds to the instant of time of a partial wear through of the surface material which leads to initial instabilities of electrical contacts. The linear wear rate by cycle in phase I of wear represents the wear performance of the surface material and is therefore relevant for the study of the surface material.

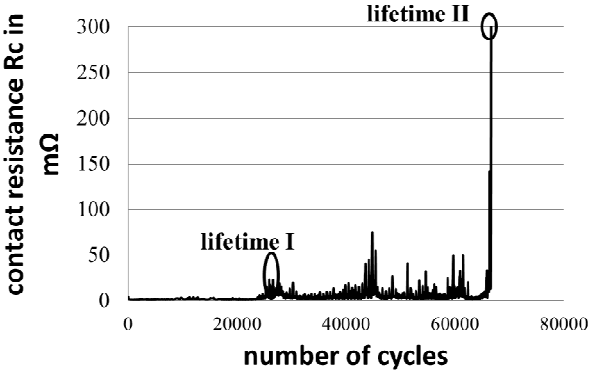

Fig. 3 Increases in contact resistance due to fretting corrosion

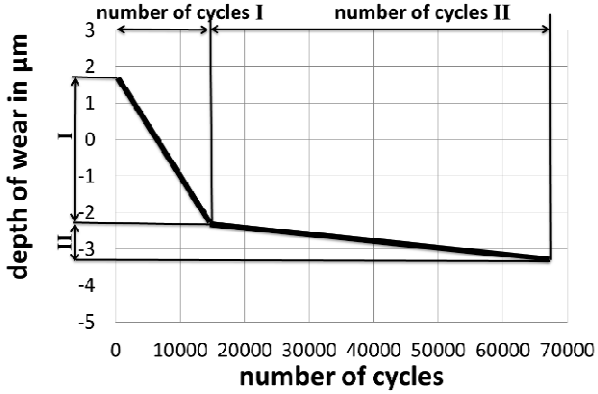

Fig. 4 Two phases of wear

Different coating materials were used in the study. Most of the gold coatings were modified using different alloy elements or nanoparticles, in order to increase their hardness.

3 RESULTS AND DISCUSSION

Figure 5 shows the wear rate by cycles of different coating materials over the hardness. Sn has the highest wear rate and Au has, on average, the lowest wear rate. The modification of the gold coating results in a large range of the wear rate. In general, the tendency of the relationship between the hardness and the wear rate according to the equation (3) can be observed. It should be mentioned that although the hardness (HV) is proportional to the indentation hardness in (3), in numerical terms they are however not equal due to different definitions. The results of the hardness measurement show some differences to literature values because of the thin coating.

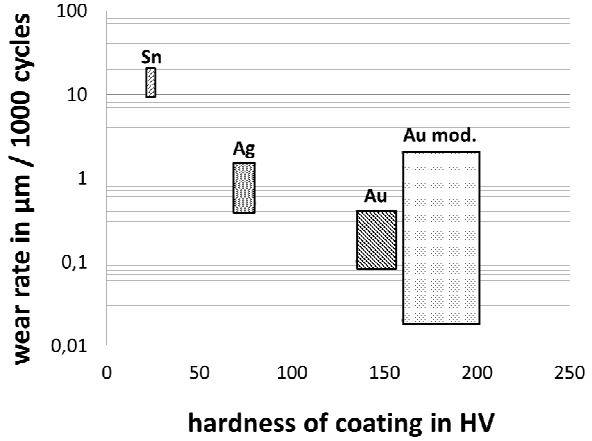

Fig. 5 Wear rate by cycles and hardness of different coating materials

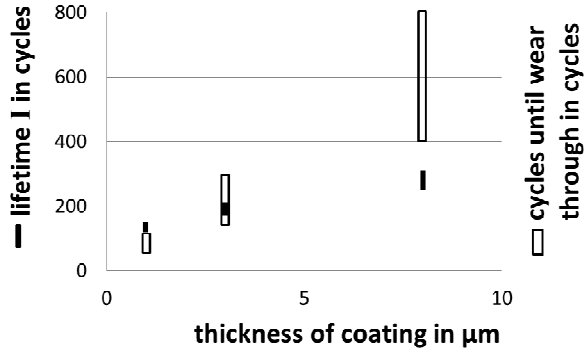

Fig. 6 Lifetime I and thickness of tin coating

Since ignoble coating materials such as tin and nickel oxide and the fretting corrosion of the coating material can lead to the lifetime end of electrical contacts theoretically speaking, the wear through of the coating material must not necessarily be a determining factor for the lifetime. In order to clarify this point, tin coatings with different thicknesses were investigated. Fig. 6 shows the clear correlation between the thickness of the tin coating and the lifetime of electrical contacts. With the increasing thickness lifetime I increases and the number of the cycles at the end of the lifetime I is within the range of the number of cycles, which leads to the wear through of the tin coating at least for the thickness of 1 and 3 µm. This

means that not only the fretting corrosion of the tin coating but also the fretting corrosion of the nickel interlayer determines the lifetime of electrical contacts with a thin coating.

The relationship for the variously modified gold coatings is much more complicated. Not only the hardness, but also the lifetime and wear rate display a large range. The extremely large ranges of wear rate and lifetime of modified gold coatings provide evidence for further parameters, which influence the wear rate and lifetime, Fig. 7. The diagram of the lifetime I over wear rate by cycles of variously modified gold coatings shows that there is a clear correlation between the maximum lifetime and the wear rate. However taking all the points in the diagram into account, the relationship between the lifetime and the wear rate presents a confusing picture, which means a high wear resistance is a necessary condition for a long lifetime, but not the sufficient condition. The types of wear also have a strong impact on the lifetime. The bond between the gold coating and the interlayer, the ductility of the coating material and the asperity also determines the lifetime significantly. Only the influence of the types of wear is discussed in this paper. Other factors will be investigated in a further study. The cracks on the coating can lead to a local oxidation of the interlayer, which then causes the first instability of the electrical resistance, which is the end of lifetime I. Lifetime II is more determined by the overall characteristics of coatings. For example all samples with a wear rate of less than 0.1 µm/1000 cycles have a lifetime of 100000 cycles or more, Fig. 8.

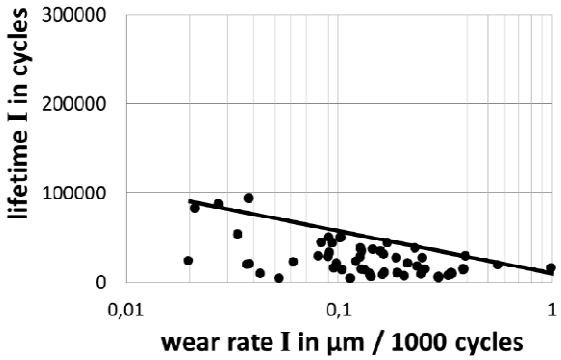

Fig. 7 Lifetime I and wear rate of gold coatings

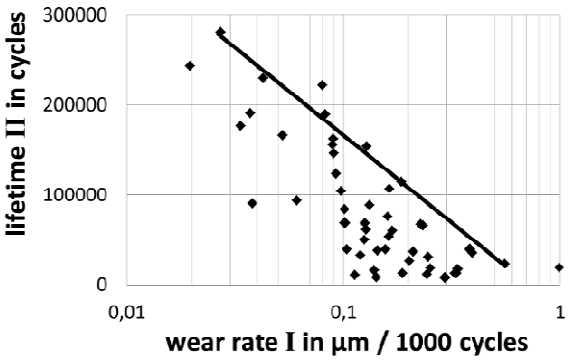

Fig. 8 Lifetime II and wear rate of gold coatings

Starting with a plating system with an interlayer, three wear types can possibly develop [12]:

The first wear type is the total wearing through of the coating, Fig. 9. In this case we have the direct contact of the interlayers, which is prone to oxidation and sensitive to fretting corrosion. Therefore the electrical contacts fail shortly after this stage has been reached.

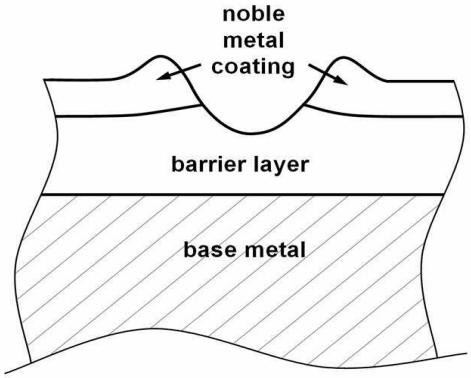

Fig. 9 Wear pattern I – total wearing off of the upper layer. Cross section of plating system of electric contacts after the wear and fretting corrosion test

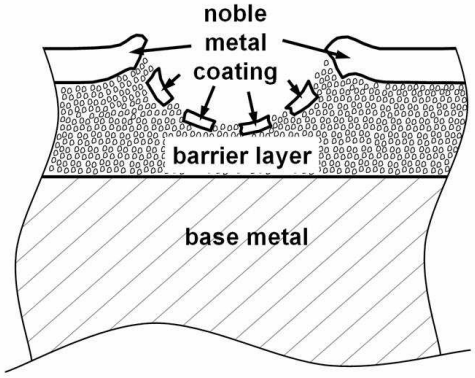

Fig. 10 Wear pattern II - partial wearing off of the upper layer and contact surface not totally covered with oxide.

The second wear type is the most uncritical one for electrical contacts. Noble metal pieces are found in the contact area and they are not covered with oxide, Fig. 10. Therefore a relatively low contact resistance is measured in this case. The electrical contacts function properly in most cases and a very long lifetime II can be expected. In order to achieve the second wear type, it is very important that coatings have a high ductility. Since the development of ductility and hardness is contradictory, gold coatings with a very high hardness do not result in a long lifetime of electrical contacts

However noble metal at the bottom of the wear crater is not the only criterion for the correct functioning of electrical contacts. If the noble metal pieces are covered with debris of oxide (the third wear type), the contacts will also fail.

4 CONCLUSIONS

Our study shows the relationship between the wear behaviours of different coating materials and the lifetime of electrical contacts. Due to various degradation mechanisms of electrical contacts, the correlation between the wear and electrical properties can be rather different for ignoble coating materials such as tin and nickel and for noble coating materials such as gold and silver. The wear through of coatings of noble coating materials is a determining factor for the lifetime, whereas the oxidation and the fretting corrosion of ignoble coating materials can lead to the lifetime end of electrical contacts without wear through of coatings. For noble coating materials, an extension in lifetime can be achieved by the modification of coating materials. This study provides suggestions for the development of new coatings for electrical contacts. It also shows that in the case of electrical contacts both the fundamentals of tribology and the physics of electrical contacts have to be considered in order to understand the results of the study correctly and that the special aspects of the wear of electrical contacts must be taken into account.

5 ACKNOWLEDGEMENTS

The authors would like to acknowledge the financial support of the European Union (EU, Project Nanogold), the German Federal Ministry for Education and Research (BMBF) and the German State of North Rhine-Westfalia (NRW). Enthone GmbH, Langenfeld, RWTH University, Aachen, University of Paderborn, KME, Stolberg and Phoenix Contact, Blomberg supported the investigation with materials, specimens and measurements. Mr. C. conducted the hardness measurements.

6 REFERENCES

[1] Holm. R., Electric Contacts, Springer, Berlin, pp. 2–11, 1967.

[2] Vinaricky, E. (Ed.), Elektrische Kontakte, Werkstoffe und Anwendungen, Springer, Berlin, 2002

[3] Slade, P., Electrical contacts. Principles and applications, Dekker, New York, 1999

[4] N.N., Surfaces, Interfaces, and their Applications II - Introduction to Wear, ETH, Zurich, 2014

[5] Popov, V. L., Kontaktmechanik und Reibung, , Springer, Berlin Heidelberg 2009

[6] Antler, M., “Tribology of Electronic Connectors” in P.G. Slade (Ed.), Electrical Contacts – Principles and Applications. Marcell Dekker, New York, 1999, pp. 332-364

[7] Ben Jemaa, N., Swingler, J., Correlation between Wear and Electrical behaviour of contact interface during fretting vibration. ICEC 2006, pp. 215-219

[8] McBride, J.W., On the Relationship between Surface Wear and Intermittency during Fretting in Electrical Contacts. Proc. of 52nd Holm Conf, Montreal 2006, pp. 273-280

[9] Song, J., Wear of electric contact surfaces. Proceedings of the STLE/ASME International Joint Tribology Conference (IJTC2007), San Diego, 2007

[10] Noel, S., Lecaude, N., Correia, S., Gendre, P. and Grosjean, A.: Electrical and tribological properties of tin plated copper alloy for electrical contacts in relation to intermetallic growth. Proc. of 52nd Holm Conf, Montreal 2006

[11] N.N., SP 8063, NASA, 1971, pp. 8-9.

[12] Song, J., Koch, C.: Wear Patterns and Life Time of Electric Contacts. Proceedings of 54 IEEE Holm Conference on Electrical Contacts, pp. 238-244, 2008.

Proceedings of the 3rd International Conference on
Fracture Fatigue and Wear, pp. 281-287, 2014

FRICTION WEAR BEHAVIOUR OF CARBON BASED EPOXY NANOCOMPOSITES

J. Abenojar[1], J. Tutor[2], Y. Ballesteros[2], J.C. del Real[2], M.A. Martínez[1]

[1] Universidad Carlos III de Madrid, Leganés, Spain
[2] Universidad Pontificia Comillas, Madrid, Spain

Abstract: Mechanical erosion and friction can be a major problem in many mechanical systems such as hydraulic equipment, fluid pump impellers, ship propellers, hydrodynamic bearings, fluid seals, inlets to heat-exchanger tubes, diesel engine wet cylinder liners, hydrofoils, liquid metal power plants, steam turbines, etc. Cavitation erosion is one of the most dangerous degradation mechanisms, since it causes huge surface damages. It is induced by the explosion of vapour bubbles that exert a pressure pulse. Anti-wear coatings based on epoxy resins are used to protect the equipment. The carbon-based nano-materials can change the mechanical, thermal and electrical properties of coatings, but only few studies on tribological properties have been published. Therefore, this work was carried out to investigate the effect of carbon based epoxy nano-composites on the wear performance. The wear tests (ASTM G99) were carried out in bulk and with a coating of 1 mm thickness on aluminium substrate. Pin on disk wear test were carried out in dry sliding conditions against an alumina ball. The epoxy resin was Hysol 9483, while (G), graphene oxide (GO) and carbon nanotubes (MWCNT) were used as carbon additions at 0.5 wt.% loading. The tracks wear were tested and characterized by optical microscopy and the wear debris powders were characterized by X-ray diffraction.

Keywords: wear; epoxy; carbon nano-composite; x-ray diffraction

1 INTRODUCTION

Today's polymer matrix polymer composites (PMC's) are used in all industrial applications which require their components to have highly specific properties such as reduced weight, complex form and very high performance. The reinforcement or filler for these composites varies according to the required properties. The epoxy matrix is widely used in many composites because of its excellent characteristics in erosion resistance, thermal stability and processing capability. When its properties are modified with micrometer-sized inorganic particulate composites, the fillers detach from the composites during wearing used to act as additional abrasives and originate a three-body wear mechanism [1,2]. These fillers can be treated with silane to improve the mechanical properties, because epoxy resin bonds are created [3]. In contrast with microparticles, nanoparticles have a much greater surface area-to-volume ratio. This ratio is important for bonding the particles to the polymer matrix in the composite material. Moreover, the angularity of the particles is remarkably reduced with decreasing particle size, so that the hard nanoparticles which cannot be used as fillers in the microscale particulate form might be suitable for sliding applications because they are not expected to abrade the counterface [4]. Also, these nanoparticles are modified, thus Long Ji et al. [5] used nano-alumina modified with polystyrene (PS). In this case, the wear rate is reduced to 99% with respect clear epoxy.

Few studies are found with carbon nano-materials as composites filler for wear applications. Only nanotubes based fillers have been extensively investigated in the literature. Among them, wear studies with multi-wall carbon nanotubes (MWCNT)/epoxy composites carried out by Jacobs et al. [6] showed a 50% decrease in the wear when MWCNT are treated with acid or a 90% if, in addition, during the manufacturing process, a speed mixer is used. However, if MWCNT are untreated an increase in the wear is observed. This same work on MWCNT/epoxy composite [7] presents the combined effect, different percentages (between 0.2 – 2 wt.%) and different treatments. The main conclusion of this work was *"The addition of CNTs to an EP matrix can significantly enhance its wear resistance. However, the performance of these composites sensitively depends on the pre-treatment of the CNTs and the mixing procedure".* Though, also friction and wear are system properties and cannot be attributed to a material. So, each system must be researched.

Due to their superior mechanical properties and relatively low cost, graphene composites have been studied for other structural applications, and for highadded value technologies, such as batteries, supercapacitors, fuel cells photovoltaic devices, photocatalysis, sensing platforms, and so on [8]. Although, not many studies on wear properties of grapheme composites are available, Zhu et al. [9] have revealed that the 2-monolayer graphene shows great potential for application as an anti-wear coating.

All these nanomaterials are difficult to disperse and they can produce agglomerations in the composite. The nano-composite can worsen its properties as a consequence of the manufacturing process. So, GO is more used; it is flat sheets of easier dispersion [10]. Anyhow, special techniques must be used.

GO have been extensively used as fillers into composites to improve the mechanical properties. However, the oxygen contained in the functional groups attached to the GO surface make it almost insulating, limiting its electrical and thermal properties. To make GO conductive, a reduction process must be carried out. Among the existing techniques of reduction, the GO used in this study were chemically reduced in an alkaline solution of KOH [11]. The study carried out by Mo et al. [12] on GO/ polyacrylonitrile has showed that GO modified with a silane has potential to industrial applications involving the lubrication and anti-wear of the nano-composite.

From this literature review it turns out that more studies on nano-composites are needed. Consequently, the main objective proposed in this paper is to study and compare chafing in epoxy matrix composites filled with different carbon nano-materials (MWCNTs, G, G modified and GO). The studies of the wear mechanisms for the different nano-composites and their properties to other types of wear (i.e. erosion wear) are beyond the scopes of this work but suggestions for further studies are provided.

2 EXPERIMENTAL PROCEDURE

2.1 Materials

The selected epoxy was Hysol 9483 (named hereafter Hysol), supplied by Henkel Adhesivos y Tecnologías S.L. (Navalcarnero, Madrid, Spain). It has low viscosity (7 Pa·s) at 25 ºC, high mechanical strength (UTS of 47 MPa according to the manufacturer) and it cures at room temperature for 12 h. Its chemical composition is based on resin (component A), on 4,4'-Isopropylidendiphenol and the hardener (component B) is 4,7,10-trioxa-1,13-tridecanediamine. The resin-hardener mass ratio is 100:46.

All specimens were prepared containing 0.5% by weight of nano-filler. The nano-fillers used were: Graphene (G): avanGRAPHENE (1-2 layers) by Avanzare Innovacion Tecnologica S.L. (Logroño, Spain); Graphene oxide (GO by Nanoinnova Technologies S.L. (Madrid, Spain); Thin Multi-wall Carbon nanotubes (MWCNT) Nanocyl™ NC 7000 by Nanocyl (Sambreville, Belgium); and functionalized graphene (G-KOH): supplied by Nanoinnova Technologies S.L. (Madrid, Spain).

2.2 Preparation of carbon/epoxy nano-composites

Table 1 shows all composites used in this work and the acronym hereafter used in this paper.

Table 1 Composites and nomenclature used in this work

Hysol	Hysol+0.5 wt. % thin multi wall carbon nanotubes	Hysol+0.5 wt. % graphene	Hysol+0.5 wt. % graphene oxide	Hysol+0.5 wt. % graphene treated with KOH
H	H05MWCNT	H05G	H05GO	H05GKOH

For each type of nano-composite, 50 g of mixture were prepared by weighing 0.25 g of nano-filler on an analytical balance (by Mettler Toledo, Greifensee, Switzerland) with an accuracy of 0.01 mg. 34.08 g of the component A were added. Afterwards, the mixture was blended for 5 min with the propeller of the overhead stirrer (by Schott Iberica S.A, Barcelona, Spain) at 500 r.p.m., and sonicated in Digital Sonifier® Cell Disruptor 450 by *Branson* Ultrasonics Corporation (Connecticut, USA), employing a microtip. The amplitude was 40% and the time of sonication 10 min. To avoid the overheating, the mixture was immersed in a stirred cold water bath and the sonication was carried out with periods of 10 seconds on and 10 seconds off. Due to the cavitation effect during sonication, the mixture contained lots of bubbles. The deaeration was carried out in a vacuum oven Nüve EV018 (by Nüve, Ankara, Turkey) for about 10 minutes or until complete disappearance of the bubbles. The pressure reached in the oven was -0.9 bars. Finally, 15.67 g of the component B were added to the mixture. After mixing with a glass rod, the bubbles are removed in the vacuum oven for 2 min. The final adhesive blend is poured into a silicone mold to obtaining specimens of 30x30x4 mm. The mold is covered with a Teflon sheet and a weight of 5 Kg thereon. Curing

took place heating to 40 ºC in an oven for 60 min and then increasing the temperature to 80 ºC for 60 more min, including the heating ramp, to ensure full curing of the adhesive and its maximum strength.

2.3 Wear properties

Dry wear tests were carried out at room temperature using a pin-on-disk tribometer (Microtest, Madrid, Spain) according to ASTM G99-05 on cylindrical specimens (Eq. 1). A 6 mm-diameter alumina ball was used for the pin. Test conditions were 120 rpm, with an applied load of 15 N, and relative humidity below 30%. The sliding distances were 500, 1000, 2000 and 4000 m. Thus, it is possible to construct a graph wear versus distance.

$$W\,(\mathrm{mm^3/N\cdot m}) = \frac{\mathrm{Volumen\,loss\,(mm^3)}}{\mathrm{Load\ (N)\cdot distance(m)}} \tag{1}$$

Where volume loss can be calculated according to Eqs. 2 and 3. According to Eq. 2 the mass loss and density of all materials was obtained weighing and measuring samples (Density = Mass/Volume)

$$\mathrm{Volumen\,loss\,(mm^3)} = \frac{\mathrm{Mass\,loss\,(g)}}{\mathrm{Density\,(g/cm^3)}}\ \mathrm{x}\,1000 \tag{2}$$

Also, volume loss were calculated by a geometric relationship (Eq. 3) using a Nikon Profile Projector V profilometer 20 (Nikon Instruments Inc, Melville, NY), in this case no significant pin wear was assumed. In two cases the wear were defined in $(\mathrm{mm^3/N\cdot m})\cdot 10^{-4}$.

$$\mathrm{Volumen\,loss\,(mm^3)} = \frac{\mathrm{(Wear\,scar\,diameter\,(mm))\ x\ (Track\ width\,(mm))^3}}{6\,/\mathrm{(sphere\,radius\,(mm))}} \tag{3}$$

Aluminium specimens coated with the composite were also tested in the same conditions, for 1000 m distance.

The average friction coefficient was obtained by the tribometer (as bending-type force transducer). Finally, the wear tracks were studied with optical microscopy Olympus GX71 by Olympus Corporation (Tokyo, Japan).

All samples were sanded manually before testing with sandpaper 600. Moreover, wear debris powders were characterized by X-ray diffraction. Analysis of the powder can give information if the nano-particles or nano-tubes were released during wear.

3 RESULTS

Table 2 shows the density calculated for the materials, which were used for the volume estimation exploiting Eq. 2. The relative densities obtained were around 98-99%. Consequently, although the materials were not 100% dense and had some bubbles therein, the processing method can be considered acceptable.

Table 2 Materials density used for the volume calculation according Eq. 2

Material	Hysol	H05MWCNT	H05G	H05GKOH	H05GO
Density (g/cm^3)	1.11 ± 0.02	1.15 ± 0.03	1.19 ± 0.01	1.19 ± 0.01	1.17 ± 0.004

Figure 1 shows the wear curves vs distance for Hysol (clear epoxy). The two methods used for wear calculation are compared. The two curves are quite similar; the small differences observed may be due to errors in the measurements of the profiles or to the density estimation. Furthermore, in the case of coatings, the wear values obtained match for the two methods. A maximum is observed at 1000 m distance. For longer distances, low wear remains more or less constant. At the beginning, track is formed, between 500 and 1000 m, yet the increase in track width is important, but after that time the increase is small. In micrographs (Fig. 1) the wear tracks with 5x magnification are observed. Abrasive scratches and material accumulation zones are found. Therefore, wear is abrasive-adhesive, more abrasive during the initial phase and more adhesive with the distance.

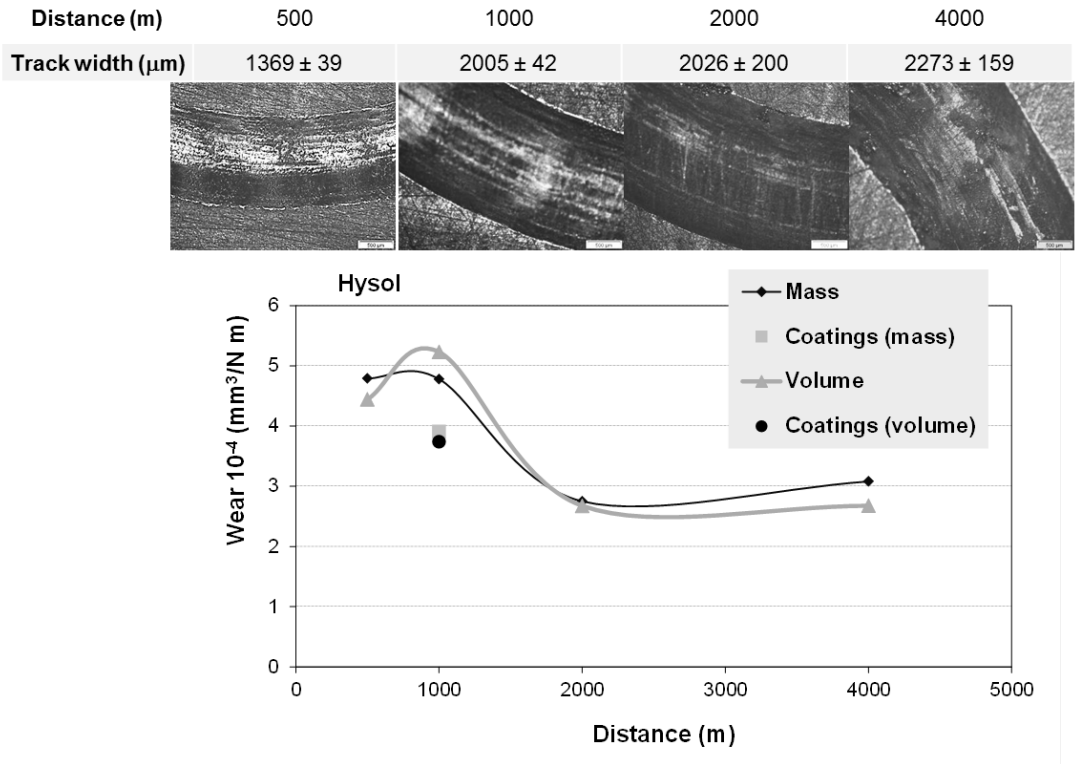

Fig. 1 Wear vs distance, wear track micrographs and track width for Hysol

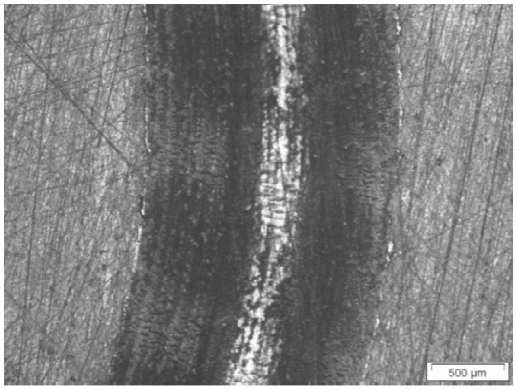

Fig. 2 Wear track micrographs of Hysol coating on aluminium, after 1000 m of distance

The wear of coatings is lower than that of the bulk material (Fig. 1). A micrograph of the wear track on the coating is shown in Fig. 2. Abrasive scratches are found in the centre of the track, and there is resin accumulated at the edges of the track. For the coating, the track width is 1705 μm, intermediate value between those obtained in the bulk material tested for 500 and 1000 m.

In Table 3 the wear for all nano-composites with clear resin are compared. All nano-composites show a maximum, although this is not at the 1000 m. For H05MWCNT, H05G and H05GKOH the maximum appears at 500 m; then the value of wear decreases and at 1000 m it is slightly lower than for the clear resin. However, it is higher for 2000 and 4000 m, except for the H05GKOH, where it shows a decrease at 4000m.

The H05GO nano-composite has a different behaviour, the wear varies little with distance, at 4000 m a small decrease is observed.

In all tracks, wear is observed at specific accumulative zones of the material (Fig. 3). This is due to an adhesive wear mechanism. Only for H05G, it is observed a larger track width (Fig. 3), although wear is not significantly higher (Table 3). This could be due to an elastic recovery of the material after the test. Recovery would be confirmed by a big difference in the wear according to the method used, but the wear is similar, 3.26×10^{-4} $mm^3/N \cdot m$ for mass method and 3.54×10^{-4} $mm^3/N \cdot m$ for geometric or volumetric method. Therefore, it must be assumed that the pin has moved during the test, in particular it has jumped as a result of the material accumulation.

Table 3 Wear ($mm^3/N \cdot m$) 10^{-4} values obtained according to volume calculation Eq. 3

		Materials				
	Distance (m)	**H**	**H05MWCNT**	**H05G**	**H05GKOH**	**H05GO**
	500	4.44	**6.52**	**7.78**	**10.00**	4.27
	1000	**5.23**	4.58	4.93	4.86	4.69
	2000	2.67	3.75	4.03	2.76	**4.89**
	4000	2.67	3.01	3.54	1.83	3.46
Coating	**1000**	3.74	4.56	4.30	5.53	5.05

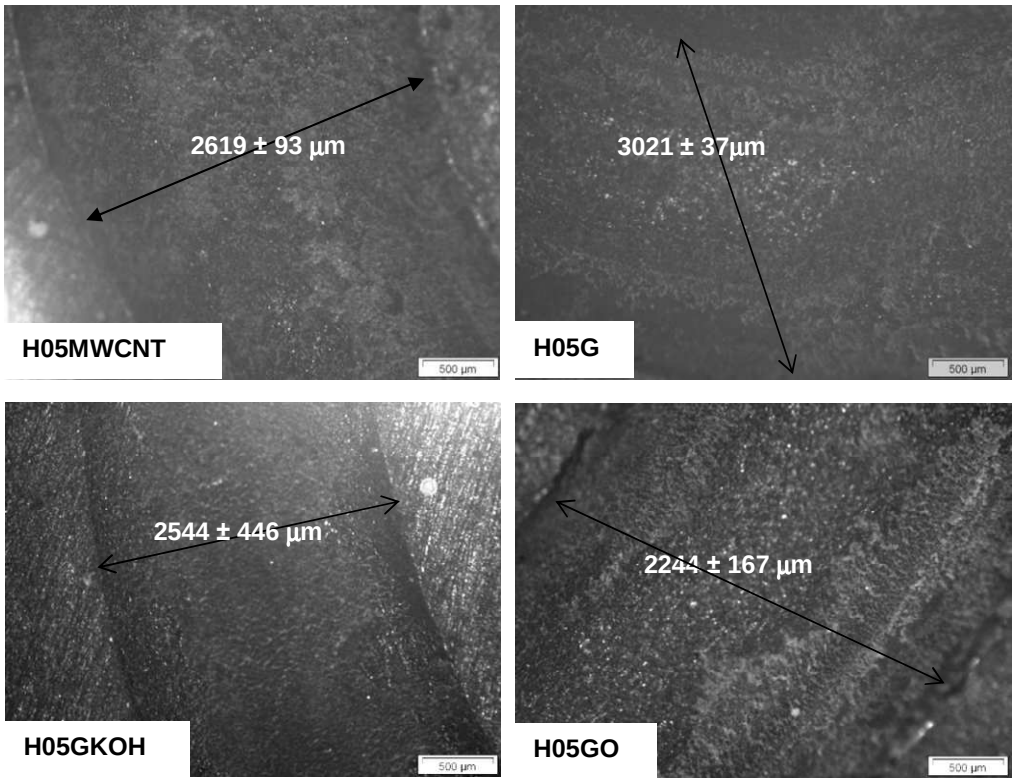

Fig. 3 Wear track micrograph and track width for nano-composites after 4000 m of distance

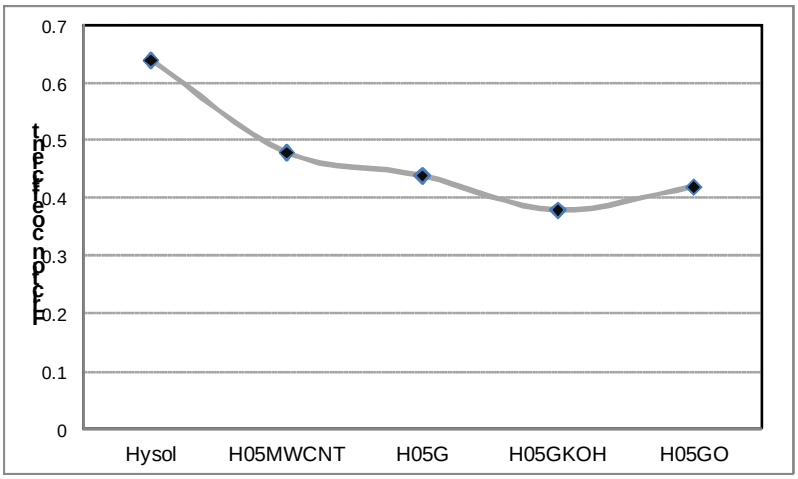

Fig. 4 Friction coefficient for all materials to 4000 m track distance

Friction coefficients were obtained directly from the tribometer. The calculation was performed as an average value of the stable region of the curve friction coefficient versus distance. In all nano-composites the value is stable around 0.4-0.5 for all tested distance (including coatings), while the clear resin has a minimum of 0.48 (500 m) and a maximum of 0.64 at 4000 m. Fig. 4 shows the friction coefficients for 4000 m to track distance.

Carbon additions, composites and debris powder were analyzed by X-ray diffraction. When diffracto-grams are compared with XRD patterns of the GO and the MWCNTs [13] they show no free MWCNT, G, or GO GKOH. In all samples, a broadband, centred of 20º approximately, is observed. This broadband is equal to that found in the composite before testing; therefore nano-materials used as reinforcement are embedded in the epoxy resin. Debris powder is micrometric and it is not hazardous either to the environment or health.

4 CONCLUSIONS

Except for H05GO nano-composite, the value of maximum wear of nano-composites appears at sliding distances short than those found for the clear epoxy resin. Moreover, nano-composites suffer more wear than the clear epoxy resin at short distances. Overall, wear stabilization in the nano-composites does not take place as clearly as in the resin and continues to slightly decline with distance.

In H05GO nano-composite, the wear is practically constant over the entire studied distance.

The nano-composites have a friction coefficient lower that the clear epoxy resin, revealing the presence of a lubrication effect.

The added nano-carbon fillers do not detach freely to the environment in the wear debris, hindering any type of harmful emission.

5 ACKNOWLEDGEMENTS

The authors would like to acknowledge the support of this research to the Spanish Ministry of Science and Innovation (through project MAT2011-29182-C02-02).

6 REFERENCES

[1] J. Abenojar, M.A. Martínez, M. Pantoja, F. Velasco, J.C del Real, Nano and micro SiC particles reinforced epoxy composite: Curing kinetics and mechanical properties, Journal of Adhesion, 88(4-6), 418-434, 2012.

[2] J. Abenojar, M. A. Martínez, F. Velasco, V. Pascual-Sánchez, J.M. Martín-Martínez. Effect of boron carbide filler on the curing and mechanical properties of an epoxy resin. Journal of Adhesion, 85(4-5) 216-238, 2009.

[3] J. Abenojar, J.C. del Real, M. Cano de Santayana, M.A. Martinez, Effect of silane treatment on SiC particles used as reinforcement in epoxy resins, Journal of Adhesion, 85(6) 287-301, 2009.

[4] C.J. Schwartz, S. Bahadur, Studies on the tribological behaviour and transfer film–counterface bond strength for polyphenylene sulfide filled with nanoscale alumina particles. Wear, 237, 261-267, 2000.

[5] Q. Long Ji, M. Qiu Zhang, M. Zhi Rong, B. Wetzel, K. Friedrich, Tribological properties of surface modified nano-alumina/epoxy composites, Journal of Materials Science, 39, 6487–6493, 2004.

[6] O. Jacobs, W. Xu, B. Schadel, W. Wu, Wear behaviour of carbon nanotube reinforced epoxy resin composites, Tribology Letter, 23(1), 65–75, 2006.

[7] O. Jacobs, B. Schädel, Wear behaviour of carbon nanotube-reinforced polyethylene and epoxy composites in: B.J. Briscoe (Ed.), Tribology of polymeric nanocomposites, Elservier Ldt.,Oxford, 2008, pp. 209-242.

[8] X. Huang, X. Qi, F. Boey, H. Zhang. Graphene-based composites. Chemical Society Reviews. 41, 666-686, 2012.

[9] Q.R. Zhu, H.Q. Li, N. Li, J. Chai, R.G. Gao, Q. Liang. Nanotribological and wear properties of graphene. Acta Physico-Chimica Sinica, 29 (7) 1582-1587, 2013.

[10] J. Du, H.M. Cheng. The Fabrication, properties and uses of graphene/polymer composites. Macromolecular Chemistry and Physics, 213, 1060−1077, 2012

[11] X. Fan, W. Peng, Y. Li , X. Li, S. Wang, G. Zhang, F. Zhang. Advanced Materials, 20(23) 4490–4493, 2008.

[12] Y. Mo, M. Yang, Z. Lu, F. Huang. Preparation and tribological performance of chemically-modified reduced graphene oxide/polyacrylonitrile composites. Composites: Part A, 54, 153–158, 2013.

[13] X-J, Shen, X-Q, Pei, Y, Liu, Sh-Y, Fu. Tribological performance of carbon nanotube–graphene oxide hybrid/epoxy composites. Composites Part B, 57, 120-125, 2014.

Proceedings of the 3rd International Conference on
Fracture Fatigue and Wear, pp. 288-294, 2014

STUDY ON THE SLIDING WEAR MECHANISM OF THE WHITE METAL

K. Masuda[1], S. Ishihara[2], T. Kobata[1] and M. OKane[2]

[1]University of Toyama, Toyama, Japan
[2]Toyama National College of Technology, Toyama, Japan

Abstract: In the present study, sliding wear tests were performed in laboratory air, in several lubricant oils with different viscosities and in water. The pin-on-disk type abrasion testing machine was utilized in the present study. In the machine, the pin was made of white metal JIS WJ2, and the disk was made of steel (JIS S45C). The results obtained showed that the rate of wear, *dW/dL* increases with an increase in the compressive normal stress that is applied to the contact area, where *W* and *L* are the amount of wear volume per unit area and the sliding distance, respectively. Similarly, it was found that the rate of wear is proportional to the shearing stress that acts on the contact area. In addition, it was found that the threshold values of the compressive normal as well as the shearing stresses exist, below which the amount of wear does not occur. The constitutive wear law for the material JIS WJ2 was realized, which is independent of the environment used. Sliding wear lives for the different lubricant oils and water were successfully estimated using the above constitutive wear law that was obtained experimentally. The estimated results correspond well with the experimental ones. It means that this evaluation method for the sliding wear lives on the basis of the wear constitutive law is useful and has a wide application. A SEM (Scanning Electron Microscope) was also performed to investigate the sliding wear mechanism.

Keywords: Friction; Wear resistance; Tribology; Sliding contact; White metal; lubrication

1 INTRODUCTION

Oil-lubricated sliding bearings employing white metal are widely used in many industrial, marine and automotive applications. These bearings normally operate in a stable, hydrostatic condition wherein a proper film thickness of oil is formed and maintained between the shaft and bearing. However, when a sufficiently thick oil film is not formed between the shafts and bearing due either to excessively high loads, high shaft speeds or improper lubricating conditions, the white metal of the bearing may be damaged [1, 2]. White metal can be fundamentally classified into two types; one has lead as its main component, the other tin [3].
In the present study, sliding wear tests were performed using tin-based white metal in laboratory air, in several lubricant oils in order to clarify the wear resistance mechanism. The sliding wear life was successfully evaluated using a wear constitutive law proposed by the one of the authors [4].

2 SPECIMEN AND EXPERIMENTAL PROCEDURE

2.1 Specimen

Shapes and dimensions of the pins used are shown in Fig. 1. The pin shown in Fig. 1(a) was used at the high and medium compressive stress region. In the tests at the low compressive stress region, the pin on the right side (Fig. 1(b)) was adopted in order to avoid the partial contact between the pin and the disk. The pin was made of tin-based casting white metal. Chemical compositions and mechanical properties are listed in Tables 1 and 2, respectively. Carbon steel, JIS S45C was used as the counter material, i.e. the circular disk that has a diameter 200 mm and thickness 40 mm.

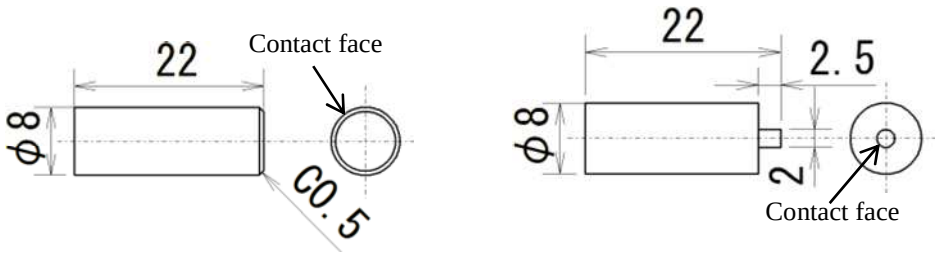

(a) (b)

Fig. 1 Shapes and dimensions of the pin used in the present study.

Table 1 Chemical compositions of the pin.

Sb [%]	Cu [%]	Sn [%]
5	2-3	bal.

Table 2 Mechanical properties of the pin.

0.2% proof stress[MPa]	Shear yield stress[MPa]	Poisson ratio[-]	Density [g/cm^3]
32	16	0.38	7.27

2.2 Experimental procedures

A schematic representation of the wear testing equipment is shown in Fig. 2. Pin-on-disk type abrasion testing machine was utilized in the present study. The definition of the compressive normal stress was $\sigma=P/A$, where P is the applied load, A is the contact area. The pin was located just 65 mm from the centre of the disk. The rotating speed was set to 2 m/s. Two kinds of oils were used as lubricating liquids. One was Diluted HOCOT 800 (described as Oil (A) hereafter) having viscosity 21.4 Pa·s at 313 K, the other was MOBIL DTE VG100 Heavy (described as Oil (B) hereafter) having viscosity 409.7 Pa·s at 313 K. In addition, water was also employed as a lubricant.

The frictional force F during the sliding wear process was continuously monitored using electric signal from the strain gauges that is cemented to the pin-support bar (Aluminium alloy), as shown in Fig. 2(b). The shearing stress τ was defined as $\tau=F/A$.

The sliding wear tests were interrupted at a constant interval to measure the pin's weight. First, the pin was removed from the testing machine, and was cleaned by ultrasonic cleaning. Then the pin was weighed. The wear volume per area, W, was determined by the next equation, $W=\Delta M/(\rho A)$, where ΔM: weight loss of the specimen, ρ: density of the material, A: the area of the contact surface. So the wear volume per area determined as above actually means the wear depth of the material.

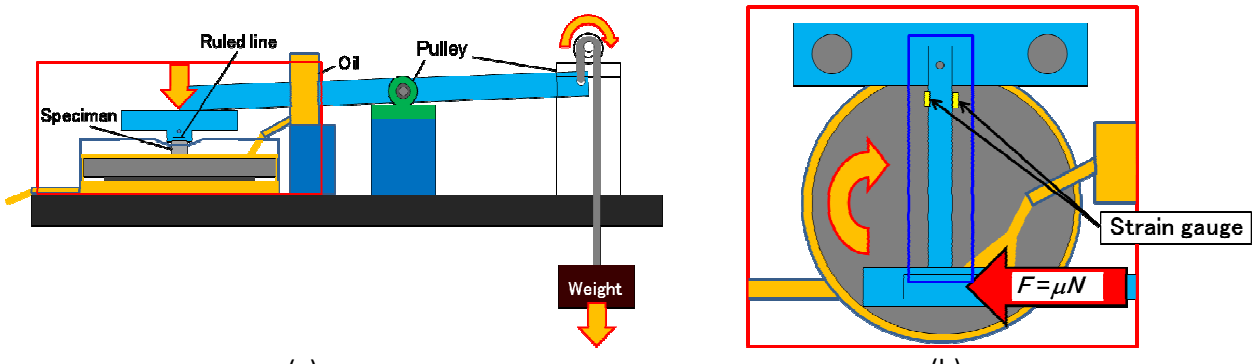

(a) (b)

Fig. 2 Schematic representation of the wear testing equipment : (a) Side view ; (b) Top view

3 EXPERIMENTAL RESULTS

3.1 Effects of environment used on the amount of wear

Fig. 3(a) shows the changes of the wear volume per area, *W*, as a function of the sliding distance, *L* for the eight levels of the compressive normal stress σ in laboratory air (dry condition). As seen from the figure, the relations of *W* and *L* can be represented by the straight lines, which are differed by the compressive normal stresses. The slope of the relation, *dW*/*dL* means the rate of wear for each of the stress level. As can be seen from the figure, the slope, i.e., the rate of wear *dW*/*dL* increases with an increase in the compressive normal stress. In addition, it is found that the amount of wear does not occur at the threshold compressive stress σ_{th}, less than 0.0008 MPa. Figs. 3(b), 3(c) and 3(d) show the *W* - *L* relations in three different lubricants, i.e., in water, in oil(A) and in oil(B), respectively. As seen from these figures, the same tendency with the results in the dry condition shown in Fig. 3(a) can be observed. However, it is found that the amount of wear decreases with an increase in the viscosity of the lubricant.

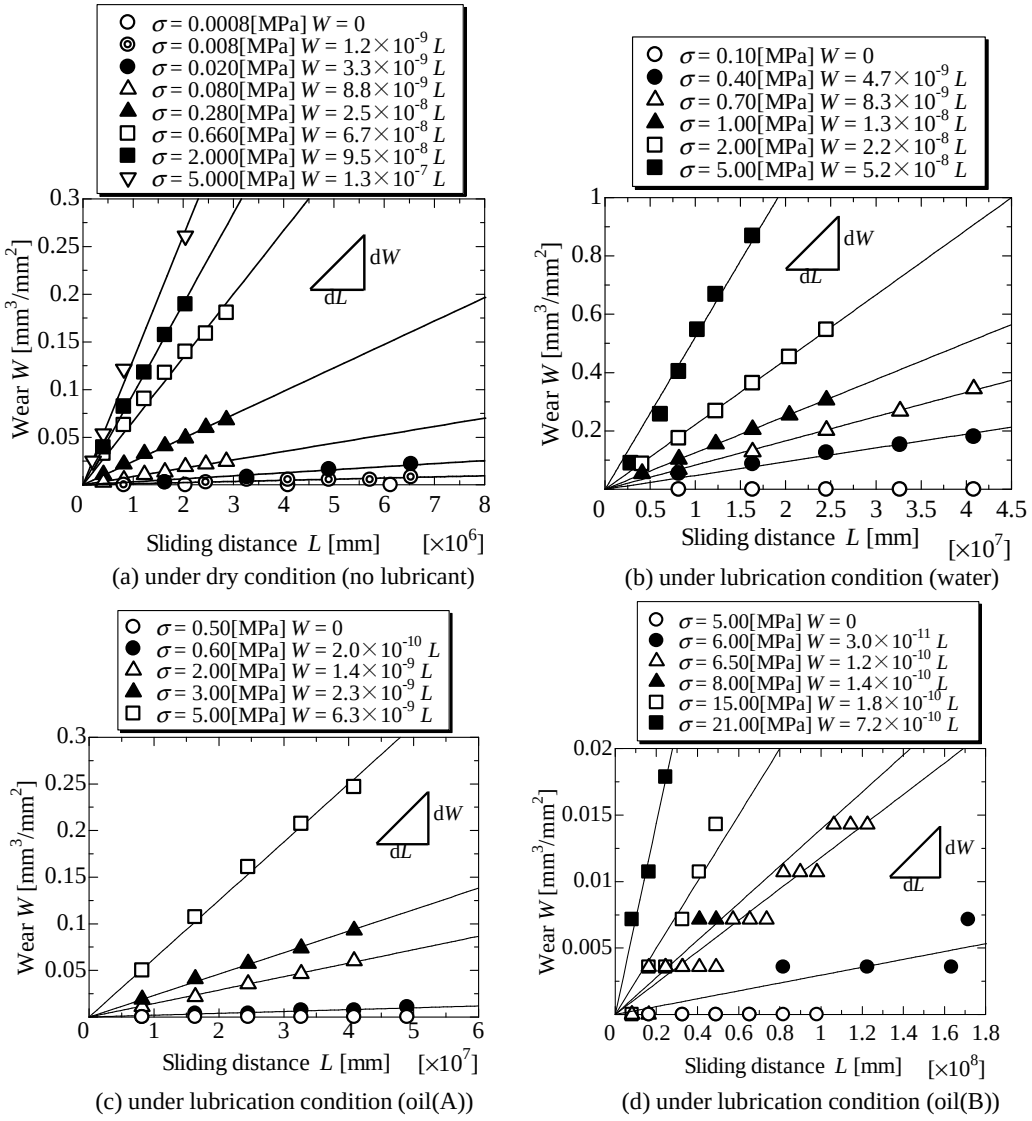

Fig. 3 Relations between *W* and *L* in the different environment.

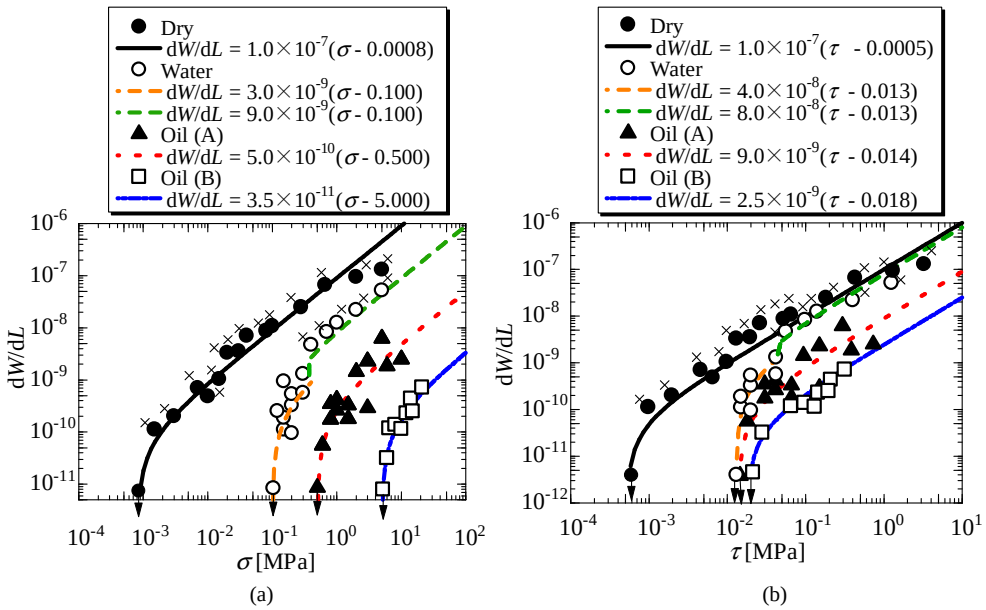

Fig. 4 (a) Relations of *dW*/*dL* and σ and (b) Relations of *dW*/*dL* and τ.

Figure 4(a) shows the log-log plot between the rate of wear, *dW*/*dL* and the compressive normal stress σ . The same data *dW*/*dL* was plotted as a function of the shearing stress τ in Fig. 4(b). As seen from these figures, the *dW*/*dL* vs. σ relations differ with the experimental conditions, i.e., in the dry condition and in the three lubricants. However in the *dW*/*dL* vs. τ relations, the above differences in the *dW*/*dL* vs. σ get fewer. In the three lubricants, i.e., water, oil(A) and oil(B), they are almost the same with each other, especially at the low τ region. At the high τ region, the value *dW*/*dL* in the water is higher than those in the oil(A) and oil(B). This dissimilarity is referred from the different wear mechanism. In Fig. 4(b), the open circles with "x" means that the severe wear was occurred at those region. In the other region, mild wear was observed as indicated by the open circles without "x". In the dry condition, the severe wear was seen at the whole region of the shearing stress as indicated by the solid circles with "x".

3.2 Observations of sliding surfaces

Figure 5 compares the appearances of the sliding surfaces of the specimens due to the different conditions, i.e., dry condition, water, oil (A) and oil (B). The comparison was made at the constant compressive normal stress of 5 MPa, and at the constant sliding distance of 8.2 km. The sliding wear direction is from the right side to the left one.

As seen from Fig. 5(a) (Dry condition), severe abrasion flaws can be seen on the sliding wear surface. This observation result was confirmed in the entire region of the sliding surface. So, the severe wear occurs in the whole region of the dry condition, as stated above with Fig. 4.

In the water condition, the sliding-wear damage changed with the applied stress. When the high compressive stress was applied to the specimen, the boundary lubrication or the mixed-mode lubrication was seen. So, as seen in Fig. 5(b), the abrasion flaws are seen due to the partial contact between the pin and the disk. On the other hand, at the low compressive stress region, the sliding was in the condition of the fluid lubrication. On the other hands, as seen from the Figs. 5(c) and 5(d), a few flaws can be seen on the sliding surface, which indicating that mild wear occurs in the oil-lubricant condition.

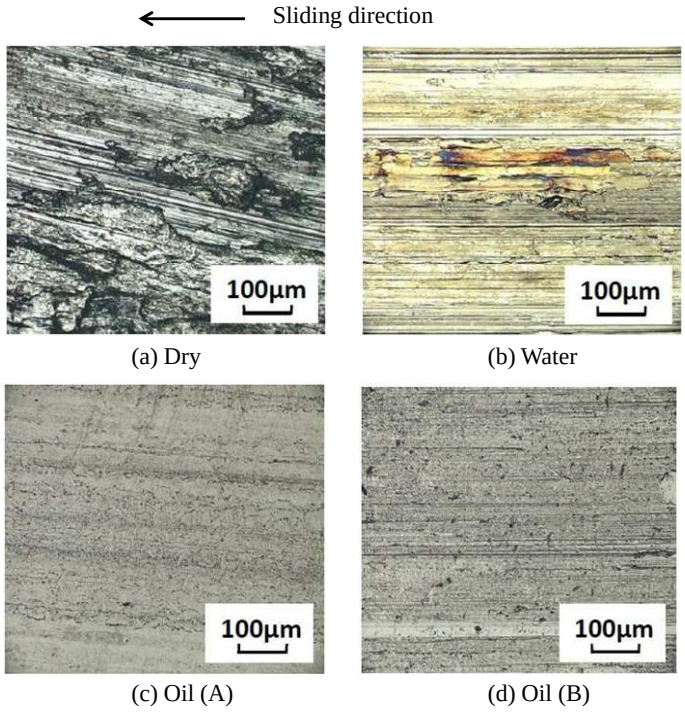

(a) Dry (b) Water

(c) Oil (A) (d) Oil (B)

Fig. 5 Sliding surfaces of the pins

3.3 Wear constitutive law

The solid and broken curves in the Figs. 4(a) and 4(b) are represented by the equations (1) and (2):

$$\frac{dW}{dL} = A_1\left(\sigma - \sigma_{th}\right) \tag{1}$$

$$\frac{dW}{dL} = A_2\left(\tau - \tau_{th}\right) \tag{2}$$

Where, σ_{th} and τ_{th} are the threshold stresses below which the wear damage does not occur, and A_1 and A_2 denote material constants. As seen from the Figs. 4(a) and (b), dW/dL-σ and dW/dL-τ relations are in accordance well with the equations (1) and (2).

4 DISCUSSIONS

4.1 Evaluation of the wear lives

The wear constitutive law of the material, Eq. (1) was utilized for evaluations of the wear lives. Integrating Eq. (1) from the initial wear value W_0 to the given wear-depth W_f, wear lives L_f at the given wear-depth can be estimated as follows, where L_o indicates the initial sliding distance.

$$\int_{L_0}^{L_f} dL = \frac{1}{A_1}\int_{W_0}^{W_f} \frac{1}{\left(\sigma - \sigma_{th}\right)} dW \tag{3}$$

$$L_f - L_0 = \frac{1}{A_1}\frac{W_f - W_0}{\left(\sigma - \sigma_{th}\right)} \tag{4}$$

Putting W_0=0 at L_0=0, then the following relationship between the compressive stress σ and sliding wear lives L_f can be obtained,

$$L_f = \frac{1}{A_1}\frac{W_f}{\left(\sigma - \sigma_{th}\right)} \tag{5}$$

By using a similar calculation process with eq. (2), the relation τ and L_f can be derived as follows.

$$L_f = \frac{1}{A_2}\frac{W_f}{(\tau - \tau_{th})} \tag{6}$$

Figs. 6(a) and (b) show the comparison between the experimental and the calculation results for σ-L_f and τ-L_f relations, respectively. The comparison was made for the dry condition. For the given wear-depth W_f, three different values of W_f were adopted (W_f=0.005 mm, 0.05 mm and 0.5 mm). For the calculation, Eq. (5) and Eq. (6) were used in A_1=1.0x10^{-7} MPa^{-1} and A_2=1.0x10^{-7} MPa^{-1}. As can be seen from these figures, the experimental results are in accordance well with the calculation ones. So, the wear constitutive law, Eq. (1) is useful for predicting the wear lives of the material.

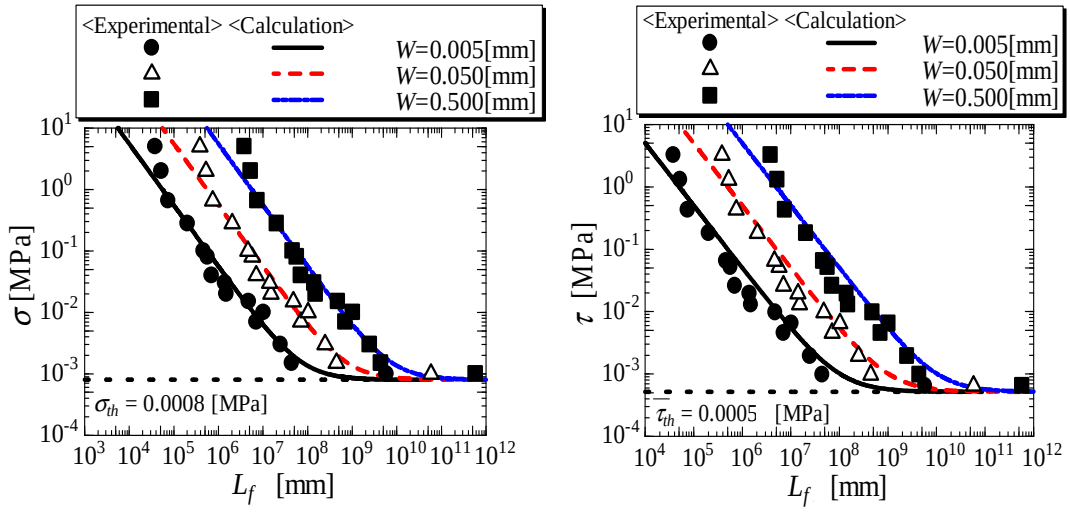

(a) Relations of L_f and σ of the dry condition

(b) Relations of L_f and τ of the dry condition

Fig. 6 Comparison between the experimental results and the calculation results for three levels of W_f

4.2 On the physical meaning of the threshold values

To discuss on the physical meaning of the threshold stresses, σ_{th} and τ_{th}, the oil film thickness, h_0 was measured during the sliding process, where h_0 was defined as the distance from the pin surface to the disk surface. Figure 7 shows the h_0-σ and μ-σ relations obtained from the tests in the oil(B) condition. μ is the coefficient of friction between the pin and the disk. As seen from the figure, h_0 decreases with an increase of the compressive stress σ, and reaches to the minimum value of 1~3 μm at σ= 5~8 MPa. Then, the value of h_0 takes a constant value less than 1 μm for the region σ > 5 MPa. On the other hand, the value of μ takes the minimum value at the compressive stress σ = 5 MPa. Based on both the reference [5], and the above experimental result, it is expected that the fluid lubrication occurs at the region, σ < 5 MPa and the mixed-mode lubrication occurs for the region, σ > 5 MPa. In other words, below the threshold value (σ_{th} =5 MPa), the wear damage does not occur, because a direct contact between the pin and the disk never occurs in that region with a help of the fluid lubrication.

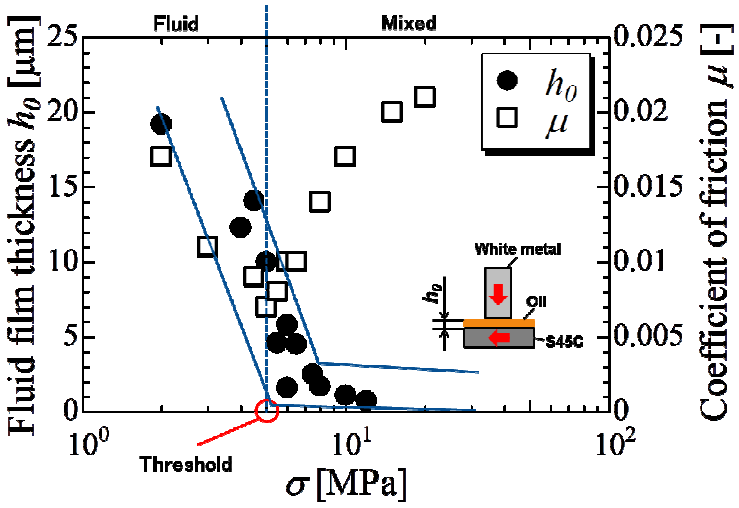

Fig. 7 h_0-σ relation and μ-σ relation in the oil (B) condition

5 CONCLUSIONS

Sliding wear tests were performed using white metal in laboratory air, in several lubricant oils with different viscosities and in water. The following conclusions were reached from the present study.

1) The *dW*/*dL* vs. σ relations differ with the experimental conditions, i.e., in the dry condition and in the three lubricants. However in the *dW*/*dL* vs. τ relations, the above differences get fewer. In the three lubricants, i.e., water, oil(A) and oil(B), they are almost the same with each other, especially at the low τ region. At the high τ region, the value *dW*/*dL* in the water is higher than those in the oil(A) and oil(B).

2) The sliding wear lives were successfully evaluated using the wear constitutive law. The evaluated results are in good agreement with the experimental results. So the wear constitutive law is useful for evaluations of the σ -L_f relation as well as the τ -L_f relation.

3) It is expected that the fluid lubrication occurs at the region, σ < 5 MPa and the mixed-mode lubrication occurs for the region, σ > 5 MPa. In other words, below the threshold value (σ_{th} =5 MPa), the wear damage does not occur, because a direct contact between the pin and the disk never occurs in that region with a help of the fluid lubrication.

6 REFERENCES

[1] Propeller and Shafting Committee. Allowable minimum revolution of shafting., J. Mater. Eng. Soc. Japan, 23(8), 42-49, 1988.

[2] S. Asanabe, Stern tube bearing, J. Mater. Eng. Soc. Japan, 27(9), 645-652, 1992.

[3] Japan Society of Tribologists, Jyunkatu Handbook., Tokyo, Yokendo Limited, 1975.

[4] S. Ishihara et al., Effect of amount of antimony on sliding wear resistance of white metal, Trib. Int., 43, 935-938, 2010.

[5] Horst Czichos, Tribology, Elsevier Scientific Publishing Company, 1978.

Proceedings of the 3rd International Conference on
Fracture Fatigue and Wear, pp. 295-300, 2014

MULTIGRID SOLUTION OF THE 3D ELASTIC SUBSURFACE STRESS FIELD FOR HETEROGENEOUS MATERIALS IN CONTACT MECHANICS

H. Boffy and C.H. Venner

University of Twente, Faculty of Engineering Technology (CTW), Department of Engineering Fluid Dynamics, The Netherlands

Abstract: The need to increase efficiency, stimulates the development of new materials tailored to specific applications and thermal/mechanical loading conditions, e.g. by controlling the property variations on a local scale: layered, graded, granular, porous and fibre-reinforced. For design and optimization of such materials the response to specific load conditions must be predicted which requires computer simulations. For applications in contact mechanics and lubrication failure criteria need to be developed which require the stress fields inside the (strongly heterogeneous) material induced by surface loading. The geometrical complexity of the subsurface topography and the need of an accurate solution require the use of a very fine discretization with a large number of elements, especially for three-dimensional problems. This requires optimally efficient numerical algorithms. In this paper the authors demonstrate the capability of Multigrid techniques to compute displacement and stress fields with great detail in strongly heterogeneous materials subject to surface loading, and in a contact mechanics application. Results are presented for a ceramic application and a contact problem of material with multiple inclusions. The efficiency of the method will allow extensive parameter studies with limited computational means. Moreover, it can efficiently be used to derive macroscopic stress-strain relations by simulations of microscopic problems. Also the method can be used for computational diagnostics of materials with specific heterogeneities.

Keywords: multigrid; elasticity; contact problem; heterogeneous materials

1 INTRODUCTION

Stimulated by environmental and efficiency constraints machines and their components need to reliably operate under increasingly extreme conditions. In bearings and gears forces need to be transmitted at higher loads, higher temperatures, smaller lubricant film thicknesses, and at the same time reduced friction levels. Existing failure criteria are generally based on the knowledge of the subsurface stress fields assuming homogeneous materials [1,2]. However, in many cases the conditions are nowadays such that local variations in the material properties, for example, (clusters of) inclusions, the granular structure, possibly with interstitial matter, may have a significant effect on the service life of machine components. Also, for many new (composite) materials failure criteria are lacking.

Accurate prediction requires models and simulation algorithms which can account for the effects of increasingly small scale phenomena in surface topology [3] and material properties (as shown in Fig. 1) also in response to variations in operating conditions and lubricant supply. Advanced numerical computational algorithms to compute the local displacement and stress fields in such materials are prerequisite for these studies. The geometrical complexity of the subsurface topography and the need of an accurate solution require the use of a very fine discretization with a large number of elements and many (millions) of unknowns, especially for three-dimensional problems. Standard methods used in engineering which are easy to us and flexible for larger scale structural computations are often not sufficiently efficient to allow simulations with the small resolution required.

In the past decades Multilevel/Multigrid techniques [4] have greatly enhanced the capabilities of numerical simulations in many fields in science, including contact mechanics and lubrication for homogeneous materials. Their efficiency has allowed much larger and realistic problems to be solved on smaller scale computers [5]. In this paper it is demonstrated that such algorithms can also successfully be used to face today's challenges: to analyse the effect material heterogeneity on a local scale on stresses and contact performance. The developed method can be used for efficient parameter studies to develop failure criteria, but also to derive macroscopic stress-strain relations from detailed microscopic simulations, in

computational diagnostics using input from mapped subsurface properties of actual material, and in topology optimization.

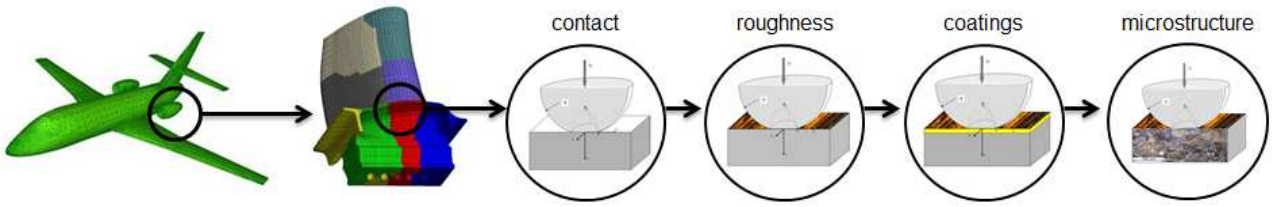

Fig. 1 From macro scale to micro scale in a contact problem

2 MODEL

2.2 Elasticity equations

The 3D heterogeneous linear elastic problem can be described as the solution of the unknown displacements u, v and w in a 3-D domain from the Navier-Cauchy equations:

$$(\lambda u_{j,j})_{,I} + (\mu u_{i,j})_{,j} + (\mu u_{j,i})_{,j} = 0 \quad j,j=1,2,3. \tag{1}$$

where λ and μ are the Lame's coefficients, which are assumed to vary as a function of space:

$$\lambda(x,y,z) = \frac{E(x,y,z)\vartheta(x,y,z)}{(1+\vartheta(x,y,z))(1-2\vartheta(x,y,z))}$$

$$\mu(x,y,z) = \frac{E(x,y,z)}{2(1+\vartheta(x,y,z))}$$

The problem is discretized using a uniform grid in a bulk with dimensions are (L_x,L_y,L_z) along x, y and z respectively. This can represent a local piece of material around a contact. It can also represent a local piece of material of a larger structure. A second order finite difference method is used to construct a system of equations that can be solved by computer. To solve the system a standard iterative method (Gauss-Seidel relaxation) is used. To accelerate convergence so as to be able to provide a solution containing millions/billions of degree of freedoms, multigrid techniques are used.

2.3 Multigrid methods

Multigrid techniques were introduced by Brandt to solve partial differential equations [6]. Subsequently they have been generalized for many scientific problems. They were introduced in tribology by Lubrecht for the fast solution of the Elasto-Hydrodynamic Lubrication problem [7,8]. The upshot of (geometrical) Multigrid is to use a conventional iterative methods for the solution of the problem. However, the drawback of these methods of slow convergence for smooth components is eliminated by introducing coarser grids on which such components can efficiently be solved. In a Multigrid algorithm a problem on a target grid is solved using a series of coarser grids. A flow diagram of a Multigrid algorithm is shown in Fig. 2. As a result of approximating and solving each error component on a scale at which the iterative method is efficient the convergence speed of the method is grid independent and the required computing time linearly proportional to the number of unknowns. The major complication is that Multigrid methods are not "black-box" methods. Optimal efficiency for non-standard applications (such as strongly heterogeneous materials) requires understanding of many details regarding the appropriate choice of transfer operators and coarse grid operators. Further details can be found in [9,10].

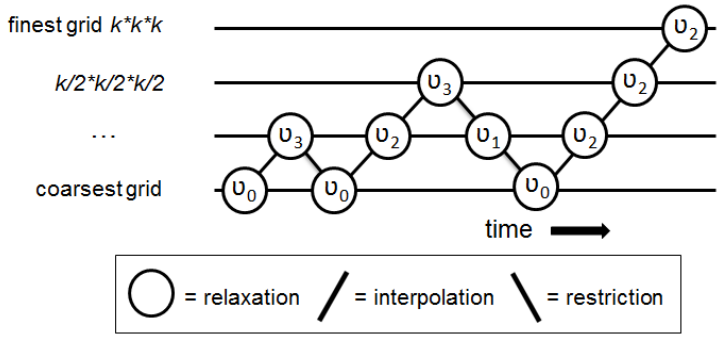

Fig. 2 A common multigrid schedule. υ represents the number of relaxation used during the different steps of the algorithm with $\upsilon_3 = \upsilon_1 + \upsilon_2$

3 Results

In this paper characteristic (tribological) problems are considered to demonstrate the potential of the developed method. The first computation of a subsurface displacements and stress fields in a ceramic material subjected to a prescribed surface loading. The second is the case of the simultaneous solution of surface pressure fields and subsurface stresses in homogeneous material with multiple inclusions with different properties.

3.1 Granular material with inclusion

The first case is a ceramic material subject to a Hertzian contact pressure. The ceramic is modelled as a granular material with interstitial matter (glue). Inclusion is modelled as an ellipsoid (see Fig.3). To model the grains, a 3D Voronoi tessellation is used. The glue is modelled as a fixed layer around each grain. For the case presented here, the volume ratio of glue is 10%. The mechanical properties are: for the grains E_g=305 GPa, υ_g=0.26 and for the glue E_{gl}=60 GPa, υ_{gl}=0.2. The properties of the inclusion are the same as the ones of the grains.

The computational domain is a parallelepiped of size [25;10;5] µm. The centre of the inclusion is located at M_i(0,0,-2) µm and its radii are c=1 µm and d=4.5 µm oriented along x and y respectively.

On the top surface an ellipsoidal pressure is imposed. Its characteristics are: a=1 µm and b=20 µm oriented along x and y respectively and a maximum pressure P_0=3 GPa.

The displacement fields are solved in the entire bulk. Subsequently, the stress fields are obtained using Hooke's law.

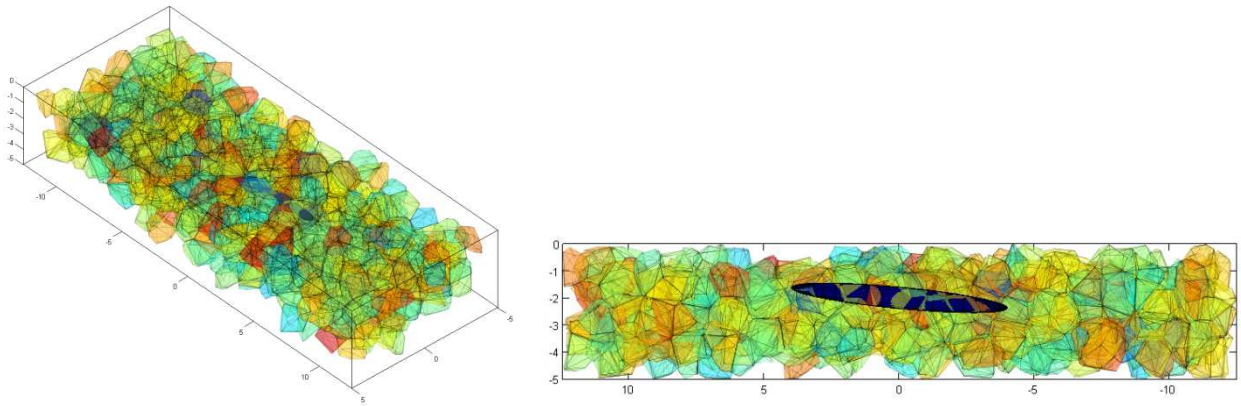

Fig. 3 Polycrystalline material with an ellipsoidal inclusion. The grains are modelled trough a 3D Voronoi tessellation. Each grain is separated from the other one by a glue layer that represents 10% of the total volume. The centre of the inclusion is located at M_i(0,0,-2) and it's radii are a=1 µm and b=4.5 µm

Figure 4 shows the tensile stress σ_{xx} in the plan (x,y,z=2). The colour scale allows one to well identify the locations where a failure may initiate. It can be seen that the tensile stress maxima appears at the rim of the inclusion, where some glue is located. Secondary maxima appear at the edge of some grains, probably due to their location and orientation in the material.

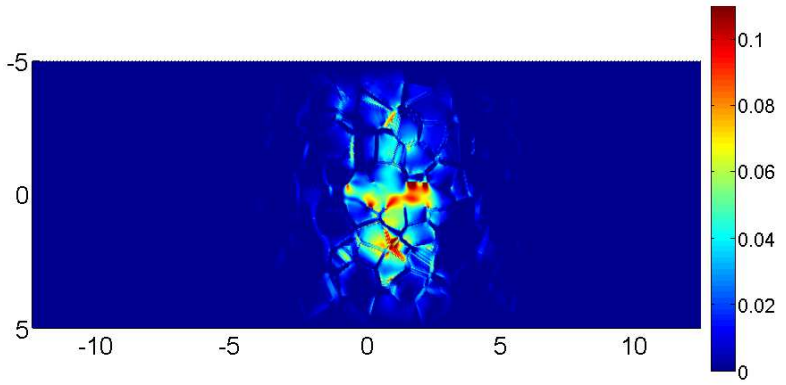

Fig. 4 Tensile stress σ_{xx} in the plan (x,y,z=2) for a polycrystalline material (ceramic) with an ellipsoidal inclusion. The mechanical properties are: for the grains E_g=305 GPa, υ_g=0.26 and for the glue E_{gl}=60 GPa, υ_{gl}=0.2. The properties of the inclusion are the same as the ones of the grains. The bulk is submitted to an ellipsoidal pressure with a maximum equal to P_0=3 GPa

This kind of study may be realised in parallel changing the parameters (loading, grain size, type of defect, …) to determine the best and worst configurations, thus helping for the design of new materials. However when a defect is big and close enough to the top surface it may affect the pressure field and consequently the stress fields inside of the structure. In order to identify the real pressure field, one has to solve the contact problem in addition to the elasticity equations (Eq. 1). In the case of complex structure, this operation is not trivial and requires the use of advanced numerical tools. The next section briefly explains how to proceed using multigrid methods.

3.2 Solution of the contact problem

In the previous example the pressure distribution at the surface was assumed to be known. However in reality this pressure is affected by the property variations of the material particularly when inclusions occur close to the surface. In that case it cannot be assumed Hertzian and needs to be solved simultaneously with the displacement equations. This can be done using a conjugate gradient method with an FFT method for the surface displacement matrix [11,12]. However Multigrid methods by their nature allow very efficient incorporation of boundary contact problem into the solver. The entire problem is solved and the amount of work is a bit larger than the single solution of the displacement fields. Some results of the effect of heterogeneities on the contact pressure are shown in Fig. 5. The pressure fields between a rigid indenter and a homogeneous material with multiple inclusions. The numerical parameters used of the different calculations are the following ones: the volume of computation is a parallelepiped whose size is [8;8;4] and the top surface is discretized using 257*257 or 513*513 points on the finest grid. The simulations involve a homogeneous material (academic Hertzian solution) and 3 cases with defects (spherical inclusions) that may be soft or hard. Details on the different configurations are given in the caption of Fig. 5.

3.3 Performance

Multigrid techniques can be a fast and accurate alternative method for numerical simulation of 3 dimensional elastic contact problems with heterogeneous materials. The convergence speed is grid independent and as a result the computational cost is linearly proportional to the number of unknowns. Table 1 gives some details of the number of points used for the different simulations. As a convergence criterion a residual of 10^{-8} on the solutions was used. This is very strict and ensures a result with an error that is much smaller than the discretization error in any case presented. Calculations have been performed on a computer with Intel X5650: 2.67Ghz, single core. Obviously the computing time can be reduced by parallel processing.

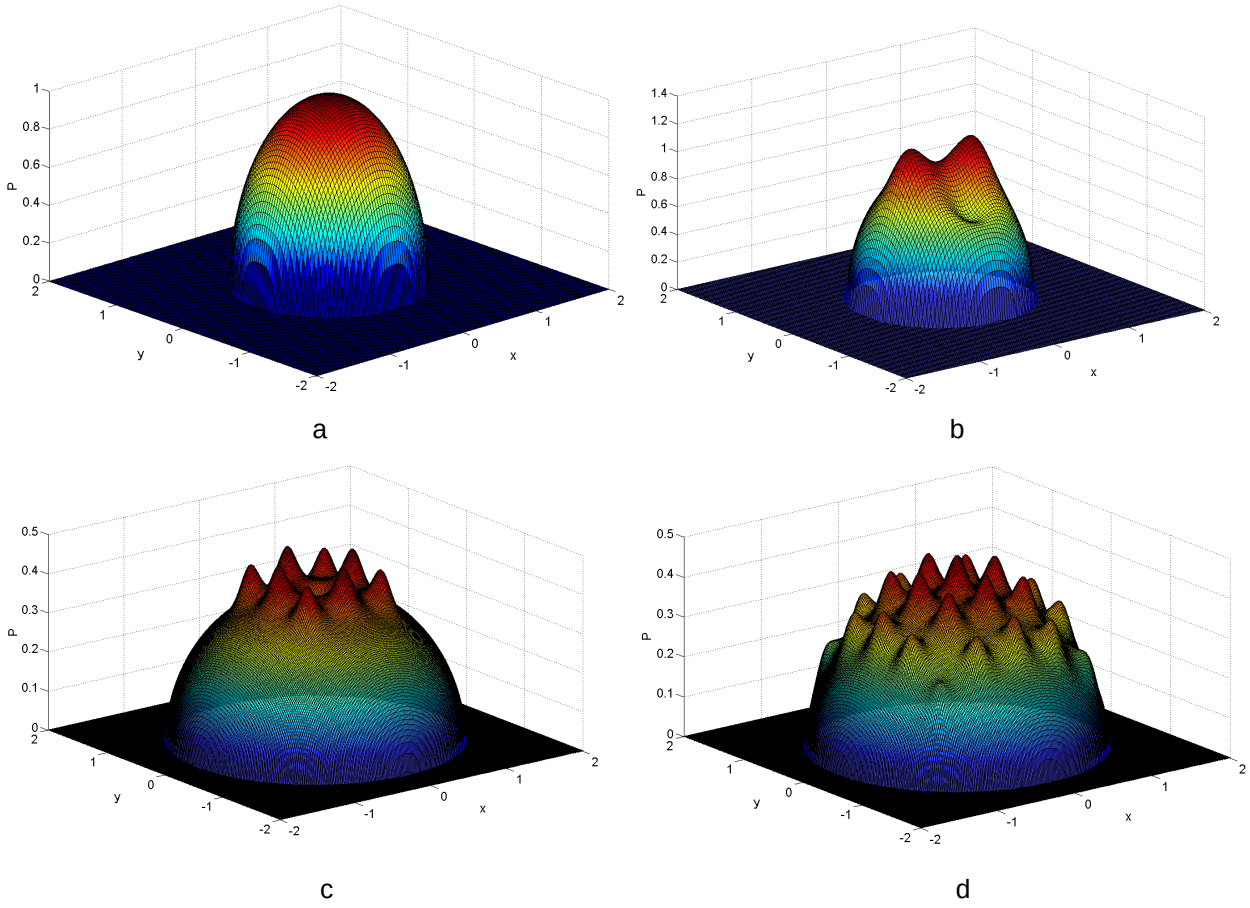

Fig. 5 Pressure fields (σ_{zz}) solved for the contact problem between a rigid indenter and a) an homogeneous material b) an homogeneous material containing 2 spherical hard inclusions ($E_i/E=3.0$, $\upsilon_i/\upsilon=1.0$, $R_i=0.25$) and two soft ones ($E_i/E=0.3$, $\upsilon_i/\upsilon=1.0$, $R_i=0.25$) c) an homogeneous material containing 8 spherical hard inclusions ($E_i/E=3.0$, $\upsilon_i/\upsilon=1.0$, $R_i=0.125$) and a spherical soft inclusion ($E_i/E=0.3$, $\upsilon_i/\upsilon=1.0$, $R_i=0.125$ d) an homogeneous material containing 25 spherical hard inclusions ($E_i/E=3.0$, $\upsilon_i/\upsilon=1.0$, $R_i=0.125$). The geometry of the indenter is spherical ($f(x,y)=x^2/4+y^2/4$ for the two first cases and $f(x,y)=x^2/16+y^2/16$ for the two other ones) and the imposed load is ($F=2*\pi/3$)

Table 1 Performance details for the different simulations. Calculations have been performed on a computer with Intel X5650: 2.67Ghz, single core

Simulation	level	Total number of points	Finest mesh size	CPU time
Ceramic	6	135 Millions	5/256	10h13
Homogeneous contact	5	8.5 Millions	1/32	1h27
Inclusions contact	5	8.5 Millions	1/32	1h36

4 CONCLUSIONS

In this paper the potential of the multigrid methodology is demonstrated for the simultaneous solution of contact mechanic problems and the associated subsurface stress fields for strongly heterogeneous materials. The developed method allows fast solution of problems using a large number of degrees of freedom such that property variations on a highly local scale can be modelled. Results have been shown for a ceramic subject to surface loading, modelled as a granular material with interstitial matter. It is also shown that solution of the contact problem can be efficiently incorporated. Pressure distribution was shown for homogeneous material with clusters of inclusions located close to the surface. The developed method offers great possibilities for parameter studies of composite and complex materials in optimization and design. Moreover, the method can be used for the development of macroscopic relations, e.g. as input to conventional computational methods (FEM), from microscopic material simulations as shown in this paper.

5 NOMENCLATURE

E Young's modulus GPa

υ Poisson coefficient -

λ, μ Lame's coefficient GPa

σ Stress fields GPa

6 REFERENCES

[1] T. A. Harris, Rolling Bearing Analysis Fourth Edition, Wiley, 2001.

[2] E. Ioannides and T. A. Harris, A New Fatigue Life Model for Rolling Bearings, Journal of Tribology, 107(3), 367-377, 1985.

[3] A. F. Bower, Applied Mechanics of Solids, CRC Press, 2009.

[4] A. Brandt, Multigrid Techniques: Guide with Application to Fluid Dynamics, BOHN: Gesellschaft für Mathematik und Datenverarbeitung, 1984.

[5] H. Boffy, M. C. Baietto, P. Sainsot, A. A. Lubrecht, An Efficient 3d Model of Heterogeneous Materials for Elastic Contact Applications Using Multigrid Methods, Journal of Tribology, 134(2), 021401, 2012.

[6] A. Brandt, A multi-level adaptative technique (mlat) for partial differential equations: ideas and software, Mathematical Software 3, 273–314, (1977).

[7] C. H. Venner and A. A. Lubrecht, Multi-Level Methods in Lubrication, Elsevier Tribology Series, Amsterdam, 2000.

[8] A.A. Lubrecht, G.A.C. Breukink, H. Moes, W.E. ten Napel, R. Bosma, Paper VI(i) Solving Reynolds' Equation for E.H.L. Line Contacts by Application of a Multigrid Method, Tribology Series, 11, 175-182, 1987.

[9] W. L. Briggs, V. E. Henson, S. F. McCormick, A Multigrid Tutorial, SIAM, 2000.

[10] F. J. Gaspar, J. L. Gracia, F. J. Lisbona, C. W. Oosterlee, Distributive smoothers in multigrid for problems with dominating grad-div operators, Numerical linear algebra with applications, 15, 661-683, 2008.

[11] P. Sainsot, A. A. Lubrecht, Efficient Solution of the Dry Contact of Rough Surfaces : a Comparison of FFT and MG methods, Proceedings of the Institution of Mechanical Engineering, Part J: Journal of Engineering Tribology, 225, 441-448, 2010.

[12] J. Leroux, B. Fulleringer, D. Nélias, Contact Analysis in Presence of Spherical Inhomogeneities within a Half-Space, International Journal of Solids and Structures, 47, 3034-3049, 2010.

Proceedings of the 3rd International Conference on
Fracture Fatigue and Wear, pp. 301-307, 2014

FRICTION AND WEAR BEHAVIOUR OF CARBURIZED STAINLESS STEEL UNDER FRETTING-RECIPROCATING SLIDINGS

L. Haviez[1,2], S. Fouvry[1], R. Toscano[1], G. Yantio[2] and G. Moreau[2]

[1]LTDS - Ecole Centrale de Lyon, Lyon, France
[2]Sagem Défense Sécurité, Paris, France

Abstract: In this research, we develop an original experimental strategy to investigate the effect of contact conditions on friction and wear behaviour of a carburized stainless steel subjected to reciprocating slidings. Tests were performed with and without the decarburized top phase, in order to determine the importance of this layer on the fretting wear behaviour as a function of the sliding amplitudes. 90°-crossed cylinder contact configuration (carburized steel / mass quenched steel) was investigating focusing on the displacement amplitude and sliding speed effects. For such equivalent sphere/plan configuration, the ambient air exposition is function of the configuration position: the fretted surface of the sphere is always hidden (H) from the ambient air, and the plan is alternatively exposed (E). Scanning and optical microscopy and 2D wear profiles were used to characterize the contact surface evolution. The results show an important influence of the air exposition when the decarburized top layer is present. Depending on the exposition, adhesive or predominant abrasive wear processes can be activated. These phenomena have been quantified by the evolution of the shape of the fretting loop, the surface roughness inside the fretting scars and the wear rate. A bilinear friction energy wear approach is introduced to quantify the wear kinetic of the carburized tribosystem. The transition from the initial high wear rate to a lower running wear response has been related to the full elimination of the decarburized top layer.

Keywords: wear rate; friction; size effect; fretting; sliding amplitude; energy wear approach, stainless steel

1 INTRODUCTION

Fretting phenomenon is considered as a critical damage process inducing wear and cracking. Fretting occurs in the contact between two bodies subjected to a normal load and sliding induced by external cyclic forces or vibration [1]. Depending on the relative displacement at the interface, Partial Slip (PS) or Gross Slip (GS) condition can be observed in the contact. In this investigation, we focus on the gross slip condition. The air ambient exposition and the oxygen “accessibility” aspect have been extensively investigated by C. Mary and al. [2] for a titanium interface. It was shown that when oxygen accessibility is low, transfer and adhesive wear processes are predominant.

In this investigation, we analyze the fretting wear response of two stainless steels: one is carburized; the other is mass quenched. A first objective of this research is to establish how the air ambient exposition can influence friction and wear response of the tribosystem. For this, exposed and non-exposed situation will be investigated by inverting the cross cylinder specimens from the fix to the mobile position. A second objective is to establish how a friction energy wear approach can be considered to quantify the wear rate taking into account the presence or not of the top decarburized layer. Through this research a more fundamental description of the fretting loop evolution will be addressed including the fretting scar roughness.

2 EXPERIMENTAL PROCEDURE

2.1 Material and contact type

Tests were performed on two chromium-molybdenum stainless steels: one carburized stainless steel (M1_C) and one stainless steel with mass quenching (M2). The M1_C specimen comprised 3 layers: the external decarburized layer (DL) with less than 200HV hardness; the second was the carburized phase (CL), with hardness gradient between 760 HV and 550HV (Fig. 1a); the third was the bulk, with 500 HV hardness. These materials were studied to determine the wear kinetics of a two cross-cylinder configuration. According to Hertz, this configuration is equivalent to a sphere/plane configuration where

M1_C is mobile and M2 fixed. The two cylinders display the same radius (7.5 mm) and the same length (20 mm). The normal force was adjusted to reach 2,200 MPa Hertzian maximum contact pressure [3]. Surface roughness was Ra=0.4µm for both materials.

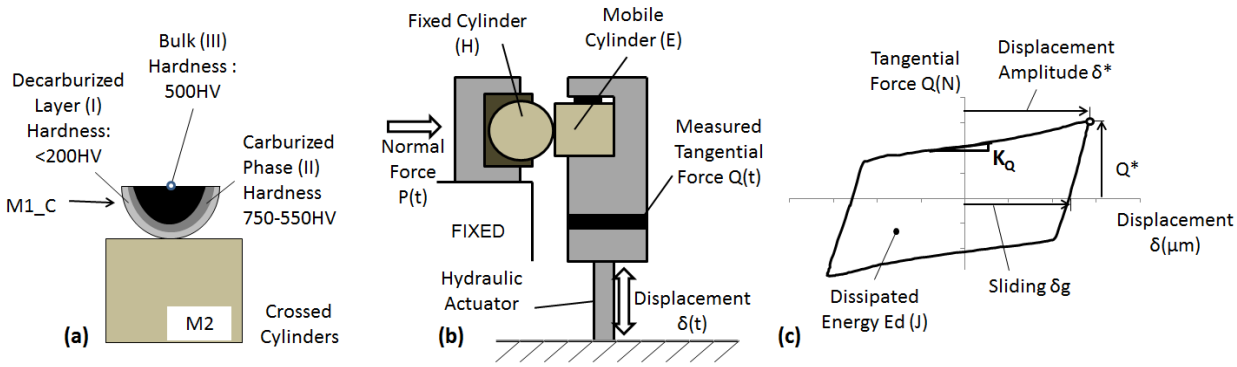

Fig. 1 (a) Contact configuration (crossed cylinders); (b) Fretting setup; (c) Fretting cycle analysis and K_Q slope definition.

2.2 Testing system

Figure 1b shows a schematic of the fretting wear test. An MTS hydraulic tension-compression machine regulated displacement between cylinders (further details of this setup and experimental method used can be found in [4]). During tests, normal force P was kept constant by a feedback system, and the cyclic sinusoidal displacement δ* was applied to generate an alternating tangential load Q* on the contact. All tests were performed with a constant frequency of 3 Hz, at room temperature. This enabled the fretting loop Q-δ to be plotted (Fig. 1c). By integrating the area of the fretting loop we can determine the friction energy Ed (J) for a given cycle. By integrating the whole fretting cycle the accumulated friction energy is determined.

$$\sum Ed = \sum_{i=1}^{N} Ed(i) \approx 4 * N * \delta g * \mu * P \qquad (1)$$

Tests were performed with δ*±300µm and different number of cycles N. Because of system stiffness, the sliding amplitude δg was not always exactly the same for a given displacement amplitude. For each test, slip was generalized in the interface thanks to the sliding ratio e, defined as the ratio between the sliding amplitude δg and the contact radius. This initial ratio e was larger than 1 but tends to decrease with the contact area extension. The friction coefficient is defined by the ratio µ=Q*/P. To study the influence of air exposition, M1_C and M2 were switched so that M1_C becomes the fixed cylinder (H) and M2 the moving cylinder (E). The last test campaign was done with M1_C and M2 in both positions (E) and (H) but M1_C was rectified in order to remove the decarburized top layer (M1_CR). The wear volume (V) of the fretting scars is measured using a 3D surface profile after ultrasonic cleaning in alcohol.

3 RESULTS

3.1 Adhesive/abrasive wear behaviour

Experiments were done on two configurations (Fig.2a): on one hand, M1_C is hidden from the air (H) and M2 is exposed (E); on the other hand, positions are switched so that M1_C is exposed (E) and M2 is kept hidden (H). Fig.1c defines the K_Q slope of the fretting loop. In the first place, we observed a large distinction between the two contact configurations (Fig.2b). When M1_C was exposed (E) and M2 was hidden (H), the K_Q slope increased with the number of cycles N and then stabilized at 0.14 N/µm by contrast the M1_C(H)/M2(E) configuration where the K_Q slope remains almost zero whatever the test durations. Moreover, we noted that the fretting scars are different for both test campaign (Fig.2c): for M1_C(E)/M2(H), scars seemed coarsen on the contrary to fretting scars of M1_C(H)/M2(E) which seemed smooth for both M1_C and M2 materials. K_Q slope increasing could be related to an adhesive wear process observed from the fretting scars. When the friction slope K_Q is small, the fretting scars could rather be characterized by abrasive wear morphology. Indeed, many researches have tried to understand the origin of the friction K_Q slope assuming it is related to the material characteristics (roughness, asperities, hardness) or to the velocity during the sinusoidal displacement called “velocity weakening” effect (the increase in friction as velocity decreases) [5].

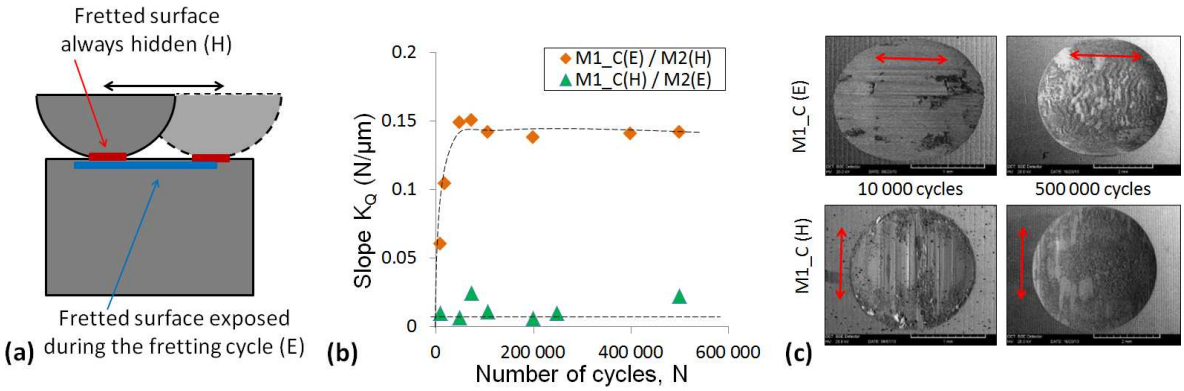

Fig. 2 (a) Illustration of the contact position hidden (H) and exposed (E), (b) K_Q slope evolution of M1_C(E)/M2(H) and M1_C(H)/M2(E) versus the number of cycles and (c) BSE micrographs of fretting scars

Two hypotheses can be considered to explain the K_Q slope: a first one assumes a ploughing interaction at the lateral borders (Fig. 3a) [5,6]. A second hypothesis considers the roughness inside the fretting scars throughout the entire contact region which by inducing an interlocking process promotes an increase of the tangential force with the displacement (Fig.3b).

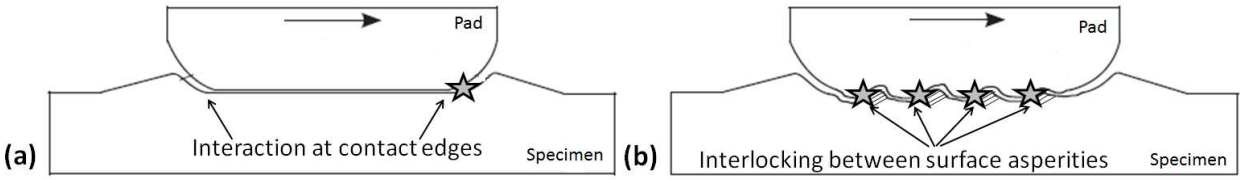

Fig. 3 Schematic diagram of wear–scar interaction types: (a) interaction at contact edges and (b) distributed local interactions (as well as the 'end' interaction) [5]

To verify the first assumption, we propose to investigate the evolution of a global description of the fretting scar morphology by computation a so called fretting scar slope defined as the ratio between the maximum depth h_{max} and the half-width a of the fretting scar $Ks=h_{max}/a$ (Fig.4a). The Ks evolution is the same for both studied configurations (Fig.4b) and we can conclude that the ploughing hypothesis at lateral borders of the contact is not at the origin of the K_Q slope parameter.

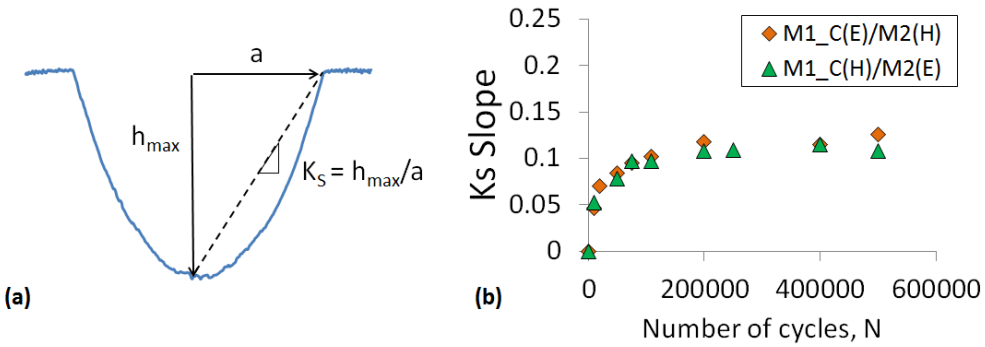

Fig. 4 (a) Schematic diagram of Ks slope definition and (b) K_S slope evolution of M1_C(E)/M2(H) and M1_C(H)/M2(E) versus the number of cycles

To verify the second assumption concerning the inner fretting asperities interlocking, we propose to investigate the evolution of the fretting scar roughness as function of the contact position (E)/(H). For each 2D longitudinal wear profile, the experimental data are fitted with a parabolic curve (Fig.5a) and the roughness R_a and R_t are extracted from the subtraction curve of the data and fit curves. This technique is applied to both materials to obtain the mean roughness Ra_{moy} defined by the mean of $Ra_{(E)}$ and $Ra_{(H)}$ (Fig.5b), except for the shortest tests of M1_C(E)/M2(H) configuration because the wear profile cannot be fitted by a curve. Two distinct evolutions can be observed. The fretting scars roughness of M1_C(E)/M2(H) configuration is larger than the one obtained for the M1_C(H)/M2(E) configuration as qualitatively deduced by SEM micrographs and Ra_{moy} analysis (Fig.5c).

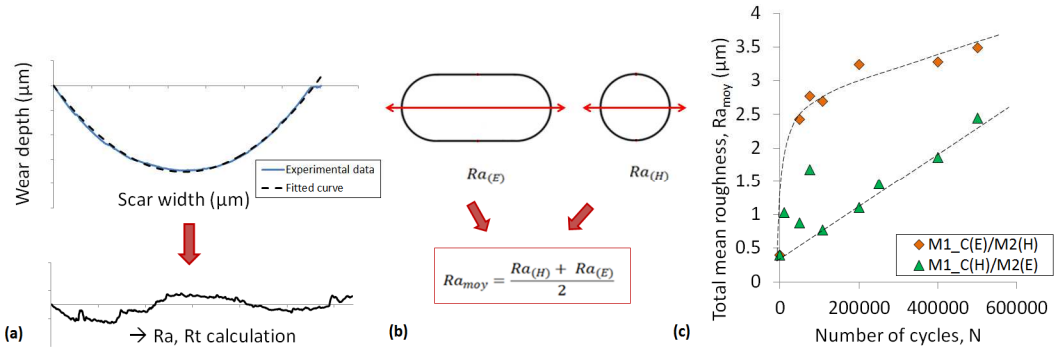

Fig. 5 (a) Extraction of the surface roughness, (b) Fretting scar surface profile measurement and (c) Total mean roughness evolution of M1_C(E)/M2(H) and M1_C(H)/M2(E) versus the number of cycles

These results suggest that the shape of the fretting loop and the roughness inside the fretting scars (Ra and Rt) can be correlated (Fig.6). Indeed when the fretting scar roughness is low the contact slips without significant resistance which induces smooth evolution of the friction plateau leading to a low K_Q value. By contrast, for the sliding condition M1_C(E)/M2(H) which tends to promote a significant fretting scar roughness, the interlocking process between asperities is increased which promotes a severe increase of the K_Q slope. Fig.6 compares the evolution of K_Q versus the Ra_{moy} fretting scar roughness measured at contact opening. A discontinuous evolution is observed. Below a threshold $Ra_{th} \approx 2.5\mu m$ and $Rt_{th} \approx 14\mu m$ (Fig.6), the K_Q slope is small (A). Above Ra_{th} and Rt_{th} a severe increase of the K_Q slope is observed reaching a plateau evolution (B) around 0.14 N/µm. Both evolution A and B are respectively observed for the M1_C(H)/M2(E) and M1_C(E)/M2(H) configurations.

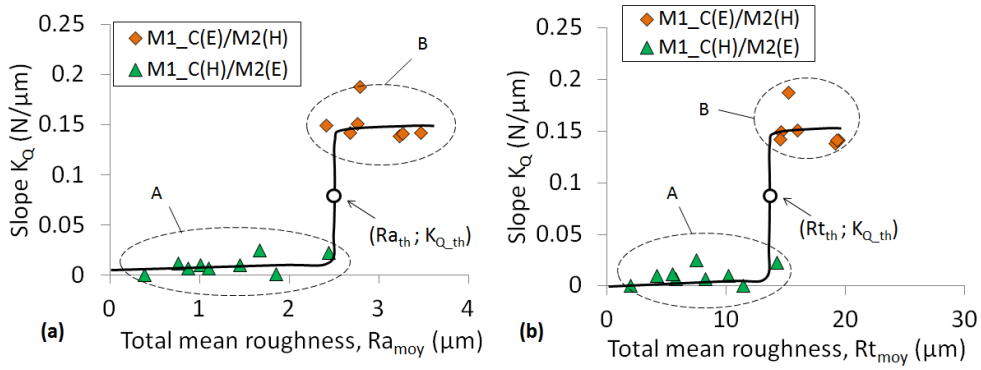

Fig. 6 Slope K_Q evolution of M1_C(E)/M2(H) and M1_C(H)/M2(E) versus (a) the total mean roughness Ra_{moy} ; (b) the total mean roughness Rt_{moy}

This result tends to confirm the second hypothesis (i.e. interlocking between surface asperities) (Fig.3b) and suggests that the K_Q slope is activated above a threshold fretting wear roughness $Ra_{th} \approx 2.5\mu m$ and $Rt_{th} \approx 14\mu m$. This analysis also shows that the K_Q parameter extracted from the fretting cycle analysis can be considered to establish if the wear process is rather dominated by adhesive wear or abrasive wear process:

- If $K_Q < K_{Q\_th}$ → Abrasive wear response (A)
- If $K_Q > K_{Q\_th}$ → Adhesive wear response (B)

(2)

where $K_{Q\_th} \approx 0.08$ N/µm.

3.2 Influence of the decarburized layer on wear and friction response

The wear volume extension of both M1_C(H) and M2(E) surfaces are compared versus the accumulated friction energy (Fig.7) [7,8]. The wear volume evolution is linear for M2 but shows a bilinear tendency for M1_C specimen, due to the structure of the M1_C interface (Fig. 1a): the fretting wear interface initially involves the decarburized layer of M1_C (DL (I)) before reaching the subsurface carburized layer (CL (II)). It is noteworthy that the wear rate of the DL layer (phase I) is about ten time faster than the successive CL

layer (phase II). The wear rate of the M2 counterbody is constant and slightly smaller than the M1_C sub-carburized layer response.

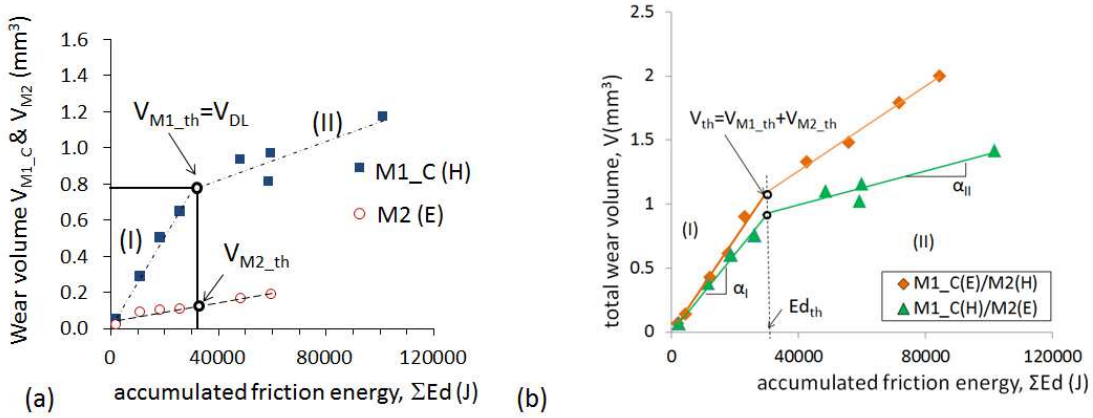

Fig. 7 (a) Evolution of wear volume V_{M1_C} and V_{M2}; (b) Total wear volume evolution ($V=V_{M1\_C} + V_{M2}$) versus accumulated friction energy

The total wear volume evolution (i.e. $V = V_{M1\_C} + V_{M2}$) is compared to the accumulated friction energy (Fig. 7b). Considering the difference between the top DL response and sub-carburized layer (CL), a bilinear energy wear model can be introduced as follows:

- If $V < V_{th}$, the interface involves the $M1_{DL}$ domain, and $V_{Ed} = \alpha_I . \Sigma Ed$
- If $V > V_{th}$, all the $M1_{DL}$ phase has been worn out and the interface involves only the $M1_{CL}$ sub-carburized layer, and $V_{Ed} = \alpha_{II} . (\Sigma Ed - Ed_{th}) + V_{th}$ (3)

where $Ed_{th}=V_{th}/\alpha_I$, with V_{th} is the threshold wear volume related to M1 decarburized top layer elimination (V_{DL}) plus the corresponding M2 wear volume and α_I is the energy wear rate of the $M2/M1_{DL}$ interface, and α_{II} is the energy wear rate of the $M2/M1_{CL}$ interface. Note that the V_{DL} volume can also be expressed as a function of the contact area A_f and the DL thickness (h_{DL}) so that $V_{DL}=h_{DL}*A_f$.

On the other hand, similar experiments were done using a M1 carburized rectified specimen, called M1_CR, where the top decarburized layer was removed. Fig.8a shows a common linear evolution of the total wear volume whatever the contact position of the M1_CR steel. This linear energy wear rate evolution is in fact equivalent to phase II M1_C(H) wear rate response (Fig.7b). The comparison between M1_C and M1_CR responses suggested that the presence of the DL layer significantly modifies the fretting wear response of the M1/M2 interface. It emphasizes the wear rate dependency regarding the ambient air exposition even after elimination of the DL layer and above all sharply increases the wear rate during the incipient phase (I) when the DL layer is still present in the interface. By contrast, by removing the DL layer using a rectification, a low constant linear evolution, independent of the contact position (E) or (H) can be observed.

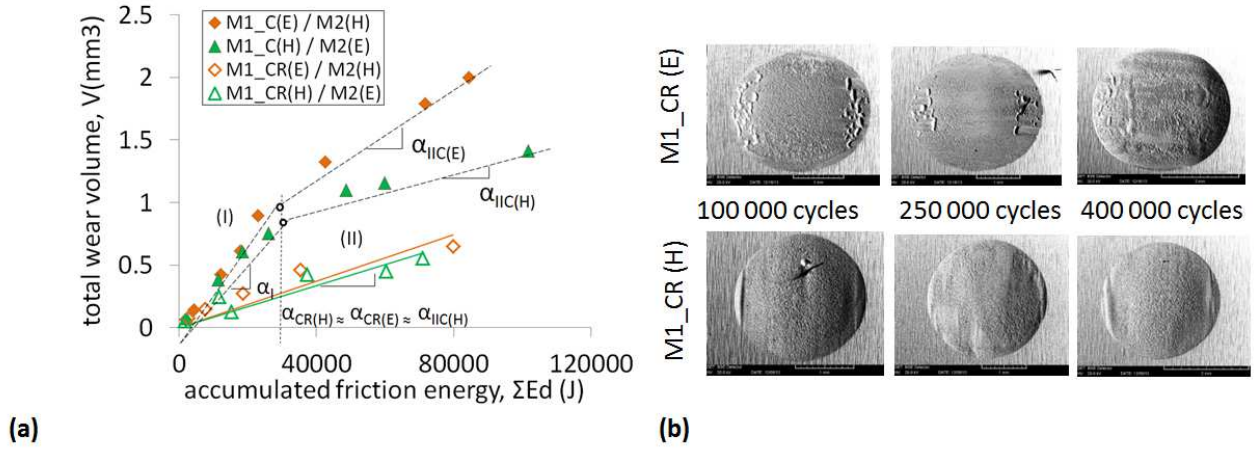

Fig. 8 (a) Total wear volume evolution versus the accumulated friction energy and (b) BSE micrographs of some fretting scars

As confirmed by the SEM fretting scar observations (Fig.8b), when the DL layer is removed smooth interfaces can be observed leading to rather low Ra_{moy} values. Fig.9 presents the same analysis than previously and compares the K_Q-R_{moy} evolution for M1_C/M2 and M1_CR/M2 configurations. Note that the threshold Ra_{th} and Rt_{th} values are equivalent to the M1_CR results and confirmed that the K_Q slope evolution is controlled by the inner fretting scar roughness through an interlocking process.

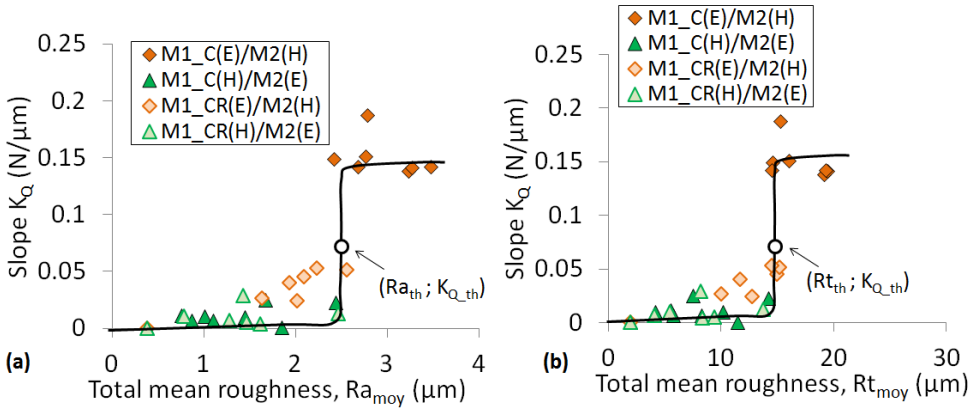

Fig. 9 Slope K_Q evolution versus total mean roughness (a) Ra_{moy} and (b) Rt_{moy}

The K_Q-R_{moy} evolution is confirmed however deeper investigations are now required to quantify this aspect including the tangential but also the normal complaisance of the interface. Further investigations will also developed to study the rheological properties of the third body trapped in the interface of adhesive fretting wear scars.

4 CONCLUSIONS

A fretting wear analysis of a carburized stainless steel interface including the presence or not of the decarburized top layer has been undertaken. It was shown that removing the top decarburized layer through a rectification machining, a linear energy wear rate evolution can be observed independent of the contact position of the carburized alloy (i.e. E or H). The fretting scars display a smooth morphology related to an abrasive wear process and a constant friction plateau during the gross slip stage (i.e. $K_Q < K_{Q\_th}$). By contrast the presence of the decarburized layer promotes a high dependency of the position. Whatever the contact position a bilinear evolution related to the initial high wear kinetic of the softer top decarburized layer can be observed, this analysis shows that if the decarburized layer is exposed, adhesive wear processes are predominant whereas abrasive processes are observed for the reverse hidden configuration. Hence, for the exposed configuration, an exotic wave structure consisting of compacted third body is observed. This tends to increase the wear rate and modify the friction response through an asperity interlocking process increasing the K_Q fretting slope. The introduction of the K_Q criteria provides an online analysis of the abrasive/adhesive wear process and appears as a pertinent parameter to investigate the rheological properties of the interface.

5 ACKNOWLEDGEMENTS

The authors would like to especially thank Safran Group, SAGEM, for financial support.

6 REFERENCES

[1] R.B. Waterhouse, D.E. Taylor, Fretting debris and the delamination theory of wear, Wear 29, 337-344, 1974.

[2] C. Mary, T. Le Mogne, B. Beaugiraud, B. Vacher, J.M. Martin, S. Fouvry : Tribochemistry of a Ti alloy under fretting in air : Evidence of titanium nitride formation. Tribology Letters 34, 211-222, 2009.

[3] K.L. Johnson, Contact Mechanics, Cambridge University Press, Cambridge, p154, 1994.

[4] S. Fouvry, Ph. Kapsa, L. Vincent: Quantification of fretting damage. Wear 200, 186-205, 1996.

[5] D.M. Mulvihill, M.E. Kartal, A.V. Olver, D. Nowell, D.A. Hills: Investigation of non-Coulomb friction behaviour in reciprocating sliding. Wear 271, 802-816, 2011.

[6] S. Fouvry, P. Duó, Ph. Perruchaut: A quantitative approach of Ti–6Al–4V fretting damage: friction, wear and crack nucleation. Wear 257, 916-929,2004.

[7] J. F. Archard: Contact and Rubbing of Flat Surfaces. Journal of Applied Physics 24(8), 981-988, 1953.

[8] S. Fouvry, T. Liskiewicz, Ph. Kapsa, S. Hannel, E. Sauger, An energy description of wear mechanisms and its applications to oscillating sliding contacts, Wear 255, 287-298, 2003.

Proceedings of the 3rd International Conference on
Fracture Fatigue and Wear, pp. 308-313, 2014

MECHANICAL BEHAVIOR OF DLC COATINGS UNDER VARIOUS SCRATCH CONDITIONS

G. Pagnoux[1,2,3], S. Fouvry[1], M. Peigney[2], B. Delattre[3], G. Mermaz-Rollet[3]

[1]LTDS, Ecole Centrale de Lyon, 36 Avenue Guy de Collongue, 69134 Ecully Cedex, France
[2]Laboratoire Navier, Université Paris-Est (Ecole des Ponts ParisTech, IFSTTAR, CNRS),
F-77455 Marne-la-Vallée Cedex 2, France
[3]PSA Peugeot Citroën, Route de Gisy, 78140 Vélizy, France

Abstract: In lubricated sliding contact systems with Diamond-Like Carbon (DLC) coated solids, several studies have shown DLC coatings are highly sensitive to asperities breaking through the lubricant film within the contact area. Those asperities produce damages similar to those obtain from scratch tests, from where coating delamination can initiate and propagate. In the present study, controlled scratches have been performed on DLC-coated samples by varying the tip radius, the normal load and the sliding speed. From one hand, the different fracture mechanisms are compared to those observed on a coated cam-tappet system. They both lead to similar damage and wear, from substrate plasticity to gross spallation, via tensile and angular cracking. On the other hand, a numerical analysis is conducted with a finite element model. It reveals the fracture mechanism can be qualitatively predicted. Additional computations show the scratch severity increases by considering a thinner coating. This upholds the observed experimental coupling between tribochemical wear, scratch networks and coating delamination.

Keywords: DLC; scratch; coating failure; FE model; wear

1 INTRODUCTION

DLC coatings are widely used for their great tribomechanical properties such as their low wear rate and their low coefficient of friction compared to non-coated solutions [1]. Many studies pointed DLC wear mechanisms depend on the atmosphere, on their thickness, their microstructure (hydrogenated or not, doped or not, mono or multi-layered), their interface quality with the substrate and the imposed loading. When applied to an industrial system with complex and various loading, several wear mechanisms can become coupled and a predictive wear model must be seen as a long-term goal.

In lubricated conditions, recent studies highlight the DLC sensibility to particles in the lubricant [2]. In a previous work, the analysis of a cam-tappet system with DLC-coated tappets led to a complete wear scenario where coating delamination starts around scratch networks and inside tribochemical areas [3]. Scratches may come from particles in the lubricant or asperities on the initial surface of the uncoated counterpart. They are particularly numerous on delaminated tappets, but they do not all lead to delamination. It is then assumed there is a specific scratch severity promoting untimely delamination.

To better understand the link between local scratches and generalized coating failure, simplified tests with controlled scratches need to be conducted. Scratches are performed by a standard scratch tester. Those have been used for many years to assess coating-to-substrate quality, though they do not systematically match the actual scratch conditions. In this study, two DLC coatings have been scratched under various and calibrated conditions and the observed failures are compared to both worn coated tappets and a numerical model.

2 SCRATCH MECHANICS

A scratch test consists in moving at a constant speed a tip on a surface while applying an increasing normal load. Standard scratch tests are performed using a Rockwell C diamond indenter with a 200µm tip radius and a normal load going from 0 to several tenth of Newton. In the case of a coated surface, at a certain critical load the coating will start to fail. The critical loads can be very precisely detected by means of an acoustic sensor attached to the load arm but can also be confirmed and collated with observations from a built-in optical microscope. The critical load data is used to qualify and compare the adhesive or

cohesive properties of different film - substrate combinations. In this study, the critical load corresponds to the first observable massive spallation. Multiple failure modes can be observed [4]. It usually starts from substrate plasticity and a slight residual groove. At a certain point, angular or parallel cracks can be seen at the edge of the groove. Those cracks can also be fully developed beyond the indenter and form conformal or Hertz cracks. With increasing load, a ploughing effect can be seen ahead of the moving tip and several spallation mechanisms appear, from localized chipping to gross spallation. The system response to a scratch test depends on a lot of intrinsic and extrinsic parameters [5]. Holmberg et al. developed a systematic numerical approach to analyze the scratch mechanics, focusing on local stress fields and first crack location [6]. The effect of contact geometry was studied by Xie [7] who pointed out the tip radius highly influences the failure mode.

3 EXPERIMENTAL DETAILS

3.1 Sample description

Circular samples are made of AISI M2 steel. They are coated with two different DLC coatings. The first one, named DLC 1, is a hydrogenated multi-layer and doped DLC with an adhesive layer made of chrome. The second one, DLC 2, is a multi-layer coating but non-doped DLC, without adhesive layer. They are similar to those used in the cam-tappet system evoked previously. Both substrate and coating were characterized by nanoindentation and EDX analysis. The coating structure and thickness and the different material parameters are listed in table 1 (where data with "*" means values which were not measured).

Table 1 Material properties

	Substrate	DLC 1	DLC2
Structure	AISI M2	Cr+CrN+a-C:H:Si+a-C:H	WC+WCC+a-C:H
Thickness [mm]	5	$0.9e^{-3}$ (Cr+ CrN) + $2.5e^{-3}$ (a-C:H :Si + a-C:H)	$0.9e^{-3}$ (WC+ WCC) + $2.5e^{-3}$ (a-C:H)
Hardness	62 [HRC]	3600 [HV]	3900 [HV]
Ra [µm]	0.02	0.21	0.15
E [GPa]	210*	223	239
v	0.27*	0.2*	0.2*
Yield limit [MPa]	4500*		

3.2 Scratch tests

Scratches have been performed using a CSM scratch tester and a Rockwell C diamond indenter with a spherical tip and a 120° cone angle. In a previous work, a simplified numerical model has been created to estimate the load transmitted by asperities [8]. As a result, a scratch map has been defined to represent the contact conditions of a coated cam-tappet system from an automotive engine which encounters asperities. The tip radius (10, 20, 50, 100 and 200µm) and scratch length (1 to 5mm) have been chosen to cover the range of observed ones on cam-tappet systems, while the normal load is raised until failure or until the maximum load given by the scratch map. The tip speed has been set to 1 and 100mm/min. Before tests, the specimens where cleaned with acetone.

4 OBSERVATIONS

In the following section, the main results from DLC 1 tests will be highlighted. For 10µm and 20µm tip radius tests, either nothing or only a slight residual groove coming from substrate plasticity is observed. This means the main stress field generated (up to a maximal contact pressure of 20GPa) is restricted to the coating and do not exceed the yield limit of the substrate, so a quasi-full elastic recovery arises after the tip transit. With the 50µm tip radius tests come the first observable cracks, which can be classified as tensile to Hertz cracks (Fig. 1). However, at the maximum imposed normal load, no critical failure can be observed.

There are multiple mechanisms of failure with 100 µm tip radius tests (Fig. 2). The coating exhibits substrate plasticity between 0 and 2.5 N. Surface angular cracks located at the groove edge start to appear at 2.5 N and become more numerous up to 5.8 N. They also become longer by propagating toward the groove centre with a slight curvature. At 5.8 N, the first critical failure is observed with the creation of large circular spalls alternatively located from one side of the wear track to another. The entire coating is removed as the remaining material is the substrate. Spalling occurs until the end of the scratch.

200µm scratch tests (Fig. 3) are quite similar to 100 µm ones. Angular cracks appear at 12.1 N and propagate to the groove centre with a slight curvature at low load, then straight to the centre with higher ones. Chipping occurs at 17.8 N, followed closely by critical failures from 18.2 N to the end of the scratch.

The spalls from 200µm tests seem to have a thinner profile than those of 100 µm, but a comparative analysis indicates all spalls have actually the same average dimensions.

There is no major difference between scratches at 1 and 100 mm/min, meaning there is no viscous effect acting at such speed. Despite the sliding speeds are widely inferior to those acting in the actual cam-tappet systems (up to several m/s), the present scratches exhibit similar failure modes, although spalling is rarely observed on coated tappets (examples on fig. 4). This is relevant with the scratch map, in which most of the calculated loads transmitted by asperities do not exceed the observed critical load.

The same scratches have been performed on samples coated with DLC 2. While both DLC are hydrogenated DLC and have the same thickness, they behave differently. DLC 2 exhibits similar failure modes but with higher critical loads. Thus, DLC 2 has a better fracture resistance, although it does not have an adhesive layer. This confirms the high dependence of the coating mechanical behaviour to its intermediate layers.

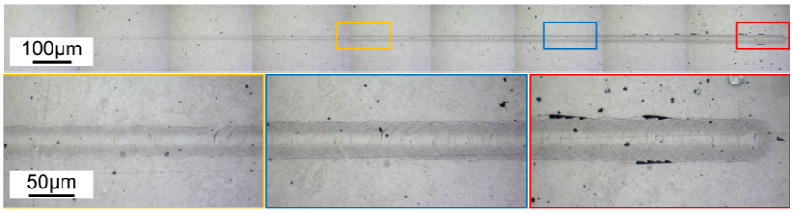

Fig. 1 R = 50 µm, Fn = 0.03 – 2.0 N, L = 2 mm, v = 1 mm/min

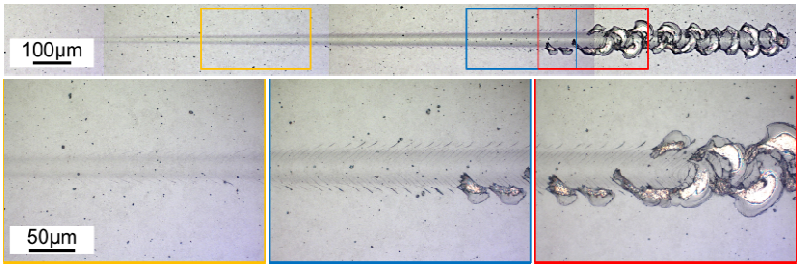

Fig. 2 R = 100 µm, Fn = 0.03 – 7.5 N, L = 2 mm, v = 1 mm/min

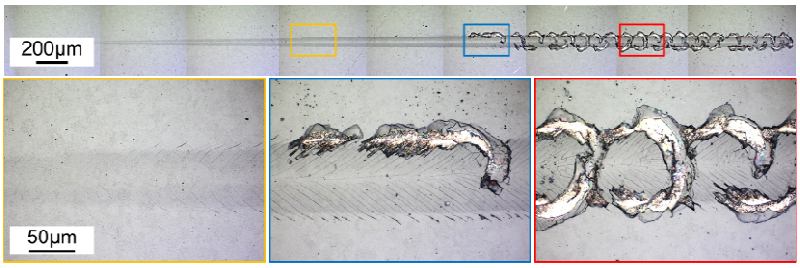

Fig. 3 R = 200 µm, Fn = 0.03 – 23.5 N, L = 5 mm, v = 1 mm/min

Indeed, the reduction of intrinsic coating residual stress is not their only benefit. Crack fronts propagate differently from one layer to another, meaning it would be necessary to identify the associated fracture toughness of each constitutive layer to correctly catch the full coating fracture behaviour. By extrapolation, this knowledge would be of great matter to estimate the coating behaviour under complex loadings, such as those experienced in cam-tappet systems. Unfortunately, the thickness of DLC coatings makes it difficult if not impossible to obtain. Thus, a numerical approach with a homogeneous coating has been chosen to identify the different failure modes and there governing parameters.

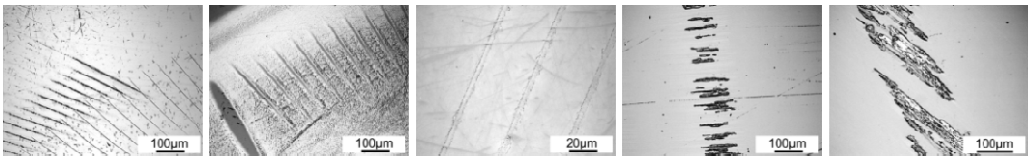

(a) (b) (c) (d) (e)

Fig. 4 Scratch network examples from a cam-tappet system [3]

5 NUMERICAL ANALYSYS AND DISCUSSION

In this numerical analysis, we focus on one substrate, one coating (DLC 1) and several scratch conditions. The substrate is chosen elastic perfectly plastic, without hardening. The coating is assumed homogeneous, isotropic and fully elastic. The surface and interface are perfectly smooth and the indenter is chosen has a perfectly rigid sphere. No residual stress is taken into account, as they were not measured on the scratched samples. The material parameters are taken from table 1, and the coefficient of friction has been set to 0.15, according to the average data measured during tests. The boundaries are at least 5 to 10 times

the contact width away from the contact area. Due to theoretical symmetry from both side of the scratch track, only half of the geometry was modeled. There is a minimum of 10 elements in the contact width and at least 7 elements in the coating thickness. All elements are three-dimensional tetrahedral elements, for a total of around $2e^5$ elements (fig. 5).

The loading is chosen as a 3 phases loading. The tip is firstly put into contact with the surface then a constant normal force is imposed as well as a longitudinal displacement. The last step consists in removing the indenter by applying an imposed normal and longitudinal displacement. The scratch length is chosen so that a steady state is reach at the end of the loading step. The full scratch test (i.e. with an increasing load) is not represented as it would require too many elements. As a result, the model can only be representative of an instant of the scratch test. The numerical model has been run for every scratch configuration. The chosen constant load was either the identified critical load or the maximal load, depending on whether or not a critical failure has been observed during scratch.

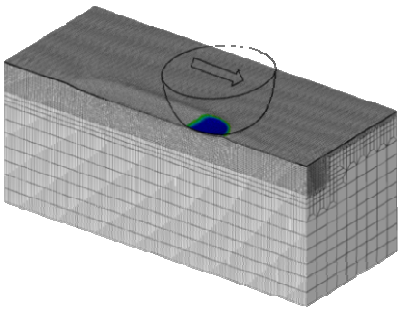

Fig. 5 Illustration of the FE model

The first result to highlight is the correlation between the observed cracks before critical failure (dashed line on Fig. 6 (a-c), top) and the direction perpendicular to the direction of the maximal principal stress on the surface (figure 6 (a-c), bottom). This means, as expected, that the coating behaves as a brittle material and the first cracks initiate on the surface, driven by the principal stress directions, and propagates toward the interface. Those results are similar to the mechanism of crack initiation developed in [6].

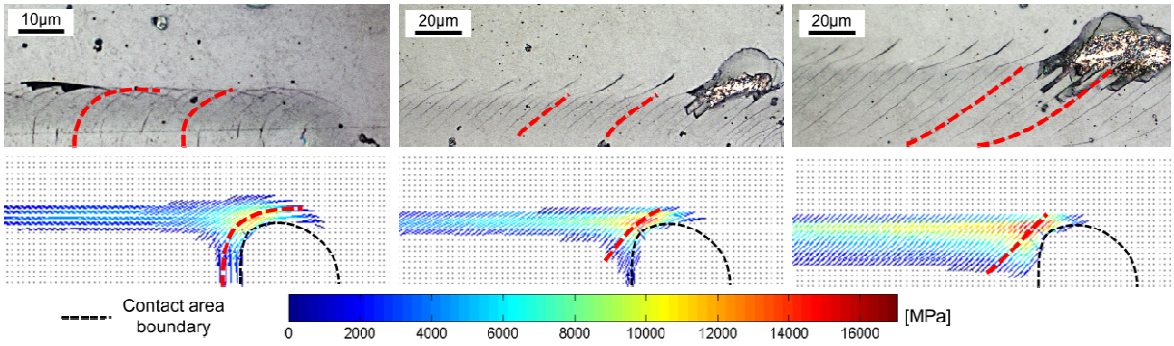

(a) R = 50 µm, at 2.0 N (b) R = 100 µm, at 5.8 N (c) R = 200 µm, at 18.2 N

Fig. 6 Surface cracks before failure (top) and first principal stress at the critical load (bottom)

The critical failure is characterized here by massive spall creation up to the interface. This means the system dissipates the stored energy accumulated in the coating by cracking in the surface as well as in the interface, via through-thickness cracking. In fact, scratches produce multi-axial stress states (shear, traction-compression) widely varying from the surface to the interface and leading to multi-physic failure mechanisms (bending, buckling …). Each mechanism tends to dissipate energy so, as a global approach; one can analyze the recoverable energy density in the coating, at its surface and in the interface. However, the entire recoverable energy does not contribute to crack initiation and propagation. By assuming a virtual surface crack front initiated perpendicularly to the direction of the maximal principal stress ($\underline{n}_s$, Fig. 7), the surface energy density required for it to propagate can be seen as part of the total available energy density.

At the interface and based on the work of Pradeilles-Duval [9], the calculated energy release rate corresponds to the jump of energy density across the interface minus the normal part of it, as it is the only part which does not participate in any mode of failure. The energy is expressed as in eq. (2), where $\underline{n}_i$ refers to the normal at the interface (see Fig. 7), $|[\ ]|$ to the jump of value across the interface, $< >$ to the mean value at the interface, and w is the total energy density.

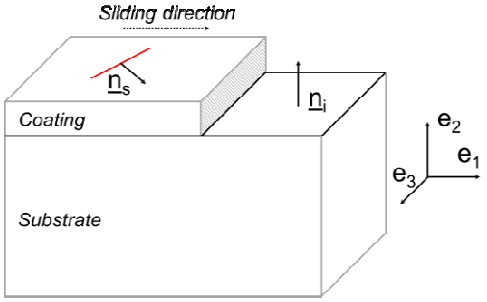

Fig. 7 Virtual surface crack and normal vector illustration

It can be expressed as in eq. (1), where $\underline{n_s}$ refers to the projection of the direction of the maximal principal stress on the surface and $\underline{\sigma}^*$ equals $\underline{\sigma}$, except ${\sigma_{jj}}^* = \max(0, \sigma_{jj})$. This means compressive stresses are not included in the calculated energy density, as they do not contribute to initiate nor propagate the considered virtual crack.

$$w_s = \frac{1}{2}\left(\underline{n_s} \cdot \underline{\sigma}^* \cdot \underline{\varepsilon} \cdot \underline{n_s}\right). \quad (1)$$

$$w_i = |[w]| - \frac{1}{2} < \underline{n_i} \cdot \underline{\sigma} > \cdot \left|\left[\underline{\varepsilon} \cdot \underline{n_i}\right]\right|. \quad (2)$$

The tensors $\underline{\sigma}$ and $\underline{\varepsilon}$ used in eq. (1) and (2) are those obtain at the end of the second phase (loading step). The stress state complexity before critical failure implies the used numerical model cannot be as representative of the system as it is at lower loads, especially considering it does not take into account the energy released by previous existing cracks. However, there is an acceptable correlation between the calculated energy densities and the failure modes. On surface, for 50µm scratch test, the recoverable energy concentrates at the indenter side and is split in two behind it (Fig. 8 (a), top). One part remains in the groove edge due to substrate plasticity and coating residual strain while the other follows the tip back. Since there is no noticeable ploughing, the energy at the interface is almost homogeneously located under the indenter (Fig. 8 (a), bottom). As a result, there are few risks of developing spalls in this circumstance and only tensile or Hertz cracks may appear.

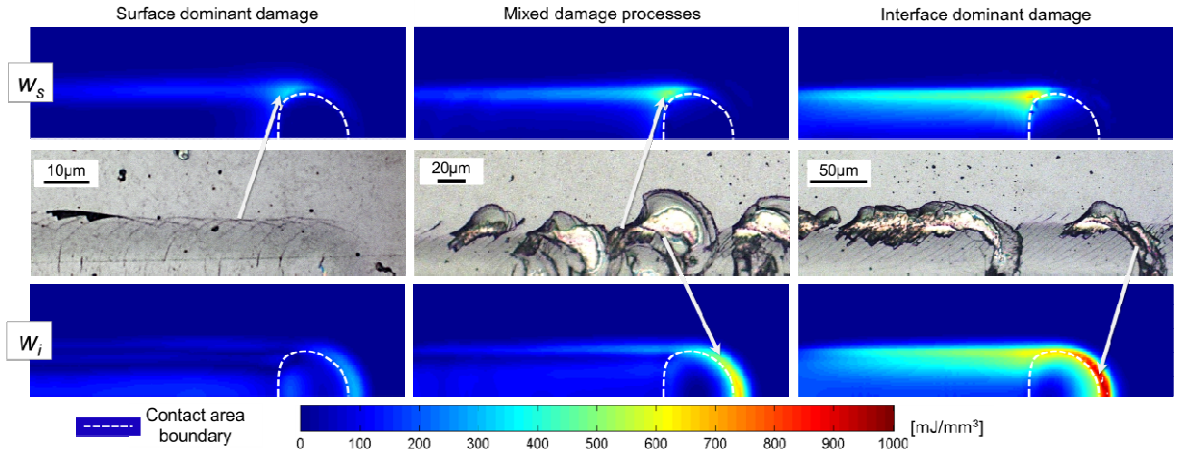

(a) R = 50 µm, at 2.0 N (b) R = 100 µm, at 5.8 N (c) R = 200 µm, at 18.2 N

Fig. 8 Surface (w_s, top) and interface (w_i, bottom) energy density

For 100 µm and 200 µm scratch tests, the energy levels dramatically increase as a result of a significant ploughing effect. At the surface, the higher values of the energy density extend from the side to the back-side of the contact area (Fig. 8 (b-c), top). At the interface, the recoverable energy concentrates in the tip front, mainly due to the compression of the coating in the sliding direction (Fig. 8 (b-c), bottom). For 200µm tests, there is a massive overlap between the area of maximal energy density at the surface and at the interface. Thus, the following failure's kinetics is proposed: first cracks are developed on surface, behind the tip and at the groove edge and propagate toward the interface. This propagation depends on the direction of the maximal principal stress. Cracks are likely to bifurcate toward the area of highest energy density, facilitated by the overlap between areas of maximal energy density. Consequently, they turn into the initial defects required for the coating to buckle, due to excessive compression at the front-side and front of the tip. This kinetics is consistent with the nano-scratch failure behaviour proposed in [11]. Furthermore, it has been shown a bigger tip radius leads to an increase of the compressive stress and a

decrease of the bending one [7]. This effect, combined with the decrease of the critical buckling stress with the radius of the loaded region [10], drastically enhances the probability of coating spallation.

The numerical model was also used to simulate the same scratch conditions but with a partially worn coating (i.e. with a reduced thickness). Results show higher stress levels (and energy density) for the worn coatings. This upholds the scratch severity increases with wear, and that scratches made by asperities after a long-term test may be more severe than those realized during a running-in period. After the indenter removal, the recoverable energy stored in the coating is of the same order than the one existing during scratch, particularly at the groove edge. Therefore, in the cam-tappet system, the initial scratches created by asperities are more likely going to evolve into generalized coating delamination when coupled with tribochemical wear. Further experimental tests will help to confirm or nullify those assumptions.

6 CONCLUSIONS

Two different hydrogenated DLC coatings have been scratched under various conditions by varying the tip radius, the normal load and the sliding speed. The wear mechanisms include substrate plasticity, cracks and spallation. The more severe scratches are those with the bigger tip radius. This is due to the ploughing effect arising at bigger loads, which promote compressive stress and buckling-like failure mode ahead of the indenter. Observations demonstrate the mechanical behaviour of each constitutive layer of the coating has to be evaluated to correctly catch the actual coating behaviour under fracture. Before critical failure, the numerical model confirms the coating behaves as a brittle material and first cracks appear at the surface, behind the contact area and at the groove edge, driven by the maximal principal stress. The analysis of the maximal energy density areas at the surface and at the interface allows suggesting a failure's kinematics explaining the origin of the initial defect required for the coating to buckle. The numerical model also highlights that for a given scratch, a worn (i.e. thinner) coating is more sensitive than an unworn one by storing a higher recoverable energy after the indenter removal. This is in agreement with observations on complex environments like coated cam-tappet systems, where generalized delamination initiates around scratch networks and inside tribochemically worn area.

7 ACKNOWLEDGEMENTS

The authors would like to acknowledge the support of HEF Group for providing the DLC-coated samples.

8 REFERENCES

[1] C. Donnet, A. Erdemir, Tribology of diamond-like carbon films: Fundamentals and applications, Springer, 2008.

[2] T. Haque, D. Ertas, et al., The role of abrasive particle size on the wear of diamond-like carbon coatings, Wear, 302(1-2), 882-889, 2013.

[3] G. Pagnoux, S. Fouvry, et al, Usures et endommagements des revêtements DLC sur systèmes came-poussoir, Tribologie: Fondamentaux et Applications Complexes, 1-8, 2013.

[4] S. Bull, Failure modes in scratch adhesion testing, Surface and Coatings Technology, 50(1), 25-32, 1991.

[5] S. Bull, E. Berasetegui, An overview of the potential of quantitative coating adhesion measurement by scratch testing, Tribology International, 39(2), 99-114, 2006.

[6] K. Holmberg, A. Laukkanen, et al., Tribological analysis of fracture conditions in thin surface coatings by 3D FEM modelling and stress simulations, Tribology International, 38 (11-12), 1035-1049, 2006.

[7] Y. Xie, H. M. Hawthorne, Effect of contact geometry on the failure modes of thin coatings in the scratch adhesion test, Surface and Coatings Technology, 155(2), 121-129, 2002.

[8] G. Pagnoux, S. Fouvry, et al, A model for single asperity perturbation on lubricated sliding contacts with DLC-coated solids, 40th Leeds-Lyon Symposium on Tribology and Tribochemistry Forum, Lyon, France, 2013.

[9] R. M. Pradeilles-Duval, C. Stolz, Mechanical transformations and discontinuities along a moving surface, Journal of the Mechanics and Physics of Solids, 43(1), 91-121, 1995.

[10] H. E. Evans, Modelling oxide spallation, Materials at high temperatures, 12(2-3), 219-227, 1994.

[11] L. Huang, J. Lu, et al, Elasto-plastic deformation and fracture mechanism of a diamond-like carbon film deposited on a Ti–6Al–4V substrate in nano-scratch test, Thin Solid Films, 466(1), 175-182, 2004.

Proceedings of the 3rd International Conference on
Fracture Fatigue and Wear, pp. 314-319, 2014

WEAR BEHAVIOR OF POWDER METALLURGY IRON COMPOSITE REINFORCED WITH 20WT.% SILICA PARTICLES

A. Amir[1] and O. Mamat[2]

[1]International Islamic University Malaysia, Kuala Lumpur Malaysia
[2]Universiti Teknologi PETRONAS, Tronoh Perak, Malaysia

Abstract: In an effort to find a cheaper production of particles reinforced metal matrix composite for tribological applications, this study focuses on iron, which is known as the oldest and cheapest tribological material. The composite was prepared via powder metallurgy fabrication technique and silica particles processed from natural sand used as the reinforcement. Wear test was performed with ball-on-disk apparatus in dry sliding condition. The effects of sliding distances, rotational speeds, and applied loads on the wear behaviour of the composite were investigated. Examination from Scanning Electron Microscopy (SEM) had revealed that the dominant wear mechanisms for the composite were delamination, followed by oxidation while pure iron exhibited adhesion, delamination and oxidation as the wear mechanisms. Interestingly, reinforcement of silica particles had evidently changed wear behaviour of the iron composite.

Keywords: silica particles; iron composite; powder metallurgy; wear mechanism; ball-on-disk

1 INTRODUCTION

Everything that man makes wears out, almost always as a result of relative motion between surfaces. From the perspective of a single machine, the losses seemed insignificance, however, when the same loss is repeated on a bulk of machines, then it become very costly. The enormous cost of tribological deficiencies to any national economy is mostly caused by the large amount of energy and material losses occurring simultaneously on virtually every mechanical device in operation. According to Tribology Centre in Danish Technological Institute, the cost of friction and wear is approximately 2-4% of an industrialized country's Gross Domestic Product [1]. In an order to curb this enormous loss, there have been extensive works on wear behaviour of ceramic reinforced metal matrix composites [2-5]. However, study in iron composite reinforced with ceramic particulates is scarce despite the fact that iron is the oldest and cheapest tribological material. Many studies on ceramic reinforcement in metal matrix composites found delamination wear to be dominating the wear mechanisms [6-9]. The worn surfaces usually consist of massive plastic deformation with pulled out wear debris accumulated on the surface and along the wear track. Another important characteristic of wear behaviour in ceramic reinforced metal matrix composite is the oxidation wear [6,8,10,11]. In this study, authors attempt to examine wear behaviour of iron composite reinforced with silica particles in dry sliding condition tested using ball on disk apparatus.

2 METHODOLOGY

2.1 Materials

Iron powder (10 μm) in this study was commercially supplied. The silica particles (0.4 μm) was produced in-house from raw sand collected from Tronoh ex-mining land and subjected to series of milling process. The iron powder was mixed with 20wt.% of silica particles then compacted using hydraulic press Carver PW 190-60 with pressure 50 MPa. The compact mixture was measured for green density using Densitimeter Mettler Toledo AX 205. Then, it was sintered in Hot Isostatic Press in argon atmosphere for 2 hours at temperature 1150°C. After that, the composite was measured again for sintered density. Three point bending test was performed using a 5 kN Universal Testing Machine Llyod LR5K Plus adhered to ASTM 133. The macrohardness of the sample was determined on the Rockwell 15T superficial scale using a 1/16 inch diameter steel ball indentor with 60 kgf load, in accordance with ASTM E18-94. These mechanical properties are presented in Table 1. Details of the fabrication process and characterization was provided elsewhere [12].

Table 1 Mechanical properties of wear sample used in this study

Wear Sample	HRF	Bending Strength (Pa)	Green Density (g/cm^3)	Sintered Density (g/cm^3)
Pure Iron	59.3	184	5.3	6.5
Iron with 20wt.% silica particles	75.9	1650	4.0	4.6

2.2 Wear Test

CSM Instrument Tribometer was used to carry out the wear test. The apparatus is ball-on-disk in dry sliding condition at room temperature. Disk specimen of diameter 6 mm and thickness 4 mm was made of iron composite reinforced with 20wt.% silica particles. The ball is Inconel of 3 mm diameter. Prior to wear test, the disk was ground against silicon carbide papers grit size 320, 600 and 800 then it was carefully cleaned with acetone and weighed. After wear test, the disk was cleaned with acetone, dried and weighed for weight loss. Load was applied from 1 to 10 N, while rotational speed selected were 0.05, 0.1, 0.15, 0.2 and 0.25 m/s. As for the sliding distance, the distance ranges from 25 to 225 m. All weight loss data were converted to volume loss using the measured densities. Volumetric wear rates were calculated from the volume losses. The worn surfaces of the composite disk were observed and analyzed using Scanning Electron Microscopy (SEM) model Leco 1430VP.

3 RESULTS AND DISCUSSIONS

3.1 Wear Rates

Volume rate for pure iron and iron composites reinforced with 20wt.% silica is plotted against rotational speed in Fig. 1. Apparently, the composite's wear behaviour only differs slightly from pure iron's. It started a little bit higher in volume rate then ended a little bit lower. Both samples showed a linear increase from sliding speed 0.05 to 0.15 m/s then, volume rate for both samples declined when the rotational speed was increased to 0.2 m/s. After that, volume rate for the composite continued to decrease whereas pure iron showed an increase at rotational speed 0.25 m/s. Fig. 2 depicted volume rate for pure iron and iron composites reinforced with 20wt.% silica versus sliding distance. The graph showed a notably big gap between volume rate of pure iron and its composite. From the graph, it can be seen that the composite demonstrated higher wear resistance than pure iron at all distances. Next, in Fig. 3, volume rate for pure iron and iron composites reinforced with 20wt.% silica against applied load is shown. The trend for both samples is quite similar, with the composite produced lower volume rate compared to pure iron, which implied the composite had higher wear resistance than pure iron, and the same trend is displayed at all applied loads. Overall, wear test using rotational speed variable produced lowest volume losses, that is in the range of 0.0045 to 0.0035 mm^3/s, while wear tests using another two variables, namely applied load and sliding distance produced volume losses in similar range, that is from 0.007 to 0.005 mm^3/s.

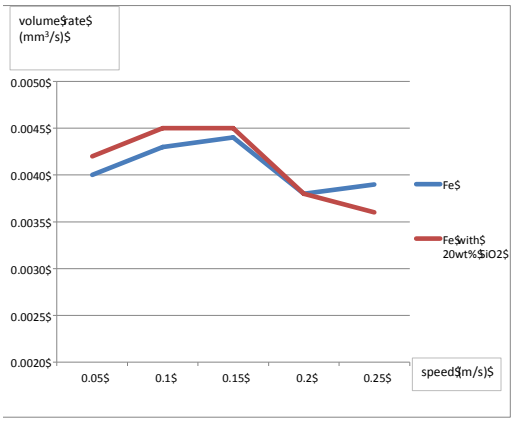

Fig. 1 Volume rate of iron composite reinforced with 20wt.% silica against rotational speed

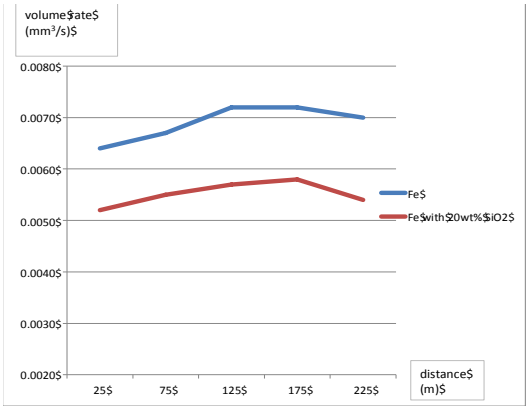

Fig. 2 Volume rate of iron composite reinforced with 20wt.% silica against sliding distance

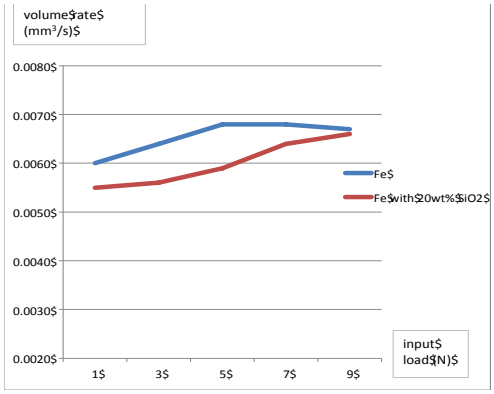

Fig. 3 Volume rate of iron composite reinforced with 20wt.% silica against applied load

3.2 Wear Mechanisms

Figure 4 displayed the worn surfaces of composite's samples from wear test using rotational speed as the variable. All samples tested against rotational speed were covered with intersection cracks and subsurface cracks, features linked to delamination type of wear. Detachment of wear debris was also found on the worn surfaces of the composite, while Fig. 5 depicted worn surfaces of pure iron under the same condition. Although pure iron displayed more or less comparable wear resistance as the composite, its worn surface shown lesser damage compared to the composite. It consists of smearing marks along the sliding direction and some irregular pits were identified. This suggests that pure iron's surface layers is more compact compared with composite. This observation supports previous finding by Y. Zhan and G. Zhang [7], whom noted reinforced composite is less compact than its alloy by comparing degree of damages seen on the worn surfaces of both samples.

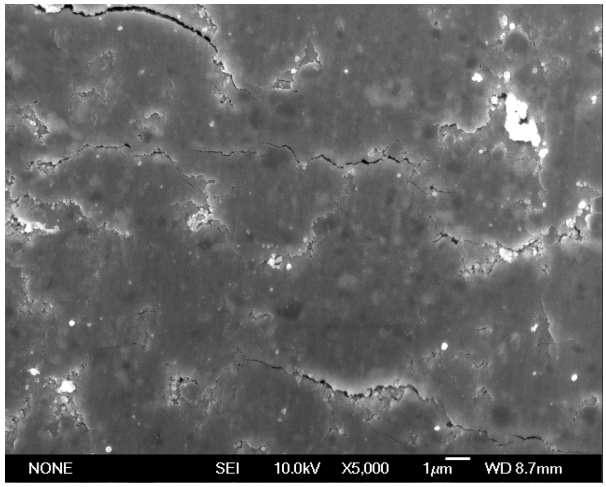

Fig. 4 Fine cracks are indication of delamination process

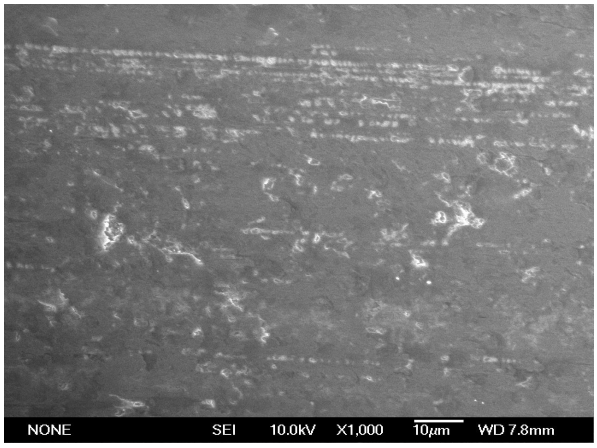

Fig. 5 Irregular pits and smearing along the sliding direction

Figure 6 displayed the composite's worn surface from wear test using load variable. Delamination is clearly to be more extensive when higher load is applied. Previous researchers have similarly found increasing dominance of delamination with load [6,7,13]. Since delamination involves subsurface deformation, crack nucleation and crack propagation, an increase in load will hasten these processes and produce greater wear. As the reinforced silica particles provide void nucleation sites, it easily turned into crack propagation paths [9-10]. This agrees with the findings of C. Lim whom reported that particulate reinforcements were not beneficial when delamination was dominant [6]. The composite had massive plastic deformation resulted from severe case of delaminated wear. H. Gulsoy et al [9] had recorded mechanism of delamination with deformed layers and tracks along the direction of sliding during wear, thus, concluded that contact pressure of wear surface increased with the increasing amount of porosity. Nevertheless, worn surface of pure iron of the same condition revealed lesser damage than its counterpart as viewed in Fig. 7, it has quite pronounce subsurface layers, which indicated delaminated wear is dominant.

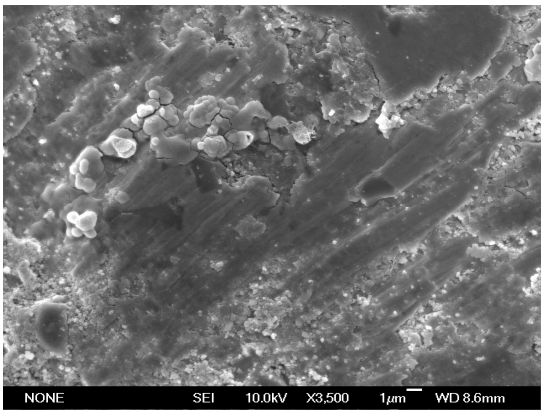

Fig. 6 Severe delamination wear

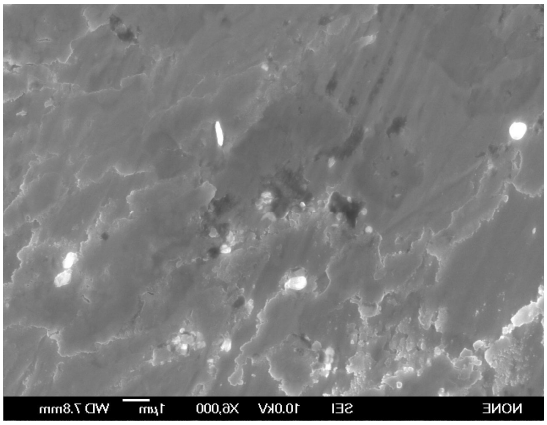

Fig. 7 Subsurface deformation

Existence of oxide films was noticed in all sliding conditions, however it is more pronounce in worn surface from wear test using distance variable. Probably, at both high load and high speed, frictional heating became more intense, which lead to oxidation wear. Fig. 8 shows an extensive oxide layer covered the composite's surface. Dominance of oxidation wear within this range of condition agrees with previous finding of Chen and Alpas [13]. Pure iron is presented in Fig. 9, where patchy oxide film appears on the edge of the surface, along with adhesion furrows marks at the centre. Gradual transition from adhesive wear to delamination wear as witnessed in pure iron was not evident in the composite. Probably it was due to composite's higher hardness. The advantage of possessing higher hardness had improved the composite's load-bearing capacity and imparted better resistance to adhesive wear [6,14]. From the examination on the worn surfaces, it become clear that composite had performed better wear resistance due to the accumulation of oxidation wear. When a near continuous oxide film formed on the surface, it prevents metal to metal contact during sliding, therefore the composite only suffers minimal volume losses compared to its counterpart that encountered direct metal to metal contact all the way during sliding.

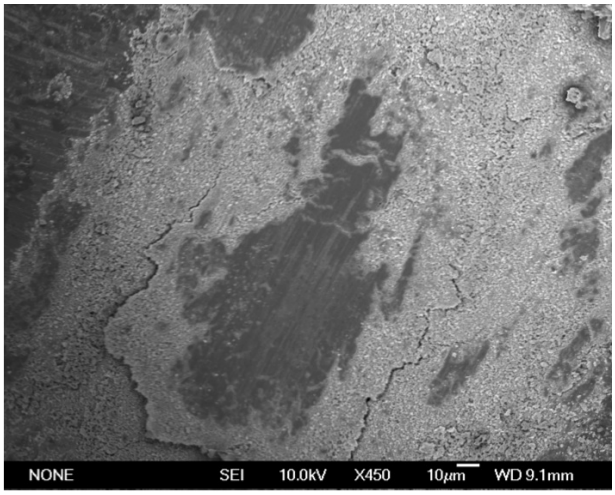

Fig. 8 Continuous oxide film formed on composite's surface

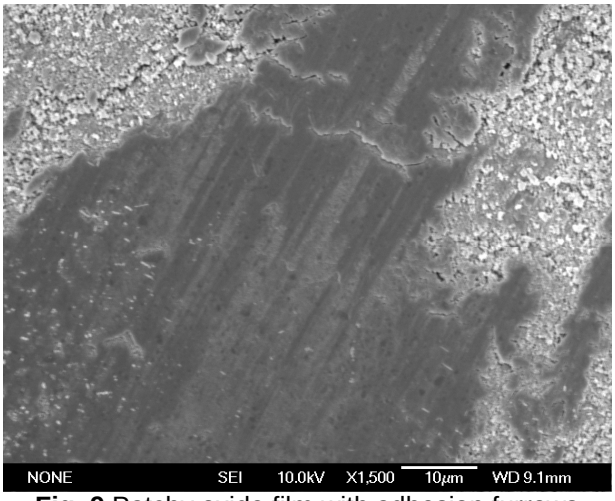

Fig. 9 Patchy oxide film with adhesion furrows

Present observation in pure iron and its composite proved that volume losses are not parallel with wear damage on contact area. Pure iron has demonstrated massive volume losses yet the damage to its worn surface was not as severe as observed in the composite. Altogether, reinforcement of silica particles into iron composite had evidently improved the mechanical properties which contributed to improve its wear resistance, however what is much more obvious is the reinforcement had changed the wear behaviour. The type of wear mechanism occurred in both samples is different. Dominant wear mechanism in composite is delamination wear but in pure iron it started with adhesive wear. Wear in composite was accelerated by propagation of intersections cracks and subsurface formation to the point it suffered a severely destructive plastic deformation with formation of large pits and accumulated large amount of wear debris. In the contrast, pure iron was worn out by smearing action of metal to metal contact during the sliding, which generated by adhesion. Then, the wear mechanism shifts from adhesion to delamination wear when subsurface deformation took place. Oxidation wear was present in both types of samples but pure iron only

exhibit mild oxidation wear whereas its composite display severe oxidation wear.

4 CONCLUSIONS

Iron composite reinforced with 20 wt.% silica particles demonstrated an improvement in mechanical properties compared to pure iron. It produced higher hardness and higher bending strength. In the wear test using sliding distance and applied load as the variables, the wear resistance displayed is slightly higher wear resistance than pure iron, only during sliding with speed variable there is no significant improvement in wear resistance. Moreover, when the worn surfaces of the samples were examined, it was shown that delamination wear dominating the wear mechanisms, followed by oxidation wear, while wear mechanism found in pure iron was adhesive wear before shifting to delamination and oxidation.

5 ACKNOWLEDGEMENTS

The authors would like to thank International Islamic University Malaysia for sponsoring this study. The authors are also grateful to Universiti Teknologi PETRONAS for providing the facilities to conduct this study.

6 REFERENCES

[1] Information on:

http://www.trelleborg.com/en/Media/Products-and-Solutions-News/Archive/Reducingfriction-can-save-energy-/

[2] S. Lim, M.F. Ashby, Wear-mechanism Maps, Acta Metall, 35, 1–24, 1987.

[3] H. Kato, T.S. Eyre, B. Ralph, Wear Mechanism Map of Nitrided Steel, Acta Metall. Mater. 42 (5),1703, 1713, 1994.

[4] S. Wilson, A.T. Alpas, Wear Mechanism Maps for Metal Matrix Composites, Journal of Wear, 212, 41, 49, 1997.

[5] A.R. Riahi, A.T. Alpas, Wear Map for Grey Cast Iron, Journal of Wear, 255, 401 – 409, 2003.

[6] C. Lim, Wear Behaviour of SiCp Reinforced Magnesium Matrix Composite, Journal of Wear, 255, 629-637, 2003.

[7] Y. Zhan, G. Zhang, Friction and Wear Behaviour of Copper Matrix Composites Reinforced with SiC and Graphite Particles, Tribology Letters, 1(17), 91-98, 2004.

[8] A. Emamian, S. Corbin, A. Khajepour, Tribology Characteristics of in-situ Laser Deposition of Fe0TiC, Journal of Surface & Coatings Technology, 206 (22), 4495-4501, 2012.

[9] H. Gulsoy, M. Bilici, Y. Bozkurt, S. Salman, Enhancing the Wear Properties of Iron Based Powder Metallurgy Alloys by Boron Additions, Journal of Materials and Design, 28, 2255-2259, 2007.

[10] B. Gomez, A. Jimenez-Suarez, E. Gordo, Oxidation and Tribological Behaviour of an Fe Based MMC Reinforced with TiCN Particles, International Journal of Refractory Metals and Hard Materials, 27 (2), 360-366, 2009.

[11] G. Straffelini, M Pellizzari, L Maines, Effect of Sliding Speed and Contact Pressure on the Oxidative Wear of Austemperred Ductile Iron, Journal of Wear, 277 (9-10), 714-719, 2011.

[12] A. Amir, O. Mamat, Effects of SiO_2 Particles in Mechanical Properties of Iron Composite, Journal of Applied Mechanics and Materials, (465-466), 886-890, 2014.

[13] H.M. Chen, A.T. Alpas, Sliding Wear Map for the Magnesium Alloy Mg-9Al-0.9Zn (AZ91), Journal of Wear, 246, 106-116, 2000.

[14] J. Williams, Wear and Wear Particles, Some Fundamentals, Journal of Tribology International, 38 (10), 863-870, 2005.

Proceedings of the 3rd International Conference on
Fracture Fatigue and Wear, pp. 320-325, 2014

FINITE ELEMENT ANALYSIS OF HYDROGEN-ASSISTED ROLLING-CONTACT FATIGUE IN BEARINGS FOR WIND TURBINES

J. Toribio, V. Kharin, M. Lorenzo and D. Vergara

Fracture of Materials and Structural Integrity Research Group, University of Salamanca, Spain

Abstract: Offshore wind parks at locations further from the shore often involve serious difficulties, e.g. the maintenance. The bearings of offshore wind turbines are prone to suffer hydrogen-assisted rolling-contact fatigue (HA-RCF). Three important aspects linked with bearing failures are being extensively researched: (i) rolling contact fatigue (RCF), (ii) influence of carbide particles on fatigue life, (iii) local microplastic strain accumulation via ratcheting. However, there is no reference related to bearing failure in harsh environment. This paper studies the influence of hydrogen on the life in service of offshore wind turbine bearings through a numerical study. So, the widely used RCF ball-on-rod test was simulated by finite element method to obtain the stress-strain state inside the bearings during their life in service life and, from this, to calculate the steady-state distribution of hydrogen concentration, thereby revealing the potential damage zones.

Keywords: hydrogen-assisted rolling-contact; fatigue; bearings

1 INTRODUCTION

Offshore wind farms reach higher levels of energy production than onshore installations. There are several reasons to this fact: (i) the wind turbine size does not have the usual onshore limitations related to road transportation or noise regulations, (ii) offshore wind speeds are considerably higher than onshore ones [1]. However, offshore wind parks present maintenance problems. The bearings of offshore wind turbines can suffer hydrogen-assisted rolling-contact fatigue (HA-RCF) due to: (i) the use of long-life lubricants with certain additives to extend the turbine maintenance intervals, thus contributing to lubricant decomposition and hydrogen generation; (ii) the increased likelihood of moisture entering the bearing; (iii) the salty environment that increases the corrosion of materials and hence the probability of hydrogen penetration.

Three important aspects linked with bearing failures are being extensively researched: (i) rolling-contact fatigue (RCF) [2-5], (ii) influence of carbide particles on fatigue life [6,7], and (iii) local micro-plastic strain accumulation via ratcheting [8-10]. However, there is no literature related with bearing failure in harsh environments. This way, this paper helps to gain a better understanding of the influence of hydrogen on the life in service of offshore wind turbine bearings through a numerical study. So, the widely used RCF ball-on-rod test [10-13] was simulated by the finite element (FE) method to obtain the stress-strain state of bearings during life in service and, from this, to elucidate the potential places where the hydrogen could be more harmful causing final catastrophic failure by hydrogen embrittlement (HE) related phenomena.

2 PROBLEM STATEMENT/NUMERICAL MODELLING

The study was divided into two uncoupled analysis. On one hand, the numerical simulation by means of a commercial FE code was used for obtaining the stress and strain states after one revolution of the bar. From the results of this analysis, a simple estimation of the hydrogen accumulation for long time of exposure to hydrogenating environment was carried out allowing the estimation of the potential hydrogen damage places. The geometry analysed consist of a steel bar of length L= 6 mm and diameter d = 9.53 mm which rotates in contact with three equidistant steel balls of diameter D = 12.70 mm which apply a point load of F = 300 N over the bar surface as reflects the scheme of Fig. 1a. The complete 3D geometry can be simplified to a half just considering the symmetry plane r-θ shown in Fig. 1b and applying the corresponding boundary conditions as restricted displacement on the bar axial direction for all the nodes placed inside the symmetry plane. Thus, an important saving of computing time is achieved optimizing the available resources. In addition, the geometry of the contacting balls can be also simplified considering the symmetry plane r-z of such components. Taking this into account, only a quarter of the whole geometry of the ball is modelled, as can be seen Fig. 1b.

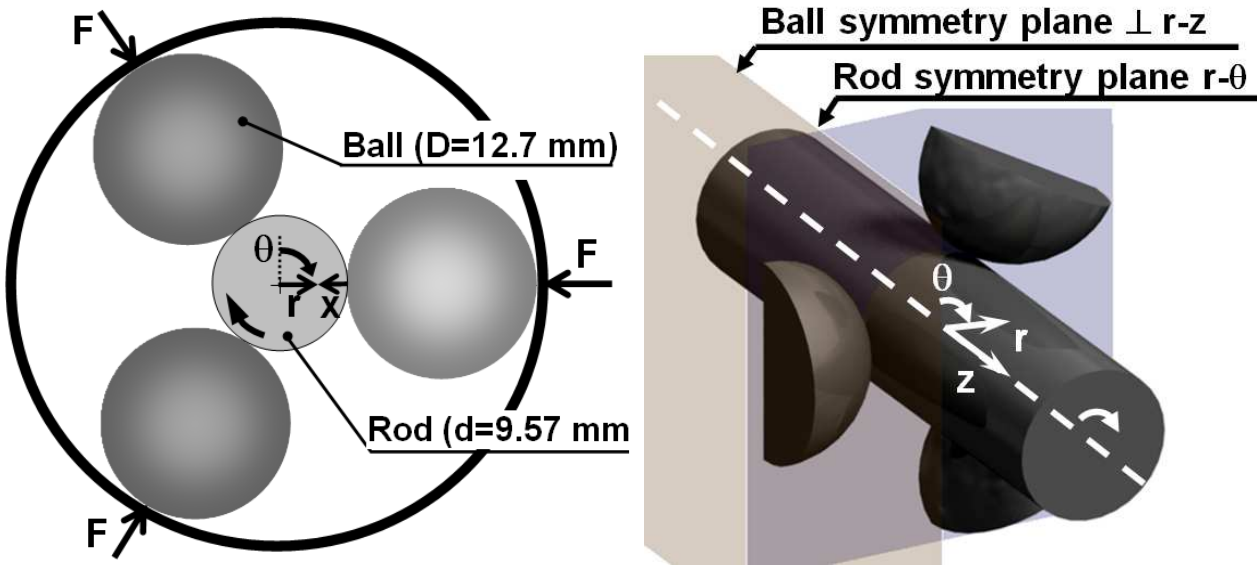

(a) (b)

Fig. 1 (a) Scheme of analysed geometry for a ball on rod test and (b) 3D geometry

The numerical modelling of the ball-on-rod test (only one revolution to save computing resources) was carried out considering the material constitutive law to be elastic perfectly plastic corresponding to a steel with the following material properties for both rod and balls: Young modulus, E = 206 GPa, Poisson coefficient, ν= 0.3 and material yield stress σ_Y = 2065 MPa. The analysis was carried out considering the isotropic strain hardening of the material and updated Lagrange procedure. According to the Hertz theory considering only the elastic response of the components [14], a very localized effect can be expected in the contact zone between rod and balls. According to this, a ball pressuring a cylinder must undergo a contact pressure of 5.5 GPa with an elliptic contacting zone whose axis length are 160 μm and 231 μm respectively.

From results of the mechanical simulation, a simple estimation of the behaviour against HE of the bar can be carried out considering that hydrogen diffusion proceeds from the bar surface to inner points as a function of the gradients of both hydrostatic stress (σ) and hydrogen solubility ($K_{S\varepsilon}$) [15-17]:

$$\mathbf{J} = -D(\varepsilon_P)\left\{\nabla C - C\left[\frac{V_H}{RT}\nabla\sigma + \frac{\nabla K_{S\varepsilon}(\varepsilon_P)}{K_{S\varepsilon}(\varepsilon_P)}\right]\right\} \quad (1)$$

R being the universal gases constant, V_H the partial volume of hydrogen, T the absolute temperature and $K_{S\varepsilon}$ the hydrogen solubility that is itself a one-to-one monotonic increasing function of equivalent plastic strain, as explained in detail elsewhere [15-17]. In particular, a linear relationship between plastic strain and solubility in the form $K_{S\varepsilon} = 1+4\varepsilon_p$ was considered to be adequate, cf. [15-17].

After using the matter conservation law and applying the Gauss-Ostrogradsky, the following second-order partial differential equation of hydrogen diffusion is obtained:

$$\frac{\partial C}{\partial t} = \nabla\cdot\left[D\nabla C - DC\left(\frac{V_H}{RT}\nabla\sigma + \frac{\nabla K_{S\varepsilon}(\varepsilon_P)}{K_{S\varepsilon}(\varepsilon_P)}\right)\right] \quad (2)$$

The equilibrium concentration of hydrogen for infinite time of exposure to harsh environment is the steady-state solution of the differential equation. It takes the form of a Maxwell-Boltzman distribution as follows:

$$C_{eq} = C_0 K_{S\varepsilon}(\varepsilon_P)\exp\left[\frac{V_H}{RT}\nabla\sigma\right] \quad (3)$$

where C_0 is the equilibrium hydrogen concentration for the material free of stress and strain. According to previous equations, hydrogen diffusion is driven by: (i) the negative gradient of hydrogen concentration (in the classical Fick´s sense); (ii) the positive gradient of hydrostatic stress; (iii) the positive gradient of hydrogen solubility, the latter is one-to-one related to the gradient of equivalent plastic strain so that the

plastic strain gradient (a continuum mechanics variable that appears as an output after the FE computation) can be analysed instead of the hydrogen solubility gradient.

3 MECHANICAL ANALYSIS: STRESS AND STRAIN

Numerical simulation allows the determination of the stress and strain state under cycling loading during the ball-on-rod test. Fig. 2a shows the global view of the distribution of von Mises stress in the steel rod and the contacting balls at the end of the first cycle, thereby after passing three contacting balls and Fig. 2b shows a detail view of the von Mises distribution at the contact of one of the balls.

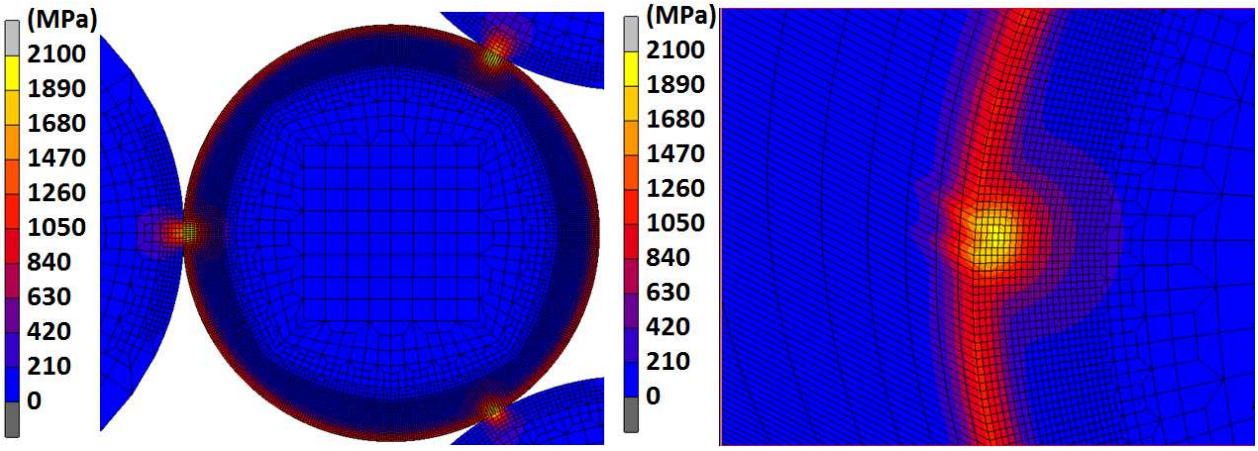

(a) (b)

Fig. 2 Distribution of von Mises stress after the first loading cycle: (a) 2D view of the contacting plane and (b) 3D detail view at the contact of one of the balls

Results shown in Fig. 2 reveal a heavy stress concentration localized at the contacting zones of each ball with the rolling rod. This effect progressively vanishes as the distance from the contact zone increases. Outside of the locally affected zone, the von Mises stress is homogenously distributed with a heavy stress concentration ring located in the vicinity of the rod surface. Within the stress concentration zone, the values of the von Mises stress reach the material yield stress what implies the appearance of plastic strains near the rod skin, as discussed in further sections. For a more detailed analysis, the radial distribution of Von Misses stress for different values of the circunferential coordinate θ are represented in Fig. 3 considering the following sections: (i) θ = 45º, (ii) θ = 20º, (iii) θ = 10º, two planes placed close to the contacting ball (iv) θ = 5º, (v) θ = 2º and finaly (vi) θ = 0º representing the contact plane between one of the balls and the rod.

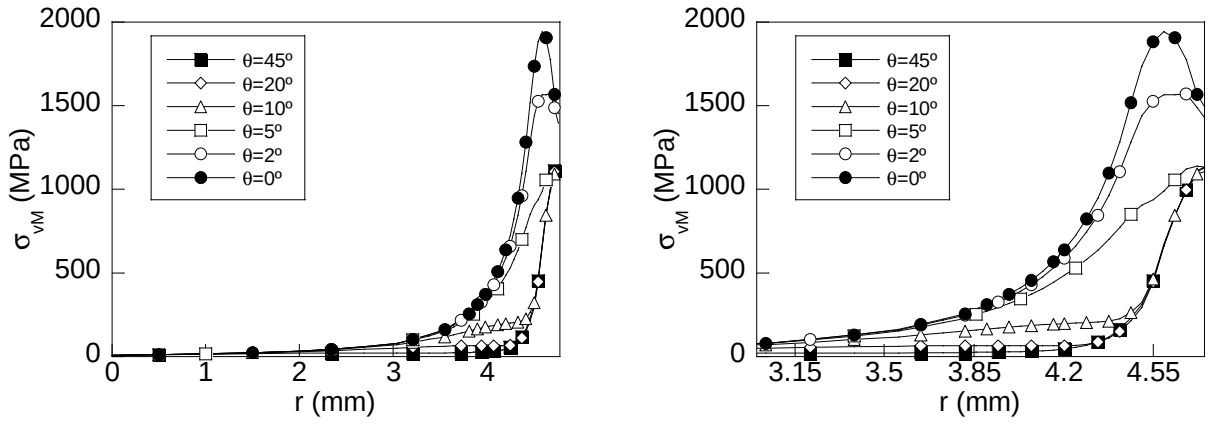

(a) (b)

Fig. 3 Radial distribution of von Misses stress for diverse circumferential coordinate θ: (a) general plot and (b) detail plot near the rod surface (zone with strong gradients)

The radial stress distribution reveals the localized effect at the contact zone with the balls which is spread through a depth from the rod surface about 1.5 mm, reaching null values at the rod centre. At the contact

radius ($\theta = 0^o$) the maximum stress is placed out of the rod surface for an approximate depth of 165 μm reaching there the material yield stress and, therefore, generating plastic strains at the surroundings of this place. The distributions for the other points in contact with the remaining balls ($\theta = 120^o$ and $\theta = 240^o$) is equivalent to that shown in Fig. 3.

As a consequence of the values of the von Mises stress in the rod surface vicinity, plastic strains are distributed through such a zone. Fig. 4 shows the 3D view of the field of equivalent (cumulative) plastic strain after the first cycle of the test was completed and the radial distribution of such a variable is plotted in Fig. 5. In the same way, Fig. 6 shows the 3D view of the field of hydrostatic stress after the first cycle of the test was completed and Fig. 7 shows the radial distribution of such a variable for diverse values of θ.

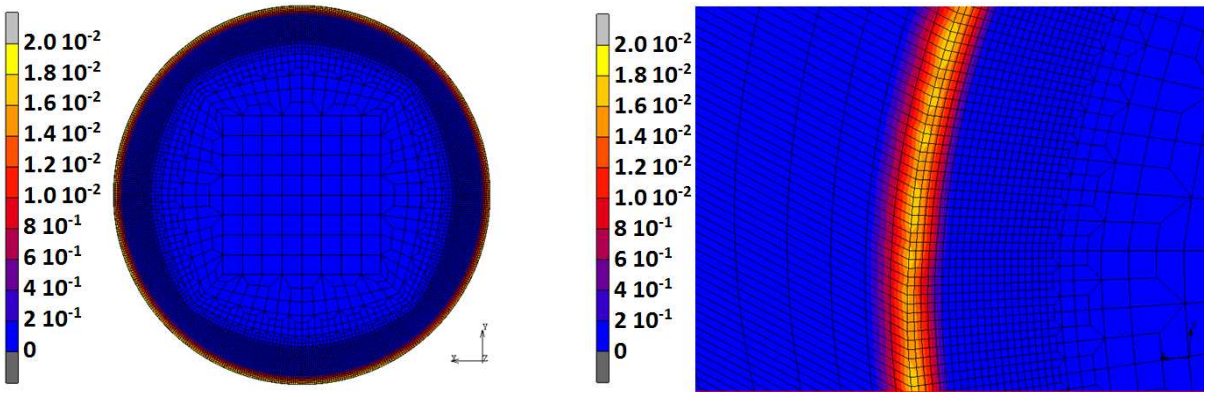

Fig. 4 Field of equivalent (cumulative) plastic strain on the cylinder after one cycle of the ball on rod test

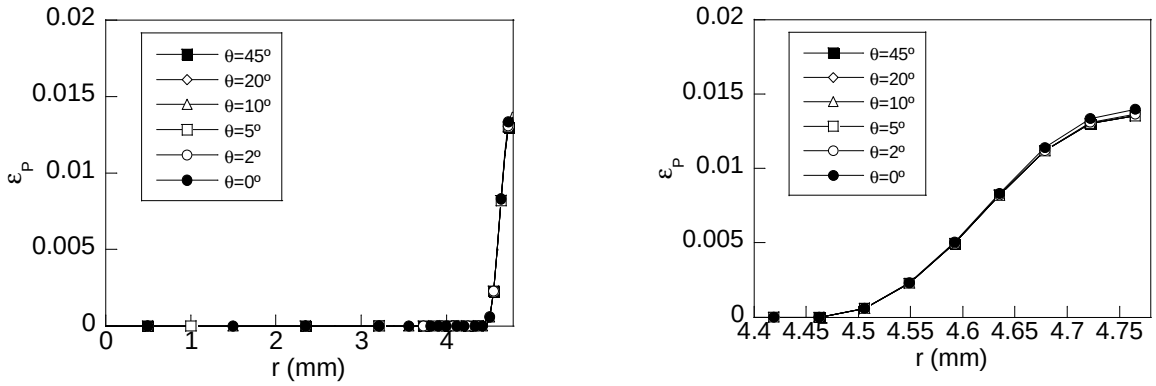

Fig. 5 Radial distribution of equivalent plastic strain for diverse circumferential coordinate θ: (a) general plot and (b) detail plot near the rod surface (zone with strong gradients)

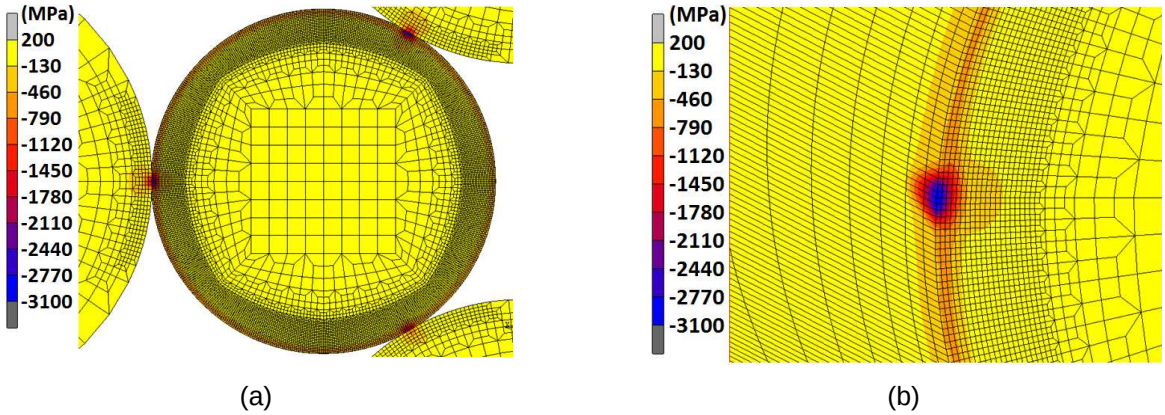

Fig. 6 Distribution of the hydrostatic stress after the first loading cycle: (a) 2D view of the contacting plane and (b) 3D view

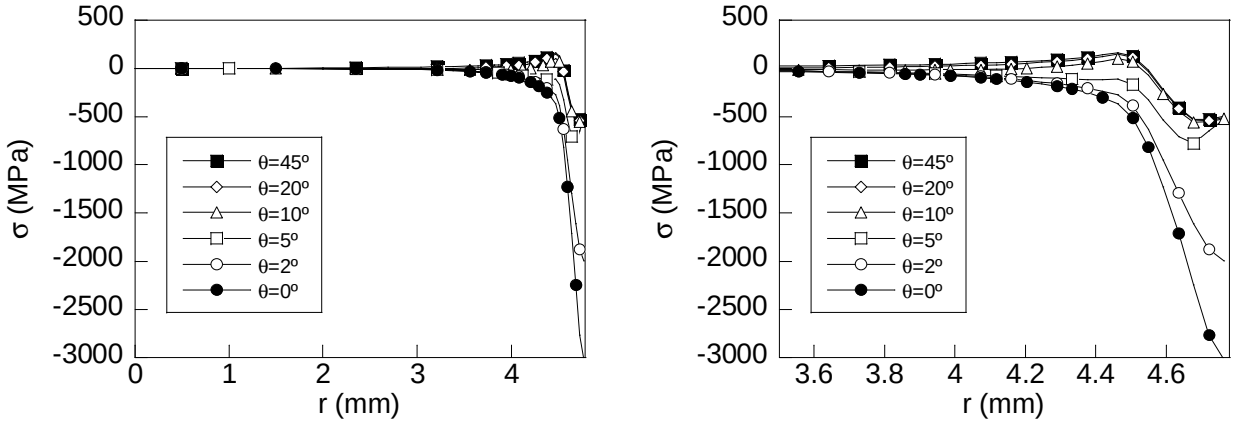

Fig. 7 Radial distribution of the hydrostatic stress for diverse circumferential coordinate θ: (a) general plot and (b) detail plot near the rod surface (zone with strong gradients)

The first driving force for hydrogen diffusion, the gradient of equivalent plastic strain, is negative and only affects the plastic strain ring near the rod surface. With regard to the second driving force for hydrogen diffusion, the gradient of hydrostatic stress, at the contact plane (θ = 0º), a distribution of compressive nature in radial direction is obtained for such a variable, it progressively decreasing with depth up to becoming null for a depth from the rod surface of about 1 mm.

4 CHEMICAL ANALYSIS: HYDROGEN TRANSPORT BY DIFFUSION

For assessing the HE of the rolling rod, it is interesting to analyse the long-time behaviour of the component under hydrogen exposure. To this end, the steady state distribution of hydrogen concentration through the rod radius was obtained (Fig. 8) using eq. (3) and taking into account both hydrostatic stress and equivalent plastic strain. Plot is associated with infinite time (steady state solution from the mathematical point of view) or with thermodynamical equilibrium of the hydrogen-metal system (from the physical view point).

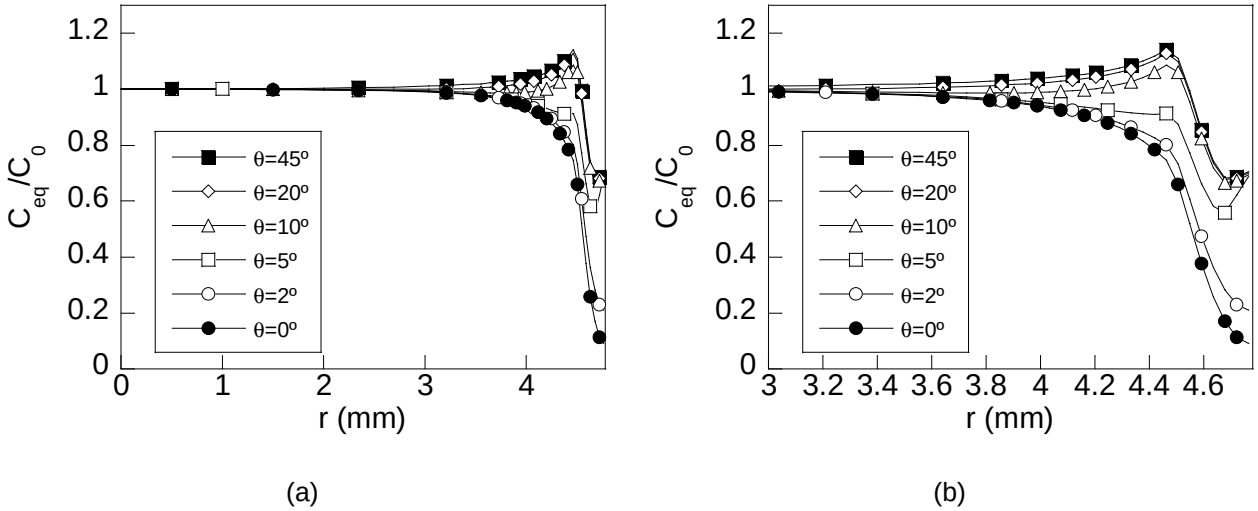

Fig. 8 Radial distribution of the hydrogen concentration for diverse circumferential coordinate θ: (a) general plot and (b) detail plot near the rod surface

According to these results, for long time of exposure to the hydrogenating environment, the hydrogen amount at the rod surface vicinity (within the stress and strain affected zone of the rod, i.e., for depths from the rod surface lower than 1 mm) is progressively increased with the circumferential distance to the contacting ball. Thus, for the plane where the ball is contacting the rod, a huge reduction of the hydrogen amount is observed due to the high compressive stresses produced by the contact pressure which promote hydrogen movement out of the contact affected zone due to the negative gradient of both driving forces for hydrogen diffusion: the inwards gradient of plastic strain and the inwards gradient of hydrostatic stress.

5 CONCLUSIONS

In a ball-on-rod test, non-uniform plastic strains are generated on the contact plane where the ball applies a huge pressure to the rod, overcoming material yield strength. This state is located near the rod surface with a plastic zone spreading over a maximum depth of 300 μm. A huge compressive stress appears in the vicinity of the rod surface; it is progressively reduced as the distance from the surface increases in radial direction. As a result, hydrogen is accumulated out of the contact plane where a huge reduction of the hydrogen amount is achieved for long times of exposure to the environment due to the high compressive hydrostatic stress in the radial direction, thereby pumping hydrogen towards points outside the contact plane. The maximum hydrogen amount appears for a depth from the surface of about 250 μm.

6 ACKNOWLEDGEMENTS

The authors acknowledge the financial support provided by the EU Project **MultiHy** (http://multihy.eu): Multiscale modelling of hydrogen embrittlement of crystalline materials (EU-FP7-NMP Project No. 263335).

7 REFERENCES

[1] Europe's onshore and offshore wind energy potential: an assessment of environmental and economic constraints. European Environment Agency, Copenhagen, 2009.

[2] A. Kumar, G. Hahn, C. Rubin, A study of subsurface crack initiation produced by rolling contact fatigue, Metallurgical Transactions A, 24, 351–359, 1993.

[3] V. Bhargava, G.T. Hahn, C.A. Rubin, Rolling contact deformation and microstructural changes in high strength bearing steel, Wear, 133, 65–71, 1989.

[4] V. Gupta, P. Bastias, G.T. Hahn, C.A. Rubin, Elasto-plastic finite-element analysis of 2-D rolling-plussliding contact with temperature-dependent bearing steel material properties, Wear, 169, 251–256, 1993.

[5] Y. Jiang, B. Su, H. Sehitoglu, Three-dimensional elastic-plastic stress analysis of rolling contact, Journal of Tribology, 124, 699–708, 2002.

[6] E. Kabo, A. Ekberg, Fatigue initiation in railway wheels—a numerical study of the influence of defects, Wear, 253, 26–34, 2002.

[7] E. Kabo, A. Ekberg, Material defects in rolling contact fatigue of railway wheels—the influence of defect size, Wear, 258, 1194–1200, 2005.

[8] R.J. Rider, S.J. Harvey, H.D. Chandler, Fatigue and ratcheting interactions, International Journal of Fatigue, 17, 507–511, 1995.

[9] C.B. Lim, K.S. Kim, J.B. Seong, Ratcheting and fatigue behaviour of a copper alloy under uniaxial cyclic loading with mean stress, International Journal of Fatigue, 31, 501–507, 2009.

[10] A.S. Pandkar, N. Arakere, G. Subhash, Microstructure-sensitive accumulation of plastic strain due to ratcheting in bearing steels subjects to rolling contact fatigue, International Journal of Fatigue, 63, 191–202, 2014.

[11] D. Glover, A ball-rod rolling contact fatigue tester, in: Rolling Contact Fatigue Testing of Bearing Steels. ASTM STP 771, , Baltimore, MD, 1982, pp. 107–124.

[12] A. Bhattacharyya, G. Subhash, N. Arakere, Evolution of subsurface plastic zone due to rolling contact fatigue of M-50 NiL case hardened bearing steel, Int J of Fatigue, 59, 102–113, 2014.

[13] N.K. Arakere, G. Subhash, Work hardening response of M50-NiL case hardened bearing steel during shakedown in rolling contact fatigue, Material Science and Technology, 28(5), 34–38, 2012.

[14] W.D., Pilkey, Formulas for Stress, Strain, and Structural Matrices, Second ed., John Wiley & Sons, Inc., Hoboken, NJ, USA, 2008.

[15] J. Toribio, M. Lorenzo, D. Vergara, V. Kharin, Hydrogen degradation of cold-drawn wires: a numerical analysis of drawing-induced residual stresses and strains, Corrosion, 67, 075001–075008, 2011.

[16] J. Toribio, V. Kharin, M. Lorenzo, D. Vergara, Role of drawing-induced residual stresses and strains in the hydrogen embrittlement susceptibility of prestressing steels, Corrosion Science, 53, 3346–3355, 2011.

[17] J. Toribio, V. Kharin, D. Vergara, M. Lorenzo, Two-dimensional numerical modelling of hydrogen diffusion in metals assisted by both stress and strain, Advanced Material Research, 138, 117–126, 2010.

Proceedings of the 3rd International Conference on
Fracture Fatigue and Wear, pp. 326-332, 2014

FEA OF STRESS SINGULARITY IN PARTIAL SLIP AND GROSS SLIDING CONDITION

T. Yue, M. Abdel Wahab and R. Hojjati-Talemi

Department of Mechanical Construction and Production, Faculty of Engineering and Architecture, Ghent University, Belgium

Abstract: Finite Element Analysis (FEA) is used widely to simulate the process of fretting wear. Usually the denser mesh size means more accurate results with less efficiency. There is a need to find the appropriate mesh size to get a balance between accuracy and efficiency. In this paper, singularity signature is used to check if stress singularity exists in cylinder on flat contact during fretting wear. It is found that a) stress singularity exits in partial slip regime and b) for gloss sliding condition, there is no stress singularity. Eventually, it is concluded that more attention should be paid to the mesh size at contact interface, when the contact condition is under partial slip regime.

Keywords: fretting wear; stress singularity; partial slip; gross sliding

1 INTRODUCTION

Fretting is a small oscillatory motion between two contact surfaces, which may cause wear or fatigue damage. Although fretting wear may happen in every contact surfaces suffered from cyclic load, researchers usually focus on stem / cement of hip joint [1], blade / disk of dovetail joint in turbine [2] and contact between strands in steel wire ropes [3]. Many parameters can affect fretting wear including normal load, applied displacement, material properties, surface roughness of the contact bodies, frequency, etc. The design of engineering components subjected to fretting wear, such as couplings and splines, jointed structures, is still a challenge to engineers. This is because of the continuous change in the contact surfaces of component during fretting wear. Therefore, a predictive technique that takes into account the wear progress during life cycle is desirable. Analytical solutions of wear problems are very difficult and limited to simple 2-D configuration steady state analysis. In contrast, numerical modelling techniques such as Finite Element Analysis (FEA) can be used for any type of structures in 3-D configuration with many complicated details such as large deformation, material non-linearity, changes in geometry and time integration effect.

When FEA of fretting contact is carried out, mesh size has significant influence on the results. Usually, the denser mesh size, the more accurate results, but the less efficiency. Researchers often refine the mesh and compare with analytical method to get accurate results with less computation time. When there is no analytical solution, the mesh could be refined to get converged results. However, if the results seem not converged with a refined mesh, is it a good idea to keep refining the mesh? In this situation, stress singularity may exist.

In flat on flat contact problems, researchers [4] have analysed the stress singularity under frictional slip in different wedge angles θ and different Coefficients Of Friction (COF). From the photo-elastic tests, both factors could influence stress singularity. Based on the contact configuration of cylinder on flat, Xu and Yuan [5] have studied stress singularity under sticking and slipping friction using FEM approach. The influence of radius of rounding pad on stress singularity has been investigated in reference [6].

Besides the basic analysis of stress singularity, researchers also have been trying to detect stress singularity from simulation results. Sinclair [7] have presented an approach to check whether or not there was a stress singularity based on the divergence of the peak stress values of different mesh sizes. Evidence of divergence requires a suitable refined sequence of discretizations. The sequence of mesh sizes recommended was h, λh, $\lambda^2 h$, where h is the fine mesh size and λ is a factor to scale mesh size. This means that at least three analyses are required.

In this paper, stress singularity is studied after one quarter of a fretting wear cycle and after 20,000 fretting wear cycles in both partial slip and gross sliding conditions.

2 COMPUTATIONAL METHODOLOGY

2.1 Singularity signatures

In elasticity, stress singularity can be divided into two forms, namely power singularity and logarithmic singularity. According to mesh sizes, types of singularity can be checked by the following formulas [8].

For power singularity, the relation between local stress σ and the distance r from singular point can be written as:

$$\sigma = O(\sigma_0 r^{-\gamma}), \qquad as \quad r \to 0, \tag{1}$$

where σ_0 is the stress of interest (e.g. axial stress or shear stress) and γ is the singularity exponent. For numerical simulations, series of mesh sizes is defined based on the fine mesh size h and the scale factor λ as:

$$h, \lambda h, \lambda^2 h. \tag{2}$$

This sequence has been demonstrated to be effective by progression theory [9]. Employing the sequence of eq. (2) for eq. 1 yields:

$$\frac{\sigma_m}{\sigma_c} \sim \frac{\sigma_f}{\sigma_m} \sim \lambda^{\gamma} \qquad as \quad h \to 0, \tag{3}$$

where c, m, f mean coarse mesh, middle mesh and fine mesh, respectively. Therefore the singularity exponent can be calculated by:

$$\gamma_c = \frac{[\ln \sigma_m/\sigma_c]}{\ln \lambda}, \qquad \gamma_m = \frac{[\ln \sigma_f/\sigma_m]}{\ln \lambda} \tag{4}$$

The power singularity present when

$$\frac{2|\gamma_c - \gamma_m|}{\gamma_c + \gamma_m} < 0.1 \tag{5}$$

This means that a power singularity presents, when the change of singularity exponent is less than 10% of its average value. This percentage has been demonstrated to be effective in the numerical experiments of stress analysis.

For logarithmic singularity, the relation between local stress σ and the distance r from singular point is:

$$\sigma = O(\sigma_0 \ln r), \qquad as\ r \to 0. \tag{6}$$

Successive estimates of the increment in the stress are written as:

$$\Delta\sigma_c = \sigma_m - \sigma_c, \qquad \Delta\sigma_m = \sigma_f - \sigma_m. \tag{7}$$

The type of singularity can be judged as logarithmic singularity when:

$$\frac{2|\Delta\sigma_c - \Delta\sigma_m|}{|\Delta\sigma_c + \Delta\sigma_m|} < 0.1, \tag{8}$$

Which has also been validated by stress analysis.

2.2 FE model

The FEA software ABAQUS / STANDARD was used to solve the contact problem and fretting wear analysis. Two-dimensional cylinder on flat FE model was developed, dimensions of cylinder and specimen are shown in Fig. 1, where P is the normal load and S is the applied displacement. Both P and S were applied on the middle point of top of cylinder, where the multi-point constraint (MPC) was used in order to avoid rotation due to the applied normal load.

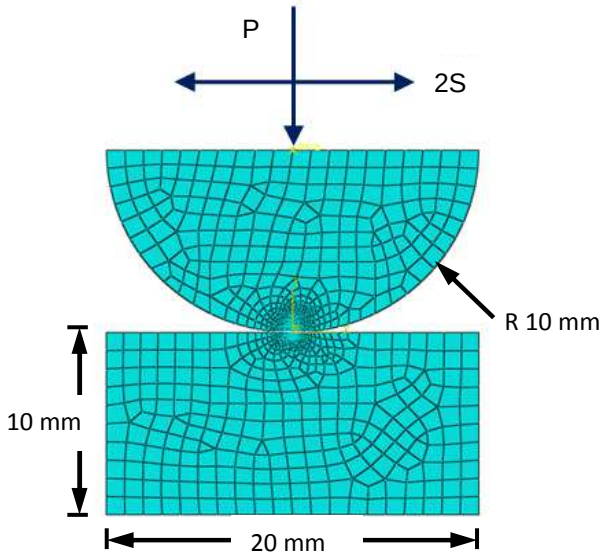

Fig. 1 Cylinder on flat FE contact model

Four-node, plane strain quadratic elements (CPE4) were used in contact zone of FE models. In order to compare the stress singularity results with the singularity signatures, three elements sizes 5 μm, 10 μm and 20 μm in the contact area were used. Ti-6Al-4V was selected as material for both pad and specimen, for which material properties are listed in Table 1 taken from reference [10]. Contact properties of contact interface are of great importance. The Coulomb friction model with isotropic friction tangential behavior was employed. Lagrange multiplier approach was chosen to impose frictional constraints, which ensure the exact sticking between closed surfaces. The interaction of contact surface was defined as surface to surface contact and finite sliding. The minimum allowable distance between the initial coordinates of adjacent nodes on the contact interface was 0.001 μm to make sure that the pad and specimen were in contact with each other. These contact parameters are similar to previous studies, such as in references [11] and [12].

To study the effect of displacement on stress singularity, 5 displacements were chosen from partial slip to grossing sliding regimes. Loading conditions are shown in Table 2.

Table 1 Material properties of FE contact models

Young's modulus [MPa]	121000
Poisson's ratio	0.29
Wear coefficient	1.12×10^{-8}

Table 2 Loading condition of FE contact models

P [N]	S [μm]
400	4, 5, 6, 7, 15

Usually, two wear models are utilized to predict wear process, namely Archard model and energy model. One of differences between them is that the influence of a variable COF is not considered in Archard equation. For this reason, energy model is more stable. Therefore in this paper, energy method was utilized as wear model.

The relationship between fretting wear volume V and dissipated energy of each cycle Ed_i is defined as [13]:

$$V = \alpha \sum_{i=1}^{N} Ed_i, \tag{9}$$

where α is the energy wear volume coefficient of the studied interface for a given sliding amplitude. N is the total number of fretting wear cycles. Considering an incremental formula, the increment of wear depth for the specimen at x position in the ith fretting cycle Δh_i is given by:

$$\Delta h_i(x) = \alpha_h E d_i(x) = \alpha_h \int_{t=0}^{T} q_i(x)\, ds_i(x), \tag{10}$$

where α_h is local energy wear coefficient, $Ed_i(x)$, $q_i(x)$, $ds_i(x)$ are the dissipated energy, tangential force and relative sliding at x position at the ith fretting cycle of period T, respectively. The updated vertical coordinate of specimen at x position in the $(i+1)th$ fretting cycle is:

$$y_{i+1}(x) = y_i(x) - \Delta h_i(x), \tag{11}$$

where $y_{i+1}(x)$ is the vertical coordinate of specimen at position x in the $(i+1)th$ increment. Repetition of these calculations for the total number of wear cycles achieves the wear simulation and the accumulated dissipated energy is updated by the relation:

$$\sum Ed_i(x) = \sum Ed_{i-1}(x) + \sum Ed_i(x) \tag{12}$$

Based on the formulas above, the process of fretting wear is predicted by UMESHMOTION subroutine [14] in conjunction with Python script.

3 RESULTS

Firstly, the variation of relative slip based on different applied displacements after one quarter of a fretting wear cycle was analysed, with the purpose of defining the slip regime. Fig. 2 indicates that partial slip occurs when the applied displacement is 4 μm, 5 μm and 6 μm. By increasing the applied displacement to 7 μm, gross sliding takes place.

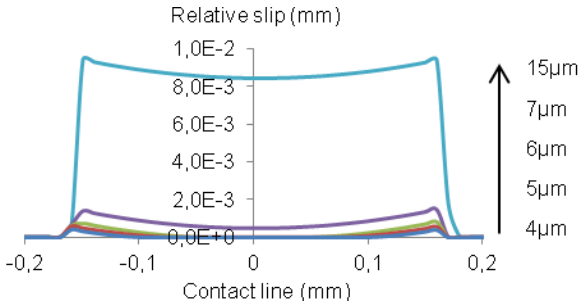

Fig. 2 The relative slip when mesh size is 10 μm

Then the $|\sigma_{xx}|_{max}$ was compared at different mesh sizes and displacements. From Fig. 3, two points might be concluded, (a) the $|\sigma_{xx}|_{max}$ is decreasing with increasing the mesh size at certain displacement, no matter the magnitude of displacements presented here and (b) the $|\sigma_{xx}|_{max}$ is higher at larger displacement if using the same mesh size in partial slip condition, while it is constant at gross sliding. This is because both shear stress and contact pressure have effect on σ_{xx}. At partial slip, shear stress distribution is changing with displacement due to the evolution of ratio between stick area and slip area. At gross sliding condition, the whole contact area is in sliding mode so that the shear stress follows Coulomb friction. At this situation, for which the applied displacement is 7 μm or 15 μm in this paper, displacement has no influence on the value of peak shear stress (Fig. 4).

Because the $|\sigma_{xx}|_{max}$ is increasing with decreasing mesh sizes, the $|\sigma_{xx}|_{max}$ at mesh size 5 μm, 10 μm and 20 μm were taken into Eq. 3 and Eq. 6 to check the type of singularity at partial slip (4 μm) and gross sliding (7 μm). From Table 3, all results are more than 0.1, therefore there is no singularity at this situation according to singularity signature.

Using energy concept as wear model, 4 μm and 15 μm were applied as displacements to simulate fretting wear in partial slip and gross sliding. The total number of fretting wear cycle was 20,000. Fig. 5 shows the difference of $|\sigma_{xx}|_{max}$ at different loading conditions. At partial slip, the $|\sigma_{xx}|_{max}$ has similar tendency to the one before worn. While for gross sliding, evolution of $|\sigma_{xx}|_{max}$ with different mesh sizes become flatten. It is because the profile changed significantly after 20,000 cycles at gross sliding condition. For peak shear stress, almost the same evolution as Fig. 4 after one quarter of a fretting cycle, is obtained as shown in Fig. 6.

The singularity signature of $|\sigma_{xx}|_{max}$ after 20,000 cycles was calculated, both power singularity and logarithmic singularity exist at partial slip, as indicated in Table 4. On the contrary, there is no singularity in gross sliding condition. From Fig. 7, it is found that fretting wear plays an important role at gross sliding. The evolution of profile changes the stress distribution markedly.

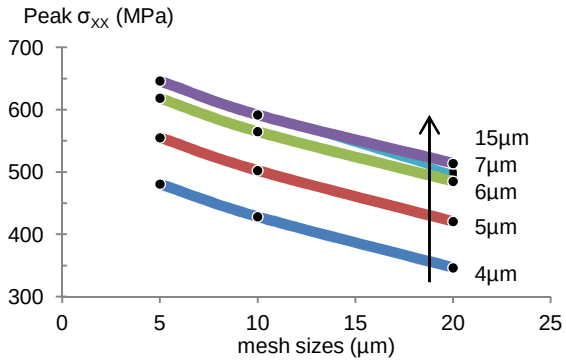

Fig. 3 The $|\sigma_{xx}|_{max}$ at different displacements with different mesh sizes

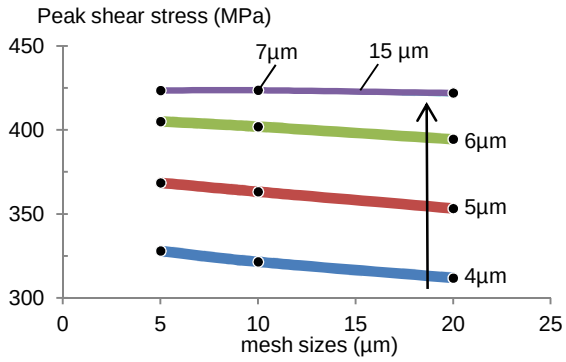

Fig. 4 The peak shear stress at different displacements with different mesh sizes

Table 3 Results of singularity signature of the peak σ_{xx}

signature	displacement	
	4 μm	7 μm
Power σ_{xx}	0.5921	0.4688
Logarithmic σ_{xx}	0.4405	0.3557

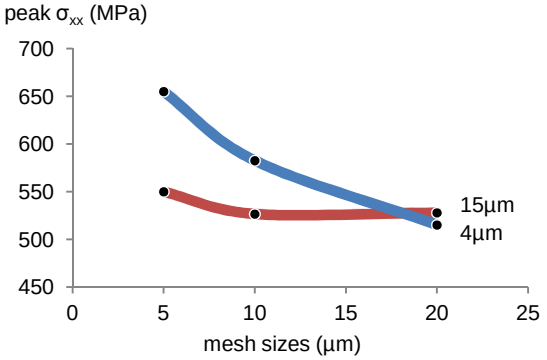

Fig. 5 The $|\sigma_{xx}|_{max}$ at different displacements with different mesh sizes

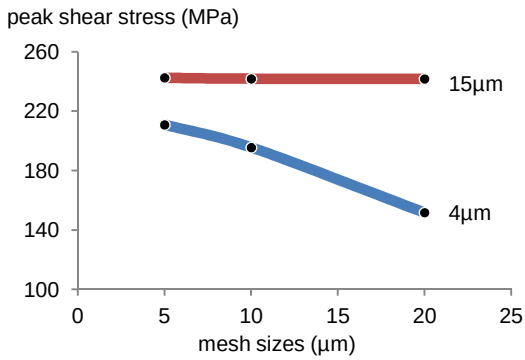

Fig. 6 The peak shear stress at different displacements with different mesh sizes after 20,000 cycles

Table 4 Results of singularity signature of the peak σ_{xx} after worn

signature	displacement	
	4 μm	15 μm
Power σ_{xx}	0.0493	2.2496
Logarithmic σ_{xx}	0.0708	2.2442

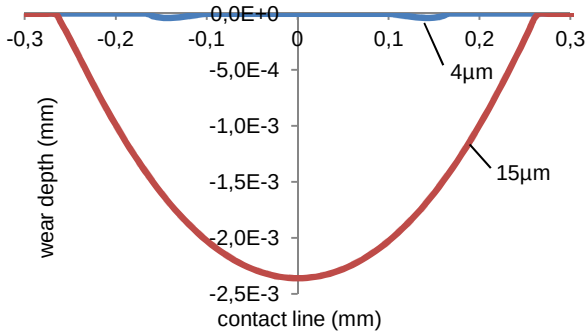

Fig. 7 Wear profiles when displacement is 4 μm and 15 μm at mesh size 5 μm

4 CONCLUSIONS

Fretting wear of cylinder on flat contact was simulated using FEA with different mesh sizes. Singularity signature was utilized to identify if stress singularity existed for different slip regimes during fretting wear. It was found that there was no stress singularity neither in partial slip nor gross sliding after one quarter of a fretting wear cycle. However, stress singularity exited in partial slip after 20,000 cycles while there was no stress singularity for gross sliding condition. Results revealed that, after 20,000 cycles, both $|\sigma_{xx}|_{max}$ and peak shear stress were roughly the same in mesh size 5 μm, 10 μm and 20μm in gross sliding, while these variables were still sensitive to the mesh sizes in partial slip. It is concluded that more attention should be paid on the mesh size for partial slip than gross sliding when simulating fretting wear.

5 ACKNOWLEDGEMENTS

The authors would like to acknowledge the support of Chinese Scholarship Council and Special Funding of Ghent University (Bijzonder Onderzoeksfonds), in the framework of BOF project BOF 01N02410.

6 REFERENCES

[1] S. Barrans, L. Blunt, H. Zhang and L. Brown, Reproduction of fretting wear at the stem-cement interface in total hip replacement, Proceedings of the Institution of Mechanical Engineers, Part H: Journal of Engineering in Medicine, 221 (8), 963-971, 2007.

[2] L. Gallego, B. Fulleringer, S. Deyber and D. Nélias, Multiscale computation of fretting wear at the blade/disk interface, Tribology International, 43 (4), 708-718, 2010.

[3] L. Xu, D. Zhang, Y. Yin, S. Wang and D. Wang, Fretting wear behaviors of hoisting rope wires in acid medium, Materials & Design, 55 (0), 50-57, 2014.

[4] M. Comninou, Stress singularity at a sharp edge in contact problems with friction, Zeitschrift für angewandte Mathematik und Physik ZAMP, 27 (4), 493-499, 1976.

[5] Y. Xu and H. Yuan, Computational analysis and characterization of fretting stress fields, Computational Materials Science, 45 (3), 674-679, 2009.

[6] H. Yuan and Y. Xu, Fracture mechanics assessment of stress concentrations in incomplete fretting contacts, Engineering Fracture Mechanics, 76 (15), 2344-2358, 2009.

[7] G. B. Sinclair, Stress singularities in classical elasticity–I: Removal, interpretation, and analysis, Applied Mechanics Reviews, 57 (4), 251-297, 2004.

[8] G. Sinclair, J. Beisheim and S. Sezer, Practical convergence-divergence checks for stresses from FEA, Proceedings of the 2006 international ANSYS conference. 2006.

[9] G. B. Sinclair, X. Chi and T. I. P. Shih, On the pressure and stress singularities induced by steady flows of incompressible viscous fluids, Acta Mechanica Sinica, 25 (4), 451-462, 2009.

[10] C. Paulin, S. Fouvry and S. Deyber, Wear kinetics of Ti–6Al–4V under constant and variable fretting sliding conditions, Wear, 259 (1–6), 292-299, 2005.

[11] I. R. McColl, J. Ding and S. B. Leen, Finite element simulation and experimental validation of fretting wear, Wear, 256 (11-12), 1114-1127, 2004.

[12] T. Zhang, P. E. McHugh and S. B. Leen, Computational study on the effect of contact geometry on fretting behaviour, Wear, 271 (9-10), 1462-1480, 2011.

[13] E. Sauger, S. Fouvry, L. Ponsonnet, P. Kapsa, J. Martin and L. Vincent, Tribologically transformed structure in fretting, Wear, 245 (1), 39-52, 2000.

[14] ABAQUS, 6.11. User's manual, Inc. and Dassault systemes, 2011.

Proceedings of the 3rd International Conference on
Fracture Fatigue and Wear, pp. 333-339, 2014

EXPERIMENTAL STUDY ON THRESHOLD BEHAVIOR OF INTERGRANULAR STRESS CORROSION CRACKING OF 316L STAINLESS STEEL BY USING FRETTING FATIGUE

Tomoya Kishino[1], Yuichi Otsuka[2], Yukio Miyashita[2] and Yoshiharu Mutoh[2]

[1]Graduate School of Engineering, Nagaoka University of Technology, Japan
[2]Nagaoka University of Technology, Japan

Abstract: The threshold behaviours of small intergranular stress corrosion cracking (IGSCC) in austenitic stainless steels used in boiling water reactor (BWR) environment is necessary in order to evaluate the integrity of aged components. Since conventional crack initiation test methods have some disadvantages such as long experimental time, effect of large scale yielding, and difficulty in determination of fracture mechanics parameters, a new intergranular crack initiation method by using fretting fatigue is developed in this study. Specimens made by 316L stainless steel were subjected to (a) solution-annealing and (b) 20% tensile prestrained in order to investigate the effect of strain on the crack initiation behaviour. After the fretting fatigue tests, cracks on the surface of specimens were observed by a scanning electron microscope (SEM). In the cases of the solution-annealed specimens, IGSCCs were observed. On the other hands, no crack was initiated on the prestrained specimens due to relatively high yield strength of the material. The number of cracks tended to increase as the number of fatigue cycles increased. Crack length distribution statistically corresponded with Gumbel distribution. Crack growth rates were much higher compared with those in the reference curve, especially at lower cycles. The crack growth rates decreased with increasing the number of fatigue cycles. Though fretting fatigue method contains concerns such as multiaxial stress field at contact area and large scale plastic deformation, it is suitable for the accelerated crack initiation test.

Keywords: SCC; 316L; fretting fatigue; BWR; small crack

1 INTRODUCTION

Stress corrosion cracking (SCC) of austenitic stainless steels is a serious problem for aged reactors. SCC is a typical fracture mode influenced by three factors of mechanical loading, environmental condition and material used. In the boiling water reactor (BWR) environment, stainless steels are subject to a severe environmental condition from the pressurized high temperature water at the pressure of 7.3 MPa and the temperature of 288℃. Moreover, the thermal stress during service, the residual stress from machining process, and the heat affected zone (HAZ) due to welding as mechanical loading factors determine SCC behaviour of stainless steels. As the material factor, the sensitization of stainless steels due to welding and hardening of surface of low carbon stainless steels due to machining are considered.

Since the processes of initiation and propagation of small SCC cracks occupy more than half period of the SCC life, it is necessary to investigate the behaviour of the small cracks in order to evaluate the integrity of reactor structural materials. Unfortunately, the conventional fracture mechanics methods such as using compact tension specimen are applicable only for long cracks. In some previous works, constant strain test [1], constant load test, small strain rate test (SSRT) and small punch test [2] were conducted to evaluate the crack initiation and small crack behaviour. However, these testing methods have some disadvantages such as long experimental time, effect of large scale yielding, and difficulty in determination of fracture mechanics parameters.

In the previous works [3, 4], fretting fatigue test method was proposed as a method to accelerate the crack initiation. Due to the interaction between the high contact stress and crevice corrosion, fretting fatigue test could initiate small cracks in relatively short time. Seangsai *et al.* studied small crack behaviour of sensitized 304 stainless steel. They have successfully applied fretting fatigue test to accelerate crack initiation and to investigate the small crack behaviour of sensitized 304 stainless steel [3,4]. However, it has not been clarified whether or not the fretting fatigue method is applicable for low carbon stainless steels which mainly used in BWR environment. Thus, it is the objective of this study to confirm the applicability of fretting fatigue test for 316L stainless steel.

Table 1 Chemical composition (wt%) of 316L stainless steel

C	Si	Mn	P	S	Ni	Cr	Mo
0.0023	0.70	0.97	0.030	0.003	12.10	17.47	2.03

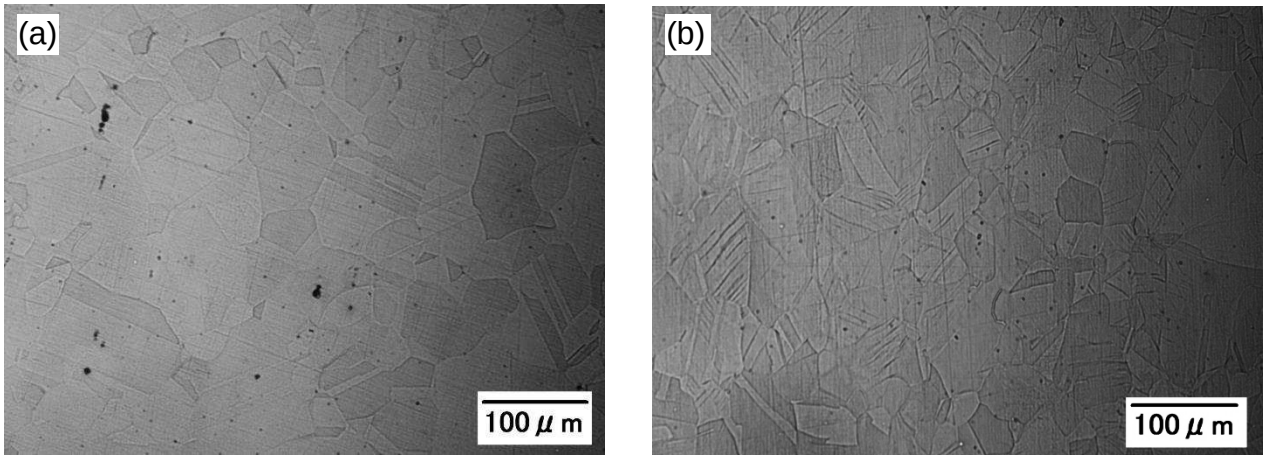

Fig. 1 Microstructures of 316L stainless steels (a) Solution annealing and (b) 20% prestrained

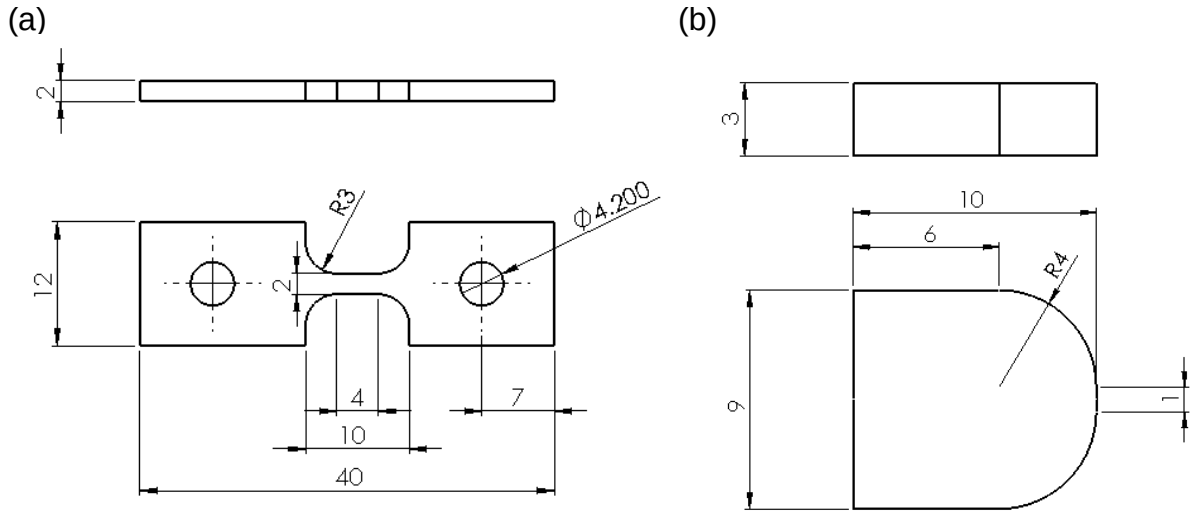

Fig. 2 Dimensions of (a) specimen and (b) contact pad (units in mm)

2 EXPERIMENTAL PROCEDURES

2.1 Material and Specimen preparations

The chemical composition of 316L stainless steel used in this study is shown in Table 1. Since work hardening affects on SCC initiation and crack growth behaviour of low carbon stainless steels in BWR environment [5,6], two types of specimens, (a) solution annealed specimen and (b) 20% prestrained specimen after solution annealing, were used. Prestrained samples simulate the hardening due to the effects of heat affected zone (HAZ) of welding, machining or irradiation. These microstructures are shown in Fig.1. Average grain size of solution-annealed specimen is 68μm. Prestrained grains consist of slip bands. The hardness of solution annealed and prestrained specimens were HV124 and HV230, respectively. The geometries of the specimen and the contact pad are shown in Fig.2. Solution annealed specimens were solution annealed after machining. On the other hand, In case of 20% prestrained specimens, first the material was solution annealed, then induced 20% strain by tensile load, manufactured at last. Prepared specimens were grinded and polished with grade 240, 600, 1000, 1500, 2000, 4000 of emery paper and 6,3,1 μm of diamond particles. Contact pads were grained in one direction along principal stress by using grade 1500 emery paper. Contact pads were not conducted any treatments. A specimen

was assembled with two contact pads by using a proving ring. Contact pressure was adjusted by tying bolts which are mounted on the ring sides.

2.2 Fretting fatigue test condition

Fretting fatigue test was conducted at the following condition: σ_{max}=177 MPa, stress ratio R = 0.9, frequency f=20 Hz, number of loading cycle N=10^3,10^4,10^5,10^6 cycles, respectively. The fretting fatigue tests were conducted in pressurized high temperature water at 288℃ under a pressure of 7.3 MPa. Dissolved oxygen (DO) was controlled at 2 ppm by bubbling nitrogen gas periodically.

2.3 Crack observation

After finishing the fretting fatigue test, the surfaces of specimens were observed by using scanning electron microscope (SEM). Observation areas were limited only within contact region and maximum principal stress region which is located 200 μm around the contact region. Stress intensity factors of the cracks were calculated by using Newman-Raju equation [7] in equation (1) based on the assumption that average crack shape had an aspect ratio of 1.

$$K_I = \sigma\sqrt{\frac{\pi a}{Q}}F \tag{1}$$

Where

$$\mathrm{Q} = 1 + 1.464\left(\frac{a}{c}\right)^{1.65}$$

$$\mathrm{F} = \left[1.13 - 0.09\left(\frac{a}{c}\right) + \left(-0.54 + \frac{0.89}{0.2+{}^{a}/_{c}}\right)\left(\frac{a}{t}\right)^2 + \left\{0.5 - \frac{1.0}{0.65+{}^{a}/_{c}} + 14\left(1.0 - \frac{a}{c}\right)^{24}\right\}\left(\frac{a}{t}\right)^4\right]\left[sec\left(\frac{\pi c}{2W}\sqrt{\frac{a}{t}}\right)\right]^{1/2}$$

3 RESULTS AND DISCUSSIONS

3.1 Crack morphology and distribution

The surface conditions of each sample are shown in Fig. 3. Crack morphology was intergranular one which initiates along with the pass of grain boundary in all testing conditions for solution-annealed specimen. Cracks located mainly within the maximum principal stress region. Detail of the cracks observed is shown in Table 2. These values include only the cracks initiated in maximum principal stress region. In case of solution annealing, number of cracks increases as the number of fatigue cycles increased. Moreover, the average crack length almost unchanged with increasing the number of fatigue cycles. On the other hands, no crack was initiated on the prestrained specimens. The yield strength of solution annealed 316L stainless steel seems to be around 200MPa at the testing temperature [8]. Furthermore, the yield strength of prestrained 316L stainless steels became much higher compared with the one in solution annealed specimen. Since the principal stress at the maximum principal stress region calculated from FEM is about 232 MPa, crack initiation seems be affected by yield strength. The fretting tests at higher principal stress level for prestrained 316L are required in order to confirm this hypothesis.

The distribution of initiated crack length by constant strain test in BWR environment was accordance with some statistical distribution [9,10]. The crack distributions of solution annealed specimens obtained from fretting fatigue test were also summarized in Gumbel distribution, as shown in Fig.4. Figure 4 demonstrated that crack length initiated by fretting fatigue also corresponds with the same statistical distribution. Although the data points of 10^4 and 10^5 cycles are low, the result of 10^6 cycles clearly shows two stage kinked curve. These stages seem to mean intergranular corrosion stage and stress corrosion cracking stage [9]. Since crack distributions are concentrated in intergranular corrosion stage at low cycle and in stress corrosion cracking stage at high cycle, the cracks have been initiated mainly due to corrosion and then grew up to a certain length as the results of the stress corrosion cracking.

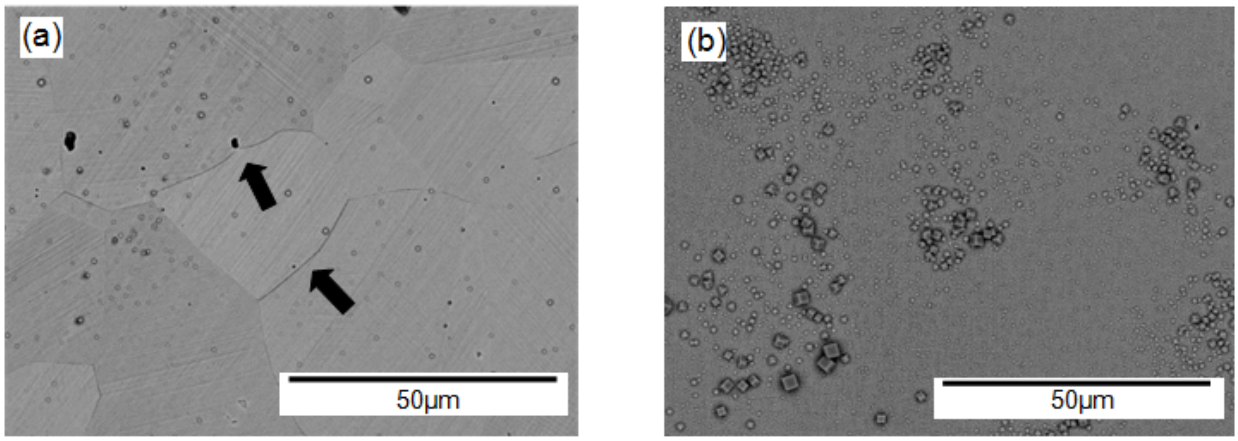

Fig. 3 Surface condition of specimens after fretting fatigue test (10^6cycle), (a) Solution-anealed specimen which contains IGSCCs and (b) 20% prestrained specimen has no cracks

Table 2 The results of fretting fatigue test on 316L stainless steel in pressurized high temperature water

Material type	Number of cycle	Number of crack	Average length [μm]	Maximum length [μm]
Solution annealing	10^3	0	-	-
	10^4	8	23	53
	10^5	10	27	90
	10^6	72	29	75
Solution annealing + 20%strain	10^3	0	-	-
	10^4	0	-	-
	10^5	0	-	-
	10^6	0	-	-

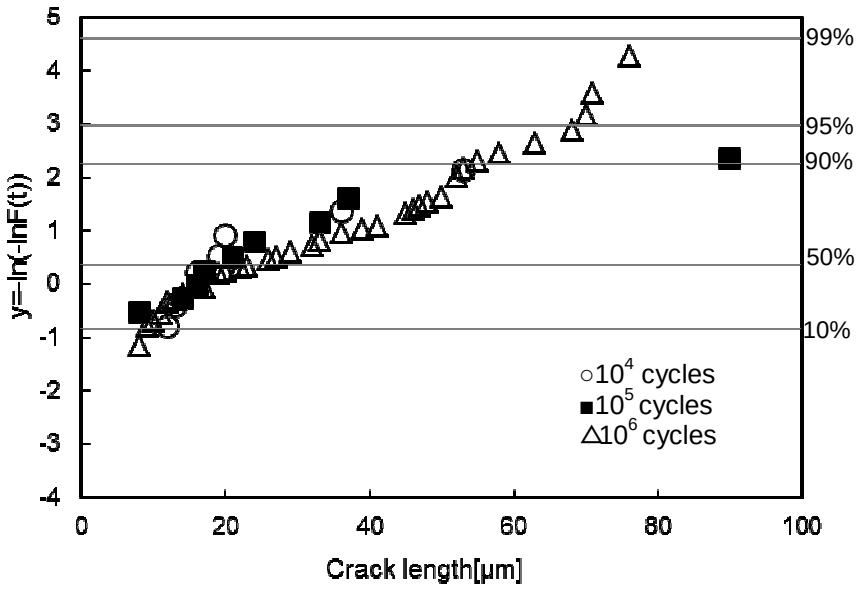

Fig. 4 Gumbel distibution observed on solution annealed 316L stainless steels after fretting fatigue test

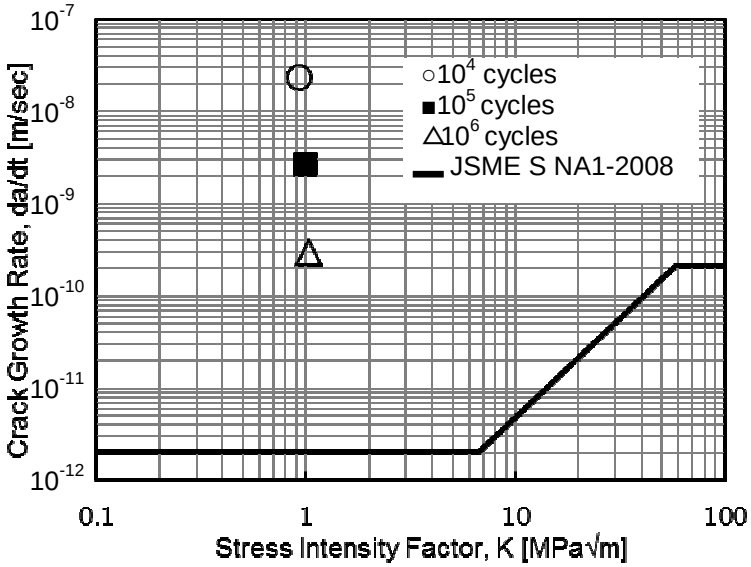

Fig. 5 The Relationship between crack growth rate and stress intensity factor at 10^4,10^5,10^6 cycle

3.2 Crack growth rate

The relationship between crack growth rate and stress intensity factor of each cycles is shown in Fig.5. Stress intensity factors of all conditions at crack bottom are calculated as aspect ratio of 1 and principal stress of 232MPa. Crack growth rates were extremely high comparing to the reference curve which is defined by JSME S NA1-2008 throughout all period. The acceleration of crack growth rate is caused by the contiguous destruction of passive and oxide film and crevice corrosion due to the existence of contact pad. The crack growth rates decreased with increasing the number of fatigue cycles. Three factors, mechanical factor, material factor and environmental factor can be the cause of the phenomena. The propagation of cracks was affected by the decrease of crack driving force due to the decrease of principal stress near crack tips or the increase of crack extension resistance at grain boundary. Moreover long time exposure made the oxide film at crack tip thicker, which can protect metal matrix at crack tip from corrosion.

3.3 Validity of fretting fatigue as the accelerated crack initiation method

Process of SCC initiation is defined as 6 stages, i.e. (1) incubation stage, (2) pitting corrosion incubation stage, (3) pitting corrosion growth stage, (4) small crack initiation stage, (5) small crack growth stage and (6) small cracks incorporation stage [11]. From above results, fretting fatigue method skips around from stage (1) to (5) because contiguous destruction of passive oxide film due to wear by contact pad exposes stainless steel substrate to corrosive environment. Then the proposed method can shorten the testing time until crack initiation. The validity of fretting fatigue is now discussed as an accelerating crack initiation method. Especially multiaxial stress field at contact area and large scale plastic deformation are concerned. At contact area, the surface is affected by shear stress due to contact pressure. However, to limit the evaluation area within 200 μm area from contact region makes it possible to consider the stress direction as only principal stress direction. Moreover, plastic deformation area is limited at the near surface and then exhibits nonlinear cyclic deformation curve, which has little effects in calculations in stress intensity factors. On the other hand, the effect of corrosion is enhanced by crevice by contact pad. The crevice corrosion test which simulates the contact region is necessary in order to convert a corrosion rate in crevice by contact pad to the one in normal SCC test. The conversion of corrosion rate makes it possible for the fretting fatigue test to simulate the corrosion conditions in normal SCC test. Consequently, the above discussions supports that the fretting fatigue test method are valid for the accelerated crack initiation test. Post constant load test after fretting test, which can be set in the same maximum stress intensity factors at the finished time of fretting fatigue test, is necessary to consider whether the IGSCC retains. Microstructure observations on oxide film at the tip of IGSCCs are also required in order to consider whether the microstructure of oxide film, which is a determination factor of corrosion resistance at crack tip, can be similar as the one made in normal SCC test.

4 CONCLUSIONS

In this study, IGSCC was successfully initiated in shorter time by using fretting fatigue. The effects of the testing condition on the crack behaviour are concluded as the follows:

(1) IGSCC was initiated only on the surface of solution annealed 316L. No cracks were found on the prestrained 316L stainless steel at the condition. A relative stress level comparing to the value of material's yield strength probably affects to these crack initiation behaviours.

(2) The crack distribution obtained from the fretting fatigue tests corresponds with a distribution as well those reported by another method of constant strain test.

(3) The crack growth rate obtained from the fretting fatigue test was much higher comparing to the reference curve because of the contiguous destruction of passive and oxide film and crevice corrosion due to the existence of contact pad. At lower cycle, the crack growth rate was higher than the crack growth rate of at high cycle. Decreases in the values of resolved shearing stress at grain boundary and thicker oxide film on the surface of crack tip can be the determination factors of threshold values of IGSCC.

(4) Though fretting fatigue method contains concerns such as multiaxial stress field at contact area and large scale plastic deformation, it is valid for the accelerated crack initiation test.

5 NOMENCLATURE

σ: principal stress [MPa]

a : depth of surface crack

c : half-length of crack

t : specimen thickness

W : half-length of specimen width

6 REFERENCES

[1] Isselin. J, Kasada. R, Kimura. A, Work Hardening, Sensitization, and Potential Effects on the Susceptibility to Crack Initiation of 316L Stainless Steel in BWR Environment, Journal of NUCLEAR SCIENCE and TECHNOLOGY, Vol. 48, Issue. No. 12, p1462-1470(2011)

[2] Isselin. J, Kai. A, Sakaguchi K, Shoji. T,Assessment of the Effects of Cold Work on Crack Initiation in a Light Water Environment Using the Small-Punch Test, Metallurgical and Materials Transactions A: Physical Metallurgy and Materials Science, 39 A (5), 1099-1108,2008.

[3] Saengsai. A, Otsuka. Y, Mutoh. Y, Fretting fatigue behaviour of SUS304 stainless steel under pressurized hot water, Tribology International,Volume 79, 2014, Pages 52–58

[4] Saengsai. A, Otsuka. Y, Mutoh. Y, Failure Behaviour of Sensitized SUS304 Stainless Steel with Small Surface Pre-Crack under Constant Load Condition in Simulated BWR Environment, Journal of Solid Mechanics and Material s Engineering Vol.5(2011)No.12 Special Issue on Recent Advance in Materials and Processing[ICMM&P2011]P898-907

[5] Ishiyama. N, Mayuzumi. M, Mizutani. Y and Tani. J, The Effect of Cold Rolling and Treatment on the Stress Corrosion Cracking of SUS316L and SUS316 Stainless Steels in High Temperature Water, J. Japan Inst. Metals, Vol.69, No. 12(2005), pp.1049-1052

[6] Lu. Z, Shoji. T, Takeda. Y, Ito. Y, Yamazaki. S, The dependency of the crack growth rate on the loading pattern and temperature in stress corrosion cracking of strain-hardened 316L stainless steels in a simulated BWR environment, Corrosion Science 50 (2008), 698-712

[7] Newman. J.C. and Raju. I.S., Stress Intensity Factor Equations for Cracks in Three-Dimentional Finite Bodies Subjected to Tension and Bending Loads, NASA Technical Memor andum 85793,NASA Langley Research Center, Hampton, VA, April 1984.

[8] Kato. K, Miyahara. Y, Hide. K and Mayuzumi. M, Effect of Temperature and Strain Rate on Dynamic Strain Aging in Heat-Affected-Zone of Type 316L Stainless Steel, J. Japan Inst. Metals, Vol. 72, No. 3 (2008), pp. 206-210

[9] Kamaya. M, Chiba, G. Nakajima. N, Totsuka. N, Multiple Cracks Initiation and Propagation Behaviour of Stainless Steel in High Temperature Water Environment,Zairyo-to-Kankyo, 50, 57-64,2001

[10] Onaka. K, Mayuzumi. M, Mizutani. Y,and Tani. J, Stress Corrosion Cracking Susceptivity of Solution Annealed Type 316 and Type 316L Stainless Steels with Different Hot Working Directions in High Temperature Water, J. Japan Inst.Metals, Vol.71,No.2(2007),pp.291-294

[11] Nakanisi. K, Tanaka. Y, Yoshida. K and Akashi. M, Effect of applied stress on the stress-corrosion cracking lifetime of carbon steel weld metal in high-purity water environment at 250C, Proceeding of international symposium on plant aging and life predictions of corrodible structures, pp.691-698(1997) NACE International.

Proceedings of the 3rd International Conference on
Fracture Fatigue and Wear, pp. 340-346, 2014

COMPARATIVE STUDY ON TRIBOLOGICAL PERFORMANCE OF ORTHOPEDIC PLASTER REINFORCED RESIN

R.M. Nasir [1,2]* and M.S.A.M. Sabir[1]

[1]School of Mechanical and Aerospace Engineering, Engineering Campus, Universiti Sains Malaysia(USM), 14300, Nibong Tebal, Seberang Perai Selatan, Pulau Pinang, Malaysia
[2]Cluster of Polymer Composite (CPC), Science and Engineering Research Centre (SERC), Engineering Campus, Universiti Sains Malaysia, Nibong Tebal, 14300, Malaysia
*corresponding author: ramdziah@usm.my

Abstract: The tribological properties of three different materials are investigated, industrial ceramic composite (IC), orthopedic plaster of paris (POP) and orthopedic plaster of paris hardened with resin (POPR.). These materials are used as a pin-on-disk(POD) cylinder sliding against a plate of steel plate AISI 316. POP was tested on dry condition while IC and POPR were ran in deionised distilled water. IC has a lowest volume loss amongst the three, followed by POP material and POPR. The average torque per volume loss of POPR material lies between 0.142 to 0.333 (N.m/mm^3) followed by IC lies between 0.143 to 0.250(N.m/mm^3) and POP material lies between 0.167 to 0.333 (N.m/mm^3). Average COF for POP was recorded as the highest, followed by IC and POPR (lubricant water condition). Reduction of the interfacial temperature and the formation of a hydroxide layer due to hydrophilicity property of ceramics during tribo-surface contact has a positive effect on wear resistance.The hardness value was recorded,with IC being the hardest, followed by POPR and POP. The worn abraded surface was observed using SEM for its wear mechanisms.

Keywords: orthopedic plaster of paris; orthopedic plaster with resin; wear; friction; hardness

1 INTRODUCTION

Over the years, high temperature chemical inert ceramic composites have been used due to its high melting point, simple refractory and excellent mechanical properties. Advances in furnaces and heat engines technology, modern high voltages electrically insulating ceramic, new specifications magnetic and optical ceramics, aircraft, aerospace and medical applications, cutting tools, advanced photonics, ultraconductivity and in nuclear reactors has given an impetus to the success of the ceramic industrial revolution. Ceramics pairing has an excellent potential in tribological performance and mechanical properties of the system [1]. In the ceramic-steel sliding pairs, strong surface interactions occurred [2]. When metal slides against metal, oxides and hydroxides often induced deformation and degradation. Further sliding requires shearing of the metallic interface, which increases the coefficient of friction and temperature [3]. Typically, in tribological contacts between ceramics and metals, the metal adheres to the ceramic surface upon sliding creating metal-metal interface [4]. Typical abrasion tests are shown in Fig.1.

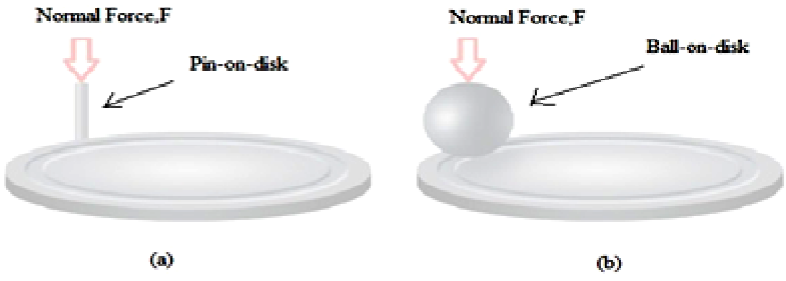

Fig. 1 Typical abrasion test; (a) pin-on-disc and (b) ball-on-disc

Effect of loose PMMA debris on orthopedic cement has been investigated[5-6]. In fabricating orthopedic cement, gypsum is heated to about 150°C to lost its water and produces the powder,i.e. cement:

Gypsum +heat=> cement + steam

$2CaSO_4 \cdot 2H_2O$ +heat=> $2CaSO_4 \cdot ½H_2O$ +$3H_2O$

Reaction of plaster of paris with present of water:

Plaster of Paris + water ==> Gypsum

$2CaSO_4 \cdot ½H_2O$ +$3H_2O$ ==> $2CaSO_4 \cdot 2H_2O$ + heat

At low contact pressures, abrasion wear is expected to be mild as the surfaces were polished at low pressures giving lower coefficients of friction. In contrary, at higher contact pressures severe wear might occur. Stresses normally exceed the tensile strength and grain fracture lead to formation of wear debris hence, an increased in abrasive wear [5]. Wear was mostly influenced by the hardness of ceramic materials[7]. The volume loss of ceramic materials during the wear tests, *V,* depends inversely proportional to the hardness of ceramics, *HV* [8] as in Eq. 1.

$V \sim (HV)^{-1}$. (1)

Two bodies sliding against each other are subjected to high local stresses and pressures. This results in shear deformation, fracture of the surfaces and high concentration temperature zone. At high temperature, chemical reactions occurs on the surfaces or even melt the surfaces. These conditions are responsible for the formation of new surface compounds, i.e. tribofilms [9]. In this study, the author wants to relate the work based on fracture beget fracture: whereby in elderly, bone fracture is common, hence, is the fracture in othopedic cement could trigger fracture in bone upon failure? The focus will be studied on the cement fracture rather than in bone to simplify the phenomenon of wear failure.

The Vickers hardness test method consists of indenting the test material with a diamond indenter, in the form of a right pyramid with a square base and an angle of 136 degrees between opposite faces subjected to a load of 1 to 100 kgf. The full load is normally applied for 10 to 15 seconds. The two diagonals of the indentation left in the surface of the material after removal of the load are measured using a microscope and their average calculated. The area of the sloping surface of the indentation is calculated. The Vickers hardness is the quotient obtained by dividing the kgf load by the square mm area of indentation [10-11] as shown in Fig. 2 and Eqs. (2-3).

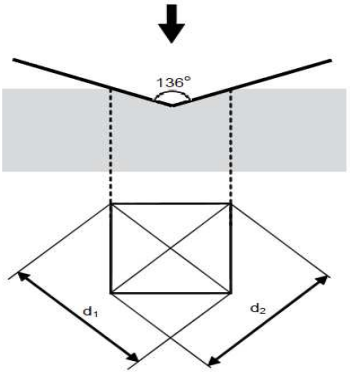

Fig. 2 Illustrated diamond intender shape on surface

$$HV = \frac{2Fsin\,(136°/2)}{d^2} \quad (2)$$

Then simplified as

$HV = 1.854 \times F/d^2$ approximately (3)

Where F=Load in kgf, *d* = Arithmetic mean of the two diagonals, d_1 and d_2 in mm, HV = Vickers hardness and HV= Vickers Hardnes

Scanning electron microscope (SEM) was used to analyzed the effect of the tribology testing on the surface of specimen. The effect of tribology testing on specimens will be analysed to obtain the behaviour and explanation of wear mechanisms. Besides that, the energy-dispersive x-ray (EDAX) was used to analyzed the element contain in the specimens. The presence of new element will be disscuss after the analysis.

Grain size is an important factor of tribological properties of ceramic material determination. Wear resistance of ceramics decreased with the grain growth and with the transformation phase. The weakest microstructure constituent was the brittle crystal boundary phase that broke and chipped off during the wear tests[12]. Alumina ceramics AL91 with mullite phase reinforcing a glassy phase exhibited high wear resistance. Wear resistance of this material is superior comparatively to different kinds of alumina ceramics with higher Al_2O_3 contents but containing only corundum crystalline phase bonded by a glassy phase[13]. In this work, orthopedic plaster bandages was used with and without epoxy resin and was compared. Wear abrasion was carried out and mechanical properties was determined. Abraded surfaces was observed and microstructure was monitored.

2 EXPERIMENT

Three selected specimens are industrial ceramics, orthopedics plaster of paris (POP) and orthopedics plaster hardened with epoxy resin (POPR). The resin used was epoxy EP431(Fisher Co.) with density of 1.21 g/cm^3. The hardener used was Jeffamine JD-230 (Shell Com.) with density of 0.948 g/cm^3. Firstly, the bandages was dipped into the container filled with water for around 3-4 second. Then the bandages was removed from the container and quickly shape into square.The square shape form bandage was left at room temperature for 24 hours prior to usage. Then the bandages was cut into pieces with the dimensions of 8mm x 8mm x 30 mm using hand grinder as in Fig. 3 (a+b). Steps were repeated to prepare the orthopedics plaster bandages. For industrial ceramics the dimension was shown in Fig. 3 (b).

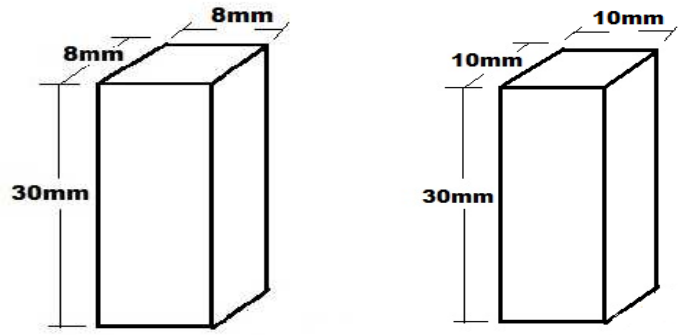

(a) (b)

Fig. 3 Dimension of (a)orthopedic specimens and (b) for industrial ceramics

For abrasion tests, the fixed specimens were tested for 30 minutes and the manipulated variables were rotation speeds (100-500 rpm) and loads (50-70 N) using Ducom TR20 with computer aided software Winducom 2010®. The weight of mass loss was measured using sensitive weighing balance Shimadzu (10^{-5}g). Specimens were dried using Metaserve drying machine before weighing. The density of each specimen was obtained from density test machine (Micrometric Acccupye 1330). Finally, the morphological surfaces (randomly selected specimens were coated with gold /palladium target using Mini Sputter Coater (SC7620) machine) was observed and EDAX was analysed using SEM Hitachi S3400N.

3 RESULTS AND DISCUSSION

The hardness measurements of control samples were measured using Vickers hardness tester and the density results were presented in Table 1 while of each material was recorded in Table 2.

Table 1 Hardness test on different material.

Material	Load	1st	2nd	3rd	Average	Density, ρ (g/mm$^{3)}$
Industrial ceramics	HV_3	617.1	570.8	479.8	555.9	$\rho_{ceramics}$=0.00207g/mm^3
POP(pure)	HV_3	57.3	70.6	53.6	60.5	$\rho_{pop(pure)}$= 0.001005 g/mm^3
POPR(resin)	HV_3	200.4	160.5	150	170.3	$\rho_{popr(resin)}$= 0.001102g/mm^3

During examining the worn surfaces there is a typical wear mechanisms occurred. The specimen was taken randomly to observed the behaviour of tribology effect of ceramic against the metal pair. The sample

of industrial ceramic and POPR was sampled at the normal load 58.86 N. Both samples show the significant result at the surfaces of material before and after test.

From Fig.4(a) ,the volume loss is increasing rapidly for three different load at the same sliding distance which is 424.115m (300rpm) and then slightly drop at distance 565.487m (400rpm) and 706.858m. (500rpm). On changing the speed from 300rpm to 500rpm under water lubricated condition, the industrial ceramic specimen experience the sliding phenomenon due to high speed. This is similar to stream drifting phenomenon in tyres and asphalt condition. At high speed rotation it gives less gripping between specimen surface to the steel plate, hence the volume lost is lowered. In Fig. 4(b) show that the lost of volume of P.O.P does not have the same behaviour as previous material. It is increasing linearly and decreased after reach the 282.743 m sliding distance (200rpm). In contrasting Fig. 4(c) it shows that the volume lost of POPR increase linearly and decreased after reach the 424.115m sliding distance (300rpm). Again at 68.87N, the specimen experiences high volume loss. Based on the material hardness in Table 1, POPR can hardly withstand the normal force exerted on it.

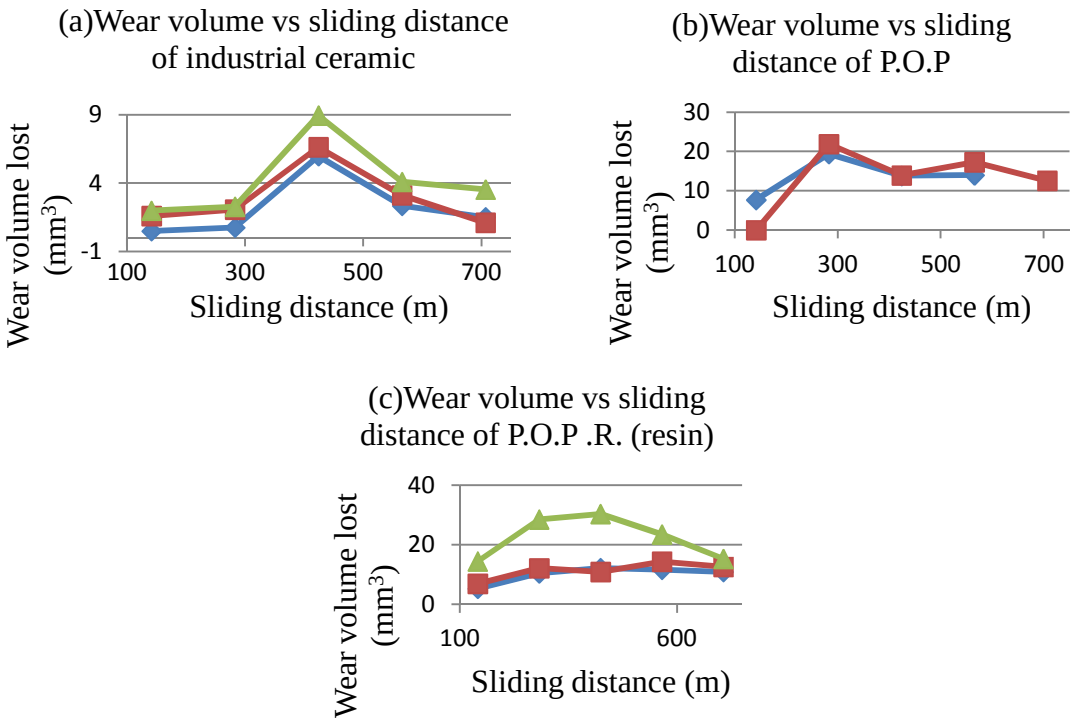

Fig. 4 Graph of wear volume against sliding distance for (a)industrial ceramic (b) P.O.P. and (c) P.O.P.R. at load 49.05N (blue), 58.86N (red) and 68.87 N (green) respectively

P.O.P material show the high average of the coefficient of friction (COF) as we can see in Fig. 5(a) ,follow by industrial ceramic and P.O.P.R. This is due to industrial ceramics material is hardest followed by P.O.P hardened by resin and P.O.P . This harder materials is expected to give the strongest interaction between the specimen and steel plate. But, in the presence of water in this tribological test result the different behaviour of coefficient of friction (COF) acting slightly different. In dry condition, (P.O.P material) shows the strongest inetraction between the surface, hence it shows higher COF compared to those two.

The frictional behaviour of ceramic-metal couples depended on a metallic layer transferred from the steel plate to the ceramic pin. A relation was determined between surface hardness and friction of ceramic-metal pairs. It was shown that the affinity for the transfer of the metal towards ceramic surfaces depended on the physical properties of the materials. The industrial ceramic COF show increases at the highers load (68.67N) except for the ceramic which is sliding at 300rpm. Next , the coefficient of friction of material P.O.P.R. as in Fig. 5(b), does not show the significant different when increasing the load for different speed. But at speed 200 rpm and 400 rpm the value of COF is deviate from the average value of COF for P.O.P.R. material. The value of COF for P.O.P as in Fig. 5(c) shows increse linearly when the load is increasing.

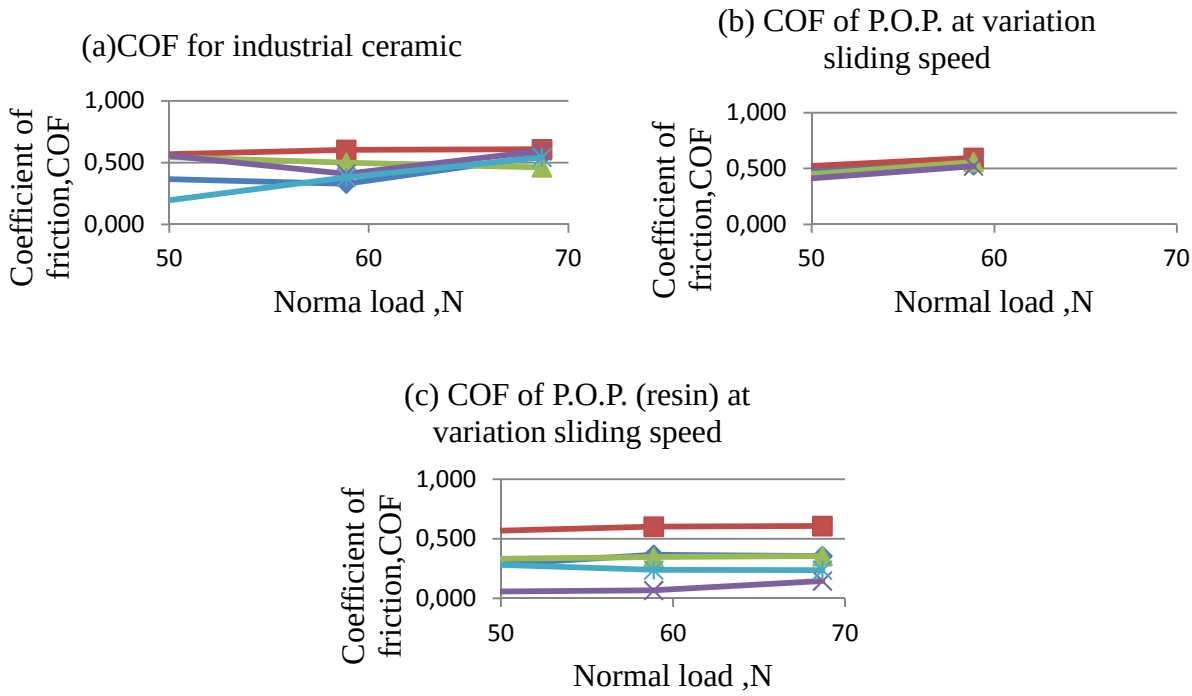

Fig. 5 Graph of coefficient of friction of (a) industrial ceramic and (b) P.O.P and (c) P.O.P R., against normal load at variation of sliding speed.

The common feature of almost all ceramic-metal interactions is that the metal adheres to the ceramic to form a transfer film. The formation of a transfer film is the result of two factors which is strong adhesion between clean ceramic and metal surfaces and the lower plastic flow stress of most metals compared to ceramics as shown in Fig. 6 (a)industrial ceramics and (b)P.O.P. respectively. Adhesion and friction between metal and ceramic surfaces strongly depend on the ductility of the metals .Soft metallic counterfaces such as brass and bronze usually generate thicker transfer films while steel and cast iron transfer films are fragmentaric [14].

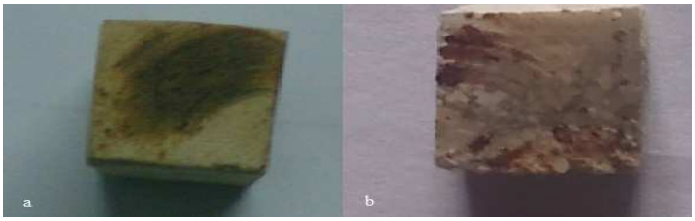

Fig. 6 (a) Industrial ceramic after the tribology test at speed 200 rpm and loaded by 58.86 N and (b) P.O.P after the tribology test at speed 200 rpm and loaded by 58.86 N.

For metal-ceramic interaction during abrasion test usually resulted in adhesion wear of metal to ceramic toform a transfer film. From the scanning electron microscopic test and Energy-dispersive X-ray (EDAX) shows the elements such as aluminum (Al) and nobidium (Nb) existed as in Fig. 7 (a) before and (b) after abrasion tests respectively. This two element was found in the composition of steel plate that use to counterface the specimens during the tribology testing. From the ceramic –metal pair sliding ,it is found that wear and friction of metals against ceramics strongly depends on the chemical reactivity of the metal [13]. Mechanism of wear was dominated by pitting, crevis wear and stress induced corrosive wear due to its brittleness and hydrophilicity. The SEM and EDAX analysis on P.O.P.R also shows (in Fig. 8 (a) before and (b) after abrasion tests, molybdenum (Mo) was found.

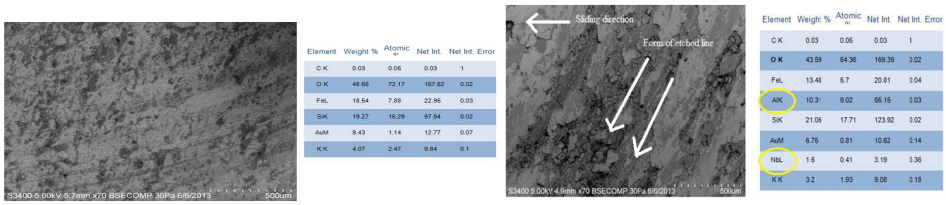

(a) (b)

Fig. 7 SEM and Edax analysis at the wear line at the surface of industrial ceramic (a) before and (b) after the tribology test

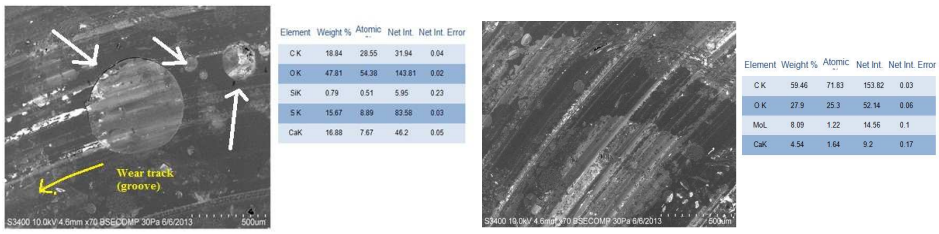

(a) (b)

Fig. 8 SEM and Edax analysis at the wear line at the surface of P.O.P.R.(a) before and (b) after abrasion tests

4 CONCLUSIONS

Amongst the ceramic selected , industrial ceramic properties have a lowest specific wear rate which lies between 2.2061x10^{-7} to 3 06 x10^{-6}(mm^3/N.m) ,followed by P.O.P material specific wear rate lies between 1.0135x10^{-6} to 1.463x10^{-3} (mm^3/N.m) and P.O.P.R. lies between 1.2775x10^{-7} to 1.396x10^{-3} (mm^3/N.m). Besides that,the value of hardness of the material was recorded for industrial ceramic is at 555.9HV, followed by P.O.P.R. at 170.3 HV and 60.5 HV for P.O.P. The experiment show that the hardness of material indeed give the effect to the specific wear rate and coefficient of friction (COF) . The P.O.P specimen which underwent the dry condition during the tribological testing recorded highest COF reading which lies between 0.400-0.598, followed by industrial ceramic specimen (lubricant water condition) between 0.602-0.175 and P.O.P.R. between 0.057-0.421. From the observation of SEM and EDAX analysis ,the transfer film phenomenon was observed. The strong contact between surface of specimen and steel plate resulting the transfer of material between the surfaces. Main wear mechanism observed were pitting, crevice corrosion and stress corrosion cracking (SCC).

5 ACKNOWLEDGEMENT

The authors gratefully acknowledge the Universiti Sains Malaysia for the Short Term Grant numbers as 304/PMEKANIK/60311052.

6 REFERENCES

[1] H. P. Kirchner and R. M Gruver, The Elevated Temperature Flexural Strength and Impact Resistance of Alumina Ceramics Strengthened by Quenching, 13, 63–69, 1974
[2] P.Andersson,. Water-lubricated pin-on-disc tests with ceramics.,Wear,01/1992, 154, 37–47,1992
[3] D.H. Buckley and K. Miyoshi, Friction and Wear of Ceramics, Wear, 100, 333–353, 1984
[4] He, Y. J., Winnubst, A. J. A., Schipper, D. J., Bakker, P. M. V., Burggraaf, A. J., & H.Verweij, Friction and wear behaviour of ceramic-hardened steel couples under reciprocating sliding motion. Wear, 184(1), 33–43, 1995
[5] F. Zivic, M. Babic, N. Grujovic, S. Mitrovic, D. Adamovic, Influence of loose PMMA bone cement particles on the corrosion assisted wear of the orthopedic AISI 316LVM stainless steel during reciprocating sliding, Wear, Vol. 300, Issues 1–2, , 65-77, 2013
[6] A. Bistolfi, G. Massazza, E. Vern´e, A. Mass`e, D. Deledda, S. Ferraris, M. Miola, F. Galetto, and M. Crova, *Review Article:*Antibiotic-Loaded Cement in Orthopedic Surgery: A Review, International Scholarly Research Network, ISRN Orthopedics, Volume 2011, Article ID 290851, 8 pages, 2011
[7] P. Švec, A. Brusilová, J. Kozánková, Effect of Microstructure and Mechanical Properties on Wear Resistance of Silicon Nitride Ceramics, Materials Engineering, Vol. 16, No. 1, 2008
[8] T.Macke, J. M.Quenisset, D.Neuilly, J. P Rocher, and R.Naslain, A comparative study of the impact behavior of ceramic matrix composites. Composites Science and Technology, 37(1-3), 267–278,1990.

[9] V. Aronow and T. Mesyet, Wear in ceramic/ceramic and ceramic/metal reciprocating sliding contact. Part 1, JTribol., 108 16 21, 1986
[10] Strues Company, Hardness Testing and Specimen Preparation Application Notes, 1–12, 2010
[11] H.Kim and T.Kim, Measurement of hardness on traditional ceramics. Journal of the European Ceramic Society, 22(9-10), 1437–1445, 2002
[12] V. E Schmidt, J. H Somerset and R. E. Porter, Mechanical properties of orthopedic plaster bandages. Journal of biomechanics, 6(2), 173–85, 1973
[13] E.Medvedovski, Alumina–mullite ceramics for structural applications. Ceramics International, 32(4), 369–375, 2006
[14] W.Gwidon and A. W. B. Stachowiak, Engineering tribology, Amsterdam: Elsevier Butterworth-Heinemann 2005